J Dawidyk

S A U P E C - 9 1

17 - 18 JANUARY 1991

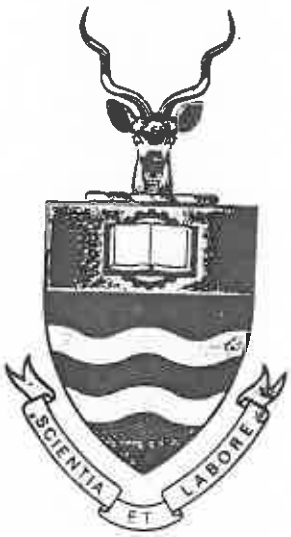

JOHANNESBURG

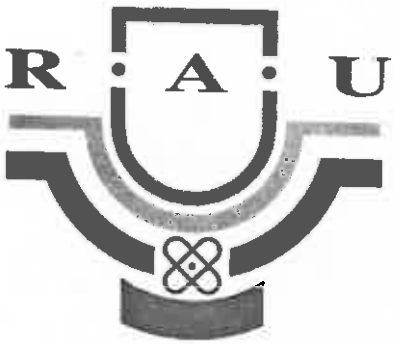

University of the Witwatersrand

Randse Afrikaanse Universiteit

17 - 18 JANUARIE 1991

S A U K I K - 9 1

1991 - ORGANISING COMMITTEE / ORGANISERENDE KOMITEE

J.A. Ferreira

M.F.K. Holm

I.R. Jandrell

J.P. Reynders ✓

J.J. Schoeman

J.D. van Wyk ✓

SAUPEC - 91 - PROGRAMME

THURSDAY, JANUARY 17, 1991

08:00	Registration	
08:40	Opening remarks Prof. J.P. Reynders	
08:45	Opening address: Prof. J.H.R. Enslin	The new IEEE Energy Chapter and the SAIEE
09:00 - 11:00	Session 1 Chair: A.C. Britten	Distribution and Transmission
11:00 - 11:30	Refreshments	
11:30 - 12:50	Session 2 Chair: I.D. Braude	Drives applications
12:50 - 14:00	Lunch	
14:00 - 15:20	Session 3 Chair: P.V. Goosen	Power quality improvement
15:20 - 15:50	Refreshments	
15:50 - 17:20	Workshop 1 Chair: J.P. Reynders	HV Technology
19:00 - 22:00	Conference Banquet	

FRIDAY, JANUARY 18, 1991

08:30 - 10:30	Session 4 Chair: R. Becker	Induction machines
10:30 - 11:00	Refreshments	
11:00 - 13:00	Session 5 Chair: S. Boshoff	Power Electronics
13:00 - 14:00	Lunch	
14:00 - 15:20	Session 6 Chair: G.R. Cardwell	Synchronous machines
15:20 - 15:50	Refreshments	
15:50 - 17:00	Workshop 2 Chair: J.A. Ferreira	Computer applications in Power
17:00 - 17:10	Closing remarks Prof. R.G. Harley	

POSTER SESSIONS

All posters will be up for discussion near the refreshment area for the duration of the Conference from 09:00, January 17 to 17:10, January 18, 1991.
Chair: Poster session: I.R. Jandrell.

SAUKIK - 91 - PROGRAM

DONDERDAG, 17 JANUARIE 1991

08:00	Registrasie	
08:40	Opening Prof. J.P. Reynders	
08:45	Openingsrede: Prof. J.H.R. Enslin	"The new IEEE Energy Chapter and the SAIEE"
09:00 - 11:00	Sessie 1 Voorsitter: A.C. Britten	Distribusie en Transmissie
11:00 - 11:30	Verversings	
11:30 - 12:50	Sessie 2 Voorsitter: I.D. Braude	Aandrywingstoepassings
12:50 - 14:00	Middagete	
14:00 - 15:20	Sessie 3 Voorsitter: P.V. Goosen	Verbetering van energievoorsieningskwaliteit
15:20 - 15:50	Verversings	
15:50 - 17:20	Werkswinkel 1 Voorsitter: J.P. Reynders	Hoogspanningstegnologie
19:00 - 22:00	Konferensiedinee	

VRYDAG, 18 JANUARIE1991

08:30 - 10:30	Sessie 4 Voorsitter: R. Becker	Induksiemasjiene
10:30 - 11:00	Verversings	
11:00 - 13:00	Sessie 5 Voorsitter: S. Boshoff	Drywingselektronika
13:00 - 14:00	Middagete	
14:00 - 15:20	Sessie 6 Voorsitter: G.R. Cardwell	Sinchrone masjiene
15:20 - 15:50	Verversings	
15:50 - 17:00	Werkswinkel 2 Voorsitter: J.A. Ferreira	Rekenaartoepassings in elektriese energietegniek
17:00 - 17:10	Afsluiting Prof. R.G. Harley	

PLAKKAATSESSIES

Alle plakkate sal vertoon word naby die gebied waar verversings bedien word vir die duur van die Konferensie vanaf 09:00, 17 Januarie tot 17:10, 18 Januarie 1991.
Voorsitter: Plakkaatsessies: I.R. Jandrell.

SAUPEC 91 - INDEX / INHOUDSOPGAWE

POSTERS / PLAKKATE Chair/Voorsitter: I.R. Jandrell		
P1 J.F. Gieras, E.E. Moos, M. Wing	Calculations of cross MMF of armature winding for permanent magnet DC motors	273-279
P2 G.M.J. Parsley, C.F. Landy	An investigation into improving the commutation of a D.C. machine	280-285
P3 H.T.W. Tromp, P.H. Swart, H.M. von Bergmann	Bipolar pulsing circuits for high power high rep rate lasers	286-290
P4 E.P. Wilke, P.C. Theron, J.D. van Wyk, J.A. Ferreira, J.J. Schoeman	'n Gestandaardiseerde hekstuurbaan vir die bipolêre isoleerhektransistor (BIHT)	291-297
P6 C.H. van As	Reluktansiemeter om Tou- spannings te bepaal	298-305

INVESTIGATION INTO VOLTAGE REGULATION IN FOUR CORE RESIDENTIAL FEEDERS

R Herman

INTRODUCTION

Unbalanced phase currents flow when single phase domestic loads are connected to a three phase system. Domestic loads are stochastic by nature. Load estimation for the purpose of calculating voltage drops has to take this into consideration. The derivation of the after diversity maximum demands for domestic consumers has been the subject of much controversy in the past. A variety of formulations have been postulated. The greatest difficulty is found in applying these estimated loads to voltage drop calculations. Generally, empirical correction factors have been used to compensate for the imbalances that might occur. The nature of the neutral current under these conditions is generally misunderstood. A complex analysis of voltage regulation is given by Davis [1]. Notwithstanding the complexity of this analysis, ceratin assumptions had to be made. Monitoring equipment for the simultaneous sampling of load currents was not available at that time.

CALCULATION OF VOLTAGE DROPS IN 4-CORE CABLES

The power factor of domestic loads is very nearly unity. This is because the largest components of the loads are heating elements. We can therefore safely assume that consumer load current and consumer voltage are in phase. It is further acceptable to assume that the low voltage cable feeding the particular group of consumers is purely resistive. The cable lengths are generally short and at 50 Hz the reactance is negligible.

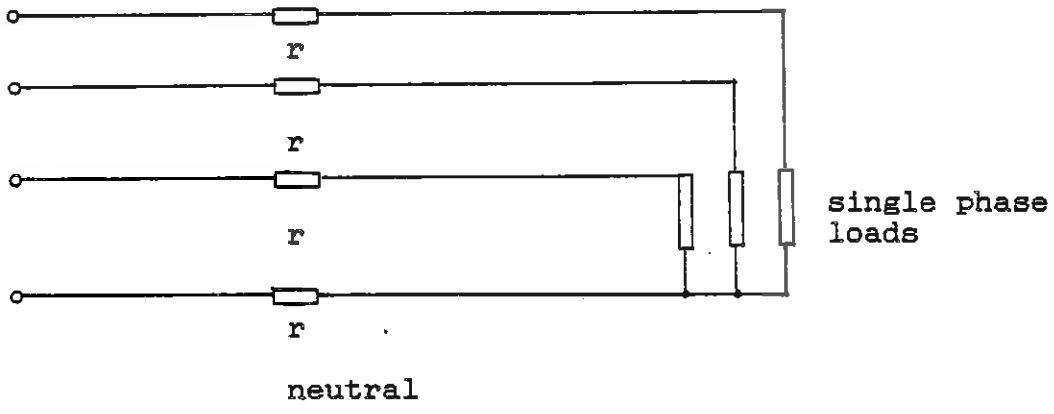

FIG 1 4-CORE CABLE FEEDING SINGLE PHASE LOADS

Assume that there are three single phase loads connected to the red, yellow and blue phases. Let the currents be I_R, I_Y, I_B and I_N respectively. Then the neutral phasor current is given by:

$$I_N = I_R + I_Y + I_B \quad \ldots\ldots\ldots\ldots\ldots\ldots\ldots\ldots\ldots\ldots\ldots\ldots (1)$$

Since the voltages are symmetrical and the power factors are unity (1) can be written

$$I_N = I_R + \lambda I_Y + \lambda^2 I_B \quad \ldots\ldots\ldots\ldots\ldots\ldots\ldots\ldots\ldots (2)$$

Where $\lambda = 1\angle 120^\circ$ and $\lambda^2 = 1\angle 240^\circ$ and I_R, I_Y and I_B are the magnitudes only.

Let V_r, V_y and V_b be the consumer phase-to-neutral voltages. Then the sending end voltage equations are:

$$V_R = rI_R + r[I_R + \lambda I_Y + \lambda^2 I_B] + V_r$$

Applying this to each phase we get the set of equations for the voltage regulation in each phase as:

$$\begin{aligned} V_R - V_r &= r[2I_R + \lambda I_Y + \lambda^2 I_B] \\ V_Y - V_y &= r[I_R + 2\lambda I_Y + \lambda^2 I_B] \\ V_B - V_b &= r[I_R + \lambda I_Y + 2\lambda^2 I_B] \quad \ldots\ldots\ldots\ldots\ldots\ldots (3) \end{aligned}$$

The equations (3) are valid for steady state deterministic loads. The load currents encountered in residential distribution systems vary stochastically as various appliances are switched on and off. The resultant neutral currents (from equation (1) will also undergo many changes in magnitude and phase angle.

SIMULATED BEHAVIOUR

To illustrate the behaviour of the neutral current and the voltage drops under random switching conditions a simple simulation was performed. The magnitude of each load current was taken to be 10 amps, of each sending end phase voltage to be 220 volts and the conductor resistance 1 ohm. The loads were then switched on and off at random, using a random number generator. Neutral currents and voltage drops were calculated for each condition (trial) simulated.

After 10 trials the results were:

Phase	Red	Yellow	Blue
Average Amps	4,0	4,0	6,0
Av Phase Amps	4,67		
Av Neutral Amps	9,0		
Av Voltage	217,2	217,2	212,1
Max Volt Drop	7,9		

After 22 sets of trials the results were:

Phase	Red	Yellow	Blue
Average Amps	5,0	5,0	4.55
Av Phase Amps	4,85		
Av Neutral Amps	8,64		
Av Voltage	214,9	214,9	216,0
Max Volt Drop	5,1		

It can therefore be seen that if the average volt drop is calculated from the average phase current, the result for the two cases is 4,67 and 4,85 volts respectively. The ratio of the maximum to average volt drop for the two cases is 1,7 and 1,05 respectively. Clearly, the ratio tends to unity as the number of trials increases. However, the magnitude of the neutral current does not change very much with increase in trials (9,0 to 8,64). The reason for this is that the phase angle of the neutral current undergoes radical changes.

This leads to the following important observation: Measurement of the mean neutral current over a period during which these variations take place have little meaning in voltage regulation calculations. It does, however, have significance with respect to the current carrying capacity of the neutral conductor. After the 22 trials simulated the accumulated vector sum of the neutral currents amounted to only 10/60 amps (mean of magnitudes = 8,64).

In practical distribution design, voltage drops are generally calculated using a balanced three phase approach with correction factors. The first of these, k_1, compensates for the lack of diversity on maximum demand current. It is a function of the number of connected consumers, n. It increases in value as the number of consumers decreases.

The second factor, k_v, needs to be introduced to correct for the effect of the voltage drop in the neutral conductor, as discussed earlier.

The voltage drop can then be given as:

$$VD = k_1 k_v I_{ADMD} \times n/3 \times r \quad \ldots\ldots\ldots\ldots\ldots\ldots\ldots\ldots \quad (4)$$

Where I_{ADMD} = the average load current per consumer.

Some preliminary field tests have been carried out to investigate the extent and nature of this correction factor.

FIELD MEASUREMENTS

A data logger was developed for collecting electrical distribution load data during 1988 and 1989 [2]. The measuring points chosen for the survey are shown in figure 2.

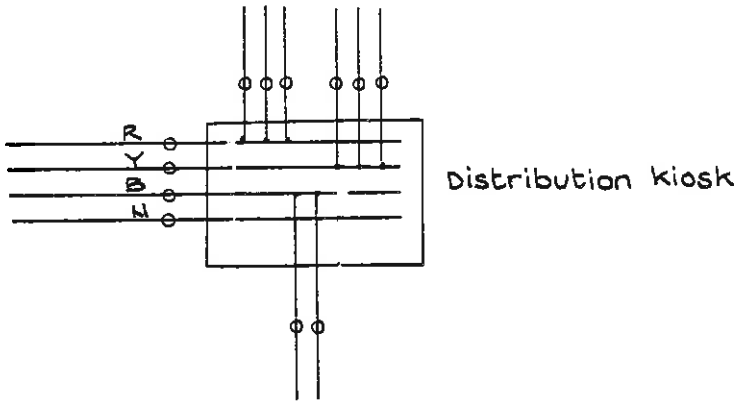

FIG 2 CONSUMER LOAD CURRENT MEASUREMENT

In this investigation steady state conditions were approximated by reducing the sampling rate to 1 minute intervals (10 minute intervals were used in the 1989 tests). A steady state condition permits the calculation of the neutral current magnitude and phase angle. Currents and phase voltages are monitored over the sampling interval and an average value for each logger channel is stored in the logger memory.

The maximum demand occurs once a year during Winter. Although the measurements described here were done during the Spring, the data could be analysed in a manner that would give information about the nature and behaviour of the correction factor, k_v.

In order to determine k_i and k_v experimentally, one must be eliminated while the effect of the other one is examined. k_i can be eliminated from the test results by normalising it , so that currents are reduced to per unit values. The measurements at different time intervals can then be compared with one another.

Load data were collected over a number of days at the rate of 900 samples per hour. These data were analysed using standard spread sheet software. From the one-minute sampled phase currents the orthogonal phasor components of the resultant neutral currents were calculated. The currents were normalised with the average phase current for each sample interval. The phasor voltage diagram for a phase is shown in figure 3.

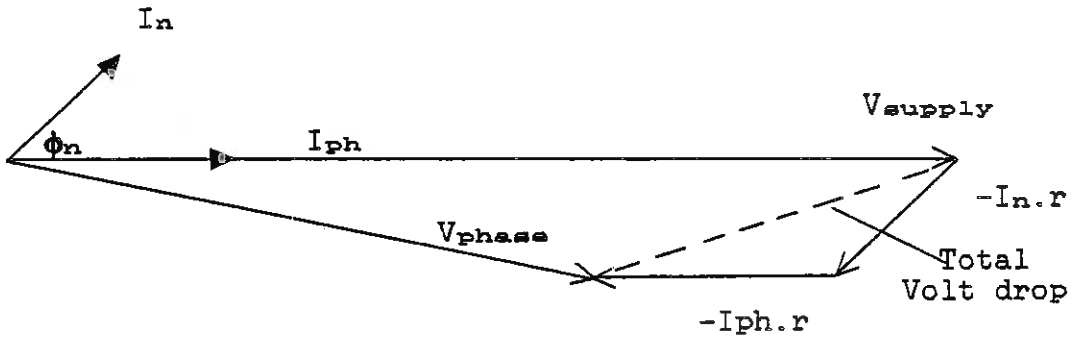

FIG 3 VOLTAGE PHASOR DIAGRAM

The average voltage drop for the three phases can then be calculated for each sample period.

The variation of k_v with respect to n was found by combining the 8 consumer currents in random groups of n = 2, 3, 4 etc. Figure 4 shows the relationship between k_v and the number of consumers. As n becomes large, k_v tends to unity.

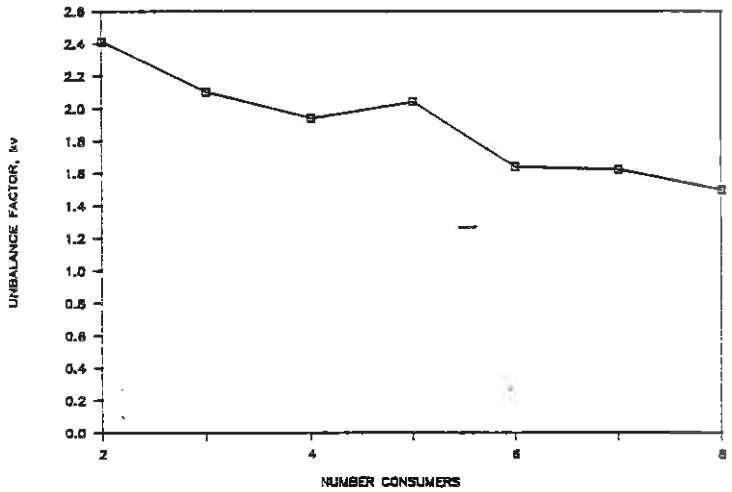

FIG 4 kv VS NUMBER OF CONSUMERS

Voltage drop calculations associated with the design of low voltage networks use maximum demand data. Periods of highest demand were extracted from the sampled data and the average k_v was calculated for 10 minute periods. k_v was also calculated using phase currents which were averaged over 10 minutes. Obviously this would yield a neutral current of dubious significance. However, it was found that the average of the 1-minute k_v values was 1,365 and the ratio of the 10-minute to 1-minute k_v values was 0,95. This indicates that the k_v value calculated from 10-minute samples is about 5% low.

CONCLUSION

This preliminary investigation into voltage regulation in four-core residential feeders has yielded some interesting results. To ensure that these calculations are both valid and uncomplicated a methodology based upon sound research has to be developed. The work reported in this paper attempts to address this problem. The statistical aspects need further investigation and will be attended to in follow up work.

REFERENCES

1. Davies, M. & Paterson, R, "Phase unbalance in low-voltage distribution Systems", p535, Proc. IEE, Dec 1962.

2. Herman, R, "Residential electrical load estimation - a pilot study", SAUPEC90, Stellenbosh, Jan 1990.

RESEARCH INTO THE DETECTION OF FIRES UNDER HIGH VOLTAGE LINES

W.L.Vosloo & J.P.Holtzhausen

Department of Electrical Engineering, University of Stellenbosch

ABSTRACT

The article describes current work being done at the University of Stellenbosch on simulating the conditions under which a sugar cane or grass fire takes place. This research will hopefully lead to fingerprinting the different noise patterns generated by corona due to heavy rain, polluted insulators, fittings and the fire itself.

INTRODUCTION

Eskom has for several years experienced on its 275 and 400 kV networks flashovers and resulting voltage dips caused by the presence of fires, notably sugar cane fires in Natal. It has been estimated that cane-fire faults account for approximately 70 % of all customer dip-related plant failure in Natal. Field research done in 1989 showed that the presence of a sugar cane fire under a 275 kV line causes an increase of conductor corona and hence electromagnetic interference. It is proposed to investigate how this increase of noise as measured in the power line carrier circuits may be used to provide a means of detecting the presence of such fires under a line. On the basis of this information the line concerned would then be de-energised so as to avoid the imposition of a fault on the power network. The objective of the research at Stellenbosch is to simulate the sugar cane and grass fires and investigate the difference between the noise patterns generated by corona due to heavy rain, polluted insulators, fittings, and the fire itself. The ability to discriminate between these sources will make it possible to develop a practical, reliable detection system.

WHAT IS CORONA ? [1,2,3]

Saint Elmo's Fire, named after the patron saint of sailors, was probably the first recorded form of corona. This was a reddish bluish flamelike crown observed on the top of masts due to the high electrostatic field strengths during thunderstorms. The Latin word for crown is corona. Likewise corona phenomena occur around power conductors under high field conditions. Consider two parallel overhead conductors in air as seen in fig 1a. If an

alternating voltage between the conductors is gradually increased, a point is reached at which the air at the surface of the conductors becomes ionized. The voltage between the conductors at this point is known as the disruptive critical voltage (Vo) and the cylinder of ionized air surrounding each conductor is called corona. If the voltage is further increased, a second point is reached at which a faint luminous glow of violet colour can be seen to surround each conductor. The potential difference at this point is known as the visual critical voltage (Vv) and the luminous glow is called visible corona. The capacitive current (Io) flowing through the air between the conductors is sinusoidal until corona occurs. When Vo is exceeded, the waveform of Io is as shown in fig 1b.

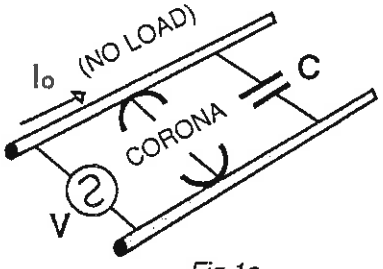

Fig 1a

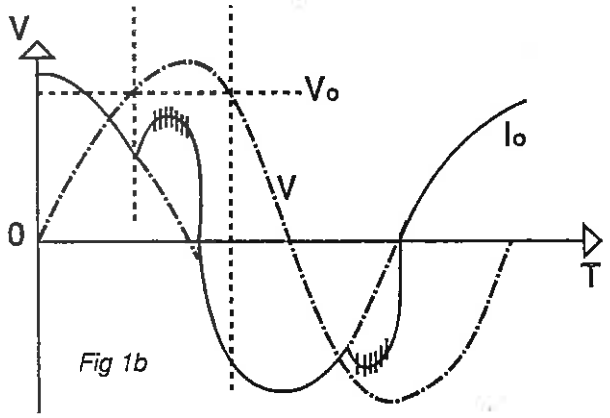

Fig 1b

Fig 1 : Voltage and current v/s time

The distortion of Io is due to the reduction in insulation resistance between the conductors caused by the ionization of some of the air. This increase commences at the point in the voltage cycle at which Vo is exceeded and Io returns to its sinusoidal waveform when the voltage falls below Vo. There is also an increase in the power loss since additional energy is used in ionizing the air. The distortion of the waveform of Io consists mainly of a fundamental and a third harmonic. The fundamental component of magnetic and electrostatic fields associated with a three-phase overhead line each sum to zero but the third harmonic fields are in phase and give a resultant which causes interference with neighbouring telephone, radio and television circuits. A 300 Hz hissing noise can be heard and ozone is formed, which can be detected by its characteristic odour, when visible corona occurs.

WHY LOOK AT CORONA ?

One of the major effects of corona is radio interference (RI). Apart from its effect on communications radio interference is important for this study in that it is related to the background electromagnetic noise appearing in power line carrier systems. Fingerprinting of the frequency spectrum and amplitude of the

various conductor corona noise sources such as heavy rain, polluted insulators, fittings, and the fire itself one would hope to be able to detect these conditions by analysing the power line carrier noise.

HOW DOES ONE SIMULATE CORONA IN THE LABORATORY ?

This is done using a corona cage as seen in fig 2. The function of the corona cage is to allow the main corona parameters of conductors to be measured as a function of the applied voltage. The corona cage allows conductors to be tested at the same field gradient as under operation but at lower voltages than the operating voltages.

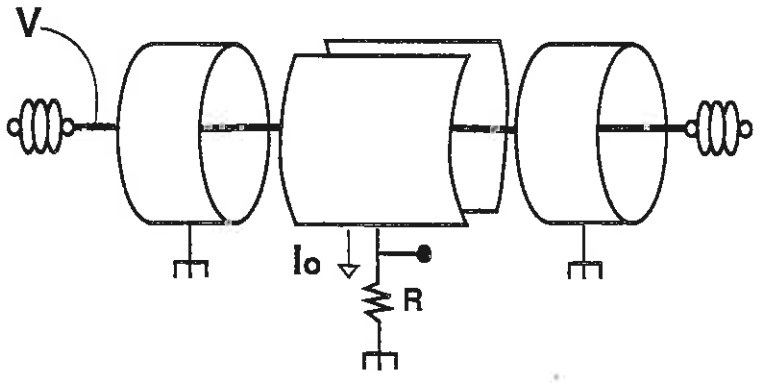

Fig 2 :Corona cage

The cage consists of three cylinders lying horizontally with the conductor under test along the central axis of the cylinders. The two cylinders on either end reduce fringing effects so that a well-defined field exists on the central cylinder from which all measurements are made. Measurements are made by observing the current (Io) flowing from the central cylinder to earth. From this waveform the intensity of corona discharges can be determined. This can be used to determine radio interference levels and power loss.

WHAT HAS TO BE SIMULATED ?

The three main contributors to corona noise on transmission lines in Natal are the following.

i) Sugar cane fires. Burning of sugar cane fields occur early morning with a high dewpoint and very little windpresent. This occurs just before harvesting to ease the process and reduce the trash content of the cane. The cane has a water content of approximately 60 %. Methane gas is produced by the burning process. Lots of dry leaves are present. Meter high flames are formed

with temperatures as high as 1000 degrees Celcius which at times leap up between the conductors causing flashovers. The temperature at the conductors are approximately 250 degees Celcius. The chemical basis of sugar cane is a carbon composite. Large plumes of smoke are formed and at times cause flashovers between conductors.

ii) Heavy rain. Rain rates of at least 1 mm/hour has to be simulated.

iii) Insulator pollution. All three of these conditions and the noise produced by line fittings has to be simulated under controlled laboratory conditions. The equipment developed must be adaptable to simulate grass fires as well.

HOW HAS IT BEEN SIMULATED ?

The structure as seen in fig 3 has been constructed to simulate the sugar cane fire.

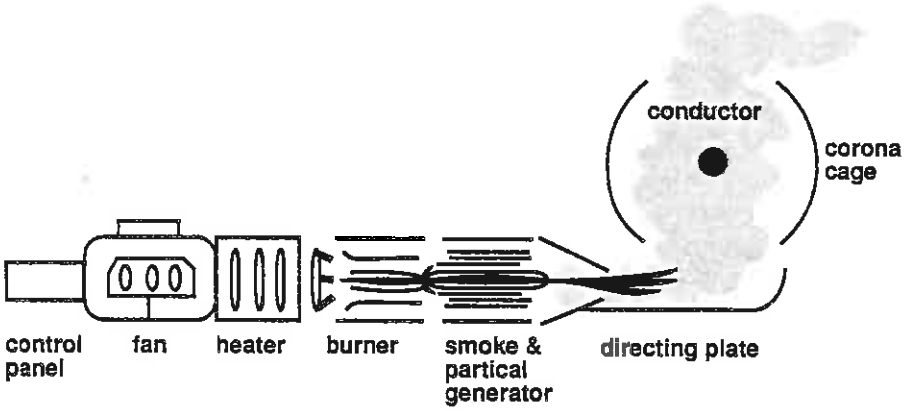

Fig 3 : Sugar cane fire simulator

The first section seen in fig 3 is the air supply fan with speed control used to generate a controllable air supply. The three 9 kW heater elements are used to pre-heat the air. The gas burner was constructed from 1/4 " copper pipe with six 1 mm injector nozzles. Three of the nozzles focus in the front of the converging tube while the other three focus at its end. The gas is regulated and controlled by a circuit installed as a safety feature. A flame plasma of approximately 1000 degrees Celcius has been formed, which is considered to be representative of a typical sugar cane flame. The smoke and particle plume is simulated in the next stage. The flame plasma flows through the centre of an 5 mm thick inner cylinder. The area between the outer expanded metal cylinder and the inner cylinder is filled by 10 kg of sugar cane, forming an coaxial tube of sugar cane. A small amount of the flame plasma leaks around the inner cylinder causing the sugar cane tube to smoulder thus leading to the production of the desired smoke

and particle plume, not unlike a smouldering cigarette. The flame plasma, smoke and particle plume is then directed to the conductor under test by the directing plate.

The structure as seen in fig 4 has been constructed to measure the corona current and to provide a controlled zone.

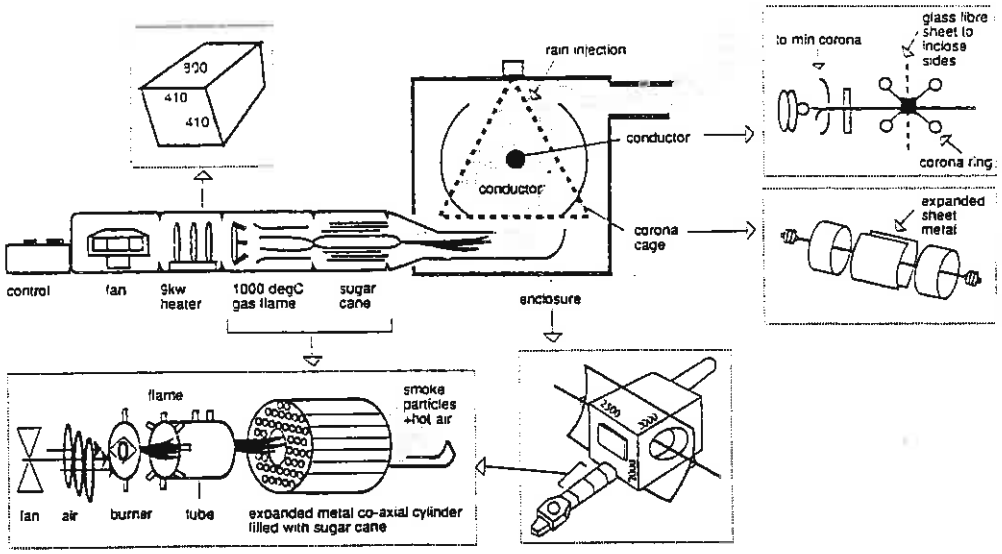

Fig 4 : Enclosed corona cage

A basic corona cage obtained from the University of Cape Town was adapted and modified to minimise any obstruction to the flow of the flame plasma and smoke plume. The cage, as seen in fig 4 has been enclosed with galvanized sheets and painted with red lead to prevent rust occurring under the harsh conditions it will be subjected to. The flame and smoke plasma enters the cage from below and leaves via the stack. The sides are closed with laminated Phenolic resin which can withstand a temperature of 400 degrees centigrade. Where the conductor enters the cage corona rings were fitted to minimise the field at this point. A rain injection nozzle has been installed to simulate heavy rain conditions. The rain rate is controlled by a regulator fitted with a pressure gauge.

The measurement schematic circuit can be seen in fig 5 and is used to look at the corona current.

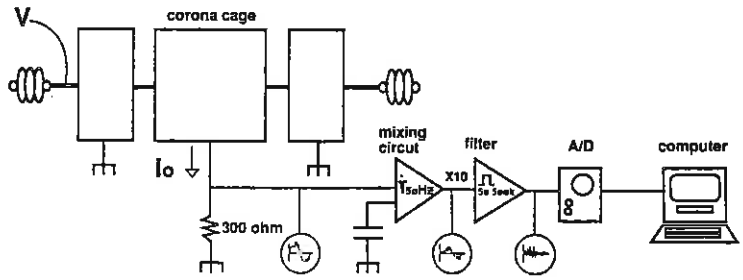

Fig 5 : Measurement circuit

REACTIVE ENERGY PRICING UNDER ESKOM'S PROPOSED TIME-OF-USE-TARIFF (R M SURTEES OCTOBER 1990)

1. BACKGROUND

In the report of the Commission of Enquiry into the Supply of Electricity in South Africa in 1984 it was stated that Eskom should be allowed greater flexibility to develop tariff structures aimed at the economic justification of load management and which comply with the following requirements:-

- That one group of customers does not subsidise another

- High occupation of generating capacity and lower average electricity prices

- Saving of electricity

Time-of-Use tariffs are considered to provide a practical means of achieving the above requirements. They have been implemented in the USA, France, the UK, Australia, New Zealand, Japan and in many other countries. They can be designed to be cost reflective and therefore enable costs to be recovered in a fair and equitable manner, thus giving users a clear indication of the supply-side requirements. Variations in cost are apparent on an hourly, daily and seasonal basis.

Eskom, after much background research, undertook, in 1989 to develop such a tariff structure. The primary emphasis of the new tariff being on cost reflectivity. This submission deals only with the reactive energy charging policy development under the TOU tariff (Tariff "T") and therefore does not attempt to explain the rationale behind the active energy structure.

2. INTRODUCTION

The two predominant tariffs employed by Eskom at present have high associated maximum demand components. ie. typically in the order 50 % of a customers' total bill. The first of which, is the kW tariff, with demand and energy consumption being measured in kW and kWh respectively. A contracted power factor (pf) limit of 0.85 is also stipulated. The existence of this tariff stems largely from historical reasons and although widely utilised, is no longer available to new customers. It is however prevalent in Eskom's Southern, Central and Western Transvaal regions, as well as the Orange Free State region.

The preferred option from Eskom's point of view is the kVA tariff, where the demand component is measured in kVA and energy consumption in kWh. A substantial incentive is provided for customers with good power factors to change to the kVA tariff. This is due to the kVA demand charge being significantly lower than the kW demand charge. In the event of power factor correction being required, pay-back periods are typically between one and two years, thus resulting in many customers having converted to the kVA tariff. The new TOU tariff requires a critical reappraisal of the methodology used in charging for reactive power (VAr's) and energy (VArh) requirements.

3. COSTS ASSOCIATED WITH THE SUPPLY OF REACTIVE ENERGY

The cost to Eskom of supplying reactive energy is a function of the system configuration, system loading and loading characteristics. Thus the problem with regard to equitable pricing, and equally important, system stability will vary by location as these parameters change. A pricing policy is therefore formulated, which is intended to demonstrate cost reflectivity in general terms.

3.1 TRANSMISSION SYSTEM COSTS

In order to quantify the kW losses associated directly with consumer's reactive power requirements and the associated costs thereof, power system simulation studies were conducted on sections of Eskom's main transmission network.(275 kV and above)
Due to the long transmission distances and predominantly reactive line characteristics on the Eskom grid, voltage support is often necessary. A major contributing component to the voltage drop problem under peak loading periods is the high reactive load requirement. (low power factor loads) In areas where the kW demand tariff is prevalent, ie. The Western, Central, and Southern Transvaal regions, as well as the Orange Free State region, Eskom has installed numerous switched shunt capacitor banks in order to maintain the specified contractual voltage levels.

The power factor present at various points on the transmission system is dependent on the extent of the loading, along with the number and position of shunt capacitor banks linked to the network.

In an attempt to quantify losses directly attributable to customers' reactive energy requirements, the investigation was conducted with the regional network loading pf's varied between unity and 0.85 and with loading conditions in the order of the regional maximum demands.

The results are summarised in Table 1.

	Capacitor Banks	
Power Factor	In service losses	Out of service losses
0.85	2.7 %	5.6 %
Unity	2.1 %	3.5 %

TABLE 1. TRANSMISSION SYSTEM LOSSES AS A FUNCTION OF LOAD POWER FACTOR

It is evident that the transmission system losses associated directly with low power factor loads are in fact comparatively small when the installed capacitor banks are in service. The hypothetical case where all banks are removed from service, gives an indication of the extent of the losses due to low power factor loading. (2.1 % increase in transmission losses)

The primary reasons for the installation of shunt capacitor banks on the transmission system are given below in order of priority.

- Increasing the power transfer capability of the inter-connected system.
- To improve the system voltage profile and reduce voltage sensitivity to disturbances and line outages.
- Reduce heating losses on the transmission system.

The major cost to Eskom is the provision of transmission line reactive support in respect of the above. In the regions where the kW tariff is predominant, there is little local reactive support and the requirements are thus taken from the transmission system. Studies conducted in order to establish further transmission system reactive requirements in 1986 have shown that approximately 75 % of the capacity of all planned installations are necessary to provide for load side reactive requirements. The remaining 25 % being for transmission system support.

Eskom would need to provide reactive compensation for the regions considered even if their power factors were close to unity for the reasons previously discussed. The problem however is that every reactive VAr "consumed" by the customer, has to be provided by the Utility. The capacity for VAr generation at the power source is not a constraint. The "bottleneck" is the transmission and distribution system and under high loading conditions the system requires added support, the degree of which is highly dependent on the load reactive requirements. Of the 5042 net MVArs required by the various regions in October 1987, 2722 MVArs were provided in the form of shunt compensation, 2148 MVArs were provided by Generation and 172 MVArs by the system itself.

The costs cannot therefore be quantified in terms of line losses alone and are related to the additional costs incurred by Eskom for the provision of shunt compensation.

3.2 DISTRIBUTION SYSTEM COSTS

Distribution voltages are normally defined by Eskom as being below 220 kV and higher than 33 kV, typically 132 kV and below.

The analysis of the costs associated with the supply of reactive energy within a distribution network is dealt with in two parts. A typical 88 kV distribution network is analysed in terms of system losses and performance under various loading conditions. Secondly, a more detailed analysis is conducted on a typical reticulation network.

3.2.1 88 kV DISTRIBUTION NETWORK

A network in the Western Transvaal (kW tariff predominant) was selected, the maximum demand of which is in the order of 500 MVA. There are 24 consumers on the network with maximum loads ranging from 2.2 MW to 104 MW and total line length in the order of 400 km. Two 48 MVAr shunt capacitor banks are utilised within the network and their effects on system performance analysed

A similar approach to that conducted on the transmission system was used. The losses and load voltage levels were monitored under various power factors, with the loading conditions remaining essentially constant.

The primary purpose of the capacitor installations is once again for voltage support. The effect on system losses is small, although some improvement could result with better placement of the capacitor banks.

The simulation results are summarised in Table 2.

	Capacitor Banks	
Power Factor	In service losses	Out of service losses
0.85	3.0 %	3.5 %
Unity	2.0 %	2.1 %
Actual	2.4 %	2.7 %

TABLE 2. 88 kV DISTRIBUTION SYSTEM LOSSES AS A FUNCTION OF LOAD POWER FACTOR

3.2.2 LOW VOLTAGE DISTRIBUTION COSTS

A typical low voltage distribution (reticulation) system is analysed in terms of losses and the effects of the positioning of various power factor correction installations. The network is also typical of a municipal type distribution section. The simplified single line diagram is given in Figure 1.

The total demand power is in the order of 55 MW, with all power factors set to 0.85 in order to determine the losses incurred due to the load reactive power requirements.

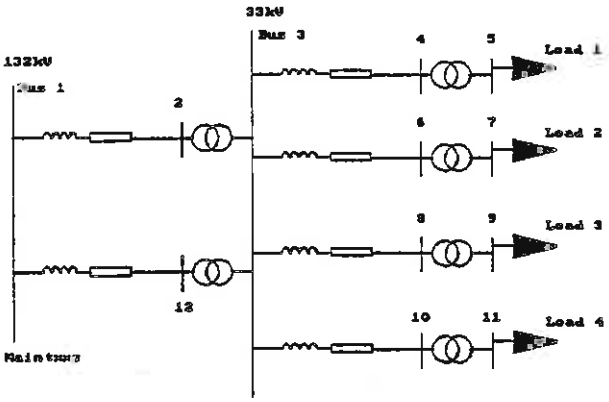

FIGURE 2. TYPICAL LOW VOLTAGE DISTRIBUTION NETWORK

TEST 1.
No power factor correction is installed and transformer tappings are set to compensate for line voltage drops and to comply with the Eskom contractual voltage level tolerances ie. +/- 7.5 %.

TEST 2.
A total of 26.5 MVAr's of compensation is provided at the loads in order to achieve power factors in the region of .99, with transformer tappings left unaltered.

TEST 3.
A 26.5 MVAr capacitor bank is connected to Bus 3. No direct load compensation is provided.

TEST 4.
A 36.1 MVAr capacitor bank is connected to Bus 1 in order to simulate the power factor condition present on the 132kV Bus during Test 1. No load compensation is provided.

	kW Losses %	132 kV Bus PF	Compensation MVAr	Bus No.
TEST 1	7.67	0.76	-	-
TEST 2	4.59	0.97	26.5	5,7,9,11
TEST 3	6.51	0.96	26.5	3
TEST 4	7.67	0.97	36.1	1

TABLE 3. SUMMARY OF LOW VOLTAGE DISTRIBUTION NETWORK TEST RESULTS

The study illustrates quite clearly the optimal positioning for power factor correction (pfc) equipment. With the installations placed at the load points, losses are reduced from 7.67 % to 4.59 %, thus representing a saving of 1.94 MW in terms of demand. With the equivalent compensation installed (26.5 MVAr) at the 33 kV Bus, a slightly reduced improvement in the 132 kV Bus power factor is evident but the loss reduction is only 0.75 MW. This is due to the reactive current still being transmitted between the 33 kV bus and the loads.

To achieve a power factor of 0.97 at the 132 kV bus, a 30.1 MVAr shunt capacitor bank would be required (TEST 4.). The compensation requirement is significantly higher than that of Test 2, where the equipment is installed at the load. The losses are unchanged, as would be expected.

In order to determine the commercial viability of power factor correction from Eskom's viewpoint, a conservative estimate of the marginal cost of generation is used and assumed to be one cent per kWhr. At a realistic cost of R 45.00 per kVAr of capacitive compensation, a payback period of 7 years is possible in terms of loss savings. It is assumed that the compensation is provided by Eskom at the customers' loads. There are however numerous practical problems associated with this hypothesis, as would be the case if the compensation was installed on the HV side of the load transformers.

The installation of the pfc equipment on the 33 kV bus by Eskom could not be justified in that payback periods are in excess of 12 years. The reasons for the installation at 132 kV would only be primarily for voltage support. For smaller installations such as this one, high voltage reactive compensation is significantly more expensive due to the high voltage switch gear required. In the event of a municipality owning such a network, the installation of pfc equipment at the 33 kV bus may be a viable option due to the rate structure.

The reactive energy charging policy should therefore provide an incentive for consumers to provide for their own reactive requirements. This practice, as discussed reduces the burden on the local distribution and transmission networks. Losses are also minimised, which, as in the case examined are substantial and certainly warrant the expense of compensation equipment.

4. TECHNICAL CONSIDERATIONS AND SUPPLY INTEGRITY

4.1 HIGH LOAD STABILITY AND CONTINGENCY PLANNING

The system is said to be secure if in it's normal operating state, including allowable outages, none of the next contingencies would cause a transition to an emergency state. (ie. no equipment overload or abnormal voltages on the system) This is the most critical aspect of the system's reactive requirement, since this can lead to unsatisfactory voltages for a large number of consumers and the possibility of voltage collapse of areas and/or cascading tripping on the system. (Ref 1)

When a major fault occurs on the system, large reactive power imbalances are often found to occur. The system inertia, in terms of load response and the ability of certain rotating plant in the affected area to provide more reactive support by over-excitation can only provide support for short periods. Voltage slide protection schemes have therefore been introduced in heavily loaded areas, situated relatively far from generating points. Automatic voltage support is provided by the fast insertion of shunt capacitors and the planned shedding of the least critical loads, thus preventing system collapse.

In the regions where the bulk loads have poor power factors, the system's power transfer capabilities are dramatically reduced. The maintenance of system security under a contingency situation in these regions is thus extremely difficult and requires the installation of further compensation. This equipment is thus not fully utilised under normal operating conditions.

4.2 SYSTEM CHARACTERISTICS

From the operating limits of a typical Generator, it is evident that the machine stability is highly dependent on the magnitude of the load and it's power factor. It is desirable however to operate large scale generation plant at high loads where they function at optimal efficiency and therefore the number of generators in service at any one time would be dependent on the prevailing system load requirements. The safety margin is dramatically reduced in the leading power factor region and only if the machine is equipped with a fast continuously acting voltage regulator, (Ref 2) can it be safely operated in the leading power factor dynamic stability zone. Only the relatively new machines are equipped with these fast acting voltage regulators and therefore leading power factor loading conditions are avoided as a general rule.

Under light loading conditions, certain parts of the transmission network become "capacitive" and compensation is required by means of reactor bank installations. These characteristics are typical of high voltage long distance systems as found in the Cape regions. The reactors therefore provide voltage control and assist in the maintenance of acceptable stability margins.

5. DESIRED SYSTEM POWER FACTOR

The analysis so far shows that ideal power factors from an Eskom point of view would differ from region to region and also vary, depending on the time variant system load requirement. If a general nationally applicable policy had to be developed, a unity transmission system power factor would therefore in fact not be optimal.

However, in an attempt to determine a power factor which would be technically optimal under medium to high loading conditions, studies, using the simulation program were again conducted at both the transmission and distribution levels. With all load power factors set to 0.98, transmission system power factors ranged from 0.95 to 0.99. The system integrity level under this hypothetical loading condition is extremely high. At power factors lower than 0.98, the system reactive requirements and line losses are increased. Under high loading conditions, with all load power factors set to unity, the losses and reactive requirements are low but the required synchronous stability margins in certain areas are not acceptable and under certain fault conditions, instability may arise.

In order to conform with the national tariff equalisation policy, a 0.98 load power factor requirement, with a prohibition on leading power factors is considered optimal under medium to high loading conditions. (Peak and Standard hours under tariff T) Under low loading or off-peak periods, the reactive power requirements are greatly diminished and the relatively stringent 0.98 power factor requirement need no longer apply.

6. CHOICE OF TARIFF STRUCTURE

The real cost to Eskom in terms of the provision of reactive power, is determined by the system peak loading conditions and a reactive demand charge would appear to be the most direct and cost reflective method of billing. Demand charges however have distinct disadvantages in that the customer's peak demand may not coincide with that of Eskom's and the customer may be unfairly penalised for short term failure of power factor correction equipment

A direct kVArh reactive energy consumption charge is deemed to be the most appropriate charging method under the proposed active energy charging structure. It achieves the desired demand type effect due to the relatively short half hourly discrete monitoring intervals without the associated disadvantages. The reactive energy component of the tariff should therefore be structured such that it creates a cost based incentive for power factor correction up to 0.98 by means of a kVArh consumption charge. This represents a reactive power requirement equal to 20 % of the active power consumed. Compensation to higher power factors approaching unity should not be encouraged and leading power factor operation should not be permitted.

6.1 CHOICE OF kVArh RATE

In the complex process of determining the active energy rates, the reactive energy consumption "revenues" were omitted from the calculations. (Ref 3) The reactive energy charges are therefore intended to recover the associated costs and not generate additional income.

As is evident in the preceding analysis concerning the costs of providing reactive support, the optimal placement, both technically and financially of this equipment is at the load itself. The economies of scale principles do not apply to the provision of reactive requirements, ie. it is generally not cost effective for Eskom to provide for "bulk" reactive support.

In order to provide a realistic cost based incentive for power factor correction, a two year payback period is used as the reference, as is the case in industry. The kVArh reactive energy consumption rate should therefore provide the customer with an incentive to operate at power factors better than 0.98.

The cost of PFC equipment, including capacitors and switch-gear is dependant on the installation voltage level, the number of discrete steps required, the degree of compensation required and physical housing or structural requirements. (Ref.4) If harmonic filters are needed, the costs are also greatly increased. An average installation, excluding major civil works, and filter requirements would cost in the region of R 45.00 per kVAr. (September 1990) The inclusion of filter banks would double the price. All calculations are therefore based on a PFC equipment cost R 45.00 per kVAr.

6.2 EFFECTS ON VARIOUS CUSTOMER TYPES

In order to determine the effects on various customers, the load data of six different customer types (All presently on the kW demand tariff) is analysed, representing a broad cross section of Eskom's consumer base. The study includes a Municipality, a Gold mine, a Foundry, a metal producer, a chemical plant and a typical Tariff "E" customer. Data for each customer was collected for a month-long period, using specifically installed instrumentation.

The kVArh charge required in order to allow a two year payback period on compensation equipment is determined in each case. The results are summarised below.

Customer	Cents/kVArh for a 24 month payback period
Gold Mine	0.7
Municipality	3.4
Chemical Plant	0.6
Metal processing Ind	0.9
Foundry	1.1
Tariff E customer	1.9

TABLE 4. VARIATION IN kVArh CHARGES FOR TYPICAL ESKOM CUSTOMER FOR A TWO YEAR PAYBACK PERIOD.

As is evident, the charges vary considerably and an incentive for one customer to install PFC equipment may not necessarily apply to another. A reactive energy charge in the order of 0.6 to 2.0 cents per kVARh appears to provide an adequate incentive for power factor correction in most instances. The range is however too broad and other factors therefore need to be considered.

Numerous customers have converted from the kW to the kVA demand tariff due to the associated financial incentives. In order therefore not to disadvantage customers who have undertaken the conversion, the kVArh rate should also provide a comparable incentive. An analysis of the kW to kVA conversion payback periods of the customers considered above and a hypothetical 100 % load factor customer show that a charge of 1.5 c per kVArh is consistent in terms of meeting both objectives. Further tests conducted on a number of other customer types have yielded similar results.

7. SUMMARY

A direct charge for reactive energy consumption, monitored over discrete half hourly intervals is the chosen billing technique, as this method avoids the disadvantages associated with a demand charge type tariff. The charge will only be effected during the peak and standard hours due to the nature of the time variant system reactive power demands.

A charge of 1.5 c/kVArh has been selected as the reactive energy rate since it is based on the cost of reactive compensation equipment as well as the existing kVA demand tariff. It also encourages power factor correction at the load itself.
Leading power factors are not generally desirable in terms of Eskom's operational requirements, since they could result in stability problems, affecting rotating plant as well as the transmission system itself, resulting in total voltage collapse in certain areas. Leading power factors are thus not permitted and a "cut off" power factor, above which no further incentive is provided, is required. A "cut-off" power factor of 0.98 (reactive energy equals 20 % of active energy) is deemed optimal, since under medium to high loading conditions it virtually ensures system stability under all fault conditions, aids with voltage control, limits system losses and assists with future planning

8. CONCLUSION

As is evident from the analysis conducted, the development of a nationally applicable cost reflective reactive energy charging policy, requires the consideration of the effects of numerous system variables. The system variables however differ considerably from area to area and therefore although a generally applicable tariff has been developed, it is not necessarily truly cost reflective in every distribution network throughout the Eskom Grid.

It is therefore recommended that an approach similar that of the United Kingdom Area Boards be adopted, where the local system reactive power flow characteristics are reflected in the various tariffs. The reactive energy charging structure as developed, should be retained, with a degree of flexibility allowed in the rates and limits, depending on the local network characteristics. For example, due to highly capacitive networks in certain Cape regions, customers with low power factors would in fact be beneficial to Eskom even under relatively high loading conditions. The 0.98 power limit could possibly be relaxed in this instance. Similarly there are certain areas in Natal and the Central Transvaal, where voltage support is a major problem and even under light loading conditions, the system remains highly inductive. In this case certain customers could be allowed operation at leading power factors.

In line with the Eskom policy of using the present surplus generation capacity to stimulate industrial growth by means of various tariff concessions, the reactive energy charge could be phased in gradually where applicable. If for example a major consumer on the kW tariff is unable to take advantage of the T tariff due to the cost of power factor correction, (filter banks required) a concessionary period could be granted, thus effectively reducing the payback period when installed. This measure would be possible in the short term in certain areas where sufficient regional capacitive compensation has been installed by Eskom.

The reactive energy charging policy developed has a sound technical and economic basis. It also has the advantage of a flexible structure and is congruent with the objectives as stated in the development of the Time-Of-Use active energy charging policy.

REFERENCES

1. Power System Reactive Requirements: Eskom,s System Operations Department. December 1985 R K Dell and M C Coetzee
2. Electrical Power Systems Volume 1. A E Guile and W Patterson.
3. Technical report on the design methodology for Eskom's proposed Time-of-Use Tariff: September 1990 D P Theron.
4. Power Factor Correction Low, Medium or High Voltage : Vector March 1989. H J Yelland.

MODELLING THE FINAL JUMP – THE VOLTAGE COLLAPSE

J.M. Van Coller
Department of Electrical Engineering
University of the Witwatersrand

Abstract

Transmission line surge voltages associated with backflashover events are characterized by very steep rates of rise. In order to accurately model the propagation and attenuation of these surges through the power system it is necessary to first derive accurate models for the generation mechanism – which implies accurate models of the voltage collapse between the pylon metalwork and the phase conductor due to the arc formation. In this paper the sensitivity of the generated phase conductor waveform to changes in the arc model is investigated using simulation.

1 Introduction

Insulation coordination involves the selection of insulation levels to successfully withstand the surge voltages anticipated.

While the peak surge voltage is an important parameter many power system components such as machines and transformers are susceptible to the rate of rise of the surge voltage since this can overstress the insulation between the end turns. In addition the rate of rise of the surge voltage waveform influences the distance over which surge arrestors are effective.

Backflashover – where lightning strikes a pylon or earth wire and flashover onto the phase conductor follows – results in surge voltage waveforms on the phase conductor with very high rates of rise. This is particularly important when the backflashover occurs at a pylon close to the terminal equipment – corona attenuation during propagation of the surge along the transmission line is then less effective in attenuating both the peak amplitude and the rate of rise.

Modelling the surges produced by backflashover implies modelling the final jump phase of breakdown – the transition of a streamer channel bridging the gap to a low impedance arc channel. The aim of this paper is to examine the sensitivity of the phase conductor waveform to changes in the models used.

2 Description of the transmission line model

Modelling backflashover requires a model of the lightning current, the impedance seen by the lightning current when it strikes the pylon, the voltage across the conductor-pylon gap, the propagation of the leader across the gap and the resulting arc channel.

A single circuit horizontal phase conductor geometry with two overhead earth wires was used in the simulation. Significant characteristics are detailed below:

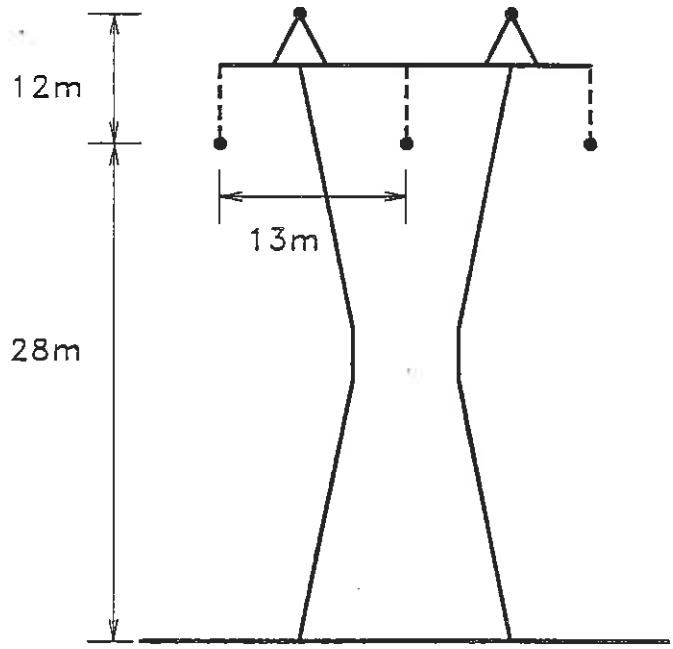

Conductor–pylon clearance: 3,5m

Midpoint sag: 7m

Tower span: 400m

Conductor bundle: 6 × Zebra

Line voltage: 765kV

Soil resistivity: 1000Ωm

The lightning current source, multiconductor transmission line, pylon, leader propagation and development of the arc channel were modelled using EMTP (Electromagnetic Transients Program).

The distributed inductance and stray capacitance to earth of the pylon was modelled by associating with the pylon a surge impedance of 160Ω [1]. The tower footing resistance was modelled as a constant 20Ω resistor (approximating the soil ionization effects but ignoring any time dependency). The earth wires above the phase conductors were assumed to be bonded to the pylons; however due to their importance in terms of coupling with the phase conductors they were modelled as phase conductors.

The instant of backflashover was determined using a leader propagation model proposed by Pigini [2].

3 Description of the arc–models

Little experimental data is available on the voltage collapse associated with long airgaps (> 3m). This can be contrasted with the considerable research into the behaviour of high voltage thyratrons (≈ 100kV) during turn-on – because of their widespread use in high-power, short-duration pulse circuits.

Although the thyratron reaches only the normal glow (or at high currents the abnormal glow) region of the v-i characteristic (rather than the arc region) is was speculated that the turn-on behaviour of thyratrons could approximate the early part of the streamer-arc transition and hence these models were examined.

During turn-on the thyratron passes through a predominantly resistive phase and then settles into an inductive phase.

The inductive phase is modelled as a series inductor with value equal to that of a straight isolated wire of length equal to that of the arc. This gives

$$L = 2 \times 10^{-7}\left[\log \frac{2\ell}{a_c} - 1 \right]\ell$$

where L is the inductance of the arc channel, in Henrys

ℓ is the length of the arc, in meters

a_c is the channel radius, in meters

The only parameter that is difficult to put a value to is the arc channel radius, a_c – a value of 1mm was use in this study, which gives for the arc channel $L \approx 1{,}5\mu H/m$.

The resistive phase can be modelled as a time-varying series voltdrop, V(t), or as a time-varying resistance, R(t):

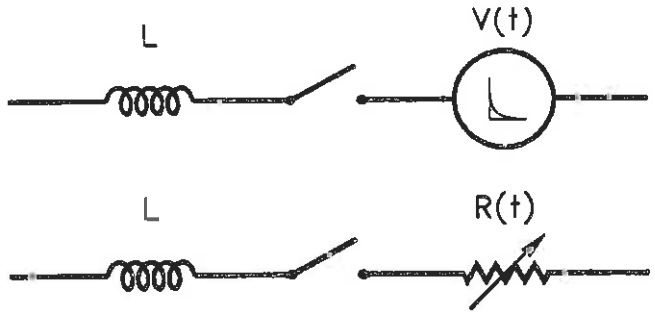

For thyratrons the form of V(t) is

$$V(t) = V_o e^{-t/\tau_R}$$

where V_o is the initial gap voltage (prior to turn-on)

t is the time from turn-on, in seconds

τ_R is the resistive phase time constant, in seconds

In the above equation the parameter that is difficult to put a value to is τ_R.

It is known that both the impedance of the external circuit and the average gap gradient immediately before breakdown influence τ_R and an equation proposed [3] is (for STP)

$$\tau_R = \frac{88}{\sqrt[3]{ZE^4}}$$

where τ_R is the resistive phase time constant, in nanoseconds

Z is is surge impedance of the external circuit as seen by the gap, in Ω

E is the average gap field at breakdown, in MV/m

– which for our example gives values of approximately 40ns.

The alternative method of modelling the arc resistance itself is in terms of an equation similar to the Toepler spark equation (although this is applicable more to streamer breakdown associated with sphere-sphere spark gaps [4]

$$R(t) = \frac{k_1 \ell}{\int_0^t i \; dt} \text{ in } \Omega$$

where R(t) is the time-dependent arc resistance, in Ω

ℓ is the gap length, in meters

i is the arc current, in amperes

For air [4] $k_1 \approx 5 \times 10^{-3}$

4 Simulation results

4.1 Inductive phase only

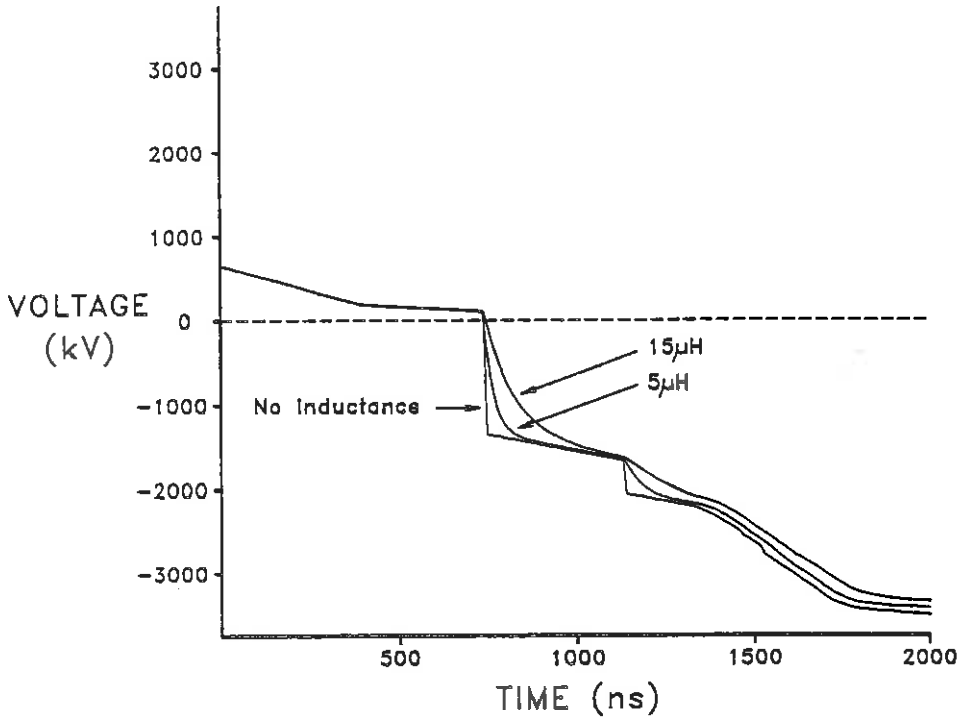

4.2 Resistive phase as well as inductive phase

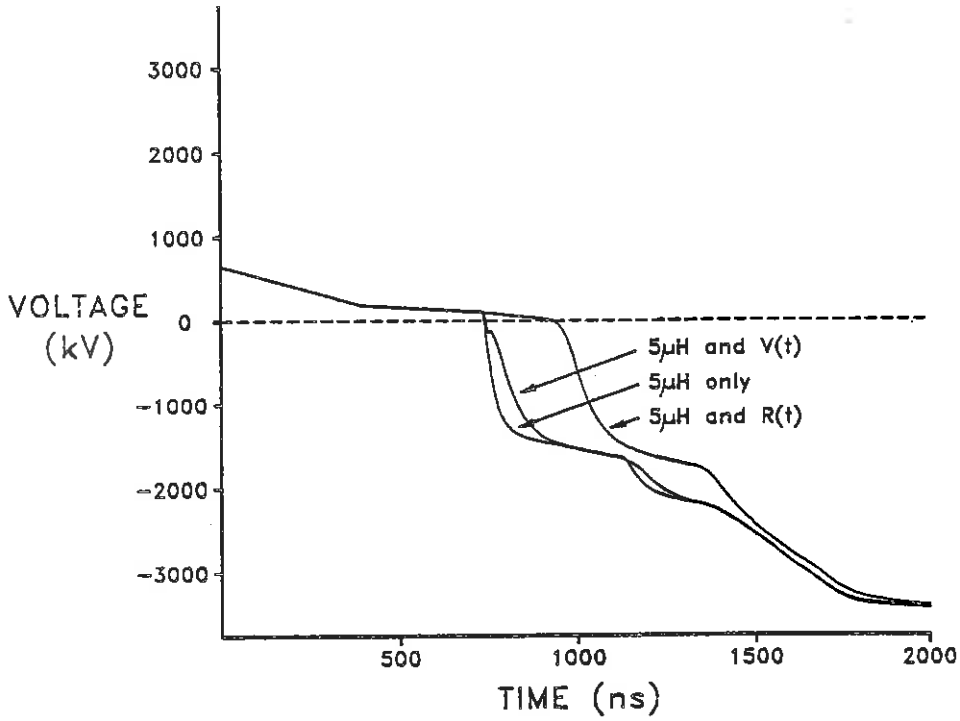

5 Discussion

The sensitivity of the surge waveform to the form of the model used has been clearly demonstrated.

The validity of the models themselves needs to be assessed using measured gap behaviour, although the associated difficulties are considerable – voltage dividers must be accurate in the ns range.

Hopefully this paper will stimulate research in this important area.

6 References

[1] Transmission line reference book – 345kV and above (Book), EPRI, chapter 12.

[2] Pigini, A et al. 'Performance of long airgaps under lightning overvoltages ... ', IEEE Transactions on Power Delivery, Volume 4, Number 2, April 1989, pp 1379 – 1392.

[3] Sargeant, W. J., Dollinger, R. E., High Power Electronics (Book), TAB, 1989, Chapter 6 and 7.

[4] Heilbronner, F. W. 'Firing and voltage shape of multistage impulse generators', IEEE Transactions on Power Apparatus and Systems, Volume PAS-90, Sept/Oct 1971, pp 2233–2238.

PROBABILITY THEORY APPLIED TO POWER SYSTEMS

Roy D Estment B Ing (Elek) (RAU)
MSc (Eng) student, University of the Witwatersrand
Senior Engineer (Transmission Expansion Planning), Eskom

1. SYNOPSIS

A method of planning extensions to a public electric power supply network is presented, which is based on the reliability of the network as well as the conventional criteria of capital cost and losses. The proposed method takes into account the cyclic variation in the failure rates of overhead transmission lines on a daily and seasonal basis, caused by the daily and seasonal variation in environmental conditions. These environmental conditions include weather patterns, pollution buildup moistened by dew, and fires (grass, bush and sugar cane). On the Eskom system, periods of high line failure rates generally coincide with periods of relatively low load. Load and overhead line failure rate patterns also differ between different climatic regions. The method is intended for use in system expansion planning, but can also be used by a system control centre for equipment outage planning.

2. INTRODUCTION

The purpose of a public electric power supply network is to meet the electricity requirements of its customers at an acceptable level of reliability and quality of supply and at minimum cost. The electric utility industry is the most capital intensive industry in the world, because of the vast sums of money that are required to construct power stations, transmission lines, and substations to meet the growing electricity requirements of its customers. The impact of the electric utility industry's funding requirements for capital projects has a major impact on the economies of the world's nations, especially in the form of higher interest rates. The impact of Eskom's capital expenditure on the South African economy is particularly severe, because of the present restrictions on access to capital.

The power system planner, who is responsible for determining what new facilities or modifications to existing facilities are required to meet South Africa's growing electricity requirements, carries a heavy responsibility to ensure that the funds available for capital projects are spent wisely. This paper proposes a method by which new transmission lines can be planned more effectively.

The operational constraints under which a power system is required to operate are component ampacity, busbar maximum and minimum operating voltages, switchgear rupturing capacities (restricts permissible fault levels), generator transient stability, and voltage stability. Assuming that the system in a healthy state is capable of meeting the demands of its customers throughout the year without violating any operational constraints, system failure can be defined as the violation of at least one system operational constraint following the loss of a system component (line, transformer, or shunt reactive device).

The loss of a system component is thus a necessary condition for system failure to occur, but is not a sufficient condition.

3. DETERMINISTIC SYSTEM PLANNING METHODS

Up to the present, Eskom has made use of the traditional deterministic approach to system planning [1]. Here, the system is designed to withstand the loss of any one system component, without system failure. This is known as the (n-1) or single contingency outage criterion. In the case of base load power stations of 1000 MW sent out capacity or more, the (n-1) criterion is used, as well as the requirement that the power station must be capable of exporting 75 % of its sent out rating without system failure following the loss of a second system component. The latter criterion is known as the (n-2) or double contingency criterion. Load flow studies are done under various contingencies to test the system for violations. Fault level studies are only done on a healthy system, as this yields the maximum fault currents the system is capable of producing, for checking against circuit breaker rupturing capacities.

The discounted cash flow method is used in the economic evaluation of system expansion proposals. Mathematically speaking, system planning is an optimisation problem in which the nett present value of supplying the customer's electricity requirements is minimised, subject to the constraints of technical acceptability (quality and security of supply), availability of funds to finance capital projects, environmental impact, and flexibility to meet changing needs. In practice, several technically acceptable options of meeting the demands placed on the system over the planning horizon (usually 10 years in Eskom) are developed. Each option is then costed in terms of capital as well as losses incurred each year, and the nett present value is calculated by means of the formula below:

$$B = \sum_{m=0}^{M} (I(m) + C_L(m))(1 + i)^{-m} \qquad (1)$$

Where: m = planning year index
M = final year in the planning horizon
$I(m)$ = capital investment in year m
$C_L(m)$ = cost of losses in year m
i = nett discount rate
B = nett present value cost of the scheme

The nett discount rate i, which represents the time value of money (one Rand today is worth more than one Rand tomorrow) is calculated as follows:

$$i = (1 + d)/(1 + e) - 1 \qquad (2)$$

Where: d = discount rate (interest rate used for financial planning studies)
e = escalation rate (inflation rate)

The discount and escalation rates are fixed by Eskom's corporate finance division to ensure uniformity in all financial planning studies.

Deterministic system planning techniques have served the electric utility industry well. However, the increasing complexity of electric power transmission systems has revealed the inadequacies of the approach. The implicit assumption made in the deterministic transmission system planning approach is that all system components have equal failure probabilities. As transmission systems increase in size and complexity, the probability of more than one component in a given part of the system being out of service at the same time, increases.

The advantages of deterministic system planning are its conceptual and computational simplicity.

4. PROBABILISTIC SYSTEM PLANNING METHODS

The shortcomings of deterministic transmission system planning methods prompted the electric utility industry to develop probabilistic transmission system planning methods. Advances in computer technology have made the necessary computational power available at a reasonable cost.

Probabilistic methods explicitly take into account the differences in failure rates between different system components. The daily and seasonal cyclic variations in failure probabilities of lines are however ignored at present. Probabilistic methods used in Britain [2] and North America [3], [4], [5], [6] are based on contingency enumeration, in which the possible contingency cases are each evaluated in turn. Methods of reducing computation time include the truncation of cases having a probability of occurrence less than a given value to eliminate cases with a low probability of occurrence, and limiting the study to the subsystem currently being investigated. In France, Monte Carlo simulation techniques are used [7], [8] in which a fixed number of contingencies are selected at random for study.

Whether contingency enumeration or Monte Carlo simulation is used, the nett present value cost of the scheme is evaluated using equation (3):

$$B = \sum_{m=0}^{M} (1+i)^{-m} \left[I(m) + \sum_{k=0}^{N(m)} P_k \left(C_L(k,m) + C_O(k,m) + C_F(k,m) \right) \right] \qquad (3)$$

Where: k = contingency index ($k = 0$ is system healthy)
$N(m)$ = number of outage contingencies studied in year m
$I(m)$ = capital investment in year m
P_k = probability of contingency k

$C_L(k,m)$ = cost of losses in year m under contingency k

$C_O(k,m)$ = cost of fuel in year m under contingency k (used in economic despatch constrained problems only)

$C_F(k,m)$ = cost to the customer of unsupplied energy in year m under contingency k

i = nett discount rate
B = total present value cost of the scheme

The number of system components varies each year as a result of proposed extensions and modifications, and hence the number of contingencies studied varies as well. The probabilities of occurrence of the truncated cases are assumed to be zero. Because the sum of probabilities of all the cases is by definition equal to one, the probability of the system being in a healthy state can be calculated as follows:

$$P_0 = 1 - \sum_{k=1}^{N} P_k \qquad (4)$$

where P_0 = probability of the system being in a healthy state.

The above calculation must be repeated for each year m in the planning horizon, due to changes in the system.

The major innovation introduced by probabilistic planning is the explicit evaluation of the cost to the customer of unsupplied energy, thereby placing a financial value on reliability. It then becomes possible to justify the enhancement of system reliability in terms of the benefit accruing to the customer.

Figure 1 shows a typical weekly load curve for a large city, compiled from R readings taken at regular intervals of t hours each. The reduction in load over the weekend is clearly visible, hence the use of a weekly load cycle in this paper. In order to determine the unsupplied energy, the first step is to sort the data used to compile the load curve in descending order of load magnitude, instead of in chronological order. The resultant curve (Figure 2) is known as the load duration curve. The load duration curve is compiled from load data over the entire period of interest, usually a whole year for system planning studies, and a few hours to a week for operations planning. The load is expressed in per unit values with the maximum load (Lmax) as base, so the curve can be applied to loads throughout the system. The assumption that loads throughout the system follow a similar pattern is generally valid for a large, meshed network. Where patterns differ widely from the system average, an independent study can be done on that part of the system.

Assume that the system capacity in its healthy state is Lsys. The system would thus be able to supply its entire load without violating any operational constraints. In this case, the unsupplied energy, and therefore its cost, would be zero. Say contingency k reduces the system's capacity to Lcont(k). In this case, operational constraints would be

violated for T'(k) hours necessitating load shedding, and the hatched area between the load duration curve and Lcont(k) yields the expectation value of unsupplied energy. The system would however be capable of supplying its load without violating any operational constraints for a period of T - T'(k) hours without shedding any load.

Thus: $P_S(k) = T'(k)/T$ (5)

$= r/R$ (6)

where $P_S(k)$ = probability of contingency k resulting in load shedding assuming contingency k occurs

r = number of load sampling intervals in T' hours = T'/t
R = number of load sampling intervals in T hours = T/t

The unsupplied energy assuming that contingency k occurs can now be calculated thus (Figure 3):

$$E_U(k) = t \sum_{j=1}^{r} (L(j) - Lcont(k)) \qquad (7)$$

where $E_U(k)$ = unsupplied energy assuming contingency k occurs

j = load sample number
L(j) = Magnitude of load in load sample j

Thus the cost of unsupplied energy can be calculated and inserted in equation (3):

$$C_F(k,m) = C_U E_U(k,m) \qquad (8)$$

where C_U = cost per kWh of unsupplied energy

$E_U(k,m)$ = unsupplied energy in year m assuming contingency k occurs (from equation (7))

The nett present value cost B of each system expansion scheme being studied is calculated using equation (3), and the scheme with the lowest nett present value cost is usually selected for implementation. Constraints such as environmental impact may however dictate otherwise, in which case the nett present value cost of selecting a more expensive scheme can be taken into account.

5. PROBABILISTIC METHOD TAKING CYCLICAL VARIATIONS IN LINE FAILURE PROBABILITIES INTO ACCOUNT

The conventional probabilistic planning methodologies described in the previous section assume that the probability of failure of system components is not a function of time of day or time of year. While this assumption may be valid for transformers, reactors, capacitors, and other components with solid or liquid insulation, it is not valid for overhead lines.

The author's investigation into this aspect was prompted by the fact that existing probabilistic planning methods yielded values for unsupplied energy that were too high. An investigation into line failure rates revealed, firstly, that the failure rate varied cyclically with time of day and seasonally. This was to be expected, as the failure mechanisms for lines are dominated by environmental factors, such as the weather, grass and sugar cane fires [9], and pollution buildup on insulators. Secondly, the periods of peak failure rate did not coincide with the periods of peak load, reducing the consequences of failure in terms of load shedding. Thirdly, the failure rate pattern was dependent on climatic zone (rainfall patterns, lightning ground flash density, frequency and type of vegetation fires etc.). A technique was developed to take account of the cyclic variations in failure probabilities.

Other factors that the new technique had to take into account were conceptual and computational simplicity, and the availability and suitability of input data from system fault statistics. A two-weather model has been used by other researchers [10], in which periods of favourable weather and stormy weather were modeled through the use of different failure probabilities for the two periods. Seasonal variations were modeled by using different proportions of favourable and stormy weather in winter and summer. No allowance was however made for the daily cyclic variation in failure probability.

In the proposed model, a weighted load duration curve is proposed to account for cyclic variations in failure probability. Figure 4 shows an example of the daily variation in failure probability, varying about its average value. Define a weighting factor w(j) equal to the per unit value of the failure probability at the time load sample j is taken, with the average value of failure probability as base. The time interval for each load sample j is then multiplied by its corresponding weighting factor w(j) to form a weighted time interval duration of tw(j). A weighted time duration curve is then obtained by sorting the load samples in descending order of load magnitude. Figure 5 shows the effect on the shape of the weighted load duration curve of peak load occurring during periods of low failure probability (curve A) and high failure probability (curve B). The figure shows clearly that the system will perform better in terms of unsupplied energy and probability of load shedding, if peak load periods correspond with periods of low failure probability.

Equation (6) now becomes:

$$P_S(k) = (1/R) \sum_{j=1}^{r} w(j) \qquad (9)$$

Equation (7) now becomes:

$$E_U(k) = t \sum_{j=1}^{r} w(j)(L(j) - Lcont(k)) \qquad (10)$$

Equations (3), (4), (5), and (8) are still directly applicable to the proposed model.

6. APPLICATIONS

The proposed method was developed for transmission system expansion planning, but can also be used for subtransmission and reticulation system expansion planning. In all three cases, a weighted load duration curve covering an entire year is used. The method can be used for operations planning, merely by using a weighted load duration curve covering a few hours to a week, depending on the nature of the problem being studied. It can also be used in transmission line optimisation studies, by basing the weighted load duration curve only on the pattern followed by a single failure mechanism such as pollution buildup. The cost effectiveness of changes in design, or operating and maintenance procedures can then be evaluated.

7. CONCLUSION

The proposed technique has a wide range of applications. It improves upon earlier methods by taking the cyclic variation in failure probabilities into account. It has a weakness in the form of the use of only the average outage duration in the calculations. This could be overcome to some extent by weighting failure probabilities according to variations in average outage duration, when calculating unsupplied energy.

The model was developed to be appropriate to the volume and type of fault statistics currently maintained in Eskom. It is acknowledged that imperfections exist in the model. A more comprehensive model would however require an increase in the volume and detail of fault statistics to find values for the additional variables of sufficient accuracy to justify the extra time and effort spent in developing and using it.

REFERENCES

[1] "Transmission System Planning Guide" Eskom Transmission Expansion Planning Division, revised January 1988.

[2] Argent S J, Hadfield DPG "Probabilistic transmission planning procedures within the CEGB" First International Symposium on Probabilistic Methods Applied to Power Systems, Toronto, Canada, 11-13 July 1986.

[3] Bhavaraju M P, Albrecht P F, Billinton R, Reppen N D "Requirements for composite system reliability evaluation models" IEEE Trans PS3 no 1 February 1988 pp 149-157.

[4] "Bulk power system reliability concepts and applications" IEEE task force on bulk power system reliability, IEEE Trans PS3 no 1 February 1988 pp 109-117.

[5] "Transmission system reliability methods, volume 1" EPRI Report EL2526 (Project 1530-1), July 1982.

[6] Desrochers G "A method for power system reliability assessment" Canadian Electrical Association Spring Meeting 1983, Vancouver.

[7] Persoz H, Santucci G, Sapet P, Lemoine J C "Planning of Electricity Networks, Volumes 1 & 2" Electricite de France, Direction des Etudes et Recherches.

[8] Batut J "EDF probabilistic approach in transmission planning studies: concepts and computer tools for a better assessment of reliability and security of an EHV transmission power system"

[9] Estment R D, Goosen P V "An investigation into the application of SVC's as a solution to voltage depressions due to line faults" Invited Paper IP01, II SEPOPE Symposium, Sao Paulo, Brazil, 21 - 25 August 1989.

[10] "Power system reliability analysis application guide" CIGRE Working Group 38.03, 1987.

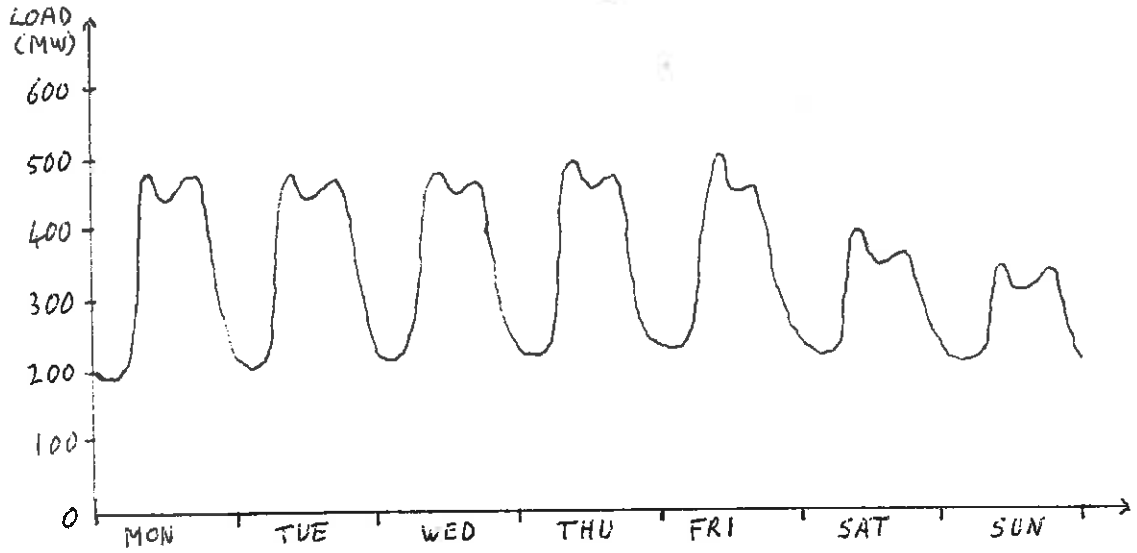

FIGURE 1: TYPICAL WEEKLY LOAD CURVE OF A LARGE CITY

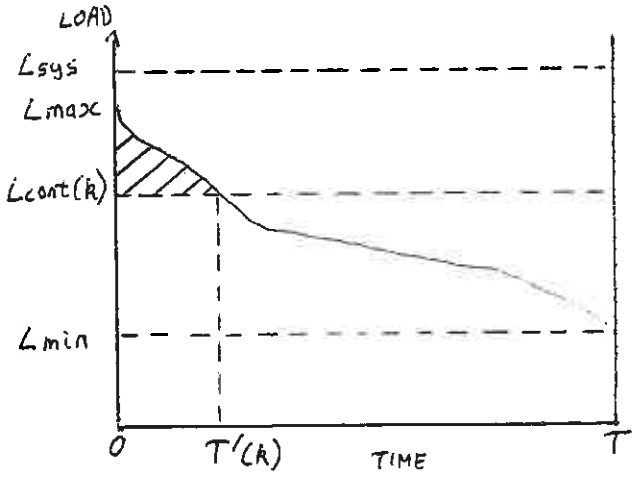

FIGURE 2: LOAD DURATION CURVE

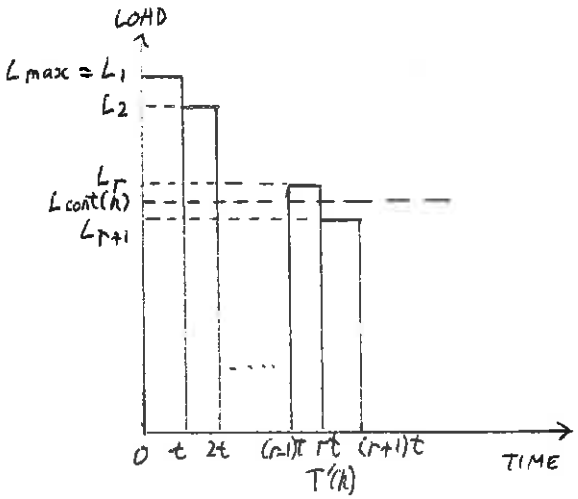

FIGURE 3: CALCULATION OF UNSUPPLIED ENERGY

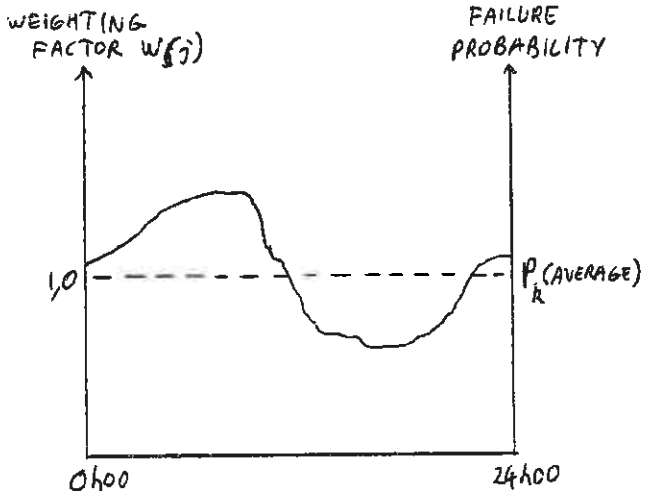

FIGURE 4: SAMPLE DAILY VARIATION IN FAILURE PROBABILITY

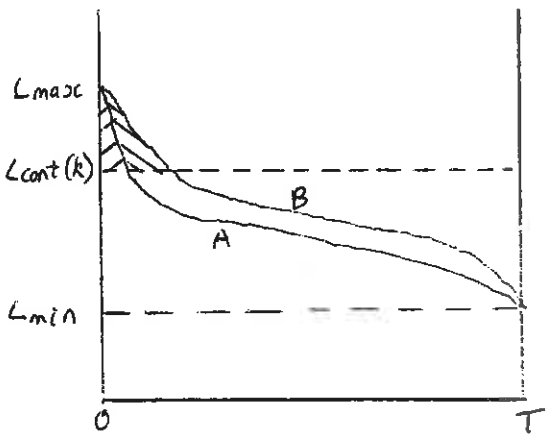

FIGURE 5: COMPARISON BETWEEN WEIGHTED LOAD DURATION CURVES

The Biological Effects of Power Frequency Electromagnetic Fields

D. R. Vogt and Prof. J. P. Reynders
University of the Witwatersrand

Abstract

There is currently considerable interest in some overseas countries about the possible effects of power frequency electric and magnetic fields on people. What evidence is there of possible effects? What research is currently going on? What legislation has been passed? Should we be concerned?

This paper briefly reviews the history of research into the area of power frequency electric and magnetic fields. It discusses the key issues of the epidemiological and biophysical evidence to date. It then examines the political implications of what has been found to date, what legislation has been passed internationally, and what rulings are currently in effect in South Africa.

Finally, it recommends a course of action for South Africa, in order to avoid the problems which have occurred in other countries where the issue has surfaced.

1. Introduction

Wherever a voltage is present on a piece of apparatus, it has an electric field associated with it. Whenever current flows in a circuit, it causes a magnetic field. Close to the apparatus, with respect to the wavelength of the alternating current, an observer is in the near field and the electric and magnetic fields can exist independently. Electric fields may be shielded easily, but it is difficult and expensive to shield against magnetic fields, so these fields are present in varying quantities wherever electricity is transported.

There is some suspicion that these fields may be linked to health effects, principally cancers.

Low frequency fields are often confused with the ionising radiation from X-rays, and nuclear sources. Such radiation has sufficient energy to break chemical bonds within the DNA of the cell, causing mutations, and hence cancer. At lower frequencies, such as microwave, television, radio or power frequencies, the waves do not possess enough energy to break bonds. In order to avoid confusion, these fields will be referred to as emissions, rather than radiation.

Emission from radio sources with a relatively high frequency can contain sufficient energy to cause significant heating effects. Such a principle is used in a microwave oven to cook food. Heating effects may lead to a breakdown of the cellular material, and possibly to cancer.

Power frequency sources have such a low frequency that they cannot damage cells by ionisation, or by direct heating effects, so there has been much scepticism among the engineering community about possible health effects.

At high intensities, effects from power frequency fields can be seen. At magnetic fields of the order of 1 Tesla, magnetophosphenes are experienced. The magnetic field is sufficiently strong to induce currents in the nerve cells from the eye to the brain, causing flashing lights appear in the eyes. To place such a field in perspective, the average 400 kV transmission line will produce a field of the order of 20 micro Tesla, about 5 orders of magnitude smaller. High intensity electric fields can induce muscle contractions and even cardiac arrest, but again, the values of such fields exceed typical transmission line values by several orders of magnitude. Extremely high fields will cause electrical breakdown of the cell membrane, but that effect will be ignored here.

2. History

The first suspicion that field emissions from high voltage equipment could cause disease came about in the 1960's with reports from Russia about effects noticed by switchyard workers. (1) The workers experienced headaches, nausea and fatigue. These effects could not be duplicated in the West, and were eventually described by one of the original authors as an exaggeration. It is likely

that the effects were caused by electric shocks, due to poor work practice, as similar workers on transmission lines had not suffered similar effects.

3. Epidemiological Evidence

Western interest was stirred by a paper by Wertheimer and Leeper in 1979. Dr. Wertheimer was collecting data about children who had died of leukaemia in the Denver, Colorado area, when she noticed that there often seemed to be transformers and heavy electrical wiring close to the homes of the leukaemia cases. She called in Mr. Leeper for an engineering perspective, and did a case-control epidemiological study. In such a study, each case is matched to a control, who is as similar as possible, except for the occurrence of the disease. The case and control homes were then assessed according to a wire code. Houses close to the primary distribution transformers were assumed to have higher magnetic fields than those further along the road. A study of the data collected (2), showed that children living in "high-current configuration" homes, had a tripled risk of cancer, with a 95% confidence interval from 1.9 - 4.6 times, over a sample of 155 cases.

There was initially considerable scepticism about the result, for the reasons outlined above, and due to doubt about the validity of the wire code. Other studies were done, one of which provoked considerable controversy when it showed a negative result, in Rhode Island (3). The Wertheimer-Leeper study has been criticised on several grounds, but it is noteworthy as the study which brought possible health effects to the attention of the public and to the wider scientific community, and also as the study which shifted interest to magnetic, rather than electric fields.

Of the later studies, some have contradicted the result, but others - including possibly the best study to date, also done in Denver, Colorado, by Dr. David Savitz (4) - produced a positive finding. Epidemiology has considerable difficulty suggesting a link between the environment and a particular disease if the relative risk is small. In addition, it can only show a link, and cannot be used to prove cause and effect. Dr. Savitz himself, concludes "it seems that interest or concern may be justified, but our study is not sufficiently convincing to warrant drastic action by homeowners." (5)

In addition to residential studies on children, a considerable amount of work has gone into the area of occupational exposure. Workers in electrical occupations may be exposed to large fields, far larger than those in the home. Two studies by Milham (6,7), have shown a link between occupations classed as electrical and tumours; and between radio amateurs and tumours. Classing an occupation as electrical is again a surrogate for measurement, and is prone to errors. Carstensen shows this in his book, (8), where he compares the ranking given by several experts to various electrical occupations. Other studies (9) have actually measured the exposure of various workers, while finding no link to any disease. It is perhaps surprising that the measured values are often well below those estimated by experts, although it is clear that workers in electrical disciplines are exposed to higher magnetic fields than those in other occupations.

Going from measurements or estimates of worker exposure to a conclusive link between field exposure and cancer is difficult, because of possible confounding factors. Many industrial occupations involve exposure to known carcinogens, such as benzene, and others involve exposure to possible carcinogens, such as aluminium workers who are exposed to very high magnetic fields, as well as to aluminium vapour and other gases associated with the smelting process.

Savitz and Calle summarise by stating that the data indicates a modest risk elevation in selected occupations, of 20% to 50%, but that the available data is inadequate to conclude that electromagnetic field exposures are the reason for that elevation (10).

4. Biological Studies

In order to show cause and effect, scientists are using laboratory animals and cells in test-tubes. No lifetime studies on animals have yet shown a link between field emissions and cancer, but there is considerable interest in studies which show that fields may influence the secretion of the hormone melatonin, by the pineal gland. (11) This hormone plays a part in the control of the circadian rhythms, the rhythms which tell the body whether it is night or day. The hormone may be suppressed, leading the body to believe that it is continuously day time. There has been a suggestion that such

an effect may cause depression in people, but there is also a tenuous link between melatonin and various types of cancer.

Among in vitro studies, the most controversial results concern the efflux of Calcium ions from brain cells, under the effect of electric and magnetic fields (12). Calcium is an important building block, and such an efflux can be linked to a breakdown of the cell physiology. The controversy stems from the extremely small fields which appear to cause such an effect. Dr. Carl Blackman has demonstrated an effect in his laboratory, at a magnetic field strength of 50 femto Tesla, at the limit of the most sophisticated measuring techniques available today. (13)

In addition, there appears to be a defined relationship between the static, or DC magnetic field and the intensity and frequency of the power frequency field. Such a result leads to the concept of "windows". Given a certain static magnetic field (the magnetic field of the earth), certain frequencies will cause Calcium efflux, and others will not, even at the same intensity (14). Similarly, at a given frequency, certain intensities will cause Calcium efflux, while higher intensities may not. If the idea of windows can be substantiated, it will cause considerable difficulty for health officials, and legislators.

5. Public Health Issues

Possible health effects are of great interest to public health officials because so many people are exposed to electric and magnetic fields. If exposure to fields above 0.2 micro Tesla leads to a doubling in the risk of leukaemia, and 20% of the population is exposed to such levels, then 16% of all leukaemias may be caused by magnetic fields. The financial and emotional cost to the public of supporting those cases is substantial enough to warrant further research.

However, the main driving force behind research is not the possible saving in taxes, but rather the more immediate and tangible saving to the utility from the keeping public happy. In the United States, planning a new transmission line is a long and costly process which almost always meets with public disapproval at some stage. In the past, such disapproval has been focussed on aesthetic considerations. Today, possible health effects are becoming a weapon in the hands of the public, as they provide a concrete objection to the building of a new line.

There are several reasons for public outcry:

Ignorance is a big problem. Even in the electrical engineering community, there are people who do not clearly understand how electric and magnetic fields propagate. Explaining those concepts to a lay person is a challenge. In addition, the equally complex field of medicine enters the picture. There are few people who understand the electrical and medical issues well enough to explain them to the general public, particularly as those issues have not bee fully explained, even in the scientific community.

To decide whether a risk is justified, its cost may be compared to the benefits coming from it. For example, the enormous benefits from chlorinating drinking water far outweigh the small risk of cancer associated with it. On a nationwide scale, the benefits of electric power are likely to outweigh any risks which may be demonstrated. Unfortunately, an individual who lives near a high voltage transmission line may perceive a large risk from that line. While the benefit of the line to society may be large, on an individual scale, the benefit is perceived to be small.

The issue of perception is crucial in dealing with the public: The actual risk is less important than whether the public perceives a risk to exist. If it perceives itself at risk, the cost in direct and indirect terms to the utility can be very large. New lines may be delayed, and existing lines may have to be rerouted away from urban areas and schools.

In addition to the perception of risk, the public also uses the issue of health effects for more selfish ends. It has been suggested that power companies are viewed in the same light as the government: huge bureaucracies that do exactly as they please, and take very little note of their consumers. A line siting issue gives those consumers power over the behemoth. In addition, health effects are a handy excuse for having unsightly lines routed away from built-up areas.

6. Legislation

Legislation has been passed in several countries, to limit the electric fields associated with high voltage transmission

lines. The levels chosen are usually based on the effects of induced currents: An electric field from a line will charge up a nearby conducting object, such as a vehicle or a fence, if it is insulated from the ground. If a person touches such an object, a current will flow to earth. If that current is large enough, it may cause death. Electric field legislation is usually based on a field strength which will keep the current flowing to a value below the let-go threshold - the point at which an uncontrollable muscle action prevents a person from letting go of the charged object.

Magnetic field legislation is not common at present. The state of Florida has adopted levels of 15-25 micro Tesla for various lines, and the state of New York is about to legislate on the issue. The values chosen are based on the status quo. In Florida (15), it was decided that the findings on health effects are not conclusive enough to allow a "safe" level to be set, so the levels are based on existing lines, as no-one has yet demonstrated that such lines cause health effects.

Even though the legislation in Florida is not based on scientific findings, it has been very helpful to the utility, because it has relieved public pressure (16).

In South Africa, there is no existing legislation on electric and magnetic field strengths. Eskom has an internal standard of 10 kV/m for electric fields, based on the let-go threshold and previous 345 kV line designs. It has, as yet, no internal standard for magnetic fields, but research is being conducted at Eskom to determine a suitable value for such a standard (17).

7. Conclusions and Recommendations

At present, there is very little public concern locally about fields due to transmission lines. Several articles have appeared in the popular and technical press, but they have stirred up little interest. Such a situation is helpful because it allows a response to public concerns to be planned in advance. Such planning is necessary, because internationally such concern has proved to be very expensive for the utilities.

Experience has shown that information can overcome public fear. If the utility provides information and has an open policy towards questions, it usually evokes a favourable response from the public, even if the information itself is not favourable. In the long run, accurate information from the utility tends to overcome sensational reports in the press.

In order to provide information to allay public concerns in South Africa, it is recommended that a nucleus of expertise be established. Locally, some research is being conducted on rats. The expertise which is being built up allows a critical evaluation of overseas publications. It also promotes contact with international bodies, such as the Bioelectromagnetics Society.

The other areas which need to be developed locally are measurement and public relations. Measurement is a powerful tool in overcoming fear, as it shows the unknown quantitatively, and allows comparisons to be made. A person near a nuclear source may be terrified, even if experts proclaim it to be safe, until a Geiger counter shows the actual level of radiation. In a similar manner, measurements can show the general public the level of magnetic fields in their homes. Measurements of the South African domestic magnetic climate will also enable authorities make decisions on reducing fields, if international research shows such a reduction to be necessary.

Measurement must be considered hand in hand with public relations. It is essential that any queries from the general public be handled promptly, efficiently, and with no attempt at withholding what is known about the effects of fields. It is recommended that a group be set up in order to handle queries in a manner which will not promote panic. In such a way, the dangerous effects of sensation may be minimised. Eskom could contribute, but the group should be seen to be impartial. It is suggested that the National Energy Council established it, as they are an independent body with sufficient stature to guarantee State support. Any organisation which has queries from the public can then pass them to the group, to be dealt with in a sympathetic and competent manner.

Bibliography

The following texts provide a more complete introduction to the biological effects of power frequency fields:

1. "Electric and Magnetic Fields from 60 Hertz Electric Power: What do we know about possible health risks?", Granger Morgan M., Dept. of Electrical Engineering and Public Policy, Carnegie Mellon University, 1989

2. "Electrical and Biological Effects of Transmission Lines", Lee J. M., et al, U. S. Department of Energy, Bonneville Power Administration, Portland, Oregon, 1989

3. Carstensen E., "Biological Effects of Transmission Line Fields", Elsevier, New York, 1987

References

1. Asanova T. P., Rakov A. I., "The State of Health of Persons Working in Electric Field of Outdoor 400-kV and 500-kV Switchyards", Hygiene of Labour and Professional Diseases, 5, 1966

2. Wertheimer N., Leeper E., "Electrical Wiring Configurations and Childhood Cancer", American Journal of Epidemiology, Vol 109, No. 3, pp 273-284, 1979

3. Fulton J. P., Cobb S., Prebble L., Leone L., Forman E., "Electrical Configurations and Childhood Leukaemia in Rhode Island", American Journal of Epidemiology, Vol. 111, No. 3, pp 292-296, 1980

4. Savitz D. A., Wachtel H., Barnes F. A., John E. M., Tvrdik J. G., "Case-Control Study of Childhood Cancer and Exposure to 60-Hz Magnetic Fields", American Journal of Epidemiology, Vol 128, No. 1, pp 21-38, 1988

5. Savitz D. A., Open letter to persons concerned about reports of electromagnetic fields and childhood cancer, University of North Carolina at Chapel Hill.

6. Milham S., "Increased Mortality in Amateur Radio Operators due to Lymphatic and Haematopoietic Malignancies", American Journal of Epidemiology, Vol. 127, No. 1, pp 50-54, 1988

7. Milham S., "Mortality in Workers Exposed to Electromagnetic Fields", Environmental Health Perspectives, 62:297-300

8. Carstensen E., "Biological Effects of Transmission Line Fields", Elsevier, New York, 1987

9. Broadbent D. E., Broadbent M. H. P., Male J. C., Jones M. R. L., "Health of Workers Exposed to Electric Fields", British Journal of Industrial Medicine, Vol. 42 pp 75-84, 1986

10. Savitz D. A., Calle E. E., "Leukaemia and Occupational Exposure to Electromagnetic Fields: Review of Epidemiological Evidence", Journal of Occupational Medicine, Vol. 29, No. 1, pp 47-51, January 1987

11. Wilson B. W., Chess E. K., Anderson L. E., "60-Hz Electric-Field Effects on Pineal Melatonin Rhythms: Time Course for Onset and Recovery", Bioelectromagnetics, 7:239-242, 1986

12. Blackman C. F., Benane S. G., House D. E., Joines W. T., "Effects of ELF (1-120 Hz) and Modulated (50 Hz) RF Fields on the Efflux of Calcium Ions From Brain Tissue In Vitro", Bioelectromagnetics 6:1-11, 1985

13. Blackman C. F., Personal Communication, June 1990

14. Blackman C. F., Benane S. G., Elliott D. J., House D. E., Pollock M. M., "Influence of Electromagnetic Fields on the Efflux of Calcium Ions From Brain Tissue In Vitro: A Three-Model Analysis Consistent With the Frequency Response up to 510 Hz.", Bioelectromagnetics 9:215-227, 1988

15. Florida State Legislature: Chapter 17-274 "Electric and Magnetic Fields", Tampa, Florida, 1988

16. McNeal M., Personal Communication, Florida Power and Light, July 1990

17. Power Line Fields Seminar, Eskom, March 1990

APPLICATION OF AN INDUCTION MOTOR IN SOLAR-WATER PUMP

M MALENGRET, J DAVIES

(1) ABSTRACT

A solar energy photovoltaic source is utilised to pump water with an induction motor. The solar panel D.C.supply is converted to a variable frequency and voltage by a 3 phase semiconductor bridge. The ratio between frequency and voltage is such as to minimise motor losses. The frequency is controlled so as to obtain maximum power from the solar array.

(2) INTRODUCTION

Solar energy applications are gaining momentum with recent accelerated solar economical improvements. Solar photovoltaic (P.V.) panels are capturing an increasing portion of the energy market - Solar is now competitive against diesel systems up to 20KVA and may even be cost effective against coal based power stations within the next 15 years. This is perhaps an optimistic speculation. However, P.V. energy is not just an interesting technology for very special applications. Cost and efficiency improvements have been more rapid than anticipated and it is true to say that this technology deserved greater recognition. [1]

Solar energy is not yet competitive in the bulk energy market, applications in specialised spheres must first be developed. This is particularly true in remote areas where grid power is prohibitively expensive. Efforts in solar research and development can therefore be rewarded immediately while promoting a wider use of the technology.

One such project is water pumping in rural areas where grid power is too expensive to connect or install. Many third world countries still rely on diesel power for water pumping. In India there are 4 to 5 million diesel powered water pumps, each consuming about 3.5 kilowatts [1]. There are 13 million people in South Africa with inadequate water supplies - the Rural Water Trust's Board is envisaging 130 solar installations at schools in Natal [4]. Many farmers in semi-desert areas such as Namibia and the Karoo are beginning to utilize solar water pumps on a larger scale.

A popular pump in rural areas is the helical positive displacement pump. The water is pushed up by a corkscrew action. These are most often powered by diesel and some suppliers offer a P.V. powered system utilizing imported D.C. permanent motors. A D.C. to D.C. converter roughly matches the load to the panels.

U.C.T. Electrical and Electronic Engineering Department in conjunction with MLT DRIVES C.C. is experimenting with an induction motor based system. A working prototype has been built utilizing a rewound standard 1/2 HP induction motor. However the motor is not suitable and is only 65% efficient at it's best. A South African manufacturer will be supplying us with a 85% efficient motor.

The induction motor is 4 to 5 times less costly than a D.C. motor and is also relatively free from wear and tear. Efficiency similar to the existing D.C. motors can be achieved. In addition a P.V. maximum power point tracker control can add an overall 20% system efficiency [3]. This technique consists of dynamic matching between energy source and respective load. Matching is achieved by monitoring the output power of the energy source and modulating a control signal. The above regulates appropriately the operation of a source-load interface device. The device in our case is a 3 phase pulse-width modulated (P.W.M.) MOSFET inverter bridge, and the load an ordinary squirrel cage induction motor. (SEE FIG 1)

(3) 3 PHASE P.W.M. INVERTER

The bridge converter consists of 6 power MOSFETS and derives the power directly from the panel with only a shunt capacitor to smooth the supply ripple current (See Fig. 1). The D.C. supply is chopped into 3 phases sine-weighted waveform. The efficiency of the converter is very high as the switching devices dissipate little energy, hence the effect on converter operating point is ignored in our assumptions. A micro controller monitors the P.V. panels voltage and current and provides the appropriate voltage and frequency control signals to the motor.

Six signals from the microcontroller switch on or off each respective MOSFETS appropriately. The signals are optically coupled for reliability and for electric isolation. Each gate receives its power from a very small capacitance charge pump.

(4) OPTIMUM EFFICIENCY APPROACH

Undoubtedly the object of the pump is to obtain maximum water delivery. The pump used has a flat torque speed characteristic apart from a high starting torque requirement due to the pump's seal tightness. Due to the effective seal, water delivery in this positive displacement pump is directly proportional to speed. It is important that the pulley ratio between motor and pump be properly selected so as to match motor torque operational point with the most significant energy supply period. This would be obtained and refined from experimental data. Having selected a particular motor, pump and pulley, a relationship between fundamental converter frequency and voltage needs to be calculated.

The speed of an induction motor is determined by the applied synchronous converter frequency and the slip. The latter in turn is a function of load torque and flux density, (namely the volts to Hertz ratio). High flux density implies low slip and in turn lower rotor copper losses. However, too high flux density brings excessive eddy and hysteresis losses and stray losses. Hence there exists an ideal applied voltage for every frequency point so as to keep power losses within the motor to a minimum.

High effiency induction motor can be achieved by keeping the current, flux density low. It is believed that this will be achieved by oversizing the motor. The motor design will be the object of further research with the help of a motor manufacturer.

Nevertheless given a particular motor an optimum relationship between volts and frequency can be aproximately calculated from motor's equivalent circuit parameters and refined experimentally.

(5) THE VOLTS TO HERTZ RELATIONSHIP

The torque development by an induction motor from a simplified equivalent circuit ignoring primary resistance is: [5]

$$T = \frac{3 S V_1^2 R_2}{R_2^2 + (S X_2)^2} \qquad (1)$$

Where R_2 is the rotor resistance per phase referred to primary.

X_2 is the rotor winding and stator leakage reactance per phase referred to primary winding.

V_1 fundamental RMS phase voltage.

W_s fundamental synchronous angular velocity: RADS/SEC.

S the slip.

If the slip is small then $R_2 << S X_2$. The torque is simplified further to:

$$T \approx 1/\omega_s \times S V_1^2 / R_2 \qquad (2)$$

$$\text{OR } S = K_1 / V_1^2 \quad \text{Where} \quad K_1 = T \omega_s R_2 \qquad (3)$$

The phase current is approximately

$$I_1 \simeq S V_1 / R_2 \qquad (4)$$

Neglecting friction and stray losses the power losses per phase are iron + copper losses and is approximately equal to

$$P_{Loss} = V_1^2/R_c + I_1^2 (R_1 + R_2) \quad (5)$$

Where Rc is the resistance representing the magnetic power losses.
Differentiating with respect to V_1 and equating to zero

$$d/dV_1 \left[V_1^2/R_c + I_1^2 (R_1 + R_2) \right] = 0 \quad (6)$$

substituting I, and S from (3) and (4) into (5)

$$V_1 = \left[K_1^2/R_c (R_1 + R_2) \right]^{1/2} \quad (7)$$

$$\therefore V_1 \propto \omega_s^{1/2} \quad (8)$$

since torque is constant and determined by the load. Optimum applied phase voltage is $v_1 = f(f_s)$ a function of fundamental frequency only. The motor will be sufficiently magnetized to keep the total slip and magnetizing losses to a minimum. From (1) the slip is determined by V_1 and f_s.The motor will hence operate at it's best efficiency if the above relationship between f and v is maintained throughout the speed range.

More accurate results can now be calculated from better motor characteristics measured experimentally at the approximate voltage and frequency determined above.

A table of optimum relationship vis a vis the motor can be drawn and stored into an Eprom. The microcontroller will ensure this relationship by modulating the mark-to-space ratio of the sine-weighted PWM signal.

The microcontroller must still establish the value of the output frequency. This depends on external climatic conditions. For the panel to deliver it's maximum power the input voltage to the converter will be kept at it's peak power point utilizing the following technique.

(5) P.V. PANEL MAXIMUM POWER POINT TRACKER

Fig. 2 shows the output characteristics of a P.V. panel array, taking the light intensity E_e as a parameter. I_s, V_s and P_s are the output current, the output voltage and the output power. These are also dependent on the panel temperature. The solar cell maximum power point shifts along with light intensity and temperature. To derive the relationship is highly complex [3]. A relatively well known simple method is to establish which side of the power curve the panels are operating and shift the point towards its maximum - See Fig. 3.

If the applied frequency to the motor is varied marginally and slowly - the current and voltage from the panel will vary. The microcontroller can multiply the latter and establish if an increase or decrease in power results. The converter frequency would then be shifted in the right direction and track the maximum point. The variation in climatic variation is slow and therefore the frequency modulation can be done very slowly in relationship to the motor time constants.

CONCLUSION

A solar photovoltaic energy source is utilised to pump water. The motor is an induction motor driven by a semiconductor 3 phase bridge.

A method to optimize volts to Hertz ratio in an induction motor driven by a P.W.M. converter is briefly presented. Nothing much about motor design has been given and will be the subject of future work.

A maximum source power tracking contol is utilised. The induction motor frequency and voltage is modulated by a microcontroller so as to minimise motor losses.

REFERENCES

[1] Scientific American September 1990 Special issue.

[2] K.C. KALAITZAICIS and G.J. VOCHTSEVANCES, "Design of a Power Conditioning Unit for Nonlinear Source - Load Systems", IEEE Transactions on Industrial Electronics, Vol 1E-31, No 4, Nov 84.

[3] H. MATSUO and F. FUROKAWA "New Solar Cell Power Supply System using a Boost type bidirectional AC-DC Converter".

[4] The Rural Water Trust c/o M.D. OLIN (Pty)Ltd P O Box 114, Bergvlei, 2012.

[5] M.G.SAY, "Alternating Current Machines Induction Machines - Theory and Performance", Fourth Edition, Page 270.

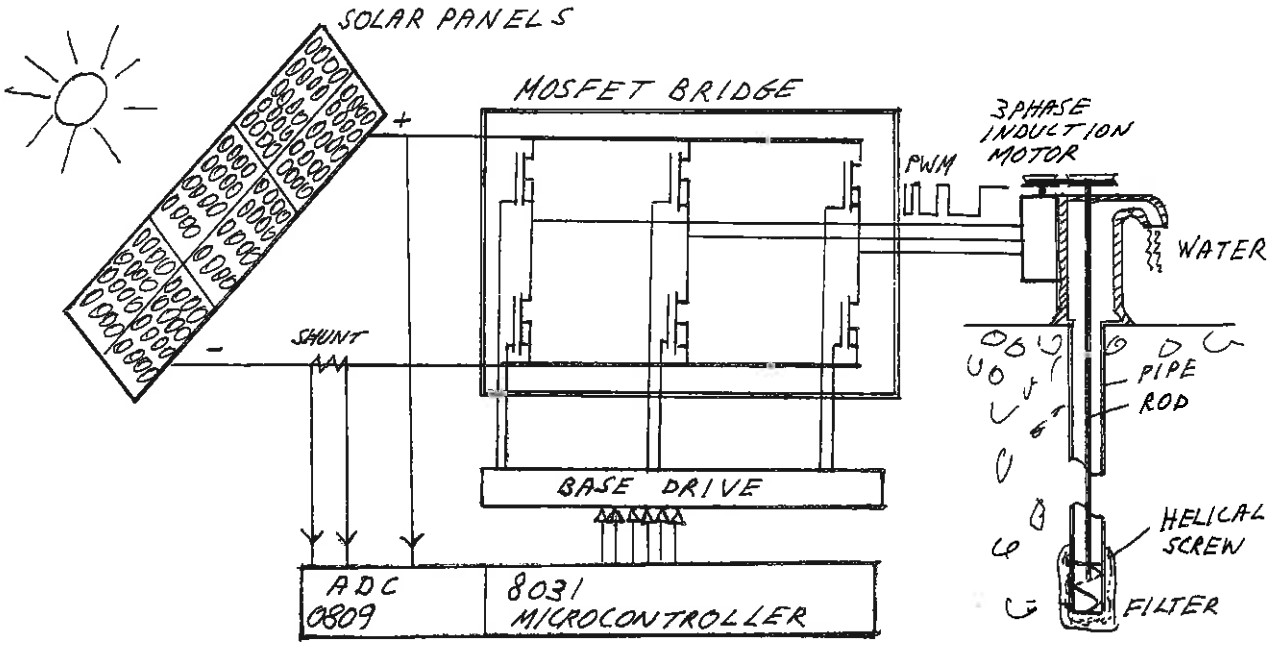

FIG 1 SYSTEM CONFIGURATION

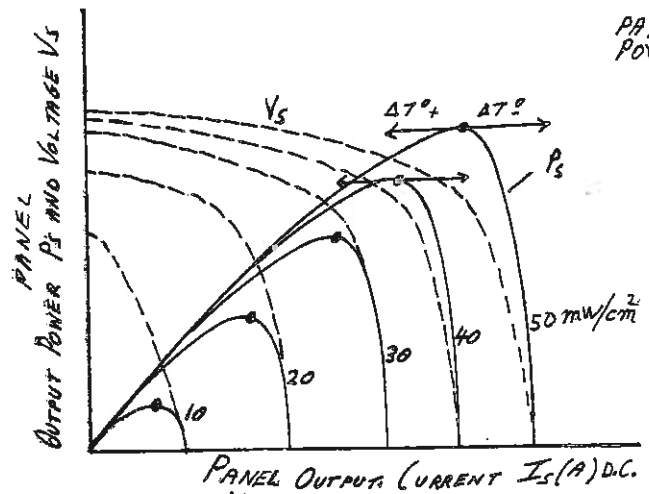

FIG 2 MAXIMUM POWER POINTS FOR DIFFERENT LIGHT INTENSITY AND PANEL TEMPERATURE

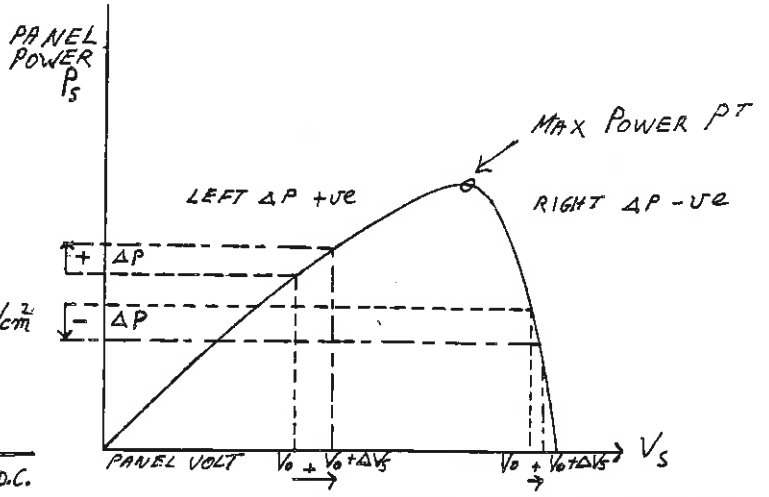

ΔV RESULT FROM Δfs MODULATION

FIG 3 MAXIMUM POWER TRACKING PRINCIPLE ASSUME OPERATING POINT V_o ON LEFT AND RIGHT OF PEAK POWER POINT

ROLLING ROTOR SWITCHED RELUCTANCE MOTOR

E. D. Smith*

SUMMARY

A new version of a motor, belonging to the class of Rolling Rotor Motors is described together with it s controller. Tests on an experimental model are compared with theoretical calculations. Attention is drawn to the motor's robustness and simplicity so that it can be considered for low cost applications where large torque and low speed is required from a gearless construction. Possible areas of application are presented.

INTRODUCTION

A particular class of machines called Torque Motors or Ring Motors have found unique application in aerospace, defence and industrial drives. The reason for this success lies in the high-torque direct drive, low cost and gearless servo-capability better than 0,5 seconds of arc [1].

The machine is a DC commutator motor of frameless construction, Fig. 1, which is mounted in cavities that have previously been machined to receive it. Fig. 2 shows a hypothetical example of an automatic sentry. The Torque motor could typically be placed in the turret and drive directly the boss or axle shown. Low cost is achieved by the elimination of the motor-frame, gearbox and coupling.

A new machine, the Rolling Rotor Switch Reluctance motor (RRSR), is described here. This has the capability of fulfilling the functions which are, at present, covered by the Torque motor. The two machines are compared below with respect to torque per unit rotor swept volume, rotor moment of inertia and cost.

---

* Department of Electrical Engineering
University of Pretoria
Pretoria 0002

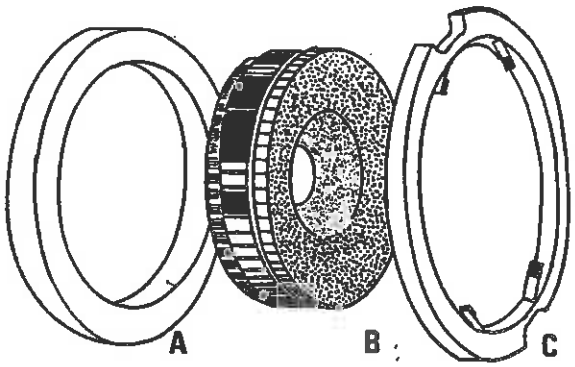

Fig. 1 : An exploded view of a Torque motor.
A) Permanent magnet stator
B) Rotor and commutator
C) Brush gear.

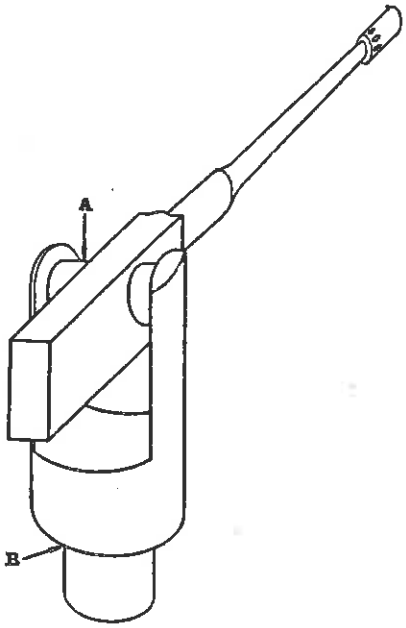

Fig. 2 : An example where gearless servo motors can be inserted into machined housings at A and B.

Present RSA technological policy is: "export rather than import replacement". The RRSR motor is examined in terms of its potential contribution in promising an improved drive, at reduced cost.

DESCRIPTION

A view along the axis of a RRSR motor is shown in Fig. 3. The central rotor is constructed of iron without windings or sliding contacts. It is free to rotate only. The stator is constrained from rotating but can execute excursions in the EB direction and its orthogonal.

The stator position has been shown with coil A energised. The next step in the sequence of motor operation is the energising of coil B while reducing current in coil A to zero. Thereafter coil C and D etc. in switched reluctance motor style. The rolling contact line between rotor and stator revolves at an angular velocity of n.

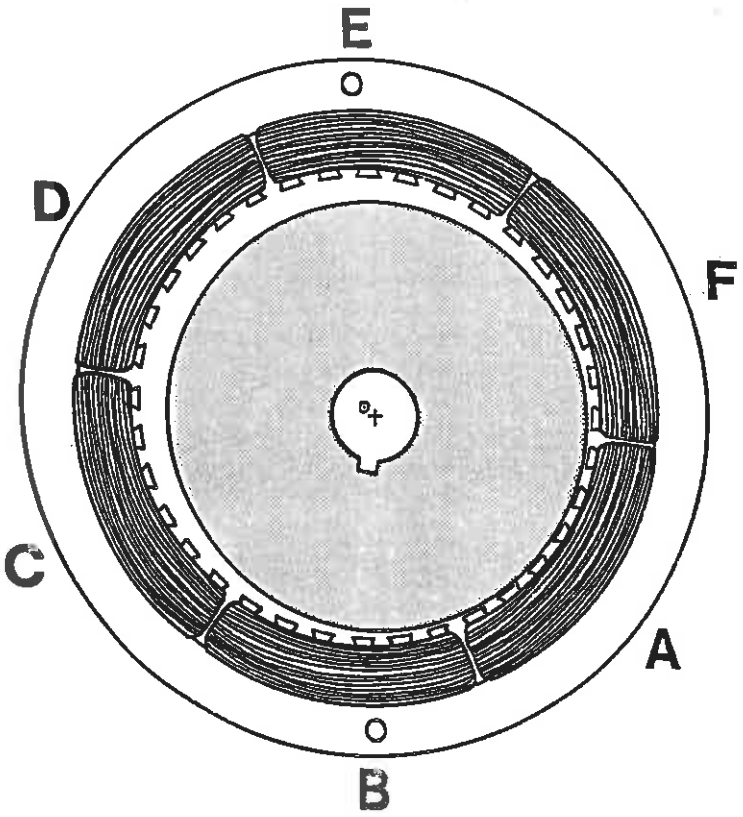

Fig. 3 : A diagrammatic representation of a RRSR motor. The stator can execute small orthogonal oscillations in the plane of the paper.

The rotor slowly turns in the opposite direction at angular velocity N given by:

$$\frac{N}{n} = \frac{D_s - D_r}{D_r} \qquad (1)$$

where D_s = stator internal diameter.
D_r = rotor diameter.

Lange torques can theoretically be delivered by the rotor which exceeds its basic torque by the effective friction gear effect.

These torques would be in the same ratio as in equation (1) if sufficient (non-slip) friction could be obtained between rotor and stator [2].

EXPERIMENTAL MOTOR

An experimental machine was constructed according to the specification below, in order to investigate the extent of the rotor-stator slipping under limiting load conditions.

SPECIFICATION

Standard AC machine laminations with 36 teeth formed the basis of the experimental machine. These laminations, however, were pressed from ordinary mild steel. The main dimensions were as follows:

Yoke thickness	=	0,0212 m
D_s	=	0,0889 m
D_r	=	0,0883 m

Each of the six coils was made as a concentric winding with 40 inner turns, 100 central and 100 outer turns.

TEST

The six windings of the motor were fed from the simple controller shown in Fig. 4. This was in turn fed from a low frequency three-phase AC supply.

The measured torque derived from the machine is illustrated graphically in Fig. 5.

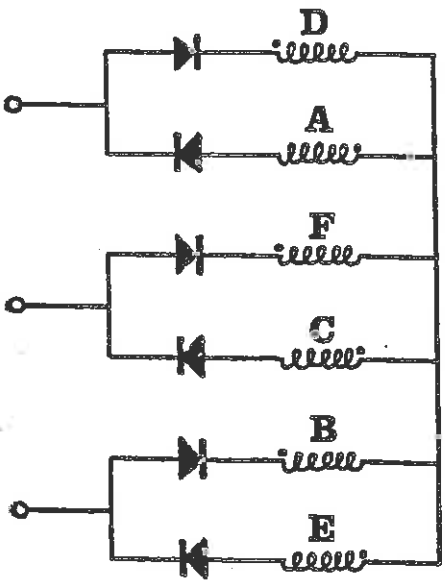

Fig. 4 : A simple controller for providing overlapping current pulses, sequentially to the six windings.

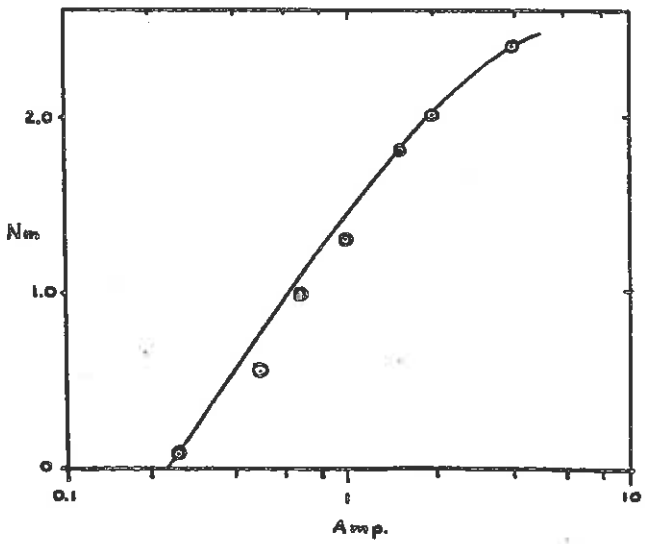

Fig. 5 : The torque provided by the experimental motor for various values of the three phase current inputs to the controller.

TORQUE

Fig. 5 shows that the maximum torque developed by the motor at 4A was 2,4 Nm. This may be compared to the calculated [2] value of 115 Nm for this machine. The large difference in these two torques can be ascribed to insufficient friction between the rotor and stator.

These values are compared to the theoretical maximum torque and obtained torque of the Torque motor of similar size in Table I.

Table I : Comparison between RRSR motor and Torque motor on the basis of torque per unit rotor swept volume.

Motor	Torque Considered	Reference	Torque in Nm/m^3
RRSR Motor	Measured	here	$1,8 \times 10^4$
	Calculated	[2]	87×10^4
Torque Motor	Typically specified by a manufacturer	[3]	2×10^4
	Calculated	[4]	$6,56 \times 10^4$

It emerges clearly from Table I that significantly higher torques can be obtained from the RRSR motor if the rotor/stator friction can be increased.

Future research on this machine will be directed at attempts to achieve this by employing a wedging action (Fig. 6) similar to that found between a V belt and pulley.

MOMENT OF INERTIA

The rotor of the RRSR motor can be in the form of a hollow pipe which allows considerable potential for reduction of the moment of inertia. This aspect compares favourably with the Torque motor which has to carry a commutator and windings on the rotor.

The RRSR rotor therefore lends itself to potential application as a rapid reacting servo motor.

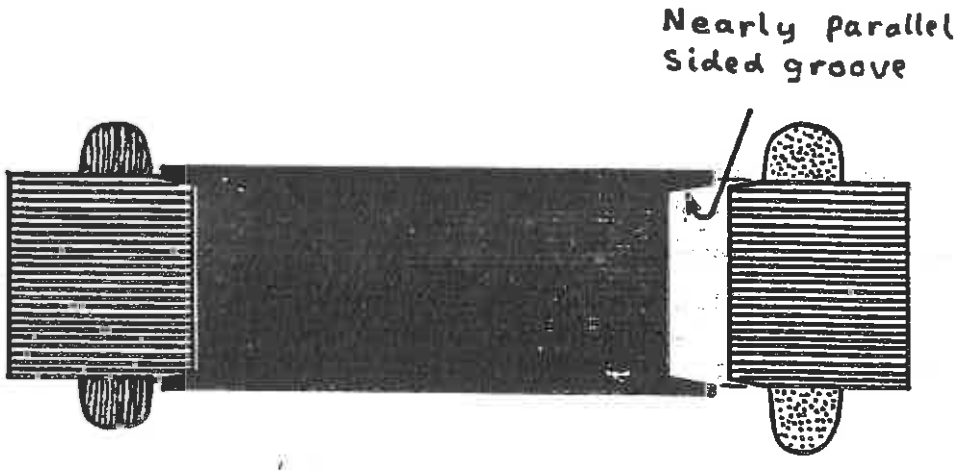

Fig. 6 : A section through a RRSR motor showing wedging action between rotor and stator as a means of increasing the friction between these two members.

COST

An examination of the component costs of DC motors usually show the commutator to be one of the most costly items. By eliminating this in the RRSR motor a significant saving becomes possible.

CONCLUSION

An experimental investigation of the RRSR motor shows it to offer potential improvements over the conventional Torque motor.

Main advantages are:

a) High torque in gearless construction.
b) Rapid response for servo applications.
c) Reduced construction cost.

APPLICATIONS

Examples of possible applications for the RRSR machine are illustrated in Figs. 2 and 7. In Fig. 7 the motor is used to steer the parabolic solar collector in azimuth by driving directly on the extended axles of the wheels.

The elevation is shown being controlled by a RRSR motor with a screw thread cut in its rotor. This rotates around the threaded shaft providing linear thrust.

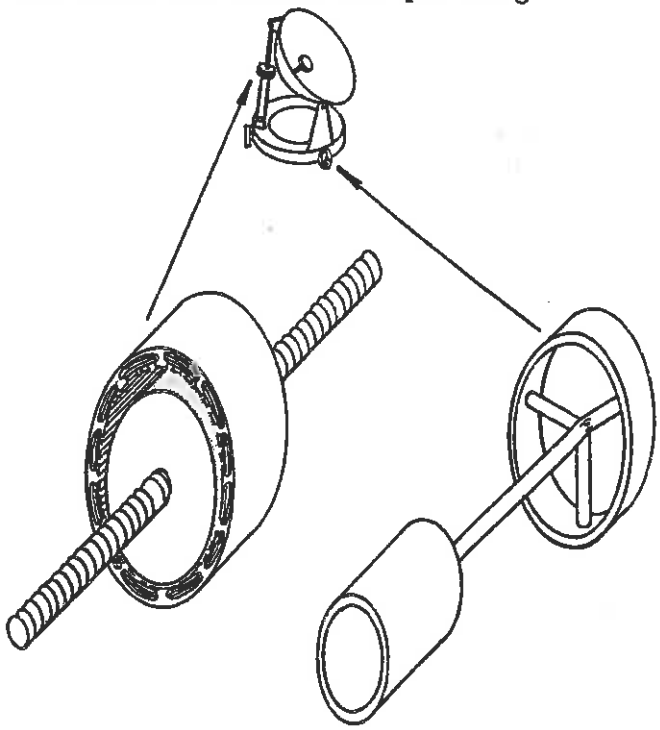

Fig. 7 : Possible applications for RRSR motors in steering a parabolic solar collector.

REFERENCES

[1] Strasheim, A., Thain, M.E., Walters, N.M., Claase, C., Human, H.G.C. and Ferreira, N.P. : "New Versatile Computer Controlled Direct Reading Emission Spectrometer", Spectro Chemimca Acta, Vol. 38B, No. 5-6, pp. 921-936, (1983).

[2] Ashen, R.A. and Bolton, H.R. : "Aspects of Hypocycloidal Reluctance Motor", IEE Proceedings, Vol. 128, Pt. B, No. 6, Nov. 1981, pp. 313-322.

[3] Inland Motor Division ; "DC Torque Motors", Kollmorgen Corporation, Radford, Virginia 24141, USA, 48 p.

[4] Mukherji, N.C. and Tustin, A. : "Vernier Reluctance Motor", IEE Proceedings, Vol. 121, No. 9, (Sept. 1974), pp. 965-974.

VERTICAL DRIVE SYSTEM WITH LINEAR INDUCTION MOTORS

J. F. GIERAS

Dept. of Electrical and Electronic Engineering
University of Cape Town
Rondebosch 7700

ABSTRACT

The application of linear induction motors (LIMs) to vertical drives seems to be promising. A single-sided LIM with a high standstill force and low synchronous speed displays a suitable performance. Typical applications include drop-towers, hoisting systems for deep shafts, elevators for rocket launchers, etc. The paper discusses LIMs with a long primary. General requirements, construction,and performance have been described. A sizing procedure of the LIM has been proposed. Advantages and disadvantages have been discussed.

INTRODUCTION

The first applications of vertical drive systems with linear induction motors (LIMs) to electric hammers and oil pumps have appeared in USSR in the early sixties [1,2]. An electric hammer with a tubular LIM is shown in Fig. 1. An oil piston pump driven by a tubular LIM is shown in Fig. 2. This idea has been abandoned. However, after nearly thirty years, promising experimental investigations on a small-scale elevator with LIMs have been made in Japan [3]. Particular attention has been paid to steady-state and dynamic characteristics by using computer control.

This paper considers an attempt of application of LIMs to elevators. Of course, at this stage only theoretical considerations and introductory calculations have been made and further experiments are necessary.

2. ELEVATOR WITH LINEAR INDUCTION MOTORS

Fig. 3 shows an elevator driven by LIMs. Flat single-sided LIMs with long primary and short secondary have been applied. Such design eliminates energy supply to the car. A long primary consists of a set of units. The length of each unit is approximately equal to the height of the car (or skip). There are two rows of units located at each side of the car. An unit is made of laminations with a three-phase double-layer winding located in slots. The magnetic flux distribution in the airgap is shown in Fig. 4. The secondary (reaction rail) consists of an aluminum cap over solid back iron fixed to the car. A secondary cage winding is sometimes recommended. Although more expensive, it gives better performance [4]. Each car is equipped with two reaction rails as in Fig. 3. Steel wheels and rails are used for the lateral support and guidance.

The parallel connected LIMs located at each side of the car are fed from a common thyristor inverter with only one central controller. Any deviation of the pole pitches of LIMs at each side of the car may cause unequal loading of the parallel connected motors. There is no effect of unequal wheel diameters on the performance (thrust produced by LIMs).

To save the electrical energy and to lower the temperature of the windings, only the units passed by the car are fed. A computer controlled power supply system

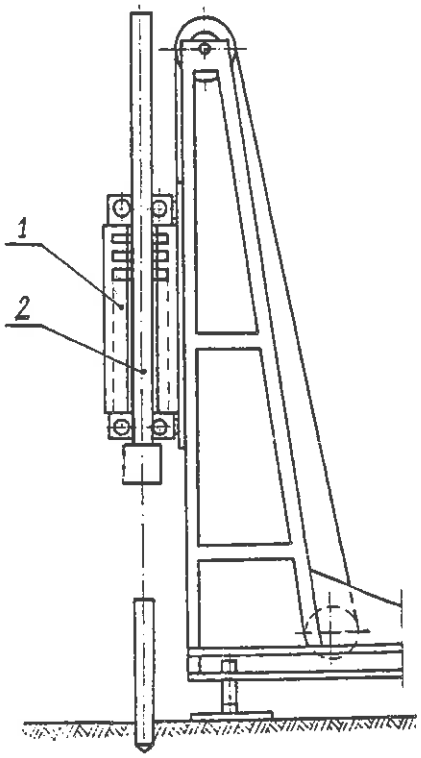

Fig. 1. Electric hammer with a tubular LIM: 1 - primary, 2 - secondary

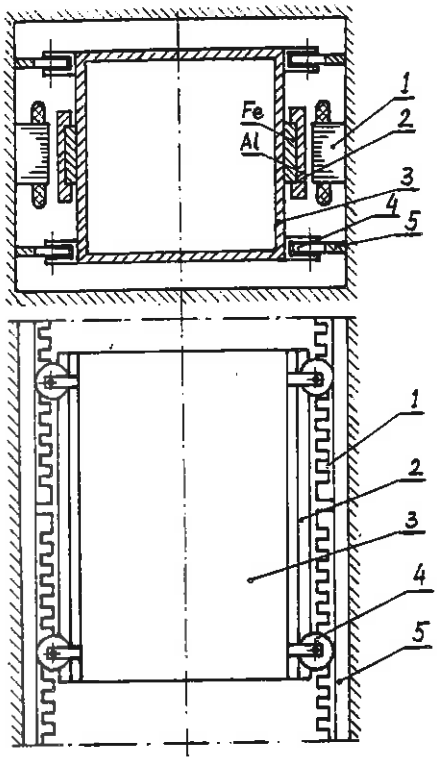

Fig. 3. Elevator driven by flat single-sided LIMs: 1- primary, 2 - reaction rail, 3 - car, 4 - guide roller, 5 - guide rail. Emergency brakes are not shown.

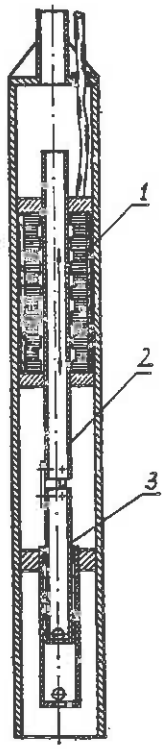

Fig. 2. Oil pump with a tubular LIM: 1 - primary, 2 - secondary, 3 - piston

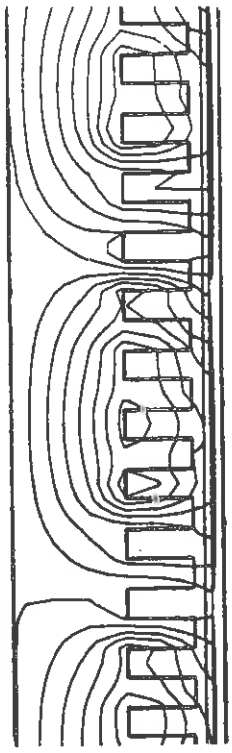

Fig. 4. Magnetic flux distribution of a single-sided LIM for $s < 1$

is required. If the car moves upward, the LIMs produce thrust to overcame the weight of the car, its inertia, and friction. If the car moves downward, the LIMs produce braking force. Plugging or dc injection braking is recommended.

Typical steady-state load characteristics of a vertical single-sided LIM are shown in Fig. 5. Deceleration and speed vs time for braking test on a small-scale vertical LIM are plotted in Fig. 6 [3].

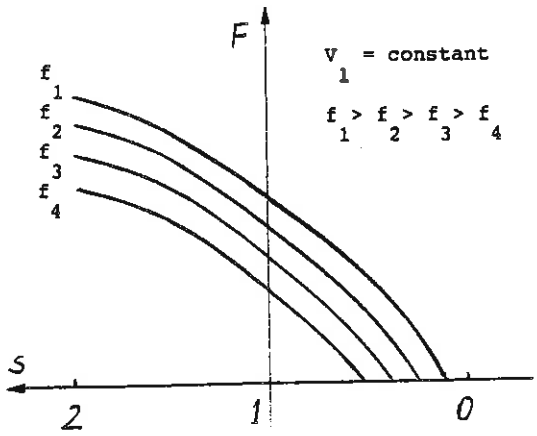

Fig. 5. Thrust F vs slip s at constant input voltage V_1 and frequency f for a single-sided LIM with $L_i/\tau \geq 2$.

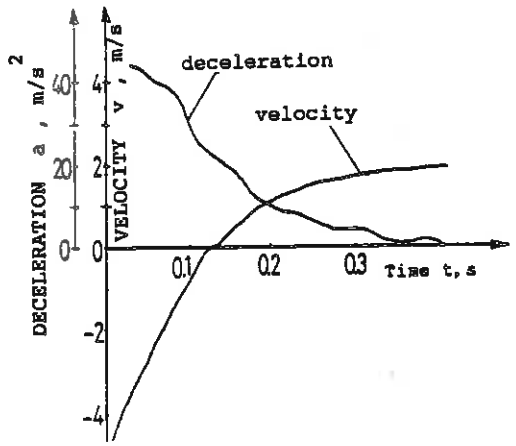

Fig. 6. Braking test obtained by reversal of the travelling-wave airgap field (plugging) using a small-scale vertical LIM (L_τ = 3 m, L_i = 0.03 m, τ = 0.075 m, m = 1 kg)[3].

3. ADVANTAGES AND DISADVANTAGES

The most important advantages of a vertical drive system with LIMs are:

(i) the rope and energy supply to the car is eliminated;

(ii) low level of noice produced by LIMs;

(iiI) computerized central control system;

(iv) high reliability;

(v) easy maintenance.

For example, as mining operations take place at depths exceeding 2000 m, multi-rope winding systems are installed. To equalize rope tensions, multi-rope winders utilise hydraulic compensators units mounted in the headgear [5]. A car (or skip) driven by LIMs can simplify the hoisting system provided that such a design is feasible. Additional benefit is an one-compartment shaft instead of a two-compartment shaft (for ascending and descending car).

On the other hand, it is impossible to avoid the following disadventages, namely:

(i) higher cost than that of a drive system with rotary motors;

(ii) higher energy consumption than in case of a drive system with rotary motors;

(iii) low power factor of LIMs due to large airgap (5 mm or even more).

4. FUNDAMENTAL EQUATIONS

By applying d'Alembert's principle to the elevator drive system, the force equation has the form

$$m \frac{dv}{dt} + Dv + K_s x \pm P = \pm F \qquad (1)$$

where: m = mass of the loaded car, t = time v = dx/dt = speed, D = coefficient of friction, K_s = spring compliance, x = distance travelled, P = m g = force of weight, g = acceleration of gravity, F =

thrust or braking force being developed by LIMs. If the car is driven upward, the LIMs develop thrust and the sign for F and P is "+". If the car is driven downward, the LIMs produce braking force and the sign for F and P is minus.

Neglecting friction and assuming $K_s = 0$, the eqn (1) is simplified, i.e.

$$m\left(\frac{dv}{dt} \pm g\right) \approx \pm F \qquad (2)$$

The main dimensions of a LIM, i.e. pole pitch τ, length of the primary core L_τ, width of the primary core L_i, and the air gap g (mechanical clearance) can be estimated with the aid of so called "output coefficient" (Fig.7 and 8)[1,6-8]:

$$\sigma_p = S_g / (v_s A) \qquad (3)$$

where:

(i) apparent power crossing the airgap

$$S_g = 3 E_1 I_1 \qquad (4)$$

(ii) active surface of the primary core

$$A = L_i L_\tau \qquad (5)$$

(iii) synchronous speed

$$v_s = 2 f \tau = v/(1 - s) \qquad (6)$$

The EMF $E_1 << V_1$, and the input phase current

$$I_1 = F v/(3 V_1 \eta \cos\phi) \qquad (7)$$

where V_1 = input phase voltage, η = efficiency, and $\cos\phi$ = power factor. Usually, $0.1 \leq \eta \cos\phi \leq 0.5$ (Fig. 9).

The output coefficient according to eqn. (1) allows to find the product $A_{my} B_{mg}$ where

$$A_{my} = 3\sqrt{2}\, I_1 N_1 / (\tau p) \qquad (8)$$

is the peak value of the primary line-current density and B_{mg} is the peak value of the airgap magnetic flux density (normal component). The airgap magnetic flux density $0.2 \leq B_{mg} \leq 0.7$ T, the line-current density $20\,000 \leq A_{my} \leq 240\,000$ A/m, and $10\,000 \leq B_{mg} A_{my} \leq 120\,000$ TA/m. For given thrust F, the width L_i in eqn (5)

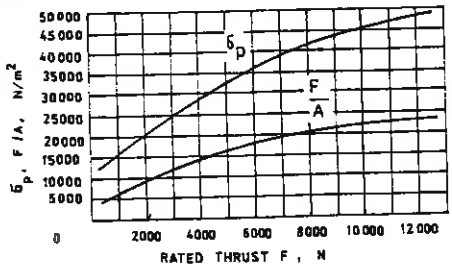

Fig. 7. Output coefficient σ_p and thrust per unit area F/A plotted against thrust at rated speed for large single-sided LIMs.

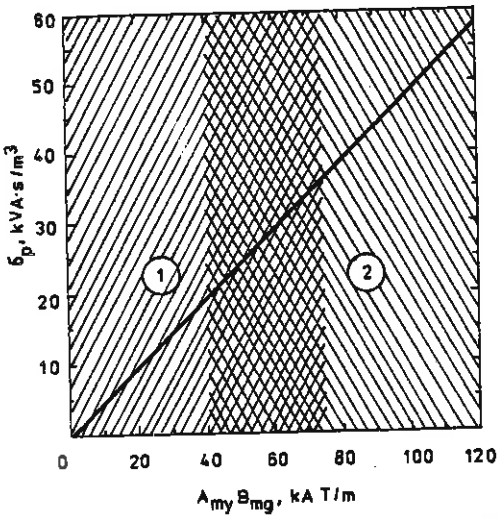

Fig. 8. Output coefficient σ_p as a function of $A_{my} B_{mg}$:

1 values of $A_{my} B_{mg}$ for small LIMs and for LIMs for industrial applications

2 values of $A_{my} B_{mg}$ for traction LIMs

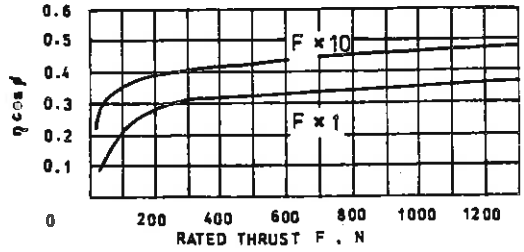

Fig. 9. (Efficiency x power factor) product plotted against thrust F at rated speed for single-sided LIMs

can be estimated using graphs plotted in Fig. 7 , where $F/A = F/(L_i L_\tau)$. Mechanical limitations allow to choose $5 \leq g \leq 15$ mm for large LIMs.

5. EXAMPLE

Find the main dimensions of LIMs for a passanger lift drive system to obtain the speed v = 3m/s and the upward acceleration a = 1.5 m/s² . The mass of the loaded car is m = 2000 kg, the input voltage (line-to line) is 380 V, and the input frequency is f = 50 Hz.

Note there is no limit to the velocity at which a passanger may travel in an enclosed lift car, but that acceleration (deceleration) should be limited to about 1.5 m/s^2 [9].

According to eqn (2) the necessary thrust developed by LIMs is $F = (a + g)\, m = (1.5 + 9.81)2000 = 22620$ N Two units, each of them developing 12-kN thrust can assure these demands. Assuming $v_s = 5$ m/s, the slip $s = (5-3)/5 = 0.4$, and, according to eqn. (6), the pole pitch $\tau = 5/(2 \times 50) = 0.05$ m. Fig. 9 gives $\eta \cos\phi \approx 0.45$. Assuming $E_1 \approx 0.5\, V_1 = 110$ V the phase current from eqn (7) $I_1 = 12000 \times 3/(3 \times 220 \times 0.45) = 121$ A, and the airgap apparent power $S_g = 3 \times 110 \times 121 \approx 40$ kVA - eqn (4). The length of the secondary as well as the length of the primary stack is assumed $L_\tau = 2$ m. Fig. 7 gives $F/A = 23\,000$ N/m^2. The active surface of the primary stack $A = 12000/23000 = 0.522$ m^2. The width of the primry stack $L_i = A/L_\tau = 0.26$ m. The width of the secondary back iron must also be at least 0.26 m. The output coefficient from eqn (3) $\sigma_p = 40\,000/(5 \times 0.522) = 15\,300$ VAs/m^3. Fig. 8 gives $A_{my} B_{mg} = 32\,000$ AT/m. If $B_{mg} \approx 0.5$ T, then $A_{my} = 32\,000/0.5 = 64$ kA/m. Since the number of pole pairs $p = L_\tau/(2\tau) = 2/(2 \times 0.05) = 20$, the number of turns per phase should approximately be $N_1 = 64\,000 \times 0.05 \times 20/(3\sqrt{2} \times 120) \approx 126$ - eqn (8). Of course, detailed electromagnetic calculations are necessary [1, 10-13]. The car is equipped with at least four guide rollers at each active surface, so that the airgap can be small, say, g = 5 mm.

Assuming the power factor $\cos\phi \approx 0.55$ and at least four LIMs (two at each side) being fed with current at the same time, the estimated electric power consumption is $P_{in} = 4\,(3\, V_1 I_1 \cos\phi) = 4 \times 3 \times 220 \times 121 \times 0.55 \approx 176$ kW. It is rather high power consumption as compared with that of a rotary motor drive system.

6. CONCLUSIONS

The fundamental advantage of the application of LIMs to elevators or hoisting systems is the elimination of ropes. On the other hand, the power consumption in case of a linear drive system is higher than that in case of a traditional drive system with rotary motors. Therefore the application of a linear drive system should be economically justified, e.g. deep shafts, light continuous arm elevators for packages, elevators with reduced level of noise, etc.

Other linear motors, for example long primary synchronous linear motors with permanent magnet excitation system should also be considered.

REFERENCES

1 Gieras J.: "Linear induction motors" (in Polish), WNT, Warsaw, 1990

2 Iżelya G.I., Rebrov S.A., and Sapovalenko A.G.: "Linear asynchronous motors" (in Russian), Technika, Kiev, 1975

3 Ebihara D., et al.: "Characteristics of a linear induction motor to vertical drive system", Int. Conf. Maglev'89, Yokohama (Japan), 1989, pp. 369-374

4 Gieras J.F.: "Design strategy of linear induction drives for industrial applications", Electrical Drives Symposium EDS'90, Capri (Italy), 1990, pp. 285-290

5 Swart R.P.: "Winding from a depth of 2400 metres", First Group Engineering Symposium, Randburg (RSA), 1986, pp. 321-329

6 Gieras J.F. : "Sizing equations and magnetic circuit design for single-sided linear induction motors", Int. Conf. on Electrical Machines ICEM'90, Cambridge, MIT (USA), 1990, pp. 498-503

7 Gieras J.F.: "Design strategy of single -sided linear induction motors for propulsion of wheel-on-rail vehicles", SAUPEC'90, Stellenbosch, 1989, Paper Number 6.3

8 Gieras J.F.: "The aspects of design of single-sided linear induction motors for transport and industrial applications", Int. Conf. MAGLEV'89, Yokohama (Japan), pp. 321-326

9 Barney G.C., and dos Santos S.M.: "Lift traffic analysis design and control", Peter Peregrinus Ltd, Stevenage, 1977

10 Gieras J.F. et al.: "Performance calculation for single-sided linear induction motors with a solid steel reaction plate under constant current excitation", IEE Proceedings, vol. 132, Pt. B, No 4, 1985, pp. 185-194

11 Gieras J.F. et al.: "Performance calculation for single-sided linear induction motors with a double-layer reaction rail under constant current excitation", IEEE Trans. on Magnetics, vol. MAG-22, No 1, 1986, pp. 54-62

12 Gieras J.F. et al.: "Calculation of thrust for a single-sided linear induction motor, taking into account phase unbalance and higher time harmonics", Archiv für Elektrotechnik, vol. 73, 1990, pp. 299-308

13 Gieras J.F. et al.: "An evaluation of the effect of varying the side-bar cross section on the performance of single-sided linear induction motor", Int. Conf. on Elec. Machines ICEM'88, Pisa (Italy), 1988, pp. 159-164

Parameterafskatting en implementering van 'n mikrodinamiese drywingsfilter.

C J Oliver G L Van Harmelen J H R Enslin

Departement Elektriese Ingenieurswese, Universiteit van Pretoria, Pretoria
Republiek van Suid-Afrika

Inleiding.

Die kompensasie van vervormde lasse is 'n onderwerp wat deesdae van meer belang word [1,2]. Die kompensasie van vervorming behels die stoor van energie en die lewering daarvan wanneer dit vereis word, sodat die belading van die toevoer minimeer word en die stroom 'n suiwer sinusverloop in fase met die spanning vertoon [2].

Die beginsel van mikrokompensasie is om 'n grootter lasvermoë te kan kompenseer met 'n kleiner mikrokompensator. So kan bv. 'n 5kVA dinamiese kompensator gebruik word om 'n 100kVA las te kompenseer. Die mikrokompensator is slegs verantwoordelik om die dinamiese vervorming en die hoë frekwensie (>500Hz) vervormingskomponente te kompenseer. Arbeidsfaktorverbetering word uitgevoer deur gebruik te maak van eksterne arbeidsfaktorkapasitors. Dus sluit sodanige mikrokompensator ook nie die 5^e en 7^e bofrekwensiefiltering in nie sodanige filtering word gewoonlik d.m.v. passiewe komponente bewerkstellig [4,5].

Die verliese intern aan die mikrokompensator is nie weglaatbaar nie. Die beheerder moet dus vir die interne verliese kompenseer om die volledige werking daarvan te verseker [1,3].

Parameterafskatting van 'n spanningsgevoerde dinamiese kompensator.

Die bepaling van verliese intern tot die dinamiese drywingsfilter is nie primêr die doel van parameterafskatting nie. Die spanning oor die kapasitor (stoorelement) is verteenwoordigend van die energie daarin.

Die afskatting van die parameters van 'n dinamiese drywingsfilter word hoofsaaklik benodig vir die syferbeheerder van die kompensator [3]. Verder word die parameters ook benodig in die aanlyn-kompensasie van die verliese van die kompensator. Die beheerder vorm dan 'n enkele mikroverwerkerbeheerder wat op gereëlde tussenposes wel die parameters van die stelsel afskat, 'n kompensasie van interne verliese doen en die drywingsskakelaars direk skakel om die verwysing i_{ref} te volg.

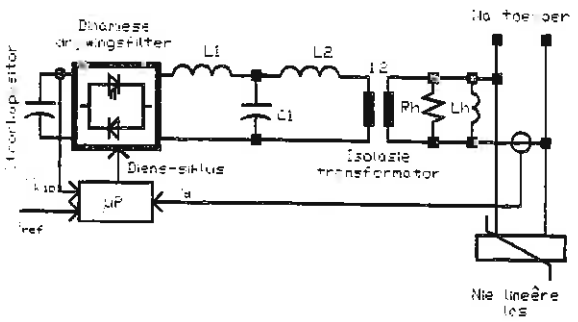

Fig 1. Die blokdiagram van die DPF (dinamiese drywingsfilter) en syferbeheerder gekoppel aan die toevoer.

Fig 1. toon die mikrorekenaar wat die komponentwaardebepaling doen asook die metings van die spannings en strome en doen dan die beheer van die skakelelemente vir toevoerkompensasie.

Die blokdiagram is 'n voorstelling van die ekwivalente baan van die DPF in 'n praktiese opstelling. Die figuur bevat die laaglaatfilter vir filtering van die hoëfrekwensiekomponente vanaf die skakelelemente. Weens die laaglaatfilter en die induktansie van die ontkoppelingstransformator moet die faseverskuiwing tussen gemete waardes en uitset in ag geneem word. Die syfer implementering van sodanige poolplasingsfilter word dan ook met die mikroverwerker onderneem [2].

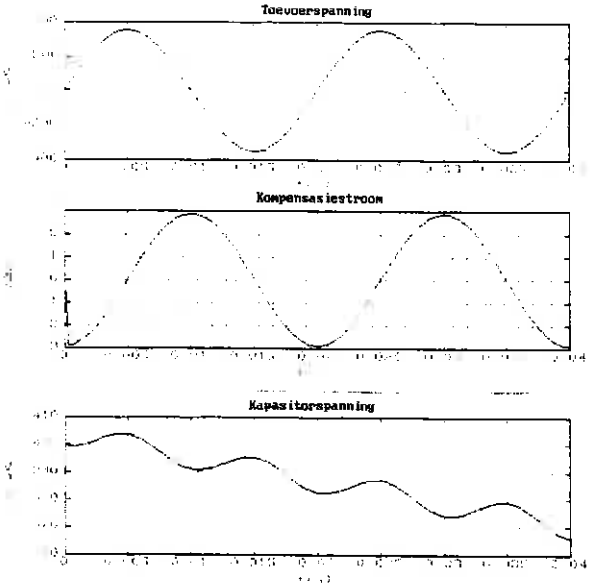

Fig 2. Spannings en strome van DPF soos gesimuleer sonder verliese van die stelsel in ag geneem.

Uit die figuur kan die faseverskuiwing tussen die toevoerspanning en die stroom uit die DPF waargeneem word. Soos gesien word is die faseverskuiwing ongeveer 90°.

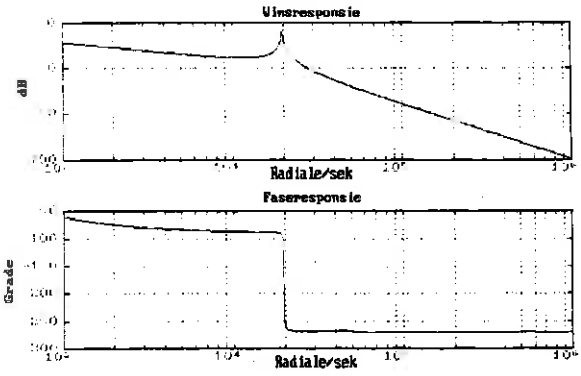

Fig 3. Bodeplot van die dinamiese drywingsfilter (DPF).

Uit die bodelot van die DPF is die fasemarge -90°. Dus is die stelsel onstabiel en nie beheerbaar nie. Vir beheerbaarheid is dit nodig om 'n fasevoorloopnetwerk saam met die beheerder te implementeer. Die fasevoorloopnetwerk sal die fasemarge positief maak en dus stabiliteit verkry.

Met die gebruik van 'n tweede orde analoog-fasevoorloopnetwerk verander die bodeplot soos volg.

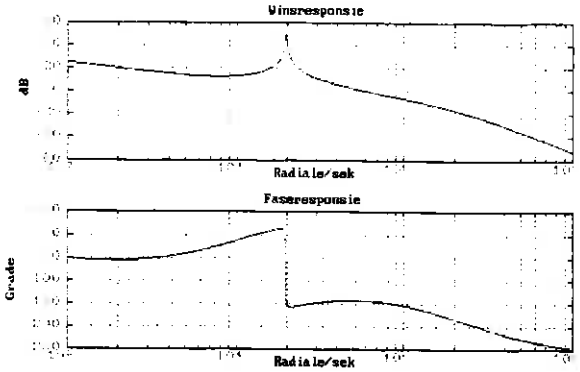

Fig 4. Bodeplot met die 2e orde fasevoorloopnetwerk.

Met die fasevoorloopbaan geïmplementeer word die fasemarge 40°. Dit is duidelik dat alhoewel die beheerder nou stabiel is die fasevoorloopbeheerder baie krities is. Indien enige van die waardes van die komponente in die ekwivalente baan verander met tyd weens temperatuur of ander faktore, sal die fasevoorloopnetwerk nie meer effektief wees nie. Die gevolg is dat die beheerder die stelsel weer onstabiel maak. Dit is nodig vir effektiewe beheer dat die fasevoorloopnetwerk aangepas word soos die waardes in die ekwivalentebaan mag verander. Die syferafskatter kan nou die waardes van die komponente gedurig bepaal en sodoende die syferfasevoorloopnetwerk vervolgens aanpas.

Ekwivalente baan.

Die ekwivalente baan wat die voorstelling is van die DPF word gebruik om die fasevoorloopnetwerk soos bespreek te ontwikkel. Fig 1. toon die opstelling soos die DPF gebruik sal word. Die toevoer waaraan die DPF gekoppel word kan gemodelleer word as 'n suiwer spanningsbron met 'n reaktansie.

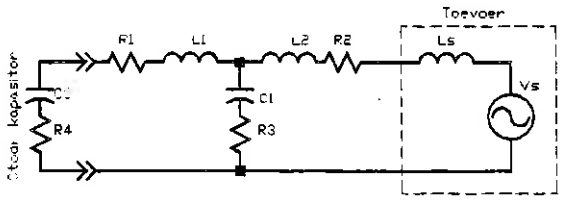

Fig 5. Ekwivalente baan van die praktiese opstelling.

As parameters van die spanningsgevoerde kompensator kan die spanningsbron van die toevoer gemodelleer word as 'n kortsluiting en die stoorkapasitor word nou die spanningsbron. Dié spanningsbron se spanning is nie konstant nie maar afhanklik van die energie wat bevat word in die kapasitor.

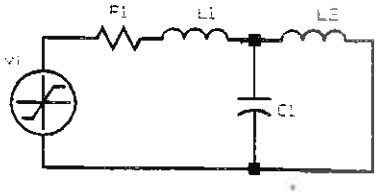

Fig 6. Ekwivalente parameters van die spanningsgevoerde kompensator.

Fig 6. dui die baan wat deur die mikrorekenaar gebruik word om die waardes van die parameters te bepaal en die golfvorms te genereer. Die simulasie genereer die golfvorms en gebruik dan die golfvorms as responsie van die DPF om die waardes af te skat.

Wiskundige werking van afskatter.

Die wiskundige modellering van die afskatter word m.b.v. toestandruimtelike voorstelling uitgebeeld [3,6].

$$\dot{\bar{X}} = (\bar{A}*\bar{X}) + (\bar{B}*\bar{U}) \quad \text{---------- (1)}$$

$$\bar{Y} = (\bar{C}*\bar{X}) \quad \text{---------- (2)}$$

waar

$\bar{U}$ - insetvektor

$\bar{Y}$ - uitsetvektor

$\bar{A}$ - sisteem-matriks

$\bar{X}$ - toestandsvektor

$\bar{C}$ - waardevektor

$\bar{B}$ - inset konstantevektor

is

In plaas daarvan om die inset U te gebruik om die uitset Y te bepaal word die uitset Y en die inset U gebruik om die waardes van C, A en B te bepaal. Vir 'n eenvoudige stelsel is:

$$\bar{Y} = \bar{X} \quad \text{---------- (3)}$$

en

$$\bar{C} = 1 \quad \text{---------- (4)}$$

Dan geld die volgende.

$$\dot{\bar{Y}} = (\bar{A}*\bar{Y}) + (\bar{B}*\bar{U}) \quad \text{---------- (5)}$$

$$\bar{Y}_{k+1} = (\bar{F}*\bar{Y}_k) + (\bar{B}*\bar{U}_k) \quad \text{---------- (6)}$$

Dus inplaas daarvan om die laaste vergelyking uit te voer word dit omskryf sodat die konstante matrikse nl. F en U bepaal kan word. Indien die konstantes in F en U saamgevat word in een konstante matriks en die inset- en uitsetwaardes Y en U word saamgevat in 'n enkele matriks lyk dit soos volg:

$$\bar{K} = \begin{vmatrix} \bar{Y}_k & \bar{U}_k \end{vmatrix} \quad \text{---------- (7)}$$

$$\bar{V} = \begin{vmatrix} \bar{F} \\ \bar{B} \end{vmatrix} \quad \text{---------- (8)}$$

$$\bar{W} = \bar{Y}_{k+1} \quad \text{---------- (9)}$$

$$\bar{W} = \bar{K} * \bar{V} \quad \text{---------- (10)}$$

$$\bar{V} = [\bar{K}^T * \bar{K}]^{-1} * \bar{K}^T * \bar{W} \quad \text{-------- (11)}$$

$\bar{V}$ = Konstante waarde matriks

$\bar{K}$ = Inset- en uitsetmatriks

$\bar{W}$ = Uitsetmatriks

Deur vergelyking (11) dan direk te implementeer word die konstantes soos bepaal in V bepaal. Die waardes bevat die waardes van die ekwivalente baan en deur omskrywing kan dit dan daaruit afgelei word.

Implemetering van afskatter.

Die verskilvergelykings wat normaalweg gebruik sou word om die responsie van die baan in Fig 6. te bepaal sien soos volg daaruit:

$$i_{k+1} = \left(1-\left[\frac{T*R_1}{L_1}\right]\right)*i_k - \frac{T}{L_1}*V_{ck} + \frac{T}{L_1}*V_{ik} \quad \text{---------- (12)}$$

$$V_{ck+1} = V_{ck} + \frac{T}{C_1}*i_k - \frac{T}{L_2*C_1}*V_{dum} \quad \text{--- (13)}$$

$$V_{dumk+1} = V_{dumk} + (T*V_{ck}) \quad \text{---------- (14)}$$

Vir Fig 6. sal die matrikse soos vervat in vergelyking (11) wat die oplossings gee van die afgeskatte waardes soos volg lyk vir ses monsterings:

$$\bar{K} = \begin{vmatrix} i_6 & V_{c6} & V_{i6} \\ i_5 & V_{c5} & V_{i5} \\ i_4 & V_{c4} & V_{i4} \\ i_3 & V_{c3} & V_{i3} \\ i_2 & V_{c2} & V_{i2} \\ i_1 & V_{c1} & V_{i1} \end{vmatrix} \quad \text{---------- (15)}$$

$$\bar{W} = \begin{vmatrix} i_7 \\ i_6 \\ i_5 \\ i_4 \\ i_3 \\ i_2 \end{vmatrix} \quad \text{---------- (16)}$$

Die matrikse word dat net so in vergelyking (11) vervang en die matriks V bepaal. Vir die geval is matriks K 'n 6x3 matriks en matriks W 'n 6x1 matriks. Gevolglik sal matriks V 'n 3x1 matriks wees wat die konstantes van vergelyking (12) bevat.

$$\bar{V} = \left| \begin{array}{ccc} \left(1- \left[\frac{T*R_1}{L_1}\right]\right) & -\left(\frac{T}{L_1}\right) & \left(\frac{T}{L_1}\right) \end{array} \right| \quad \text{---------- (17)}$$

Hieruit kan die konstantes R_1 en L_1 bepaal word. Indien die ander konstantes soos L_2 en C_1 ook bepaal wil word, moet dieselfde prosedure uitgevoer word met een van die ander verskilvergelykings.

Resultate van parameterafskatting.

Die syferafskatter soos bespreek is geïmplementeer op 'n mikrorekenaar op die ekwivalente baan van die DPF. Die ekwivalente baan in die mikrorekenaar word gebruik om die nodige golfvorms te genereer vir die afskatter.

Die akkuraathede wat verkry is met die afskatter is van so 'n aard dat dit in die finale opstelling gebruik kan word om die waardes in die ekwivalente baan te bepaal. Die akkuraathede wissel van 98 tot 94 % en is dus 'n goeie verteenwoordiging van die waardes.

Die akkuraathede is sterk afhanklik van die monsteringstempo en kan dus verhoog word indien die monsteringstempo verhoog word. Die afskatting geskied nie noodwendig altyd intyds nie maar kan geskied voordat die kompensator in werking tree. Dit sal bv. die waardes in die ekwivalente baan bepaal vir elke opstelling wat uniek is voordat die kompensator in werking tree.

Ontwikkeling van 'n mikrokompensator.

Die DPF wat gebruik word sal as 'n driefasige kompensator bestaan uit drie of alternatiewelik vier fase-arms. Elke skakelaar moet geïsoleerd gestuur word teen 'n tipiese skakelfrekwensie van 30kHz om aan die dinamiese responsie te kan voldoen. 'n 5kVA driefasige DPF word tans as mikrokompensator ontwikkel wat van IGBT's of VETTE gebruik maak.

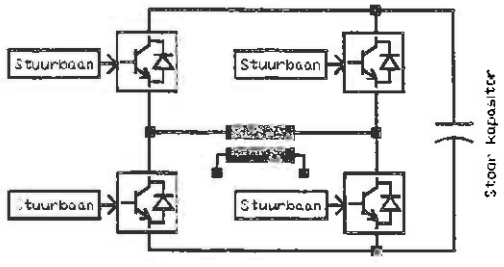

Fig 7. Uitleg van die dinamiese drywingsfilter (DPF).

Fig 7. toon die skakelelemente van 'n enkelfasige mikrokompensator. Uit die baan is dit duidelik dat die slegs die boonste skakelaars se stuuring geïsoleerd hoef te wees en nie al die skakelaars nie om die moontlikheid van grondfoute uit te skakel.

Die vereistes waaraan elk van die stuurbane moet voldoen wat die skakelaars stuur is dat dit eerstens geïsoleerd moet wees, daar moet sentrale beveiliging vir die skakelaar wees en dit moet gedesentraliseerde beveiliging bied vir die hele DPF as geheel.

Om die geïsoleerdheid te verseker en ook om die ander vereistes te verkry moet die kragbron vir elk van die stuurbane geïsoleerd wees. Die stuursein vir elk van die skakelaars moet na die stuurbaan geïsoleerd wees asook die beveiligingsein na die desentrale beveiliging.

Die multi-isolasie kragbron word verkry met 'n gesentraliseerde 30kHz 100V kragbron, wat desentraliseerd vir elke kragbron d.m.v. 'n klein transformator, gelykrigter en reguleerder bewerkstellig word. Vir die isolasie van die stuursein en beveiligingsein word van optiese isoleerders gebruik gemaak.

Die etsbaan ontwerp vir die spesifieke doel is ontwerp om 'n TO-220 of twee TO-3 pakkies in parallel te skakel. Die etsbaan maak gebuik van 'n goeie grondvlak om die robuustheid van die stuuring te vermeerder en die gevoelighied vir ruis te verminder.

Vereenvoudigde verliese en skakelvermoë.

Die etsbaan wat ontwikkel is, is prakties getoets met twee veldeffek-transistors in parallel. Die skakeling van 'n geïntegreerde-hek bipolère-transistor (IGBT) is ook ondersoek met dieselfde stuurbaan.

Twee veldeffek-transistors in parallel by hoë spanning het 'n redelike hoë aan-weerstand, van ongeveer 0,4 ohm. Indien 'n stroom van 20A geskakel word sal die aan-spanning in die orde van 8V wees. Die aan-verliese in die veldeffek-transistors sal dan 160 watt wees wat die gebruik van VETTE in hoëspanning, hoëstroomstelsels nadelig beïnvloed.

Die geïntegreerde-hek bipolère-transistor het nie 'n aan-weerstand nie maar 'n aan-spanning. Die aanspanning van een enkele geïntegreerde-hek bipolère-transistor met dieselfde drywingsvermoë as die twee veldeffek-transistor in parallel is 2V. Die verliese wanneer 20A geskakel word is dus 40 watt wat heelwat laer aan-verliese as die veldeffek-transistors tot gevolg het. Die afskakeltyd van die IGBT is egter heelwat stadiger as die van die VET wat weer 'n hoër skakelverlies tot gevolg sal hê. Met goeie gapserontwerp kan sodanige verliese egter minimeer word. 'n Aansienlike kleiner hitteput kan dus gebruik word om dieselfde drywing te skakel. Verder sal die stelsel 'n hoër totale rendement hê, indien IGBT's gebruik word.

Die stuuring van die skakelaars.

Die etsbord is gebruik om die veldeffek-transistor sowel as die geïntegreerde-hek bipolêre-transistor te skakel.

Die stuurbaan soos genoem is heeltemal geïsoleerd van die res van die kompensator om die moontlikheid van grondfoute uit te skakel. Die stuurbaan maak gebruik van 'n positiewe sowel as negatiewe spanning aanboord die stuurbaan om vinnige aan- en afkakeling te verkry. Verder bestaan die stuurbaan uit 'n stuurseinbeveiliging wat die stuursein na die skakelaar afsny indien 'n fouttoestand onstaan.

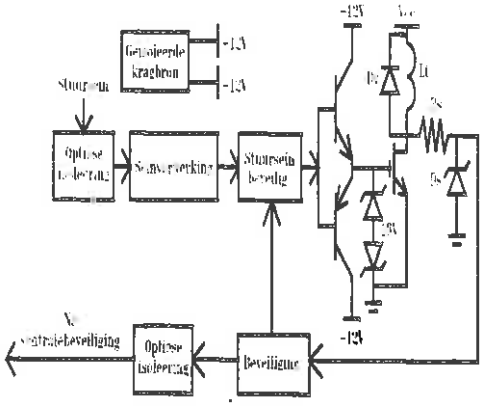

Fig 8. Blokdiagram van die stuurbaan.

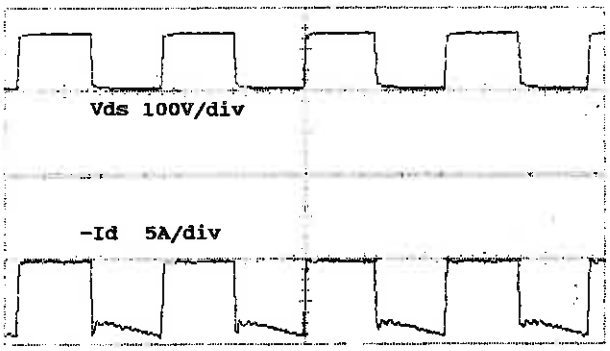

Fig 9. Skakeling van die veldeffek-transistors IRF-452.

Die ontwikkelde stuurbaan kan vir beide die veldeffek-transistor en geïntegreerde-hek bipolêre-transistor stuuring gebruik word. Die resultate toon dat die skakelaars voldoende gestuur word.

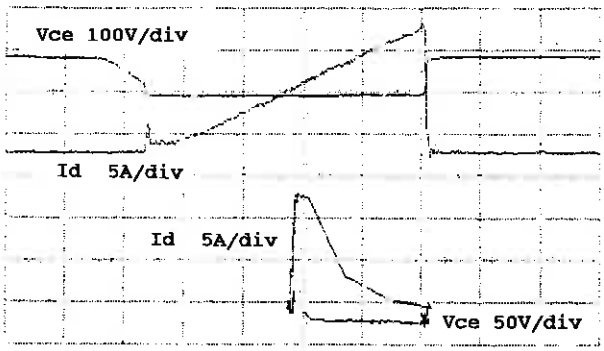

Fig 10. Skakeling van die geïntegreerde-hek bipolêre-transistor IRGBC20.

Opsomming.

In die referaat is die probleme met die verliese in die kompensator aangespreek.

Die uitsetfilters wat die hoëfrekwensie komponente van die skakelelemente uitfilter veroorsaak swak fasemarges wat die stabiliteit van die beheerder beïnvloed. 'n Mikrorekenaar word beplan wat die waardes van die komponente van die ekwivalentebaan afskat en die syferfasevoorloopnetwerk vervolgens aanpas. Sodoende word 'n stabiele fasemarge verkry vir doeltreffende beheer.

Verder is die skakeling van IGBT's en VETTE ondersoek. Die dimensies van hitteput benodig vir 'n IGBT is heelwat kleiner as dié vir 'n gelykstaande VET. Die feit maak die gebruik van 'n IGBT i.p.v. 'n VET baie meer voordelig. Die nadele verbonde aan die IGBT, soos bv. die langer afskakeltye i.t.v. 'n VET, moet ook egter in ag geneem word.

'n 5kVA mikrokompensator word ontwikkel wat van die inligting in die referaat gebruik maak om die werking daarvan te verseker.

Lys van simbole.

C_1 Kapasitor [F]
D_s Spanningsbepalingsweerstand
D_v Vryloopdiode
i_d Kompensasiestroom [A]
i_{ref} Verwysingstroom [A]
i_k Huidige stroom [A]
i_{k+1} Stroom met volgende monstering [A]
i_1 Stroom tydens eerste monstering [A]
i_2 Stroom tydens tweede monstering [A]
I_d Put-stroom [A]
I_c Kollektor-stroom[A]
$\bar{K}^T$ Getransponeerde van matriks $\bar{K}$
$\bar{K}^{-1}$ Inverse van matriks $\bar{K}$
L_1, L_2 Induktansie [H]
L_s Toevoerinduktansie [H]
L_t Lasinduktansie [H]
L_h Magnetiseerinduktansie [H]
R_1 Weerstand (Stel verliese voor) [Ohm]
R_h Ysterverliese [Ohm]
R_s Spanningsbepalingsweerstand [Ohm]
T Monsteringstyd [Sekondes]
V_i Insetspanning [V]
V_{dum} Hulpspanning [V]
V_c Spanning oor kapasitor [V]
V_{cc} Hoogspanningstoevoer [V]
V_{ck+1} Spanning oor kapasitor met volgende monstering [V]
V_{ck} Huidige spanning oor kapasitor [V]
V_{kap} Stoorkapasitorspanning [V]
V_s Toevoerspanning [V]
V_{ds} Put- bronspanning [V]
V_{ce} Kollektor- emittorspanning [V]
$\bar{X}^*$ Afgeleide van matriks $\bar{X}$

Verwysings.

[1] J H R Enslin en J D Van Wyk: " A new control philosophy for power electronic converters as fictious power compensators",Trans. on Power Electronics, Vol.5, no.1, Jan. 1990.

[2] G. Van Schoor en J.D. Van Wyk: "A study of current-fed converters as an active three phase filter", in Proceedings of IEEE Power Electronics Specialists Conference (PESC-87), pp482-490, Blacksburg, VSA, Junie 1987.

[3] C J Oliver: "Parameterafskatting en ontwikkeling van 'n dinamiese mikrokompensator vir vervormde lasse", BIng-skripsie, Departement Elektriese Ingenieurswese, Universiteit van Pretoria, Republiek van Suid-Afrika, November 1990.

[4] D A Marshall, J D Van Wyk, D Vermoten, F P Venter, J J Schoeman: "An experimental study of a hybrid power compensator", Proc. IEEE, ICHPS IV, Oktober 4-6 1990, Budapest, Hungarye.

[5] T J E Miller : "Reactive power control in electric systems", Hoofstukke 4,5,6, New York, John Wiley & Sons, 1982.

[6] Jacquot Raymond G., "Modern digital control systems", Hoofstukke 1 to 8, Universiteit van Wyoming, Laramie, Wyoming, Marcal Dekker, Inc, 1985.

ENERGY LOSS-RETRIEVAL, AND ENERGY CONTROL SYSTEMS FOR THE OPTIMIZATION OF DYNAMIC POWER FILTERS

GL VAN HARMELEN JG ROOS JHR ENSLIN

DEPARTMENT OF ELECTRICAL ENGINEERING, UNIVERSITY OF PRETORIA
PRETORIA, REPUBLIC OF SOUTH AFRICA

ABSTRACT

Efficiency optimization of dynamic power filters (DPF's) is inevitable for an effective compensation effort. A regenerative snubbing technique is proposed for switching-loss retrieval in bridge configurations. A single energy storage capacitor is used to capture the regenerative energy from the three or four bridge arms and also serves as an overvoltage clamp for the collector emitter voltages. The energy flow between this storage capacitor and the DC-bus capacitor is controlled by a buck-converter with a modified control strategy. Modifying the control parameters of this converter allows effective control of the overvoltage clamp and also the effective turn-off snubbing efficiency in each phase.

Energy is generated into the bus capacitor of the voltage-fed dynamic power filter topology by the snubbers, as well as by the compensation effort itself. An investigation is shown into the monitoring, modelling and control of the stored energy in the Dynamic Power Filter storage capacitor by monitoring the DC-bus voltage. The capacitor voltage is directly related to the energy absorbed or delivered by the bridge during compensation and a closed loop control system for control of this stored energy is proposed.

INTRODUCTION

Energy loss in dynamic power filters must be kept to the absolute minimum for effective operation. Dynamic power filters operate on-line with the network they are compensating and any losses or distortions added by the dynamic power filter itself, will deteriorate the compensation effort [4]. In high power, high switching frequency, bipolar transistor, PWM-bridge topologies, switching losses must be minimized in the bridge in order to ensure optimum operation [1].

The connection of a Dynamic Power Filter to a supply network which requires compensation is shown in Fig. 1. No external source of energy is employed in the compensation effort and thus extreme care must be taken with the control and loss of the energy stored in the compensator.

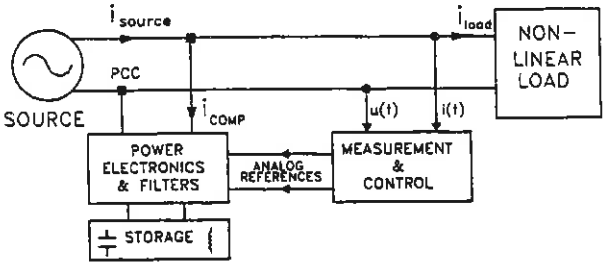

Fig. 1. Compensation system connection to a supply network.

No power electronic bridge is perfect, and even with regenerative snubber techniques employed, as will be discussed in this paper, the bridge still incurs additional losses. This implies that the energy stored in the dynamic power filter (a capacitor for a voltage-fed system, and an inductor for a current-fed system) will eventually decrease until it has reached a zero value if it is not charged in some manner.

In order to compensate for the losses occurring in the bridge, a model has to be found which adequately describes the losses occurring in the bridge, so that such losses may be compensated for.

A DPF is essentially an ideal current source and as such, takes on the system voltage at the point of common coupling (PCC). If the reference to the DPF is an active current, this implies that energy is being delivered into the DPF, which is ideally a special type of storage element. The energy which is drawn from the supply, is subsequently stored in the DPF storage element (capacitor).

$$\delta E_T = P.\delta T = U_{RMS}.Ia_{RMS}.\delta T = \frac{1}{2}C(U^2_{c+\delta T}-U^2_c) \qquad (1)$$

If however, the rate at which energy is added to the DPF by an active current, is equal to the rate at which it is dissipated internally to the DPF, then the energy balance within the DPF is maintained.

$$E_{c+\delta T} = E_c - E_{losses} + E_{loss\ compensation} \qquad (2)$$

THE REGENERATIVE SNUBBER

The proposed turn-on/turn-off snubber which protects both the transistors in one arm of a three-phase bridge, is shown in Fig. 2. This snubber configuration has several advantages:

- It has relatively few components
- It introduces lower additional stresses
- The snubber diodes do not cause difficulties due to their reverse recovery times
- The circuit has an overvoltage snubbing action
- All the snubber energy is stored within a single capacitor which makes loss retrieval (regenerative snubbing) very simple

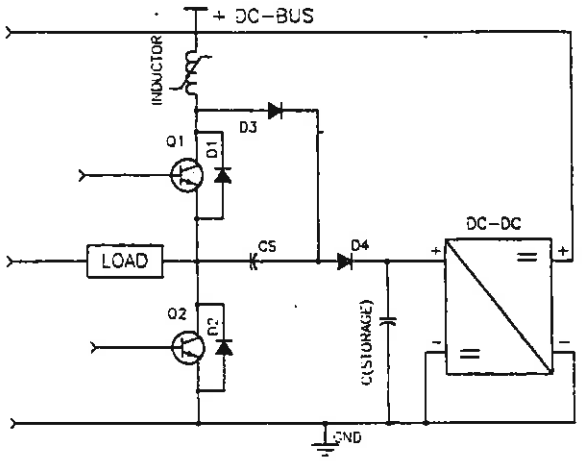

Fig. 2. Regenerative snubber topology.

This snubber has been employed in a 40 kVA, three-phase, 400 V, industrial frequency convertor, which is currently under modification to operate as a three-phase dynamic power filter. Due to a relatively slow output darlington transistor configuration on this bridge (current fall-time), relatively large turn-off snubber capacitance has to be used. This in turn implies large amounts of snubber energy which need to be regenerated.

The DC-bus of the DPF will be operated in the 300-400 V range and will be connected onto the supply network through a 1:1.5 step-up transformer.

In order to design the turn off-snubbers, the fall-time of the collector current was measured from no-load to full-load and was found to remain in the order of 2.8 μs.

$$t_f = 2.8\ \mu s \quad therefore\ \tau = \frac{5}{9} t_f = 1.6\ \mu s \qquad (3)$$

$$C_s = I_c \frac{\tau}{U_c} = 100 . \frac{1.6E\text{-}6}{400} = 0.47\ \mu F \qquad (4)$$

With the DC-bus operating at 400 V, with eight transistor's turn-off snubber energy being handled by one convertor, the energy may be calculated as follows for a DPF switching frequency of 10 kHz:

$$E_c = \frac{1}{2} CV^2 = \frac{1}{2}\ 0.47E\text{-}6\ 400^2 = 37.6mJ \qquad (5)$$

Taking this further:

$$P_{total} = 8 . E_c . f_s = 8\ .\ 37.6E\ .\ 10000 = 3\ kW \qquad (6)$$

This quantity ignores turn-on and overvoltage snubbing energy which is also to be returned to the DC-bus.

Simulated and practical results for input voltage and current to the buck converter are shown in Fig. 3a and Fig 3b respectively.

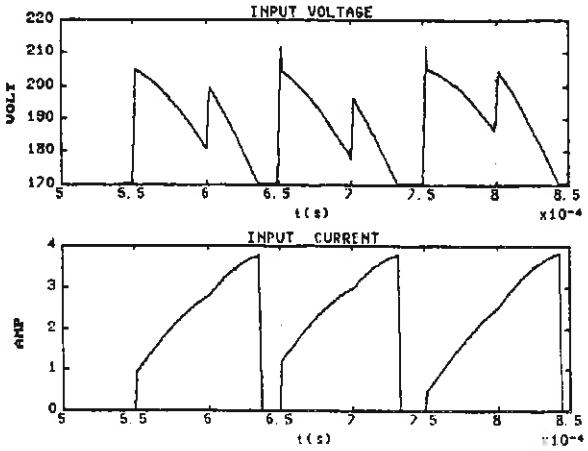

Fig. 3a. Simulated results of input voltage and input current to the buck converter during snubbing operation.

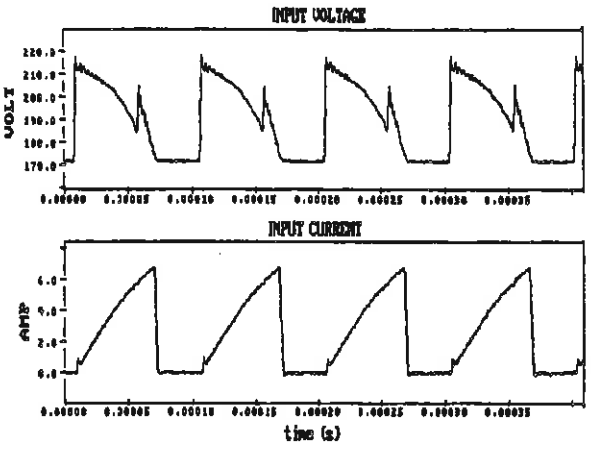

Fig. 3b. Practical results of input voltage and input current to the buck converter during snubbing operation.

A block diagram of the buck converter is shown in Fig. 4. A BUV298 bipolar transistor was used as main switch and the convertor was designed to operate at 300 V, 20 A, and in the 10-20 kHz switching frequency range.

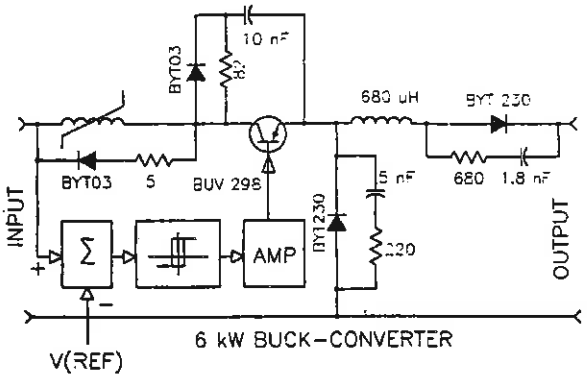

Fig. 4. Block diagram of the regenerative snubber buck-converter.

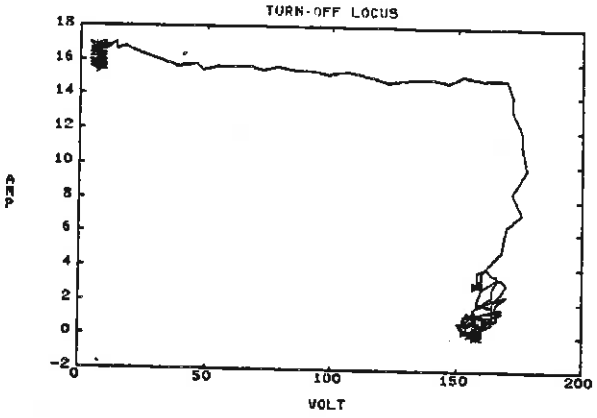

Fig. 5a. Turn-off locus without the snubber.

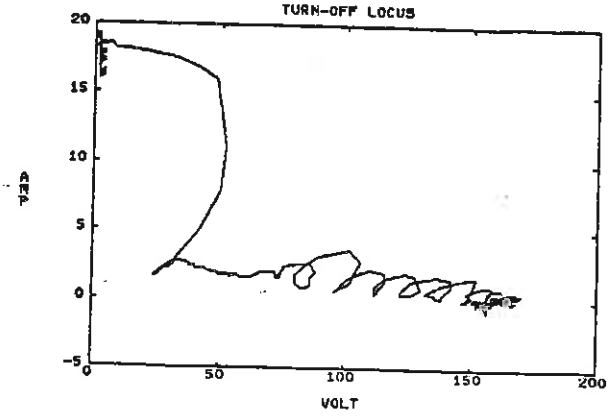

Fig. 5c. Turn-off locus with snubber working.

REGENERATIVE SNUBBER CONVERTER CONTROL

Energy from the snubbers is dumped into a single storage capacitor and it is the task of the converter controller to maintain a specified average value on this capacitor. A hysteresis controller operates from an error signal obtained by subtracting the input voltage from a reference value. When the input voltage rises above the reference value, the switch (BUV298) is turned on and the storage capacitor is discharged via the main inductor back into the supply. When the input voltage has dropped sufficiently, the switch is turned off again and the storage capacitors once again allowed to charge up.

In order to maintain control of the converter, the input voltage (reference) should be slightly higher than the DC-bus voltage in order to ensure a positive current flow into the DPF DC-bus. This implies that a residual DC- voltage is always present on the snubber capacitor which implies that U_{cs} will rise very quickly for the first part of the turn-off waveform (i.e. no snubbing action). Once U_{cs} rises above the residual value, full snubber operation comes into effect. A block diagram of the regenerative snubber is shown in Fig. 4.

SNUBBER RESULTS

On- and off-switching loci with and without the snubber are shown in Fig. 5a to Fig. 5d.

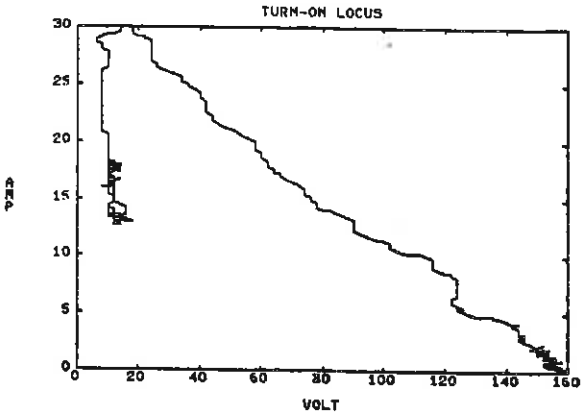

Fig. 5b. Turn-on locus without the snubber.

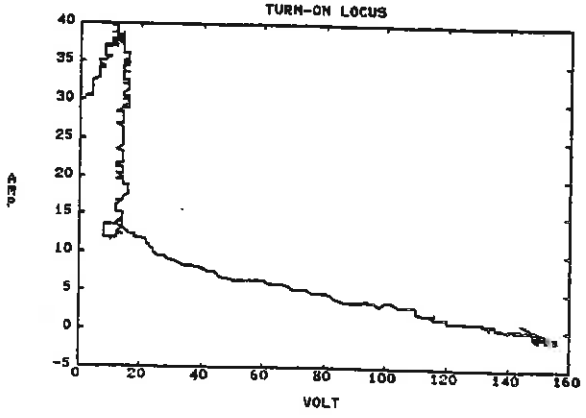

Fig. 5d. Turn-on locus with snubber working.

These result were measured at a load current of 15 Amp and a DC-bus voltage of 150 volt. This rating was chosen as an identical load with and without snubbers was required for comparison. The storage capacitor voltage control value was adjusted to ± 200 Volt.

ENERGY CONTROL WITHIN THE DPF

In the process of compensation, no external DC-source is connected to the dynamic power filter. The losses present within the bridge are therefore very important as they need to be compensated for in order to maintain a constant DC-bus voltage. In a voltage-fed dynamic power filter, energy is supplied to and from the supply source as it is interchanged with the dynamic power filter. Energy within the DPF is stored in a DC capacitor which is connected in place of the normal DC-bus for a standard inverter topology. A block diagram of the layout is given in Fig. 6.

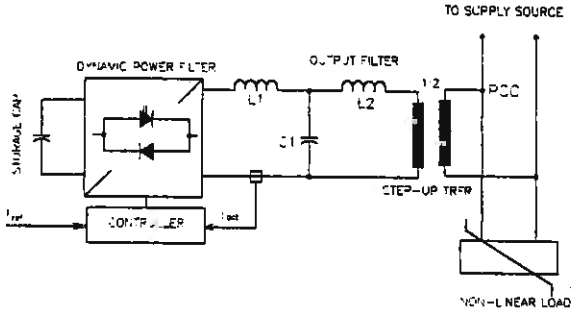

Fig. 6. Block diagram of voltage-fed DPF.

During a compensation effort, several cycles of energy may be supplied and returned by the DPF during a fundamental period of compensation. During reactive compensation, energy is supplied and demanded from the DPF at double the supply frequency as is seen in the simulation presented in Fig. 7. A practical result, measured on a 1 kVA voltage DPF is shown in Fig. 8.

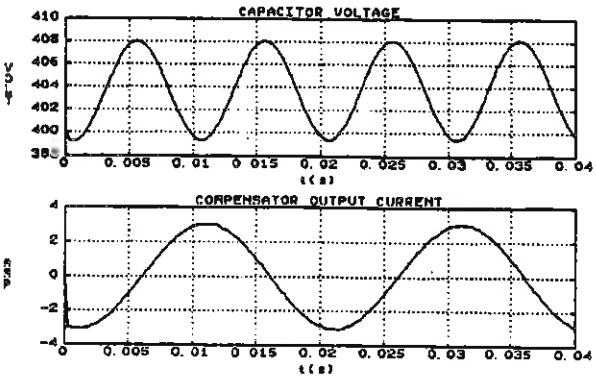

Fig. 7. Simulated result of charging and discharging of the storage capacitor during reactive power compensation.

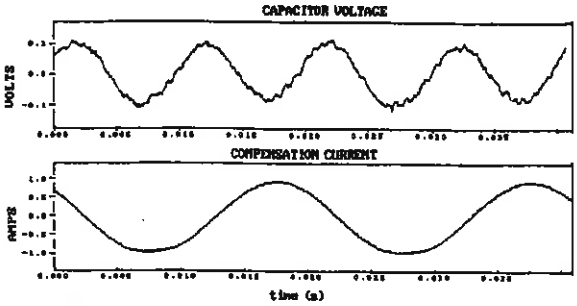

Fig. 8. Practical result of the charging and discharging of the storage capacitor during reactive power compensation.

The storage capacitor used in the practical result was 2200 μF whereas the capacitor used in simulation was 500 μF. The simulated and practical voltage deviations thus differ in absolute value but clearly show the same characteristics.

DPF LOSS MODELLING

As has been discussed, the bridge itself has losses and thus the energy in the capacitor will tend to run out under normal fictitious power compensation (reactive and distortive components). Fictitious power contains no active power components and thus the nett energy exchange with the compensator over a long period will remain zero. The active power dissipated in the bridge losses will however deplete the energy stored in the storage capacitor.

In order to combat this decrease in stored energy, which implies a decrease in DC-bus voltage, which implies a deterioration in DPF dynamic behaviour, a model for the losses in the DPF is sought. From such a model, the losses must be determined and an active current should subsequently be added to the fictitious compensation component in order to charge the DC-capacitor.

$$i'_{ref} = i_{ref} + i_{loss\ compensation} \qquad (7)$$

Losses (equivalent conductance) are modelled as a constant loss conductance, G_k added to a conductance term derived from the DC-bus capacitor error voltage.

$$G_{loss} = G_k + \alpha \cdot e_{sc} \qquad (8)$$

$$e_{sc} = U_{sc} - U_{ref} \qquad (9)$$

Having found the value of G_{loss}, which represents the equivalent amount of losses in the bridge, multiplication of this term with the system voltage, will result in an active current which is representative of the losses in the bridge.

When this active component is added to the DPF reference, it causes the DC-capacitor to be charged at the same rate at which it is being discharged by the losses associated with the DPF (switching losses, conduction losses, transformer and copper losses, low-pass output filter losses) [4].

A block diagrammatic representation of the closed loop control used for this control is shown in Fig. 9.

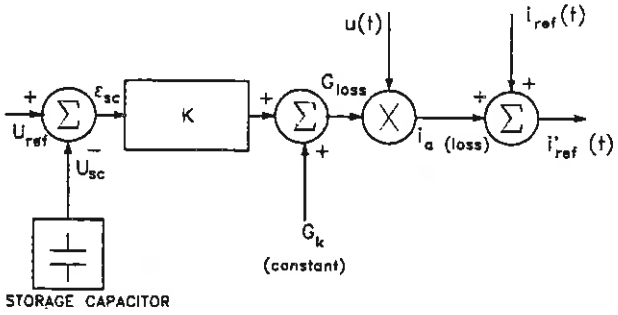

Fig. 9. Loss modelling and control of the DPF.

The total current drawn from the supply, with the load, the DPF and the loss compensation circuit connected is then:

$$i(t) = i_{load} + i_{compensation} + G_{loss}u(t) \qquad (10)$$

Due to the nature of compensation itself, $i_{load} + i_{compensation}$ is an active current, in phase with the voltage and having the same waveshape, by definition [5]. The component $G_{loss}u(t)$ is also an active current and this technique thus succeeds in drawing an active current from the supply, in order to replenish the DC-capacitor, without distorting the original compensation effort.

COMPENSATION RESULTS

In order to illustrate this effect, compensation of a half-wave rectified resistive load is shown diagrammatically in Fig. 10. Load voltage and current measurement are made and are fed into a measurement, calculation and control unit [3].

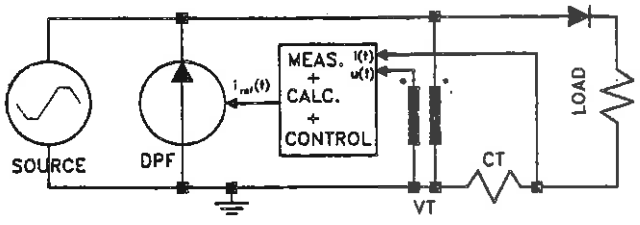

Fig. 10. Half-wave rectified load compensation circuit.

An analog compensation reference, which has the active loss-compensation component added to it, is fed to the DPF which is shown as a current source. The practical results measured on this circuit are shown in Fig. 11. The system voltage and system current (on source side) are shown in the Fig. 11a and Fig. 11b.

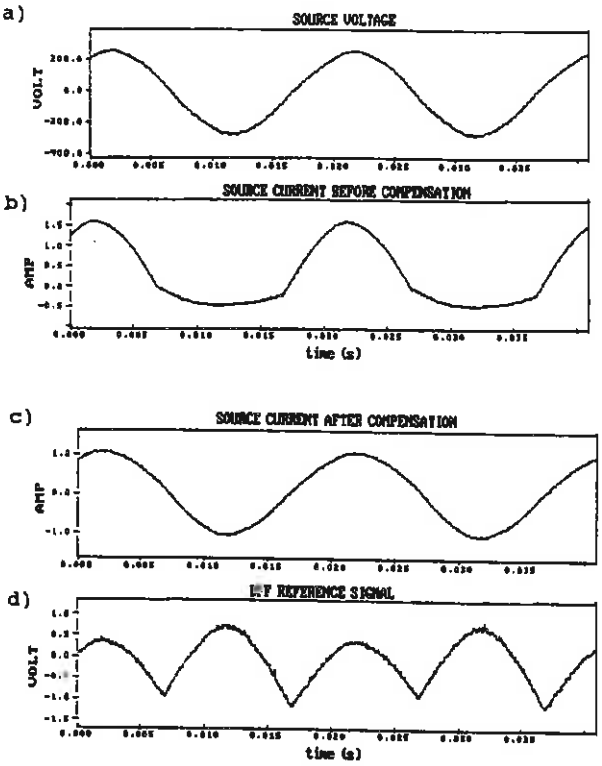

Fig. 11. Half-wave rectified load compensation effort.

During the negative half cycles, no current flows into the load due to rectification but one can clearly see an active current component being drawn from the supply in Fig. 11b. This active current is superimposed on the load current as delivers the waveshape as seen in Fig 11b. This active component is absorbed by the DPF for loss compensation. After compensation, as is seen in Fig. 11c, an active current, in phase with the voltage and having the same waveshape, is drawn from the supply. This current also contains the active component of ± 200 mA which is used to supply the losses of the DPF. The DPF compensation reference, without the loss compensation component added to it (obtained from a TMS320C25 DSP controller) is shown in Fig 11d.

CONCLUSION

Energy loss-retrieval and control circuits for voltage-fed dynamic power filters were discussed in this paper. Total efficiency of a DPF is a critical issue as it is connected on line with the load it is compensating. Any unnecessary losses in a DPF are directly related to an additional loading on the power network, the minimization of which is the ultimate goal of compensation.

A regenerative turn-on/turn-off snubber is proposed and practical results obtained with the proposed circuit are given.

Not all the losses in the bridge may however be retrieved by regenerative circuits. Heat which is generated in the DPF, and the power dissipated in auxiliary circuits cannot be retrieved. An active current must be drawn from the system the DPF is compensating in order to compensate for these losses (i.e. charge the DC-capacitor). This active current has the effect of charging the DC-bus capacitor at the same rate at which the losses of the bridge are discharging the DC-bus capacitor. The closed loop control strategy for this, and practical results measured during a compensation effort were shown.

REFERENCES

[1] Mohan, N.; Mudeland, T.M.; Robbins, W.P. : Power Electronics : Converters, Applications and Design, John Wiley & Sons, New York, 1988.

[2] Undeland, T.M.; Jenset, F.; Steinbakk, A.; Rogne, T.; Hernes, M. : "A Snubber Configuration for Both Power Transistor and GTO PWM Inverters", in Proc. of 1984 Power Electronics Specialist Conference (PESC '84), pp.42-53.

[3] Enslin, J.H.R.; Van Harmelen, G.L. : "Real-time dynamic control of a dynamic power filter in supplies with high contamination", in Proc. of 21 st IEEE Annual Power Electronic Specialists Conference (PESC-90), San Antonio, Texas, USA, pp.887-894, June 1990.

[4] Van Harmelen, G.L. : "Structure and Development of a Dynamic Compensation System Controller for Contaminated Power Networks", M.Ing dissertation, Internal Report, no.86-VA-030, Department of Electrical Engineering, University of Pretoria, Jan. 1991.

[5] Fryze, S. : "Wirk-, Blind-, und Scheinleistung in Elektrisch Stromkreisen mit nichtsinusoidalformingen Verlauf von Strom und Spannung", in ETZ, vol.53, no.25, pp.596-599, 625-627, 700-702, 1932.

LIST OF SYMBOLS

τ	Turn-off snubber design time-constant
C_s	Snubber Capacitance
DPF	Dynamic Power Filter
E	Energy function
f_s	Switching frequency [Hz]
G	Conductance [Siemens]
G_k	Constant loss conductance term [Siemens]
I	RMS value of current [Amp]
i(t)	Current time function
I_c	Collector current [Amp]
P	Power [Watt]
δT	Time increment [sec]
δE	Energy increment [Joule]
t_f	Current fall time
U	RMS value of voltage [Volt]
u(t)	Voltage time function
U_{ce}	Collector Emitter voltage [Volt]
U_{sc}	Voltage on storage capacitor

REAL-TIME FICTITIOUS POWER CALCULATION AND COMPENSATION IN THREE PHASE SYSTEMS

D.A. Marshall, J.D. van Wyk, D. Vermooten, F.P. Venter, J.J. Schoeman,

Energy Laboratory, Engineering Faculty, Rand Afrikaans University, P.O. Box 524,

Johannesburg, 2000, Republic of South Africa.

ABSTRACT

This paper suggests the combination of the classic static VAr compensator and the dynamic compensator into a hybrid compensator topology. An overall control procedure for the hybrid compensator is suggested and a novel technique for the control of the dynamic compensator is also proposed and illustrated with a computer simulation. Operating results of the hybrid power compensator is presented in its present state.

INTRODUCTION

In present conventional practice fictitious currents in electric energy systems are compensated with reactances. Typical compensator topologies comprise switched or fixed inductive or capacitive reactances connected into the network in parallel, and switched or fixed inductive and capacitive reactances connected into the network as a series combination [1][2][3]. The fixed reactance topologies compensate for the average component of a particular category of fictitious current i.e. fundamental and harmonic reactive currents and the switchable reactance topologies compensate for the slowly varying component of this particular category of fictitious current. The dynamic compensator [4] is used to compensate for the frequency range of fictitious currents that the series combinations of fixed reactances are not tuned for, or for which the switchable reactance dynamics are too slow [5]. This paper describes the integration of the dynamic compensator with the classic static VAr compensator, into a hybrid topology. The possible overall control of the integrated system is discussed, as well as the control of each individual building block. Simulated and experimental results are presented to illustrate the complimentary role of each of the hybrid compensator building blocks.

HYBRID POWER COMPENSATOR

Classic static VAr compensator topology

There are various topologies of reactive elements by which a static VAr compensator (SVC) may be realized [1][2][3]. One such a topology is a capacitor bank in parallel with a thyristor controlled reactor (TCR). A further variation on the TCR is the thyristor controlled transformer (TCT) in which thyristors periodically short circuit the secondary of a transformer and the leakage inductance is used as reactor [2][3]. In the three phase system both the capacitor bank and primary of the transformer are Y–connected (Figure 1).

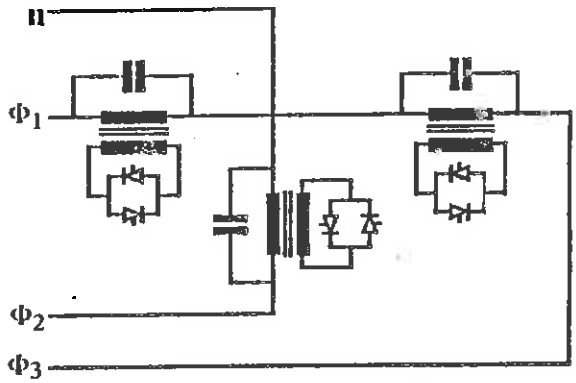

Figure 1: Static VAr compensator.

Dynamic compensator topology

The dynamic compensator has two fundamental topologies i.e. the voltage–fed and current–fed convertors [4][6] (Figures 2 and 3). The voltage–fed and current–fed converter topologies can further be implemented in two–pulse or four–pulse topologies. The converter bridge, reactive energy storage components and low pass filters are illustrated for single phase implementation in Figure 4 a–d and for three phase implementation in Figure 4e and f. The two–pulse voltage–fed and four–pulse current–fed topologies were implemented for three phase compensation in an experimental system with a rating of 15kVAr [4][7][8]. The following are general comments on the different topologies.

1. The current–fed topology has the highest losses due to the internal resistance of the dc–side coil.

2. The voltage–fed topology requires more complicated protection control to prevent a short circuit across the dc–side capacitors, while a short circuit across the current–fed topology dc–side coil will not be disastrous.

3. The voltage–fed topology requires a higher installed capacity since the dc side capacitor voltage must always be higher than the peak system voltage.

4. The current–fed topology requires more complicated compensation control since the third order characteristics of the circuit sustains a stable limit cycle reducing compensation efficiency.

5. The voltage–fed converter bridge requires more power components due to the fact that the switches require anti–parallel diodes.

6. The current–fed topology is bound to be more expensive due to the higher cost of inductors as compared to capacitors, and also the filter capacitor on the ac–side of the converter bridge.

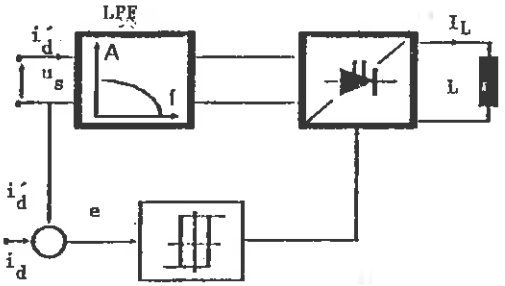

Figure 2: Topology for current–fed dynamic compensator.

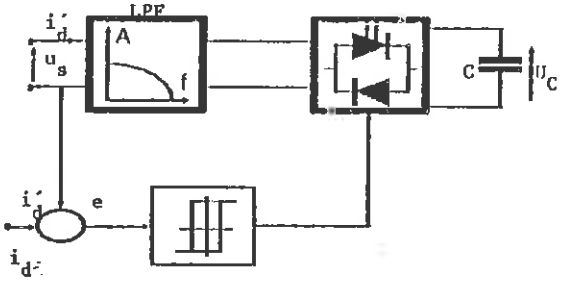

Figure 3: Topology for voltage–fed dynamic compensator.

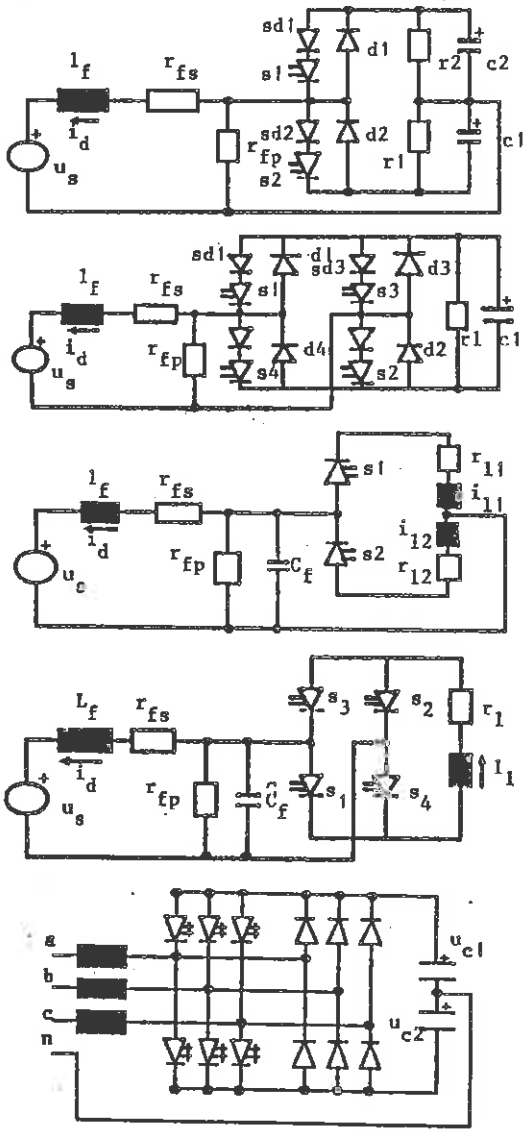

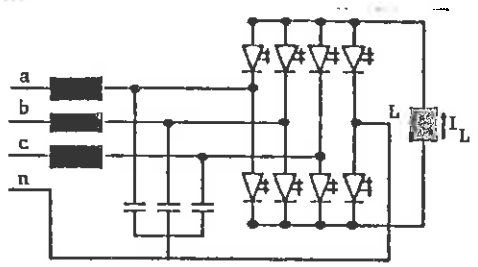

Figure 4: Single phase dynamic compensators. (a) Two–pulse voltage–fed, (b) Four–pulse voltage–fed, (c) Two–pulse current–fed, (d) Four–pulse current–fed. Three phase dynamic compensators, (e) Split capacitor topology, (f) Single inductor topology.

HYBRID POWER COMPENSATOR TOPOLOGY

Generically the hybrid power compensator can have only one topology. That is, the parallel combination of the classic static VAr compensator with the dynamic compensator. Figure 5 illustrates a single line diagram topology of a hybrid power compensator [9]. In the global control of the hybrid compensator, the supply busbar voltage u_s is used as reference.

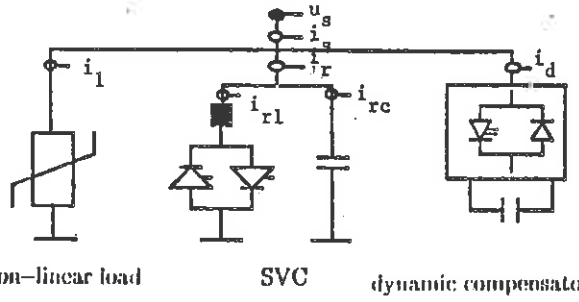

Figure 5(a): Generic topology of the hybrid power compensator.

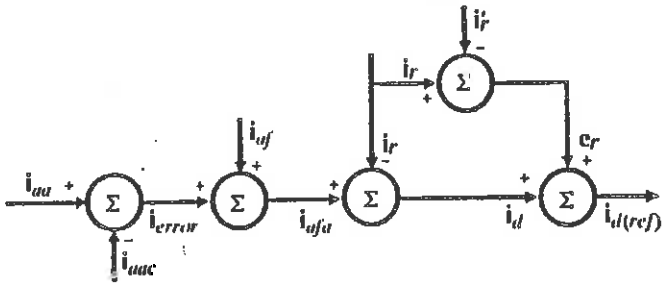

Figure 5(b): Overall control of the hybrid power compensator.

FICTITIOUS POWER ANALYSIS AND HYBRID COMPENSATOR CONTROL

From measurement of the supply busbar voltage u_s, the classic active current i_a is obtained from the original definition of active power [10].

$$G = {|P_L|}/{U^2} = \left|\frac{1}{T}\int_0^T u(t)i(t)dt\right| / \left[\frac{1}{T}\int_0^T u^2(t)dt\right] \quad (1)$$

$$i_a(t) = G\,u(t) \quad (2)$$

The active current is thus a scaled in–phase replica of the voltage. The value of conductance G used is the value calculated over the previous period, but from the original definition of active current, that is the only accurate value for i_a. Also the value of G may not be adjusted during one fundamental voltage period, since that would result in fictitious current flowing.

The fundamental frequency displaced current i_r is calculated from a $\frac{3}{4}$ cycle delayed version of the supply voltage u_s.

$$B = |Q_L| / U$$

$$= \left| \frac{1}{T} \int_0^T u(t - {}^{3T}/_4) i(t) dt \right| / \left[\frac{1}{T} \int_0^T u(t - {}^{T}/_4)^2 \, dt \right] \quad (3)$$

$$i_r(t) = B \, u(t - {}^{3T}/_4) \quad (4)$$

The delay in the calculation of B implies that the value of i_r also dates from the previous cycle. The instantaneous power theory is combined with the classic active current theory to give the revised instantaneous power theory [11]. From the revised instantaneous power theory, the correct instantaneous fictitious current, i_F is obtained. The revised instantaneous power theory does not provide a means of sub–dividing the fictitious current, but the subtraction of i_r from the fictitious current i_F results in the most accurate distortion current i_d.

$$i_d = i_F - i_r \quad (5)$$

For the hybrid power compensator in Figure 5a the suggested control is illustrated diagrammatically in Figure 5b. The control signal to the switched reactance for displaced current compensation is i_r. The current i_r is a reference value which could change with time and would accordingly result in a change in the firing angle of the switched reactance. The switching of the reactance induces current harmonics into the network, the amplitude of which varies with the firing angle.

Due to these harmonics and the possible inaccuracies in the switched reactance model, the actual static VAr compensator current i_r' should also be monitored. The distortion current value i_d is used as reference control signal to the dynamic compensator. As a feedback measure, the difference e_r between i_r and the measured value i_r' should be added to the dynamic compensator reference signal i_d in order to obtain complete compensation (Figure 5b). If fixed series tuned reactances are installed as part of the hybrid compensator, the particular current should also be monitored as part of i_r and subtracted from the calculated instantaneous reference value for i_d.

CLASSIC STATIC VAr COMPENSATOR

The classic static VAr compensator (SVC) relies on reactive components to generate or absorb reactive power [1]. The SVC forming part of the hybrid power compensator in Figure 5 consists of a fixed capacitance and a thyristor controlled transformer (TCT). The capacitance draws a steady leading current from the source. By varying the gating angle of the thyristors in the TCT, the fundamental component of the reactor current is varied.

$$I_{rl} = \frac{U_s \, (2\pi - 2\alpha + \sin 2\alpha)}{\pi \cdot \omega \cdot L\sigma} \quad (6)$$

At a firing angle of $\alpha = 90°$, full resonance between the reactor and capacitance takes place. In the absence of losses the SVC then has an infinite impedance and no current is drawn from the source. This means that the reactor has been dimensioned so that at a maximum it can absorb all the reactive power generated by the capacitance. The SVC can therefore only compensate loads with a lagging power factor characteristic.

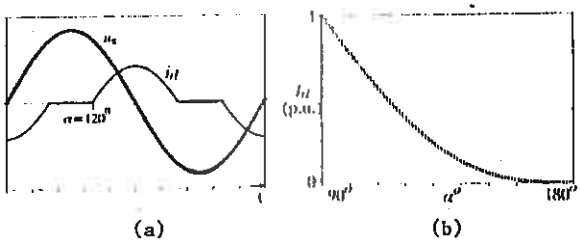

Figure 6: (a) Current and voltage waveforms of the TCT.
(b) Fundamental component I_f of the TCT current i_L as function of gating angle α.

From the fundamental frequency displaced current i_r drawn by the load, the value of the leading current to be generated by the SVC is known, $i_{svc} = i_r$.

The total line current i_{svc} drawn by the SVC is subdivided into the capacitor current i_{rc} and TCT current i_{rl} and algebraically expressed as

$$i_{svc} = i_{rc} - i_{rl} \quad (7)$$

Substituting equation (6) in (7) expresses i_{svc} as a function of the gating angle α.

$$i_{svc} = i_c - \frac{2 \cdot U_s}{\omega \cdot L\sigma} - \frac{U_s}{I_{rr}} \, (\sin 2\alpha - 2\alpha) \quad (8)$$

This is a transcendental equation in α and has to be solved numerically.

DYNAMIC COMPENSATOR CONTROL

The reference input to the dynamic compensator is the distortion current i_d. The dynamic compensator therefore is controlled as a current source, and would draw the inverse of the distortion current. The actual measured dynamic compensator current i_d' is subtracted from the reference current i_d which gives the error e, the input to a hysteresis controller (Figures 2 and 3) [13]. The output polarity of the histeresis controller determines the switching pulses for the converter bridge.

$$e = i_d - i'_d \quad (9)$$

The voltage–fed compensator (Figure 4 a,b,c) is a second order system, and the equivalent circuit for the switched conditions to generate a decreasing or increasing i'_d, is given in Figure 7 a and b respectively. L_f and r_f are the isolation / step up transformer series components combined with the equivalent network impedance, while the high transformer parallel resistance is neglected [4]. The dc voltage source is a capacitor and forms a second order circuit with L_f. The current–fed compensator (Figure 4 e,d,f) is a third order system, and Figure 8 a,b respectively illustrate the two switched conditions for a decrease and increase in i_d.

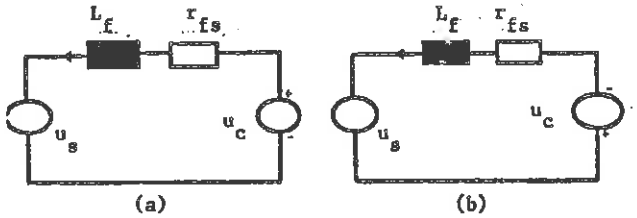

Figure 7: Equivalent voltage–fed dynamic compensator circuit for a decrease (a) and increase (b) in i_d'.

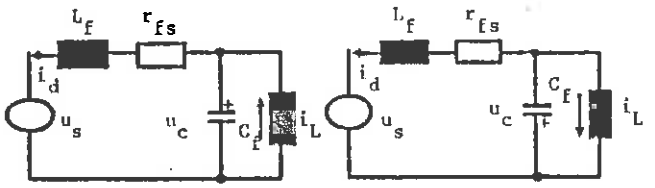

Figure 8: Equivalent current–fed dynamic compensator circuit for a decrease (a) and increase (b) in i_d'

The constant current source i_L is a coil and together with L_f and C_f forms a third order circuit. Capacitor C_f is necessary to filter the converter switching frequency. The control of the current–fed compensator with a hysteresis controller, results in a stable limit cycle, which is superimposed on the compensator generated current i_d' [14]. The limit cycle impairs the efficiency of compensation (Figure 9) [15][16]. A novel technique was implemented to control the current–fed compensator and cancel the limit cycle at its very origin. Previous attempts to cancel the limit cycle were succesful, but suffered from the drawback that the techniques were all compensator and network parameter dependent [4][7]. It is not the case with the error–modulation control technique, which would also have application in the wider control field. Due to the second order characteristics of the voltage–fed compensator, a limit cycle, as found in the current–fed dynamic compensator, does not exist in the system (Figure 10).

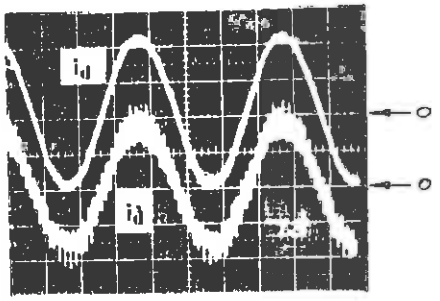

Figure 9: Stable limit cycle present in the compensating current of the dynamic current–fed compensator.

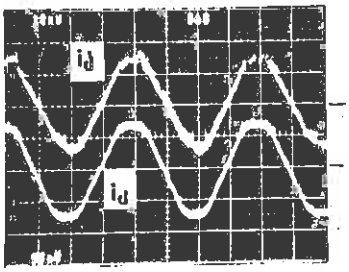

Figure 10: Generation of compensating reference i_d with voltage–fed dynamic compensator.

If the current sensed by the hysteresis controller is too small in the direction shown in Figure 4d, the controller will close switches S_3 and S_4 at time instant t_1 in Figure 11, thus charging the filter capacitor according to the equation.

$$u_c = \frac{1}{C}\int i_L \, dt \qquad (10)$$

The current i_d' will only start to increase in the direction shown if the instantaneous voltage across the filter capacitor is higher than that of the opposing supply voltage thus minimizing the error from time instant t_2 in Figure 11c. If the current is sensed as being too high, the controller will close switches S_1 and S_2, thus discharging the capacitor with respect to the supply voltage u_s and forcing the current to decrease. Results obtained in a practical circuit with this topology is shown in Figure 9.

It is clear from the results shown in Figure 9 that there is a stable but undesirable limit cycle present in the compensating current produced by the four–pulse current–fed converter [7][14]. The presence of this limit cycle is a result of the control strategy in use. The controller used is a hysteresis element with two possible outputs, namely +1 or −1. When the error, which is the difference between the reference current i_d and the compensating current i_d' exceeds a certain preset positive hysteresis limit, the output of the hysteresis element will go to −1 at time instant t_1 in Figure 11c. This will close switches S_3 and S_4, thus increasing the compensating current. The hysteresis element stays in this state until the error exceeds the preset negative hysteresis limit at time instant t_3 in Figure 11c. The output of the hysteresis element will then go to +1, causing switches S_1 and S_2 to close. This will cause the compensating current to decrease. There are thus two factors causing the limit cycle.

Firstly the current is forced to exceed the negative limit when sensed to be higher than the positive limit, and again forced to exceed the positive limit when sensed to be lower than the negative limit. This occurs because the controller can only change switching states when an error exceeding the hysteresis band is detected. This error will then be corrected for until overcorrection results, leading to the following change of state.

Secondly, there is a finite time necessary to charge or discharge the filter capacitor C_f. If r_f in Figure 8a is neglected for the purpose of illustration, the voltage equation for loop 1 in Figure 8a is

$$u_c - u_s = -L\frac{di_d}{dt} \qquad (11)$$

and from equation 10

$$\frac{1}{C}\int i_L \, dt - u_s = -L\frac{di_d}{dt} \qquad (12)$$

Equation 12 holds for time span t_0 to t_1 and t_1 to t_2 in Figure 11c and for time span t_2 to t_3 the capacitor voltage u_c is charged to a positive value with respect to the supply voltage and equation 13 holds.

$$+\frac{1}{C}\int i_L \, dt - u_s = L\frac{di_d}{dt} \qquad (13)$$

The ratio between the rates of change of current over period T_3 and period T_1 in Figure 11 is given as:

$$\frac{\left.\frac{di_d}{dt}\right|_{T_3}}{\left.\frac{di_d}{dt}\right|_{T_1}} = \frac{\left.\frac{1}{C}\int i_L \, dt - u_s\right|_{T_3}}{\left.-\frac{1}{C}\int i_L \, dt + u_s\right|_{T_1}} \qquad (14)$$

But the dc current i_L is constant and the supply voltage u_s can be approximated as constant since the switching rate is around 1kHz [4], and the capacitor voltage is charged with respect to the supply voltage.

Thus

$$\frac{\left.\frac{di_d}{dt}\right|_{T_3}}{\left.\frac{di_d}{dt}\right|_{T_1}} = \frac{\frac{i_L}{C}\int_{t_2}^{t_3} dt - U_s}{-\left[\frac{i_L}{C}\int_{t_0}^{t_2} dt - U_s\right]} \qquad [15]$$

Due to the overshoot of the compensating current at instant t_1 in Figure 11a and the fact that the capacitor voltage u_c has to be charged to zero with respect to the supply voltage u_s at time instant t_2, before the compensating current can start to increase from time t_2, the duration T_3 of charging of the capacitor until the error reaches the negative hysteresis band is longer than T_1 and therefore the numerator on the righthand side of equation 15 is larger than the denominator which implies that the rate of change of current over time period T_3 becomes greater than the rate of change of current over time T_2 because the capacitor C_f is charged for a longer time T_3. This implies that the $\frac{di_c}{dt}$ increases with each switching cycle, leading to the limit cycle. The system parameters eventually restrict the oscillation amplitude.

ERROR MODULATION

It is shown in the preceding discussion that there is an undesirable oscillation in the compensating current that is independent of the form of the reference current. It should be possible to eliminate the limit cycle if a controller that does in principle not use any hysteresis element is implemented. The impedance of the network is a variable function of time, which demands that the controller must be stable over a wide range of network impedances. Such a controller is shown in Figure 12.

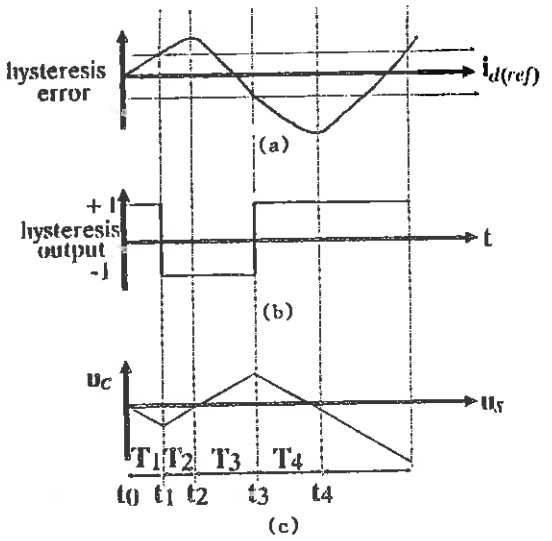

Figure 11: Error signal, hysteresis controller output and capacitor voltage in dynamic compensator.

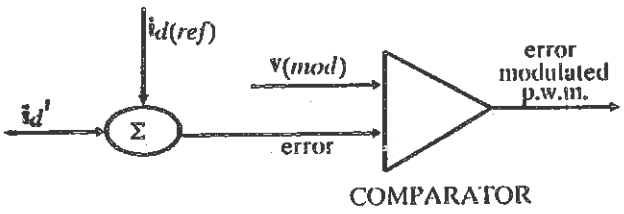

Figure 12: Error modulator.

The error value is obtained as discussed (equation 9). The error value is compared to a modulating signal which is a constant amplitude, constant frequency triangular waveform. The result is an error modulated pwm generator. As the error increases, the modulating depth is increased to ensure fast error correction. At minimum error the modulation depth adjusts to 50%.

SIMULATED RESULTS

In order to test this proposed new control technique, the system was simulated with PSPICE. Figure 13 shows results obtained with a sinusoidal reference current of frequency 50 Hz. The current i_d follows the reference with negligible error, and no limit cycle is apparent.

The reference current frequency was also varied and good results were obtained. Figure 14 shows results obtained with a reference current frequency of 1kHz, which is approaching the upper limit at which the compensator would be required to operate.

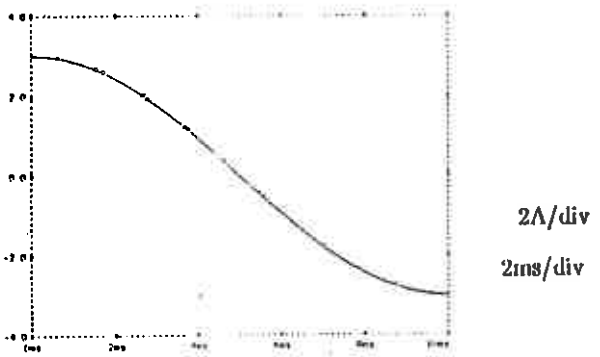

Figure 13: Error modulation generated compensating current i'_d (X) and reference current i_d (0).

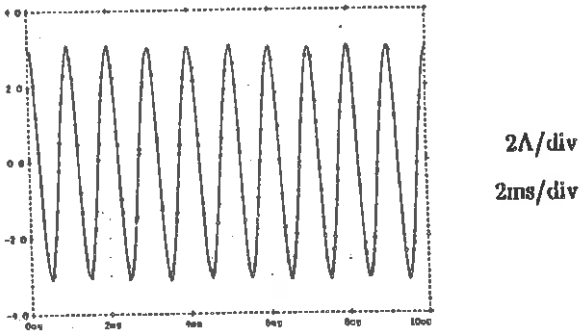

Figure 14: Error modulation generated compensating current i_d (X) and reference current i_d (0).

The influence of supply and compensator parameter variation was also investigated since in practical power systems the supply impedance is a varying function of time and there could also be variations from the design values of compensator components. The simulated error modulated pwm controller generated compensating currents with the same accuracy as in Figures 12 and 13 under conditions of changing parameters.

EXPERIMENTAL RESULTS

The revised instantaneous power theory [11], was applied to a non–linear experimental load comprising a 6–pulse static Scherbius cascade. The load operated under steady state conditions and therefore the control theory was applied off–line. Figure 15 illustrates the supply voltage u_s, the displaced current i_r, the active current i_a and the distorted current i_d. The waveforms in Figure 15 were used as control signals for the hybrid compensator. Figure 16 a–d illustrate the experimental results. The capacitor bank of the classic

static VAr compensator resonated with the supply impedance and that resulted in the distorted SVC waveform in Figure 16a. Such a resonant condition could also occur in practice, and presented an opportunity to further illustrate the versatility of the dynamic compensator. Firstly, the dynamic compensator cannot resonate with any other impedance and secondly, if a resonant condition exists in a network resulting in waveform distortion, the dynamic compensator would also compensate for that. The current distortion caused by the resonant condition, was added to the calculated i_d (Figure 5b), and the dynamic compensator generated the required current waveform (Figure 16c). Save for the low-level oscillation present in the supply current due to the SVC resonance with the supply impedance and the high frequency component due to the converter switching, the supply current is in-phase with the supply voltage and sinusoidal (Figure 16d).

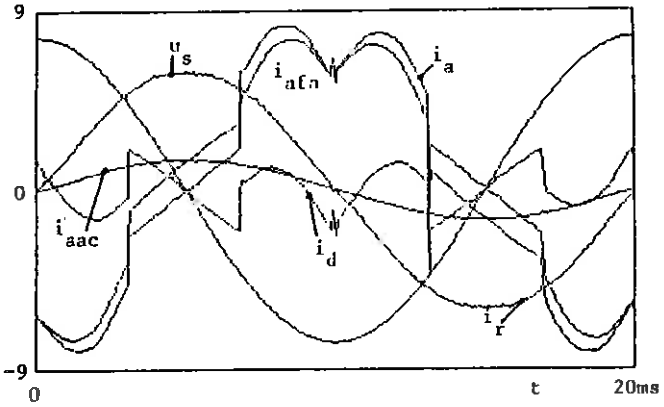

Figure 15: Supply voltage u_s, load current i_n, active current i_{aac}, displaced current i_r, distortion current i_d and fictitious current i_{afa} [11]

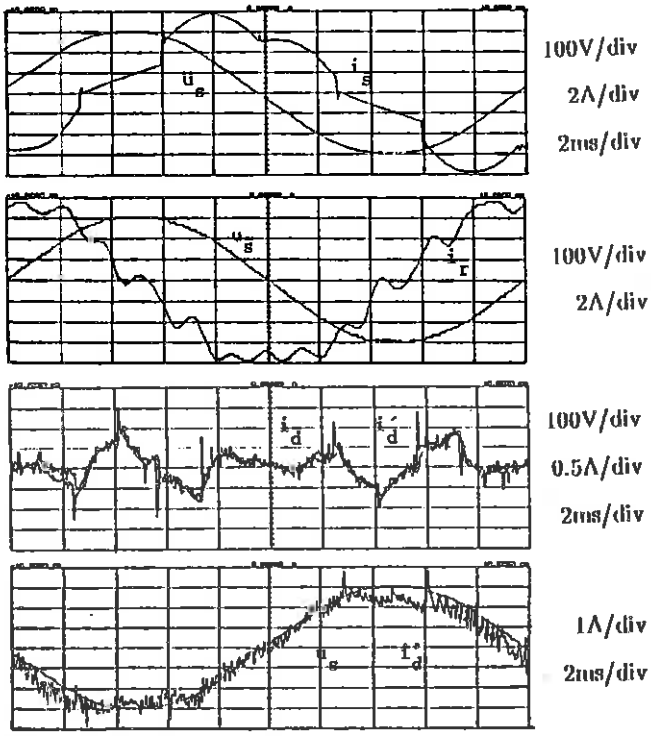

Figure 16 (a) Supply voltage u_s and load current i_s,
(b) supply voltage u_s and SVC current i_r,
(c) reference and generated distortion currents i_d and i_d
(d) supply voltage u_s and supply current i_d'

CONCLUSIONS

The paper illustrates the integration of the classic static VAr compensator and the dynamic compensator into-a hybrid topology. The control signals for each of the building blocks of the hybrid compensator are derived according to the revised instantaneous power theory. The experimental compensation results illustrate the complimentary function that each of the hybrid compensator building blocks fulfills. The error-modulation control technique allows one to control the current-fed dynamic compensator with the same accuracy than the voltage-fed compensator. Future work will include the implementation of hybrid compensator control signal calculation on computer and the extension of the hybrid compensator control to dynamic conditions. The error modulation control technique will be implemented in a practical dynamic compensator and the technique will be evaluated in terms of dynamic range and network parameter dependence.

SYMBOLS

P_L	Average power to the load.
Q_L	Reactive power between source and load.
u_s	Instantaneous supply voltage.
i_s	Instantaneous supply current.
U	Rms voltage value.
I	Rms current value.
i_F	Instantaneous fictitious current.
i_r	Instantaneous reactive current.
i_d	Instantaneous distortion current.
i_s	Instantaneous source current.
G	Average conductance.
B	Average susceptance.
i_{rl}	Instantaneous TCT current.
i_{rc}	Instantaneous SVC-capacitor current.
L_f	Lowpass filter component
C_f	Lowpass filter component
i_d'	Instantaneous compensating current.
i_r'	Instantaneous SVC current
i_r	Instantaneous displaced current.
e	Error input to hysteresis controller.
e_r	Difference between reference and generated SVC current
α	Gating angle of thyristors.
$L\sigma$	Leakage inductance of transformer.
i_{svc}	Instantaneous line current of SVC.
i_a	Instantaneous active current.

REFERENCES

[1] Sjokvist T. Thyristor switched capacitors for reactive power compensation. Iron and Steel Engineer, 1976.

[2] Gyugyi L. Reactive power generation and control by thyristor circuits. IEEE Transactions on Industry Applications, vol IA-15, no. 5, 1979, pp. 521 – 532.

[3] Gyugyi L, ER Taylor Jr. Characteristics of static, thyristor controlled shunt compensators for power transmission system applications. IEEE Transactions on Power Apparatus and Systems, vol PAS-99, no. 5, 1980, pp. 1845 – 1854.

[4] Van Wyk JD, DA Marshall and S Boshoff. Simulation and experimental study of a reactively loaded pwm converter as a fast source of reactive power. IEEE Transactions on Industry Applications, vol. IA-22, no.6, 1986, pp. 1082 – 1090.

[5] Chit A, W Horn and H Utecht. Limit of dynamic action of static power factor correction equipment. AEG-Telefunken Progress, 1976, pp. 19 – 24.

[6] Dinkel G and R Gretsch. Kompensator fur Oberschwingungen und Blindleistung. etz Archiv Bd 9, 1987, pp. 9 – 14.

[7] Van Schoor G and JD van Wyk. A study of a system of current–fed converters as an active three phase filter. Conference Record, IEEE Industry Application Society Annual Meeting, 1987, pp. 482 – 490.

[8] Smit I, JD van Wyk and JJ Schoeman. GTO–converters above 30kHz with resonant input link as power filters. Proceedings, 3rd European Conference on Power Electronics and Applications EPE–89, Aachen, BRD, October 1989, pp. 1549 – 1553.

[9] Inokuchi H, F Aoyama, T Furuhashi, Y Tanove and K Terashima. An application of the new static VAr compensator utilizing the pwm converters. Conference Record Eleventh UIE Conference, Spain, 1988, pp. 3–16.

[10] Fryze S. Wirk–, Blind–, und Scheinleistung in elektrischen Stromkreisen mit nichtsinusformingen Verlauf von Strom und Spannung. Elektrotechnische Zeitschrift, 1932, Heift 25, pp. 596 – 599, 625 – 627, 700 – 702.

[11] Marshall DA and JD van Wyk. An evaluation of the complete real–time compensation of fictitious power in electrical energy networks. ICHPS 1990 Meeting, Budapest, Paper submitted for evaluation.

[12] Miller TJE. Reactive power control in electric systems. John Wiley and Sons, 1982, pp. 181 – 217.

[13] Palaniappan RG and J Vithayathil. A control strategy for reference wave adaptive current generation. IEEE Transactions on Industrial Electronics and Control Instrumentation, vol. IECI – 27, no. 2, 1980, pp.92–96.

[14] Weischedel HR. An exact method for the analysis of limit cycles in on–off control systems. IEEE Transactions on automatic control, February 1973.

[15] Van Wyk JD, S Boshoff and DA Marshall. Compensation of distortion current in power networks by power electronic converters. Conference Record, IEE PEVD, 1986.

[16] Van Wyk JD, S Boshoff and DA Marshall. Adaptive elimination of aperiodic distortion in power systems. Conference Record, IEEE IAS Annual Meeting, Toronto, 1985, pp. 312 – 317.

[17] Atsuo Kawamura and RG Hoft. Analysis of pwm inverter with instantaneous feedback control IPEC – Tokyo, 1983, p. 259 – 373.

[18] Enslin JHR and JD van Wyk. A new control philosophy for power electronic converters as fictitious power compensators. IEEE PESC Conference Record, Kyoto, Japan, April 1988.

[19] Achenbach H, W Hanke and W Hochstetter. Controllable static reactive power compensators in electric supply systems. Symposium Preprints, 2nd IFAC Symposium Control in Power Electronics and Electrical Drives, Dusseldorf, 1977, pp. 917 – 924.

ACKNOWLEDGEMENTS

Mr. Marshall is on secondment from Eskom, the National Electricity Utility Company, and greatly appreciates their support. Financial support from the FRD, Pretoria, is also gratefully acknowledged.

A MICROPROCESSOR-BASED SYSTEM FOR MONITORING THE CONDITION OF A BATTERY ENERGY STORAGE PLANT

GP HANCKE AND GL VAN HARMELEN

Department of Electrical Engineering
University of Pretoria, Pretoria, South-Africa

ABSTRACT

The system described in this paper makes use of an electronic probe in each cell of a standby battery plant, being monitored by a dedicated microprocessor controller. These probes are scanned periodically by means of the microprocessor-controlled central unit, with status and error message outputs available on a printer connected to the controller. The probes use a fibre-optic technique for determining the specific gravity of the electrolyte of the lead-acid batteries and measurements are automatically corrected for temperature variations.

INTRODUCTION

The change in specific gravity of the electrolyte in a lead-acid cell is directly proportional to the energy taken out of the cell on discharge [1]. By measuring the specific gravity, it is possible to get an indication of how far a discharge has progressed. On charge, a specific gravity reading can be an approximate guide, but it is not directly proportional to the amount of charge received. This is due to the relatively slow diffusion of acid within the cell [2]. For accuracy, readings should only be taken after a stabilization period of several hours.

The conventional methods of measuring specific gravity are all based on the law of Archimedes. A classic example is the hydrometer, which is normally used to determine the state-of-charge of a lead-acid battery by measuring the specific gravity of the electrolyte. The measurement is made by drawing a sample of the battery acid into the glass barrel, until the hydrometer floats freely and a reading may be made. It is important to return the sample of acid to the cell from which it was taken, otherwise the specific gravity and level of the acid will be affected. This is a cumbersome and awkward procedure, especially when a large number of battery cells have to be checked. In addition, there exist certain conditions under which the use of a hydrometer is impractical. Installations where battery banks are used for emergency or primary sources of energy need to be monitored on a continuous or regular basis and are often situated in locations where accessibility is difficult. An example thereof is radio repeater stations on high mountains.

Likewise, the laboratory method of withdrawing a drop of the electrolyte and measuring its refractive index is not practical in continuous monitoring of the state-of-charge. Mas has used the gas flow from the battery [3] and its internal pressure [4] as parameters which, electrically sensed, control the charging current. These systems have been evaluated in battery chargers. Other methods use open-circuit voltage, impedance, and humidity as the charge-determining parameter. For example, Taylor employed the impedance of the battery as the critical parameter for charging [5]. Winsel [6] reported on a state-of-charge indicator based on humidity. Ofry and Singer [7] used an improved loaded voltmeter test. Other methods include the ampere-hour measurement and galvanostatic technique, both methods based on the fact that the internal resistance is a function of the state-of-charge.

It is further a well known fact that abnormally high and low temperatures affect SG measurements and a temperature correction factor has then to be applied [8].

In this paper however, a simple, cost effective method is presented whereby battery condition can be monitored on a continuous basis without the intervention of an operator. An analog voltage signal equivalent to specific gravity is available for continuous monitoring by a microprocessor and depending on the software that is loaded, any one of a host of actions may be taken by the controller. A probe is installed in each cell and all the probes are then scanned on a periodic basis with each probe having a unique address. A temperature measurement is also made by the microprocessor that the correct correction factor may be applied to the reading taken.

DESCRIPTION OF MEASUREMENT SYSTEM

The total measurement system may be subdivided into three main sections. These are the microprocessor hardware itself, the analog front and measurement interface control, and finally the software which is written to suite a specific user's requirements.

A block diagrammatic representation of the microprocessor based system is shown in Fig. 1. Cell selection and multiplexing takes place within the analog front end section. The microprocessor decides upon appropriate action by means of the software that is loaded and running. An electronic specific-gravity probe is further installed in each cell of the battery pack to be monitored and one external thermocouple is used to measure temperature.

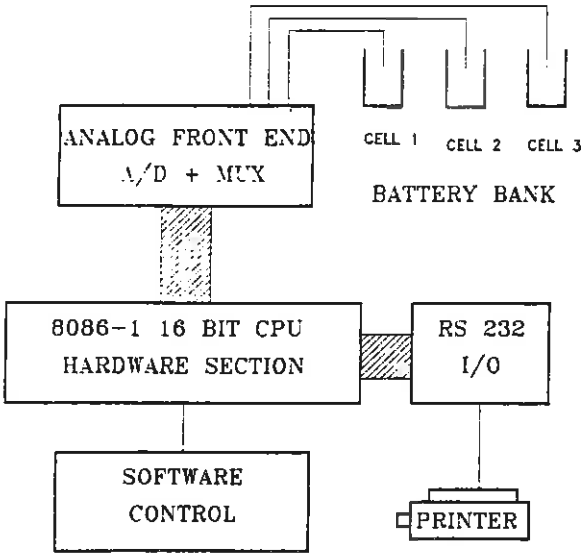

Figure 1. Block diagram of the measurement system.

The Analog front end.

CMOS 4051 analog multiplexers are cascaded and addressed so that upto 256 cells may be read with the current I/O setup. The 256 limitation is due to the use of an 8 bit output port to address the specific cell, however with a reconfiguration of the 8255 Programmable Peripheral Controller (PPI), 4096 cells may be addressed.

The second port on the PPI is used to transfer analog to digital converter data, and the third port is used to control the analog to digital converter, as may be seen in Fig. 2. A 12 bit AD 574 A/D converter was used in this application due to it's ease of operation and control. While 12 bit accuracy is not deemed necessary in this application, this facility has however been provided.

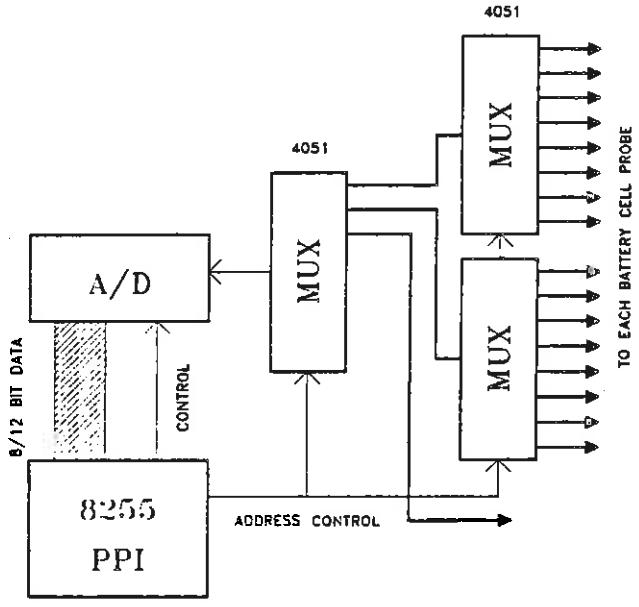

Fig. 2. Block diagram of the analog front end.

The 8086 Microprocessor

As the personal computer has become an everyday tool available to most engineers today, a dedicated, down-loadable 8086-1 CPU system was designed and constructed for this application. The basic structure is identical to any personal computer with the difference that no keyboard, CRT display or disk controllers are present in this dedicated system. Software may be written and debugged on a personal computer, and then loaded directly into the microprocessor RAM via a RS 232 interface, or two EPROMS may be burnt with the appropriate program.

Three system timers (8253), one interrupt controller (8259), a RS 232 port (8251) and an 8255 PPI are all included in this system. These provide extensive timing and interfacing control options. This is accompanied by 8 KB of EPROM memory and 32 KB of static RAM space. 2 KB of the RAM was configured at the bottom end of the memory to be used for interrupt addressing and as a stack segment.

The hardware described above is seen in Fig. 3. The user program may thus be run either, from internal EPROM memory, or may be loaded from a personal computer, via the RS 232 communication channel. Once the system is in operation, this port is also used to output data to a normal dot matrix printer.

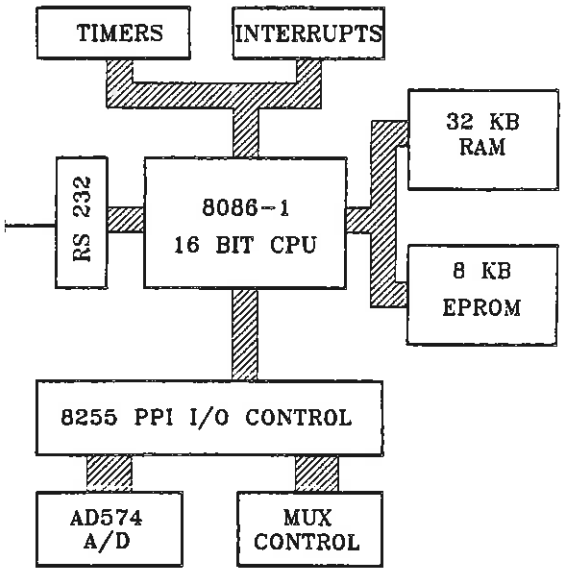

Fig. 3. Block diagram of the 8086-1 microprocessor controller card.

Software Development and Implementation

All of the software is presently written in machine code, assembled and then debugged on a personal computer. With the proliferation of assemblers and debuggers available on the market today, the implementing of code on one of these packages is almost as simple as writing a high level language such as Turbo Pascal. Once the software is written, it may be debugged on the PC itself, with only very limited software. The need for an In Circuit Emulator (ICE) and its very expensive development system is thus avoided.

A small program is further used to either split the generated program machine code into it's respective high and low byte section for burning into EPROMS, or the program may be directly loaded into the microprocessor RAM. The advantage of this option is that correct operation may be verified before the final burning of the EPROMS is undertaken.

Although applications and implementations may vary vastly from plant to plant, changing the configuration of this system is merely a matter of changing a program. The hardware was designed with maximum adaptability and versatility being key factors in its implementation. The current system checks the states of all the cells once every half hour and displays the calculated average condition of the battery bank. This is then printed on the printer.

An error level may be set at which the microprocessor will indicate a low state of charge or a faulty cell. This error message will also be printed, together with the address of the particular cell. Although all the cell data may be printed after every reading is made, this normally produces huge amounts of unused data.

This large amount of data may however be read by a personal computer for further post-processing. Storage of the data may then take place on hard or soft diskette with the added advantage that standard software packages (eg spreadsheets or databases) may be used to process the huge amounts of cell data.

THE OPTICAL PRINCIPLES OF THE PROBE

The most important part of the entire complicated system however, is the principle upon which the specific gravity sensor operates. This technique leads to a small, reliable and inexpensive probe which is inserted into all cells to be monitored. The phenomenon on which this specific sensor is based can be explained by means of the known laws of optics as illustrated in figure 4.

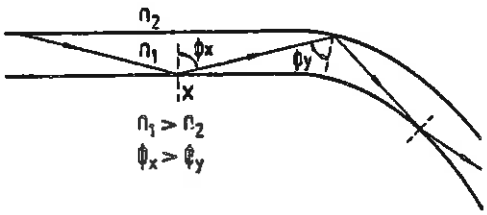

Figure 4. Reducing the angle of incidence by bending the fiber.

No losses from within the fiber will occur when the following two conditions are met:

(i) The index of refraction of the fiber, n_1, must be greater than that of the surrounding medium, n_2.

(ii) The angle of incidence must be greater than the critical angle φ_c, which is given by the following relationship:

$$\sin \varphi_c = n_2/n_1$$

When these conditions are met, total reflection will take place, otherwise refraction will take place and losses occur. The transducer under discussion utilizes the violation of the second above mentioned condition by:

(i) bending the fiber and consequently reducing the angle of incidence and

(ii) making use of the fact that the index of refraction (n_2) of the surrounding medium (i.e. the electrolyte) changes due to changes in the state-of-charge of the battery.

CONSTRUCTION OF THE PROBE

A block diagram of the relative density probe is shown in figure 5. A current source supplies a constant current to an infrared diode, which acts as source of radiation. The infrared radiation is transmitted along the optical fiber through the curved section where losses occur as a function of the specific gravity of the surrounding medium. The remainder of the radiation is detected by the infrared detector, which forms one arm of a Wheatstone bridge. The bridge output voltage is amplified by means of a differential amplifier. The output signal, voltage or current, is then used as required. In the case of this particular system, the voltage is fed to an analog multiplexer input of the address at which this probe is inserted.

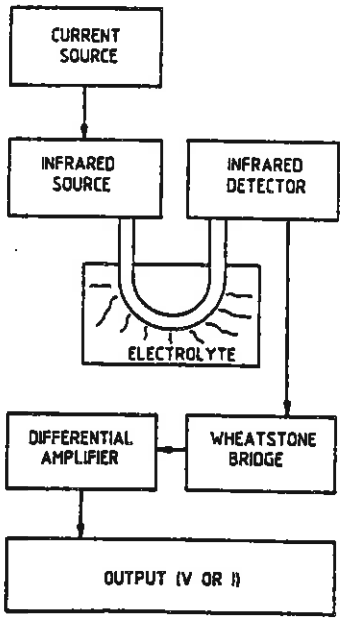

Figure 5: A block diagram of the measurement probe

The Sensing Element

The sensor element itself is very important and its construction is illustrated by means of the longitudinal sectional view of figure 6.

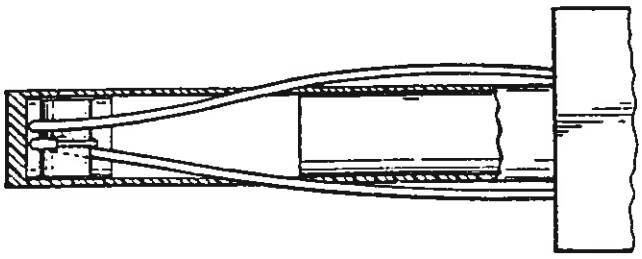

Figure 6: The construction of the sensor.

The sensor comprises a cylindrical wall of plastic material with the bottom end of the cylinder being closed off by means of an end-piece. This serves to prevent gas from accumulating on the optical fiber, resulting in inconsistent readings. The forming of gas takes place when the lead-acid battery is charged.

Provision has to be made though for the diffusion of acid within the probe. This is done by providing sufficient circulation apertures in the wall of the sensor. A circular mounting member is mounted transversely in the sensor, between the end-piece and the openings. The optical fiber is wrapped around the mounting member, with a portion of the fiber stripped of its cladding. It is in this bare piece of fiber where the actual measuring process takes place.

Calibration

The instrument has been calibrated to measure specific gravity between 1.1 and 1.3 because these are the values that correspond to a fully discharged and fully charged lead-acid cell respectively. It is also possible to calibrate the instrument in terms of state-of-charge.

These calibration charts are formed by means of lookup tables which are stored with the CPU memory. The voltage that is read by the A/D converter varies between 0 and 9 volts with the error level for a faulty or discharged battery preselectable by means of software.

CONCLUSIONS

A fibre-optic probe for measuring relative density has been developed and successfully applied to the electrolyte of a lead-acid battery in order to determine the state-of-charge of the battery. These probes are then implemented in a larger microprocessor controlled measuring system, the size of which is user selectable and will vary depending on the actual requirements. It must be mentioned that this instrument has primarily been developed in order to get an indication of the state-of-charge of lead-acid batteries without using an operator and for this application measurement accuracy is not of paramount importance.

The primary goal of this system is thus to detect a bad cell and sound an alarm by printing an appropriate error message and address on the printer. An audible or visual alarm may also be added with relative ease.

ABBREVIATIONS

CPU	Central Processing Unit
PPI	Programmable Peripheral Controller
RAM	Random Access Memory
EPROM	Erasable Programmable Read Only Memory
A/D	Analog to Digital Converter
KB	Kilobyte
I/O	Input/Output
PC	Personal Computer
MUX	Multiplexer
V	Voltage
I	Current
SG	Specific Gravity

REFERENCES

[1] K.V. Kordesch, Batteries. Vol. 2: Lead-acid batteries and electric vehicles, New York: Marcel Dekker,Inc, 1977, ch. 2, p 246

[2] G.W. Vinal, Storage Batteries, 4th ed. New York: Wiley, 1955, ch. 6, pp 260 - 263

[3] J. Mas, U.S. Pat 3 241 028 (1966)

[4] J. Mas, U.S. Pat 3 816 806 (1974)

[5] D.F. Taylor, U.S. Pat 3 816 807 (1974)

[6] A Winsel, German Pat 2 254 207 (1973)

[7] E. Ofry and S Singer, Measurement of the state of battery charge using an improved loaded voltmeter test method, IEEE Transactions on Instrumentation and Measurement, vol. IM-31, no. 3, pp 154 - 158, September 1982

[8] G. Smith, Storage Batteries, 2nd Edition, Pitman Publishing, 1971 ,ch. 10, pp 188-191

PARAMETER IDENTIFICATION APPLIED TO INDUCTION MOTORS

JA de Kock FS van der Merwe HJ Vermeulen
University of Stellenbosch, South Africa

ABSTRACT

A parameter perturbation technique used in parameter identification is applied to induction motors. The results indicate that measurements taken from voltage disturbances to the machine contain enough information to estimate the machine parameter values with good accuracy.

1. INTRODUCTION

Economic considerations have forced modern power systems to operate closer to their stability limits. This has made power system stability studies very important to utilities and large industrial concerns. As a result, the theory of and models for stability studies, have received much attention in the past number of years. Simulations of power systems, can now be done quite accurately provided that the parameter values of the elements used, are accurately known and available.

This is not always the case. Data could be lost, or was never calculated or supplied by the manufacturers to the user. If, after installation, machine parameters have to be determined, it is usually cumbersome and often not possible. Some of the parameters cannot be measured and can only be approximated from calculations, e.g. rotor resistance and the leakage inductances.

A new method is proposed that will solve these problems. The machine is perturbed by a sudden change in voltage, and the dynamic response of the induction motor is measured with a data acquisition system. The raw data is conditioned and used to drive a computer model of the induction motor. The simulated results are compared with the actual results. The error is used to update the parameter values of the model, and so improve the model's response to disturbances.

2. DATA ACQUISITIONING AND CONDITIONING

To implement the proposed method, data (i.e. the three-phase voltages, the three-phase currents and the speed signal) of the dynamic behaviour of the induction motor must be collected and stored for later processing. A digital data acquisition system (see figure 2.1) was used for this purpose. It comprises voltage and current isolation amplifiers that are coupled to the induction motor's feeder, and a speed encoder. These signals are fed to a 12-bit analog-to-digital converter with it's own controller and on-board memory. The A/D converter is software controlled from a personal computer (PC), which is also used to store the data and condition it for later processing.

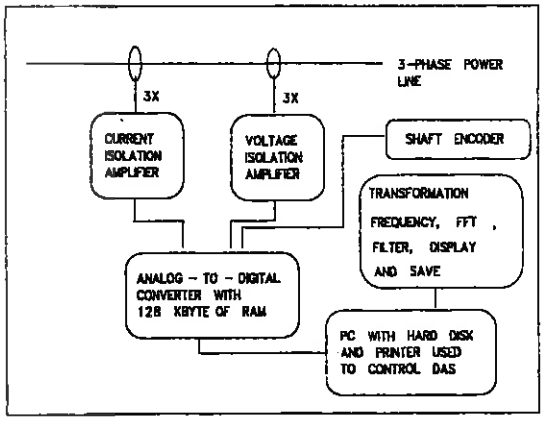

Figure 2.1 A schematic diagram of the data acquisition system and it's functions.

The machine model used for identification makes use of a synchronous rotating reference frame. Measured data must be transformed from a three-phase stationary reference frame to a two-phase synchronous rotating reference frame (see Jones [1] pp. 79 -86 and pp. 147-60, and Krause [2] pp. 133-63). To make this transformation, the frequency of the raw data must be determined very accurately.

High frequency harmonic distortion can interfere with the transformation and appears as correlated noise. The harmonic content of the raw data can be determined with a FFT [6], and acts as a guide to adjust the sampling frequency. The sampled data may be digitally filtered to remove the unwanted noise.

In figure 2.2 an example is given of the raw data sampled from the supply voltage to the induction motor during a voltage dip. If this data is transformed without filtering the noise generated from the harmonic distortion is very pronounced. This is demonstrated in figure 2.3 that makes use of the data in figure 2.2. If the data is filtered selectively the signal may be improved to that in figure 2.4 and can now be used in simulation and identification.

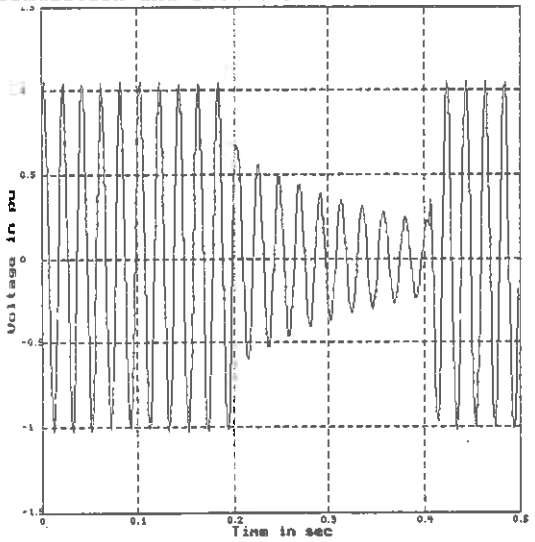

Figure 2.2 The raw data sampled from a phase of the supply voltage to the induction motor.

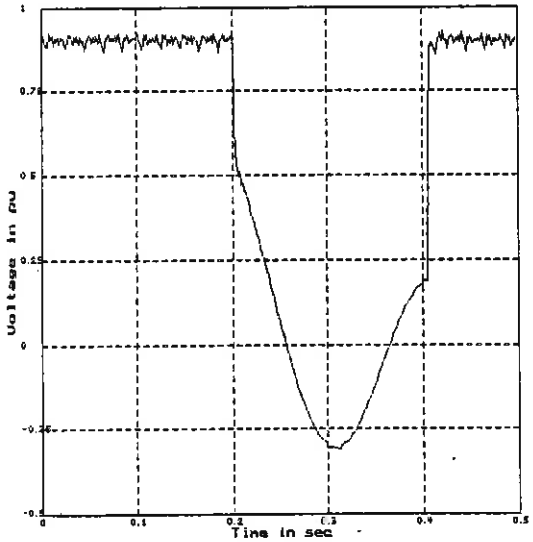

Figure 2.3 Note the harmonic distortion in the transformed Q-axis voltage of the data in figure 2.2.

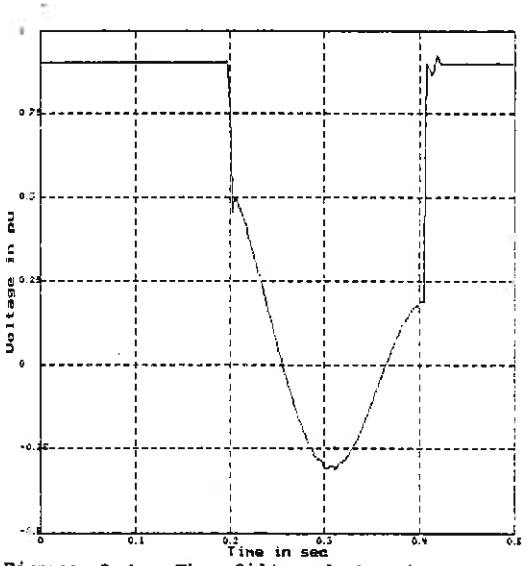

Figure 2.4 The filtered Q-axis voltage signal of the data in figure 2.2.

3. SIMULATION AND IDENTIFICATION

The speed range in which the induction motor operates prior to, during, and after voltage dips is limited to the upper speed range if the motor reaccelerates. This makes it possible to use a single rotor cage model for simulation and identification. To implement the machine model, the machine equations were transformed to obtain equation 3.1.

$$[v] = [z][i] \qquad 3.1$$

The deduction of this equation can be followed in Krause (see [2] pp. 172-5). The full equation is given in the appendix. The torque equation 3.2 does not change under the transformation.

$$T_e - T_l = \frac{1}{2H}\,s \qquad 3.2$$

where $T_e = X_m(i_{qs}i_{ds} - i_{ds}i_{qs})$

These equations can be rewritten in a block diagram format for simulation (see figure 3.1). An in-house developed program 'Non-linear Identification through SIMulation' (NISIM) [3] was used for the simulation of the motor. It can be run from a PC with 640 kbyte of RAM. This program can take the non-linear properties of an induction motor into account and has the capability to use measured data as an input to a simulation. Additional routines could also be written to take special functions into account, e.g. the electromagnetic coupling between the stator and the rotor.

By simulating the induction motor, a good knowledge of the characteristics of the system can be obtained and the importance of various parameters determined. NISIM allows a set of parameters to be perturbed and draws a family of graphs to demonstrate the effect of the change of parameter values on the system's behaviour. Simulations that are started at an non-zero operating point, need initial values for the various states.

To identify a system, prior knowledge of the system is needed to obtain a mathematical model of the system. For linear or linearized systems, identification can be done with a program like MatLab [5]. Most real systems are however non-linear, and have to be identified in this mode of operation. NISIM uses a parameter perturbation technique to minimize the error J(r) between the simulated model and the real system as seen in figure 3.2.

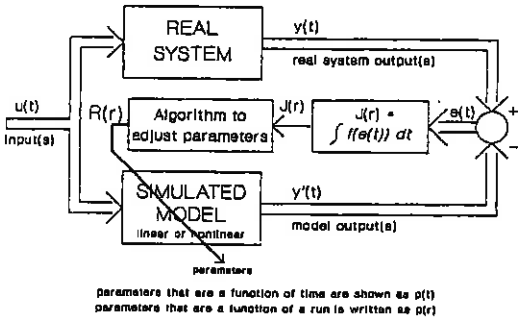

Figure 3.2 A flow diagram of the parameter perturbation technique as used in NISIM.

J(r) is a relative error of the weighted sum of the difference between the real and simulated outputs. For each of the real system outputs a weighting matrix is built for comparison with the simulated outputs (see equation 3.3).

$$J = f_1(e) + \frac{1}{T}\int_{\omega}^{T} f_2(e)dt \qquad 3.3$$

where: $f_1 = k_w[\max(\bar{Y}-\hat{Y})]$

and $f_2 = k_1(e)^3 + k_2e^2 + k_3|e| + k_4\sqrt{e}$

Knowledge of the output signal is important when building a weighting matrix. If the wrong combination is used, the program would give a false minimum value for the error and the perturbed parameter.

The value of J(r) is only relative and is a strong function of the choice of the weighting matrix and the comparative output signals. This may lead to a small change in the J(r) for a large variation in the value of a parameter.

The answer produced by the program may be incorrect. It is important to visually inspect the difference between the best simulation and the real system, and if necessary adjust the weighting matrix to improve the results.

4. RESULTS OF THE IDENTIFICATION PROCEDURE

Measurements and data used are confined to laboratory tests with a 5,5 kW induction motor. The induction motor's operation was disrupted by a dip in the supply voltage to the machine. Measurements were made of the resulting disturbance and the data was conditioned for use in the program NISIM. The prior knowledge of the system was used to set initial limits on the parameter value that was to be perturbed for identification (see table 4.1).

Table 4.1 Induction motor parameters estimated with NISIM (all values are in per unit).

Parameter	Tolerance	Estimated value	Measured value
R_s	0 to 0,2	0,045	0,058
T_{load}	-0,4 to -1,0	-0,8023	-0,8350
H	0,5 to ∞	1,890	2,1255
R_r	0 to 0,2	0,060	0,062

The model's parameters were adjusted, one at a time, during the identification process. Initially a linear scanning method was used to determine an estimated value of a parameter by minimizing the error J(r) in figure 3.2. The parameter value is varied over a large area to prevent the program from converging to a local minimum. Once a global minimum is found, a gradient method is used to find the best value.

In figure 4.1 a sample of the transformed and filtered current response is given for the disturbance in figure 2.1. This used for comparison with the simulated current in figure 4.2a. In this example of parameter perturbation the inertia (actually 1/2H) was varied from 0,1 to 0,5, as illustrated in figure 4.2c. For each run a graph of one or more of the outputs can be drawn. The response of the Q-axis stator current is illustrated in figure 4.2a and the relative error J(r) figure 4.2b.

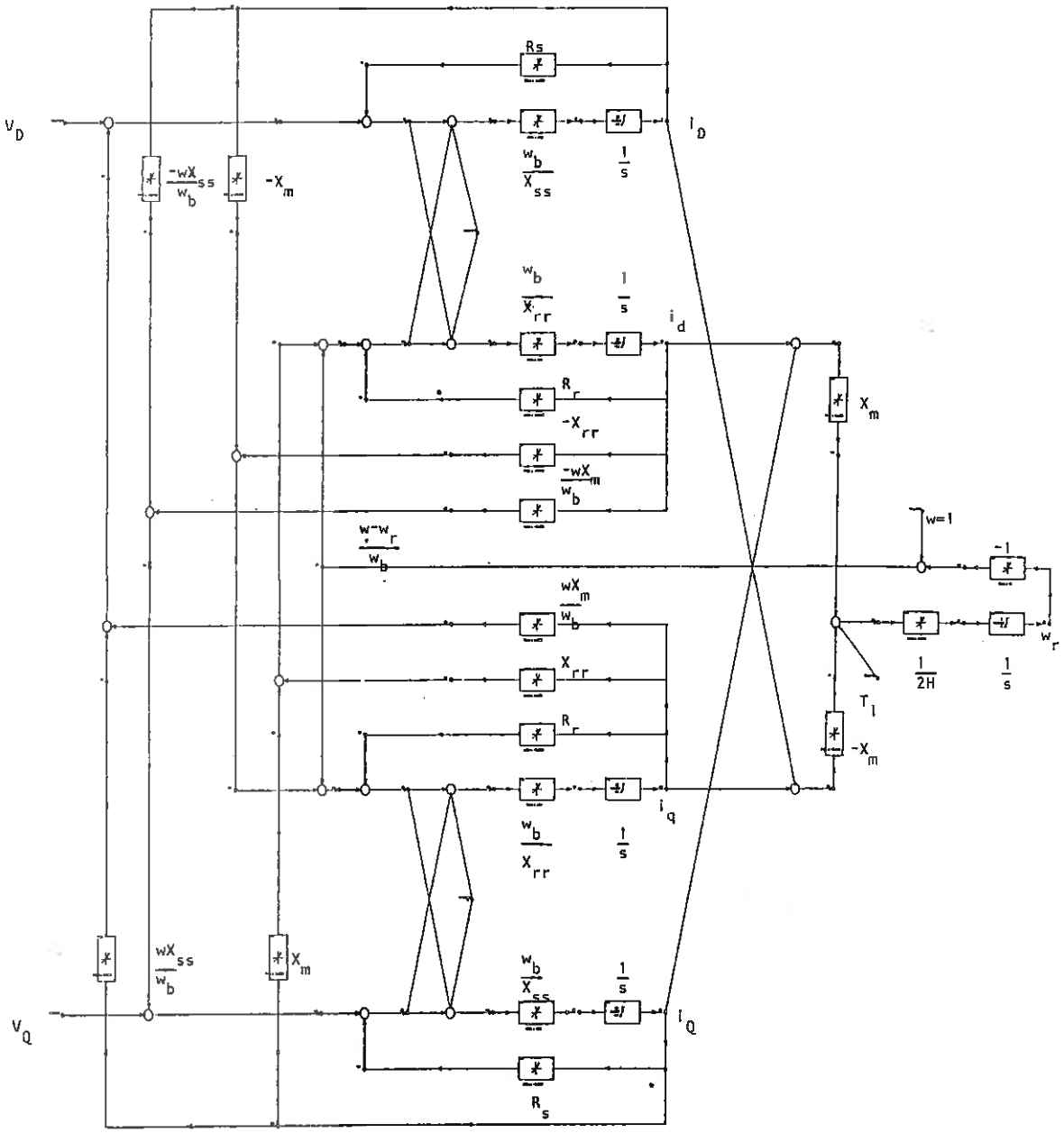

Figure 3.1 Equation 3.1 implemented in block diagram form to simulate the induction motor with NISIM.

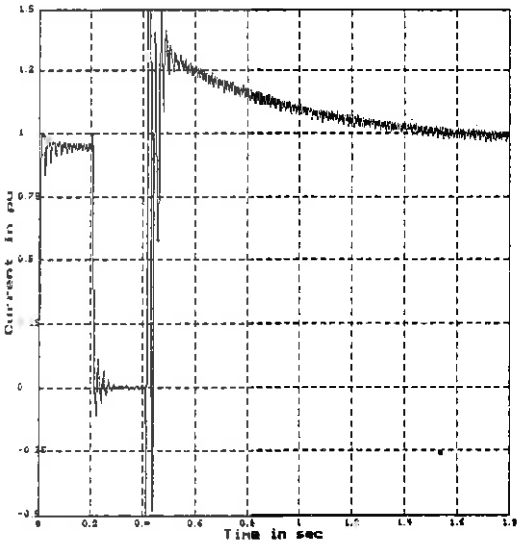

Figure 4.1 The measured Q-axis stator current of the induction motor for the voltage dip in figure 2.2.

The parameters were estimated one at a time and the whole process repeated to improve their values if possible. Note must be taken of the improvement to determine further estimation.

5. CONCLUSION

With the aid of a parameters perturbation technique, the parameter values of an induction motor can be identified. The system is lightly perturbed by forcing a voltage dip on the system and measurements are made of the voltage, current and speed responses. Using this method optimal parameter values can be obtained for the machine with a minimum of disruption caused to normal operation of the plant. The results indicate that there is a good correlation between the estimated values and values obtained from conventional tests, that are usually long and cumbersome.

At present this technique has only been used on a 5,5 kW motor, but further investigations are to be done on operational high voltage industrial machines.

6. ACKNOWLEDGEMENT

The authors wish to thank the National Energy Council (NEC) and SASOL for their financial support with the research.

7. REFERENCES

1. JONES, C.V., The Unified Theory of Electrical Machines, Butterworths, London, 1967.

2. KRAUSE, P.C., Analysis of Electrical Machinery, McGraw-Hill, New York, 1987.

3. STRYDOM, O.M. and MOSTERT, J., The NISIM Manual, Internal document of the Dept of Electronic Engineering of the Univ. of Stellenbosch, 1990.

4. HOWE, R.M., Dynamics of Real-Time Digital Simulation, Applied Dynamics International, 1982.

5. MOLER, C., LITTLE, J., BANGERT, S. and KLEIMAN, S., PC-Matlab, The MathWorks, Inc., Sherborn, 1986.

6. BERGLAND, G.D., 'A Guide Tour of the Fast Fourier Transform', IEEE Spectrum, July 1969.

8. APPENDIX

List of symbols: all values are in per unit.

R_s - Stator resistance
X_l - Stator leakage reactance
X_m - Magnitizing reactance
X_2 - Rotor leakage reactance
R_r - Rotor resistance
H - Inertia constant
T_l - Load torque
w - Frequency of reference frame
w_b - Base frequency
w_r - Rotor speed
v - Voltage
i - Current
Q - Quadrature axis of stator
D - Direct axis of stator
q - Quadrature axis of rotor
d - Direct axis of rotor

$X_{ss} = X_l + X_m$
$X_{rr} = X_2 + X_m$

The full version of equation 3.1:

$$\begin{bmatrix} v_q \\ v_d \\ v_q \\ v_n \end{bmatrix} = \begin{bmatrix} r_s+\frac{p}{\omega_b}X_{ss} & \frac{\omega}{\omega_b}X_m & \frac{p}{\omega_b}X_m & \frac{p}{\omega_b}X_m \\ -\frac{\omega}{\omega_b}X_{ss} & r_s+\frac{p}{\omega_b}X_{ss} & -\frac{\omega}{\omega_b}X_m & \frac{p}{\omega_b}X_m \\ \frac{p}{\omega_b}X_m & \left(\frac{\omega-\omega_r}{\omega_b}\right)X_m & r_r+\frac{p}{\omega_b}X_{rr} & \left(\frac{\omega-\omega_r}{\omega_b}\right)X_{rr} \\ -\left(\frac{\omega-\omega_r}{\omega_b}\right)X_m & \frac{p}{\omega_b}X_m & -\left(\frac{\omega-\omega_r}{\omega_b}\right)X_{rr} & r_r+\frac{p}{\omega_b}X_{rr} \end{bmatrix} \begin{bmatrix} i_q \\ i_d \\ i_q \\ i_n \end{bmatrix}$$

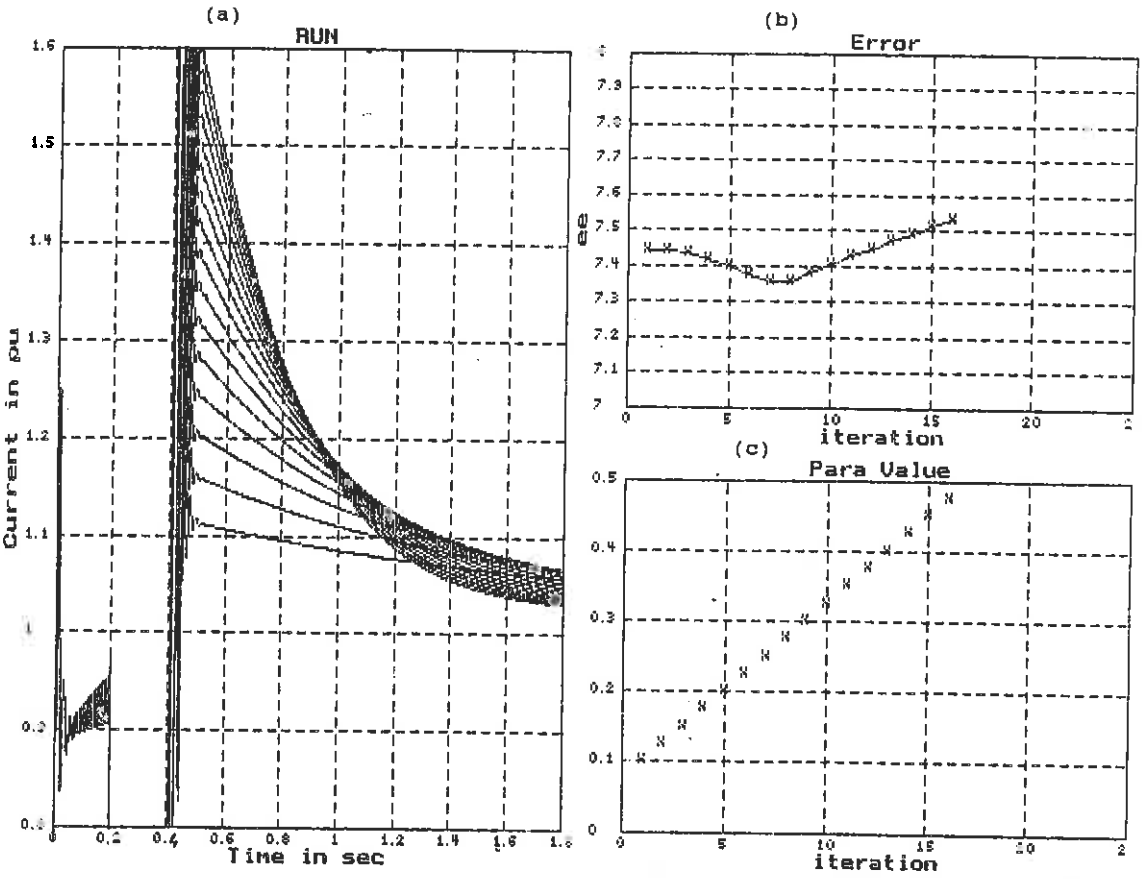

Figure 4.2 An example of the estimation process performed on the inertia of the system.

The Effects of Additional Space Harmonics induced in Induction Motors having Broken Rotor Bars

C.F. Landy, W. Levy, M.D. McCulloch

Department of Electrical Engineering
University of the Witwatersrand, Johannesburg
South Africa.

Abstract

The effects of broken bars on the current distribution in an insulated cage machine were investigated. It is proposed that the new current pattern causes additional space harmonic fields in the airgap. These space harmonic fields give rise to additional time harmonic currents in the stator winding. It is also shown that these additional space harmonic fields due to the rotor unbalance interact with some of the stator space harmonics thereby producing synchronous torques at some specific speeds. The speeds at which these synchronous torques occur is shown to be independent of the number of slots in the rotor. These synchronous torques were found for one broken bar as well as for a combination of broken bars. It is also shown that these synchronous torques will occur in an uninsulated cage motor, provided the motor parameters are such that the current flowing in the broken bar is small.

1 INTRODUCTION

With the present trends of designing more economical induction motors, the materials used are made to operate close to both their electrical and mechanical limits. Thus, especially when operating in harsh environments, the probability of rotor bars breaking will be greater now than it has been previously. Early detection of broken rotor bars can lead to a scheduled repair of the motor, before costly damage is done to the stator windings.

Williamson and Smith (1) investigated the current pattern around an insulated cage with broken rotor bars and the production of oscillatory torques at speeds near rated speed. Kerszenbaum (2) predicted a decrease in the pullout torque if the rotor had broken bars. He also verified the presence of additional stator time harmonic currents, and the presence of axial vibrations of frequency equal to four times running speed. The above authors predicted the presence of a negative phase sequence harmonic mmf, for a faulty cage.

This paper investigates the case of an insulated cage induction motor. It is shown that from the predicted current distribution around the cage for one broken bar, additional space harmonic fields are produced. These cause additional stator current frequencies and additional synchronous torques. Verification was obtained on an experimental motor developed by Cormack. This is an inverted geometry, four pole motor ie. the cage is the stationary member, thus allowing for ease of measurement of the bar currents. The cage can also be changed thereby allowing for measurements to be taken on a 22,26 and 36 bar cage. There are 24 stator slots. It was also shown that these effects were present in an uninsulated cage motor.

This machine has been designed to emphasise space harmonics which are present eg. by the stator winding not being short chorded. The slot combinations also lead to a distorted torque speed curve. However these effects do not detract from the subsequent analysis.

2 ANALYSIS OF ROTOR BAR CURRENT DISTRIBUTIONS

From the method proposed by Williamson and Smith, the current distribution around the cage was predicted for the 36 bar cage experimental motor. The current distribution was measured by placing a toroidal coil around each bar. The measured and predicted values for one broken bar are shown in Figure 1. These values were normalised to minimise irregularities found in the cage.

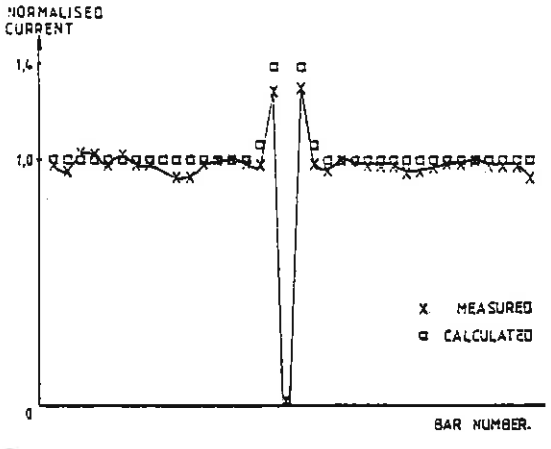

Figure 1: Calculated and measured current distribution for one broken bar

Figure 2 (a) shows the current distribution around the cage of a four pole machine at an instant of time. It must be noted that this sinusoidal pattern is moving with respect to the cage at the slip speed. Figure 2 (b) shows the distribution at the same

instant of time, but for one broken bar. Once again the sinusoidal component is moving relative to the cage, while the discontinuity set up by the broken bar is not. This can be thought of as the multiplication of the time moving wave of Figure 2 (a) with the stationary wave of Figure 2 (c). The function shown in Figure 2 (d) was used to simplify the analysis.

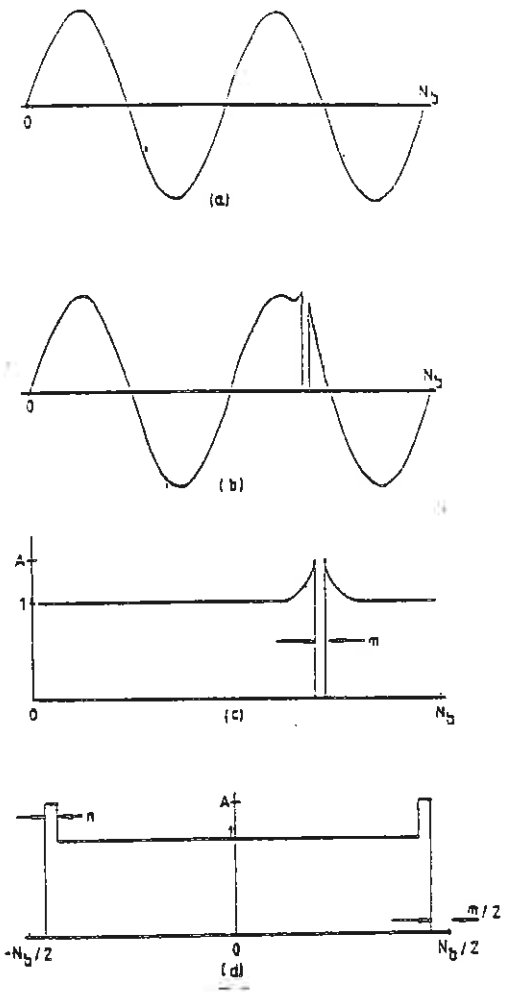

Figure 2:

(a) Current distribution for a healthy cage

(b) Current distribution for one broken bar

(c) Effective modulating wave

(d) Simplified modulating wave

From the Fourier analysis in Appendix A, the function of Figure 2 (d) can be written as

$$F = a_o + \sum \{a_k \cos(kwx) + b_k \sin(kwx)\} \qquad (1)$$

where

$$w = \frac{2\pi}{N_b} \qquad (2)$$

$$a_o = 1 - \frac{2}{N_b}\{A_n - n - m\} \qquad (3)$$

$$a_k = \frac{1-A}{\pi k}\sin\left\{\pi k\left(1 - \frac{2m}{N_b} - \frac{2n}{N_b}\right)\right\} + \frac{A}{\pi k}\sin\left\{\pi k\left(1 - \frac{2m}{N_b}\right)\right\} \qquad (4)$$

The function in Figure 2 (a) is given by

$$i = I\cos\left\{\frac{2\pi px}{N_b} - 2\pi ft\right\} \qquad (5)$$

Multiplying the k harmonic of equation 1 by equation 2 gives the function for figure 2 (b) as

$$\begin{aligned} j_k &= a_k I\cos\left\{\frac{2\pi kx}{N_b}\right\}\cos\left\{\frac{2\pi px}{N_b} - 2\pi ft\right\} \\ &= \frac{a_k I}{2}\left\{\cos\left\{\frac{2\pi x}{N_b}(k+p) - 2\pi ft\right\} + \cos\left\{\frac{2\pi x}{N_b}(k-p) + 2\pi ft\right\}\right\} \end{aligned} \qquad (6)$$

and

$$j_o = I a_o \cos\left\{\frac{2\pi px}{N_b} - 2\pi ft\right\} \qquad (7)$$

Thus the disturbance in the current pattern produces a new set of space harmonics in the cage of order (k+p) rotating in the forward direction and order (k-p) rotating in the backward direction. These mmf harmonics will interactwith the stator winding.

3 PRODUCTION OF ADDITIONAL STATOR CURRENTS

Each of the above mmf harmonics will induce an emf in the stator winding. However due to the winding factor these may be very small in magnitude. The experimental machine used has a full pitched, narrow phase spread, three phase winding. Thus only harmonics of the form p(3py+1) where y is any integer, will have a net resultant emf in the stator. These emfs will give rise to

Table 1: Magnitude of predicted additional primary currents

HARMONIC ORDER k	PREDICTED FREQUENCY FOR -520 RPM (Hz)	MEASURED MAGNITUDE (dB)
+2	50	0
+10	-19	-31
+14	-54	-46
+22	-123	-46
+26	-158	-36
-2	85	-20
-10	154	-52
-14	189	-34
-22	258	-36
-26	292	-32

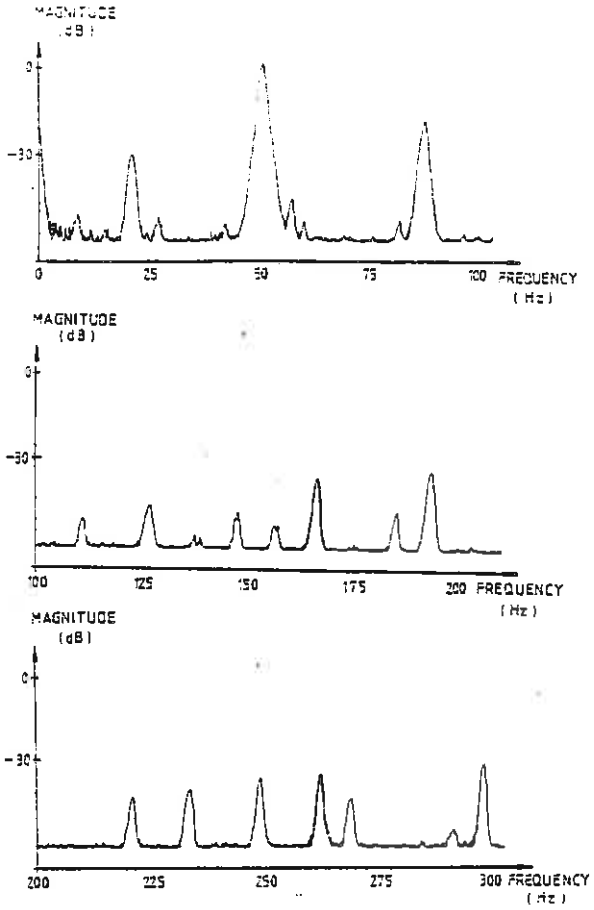

Figure 3: Frequencies of primary current measured at 520 RPM.

currents in the stator of frequency given by Appendix B as

$$f' = pN_s + N(k - p) \tag{8}$$

The experimental motor (36 bar cage) was driven at a speed of -520 RPM, so as to seperate the current components. Table 1 shows the expected frequencies that should be present. as well as the measured magnitudes for one broken bar. Figure 3 shows the actual harmonic spectrum. From the table it can be seen that the negative phase sequence component (-2) is large compared to the other harmonic components. This is due only in part to the coil winding factor.

4 PRODUCTION OF SYNCHRONOUS TORQUES

The table of harmonic content of a healthy 36 bar cage motor, as developed by Landy, is shown in Table 2. When a bar is broken, a negative phase sequence of the fundamental was previously shown to exist. By a similar analysis to that given in section 3, each of the space harmonics induced in the cage by the stator space harmonics can develop its own oppositely rotating component. Thus a second table of harmonics can be formed which will contain the same entries as for the first table, but each of the rotor harmonics will be of an opposite sign. Note that for a cage with a broken bar both of these tables will exist.

Table 2: Table of harmonic content for a healthy 36 bar machine

		-2	-1	0	+1	+2
K	q					
-8	-46	-118	-82	-46	-10	+26
-6	-34	-106	-70	-34	-2	+38
-4	-22	-94	-58	-22	+14	+50
-2	-10	-82	-46	-10	+26	+62
0	+2	-70	-34	+2	+38	+74
+2	+14	-58	-22	+14	+50	+86
+4	+26	-46	-10	+26	+62	+98
+6	+38	-34	+2	+38	+74	+110
+8	+50	-22	+14	+50	+86	+122

Consider a general table of harmonics. Let Q_a be a stator space harmonic which generates a rotor harmonic r. If the harmonic r has the same order as another stator harmonic Q_b, where $Q_b = Q_a$, then a synchronous torque will occur at a given speed. If Q_b has the same sign as r, then, from Appendix C equation C7 the synchronous torque will occur at zero speed ie. a cogging torque. When they are of opposite signs, then the synchronous torque will occur at a speed given by

$$N = \frac{2pN_s}{Q_a + Q_b} \tag{9}$$

Thus, for a healthy cage, if there is a rotor space harmonic of the same order and sign as for a stator space harmonic, then a cogging torque will occur. For the cage with one broken bar this same combination will give rise to a synchronous torque at the speed given by equation 9. Similarly, if the table of harmonics for a healthy cage has entries of opposite sign for the rotor and stator, the synchronous torque will occur at a speed given in equation 9. When one bar breaks, this combination will give rise to a cogging torque.

As shown in section 3, when a bar breaks, additional rotor space harmonics of all integral orders are produced. Each order has mmf waves travelling in both directions. However these can only interact with harmonics of the same order which are present in the stator. For the experimental machine, the dominant space harmonics in the stator are the tenth, fourteenth, twenty-second and twenty-sixth. Thus it is expected that only these orders of space harmonics will produce torque (eg. both the forward and backward rotating tenth rotor space harmonic can interact with the tenth stator space harmonic).

Each of the rotor space harmonics is stationary with respect to its corresponding stator harmonic at only one speed, hence producing a sychronous torque at that speed. From Appendix D, if the rotor and stator harmonics are moving in the same direction (for a slip of one), this synchronous torque will occur at zero speed. If these harmonics are moving in an opposite sense (for a slip of one), this synchronous torque will occur at a speed given by equation D4

$$N = \frac{2pN_s}{Q + p} \tag{10}$$

This speed is dependant only on the stator winding and is independant of the number of bars.

From Table 2, only cogging torques are produced for the healthy 36 bar cage motor. When one bar is broken, from the above section, synchronous torques will occur at $-Ns/2$, $+Ns/4$ and $+Ns/7$. From above, it is predicted that synchronous torques will occur at speeds of $-Ns/2$, $+Ns/4$, $-Ns/5$ and $+Ns/7$ for the tenth, fourteenth, twenty second and twenty sixth harmonics respectively. Although both theories predict synchronous torques at similar speeds, the former does not predict a torque at $-Ns/5$. From Figures 4 (a) and (b), synchronous torques can be seen at $-Ns/2$, $+Ns/4$, $+Ns/7$ and at $-Ns/5$, thus verifying the latter theory.

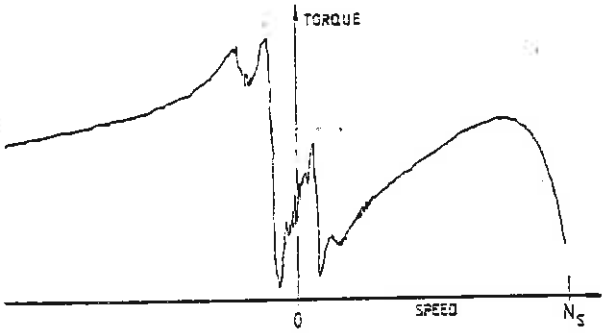

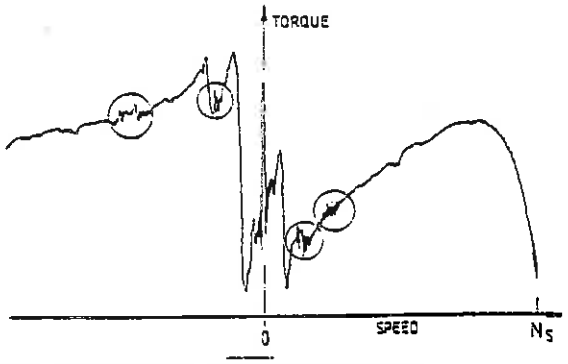

Figure 4: Torque speed curve for 36 bar machine

(a) Healthy cage

(b) One broken bar

it can be shown that for the healthy 22 bar cage, synchronous torques should appear only at $-Ns/11$. For one broken bar, from section 5.1, there should only be cogging torques and no other synchronous torques. From section 5.2, there should again be synchronous torques at $-Ns/2$, $+Ns/4$, $-Ns/5$, $+Ns/7$ and at zero speed. From the measured torque speed curves, Figures 5 (a) and (b), these effects can be seen.

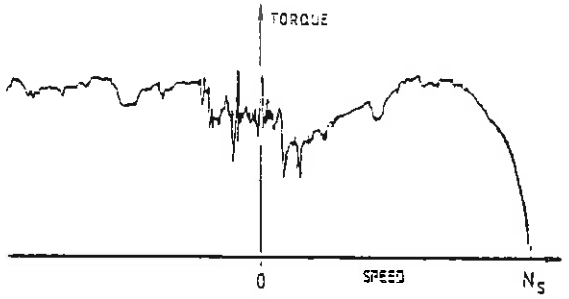

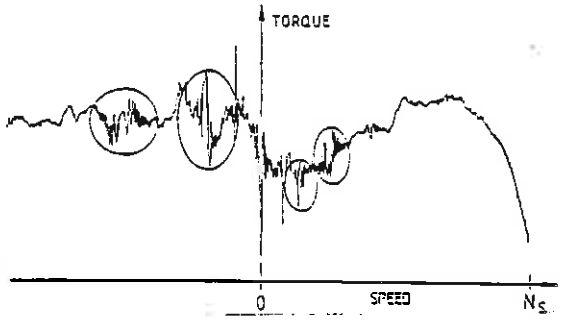

Figure 5: Torque speed curve for 22 bar machine

(a) Healthy cage

(b) One broken bar

For both the healthy 36 and 22 bar cage cases, there are small anomalies in the cage due to unequal contact resistances between each bar and the endring. This caused the appearance of the more dominant synchronous torques for a healthy cage. This shows that the production of synchronous torques is very sensitive to disturbances in the cage. Thus it is predicted that these synchronous torques will be evident for the case of an uninsulated cage motor.

An uninsulated 36 bar cage was used which has cage characteristics similar to that of large induction motors. As can be seen from Figures 4 (a) and (b), the additional synchronous torques are produced. It is hence expected that these synchronous torques will be present in large induction motors; however this is still to be verified.

5 CONCLUSION

It has been shown that, when a bar of an insulated cage induction motor breaks, a distinct current distribution is set up around the cage. This disturbance was shown to cause additional mmf space harmonics. These harmonics were shown to exist by the presence of additional stator current time harmonics.

The additional mmf harmonics also produce synchronous torques at specific predicted speeds, given by two separate theories. The "additional harmonics" theory is thought to be the more dominant since it is independant of the number of bars and the mmf waves in the rotor are larger for this theory than for the former. It was also shown that the production of synchronous torques is very sensitive to discrepancies in the cage, and it was further shown that the torques were present when a bar breaks in an uninsulated cage.

It is now put forward that by doing a torque speed curve, faults can be detected in the cage during manufacture. This technique can also be used to detect broken rotor bars for induction motors that are in service.

6 LIST OF PRINCIPAL SYMBOLS

- A – peak value of current distortion
- f – frequency
- k – harmonic order
- m – number of broken bars
- N – speed of rotor
- N_b – number of bars
- N_r – speed of stator wave relative to rotor
- N_s – speed of stator wave relative to stator
- N'_s – speed of rotor wave relative to stator
- n – width of assumed distortion
- p – number of pairs of poles
- Q – stator harmonic order
- r – rotor harmonic order

7 REFERENCES

1. **Williamson, S. and Smith, A.C.** "Steady state analysis of three phase cage motors with rotor bar and endring faults", PROC IEE Volume 129 b, May 1982, pp 93–100.

2. **Kerszenbaum, I.** "The behaviour of three phase squirrel cage induction motors with unbalance in the rotor impedance; in particular two pole machines", PhD Thesis, University of the Witwatersrand, 1983.

3. **Cormack, W.** "The measurement of the torque slip curves of induction machines", TRANS SAIEE Volume 46 (5), 1955, p127.

4. **Plowden, K.C.** "Measurements of the currents flowing in the bars of a squirrel cage induction motor", MSc Thesis University of the Witwatersrand, 1972.

5. **Landy, C.F.** "An investigation of an induction motor with a view to leakage effects and developed torque", PhD Thesis, University of the Witwatersrand, 1978.

APPENDIX A

The equation for the Fourier series is

$$F = a_o + \sum \{a_k \cos(kwx) + b_k \sin(kwx)\} \qquad \text{(A1)}$$

where

$$w = \frac{2\pi}{T} \qquad \text{(A2)}$$

For Figure 2(d), due to symmetry, $b_k = 0$ for all values of k.

$$\begin{aligned} a_o &= \frac{1}{T}\int_{\frac{T}{2}}^{\frac{T}{2}} F\,dx \\ &= \frac{2}{T}\int_0^{\frac{T}{2}-m-n} dx + \frac{2}{T}\int_{\frac{T}{2}-m-n}^{\frac{T}{2}-m} A\,dx \\ &= 1 - \frac{2}{T}\{An - n - m\} \end{aligned} \qquad \text{(A3)}$$

$$\begin{aligned} a_k &= \frac{1}{T}\int_{\frac{T}{2}}^{\frac{T}{2}} F\cos(kwx)\,dx \\ &= \frac{2}{T}\int_0^{\frac{T}{2}-m-n} \cos\left\{\frac{2\pi kx}{T}\right\} dx + \frac{2}{T}\int_{\frac{T}{2}-m-n}^{\frac{T}{2}-m} A\cos\left\{\frac{2\pi kx}{T}\right\} dx \\ &= \frac{1-A}{\pi k}\sin\left\{\pi k\left(1-\frac{2m}{T}-\frac{2n}{T}\right)\right\} + \frac{A}{\pi k}\sin\left\{\pi k\left(1-\frac{2m}{T}\right)\right\} \end{aligned} \qquad \text{(A4)}$$

For the case in question, m and n have units of numbers of bars while $T = N_b$, the total number of bars.

APPENDIX B

The speed of the fundamental mmf wave with respect to the rotor is given by

$$N_r = N_s - N \qquad \text{(B1)}$$

where

$$N_s = \frac{f}{p} \qquad \text{(B2)}$$

The k^{th} rotor harmonic (in mechanical measure) has a speed relative to the rotor of

$$N_{rk} = \frac{p(N_s - N)}{k} \qquad \text{(B3)}$$

The speed of this wave relative to the stator is

$$\begin{aligned} N'_s &= \frac{p(N_s - N)}{k} + N \\ &= \frac{pN_s}{k} + N\left(1 - \frac{k}{p}\right) \end{aligned} \qquad \text{(B4)}$$

This mmf wave induces an emf wave in the primary which causes a current of frequency

$$f' = pN_s + N(k - p) \qquad \text{(B5)}$$

APPENDIX C

The speed of the Q_a^{th} harmonic relative to the stator is

$$N_{sq} = \frac{pN_s}{Q_a} \tag{C1}$$

The speed of this wave relative to the stator is

$$N_{rq} = \frac{pN_s}{Q_a} - N \tag{C2}$$

The speed of the r^{th} rotor harmonic produced by Q_a is

$$N_{rr} = \left(\frac{pN_s}{Q_a} - N\right)\frac{Q_a}{r} \tag{C3}$$

The speed of this wave relative to the stator is

$$\begin{aligned} N_s' &= \frac{pN_s}{r} - \frac{NQ_a}{r} + N \\ &= \frac{pN_s}{r} + N\left(1 - \frac{Q_a}{r}\right) \end{aligned} \tag{C4}$$

Now for this mmf wave to interact with stator harmonic Q_b, $Q_b \neq Q_a$ and $Q_b = r$ or $Q_b = -r$.

$$N_s' = \frac{pN_s}{Q_b} \tag{C5}$$

therefore

$$\frac{pN_s}{Q_b} = \frac{pN_s}{r} + N\left(1 - \frac{Q_a}{r}\right) \tag{C6}$$

Case 1: $Q_b = r$

$$\frac{pN_s}{Q_b} = \frac{pN_s}{Q_b} + N\left(1 - \frac{Q_a}{Q_b}\right) \tag{C7}$$

therefore

$$N\left(1 - \frac{Q_a}{Q_b}\right) = 0$$

i.e. $N = 0$ since $Q_a \neq Q_b$.

Case 2: $Q_b = -r$

$$\begin{aligned} \frac{pN_s}{Q_b} &= -\frac{pN_s}{Q_b} + N\left(1 + \frac{Q_a}{Q_b}\right) \\ \frac{2pN_s}{Q_b} &= N\left(1 + \frac{Q_a}{Q_b}\right) \\ N &= \frac{2pN_s}{Q_a + Q_b} \end{aligned} \tag{C8}$$

APPENDIX D

The speed of the k^{th} rotor harmonic relative to the rotor is

$$N_{rk} = \frac{p(N_s - n)}{k} \tag{D1}$$

The speed of this wave relative to the stator is

$$\begin{aligned} N_s' &= \frac{p(N_s - n)}{k} + n \\ &= \frac{pN_s}{k} + n\left(1 - \frac{p}{k}\right) \end{aligned} \tag{D2}$$

For this wave to interact with the Q^{th} stator harmonic, either $Q = k$ or $Q = -k$.

Case 1: $Q = k$

$$\frac{pN_s}{Q} = \frac{pN_s}{Q} + n\left(1 - \frac{p}{q}\right) \tag{D3}$$

therefore

$$n\left(1 - \frac{p}{Q}\right) = 0$$

i.e. $n = 0$ for $p \neq Q$.

Case 2: $Q = -k$

$$\begin{aligned} \frac{pN_s}{Q} &= -\frac{pN_s}{Q} + n\left(1 + \frac{p}{Q}\right) \\ \frac{2pN_s}{Q} &= n\left(1 + \frac{p}{Q}\right) \\ n &= \frac{2pN_s}{Q + p} \end{aligned} \tag{D4}$$

THE EFFECT OF INTERBAR CURRENTS ON A DOUBLE-CAGE INDUCTION MOTOR

R.F.WALLISER, *BSc(Eng)*
C.F.LANDY, *PrEng, BSc(Eng), MSc(Eng), PhD, MSAIEE, SMIEEE, AMIEE*

ABSTRACT: Under certain conditions, interbar currents may flow between uninsulated bars through the core of the machine. This is known to occur if skew is present in the rotor bars; but it was also found that if a bar is broken, current still flows into it and then flows tangentially out to the adjacent bars. This phenomena has thus far only been investigated in the case of single cage machines and this paper examines the effect on double-cage machines.

1 List of principal symbols

I_n -actual average current flowing in outer cage
I_t -actual total current flowing in system comprising broken bar and adjacent bars in both inner and outer cages
I_D -inner cage current in system
I_{bb} -actual current flowing into broken bar from the healthy endring
$2I_b(x)$ -actual rotor-bar current flowing into the broken bar at a distance x from the healthy endring
$2dI_c(x)$ -current flowing from broken bar into the core at a distance x from the healthy endring
Z_o -outer bar impedance
Z_i -inner bar impedance
R_c^{oo} -interbar resistance between outer bars
R_c^{io} -interbar resistance between inner and outer bars
l -normalized gross core length

2 Introduction

The double-cage rotor carries two concentric and separate cage windings. The inner cage has an inherently low value of resistance and a high reactance, while the outer cage has a high resistance and a low reactance value. On starting, the outer cage carries most of the current and its high resistance results in a lower starting current and a higher starting torque than in the case of a comparable single-cage machine. To a first approximation, it is possible to consider the final torque-speed characteristic to be the sum of those of the individual cages. This allows the shape of the torque-speed curve to largely be determined by the designer in the way the impedance values of the two cages are varied.

Although a large amount of research has been conducted into faults in rotors of single cage machines, there has been little attention paid to those faults that occur in double-cage machines. Rotor bar faults present a rather difficult problem, because most of the rotor current flows in the outer cage at starting and in the inner cage while running. A fractured bar in the outer cage may therefore, only have an effect during starting and be difficult to detect under running conditions. Williamson and Abdel-Magied[1], did do research into this area and came up with an extremely complex method of analysis relating externally impressed voltages by a coupling impedance matrix. Bar faults are represented by altering the matrix dimensions and this relies on the fact that no current flows into the broken bar. The presence of large interbar currents could largely disrupt this form of analysis.

This paper deals with the occurrence and prediction of interbar currents in double-cage machines. A full understanding of the nature, if any, of these interbar currents is needed before any attempt should be made at methods of detecting these faults.

2 Theoretical Analysis

The predictions are based on a staggered double cage machine arrangement, with each inner cage bar centrally placed between two outer cage bars. With this arrangement, the mutual reactance between cages can be ignored.

2.1 Assumptions

a) The interbar currents flow only between the broken bar and the two adjacent bars of both cages
b) The voltages induced in all the bars in question are in phase with one another
c) The interbar resistance is mainly resistive at the supply frequency

d) The endring impedance between bars is negligible
e) The portion of the bars between endring and core is disregarded
f) The bar fracture is between the endring and the core
Although a) may not be strictly true, it is assumed most of the current flows to the adjacent bars.

2.2 Model

From the equivalent circuit of Jacobs[2] for a double-cage machine with separate end rings and no mutual reactance, the following expression is obtained relating the inner cage current to that of the outer cage

$$I_D = \frac{Z_o}{Z_i} I_n \qquad \ldots\ldots (1)$$

Fig 1 is a graphical representation of the situation of a broken outer cage bar. The current flowing in the inner and outer cages can be representing by the following expressions involving I_t and $I_b(x)$ by using eqn 1

$$I_o = \left(\frac{I_t}{2} - I_b(x)\right)\left(\frac{Z_i}{Z_i+Z_o}\right) \quad \ldots (2)$$

$$I_D = \left(\frac{I_t}{2} - I_b(x)\right)\left(\frac{Z_o}{Z_i+Z_o}\right) \quad \ldots (3)$$

Using eqns 2 and 3, the following expressions can be obtained for the voltages dropped across a portion of the bars.

$$dV_B = -2 I_b(x) Z_o dx \qquad \ldots (4)$$

$$dV_A = -\left(\frac{I_t}{2} - I_b(x)\right)\left(\frac{Z_i Z_o}{Z_i+Z_o}\right) \quad \ldots (5)$$

Following assumption (b), dV_A and dV_D should be equal

From 4 and 5 the following expression can be found for the voltage between the broken bar and the adjacent bars

$$V_{BA} = V_B - V_A$$

$$= -\frac{3Z_iZ_o+2Z_o^2}{Z_o+Z_i}\int_0^x I_b(x)\,dx + \frac{I_t}{2}\frac{Z_iZ_o}{Z_i+Z_o}x$$

Since, $dI_c(x) = -dI_b(x)$ it follows that

$$dI_c = \left(\frac{V_{BA}}{R_c^{oo}} + \frac{V_{BD}}{R_c^{oi}}\right)dx$$

$$= -\left(\frac{dI_b(x)}{dx}\right)dx$$

Rearranging and differentiating gives the following differential equation

$$\frac{d^2 I_b(x)}{dx} - \left(\frac{2Z_o^2+3Z_oZ_i}{Z_o+Z_i}\right)\left(\frac{R_c^{oo}+R_c^{oi}}{R_c^{oo}R_c^{oi}}\right)$$

$$I_b(x) + \frac{I_t}{2}\left(\frac{Z_iZ_o}{Z_i+Z_o}\right)\left(\frac{R_c^{oi}+R_c^{oo}}{R_c^{oo}R_c^{oi}}\right) = 0$$

Using the initial conditions: $I_b(x=l) = 0$ and $dI_b(x=0) = 0$; the DE can be solved and the following expression for $I_b(x)$ is obtained

$$I_b(x) = \frac{I_t}{2}\left(\frac{Z_i}{2Z_o+3Z_i}\right)\left(1 - \frac{\cosh\lambda x}{\cosh\lambda l}\right)$$

where

$$\lambda = \sqrt{\left(\frac{2Z_o^2+3Z_oZ_i}{Z_i+Z_o}\right)\frac{1}{R_c}}$$

and

$$\frac{1}{R_c} = \left(\frac{R_c^{oo}+R_c^{oi}}{R_c^{oo}R_c^{oi}}\right)$$

Now, since the change in the mmf distribution in the region of the broken bar will be compensated for by the increased currents flowing in the adjacent bars, the total ampere-turns produced in the system will remain almost constant, therefore

$$I_n = \frac{I_t - 2I_D}{3}$$

Using 1, this can be rearranged to give

$$I_t = I_n\left(\frac{3Z_i+2Z_o}{Z_i}\right)$$

Substituting this into the equation for $I_b(x)$

$$I_b(x) = \frac{I_n}{2}\left(1 - \frac{\cosh\lambda x}{\cosh\lambda l}\right) \quad ....(6)$$

With the constant lambda as defined previously. Since $2I_b(x=0) = I_{bb}$ the following expression is obtained for the current entering the broken bar

$$\frac{I_{bb}}{I_n} = 1 - \frac{1}{\cosh\lambda l} \quad ....(7)$$

Referring to Kerszenbaum[3] and Landy and Kerszenbaum[4], equations 6 and 7 are the same as those representing the case of a broken bar in a single-cage machine. The difference between the two cases being the definitions of the constant lambda and the contact resistance, which are more complex in the case of the double cage machine. Consequently, for the same value of lambda, the broken bar in the single- and double-cage machines will have the same amount of current entering it but the way it distributes into the core will differ. Fig 2 shows how the current entering the broken bar is determined by the value of lambda. For values of lambda above two, the current entering the broken bar becomes comparable to the current entering that of a normal bar.

The presence of large currents entering the broken bar, will disrupt the theory presented by Williamson and Abdel-Magied[1]. This could explain some of the discrepancies which they encountered in practice. A large value of lambda; found especially in large machines; during operating conditions could make broken bar detection difficult using present techniques as the current pattern would not be disrupted as much as would be expected.

3 Experimental Verification

3.1 Method

To prove that currents are flowing in the broken bar, a method is needed to measure the actual current flowing in a single bar. This is very difficult to achieve when the motor is rotating. There is a method of detecting currents flowing in a single rotor bar under locked rotor conditions using Rogowski coils. This method is described in detail by Kerszenbaum[3] and has been used successfully many times before. Basically, this method consists of a wound calibrated coil being secured around the bar with its output being the differential of the current flowing in the bar. The coil output is then fed into an amplifying and integrating circuit to obtain the magnitude of the current flowing in the bar. This method is used because the coil will experience very little interference from any other sources apart from the one it is wrapped around. Saturation is also not a problem because of the air core and Fig 3 shows the very linear property of one of these coils.

3.2 The Experimental Motor

The motor used was one of staggered design, with each cage having 72 circular shaped bars and a skew of one stator slot pitch. The outer cage has a 40% conductivity, while the inner has a conductivity of 100%. The machine is a 10 pole, 380V First Electric motor with a full load rating of 100kW.

With the aid of a simulation package, the bar currents at standstill at a reduced voltage of 129V were found to be 410A and 230A for the outer and inner cages respectively. The calculation of R_e proved to be a problem because the motor, when constructed, had an insulated outer cage. This insulation is known to break down once the motor has been in use, and so lambda had to be calculated for the case of the insulation still being intact and for the case of it being broken down. With the insulation still being intact, there would be very high values of R_e and thus from the definition of lambda, we expect it to be very low, and thus not much current to flow in the broken bar. Taking the insulation as being largely ineffectual, values for R_e^{oo} and R_e^{oi} need to be found. The interbar resistance per meter of effective core length was found by Kerszenbaum[3] to be in the region of 19.5$\mu\Omega$ for large machines. This value was increased to 25 and 30 $\mu\Omega$ for R_e^{oi} and R_e^{oo} respectively, due to the possible influence the remnants of the insulation on the outer cage might still have. Using these values and those from the simulation, a value for lambda of 4.86 was calculated. Referring to Fig 2, with this value of lambda, the current entering the broken bar should be approximately that of the current entering a normal bar.

An outer cage bar was broken on the NDE side of the rotor by sawing through the bar. The positioning of the coils on the rotor bar are shown in Table 1. Bar number 1 is the broken bar, and the bars are numbered from 1 to 72 in a clockwise direction facing the NDE side. The inner cage has the same

numbering system, with number 1 being the bar immediately to the right of the broken bar.

Table 1:Rogowski coil positions on rotor

Drive End				Non-Drive End			
Inner cage		Outer cage		Inner cage		Outer cage	
Bar no	Coil no	Bar no	Coil no	Bar no	Coil no	Bar no	Coil no
62	C	2	1	1	A	2	9
		1	2	71	B	72	11
		3	4	72	D		

3.3 Experimental Results

The currents flowing in the rotor bars during the locked rotor test are very high, so the tests were performed at a reduced voltage of 129V to prevent excessive overheating. The first test performed on the motor yielded results that would be expected on a cage with insulated outer bars. The current flowing in the broken bar was about 35% of that in a healthy bar. More tests were performed on the motor and the current flowing in the broken bar increased until it stabilized at a value of 103% that of the current flowing in a normal bar. This variation could only be attributed to a reduction of the interbar resistance. Reasons for this could be that the interbar voltage, caused by the disruption in the current flow of the broken bar, leads to a breakdown in the bar insulation which would in turn reduce the interbar resistance. The path through which the interbar currents travel between the broken bar and the surrounding bars also becomes better established in time which further reduces the interbar resistance.

The actual currents obtained by the various coils are shown in Table 2. Referring to Table 2, the 'insulated' case refers to the results taken when voltage was first applied and the 'uninsulated' case refers to the results taken after voltage had been applied to the machine for a period of a half hour. The difference in the results is clear, with the 'insulated' case being concurrent to the theory put forward by Williamson and Abdel-Magied[1]. The results show there is a large increase in the currents of the surrounding bars as they compensate for the broken bar. There is also an increase in both the inner and outer cage bar currents, showing that the inner cage does compensate for the broken outer cage bar.

Table 2:Currents detected by coils

Insulated		Uninsulated	
Coil no	Current in A	Coil no	Current in A
A	290	A	288
B	300	B	314
C	260	C	278
D	335	D	315
1	915	1	447
2	145	2	426
4	710	4	458
9	890	--	--
11	535	11	450

For the case of the 'uninsulated' results, it can be seen from Table 2 that the broken bar acts largely the same as a normal bar. The currents in the surrounding bars have also dropped markedly from the 'insulated' case. The results in this case, show that there is a very small disturbance in the current flow pattern in the area surrounding the broken bar. Under these conditions, the effective rotor impedance unbalance would be small and the reflected harmonic stator currents would not be very significant.

The currents flowing in the bars are all slightly larger than the predicted values for a normal rotor bar. This can be attributed to the fact that the motor is of an old design, and the simulation package could not simulate the exact bar configuration of the rotor. The results do, however agree with the predictions made for the value of lambda of this machine calculated earlier. The results show a marked increase in not only the adjacent bars, but also in bars further away. This fact can be attributed to the skew in the rotor bars.

Referring to Heller & Hamata[5], an increase in the bar current will lead to a greater interbar voltage as a result of the skew. This will in turn lead to larger circulating currents between the bars, which will 'spread' the larger currents to the surrounding bars. Although this effect is also attributable to interbar currents, it must be noted that the distribution and magnitude of these currents for the area around the broken bar is very different from those produced by skewing.

4 Conclusion

It has been shown that interbar currents do indeed exist in a double-cage machine with a broken bar and that they can be of comparable magnitude to those flowing in a normal bar. Although the machine in question was not ideal, the experimental results compare favourably with those predicted in the theory. The theory can easily be extended to an inner cage break, which merely involves interchanging the positions of Z_i and Z_o in the definition of lambda. Although the equations obtained apply to the case of staggered bars with no mutual inductance, they could be adapted for other bar arrangements, such as dumbbell shaped slots.

The tests done were at a slip of 1, and although at operating slip the impedances drop, they do not have such a large effect on the magnitude of the interbar currents because of the definition of lambda. Thus at operating slip there will still be interbar currents although they are slightly smaller in magnitude than at standstill.

The presence of these large interbar currents will reduce the production of other than main frequency components in the stator. This will reduce the effectiveness of previously used detection systems for broken bars, and other detection techniques such as vibration monitoring[4] may be needed to conclusively detect broken bars in large double cage machines.

5 Acknowledgements

The authors would like to thank ESKOM Highveld power station for the use of their motor. The authors would aiso like to acknowledge the financial support provided by the Foundation for Research and Development (FRD) and SASOL Ltd. and the facilities made available by the Department of Electrical Engineering of the University of the Witwatersrand.

6 References

[1] Williamson. S and Abdel-Magied. M A S:'Steady-state analysis of double-cage induction motors with rotor-cage faults' *IEE Proc. Vol B. July 1987. pp199-206*

[2] Jacobs. P: 'Defining the Equivalent Circuit of the Double-Cage Motor' *AIEE Trans. Vol 72. Part III. August 1953. pp651-654*

[3] Kerszenbaum. I: 'The behaviour of three-phase squirrel cage induction motors with unbalance in the rotor impedance; in particular two pole motors' *PhD Thesis, University of the Witwatersrand, Johannesburg, 1983*

[4] Kerszenbaum. I and Landy. C F: 'The detection of broken bars and/or endrings in large squirrel cage induction motors' *Trans SAIEE. July 1984. pp22-27*

[5] Heller. B and Hamata. V: 'Harmonic field Effects in Induction Machines' *Elsevier Scientific. Czechoslovakia. 1977. pp257-275*

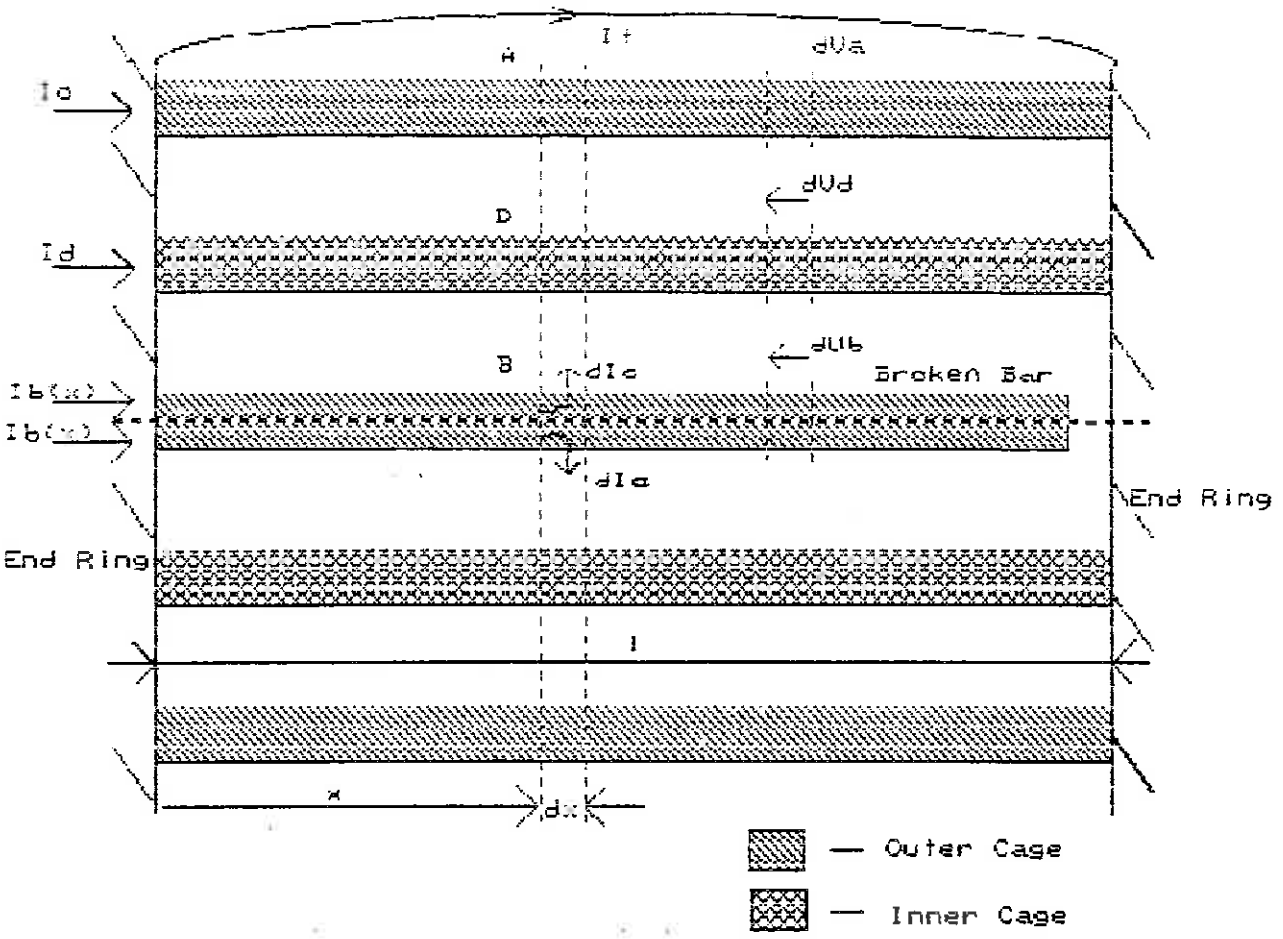

Figure 1: Graphical representation of broken outer cage bar

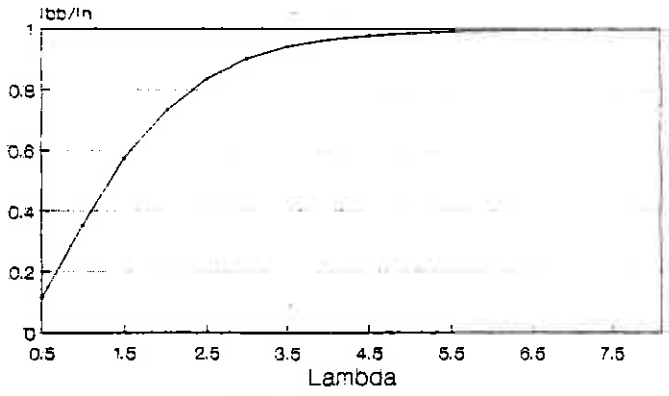

Figure 2: Plot of Ibb/In vs Lambda

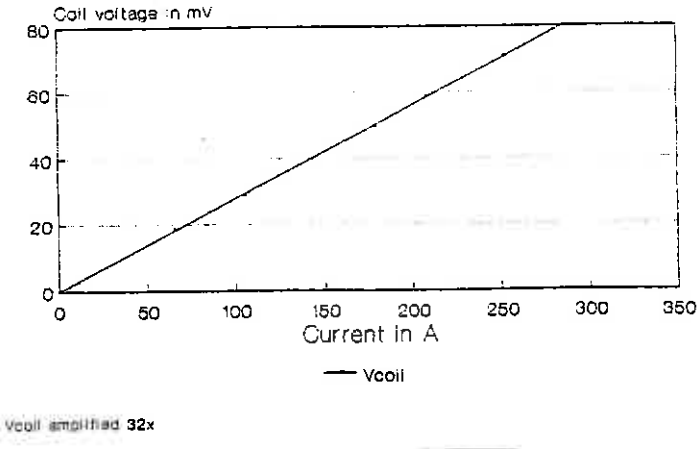

Figure 3: Calibration curve for Coil #2

THE EFFECT OF DEEP BAR PROPERTIES WHEN ASSESSING RESWITCHING TRANSIENTS IN SQUIRREL CAGE INDUCTION MOTORS

C F Landy *, W Levy **, M McCulloch * and A S Meyer *

Department of Electrical Engineering
University of the Witwatersrand, Johannesburg

SYNOPSIS

It has long been known that reswitching the supply onto a squirrel cage induction motor can result in the production of large transient torques. Generally these torques appear in the negative direction, i.e. the transient produced opposes the direction of motion of the motor. When analysing these transient torques, the motor generalized equations are usually solved for various time lags between switch-off and remake of the supply. This paper shows that when dealing with motors having deep bar properties, it is important to include the deep bar characteristics when doing the simulations. The results show that when these are included, the transient negative torques are significantly larger. Two examples of simulations done on machines having both deep bar and non-deep bar properties are shown. These results will illustrate how important it is to include the deep bar properties.

1. INTRODUCTION

Reswitching transient torques occur when the supply to an induction motor is removed and re-made within a very short time. When the supply is removed the stator currents cease to exist, but the energy stored in the magnetic field cannot change instantaneously. Consequently the rotor currents increase so that the total mmf acting on the magnetic circuit just prior to and just after switch-off remain the same. After switch-off the rotor currents, which are now no longer varying sinusoidally, decay exponentially at a rate governed by the rotor circuit time- constant. The magnetic flux produced by these rotor currents is fixed in space relative to the rotor, but rotates with the rotor relative to the stator. Also this flux will decay at the same rate as does the rotor currents. Emfs will be induced in the stator winding, due to the rotor produced flux, and the magnitude of this emf will decay with time.

The rotor speed will also decay after switch-off at a rate governed by the rotor plus connected load mechanical time- constant. This means that the rate at which the flux due to the rotor currents passes the stator coils changes with time. The frequency of the emfs induced in the stator winding therefore also changes. However on the supply side of the interruptor the supply voltage still exists with fixed magnitude and frequency, while on the motor side the induced emf appears with decaying magnitude and frequency.

⋆ Department of Electrical Engineering, University of the Witwatersrand.
⋆⋆ Formerly with the Department of Electrical Engineering, University of the Witwatersrand. Now with Eskom, Megawatt Park.

If the rotor plus load rotational moment of inertia is low, then the the speed will drop fairly quickly after switch-off. Likewise the frequency of the induced stator emfs will change. It is therefore possible to have the supply re-made when the induced emf is at a negative peak while the supply voltage is at a positive peak. At this instant the effective voltage applied to the stator winding is almost twice the peak supply voltage. The torque transient that results will be negative in the first instance, having magnitudes up to about fifteen times the Ωmotoring full-load torque. Such large negative re-switching transient torques have been known to cause damage to motors and couplings.

When the supply is re-made with the induced emfs and supply voltage being "in phase", rather than "out of phase", then the transient torque that results is positive and the magnitude is far less. This condition of re-switching is considered to be safe.

Normally, when predicting re-switching transients, it is assumed the rotor circuit parameters remain constant. The rotor resistance and reactance are usually set at their "running values" because the motor is normally running at full speed when such re- switching occurs. However, if the motor has deep rotor bars and if the speed drops markedly during the switch-off period, then the frequency associated with the rotor quantities will be significantly higher than that at running. This means that when the supply is re-made the rotor resistance can be considerably larger and the reactance smaller than during normal running. Levy et-al [9] have developed advanced models of induction motors incorporating the rotor parameter variation with rotor speed. This paper shows that when these parameter variations are included the transient re-switching torques are very significantly larger.

2. DEEP BAR MODEL

To obtain a dynamic model which includes rotor parameter variation with frequency, the rotor bar is divided into n equal sections along its depth as shown in Figure 1, which shows a rectangular bar in an open slot.

A lumped parameter circuit is then used to model the bar, where each section has a resistance and leakage inductance associated with it given by

$$R_{sec} = \frac{\rho\, l_b}{w\, d_{sec}} \qquad (1)$$

$$L_{l\,sec} = \frac{\mu_0\, l_c\, d_{sec}}{w} \qquad (2)$$

The Improved Pi Model (as suggested by [4]) has the complex form shown in Figure 2 for each section of the bar, with the inductance split in the ratio one sixth, two thirds and one sixth (1:4:1) according to Simpson's integration rule. Thus the equivalent circuit of the Improved Pi Model is obtained for both the d-axis and the q-axis as shown in Figure 3 and combining the series inductances gives the circuit of Figure 4 where

$$R_i = 2R'_i$$

$$L_{0,1} = L'_{l0} + \frac{1}{6}L'_{l1}$$

$$L_i = \frac{2}{3}L'_{li} \qquad (3)$$

$$L_{i,j} = \frac{1}{6}L'_{li} + \frac{1}{6}L'_{lj}$$

and L'_{10} is the leakage inductance of the portion of the slot above the bar (i is the number of sections of bar).

The differential equations for the circuit of Figure 4 are obtained by developing the traditional d-q axis equations of an induction motor. The system of equations is given in a rotor fixed reference frame to simplify the rotor equations. Thus the stator equations are given by

$$V_{sd} = R_s I_{sd} + L_s \frac{d}{dt} I_{sd} + M \frac{d}{dt} I'_{rd} + \omega_r M I'_{rq} + \omega_r L_s I_{sq} \qquad (4)$$

$$V_{sq} = R_s I_{sq} + L_s \frac{d}{dt} I_{sq} + M \frac{d}{dt} I'_{rq} - \omega_r M I'_{rd} - \omega_r L_s I_{sd} \qquad (5)$$

and the rotor portion of the circuit is given by the following equations. The equations for loop (0,1) of Figure 4 are

$$V'_{rd\,0,1} = 0 = (R_1 + R'_2) I'_{rd\,0,1} + L_{0,1} \frac{d}{dt} I'_{rd\,0,1} - R_1 I'_{rd\,1} + M \frac{d}{dt} I'_{rd\,0,1} + M \frac{d}{dt} I_{sd} \qquad (6)$$

$$V'_{rq\,0,1}=0=(R_1+R'_e)I'_{rq\,0,1}+L_{0,1}\frac{d}{dt}I'_{rq\,0,1} \qquad (7)$$
$$-R_1I'_{rq\,1}+M\frac{d}{dt}I'_{rq\,0,1}+M\frac{d}{dt}I_{sq}$$

for loop (1) are

$$V'_{rd\,1}=0=-R_1I'_{rd\,0,1}+2R_1I'_{rd\,1} \qquad (8)$$
$$-R_1I'_{rd\,1,2}+L_1\frac{d}{dt}I'_{rd\,1}$$

$$V'_{rq\,1}=0=-R_1I'_{rq\,0,1}+2R_1I'_{rq\,1} \qquad (9)$$
$$-R_1I'_{rq\,1,2}+L_1\frac{d}{dt}I'_{rq\,1}$$

and for loop (1,2) are

$$V'_{rd\,1,2}=0=-R_1I'_{rd\,1}+(R_1+R_2)I'_{rd\,1,2} \qquad (10)$$
$$-R_2I'_{rd\,2}+L_{1,2}\frac{d}{dt}I'_{rd\,1,2}$$

$$V'_{rq\,1,2}=0=-R_1I'_{rq\,1}+(R_1+R_2)I'_{rq\,1,2} \qquad (11)$$
$$-R_2I'_{rq\,2}+L_{1,2}\frac{d}{dt}I'_{rq\,1,2}$$

or in general, for either the d-axis or the q-axis, each group of two loops (i) and (i,j) are given by

$$V'_{r\,i} = 0 = -R_i I'_{r\,i-1,i} + 2R_i I'_{r\,i} - R_i I'_{r\,i,j} + L_i \frac{d}{dt} I'_{r\,i} \tag{12}$$

$$V'_{r\,i,j} = 0 = -R_i I'_{r\,i} + (R_i + R_j) I'_{r\,i,j} - R_j I'_{r\,j} + L_{i,j} \frac{d}{dt} I'_{r\,i,j} \tag{13}$$

and the last loop (n) is given by

$$V'_{r\,n} = 0 = -R_n I'_{r\,n-1,n} + 2R_n I'_{r\,n} + L_n \frac{d}{dt} I'_{r\,n} \tag{14}$$

Any shape of rotor bar may be implemented because the equations of this model are derived using purely the resistance and leakage inductance of each section of bar, calculated individually to create the equivalent circuit of Figure 3. Thus, as long as the bar and slot dimensions are known, any rotor bar shape can be modelled using these equations. The rotor slot/bar shapes already implemented in the simulation package include a rectangular open or semi-closed slot, a trapezoidal slot, a T-shaped bar and a double cage rotor bar.

3. RESWITCHING USING THE DEEP BAR MODEL

The stator equations are as given above in equations (4) and (5). The rotor equations for the first loop of any of the lumped parameter circuits have a similar format to equations (6) and (7). When the supply is disconnected the stator currents are zero and thus

$$V_{sd} = M \frac{d}{dt} I'_{rd} + \omega_r M I'_{rq} \tag{15}$$

$$V_{sq} = M\frac{d}{dt}I'_{rq} + \omega_r M I'_{rd} \qquad (16)$$

$$V_{rd} = 0 = (R_0 + R'_e)I'_{rd\,0} + L_0\frac{d}{dt}I'_{rd\,0} - R_1 I'_{rd\,1} + M\frac{d}{dt}I'_{rd\,0} \qquad (17)$$

$$V_{rq} = 0 = (R_0 + R'_e)I'_{rq\,0} + L_0\frac{d}{dt}I'_{rq\,0} - R_1 I'_{rq\,1} + M\frac{d}{dt}I'_{rq\,0} \qquad (18)$$

The boundary conditions necessary for the currents to maintain the balance of mmf over the interval of switching are given by

$$I'_{rd\,0_+} = I'_{rd\,0_-} + I_{sd_-} \qquad (19)$$

$$I'_{rq\,0_+} = I'_{rq\,0_-} + I_{sq_-} \qquad (20)$$

4. PREDICTED RESULTS

The predicted results shown below are for a 254kW, 3 300V, 50Hz, 4 pole, squirrel cage induction motor. For the traditional model, the (DC) running values of the rotor resistance and leakage reactance have been used. The deep bar model is the improved Pi model with the bar divided into four sections, Levy [8]. For both cases the motor was run up to full speed so that the steady state conditions were achieved. These steady state conditions were then used as initial conditions for the switch-off mode.

Figure (5) shows the torque and the speed of the motor predicted using the traditional model, with the supply disconnected for 8 cycles (0.16 secs) and then re-made. Figure (6) shows the predicted torque and speed transients, for the same conditions, using the deep bar model. For both cases the graphs show zero electromagnetic torque while the supply is disconnected. Both graphs also show that a very large negative torque is produced, but the deep bar model gives a peak of -14 PU while the traditional model gives a peak of only -10 PU. It is seen that during the off period the motor speed has dropped to 0.68 PU. As such the rotor parameters are

no longer equal to those under running conditions and the traditional model fall down because the frequency of the rotor voltages and currents has increased from nearly zero to 16Hz.

5. CONCLUSIONS

The predicted results clearly show that deep bar properties must affect the transient re-switching torques produced. If the motor speed does not change significantly over the interval of switching, then the traditional model will suffice. However, if the motor speed varies, as is the case above, then the deep bar effects must be accounted for. Likewise the predictions of the stator and rotor current transients will also be affected by the deep bar parameter variations.

6. ACKNOWLEDGEMENTS

This research has been sponsored by the National Energy Council in South Africa. The authors wish to thank the National Energy Council for this generous support without which this research would not have been possible. The authors also wish to acknowledge the co-operation received from GEC Machines of South Africa for providing the necessary data and the University of the Witwatersrand for providing many of the facilities used.

7. LIST OF SYMBOLS

d = depth
I = current
l = rotor length
L = inductance
M = mutual inductance
R = resistance
ρ = resistivity

σ = saturation factor
μ_0 = magnetic space constant

V = voltage
w = width of bar or slot
ω_r = angular speed of rotation

Subscripts
b = bar
c = core
d = d-axis
e = end ring
l = leakage
q = q-axis
r = rotor
s = stator
Superscripts
$'$ = referred to stator

8. REFERENCES

1. **Boldea, I., Nasar, S.A.** "A general equivalent circuit (GEC) of Electric Machines including crosscoupling saturation and frequency effects", IEEE Transactions on Energy Conversion, Vol. EC-3, No. 3, pp. 689-695, 1988.

2. **Ferreira de Jesus, J.M.**, "A model for saturation in induction machines", IEEE Transactions on Energy Conversion, Vol. EC-3, No. 3, pp. 682-688, 1988.

3. **Lipo, T.A., Consoli, A.** "Modelling and Simulation of Induction Motors with saturable leakage reactances", IEEE Trans Industry Applications, Vol. 20,, No. 1, 1984, pp. 180-189.

4. **Babb, D.S., Williams, J.E.** "Network analysis of A-C Machine Conductors", Transactions AIEE, Vol. 70, pp. 2001-2005, 1951.

5. **Alger, P.L.** "Induction Machines - Their behavior and Uses", Gordon and Breach, New York, 1970.

6. **Agarwal, P.D., Alger, P.L.** "Saturation Factors for Leakage Reactance of Induction Motors", AIEE Trans., Vol. 80, 1961, pp. 1037-1042.

7. **Landy, C.F.** "The prediction of transient torques produced in induction motors due to rapid reconnection of the supply", Trans. SAIEE, Vol 63, 7, 1972, p.178.

8. **Levy, W.** "Modelling and simulation of induction motors for variable speed drives, with a view to deep bar and saturation effects". PhD Thesis, University of Witwatersrand, Nov. 1990.

9. **Levy, W., Landy, C.F., McCulloch, M.** "An accurate model for deep bar and saturation effects in induction motors". Proceedings ICEM 90, Aug. 1990, p. 215.

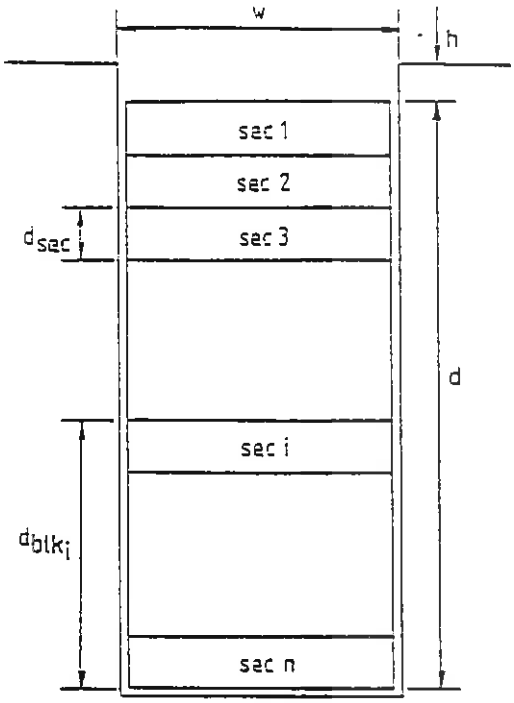

Figure 1 : Rectangular Bar in an Open Slot

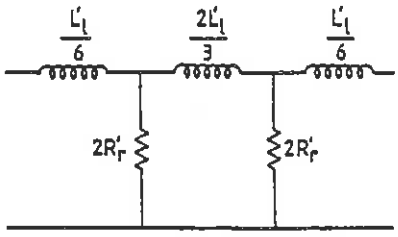

Figure 2 : One Section of the improved Pi Model

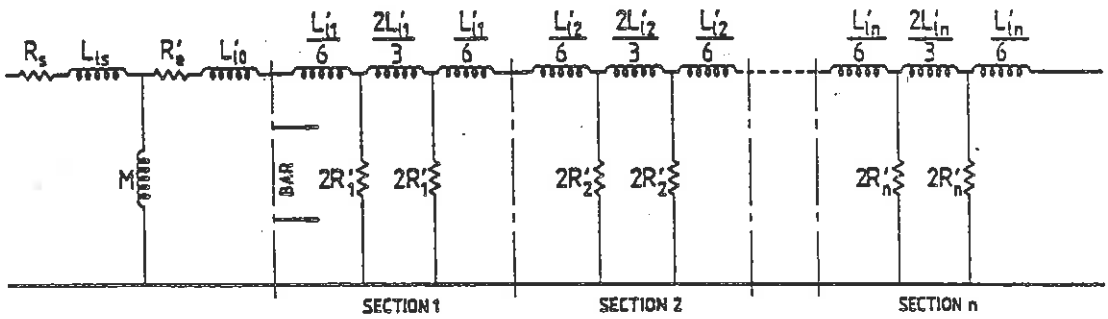

Figure 3 : Equivalent Circuit of the improved Pi Model

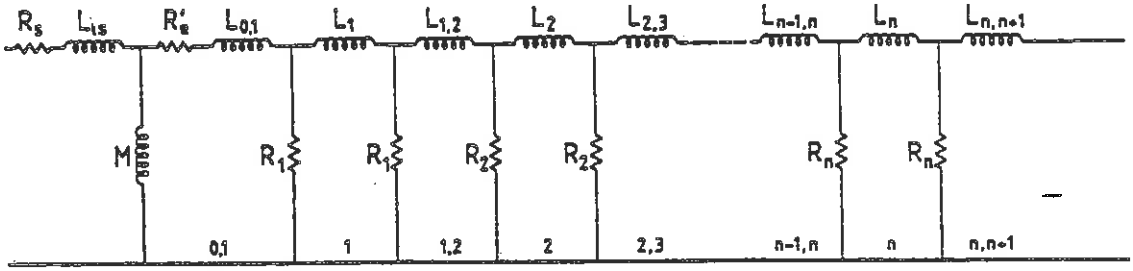

Figure 4 : Reduced Equivalent Circuit of the improved Pi Model

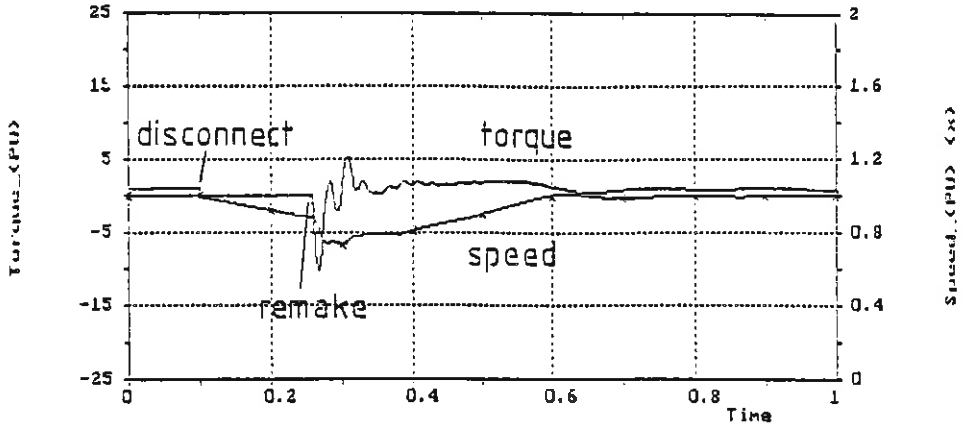

Figure 5 : Predicted Results of 254kW, 3300 V, 4 Pole Induction Motor Using the Traditional Model. The supply is disconnected at 0.1 seconds for 8 cycles (0.16 seconds) and then re-made.

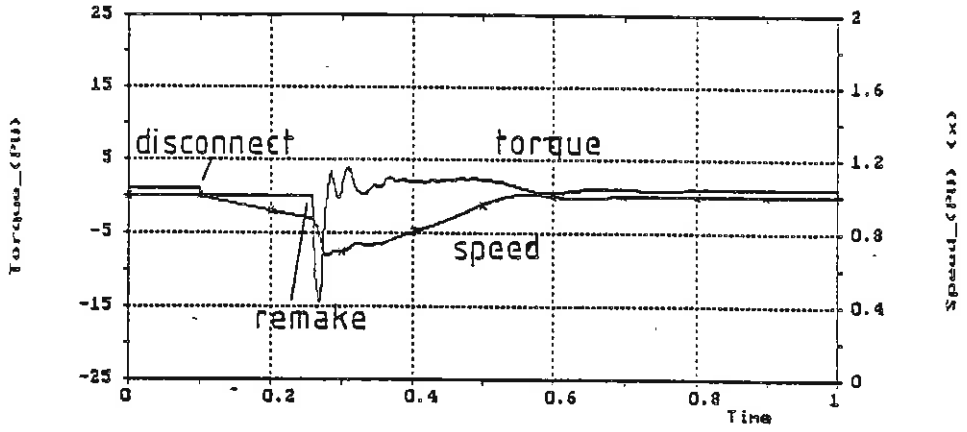

Figure 6 : Predicted Results of 254kW, 3300 V, 4 Pole Induction Motor using the Deep bar Model. The supply is disconnected at 0.1 seconds for 8 cycles (0.16 seconds) and then re-made.

VIBRATION MONITORING TECHNIQUES: A method of diagnosing rotor faults

D. Hop, C.F Landy
University of the Witwatersrand

Abstract :
An experimental motor set has been setup to allow for a broad database to be established so that criteria for the diagnosis of rotor bar faults in large squirrel cage induction motors can be formulated. A 4x RPM axial vibration signal was used as the basis for comparison with existing methods. This method proved reliable and was non-invasive.

1. INTRODUCTION

The monitoring of motors to determine when and how they will fail is well tested and has worked for many years but there exists a need for an accurate and reliable monitoring technique to detect faults in the rotor cage of induction motors. The technique must also be non-invasive. There are two methods which are being used to monitor the condition of the motor without interrupting its operation, namely stator current and vibration monitoring.
Since it is often easier to access the supply cabling than the motor itself, many researchers have developed techniques whereby the analysis of the stator current spectrum can indicate condition of the rotor bars. Hargis[2] and Tavner[3] have both shown that the existence of broken rotor bar/s in the cage produce current harmonics that appear in the stator windings. These harmonics can be detected in the current spectrum and hence a simple formula was derived -

$$R_s = \frac{\sin\alpha}{2p(2\pi-\alpha)}$$
$$\alpha = \frac{2\pi np}{N}$$

where n = no. of broken contiguous bars,
N = no. of rotor bars, N >> n.
This however, only holds true for certain types of squirrel cage motors as it relies on the assumption that rotor cage becomes electrically unbalanced since no current flows into this bar.
It has subsequently been shown by Kerszenbaum and Landy[1] that in cases where the rotor bars are uninsulated, namely large motors, and the bar is cracked or broken near the endring, as is often the case, there may exist large interbar currents between the damaged bar and the adjacent bars. This means that a percentage of the normal current flowing in a 'healthy' bar will still enter into the damaged bar. The assumption that was previously used is thus no longer valid. Hence a new approach, vibration monitoring.

2. PRODUCTION OF AXIAL VIBRATION

It has been shown [1] that the current entering the rotor core from the broken bar has a non-linear distribution along the core and is given by

$$\delta I_c(X) = \frac{I_N}{2}\lambda\frac{\sinh\lambda X}{\sinh\lambda l}$$
$$\lambda = \sqrt{3\left|\frac{Z_b}{R_c}\right|}$$

This interbar current flows tangentially from the broken bar and consequently produces axial fluxes. Due to the non-linear distribution of the current, these axial flux patterns produce four axial poles which are not symmetrically located around the circumference. It can be shown that these four poles produce an axial vibration at 4 times the running speed of the rotor due to changes in the permeability that four poles encounter on each revolution of the rotor.
The contact impedance $|Z_c|$ can be shown [1] to be equal to $|R_c|$ for frequencies < 50Hz. Since the impedance of the bar $|Z_b|$ is dependent on the slip, it can be expected that the greater the load, the greater the interbar currents and hence the greater the axial vibration.

3. VIBRATION MONITORING SETUP

To obtain a sufficient database from which data could be correlated, both methods of monitoring were used. Vibration monitoring was done in both the axial and the radial directions with the use of accelerometers. The current and vibration measurements were stored in a database using a powerful signal processing package. This allowed the use of broadband and narrowband FFT analysis.
Two 75kW Hawker Siddley squirrel cage induction motors were used, one being the reference, the other being damaged. The motor that was later damaged, was first sent through the full battery of tests, namely

1) vibration (axial and radial) analysis, from no load to 125% full load;
2) stator current analysis, from no load to 125% full load.
A torque-speed curve was also generated for the motor. The rotor was then removed and a single bar was cut (at the drive end) so that only about 25% of the bar was in contact with the endring. This was to simulate a high resistance joint or hairline crack. On replacing the rotor, the same tests were done on the motor. At each point the loading was carefully checked so the correct correlation could be done at a later stage. Finally, the partially cut bar was totally cut and the tests redone.

4. VIBRATION AND CURRENT RESULTS

The vibration spectra were generated for three frequency bands, namely 0-300Hz, 0-1000Hz and 0-10000Hz. The narrowbands were used to focus on the 1,2,4 and 6xRPM as well as 2x line frequency. The vibration due to the presence of slots in the rotor were also analysed. To establish whether there exists a definite trend that is a function of both the load and damage, it was necessary to ensure that all results were taken at the same percentage loading. These results could then be plotted to establish any trends.

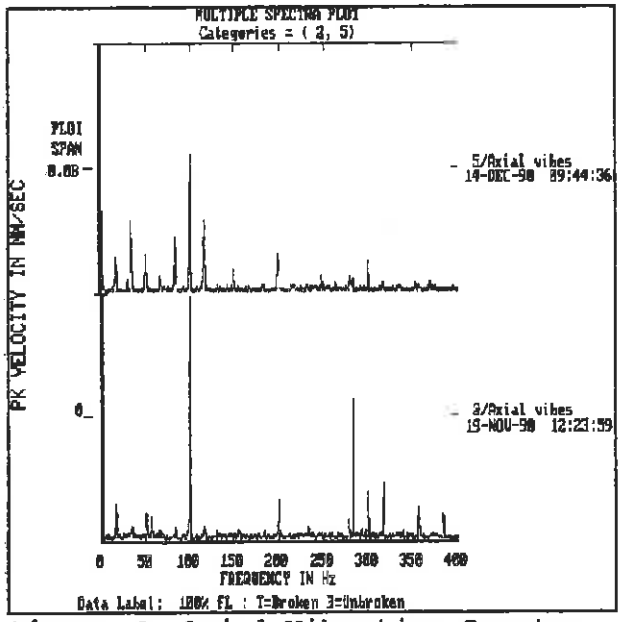

Figure 1: Axial Vibration Spectra - At 100% Full load, broken and unbroken bar.

Secondly, similar frequency bands were used for the current spectrum. The package that was used to analyze the spectra enabled the zooming in on frequencies around the fundamental so that any sidebands could be easily recognized. Graphical trending was also established for these current spectra as well as using the formula derived by Hargis and Tavner.

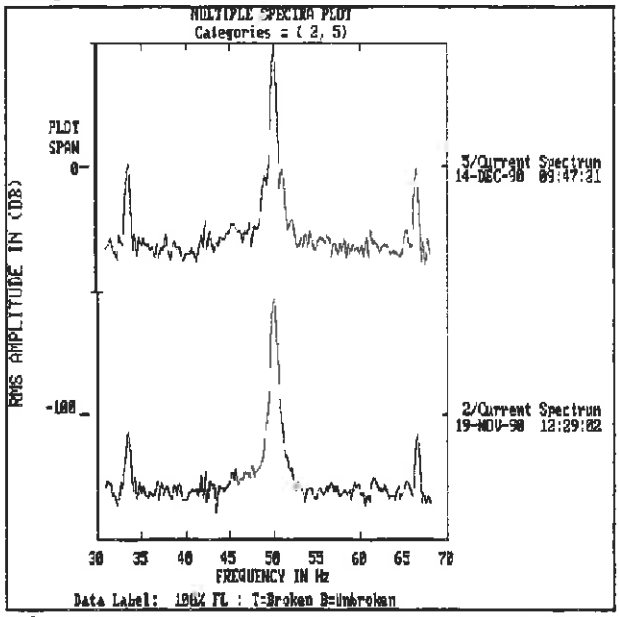

Figure 2: Stator Current Spectra - At 100% Full load, with broken and unbroken bar

It can be clearly seen from Fig. 2 that there does exist sidebands at 2x slip frequency about the fundamental signal. The limits of these sidebands that constitute damage levels have been defined by Tavner[3]. It has been established that if the lower sideband has a magnitude greater than -54dB, it means that there exists severe damage to at least one bar. If this sideband falls within the -60dB to -54dB limit, a cracked bar would be suspected. As can be seen from Fig. 2, the value of the this sideband does exceed this -54dB damage limit.

5. DISCUSSION OF RESULTS

For the motor that was to be damaged (referred to as Motor B), a set of physical data was calculated so as to predict the magnitudes of the vibrations as well as the sidebands in the current spectra.
The values of the bar impedance and contact

impedance were calculated to be as follows,

$$X_{b(50Hz)} = 922.9\mu\Omega \quad R_b = 58.13\mu\Omega$$
$$\therefore |Z_b| = 924.7\mu\Omega$$
$$X_{b(0.53Hz)} = 9.79\mu\Omega$$
$$\therefore |Z_b| = 58.95\mu\Omega$$
$$|Z_c| \approx |R_c| = \frac{20}{0.342 * 0.94} = 62\mu\Omega$$
$$Hence \left|\frac{Z_b}{R_c}\right|(50Hz) = 14.9$$
$$\left|\frac{Z_b}{R_c}\right|(0.53Hz) = 0.95$$

Since $|Z_b|$ is dependent on slip, it can be clearly seen how the magnitude of the interbar currents are severely effected by the dimensions of a particular motor.

The above values indicate that at starting approx. 100% of the normal current will flow in the broken bar and at slip frequency, this current will only reduce to approx. 60%. This means that the expected axial vibration should be present in both the high resistance bar and broken bar cases. It also indicates that the current spectrum sidebands will appear but their reliability cannot be clarified. This uncertainty establishes the basis for parallel methods of monitoring.

From these values, the exact magnitudes of the 4x RPM vibration cannot be predicted but their presence can be accurately predicted. As can be seen from Fig. 1, the magnitudes of this particular vibration is in the order of 0.001 - 0.008mm/s. This, in many cases, may be overlooked due to its magnitude but it does reveal the damage to the rotor bar.

In Fig. 2, it can be seen that as the damage to the rotor bar became more severe, sidebands at 2x slip frequency appear about the fundamental frequency. Although these sidebands appear, using the above formula (section 1), the result is inconclusive.

Fig. 3 shows the trending that was established for the 4x RPM vibration signal. Clearly, it can be seen that the influence of the loading is more pronounced in the broken bar case. Excepting for the 125% full load case, the trend of the broken bar case follows what was expected. Unfortunately, the magnitudes of the unbroken bar case appear to be higher than expected. To re-affirm these results, further tests need be done on the second motor (Motor A).

Fig's 4 and 5 show the trending established for the fundamental, lower sideband and their ratio of both the unbroken and broken bar. For the unbroken bar, the lower sideband did not exceed the -60dB limit whereas in the broken bar case, this limit was exceeded at loads greater than 100%. This indicates that the amount of current entering the broken bar reduces below a limit for which the current spectrum analysis method begins to work.

6. CONCLUSION

It can be clearly seen from the above discussions that there exists certain conditions for which both the vibration and current monitoring methods are relevant. Due to the large currents that can flow into a broken bar and hence the interbar current flowing into the core, the current monitoring method can become unreliable. This means that by using another simple method in tandem, these abnormalities can be overcome. The monitoring of the 4x RPM vibration signal can provide users of large induction motors with sufficient additional knowledge about the condition of the rotor bar to make a definite decision on the maintenance procedures of a motor.

It is of the authors opinion that this method of motor analysis will provide definite warning signals from which further action can be taken so as not to allow the damage to develop further.

7. ACKNOWLEDGEMENTS

The authors wish to acknowledge the assistance that was received for both financial support and supplying of the motors from SASOL Limited, National Energy Council and the Umgeni Water Board. The experimental work was conducted at the University of the Witwatersrand laboratories and the authors wish to acknowledge the help and facilities provided.

8. LIST OF SYMBOLS

R_s = ratio of lower sideband to fundamental

$I_c(X)$ = distribution of interbar current in the core at position X along the core

Z_b = normal bar impedance $(R_b + jX_b)$

R_c = resistive component of interbar impedence Z_c. Usually $R_c >> X_c$ so $Z_c = R_c$

9. REFERENCES

1. Kerszembaum, I. and Landy C.F. "The existence of large interbar currents in three phase squirrel cage motors with rotorbar and/or endring faults". IEEE Trans. on Power Apparatus and Systems, vol PAS-103, No 7, July 1984, p 1854

2. Hargis, C., Gaydon B.G., and Kamash K. "The detection of rotor defects in induction motors". Conf. Proc. IEE Conf. on Electrical Machines - Design and Application, London, July 1982, pp 216-219.

3. Tavner, P.J., Armin K.K, Hargis C., "An electrical technique for monitoring induction motor cages". Third International Conference on Electrical Machines and Drives, 1987, pp 43-47.

4. Bate, G.H. "Vibration diagnostics for industrial electric motor drives". Bruel and Kjaer, 1989.

AXIAL VIBRATION
4xRPM

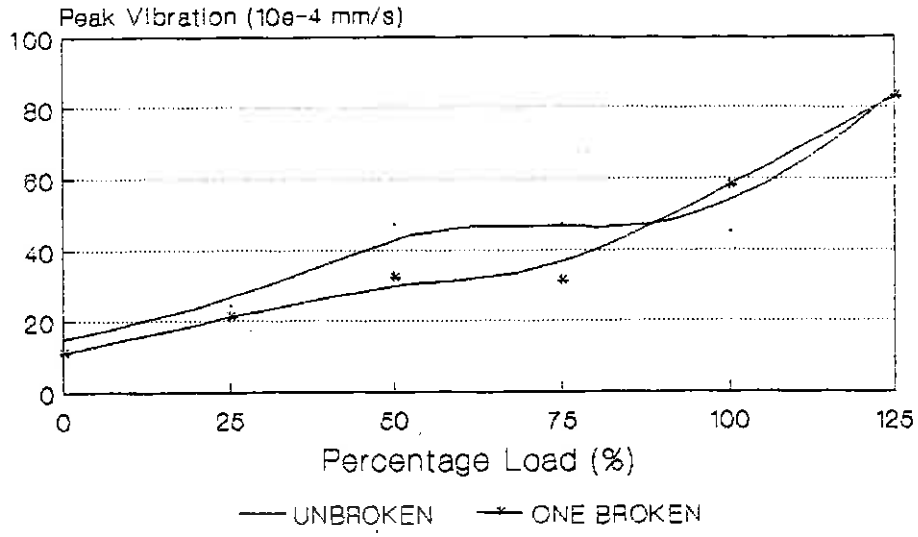

Fig 3: Axial Vibration Trending

STATOR CURRENT SPECTRA
Unbroken Bar

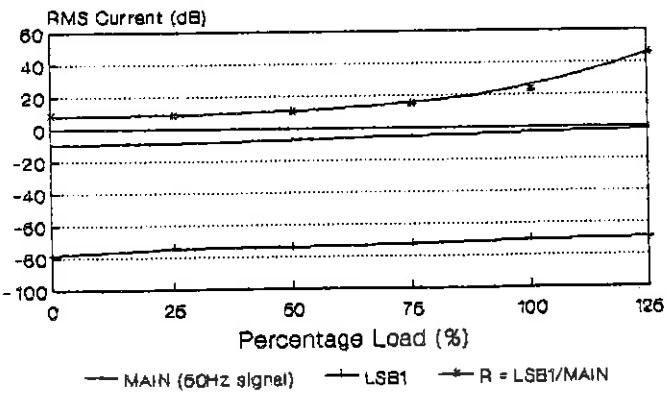

Fig 4: Current Spectra Trending

STATOR CURRENT SPECTRA
One Broken Bar

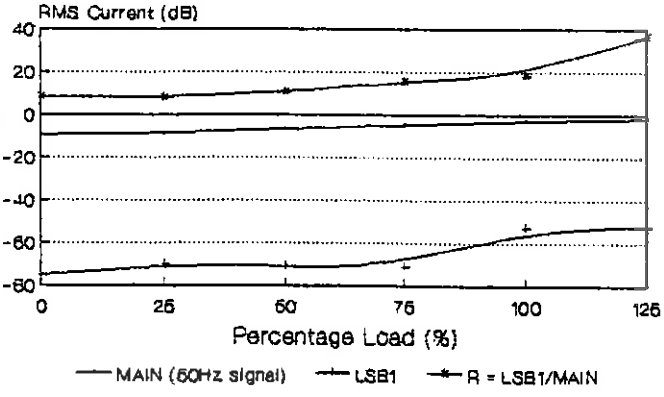

Fig 5: Current Spectra Trending

TRANSPUTER BASED SENSORLESS AC-MOTOR FLUX-CONTROL METHOD

M.J.Case, W.F. van Wyk
Department of Electrical and Electronic Engineering
University of Stellenbosch

Abstract. This paper presents a transputer based field-oriented induction motor control method which does not depend on stator resistance neither does it require flux transducers. The system is based on a paper published by A. Abbondanti in 1977. The computation algorithm as well as experimental results are presented.

Introduction

In 1977 Abbondanti published a paper (1) on a method of controlling the flux in a polyphase induction motor. The approach described is not dependent on any knowledge of the value of the stator resistance, nor is it affected by stator resistance thermal variations. Furthermore, the method is based on analogue operations on motor voltage and current and does not make use of transducers or probes to measure the flux. This paper shows a means of implementing this method to determine flux by means of a T800 Transputer.

1. Phasor transformations (2)

Phase voltages V_a, V_b and V_c may be converted to the stationary d_s-q_s frame with the help of equations (1.1) and (1.2).

$$V_{qs} = V_a \qquad (1.1)$$
$$V_{ds} = 1/\sqrt{3}\,(V_b + V_c) \qquad (1.2)$$

These voltages may be converted to the synchronously rotating d-q frame with the help of equations (1.3) and (1.4).

$$V_q = V_{qs}\cos(wt) - V_{ds}\sin(wt) \qquad (1.3)$$
$$V_d = V_{qs}\sin(wt) + V_{ds}\cos(wt) \qquad (1.4)$$

Equations (1.3) and (1.4) may be inverted to define relationships of stationary frame variables in terms of rotating frame variables as follows:

$$V_{qs} = V_q\cos(wt) + V_d\sin(wt) \qquad (1.5)$$
$$V_{ds} = -V_q\sin(wt) + V_d\cos(wt) \qquad (1.6)$$

These equations may again be inverted to define phase voltages in terms of stationary frame variables as follows:

$$V_a = V_{qs} \qquad (1.7)$$
$$V_b = \tfrac{1}{2}(-V_{qs} - \sqrt{3}V_{ds}) \qquad (1.8)$$
$$V_c = \tfrac{1}{2}(-V_{qs} + \sqrt{3}V_{ds}) \qquad (1.9)$$

Assume, for example, that the phase voltages are balanced and sinusoidal. Then

$$V_a = V_p\cos(wt) \qquad (1.10)$$
$$V_b = V_p\cos(wt-120^\circ) \qquad (1.11)$$
$$V_c = V_p\cos(wt+120^\circ) \qquad (1.12)$$

Substituting these equations in equations (1.1) and (1.2) yields

$$V_{qs} = V_p\cos(wt) \qquad (1.13)$$
$$V_{ds} = -V_p\sin(wt) \qquad (1.14)$$

Again, substituting in equations (1.3) and (1.4), we have

$$V_q = V_p \qquad (1.13)$$
$$V_d = 0 \qquad (1.14)$$

These relationships verify that the sinusoidal variables appear as dc quantities in a synchronously rotating reference frame. The amplitude of the dc quantity is the amplitude of the sinusoidal variables.

2. Method used to obtain flux related signal

The three line voltages and currents of the motor may be transformed to the synchronous reference frame. Power is invariant under these transformations. The resulting voltage and current phasors have the same relative

magnitude and phase as the voltage and current phasors supplied to one phase of a star connected load. The two phasors,

$$V = V_d + jV_q \text{ and}$$
$$I = I_d + jI_q$$

may thus be used to calculate the instantaneous power delivered to one phase of the motor.

$$VI^* = P - jQ \qquad (2.1)$$

where P = Average power and
Q = Reactive power

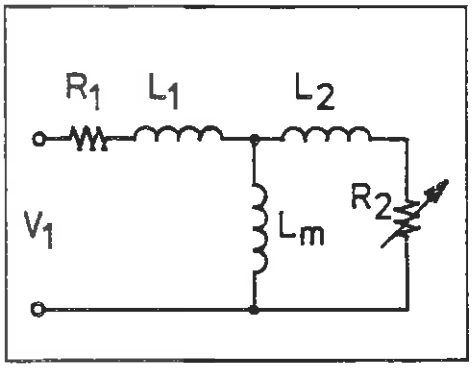

Figure 1: INDUCTION MOTOR

The flux-related signal used to obtain information on the level of the flux is defined here as the motor phase reactive power Q (see Figure 1).

$$Q = \tfrac{1}{2}wL_1I_1^2 + \tfrac{1}{2}wL_2I_2^2 + \tfrac{1}{2}wL_mI_m^2 \qquad (2.2)$$

The basic concept of the proposed flux regulation method arises from the recognition that Q is a function of and only of:

a. The magnetizing current I_m (and therefore of flux Φ).
b. The line current I_1.
c. The motor inductive parameters L_1, L_m and L_2.
d. The angular frequency w.

Since w and all the inductive parameters are known and since I_1 and Q are measurable, I_m (and Φ) may be derived from the correct processing of known and measured quantities.

One may for instance, consider the following rearrangement of Abbondanti's flux related signal:

$$(\tfrac{1}{2}L_a)wI_m^2 = Q - [\tfrac{1}{2}(L_b + L_c)]wI_1^2 \qquad (2.3)$$

where $L_a = L_m(L_m+L_2)/(L_m+2L_2)$
$L_b = (L_mL_2)/(L_m+2L_2)$
$L_c = L_1$

3. Practical Implementation of the proposed method

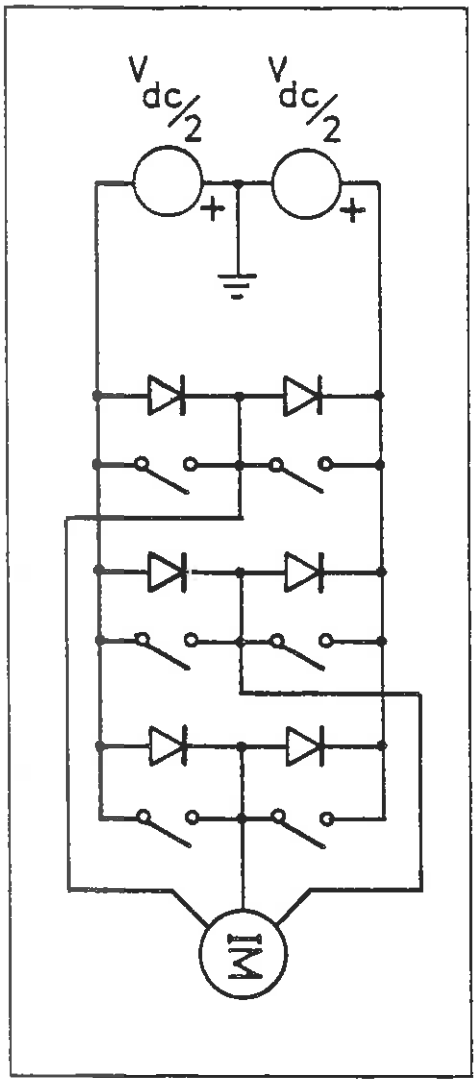

Figure 2: POWER CIRCUIT

The instantaneous flux level of the machine may be determined if the voltage phasor $V_d + jV_q$ and the corresponding current phasor $I_d + jI_q$ are known. The voltage phasor is used to control the flux level at a given frequency. Its value must therefore be under control of the microprocessor. If Pulse Width Modulation is used to generate the voltage phasor, only the instantaneous dc-link voltage needs to be known to fully determine the voltage phasor supplied to the machine. The dc-link voltage therefore needs to be sampled.

If the voltage phasor $V = V_d + jV_q$ is known, we need to know the corresponding line current phasor $I = I_d + jI_q$ to determine the reactive power delivered to one phase of the motor. If one bears in mind that the instantaneous sum of the three line currents supplied to a motor is zero, we may sample only two of the three line currents and calculate the third one. Fast analogue to digital converters are very expensive, therefore it is desirable to decrease the bandwidth. We may therefore determine the resulting line current phasor by sampling two of the three line currents.

Abbondanti states from equation (2.3) that by using the terminal characteristics of the machine, we may calculate the flux level in the machine.

If we know the right hand side of (2.3), we have a signal proportional to I_m^2 and w. If we want to keep the flux at a constant level, we must force the right hand side to be proportional to w. (See Figure 7)

To achieve this we need to know the supplied reactive power. We get it by inserting $V = V_d + jV_q$ and $I^* = (I_d - jI_q)$ in (2.1). The frequency w is under external control and is therefore a given value. We may determine the peak amplitude of the line current by calculating the amplitude of the current phasor $I = I_d + jI_q$. This may be done as follows:

$$I_1^2 = I_d^2 + I_q^2 \qquad (3.1)$$

The right hand side of (2.3) may now be determined and the loop described in Figure 7 may be closed and stabilized.

4. Transputer-based implementation

A 256 kbyte fast static memory transputer controller card designed and supplied by NetElek, (a Stellenbosch based company), is used as controller. Two memory mapped 8254 programmable counters generate the pulse width modulation while a twelve bit AD574 analogue to digital converter with eight sample and hold circuits interfaces the analogue inputs to the transputer.

At the beginning of a period, the preloaded counters and the sample and hold circuitry are activated simultaneously (all eight analogue channels are sampled simultaneously and are then selected sequentially to be converted to digital values). This results in a delay of one switching period in the measured analogue values which must be taken in consideration to ensure stability. The next step is to select the first sampled channel and activate the converter. The transputer is now free to do other calculations. After completion, the converter notifies the transputer and the next channel is selected and converted.

Only the dc-link voltage and two of the line currents as well as an angular frequency command are needed to implement Abbondanti's approach. Only four analogue channels are therefore converted to digital values.

The third line current is calculated by keeping in mind that the three instantaneous line currents add up to zero at any time. A synchronously rotating current phasor may now be determined by inserting w and the three line currents in (1.1) to (1.4).

The present voltage phasor was calculated in the previous period. The instantaneous reactive power may therefore be determined as well as the amplitude of the phase current phasor.

The per phase inductance is known and with the help of (2.3) we may determine I_m and therefore the flux level. This value is compared with a reference and the error is used to calculate the new voltage phasor $V_d + jV_q$ to force the flux to a predetermined level. This voltage phasor is transformed back to three phase values and loaded in the counters and the

transputer deschedules until the start of the next period.

In this implementation the voltage phasor is used to control the flux while the external angular frequency w input generates slip and therefore torque. The transputer still has enough calculating calculating power available to use some of the available analoque channels and implement simultaneous position and speed control loops.

5. Conclusions

Abbondanti's approach is very attractive as a modern control philosophy. It uses instantaneous values to determine the flux level. The response is therefore also instantaneous. The ease of implementation, the absence of remote sensors, the independence on the stator resistance and the inherent stability makes it very feasible to implement in commercial drives. Some of the experimental waveforms may be seen in Figures 3,4,5 and 6.

References

1. Abbondanti, A: "Method of flux control in induction motors driven by variable frequency, variable voltage supplies." IEEE/IAS Intl. Semi. Power Conf., pp. 177-184 1977.

2. Adkins, B.: "The general theory of electrical machines", Chapman and Hall, London, 1964

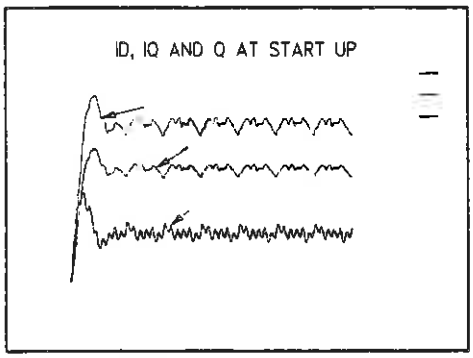

Figure 3: Start-up currents

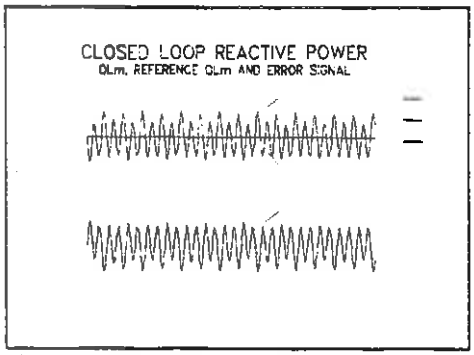

Figure 4: Closed loop reactive power

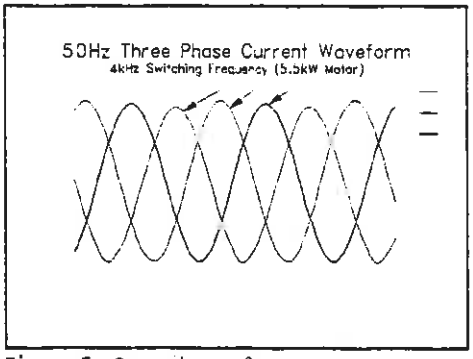

Figure 5: Current waveforms

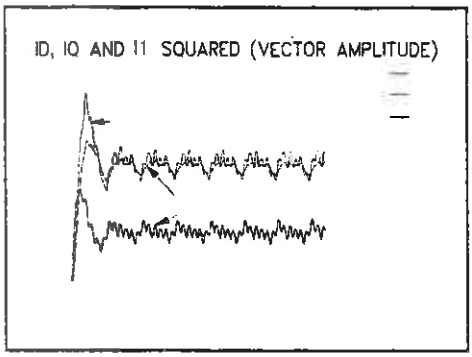

Figure 6: Vector amplitude

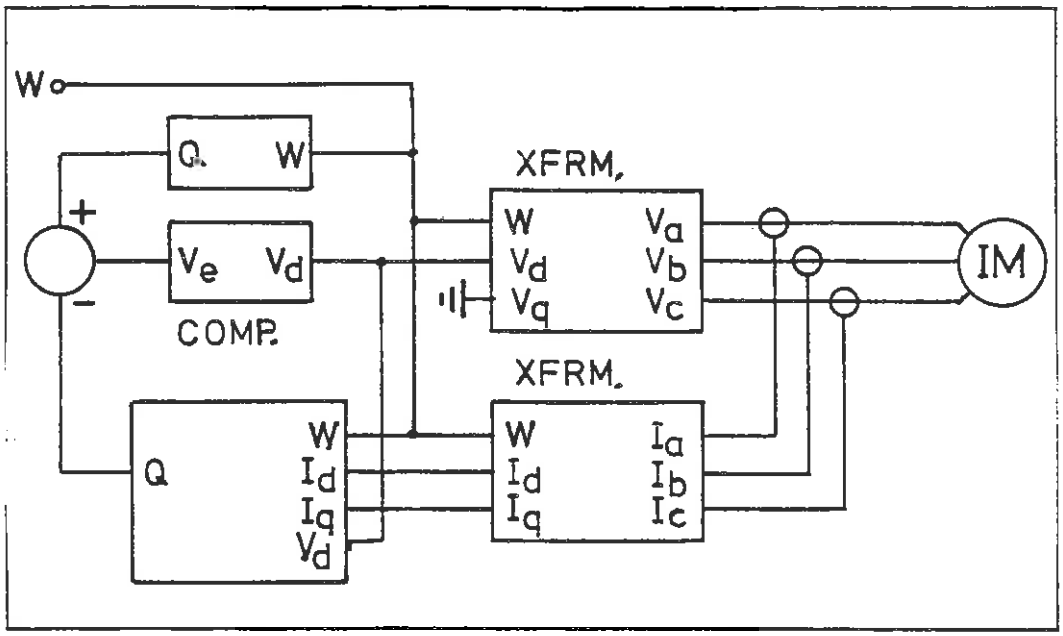

Figure 7: Control circuit

Ontwikkeling en implementering van 'n saamgestelde omsetter vir gebruik in sonenergiestelsels.

SJB HARTMAN PROF JHR ENSLIN DB SNYMAN

DEPARTEMENT ELEKTRIESE INGENIEURSWESE
UNIVERSITEIT VAN PRETORIA
SUID-AFRIKA

Uittreksel: Die voorgestelde omsetter wat hier beskryf word dien as enkele omsetter binne 'n tipiese alleenstaande sonenergiestelsel. Hierdie omsetter tree op as batterylaaier en wisselrigter terwyl maksimum drywingspuntvolging ook geïmlementeer is.

Die saamgestelde omsetter beskik oor besonder hoë rendementeienskappe en is weens die eenvoud van die stelsel baie koste-effektief. Die prototipe omsetter is geskik vir gebruik saam met 'n 96 volt sonpaneelstelsel en 'n 24 volt batterybank terwyl die wisselrigvermoë van die omsetter 1.5 kVA is. Maksimum drywingspuntvolging word verrig deur die uitsetspanning en frekwensie met behulp van 'n optimiseringsalgoritme aan te pas.

'n Volledige beskrywing van die werking asook beheer van die saamgestelde omsetter word uiteengesit.

1. INLEIDING.

Alternatiewe energiestelsels vind vandag al hoe meer toepassing in Suid-Afrika - veral in verafgeleë gebiede waar die nasionale net nie elektriese energie verskaf nie. Die gebruik van sonenergiestelsels vir klein huishoudings in sulke afgeleë gebiede is reeds 'n koste-effektiewe oplossing vir die energieverskaffingsprobleem [1,2,7,9].

Huidiglik beloop die koste van sonpanele ongeveer $5 per piek watt [2]. Hierdie hoë kapitale koste verbonde aan sonenergiestelsels noodsaak dat die omsetters wat in sulke stelsels gebruik word hoë effektiwiteit omsetters moet wees wat daarbenewens ook die sonpanele maksimaal benut. [5]

Die saamgestelde omsetter is ontwikkel ten einde 'n enkele omsetter daar te stel wat al die benodigde funksies in 'n alleenstaande sonenergiestelsel verrig. Sulke alleenstaande stelsels vereis gewoonlik 'n 220 volt of 110 volt wisselspanning, geskik om tipiese standaard toebehore byvoorbeeld yskaste, waterpompe, vrieskaste, mikrogolfoonde, televisie ens. van krag te voorsien. 'n Stoorelement is ook dikwels nodig ten einde elektriese energie gedurende die aand aan byvoorbeeld ligte en televisiestelle te voorsien. Die saamgestelde omsetter tree dus in sodanige stelsel op as wisselrigter en batterylaaier sowel as maksimum drywingspuntvolger.

2. WERKING.

'n Blokdiagrammatiese voorstelling van die saamgestelde omsetter word in figuur 1 getoon. Hierdie omsetter bestaan hoofsaaklik uit 'n middeltapmutator wat deur 'n mikroverwerkerbeheerder beheer word [4].

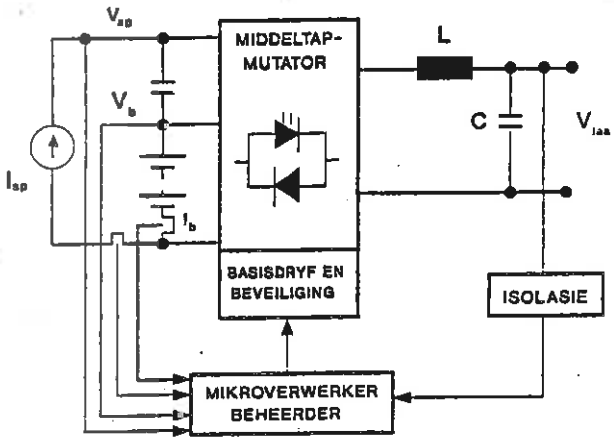

FIGUUR 1. BLOKDIAGRAM VAN DIE SAAMGESTELDE OMSETTER.

Die beheereenheid is geïmplementeer met behulp van 'n 80C31 gebaseerde mikrover-

werkerkaart. Verskeie seine word na die beheereenheid gevoer waar dit versyfer word vir gebruik deur die beheeralgoritme. Hierdie beheerder verrig benewens die uitvoering van die maksimum drywingspuntvolg-algoritme ook onder meer beveiliging van die batterye teen oorstroomtoestande en diepontlading uit.

Die middeltapmutator lewer 'n wisselspanning uitset (Vuit) na gelang van die verwysingsein soos deur die mikroverwerkerbeheerder gegenereer.

2.1 DIE MIDDELTAPMUTATOR.

Die drywingsbaan van die middeltapmutator word in figuur 2 getoon [4]. Die baan bestaan hoofsaaklik uit 'n 50 Hz transformator (N1-N5), vier diodes, twee skakelaars, twee kapasitore en die uitsetfilterelemente.

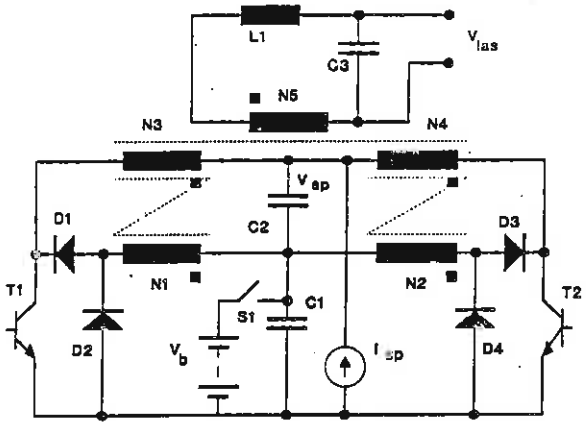

FIGUUR 2. DRYWINGSBAAN VAN DIE MIDDELTAPMUTATOR.

Die windingverhoudings van die transformator is só geskaleer dat hoëspanning sonpanele (nominaal 96 volt) saam met 'n 24 volt batterybank gebruik kan word. Die skakelaars T1 en T2 word teen 4 kHz geskakel met behulp van pulswydtemodulasie tegnieke. Hierdie skakelaars is bipolêre transistors gebaseer op die gekompenseerde darlington konfigurasie wat besonder lae aanspannings tot gevolg het [3]. Sulke effektiewe skakelaars is essensieel ten einde die effektiwiteit van die saamgestelde omsetter so hoog moontlik te kry.

Die drywingsbaan-konfigurasie laat verskeie modusse van werking toe na gelang van die transistor stuurseine en spesifieke insetspannings. Hierdie modusse word as volg uiteengesit.

BATTERYLAAI-MODUS.

In hierdie modus word die batterye vanaf die sonpanele gelaai. Wanneer T1 skakel verskyn die sonpaneelspanning (Vsp) oor N3 en indien die sonpaneelspanning hoër is as die nominale waarde sal 'n spanning groter as die batteryspanning oor N1 verskein. In hierdie geval sper diode D1 en stroom vloei deur diode D2 in die battery in. Dieselfde gebeur wanneer T2 geskakel word met D4 en D5. Diodes D2 en D4 tree in hierdie modus van werking dus op as gelykrigterdiodes. Die grootte van die stroom wat in die battery invloei kan beheer word deur die effektiewe aantyd van die skakelaars (T1 en T2) te beheer.

WISSELRIG-MODUS.

'n Sinusvormige uitsetspanning word in hierdie modus op N5 gegenereer deur die skakelaars T1 en T2 met behulp van pulswydtemodulasietegnieke te skakel. Die hoëfrekwensie pulswydtegemoduleerde sein word met behulp van C3 en L1 gefilter om die verlangde wisselspanning-uitset te lewer.

Die energie wat tydens wisselrigterwerking deur die las gebruik word, word deur die sonpanele voorsien wanneer die sonpaneelspanning hoër is as die nominale sonpaneelspanning van 96 volt. Wanneer die las meer drywing trek as wat die sonpanele kan voorsien sal die sonpanele die drywing beskikbaar teen die nominale spanning lewer terwyl die batterye verdere energie sal verskaf. In die geval waar die sonpanele nie aktief is nie (byvoorbeeld in die aand) word die energie slegs deur die batterye voorsien.

Wanneer 'n wisselspanning uitset na die las gevoer word, kan regeneratiewe strome vloei deur diodes D2 en D4 wat in hierdie modus dan optree as vryloopdiodes.

GEKOMBINEERDE WISSELRIGTER EN BATTERYLAAIER.

Die saamgestalde omsetter kan ook funksioneer as 'n batterylaaier terwyl die las van wisselspanning voorsien word. Hierdie is dan ook die modus waarin die omsetter gewoonlik gedurende die dag funksioneer.

Werking in hierdie modus geskied slegs wanneer die sonpaneelspanning hoër is as die nominale waarde. Hierdie vereiste stel dus die beperking daar, dat die drywing wat na die batterye en las vloei tesame nie meer sal wees as wat die sonpanele kan voorsien nie.

2.2 BEHEER VAN DIE MIDDELTAPMUTATOR.

Die middeltapmutator word beheer deur die 80C31 gebaseerde mikroverwerker wat die verlangde verwysingsein bereken en genereer. Wanneer wisselrigting plaasvind uit die batterye, of die batterye tesame met die sonpanele, word die uitsetspanning gelewer na die wisselstroom las konstant op 220V en 50

Hz gehou.

Wanneer die saamgestelde omsetter egter funksioneer as wisselrigter en batterylaaier (die modus waarin die omsetter gedurende die grootste deel van die dag werk) is dit noodsaaklik dat die maksimum drywingspunt van die sonpanele gevolg sal word. Ten einde op die maksimum drywingspunt te bly moet die drywing gelewer aan die batterye en las beheerbaar wees. In die geval waar die las van wisselstroom voorsien word, vind ons dat die battery se laaistroom hoofsaaklik 'n funksie is van die sonpaneelspanning.

Die lasdrywing kan egter binne perke beheer word deur die regulering van die uitsetspanning en frekwensie. Ten einde versadiging in magnetiese bane te verhoed word die spanning-frekwensie verhouding van die uitset deurgans konstant gehou. Meeste tobehore wat gedurende die dag aangedryf word kan oor 'n frekwensiebereik van 50Hz tot 60 Hz funksioneer. So byvoorbeeld dink ons aan 'n induksiemotor en waterpomp - waarvan die motorspoed en sodoende die benodigde drywing deur variasie in die toevoerfrekwensie beheer kan word [6,8].

'n Voorbeeld van die verandering in gelewerde drywing onder verskillende uitsetfrekwensies word in figuur 3 getoon. Die krommes toon die drywing wat deur die omsetter aan die las en batterye tesaam gelewer word by verskillende sonpaneelspannings. Hierdie krommes is geneem vir verskillende uitsetfrekwensies.

Wanneer die tipiese verloop van spanning teen maksimum drywing gelewer, van 'n tipiese sonpaneelstelsel bo-oor die omsetter karakteristieke geplot word (figuur 3), kan gesien word dat die werkpunt van die omsetter vir 'n bepaalde uitsetfrekwensie op die maksimum drywingspunt sal val. Dit is dan ook hierdie tegniek wat toegepas word om die sonpaneeldrywing op die maksimum drywingspunt te hou. 'n Optimiseringsalgoritme pas die uitsetfrekwensie gedurig aan totdat maksimum drywing vanaf die sonpanele verkry word.

Dit is egter belangrik om te let daarop dat 'n spesifieke las gebruik kan word om die maksimum drywingspunt slegs binne 'n bepaalde gebied te volg. Die hele sonpaneelstelsel word dus so ontwerp dat deur effektiewe lasbeheer (met byvoorbeeld tydskakelaars) die sonpanele deurgans maksimaal benut kan word.

3. EKSPERIMENTELE RESULTATE.

3.1 EFFEKTIWITEIT.

Rendementeienskappe soos gemeet op die prototipe saamgestelde omsetter word in figuur 4 tot figuur 6 getoon. Uit hierdie krommes is dit duidelik dat die rendement van die

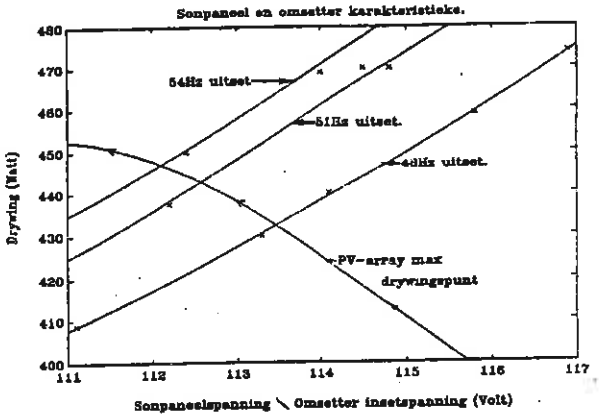

FIGUUR 3. OMSETTER KARAKTERISTIEKE SAAM MET DIE TIPIESE VERLOOP VAN SONPANEELSPANNING EN MAKSIMUM SONPANEELDRYWING.

omsetter veral tydens wisselrigting vanaf die sonpanele (figuur 4) besonder hoog is.

Hierdie hoë rendement (bokant 85% vir 'n werksgebied tussen 350 watt en 1.5 kW) is hoofsaaklik te danke aan die besonder effektiewe skakelaars asook hoë sonpaneelspanning wat gebruik word.

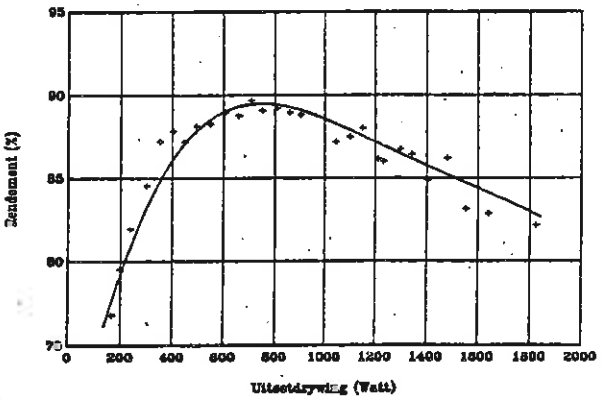

FIGUUR 4. RENDEMENT VAN OMSETTER AS WISSELRIGTER UIT DIE SONPANELE.

Tydens wisselrigting uit die batterye (figuur 5) is die rendement effens laer (in die orde van 72% vir 'n werksgebied van 150 watt tot 400 watt) weens die laer insetspanning en gevolglik hoër geskakelde strome. Die rendement neem met verdere toename in gelewerde drywing skerp af in die gebied hoër as 400 watt. Die omsetter werk egter sleg in die aand teen lae las by hierdie rendementwaardes.

Die rendement van die omsetter wanneer dit funksioneer as wisselrigter uit die batterye stem egter baie goed ooreen met huidig beskikbare batterywisselrigters.

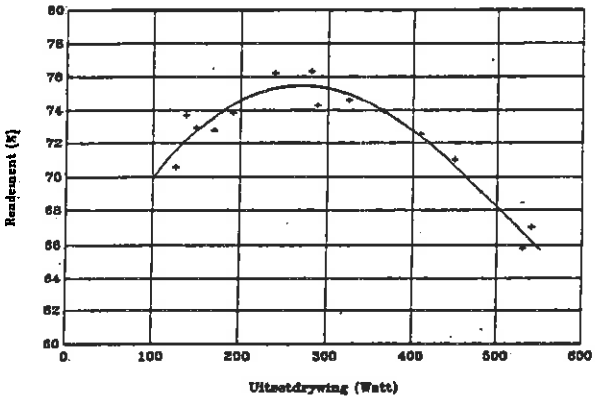

FIGUUR 5. RENDEMENT VAN OMSETTER AS WISSELRIGTER UIT DIE BATTERYE.

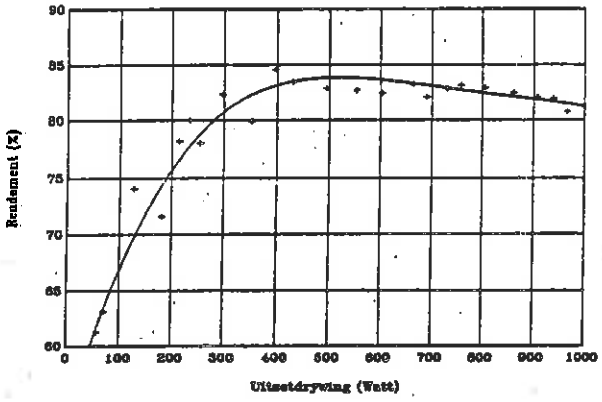

FIGUUR 6. RENDEMENT VAN DIE OMSETTER AS BATTERYLAAIER.

Die rendement van die stelsel wanneer dit funksioneer as batterylaaier (figuur 6) is hoër as 80% vir 'n werksgebied van 300 watt tot 1kW.

3.2 WISSELSTROOMUITSET

Die uitsetgolfvorms van die saamgestelde omsetter wanneer dit 'n weerstandslas voer word in figuur 7 getoon. Die spanning en stroom wat aan 'n tipiese induksiemotor met las gevoer word, word in figuur 9 getoon. Die spektrum-analises van die betrokke gelewerde spanning-golfvorms word in figure 8 en 10 getoon.

Hierdie resultate toon dat die wisselspanning uitset redelik goed sinusvormig beheer kan word deur pulswydtemodulasietegnieke.

3.3 MAKSIMUM DRYWINGSPUNTVOLGING.

Ten einde die weking van die saamgestelde omsetter onder maksimum drywingspuntvolging-beheer aan te toon is die verloop van son-paneeldrywing teen spanning gedurende 'n

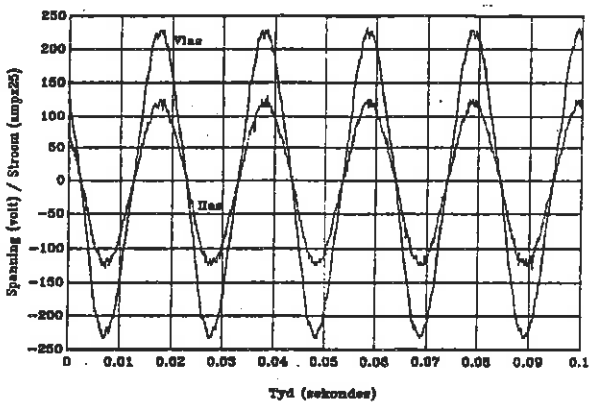

FIGUUR 7. UITSETSPANNING EN STROOM TYDENS AANDRYF VAN WEERSTANDSLAS.

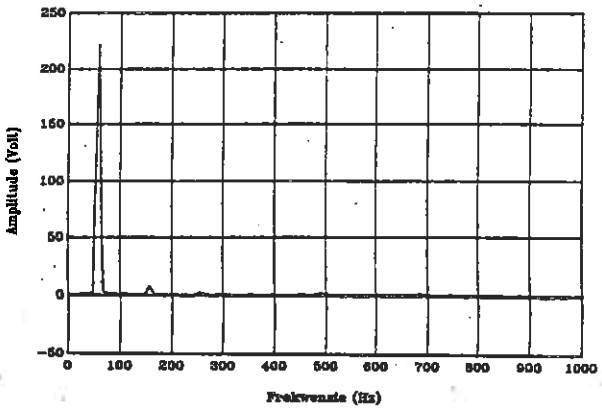

FIGUUR 8. SPEKTRUM-ANALISE VAN DIE SPANNING-GOLFVORM VAN FIG 7.

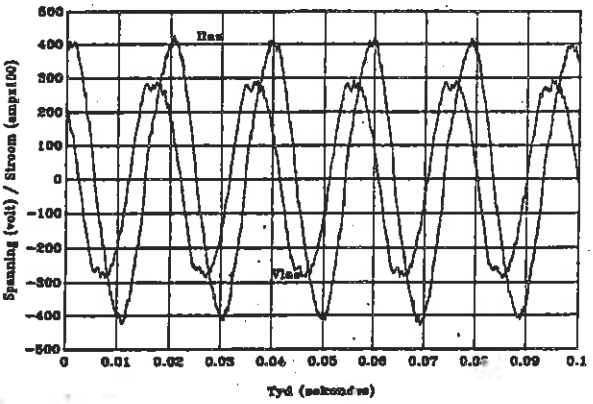

FIGUUR 9. UITSETSPANNING EN STROOM TYDENS DIE AANDRYF VAN INDUKSIEMOTOR LAS.

verandering in die insulasievlak geplot. Die sonpaneelkarakteristieke is in die laboratorium gesimuleer en die resultate hiermee behaal word in figuur 11 getoon. Die lokus van die uitsetdrywing is teen die sonpaneelspanning geplot en toon aan hoe die maksimum drywingspunt telkens deur die optimiseringsalgoritme opgesoek word. Sodoende word die sonpanele maksimaal benut.

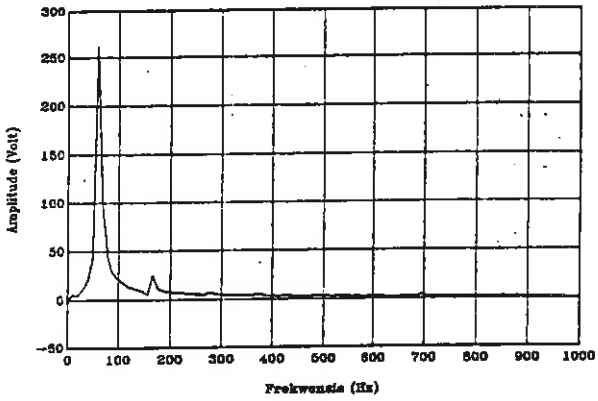

FIGUUR 10. SPEKTRUM-ANALISE VAN DIE SPANNING-GOLFVORM IN FIG 9.

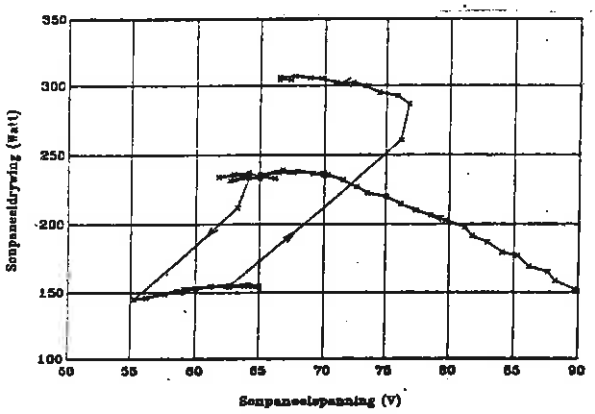

FIGUUR 11. VERLOOP VAN SONPANEELSPANNING TEEN DRYWING GEDURENDE MAKSIMUM DRYWINGSPUNTVOLGING.

3.4 WERKING AS WISSELRIGTER EN BATTERYLAAIER.

Wanneer die sonpaneelspanning bo die nominale waarde van 96 volt is sal die battery gelaai word, selfs terwyl die wisselspanning die las aangedryf. Indien die sonpanele egter sou wegval sal wisselrigting dadelik vanuit die batterye voortgesit word. Figuur 12 toon aan wat met die batterystroom gebeur wanneer die sonpanele wegval.

Terwyl die sonpanele genoeg energie verskaf vir die aandryf van die las sowel as die laai van die batterye kan daar uit figuur 12 gesien word dat 'n netto negatiewe stroom in die battery invloei (batterye word gelaai). Wanneer die sonpaneelstroom egter na nul val, neem die batterye die lasstroom oor en voorsien die energie benodig om die las te voer. In hierdie geval toon figuur 12 dus dat 'n groot netto positiewe stroom deur die batterye vloei, wat die lewering van drywing deur die batterye aandui.

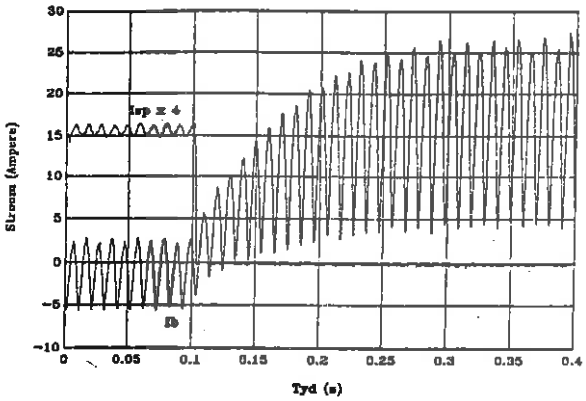

Isp - Sonpaneelstroom maal 4.
Ib - Batterystroom.

FIGUUR 12. VERLOOP VAN BATTERYSTROOM WANNEER DIE SONPANELE WEGVAL.

4. GEVOLGTREKKING.

Uit die bogenoemde resultate is dit duidelik dat die saamgestelde omsetter wel die benodigde funksies van wisselrigter, battery-laaier en maksimum drywingspuntvolger as enkele eenheid kan verrig. Die eenvoud van die drywingsbaan lewer 'n koste-effektiewe eenheid met besonder hoë rendementeienskappe - wat natuurlik 'n vereiste is vir gebruik in sonenergiestelsels.

Wanneer die saamgestelde omsetter egter in sonenergiestelsels geïmplementeer word is dit noodsaaklik dat lasbeheer toegepas sal word ten einde die suksesvolle werking van die maksimum drywingspuntvolg-algoritme te verseker.

7. VERWYSINGS.

[1] "Sun provides a cost effective solution to rural energy problem.", Engineering News, 29 Junie, 1990, pp22.

[2] "Photovoltaic power: On its way to improving South-Africa's quality of life.", Engineering News, 29 Junie 1990, pp19.

[3] VAN DER BROECK HW, VAN WYK JD, SCHOEMAN JJ, "On the steady-state and dynamic characteristics of bipolar transistor power switches in low-loss technology", IEE Proceedings, vol. 132, pt. B, no. 5, September 1985.

[4] SNYMAN DB, ENSLIN JHR, "Combined low-cost, high-efficient inverter, peak power tracker and regulator for PV applications", IEEE Power Electronics Conference, Wisconsin, VSA, Julie 1989.

[5] SCHOEMAN JJ, VAN WYK JD, "A simplified maximal power controller for terrestrial photovoltaic panel arrays", IEEE Power Electronics Conference, Massachusetts Institute of Technology, Cambridge, Junie 1982, pp 361 - 367.

[6] ALCOCK DN, "Production operation of submersible pumps with closed-loop adjustable speed control", IEEE Transactions on industry applications, vol. IA-17, no. 5, pp 481, September / Oktober 1981.

[7] RAMAKUMAR R, "Renewable energy sources and developing countries", IEEE Transactions on Power Apparatus and Systems, vol. PAS-102, no. 2, pp 502, Februarie 1983.

[8] CONNORS DP, JARC DA, DAUGHERTY RH, "Considerations in applying induction motors with solid-state adjustable frequency controllers.", IEEE Transactions on Industry Applications, vol. IA-20, no. 1, pp 113 - 121, Januarie / Februarie 1984.

[9] HUBBARD HM, "Photovoltaics Today and Tomorrow", Science, 21 April 1989, pp 297.

A NEW ULTRASONIC SERIES RESONANT CONVERTER WITH INTEGRATED L-C-T

M.C. Smit, J.A.Ferreira, J.D. Van Wyk
Energy Laboratory, Rand Afrikaans University
P.O. Box 524, Johannesburg 2000, South Africa
M. Ehsani
Power Electronics Laboratory, Texas A&M University
College Station, TX 77843

An integrated structure for the capacitor, inductor and transformer of the series resonant converter is presented. It is shown that the necessary capacitance can be achieved by using a bifilar primary and the leakage inductance of the transformer replaces the physical inductor. By integrating three components into one it is possible to save space, mass, volume and cost.

1.0 INTRODUCTION

A constant demand exists for ever decreasing size in switchmode supplies. The first step has been the introduction of resonant mode converters[1]. Such converters typically consist of a resonant tank, a transformer and an input or output filter. The soft-switching characteristics of these converters allow an order of magnitude higher frequency, thus reducing the size of the reactive components. The next logical step towards a smaller package is introduced, namely the electromagnetic integration of the resonant tank and, if possible, the transformer into a single component, which, not only saves mass and volume, but can also reduce manufacturing costs.

The particular converter to be investigated is the well known series resonant converter shown in Figure 1. In this paper it will be shown that it is possible to integrate the series circuit consisting of the capacitor, inductor and transformer into a single structure.

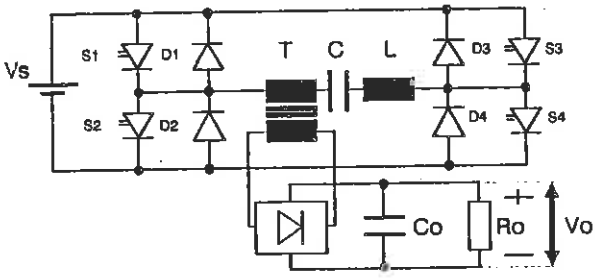

Figure 1: The series resonant converter.

2.0 THE INTEGRATED L-C-T TRANSMISSION LINE

The first step towards a practical integrated L-C-T is to recognise that a three conductor transmission line structure can behave as a series capacitor, inductor and transformer. In microstrip theory [4] it is a well known technique to create a capacitor by using short sections of transmission line of a very low characteristic impedance. In Figure 2 conductor 1 and 2 are spaced with a very thin dielectric and forms the series capacitor in the series resonant converter. In microstrip circuits coupling between two circuits can be obtained by placing two conductor sections in close proximity to each other. In Figure 2 conductor 3 has been placed so that a mutual flux Φ_m couples conductor 3 with conductor 1 and 2. Due to the space between them, a certain leakage flux Φ_l also exists. This leakage flux gives an uncoupled inductance which can serve as the series inductance L in Figure 1.

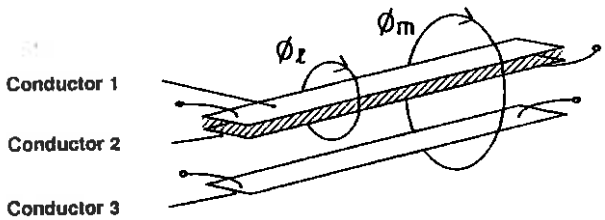

Figure 2: The integrated L-C-T transmission line.

This transmission line can be modelled as a distributed circuit network as indicated in Figure 3. Magnetic coupling between conductor 1 an 3 is indicated by M_{as}, and that between conductor 2 and 3 by M_{bs}. This network is used to simulate the behaviour of the integrated L-C-T. The transmission line structure as configured in Figure 2 is not practical for power transmission and the operating frequencies, if microstrip technology is to be used, is beyond the capability of power semiconductors with sufficient power processing capabilities. It is therefore necessary to investigate more practical lower frequency structures which can operate at frequencies below 10MHz. It is however necessary that the new structure behaves in the same manner as the transmission line structure, because the experimental and theoretical work conducted within the scope of this project, indicated that the distributed

network is a workable alternative to the lumped L-C-T.

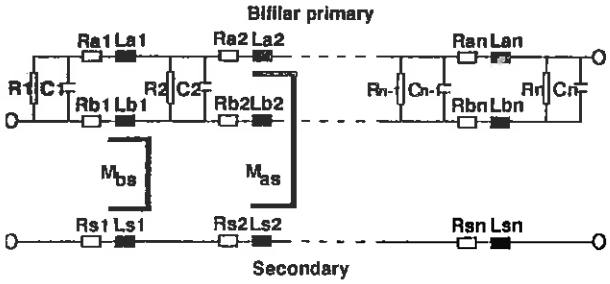

Figure 3: Distributed circuit of the integrated L-C-T transmission line.

3.0 THE INTEGRATED L-C-T IN A TRANSFORMER STRUCTURE

A suitable L-C-T structure for a series resonant converter requires a large enough LC product for a practical switching frequency, a suitable Zo to match the supply voltage and load and very good coupling between conductors 1, 2 and conductor 3 to facilitate power transmission. Good coupling can be achieved using a high frequency core, in which case the L-C-T structure becomes a transformer, as shown in Figure 4. Conductors 1 and 2 in Figure 2 have become a bifilar primary which contains the capacitor, while the leakage inductance serves as the series L (Figure 1). Two structures were investigated experimentally.

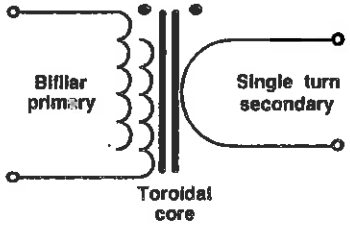

Figure 4: Transformer diagram of integrated L-C-T.

Two integrated L-C-T transformer structures are presented in the paper. The first involves a toroidal core as shown in Figure 5. The primary consists of bifilar foil windings wound directly on the core. The secondary has a single turn and forms a cup which contains the core and the primary. The space between the primary winding and the interior walls determine the leakage inductance.

An advantage of the toroidal structure is that a theoretical analysis of the structure is relatively easy due to the radial symmetry of the configuration. Manufacturing on the other hand is fairly complicated.

The second configuration is shown in Figure 6 and consists of four U-cores positioned to form a cross, and I-core sections closing the magnetic circuit in the centre leg. Barrel type windings of foil conductors are used and construction is therefore easier than in the case of the toroidal structure. Theoretical analysis of this structure is more difficult, in particular calculation of leakage inductance. An approximation can be obtained by using the method outlined in reference [4].

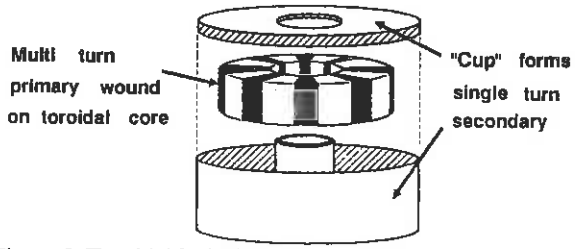

Figure 5: Toroidal L-C-T transformer structure.

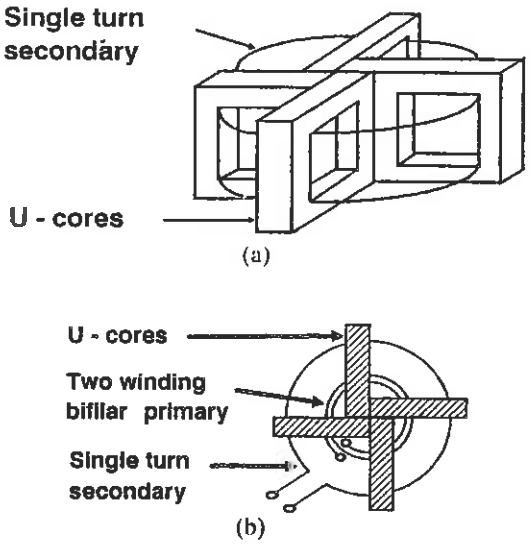

Figure 6: U core L-C-T transformer structure. a) 3D structure. b) Top view.

4.0 THE TOROIDAL L-C-T STRUCTURE

The structure investigated in the paper involves a transformer on a toroidal core, as is shown in Figure 5. The specific design entails a single turn secondary and a multiturn primary. A toroidal configuration was chosen because it permits a very large range of leakage inductance values, since, contrary to other core configurations, the winding window is unbounded. For this configuration the theoretical analysis can then be performed exactly and verified with an experimental prototype.

4.1 Theoretical analysis

4.1.1 Leakage inductance

Inductance can be computed from the following well known equation:

$$L = \frac{\int_v \mu H^2 \, dv}{I^2} \qquad (1)$$

If $\int_v dv \equiv$ total volume V, and $H \equiv$ magnetic field intensity and constant in the volume enclosed by the current, then we have the leakage inductance:

$$L_\sigma = \frac{\mu H^2 (V_s - V_p)}{I_s^2} \tag{2}$$

and magnetising inductance

$$L_m = \frac{\mu H^2 V_p}{I_p^2} \tag{3}$$

where $V_p \equiv$ *volume of primary*

$$= \frac{\pi}{4} \left(B_p + A_p\right) \left(B_p - A_p\right) h_p \tag{4}$$

$V_s \equiv$ *volume of secondary*

$$= \frac{\pi}{4} \left(B_s + A_s\right) \left(B_s - A_s\right) h_s \tag{5}$$

with $A_s = \frac{A_p + B_p}{2} - D_s$ (6)

and $B_s = \frac{A_p + B_p}{2} + D_s$ (7)

The height of the secondary is given by

$$h_s = h_p + \left(D_s - \frac{B_p - A_p}{2}\right) \tag{8}$$

The secondary has only one winding as shown in Figure 5, thus

$$I_s = N_p I_p \tag{9}$$

where $N_p \equiv$ *number of primary turns*

and from equations (2 and 3), we determine L_σ and L_m if

$$H = \frac{2 N_p I_p}{\pi \left(A_p + B_p\right)} \tag{10}$$

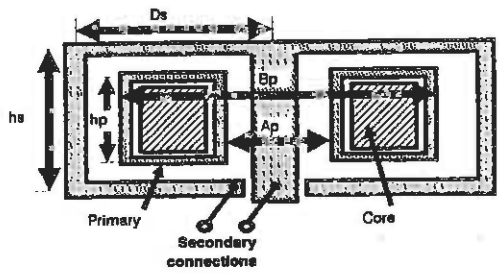

Figure 7: Cross section dimensions of structure.

4.1.2 Capacitance

As can be seen seen from Figure 2 and 4, the primary winding is constructed to form a capacitor by using a parallel strip bifilar wound winding, and bringing the opposite connections out. The capacitance is given by:

$$C = \frac{\varepsilon S}{d} \tag{11}$$

where $\varepsilon = \varepsilon_0 \varepsilon_r$

$$S = w \left[\left(B_p - A_p\right) + 2h_p\right] N_p \tag{12}$$

$d \equiv$ *bifilar primary plate separation*

$w \equiv$ *bifilar primary plate width*

4.2 Experimental prototype

An experimental prototype was constructed, and had the following dimensions

$A_p = 22.4\,mm$, $B_p = 36.0\,mm$, $h_p = 14.5\,mm$,

$D_s = 12.0\,mm$, $N_p = 8\,turns$, $\mu_r = 120$,

$w = 4.0\,mm$, $\varepsilon_r = 2.67$ and $d = 0.03\,mm$

A shown in Figures 8 and 9, an open circuit (secondary) resonant frequency of 1.4MHz was measured and a resonant frequency of 9MHz was obtained when the secondary winding is shorted out.

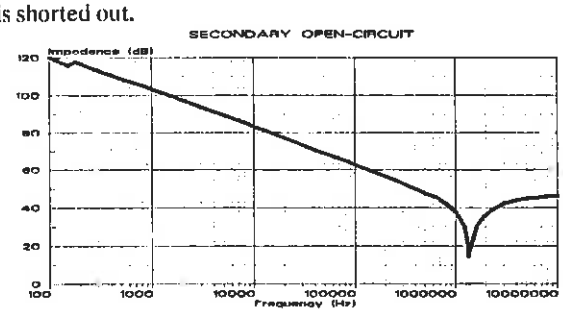

Figure 8: Open circuit response

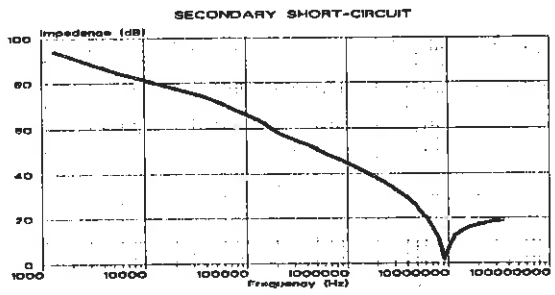

Figure 9: Short circuit response

4.3 Technological aspects

The very high resonant frequency of the particular experimental prototype renders it impractical for higher power converter applications. The capacitance value was too low, due to the fact that a dielectric with a relative permittivity of 2.67 had to be used. The required high value of capacitance can be obtained by using a ferro-electric ceramic between the windings. These ferro-electric ceramics are known from their application in multilayer chip capacitors [2] and power electronic snubbers [3], and exhibit a very high dielectric constant (> 1000). An inhouse technology has been developed to manufacture ceramic dielectrics from technology using barium titanate from sintered ceramic capacitors [7], though at the time when this paper was written, some practical implementation problems still needed to be solved.

5.0 U-CORE LCT STRUCTURE

5.1 Experimental prototype

The configuration is shown in Figure 6 and is described in paragraph 3. The two winding bifilar primary (separated by a dielectric) and single turn secondary is wound through the core window. Since this structure is much larger than the toroidal structure, it results in a lower resonant frequency.

5.2 Spice simulation

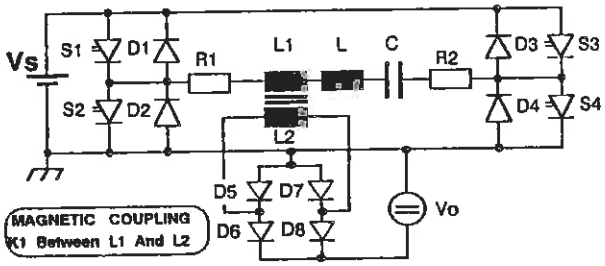

Figure 10: SPICE model of discrete component converter.

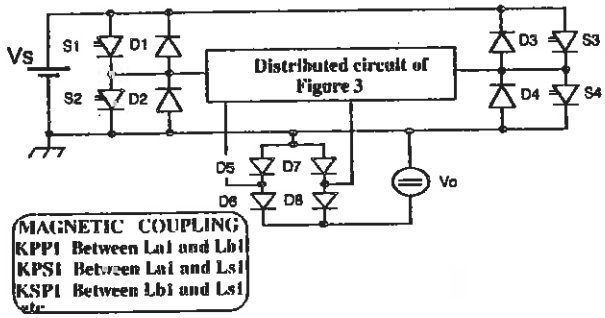

Figure 11: SPICE model of integrated component converter.

The objective of the simulation is to show that the integrated structure reacts in the same way as a discrete series inductor capacitor and transformer would do, and in turn agrees with the experimental results. Figure 10 shows the SPICE circuit model of the discrete component series resonant converter. Figure 11 shows the equivalent circuit presentation of the integrated structure. The windings are modelled in terms of the transmission line in Figure 3. These SPICE models are used to simulate both the frequency and time response described in the next paragraph.

5.3 Frequency domain performance

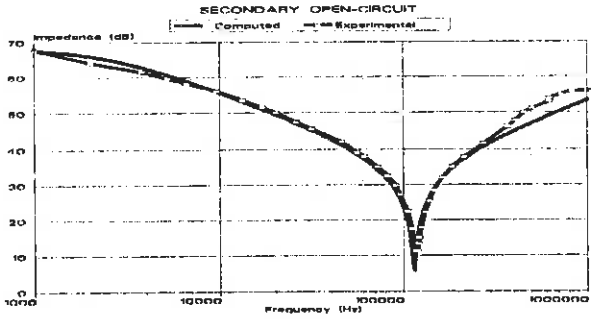

Figure 12: Open circuit response.

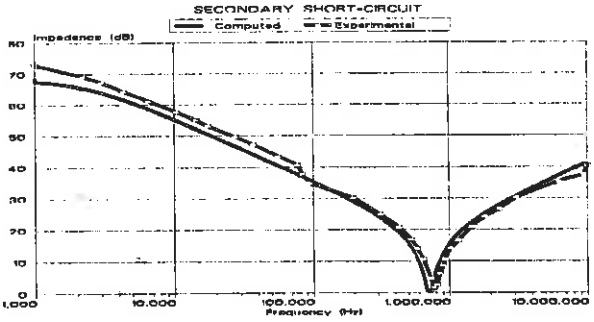

Figure 13: Short circuit response.

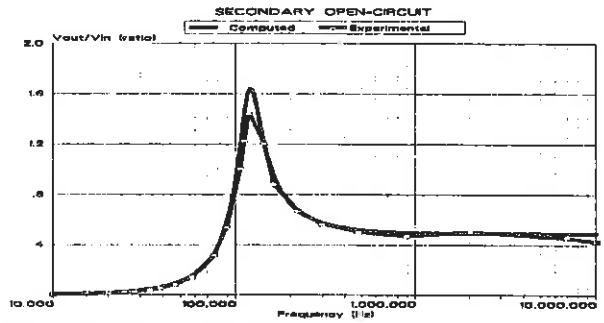

Figure 14: Vout vs. Vin ratio.

Using the capacitance of the bifilar primary (23.9 nF), the leakage and magnetising inductance can be found by short- and open circuiting the secondary winding respectively. The open circuit resonant frequency of 119kHz was measured which gives a magnetising inductance of 75 μH. A resonant frequency of 726kHz was obtained when the secondary wind-

ing is shorted out, and corresponds to a leakage inductance of 1.8 μH. Transformer action of the integrated L-C-T is evident if the frequency response of the ratio, secondary output voltage to primary input voltage, is plotted. As shown in Figure 14 the voltage ratio of 0.5 (two turn primary and single turn secondary), is only evident at high frequencies where capacitance between the bifilar primary conductors is neglible.

5.4 Time domain

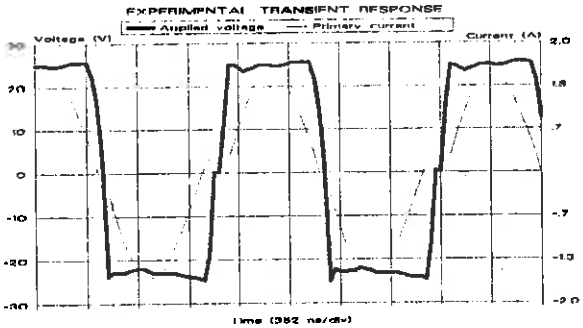

Figure 15: Measured current and voltage waveforms of integrated component.

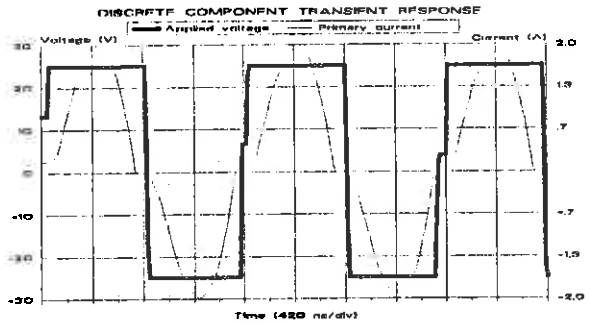

Figure 16: Simulated current and voltage waveforms of discrete component converter.

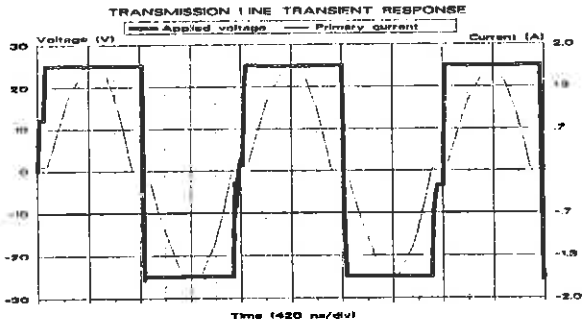

Figure 17: Simulated current and voltage waveforms of integrated component converter.

With a rectifier bridge, filter capacitor and 6.2Ω load resistance, the applied voltage across and primary current of the L-C-T structure is shown in Figure 15. From these time domain graphs it is evident that the integrated L-C-T structure functions well in a series resonant converter. Agreement between experimental and simulated waveforms, as well as the similarity between the waveforms obtained with the lumped and distributed models, confirms the theoretical approach followed.

6.0 CONCLUSION

A method to integrate the capacitor, inductor and transformer of a series resonant converter has been described. The results presented shows that an integrated L-C-T structure can succesfully be modelled and has practically been constructed and operated in a series resonant converter.

This integrated structure requires certain manufacturing technology which had been developed. A crucial technology is to be able to obtain large enough capacitance in the primary in order to get reasonable values of characteristic impedance and resonant frequency. This high permittivity would allow the integrated LCT-toroidal structure of this paper to be made in acceptable dimensions at an acceptable frequency, and would make this a competitive technology.

REFERENCES

[1] F.C. Lee; "High frequency quasi-resonant converter technologies" Proc. IEEE vol 76(4), 1988, pp. 377-390.

[2] H. Takamisawa, K. Utsumi, M. Yonezawo, T. Ohno; "Large capacitance multilayer ceramic capacitor", IEEE Trans. Comp., Hybrids, Manuf. Technol, vol CHMT-4(4) 1981, pp 345-349.

[3] A.G.K. Lutsch, J.D. van Wyk, J.J. Schoeman; "On the evaluation of ferroelectric nonlinear capacitors for application in power circuits", IEEE Tran. Comp., Hybrids, Manuf. Technol., Vol CHMT-12, 1989.

[4] T.C. Edwards; "Foundation for Microstrip Circuit Design", John Wiley & Sons, 1981.

[5] P.L. Davell; "Effects of Eddy currents in transformer winding", Proceedings of the IEE, Vol 113, No 8, August 1966, pp 1387-1394.

[6] M. Ehsani, T. Li, O.H. Stielau, J.D. van Wyk, I.J. Pitel, "Integrated Reactive Components in power electronic circuits"

[7] J.D. van Wyk, C.K. Campbell, M.K.F. Holm, J.J. Schoeman; "Studies of non-linear capacitors for applications in snubber modus for power electronic switches", Accepted for PEMC-90 (6th conference on Power Electronics and Motion Control, Budapest, October 1-3, 1990).

A HIGH PERFORMANCE GATE/BASE DRIVE USING A CURRENT SOURCE

O.H. STIELAU, J.J. SCHOEMAN, J.D. VAN WYK
Energy Laboratory,
Rand Afrikaans University,
P.O. Box 524, Johannesburg, 2000,
REPUBLIC OF SOUTH AFRICA.

Abstract- Unlike minority carrier semiconductor devices eg MOSFET's which are voltage controlled, majority carrier elements eg bipolar transistors and GTO's are current or charge controlled. To turn such a device on or off, a certain amount of charge has to be injected or extracted from the gate/base. If this is to be done quickly, very fast current rise and fall times are necessary. The gate drive discussed in this paper achieves extremely fast turn-on times due to a current pulse which is applied to the gate. The gate/base current rise time is only a function of the turn-off time of a MOSFET, resulting in extremely fast rise times. The fundamental limits of the new drive are pointed out, including minimum off-time and maximum on-time. A loss analysis is also carried out. Experimental results verify the performance of the gate drive.

INTRODUCTION

In force commutated circuits, switching losses can be divided into turn-on and turn-off losses. Turn-off losses are usually dominant, so that the gate drive is optimised to minimise turn-off losses. Once a turn-off circuit has been decided on, the turn-on circuit is added to complete the gate drive. Since the turn-on circuit is connected to the turn-off circuit via the gate, the available options are usually limited, resulting in a less than optimum turn-on circuit as can be seen in the literature [1] - [3].

In this paper, a different strategy is followed. The gate drive is optimised for turn-on with a built-in turn-off circuit. The final circuit was obtained after investigating several options, and a systematic approach is followed showing how the final circuit was arrived at. A loss analysis shows that the drive has a very high efficiency.

CONVENTIONAL GATE DRIVE

To turn a majority carrier semiconductor device on quickly, a certain amount of charge has to be injected into the gate within a specified time. The turn-on time will be determined by the rise time of the current pulse, and the amplitude of the pulse [2]. In conventional gate drives, a switching element S is switched on and gate current starts flowing as shown in Fig. 1.

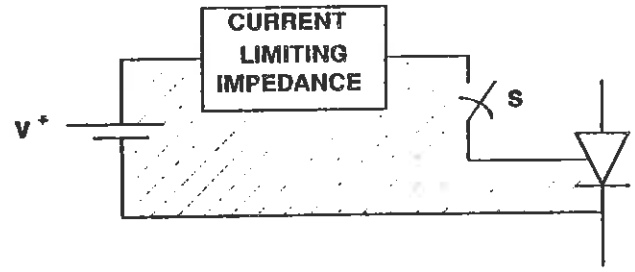

Fig. 1. Conventional gate drive.

The rise time of the gate current is determined by:

1) The supply voltage, V^+,

2) the turn-on behaviour of S, and

3) the stray inductance of the shaded loop.

The amplitude of the gate current is determined by

1) The supply voltage, V^+,

2) the gate-cathode voltage, and

3) the current limiting impedance.

For high efficiency, V^+ is usually chosen low, in the range of 5-10V, severely limiting the rise time of the gate current. For faster rise times, V^+ can be increased [2] with resultant higher losses.

Even with a low value of V^+, the efficiency of the gate circuit is still extremely low. With $V^+ = 5V$ and a gate-cathode voltage of 1V, the efficiency can not be higher than 20%.

A comprehensive study of transformer-coupled base drives has been given in the literature [4], [5]. These drives are characterised by their complexity, but relatively high efficiency. The new gate drive now proposed is not only extremely simple, but high efficiency can also be achieved.

NEW GATE DRIVE

Version 1

In the new gate drive, forced commutation is used to switch on the main device. An inductive current is switched off, and is forced to commutate into the gate. The fundamental circuit is shown in Fig. 2.

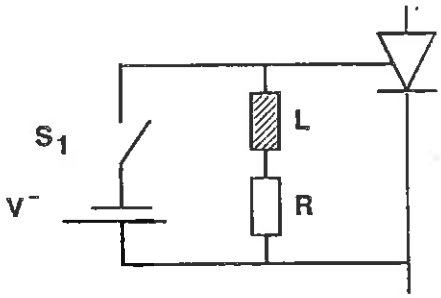

Fig. 2. New gate drive - Version 1.

With S_1 closed the gate is biased negatively. In the steady state, a current equal to $\frac{V^-}{R}$ flows through R, L, S_1 and V^-. When S_1 is opened, this inductive current is forced to commutate into the gate. The rise-time of the gate current is only a function of the commutation time of the current from S_1 to the gate, since the inductive current through L must continue flowing. The amplitude of the gate current is equal to the inductor current which will be equal to $\frac{V^-}{R}$.

In the on state, current flows through L, R and the gate. The gate current will drop roughly exponentially until turn-off, when S_1 is switched on and the gate is biased negatively again. In the off state, the inductor current rises exponentially again to a steady state value equal to $\frac{V^-}{R}$. Waveforms of inductor, switch and gate currents are shown in Fig. 3.

To keep losses low, V^- must be small. For a peak gate current of 10A and $V^- = 4V$, losses in R would be equal to nearly 40W. The efficiency of this gate drive is thus very low.

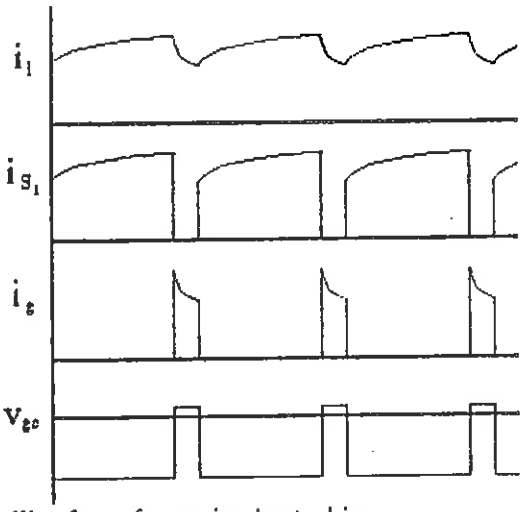

Fig. 3. Waveforms for version 1 gate drive.

Version 2

From Fig. 2, the steady state inductor current is equal to $\frac{V^-}{R}$. To increase this current level, V^- must be increased or R must be decreased. R can be decreased by placing a second switch across the resistor, resulting in the circuit shown in Fig. 4.

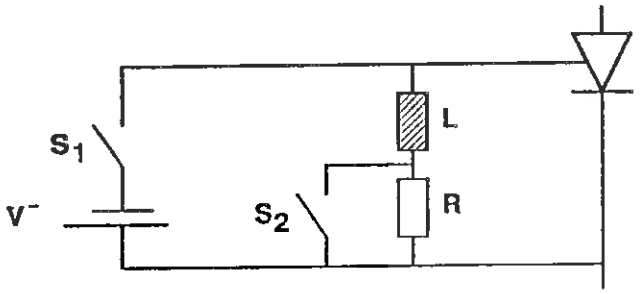

Fig. 4. Version 2.

In the off state, S_1 is on and S_2 off. A small current, in the steady state equal to $\frac{V^-}{R}$, will flow through R, L, S_1 and V^-. Just before the main device is to be switched on, S_2 is switched on. The current through L then rises linearly at a rate equal to $\frac{di_L}{dt} = \frac{V^-}{L}$ until it reaches the desired turn-on value. S_1 is then switched off, forcing the inductive current to commutate into the gate of the main device.

The inductive current flowing through S_2, L and the gate will now decay, as the energy stored in the inductor is dissipated in the gate. Gate current will thus flow until the stored inductive energy runs out, or S_2 is switched off. The gate current waveform can be aproximated by a linear decay with $\frac{di_{fg}}{dt} = -\frac{v_{gc}}{L}$, with i_{fg} the forward gate current and v_{gc} the on state gate-cathode voltage. Note that this decay is much slower than the build-up of the inductor current because V^- is much larger than v_{gc}.

To switch off the main device, S_2 is switched off and S_1 on. The gate voltage is then biased negatively with voltage source V^-. The current which flowed in S_2 (if any) is commutated to R, and the current through R will rise or drop exponentially to a steady state value equal to $\frac{V^-}{R}$.

Version 3

The main disadvantage of version 2 is the constant current flowing through R in the off state, causing unnecessary losses. The only function of this resistor is to limit the voltage across S_2 when it is switched off. If a capacitor is placed in series with the resistor, there are no DC losses in the off state. The resulting circuit is shown in Fig. 5.

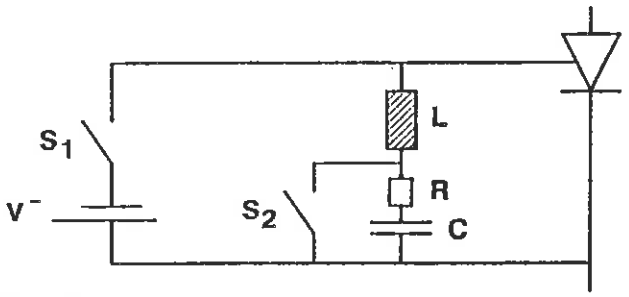

Fig. 5. Version 3.

At turn-off, L, C, and R form a damped series resonant circuit since S_2 is off and S_1 is on. When everything has settled down, capacitor C will be charged to a voltage equal to V^-. The amount of charge necessary to charge the capacitor is equal to $Q = C V^-$. The current charging up C also flowed through the source, and the source thus supplied an additional amount of energy equal to $QV^- = C(V^-)^2$. This energy represents a loss in the gate drive as it does not help in switching the main device on or off, and is also not regenerated to the source. The energy is dissipated in R and to keep this energy as low as possible, the capacitance C must be made as small as possible.

A small capacitance, however, results in a large voltage peak across S_2. Possible solutions are using a switch with an avalanche rating eg. International Rectifier HEXFETS [6], thus dissipating some of the inductive energy in S_2, or placing a zener across S_2, in which case R and C can be eliminated. No additional energy will then be supplied by the source so that the overall drive losses will decrease. The energy dissipated in the zener will be equal to the excess inductive energy in L at turn-off.

A trade-off thus has to be made between efficiency of the drive and the maximum voltage allowed across S_2. When S_2 is turned on again, the energy stored in C is dissipated in R. R is dimensioned to keep the peak discharge current at an acceptable level.

Version 4

To switch on a majority carrier semiconductor device quickly, it is advantageous to have a very large gate current peak dropping down to a certain much smaller value [2].

The ratio of the peak current to average on-state current would typically be between 3 and 20. This can easily be accomplished using the new drive by making the inductor L saturate as shown in Fig. 6.

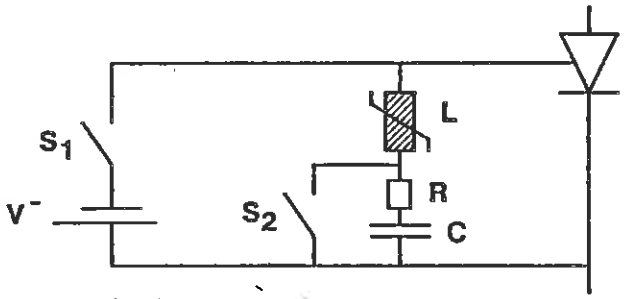

Fig. 6. Version 4.

When S_2 is switched on, the inductor current builds up slowly until the inductor saturates after which the current increases rapidly. As soon as the desired turn-on current level is reached, S_1 is switched off and this current is commutated into the gate. Since the inductor is saturated, the gate current will drop quickly until the core comes out of saturation again and the current will then drop very slowly. Using this gate drive a very large current pulse can be injected into the gate resulting in very fast turn-on times.

Since the magnetic core is only saturated in one direction, core losses will be very low. Excess energy in the inductor at turn-off will not be more than in version 4 because the inductor current has fallen to low levels at turn-off. This results in much improved performance without a premium being paid in the form of larger losses.

FUNDAMENTAL LIMITS

The following discussion refers to versions 3 and 4.

The rise-time of the gate current only depends on the commutation time of the inductor current from S_1 to the gate. This commutation time depends on the turn-off time of S_1, so that the $\frac{di_{fg}}{dt}$ is only dependent on the value of the inductor current and the turn-off time of S_1 and nothing else.

During turn-off, charge has to be extracted from the gate by a negative gate current. The rise time of this negative gate current depends on the turn-on time of S_1, the value of V^-, and the stray inductance of the turn-off loop shown in Fig. 7. This inductance should be small to ensure that the charge is extracted quickly and also that the gate always stays negatively biased even when a very high $\frac{dv}{dt}$ is applied to the main device.

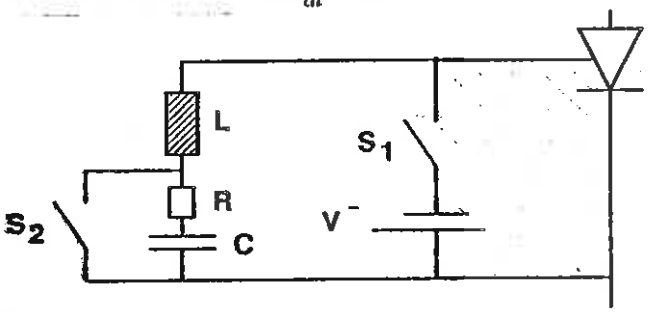

Fig. 7. Low inductance loop.

Losses can be identified in the following places:

1) For practical circuits the largest losses are conduction losses in S_1 and S_2. These losses can only be minimized by the choice of switching devices.

2) The dissipation of excess inductive energy at turn-off is the only other major loss. This energy is eventually dissipated in resistor R. In practical circuits, these losses are reasonably low and would represent about 20% of the input power to the gate drive.

Two low-inductance loops can be identified. During turn-on, current flowing through S_1 and V^- must commutate into the gate. The shaded loop shown in Fig. 7 must thus have very little stray inductance. The voltage across S_1 at turn-on will depend on the impedance of this loop, and careful layout is necessary to limit inductance as $\frac{di_{fg}}{dt}$ values of 1000A/μs can be obtained. S_1 must be able to block the induced voltage.

The second loop is the loop caused by R, C and S_2. During turn-off, S_2 is switched off and current flowing in S_2 commutates to the RC snubber. The stray inductance in this loop must be kept to a minimum to reduce voltage peaks across S_2.

The fundamental limits of the circuit in terms of switching times and losses are thus mostly determined by the performance of the switching devices S_1 and S_2. Care must be taken in the layout of the loop identified in Fig. 7 which includes the transmission line to the gate, and the source V^-, in order to reduce voltage overshoots across S_1. The positioning of S_2 and of L is totally unimportant. They can be placed far away from the rest of the circuit so that they are out the way of the other elements. V^- and S_1 must, however, be placed as close as possible to the transmission line to the gate.

The circuit has three fundamental timing limitations.

Firstly it is necessary to know before each turn-on when the turn-on will actually take place. This is because the current in the inductor first has to build up to the required turn-on value before the main device can be turned on. In applications were the turn-on signal is always fixed, eg. PWM modulation with trailing edge modulation [7], or delta modulation this is not a problem. The drive can, however, not be used in applications with indeterminate turn-on instants, eg. PWM with leading edge modulation [7] or hysteresis controllers. Version 1 does not have this problem but suffers low efficiency as already pointed out.

Secondly the maximum on-time of the main device is limited. This is due to the limited amount of energy which can be stored in the inductor. This is usually not a problem for practical circuits since power electronic switches are usually used in applications where they are switched on and off, and not left on permanently. The inductor thus has to be designed to store enough energy to keep the main device on for the maximum permissible on-time.

Thirdly the minimum off-time of the main device is limited. This is because the inductor current can only build up during the off-state of the main device. Since the current builds up with the supply voltage as driving function and decays against the gate-cathode voltage, the ratio of these two voltages will determine the ratio of the current rate of rise and rate of fall. For a supply voltage of 15V and gate-cathode voltage of 1V, the on-off duty ratio can be varied between 0% and 93%. This is enough for most power electronic applications.

From the three limitations mentioned above, it can be seen that this drive is best suited for applications with a constant on-time, eg. resonant converters, or for PWM converters with trailing edge modulation and a lower switching frequency limit.

The drive is suited for all types of current controlled devices, but will have to be adapted if it is to be used for voltage controlled devices.

LOSS ANALYSIS

For the loss analysis, the version 4 gate drive was used. The following assumptions were made:

1) The switches can be modelled as an open circuit in the off state and a resistance R in the on state. This assumption is valid if MOSFETS are used. The MOSFET is at present the ideal switching device for this gate drive due to its high switching speed and easy driving.

2) Switching losses in the switches S_1 and S_2 are neglected. Only conduction losses are thus taken into account.

3) Excess inductive energy at turn-off is dissipated in the gate drive. This energy is equal to the energy stored in the inductor at turn-off, namely $\frac{1}{2} L i^2$.

4) Losses during turn-off due to a negative gate current are neglected.

5) The saturation of L is very sharp. The inductance thus has one of two values, either L_{pre} (the inductance in the unsaturated state) or L_{post} (the inductance in the saturated state).

6) The resistance of switches S_1 and S_2 is so low that the inductor current rises and falls linearly.

Fig. 8 shows waveforms of the switch currents as well as the gate current during operation.

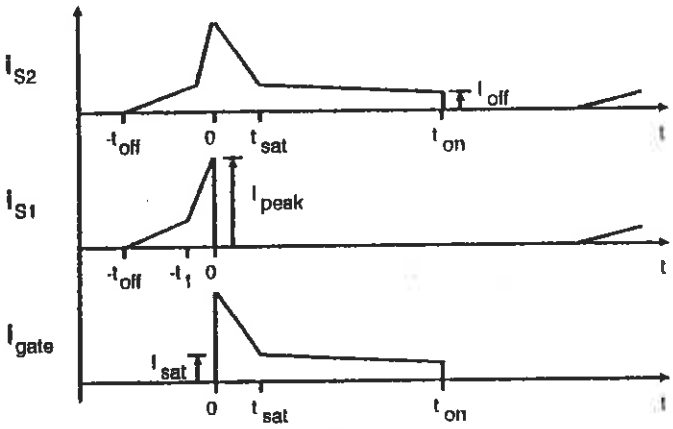

Fig. 8 Waveforms of current through S_1, S_2 and the gate.

Of the various parameters, the following are determined by the semiconductor device to be switched:

V^- : This voltage source must be smaller than the maximum reverse gate voltage.

I_{off} : This is the minimum gate current necessary to keep the device in conduction.

I_{peak} : This is the value of the peak gate current necessary to achieve minimum turn-on losses of the main device.

t_{sat} : This is the length of the gate current pulse needed for good turn-on.

The following parameters are determined by circuit considerations:

t_{off} : This is determined by the minimum off-time of the switch in the application. The inductor current can only build up during this time.

From Fig. 6 and 8, the following relations can be written down:

$$L_{pre} = \frac{v_{gc}\,(t_{on} - t_{sat})}{I_{sat} - I_{off}} = \frac{V^-(t_{off} - t_1)}{I_{sat}} \qquad (1)$$

$$L_{post} = \frac{v_{gc}\,(t_{sat})}{I_{peak} - I_{sat}} = \frac{V^-(t_1)}{I_{peak} - I_{sat}} \qquad (2)$$

From (2): $v_{gc} * t_{sat} = V^- * t_1 \;\therefore\; t_1 = \frac{v_{gc}}{V^-} * t_{sat}$ (3)

From (1): $L_{pre}\, I_{sat} = V^-(t_{off} - t_1)$ (4)

(3) into (4): $L_{pre}\, I_{sat} = V^- * t_{off} - v_{gc} * t_{sat}$ (5)

$$\therefore t_{off} = \frac{L_{pre}\, I_{sat} + v_{gc} * t_{sat}}{V^-} \qquad (6)$$

The energy loss due to conduction losses in S_1 and S_2 can be calculated if the resistance R of the switches is known. If we let $i = i_{S2}$, the energy loss, W_{cond}, in one period, τ, is equal to

$$W_{cond} = \int_0^{\tau} i^2 R\, dt = R \int_0^{\tau} i^2\, dt \qquad (7)$$

For S_1, the loss is equal to

$$W_{S_{1cond}} = R_{S_1} \int_{-t_{off}}^{0} i^2\, dt \qquad (8)$$

and for S_2 equal to

$$W_{S_{2cond}} = R_{S_2} \int_{-t_{off}}^{t_{on}} i^2\, dt \qquad (9)$$

For $-t_{off} < t < -t_1$:

$$\int_{-t_{off}}^{-t_1} i^2\, dt = \frac{I_{sat}^2}{3}\,(t_{off} - t_1) \qquad (10)$$

For $-t_1 < t < 0$:

$$\int_{-t_1}^{0} i^2\, dt = \frac{t_1}{3}\,(I_{sat}^2 + I_{sat}\, I_{peak} + I_{peak}^2) \qquad (11)$$

For $0 < t < t_{sat}$:

$$\int_0^{t_{sat}} i^2\, dt = \frac{t_{sat}}{3}\,(I_{sat}^2 + I_{sat}\, I_{peak} + I_{peak}^2) \qquad (12)$$

For $t_{sat} < t < t_{on}$:

$$\int_{t_{sat}}^{t_{on}} i^2\, dt = \frac{(t_{on} - t_{sat})}{3}\,(I_{off}^2 + I_{off}\, I_{sat} + I_{sat}^2) \qquad (13)$$

The energy loss per period in S_1 is thus equal to

$$W_{S_{1cond}} = R_{S_1} \int_{-t_{off}}^{0} i^2\, dt$$

$$= R_{S_1}\left(\frac{(t_{off} - t_1)}{3}\,(I_{sat}^2) + \frac{t_1}{3}\,(I_{sat}^2 + I_{sat}\, I_{peak} + I_{peak}^2)\right) \qquad (14)$$

and in S_2 equal to

$$W_{S_{2cond}} = R_{S_2} \int_{-t_{off}}^{t_{on}} i^2\, dt$$

$$= R_{S_2}\left(\frac{(t_{off} - t_1)}{3}\, I_{sat}^2 + \frac{t_1}{3}\,(I_{sat}^2 + I_{sat}\, I_{peak} + I_{peak}^2) + \right.$$

$$\frac{t_{sat}}{3}\,(I_{sat}^2 + I_{sat}\, I_{peak} + I_{peak}^2) +$$

$$\left.\frac{(t_{on} - t_{sat})}{3}\,(I_{off}^2 + I_{sat}\, I_{off} + I_{sat}^2)\right) \qquad (15)$$

The loss due to excess energy stored in the inductor can be calculated as

$$W_L = \frac{1}{2}\, L_{off}\, I_{off}^2, \qquad (16)$$

with L_{off} the inductance of the inductor at turn-off.

Total losses in the gate grive are now simply equal to

$$W_{total} = W_{S_{1cond}} + W_{S_{2cond}} + W_L. \qquad (17)$$

THE GATE DRIVE UNDER TEST

The gate drive shown in Fig. 9 was used to obtain the results presented in the next section. The main device was a DZT300RE zero turn off thyristor (ZTO) from MEDL [8] rated at 230A mean on-state current and 1600V repetitive off-state voltage.

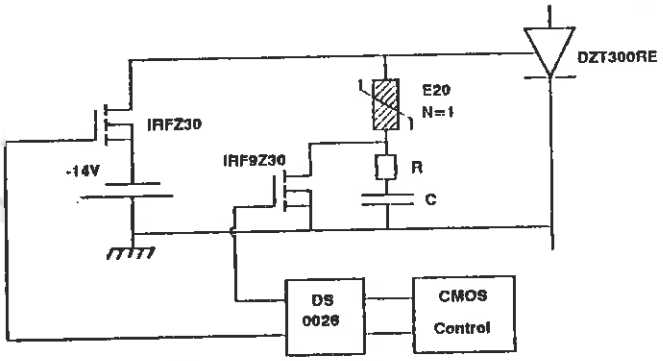

Fig. 9. Circuit diagram of gate drive.

S_1 was a IRFZ30 MOSFET with $R_{S1} = 0.05\Omega$, and S_2 a IR9FZ30 MOSFET with $R_{S2} = 0.14\Omega$. To simplify the drive of the MOSFETs, both are switched by a dual MOS driver IC, the DS0026. The RC snubber consisted of a 47nF capacitor and a 47Ω resistor. This combination resulted in a peak voltage across S_2 of less than 25V.

The maximum reverse gate voltage of the ZTO is equal to 16V, and V^- was thus chosen as $V^- = -14V$. The inductor consisted of a single winding on a E20 core made of 3E1 material.

The application is in an induction heater operating at a resonant frequency of 100kHz. The on-time is constant and equal to $t_{on} = 6\mu s$. The gate voltage was measured as $v_{gc} = 1V$. It was found experimentally that a peak current of $I_{peak} = 30A$ was needed to turn the ZTO on without excessive losses.

Fig. 10 shows the inductor current and gate voltage for a peak gate current of 30A. The inductor saturates at about 6A, and comes out of saturation about $2\mu s$ after turn-on. The minimum off-time for this drive is equal to $t_{off} = 1.2\mu s$ and t_1 can be read off as $t_1 = 600ns$. At turn-off, the rate of change of the inductor current is equal to $2A/\mu s$, and the inductance at turn-off, L_{off}, can thus be calculated as

$$L_{off} = \frac{(\frac{di}{dt})}{v_{gc}} = 2\mu H. \qquad (18)$$

The rise in gate voltage just before turn-on is due to the on-resistance of S_1.

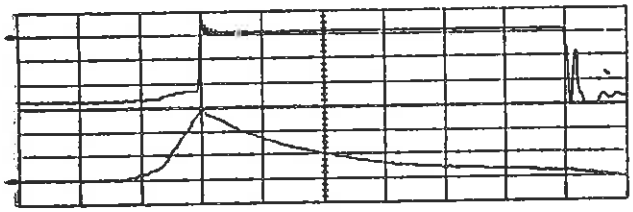

Fig. 10. Inductor current and gate voltage.

Top:	Gate voltage	5V/div
Bottom:	Inductor current	10A/div
Time:		1μs/div

We thus have: $V^- = 14V$, $I_{peak} = 30A$, $v_{gc} = 1V$, $I_{sat} = 6A$, $t_{on} = 6\mu s$, $I_{off} = 2A$, $t_{sat} = 2\mu s$, $t_{off} = 1.2\mu s$, $L_{off} = 2\mu H$, $t_1 = 0.6\mu s$

If will be noted that the measured figures do not correspond with (1) and (2). This is due mainly to the non-negligible resistance of the two MOSFETs which was neglected when deriving the equations. Equations (14) to (17) can, however, be used to determine the losses in the gate drive since they are based on the physical current though the switches as shown in Fig. 8. Results are as follows:

$W_{S1cond} = 11\mu J$,

$W_{S2cond} = 146\mu J$,

$W_L = 4\mu J$, and

$W_{total} = 161\mu J$.

Losses in the gate drive were measured by loading the drive with two Schottky diodes in series with an on-state voltage of 1V. The switching frequency was 10kHz and the input power to the gate drive was measured as equal to 1.85W. The energy added to the drive per cycle is thus equal to $185\mu J$. Of this energy, an amount equal to the charge Q which flowed through the Shottky diodes multiplied by the on-state voltage (1V) of the diodes is dissipated in the diodes, and the rest is dissipated in the gate drive. From Fig. 10 this charge can be measured as $53\mu Q$, and the amount of energy dissipated in the diode thus calculated as $53\mu J$. Measured losses thus equal $132\mu J$, which compares very well with the calculated result of $161\mu J$, and the measured efficiency is thus equal to 28.6%.

To achieve comparable gate current rise times in a conventional gate drive, a voltage source of about 100V would be needed. Such a gate drive would thus have a theoretical maximum efficiency of 1%, and the improvement in efficiency of the new gate drive is thus substantial.

Furthermore the new gate drive uses only one voltage supply instead of two needed for a conventional gate drive, making the gate drive power supply much simpler.

EXPERIMENTAL RESULTS

Measurements were made on a series resonant circuit shown in Fig. 11.

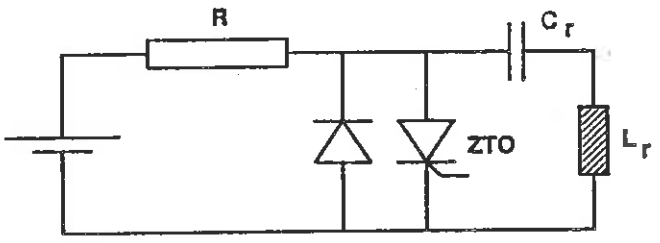

Fig. 11. Measurement circuit.

The ZTO was a DZT300RE device from Marconi and the freewheeling diode consisted of two MUR 1560 diodes in parallel. No snubbers were used.

When the ZTO is switched on, current resonates through C_r, L_r and either the ZTO or the freewheeling diode. When the diode conducts, the ZTO is switched off. Lost energy is replaced by the source via R, which in this case was a 10kΩ resistor.

Fig. 12 shows the the ZTO current and voltage for a peak forward gate voltage of 30A. The inductor current is shown in the bottom trace.

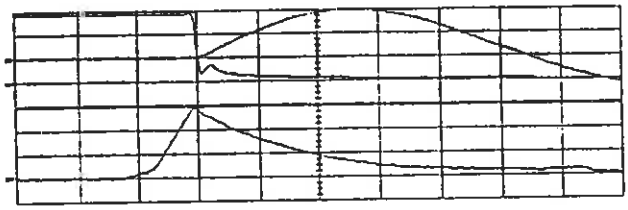

Fig. 12. ZTO voltage and current, and inductor current.

Top:	Voltage across the ZTO	75V/div
	Device current	100A/div
Bottom:	Inductor current	10A/div
Time		1μs/div

Fig. 14 shows the power dissipation of the ZTO during conduction. The on-state voltage was measured using the circuit shown in Fig. 13, where the voltage is measured at point X and the on-state voltage of diode D subtracted from this value. The voltage source V consisted of two 9V batteries in series. There is no typical peak power dissipation at turn-on, but the on-state voltage drops reasonably slowly and reaches a value of 5V after about 2.6μs.

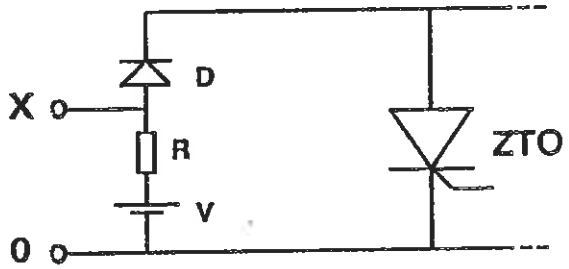

Fig. 13. On-state voltage measurement circuit.

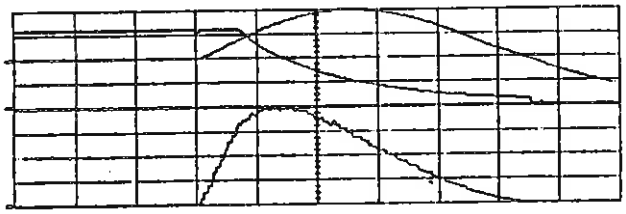

Fig. 14. On-state voltage, device current and power dissipation for I_{peak} = 30A.

Top:	On-state voltage	5V/div
	Device current	100A/div
Bottom:	Device power dissipation	400W/div
Time:		1μs/div

Fig.15 shows turn-on at a peak gate current of 40A. The power dissipation is much less, and an energy saving of about 400μJ is achieved. Gate drive losses increase by about 120μJ but the overall saving is still substantial. The advantages of this high performance gate drive are obvious.

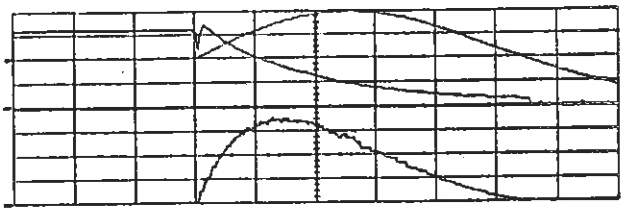

Fig. 15. On-state voltage, device current and power dissipation for I_{peak} = 40A.

Top:	On-state voltage	5V/div
	Device current	100A/div
Bottom:	Device power dissipation	400W/div
Time:		1μs/div

CONCLUSION

The gate/base drive presented is optimised for turn-on of a majority carrier semiconductor device. The efficiency of the final version is exceptionally high compared to conventional gate drives, and measured turn-on times of a ZTO are extremely low. The gate drive is extremely simple with only one voltage source and layout restraints are not as critical as in conventional gate drives. Some timing limitations exist in the form of minimum off-time and maximum on-time. These and other fundamental limits are discussed.

REFERENCES

[1] C. J. Hammerton and F. A. Woodworth, "The GTO as a fast Thyristor," Proc. of the European Power Electronics Conference (EPE 87), Grenoble, Sept 1987, pp. 81-85.

[2] R. J. Morris, F. J. Wakeman et al., "A New Family of G.T.O. Devices for Medium Frequency Applications," IEEE IAS Annual Meeting (IAS 89), San Diego, Calif., U.S.A., Oct 1989, pp. 1264-1269.

[3] W. F. Wirth, "High-Speed Snubberless Operation of GTOs Using a New Gate Drive technique," IEEE Trans. on Industry Applications, Vol. 24 No.1, Jan/Feb 1988, pp. 127-131.

[4] P. H. Swanepoel, J. D. van Wyk and J. J. Schoeman, "Transformer Coupled Direct Base Drive Technology for High Power, High Voltage Bipolar Transistor PWM-Converters," IEEE IAS Annual Meeting (IAS 87), Atlanta, GA., U.S.A., 18-23 Oct 1987, pp. 906-913.

[5] R. B. Prest and J. D. van Wyk, "Pulsed Transformer Base Drives for High-Efficiency High-Current Low-Voltage Switches," IEEE Trans. on Power Electronics, Vol. 3 No.2, April 1988, pp. 137-146.

[6] International Rectifier, Power Mosfet HEXFET Databook, Third Edition, HDB-3, 1985.

[7] H. Stemmler, Steuerverfahren für Ein- und Mehrpulsige Unterschwingungswechselrichter zur Speisung von Kurzschlussläufermotoren. Doctoral Thesis at the faculty of electrical engineering at the University of Aachen, Germany, 1970.

[8] Marconi Electronic Devices, "The ZTO Zero Turn-off Thyristor," Application note, Oct 1987.

AN INTEGRABLE BASE DRIVE TECHNOLOGY FOR VERY HIGH CURRENT BIPOLAR TRANSISTOR SWITCHES

G. J. van der Merwe, J.D. van Wyk, J.J Schoeman

Energy Laboratory, Rand Afrikaans University,

P.O.Box 524

Johannesburg 2000

REPUBLIC OF SOUTH AFRICA,

ABSTRACT - In high current transistor switching, the losses involved in the base drive supply are often more than the losses in the main switching device itself. Today Schottky diodes with an ultra low voltage drop (0.3V at 20A) are available. In high current supplies (>50A), these diodes can be a great advantage in obtaining high efficiency. The internal frequency range is limited by the high current and low voltage on the secondary which will tolerate only a very small leakage inductance.

An integrable structure for a base drive is presented. It is shown that a basic supply with an effective efficiency in excess of 65% can be achieved. The supply that was built delivers a continuous current of 400A at 1.5V output at an efficiency of 60% with an input voltage of 150V. The supply was built on the basis of the concept of matrix transformers that was introduced earlier.

The concept makes the integration of high current low voltage supplies more feasible (as shown in this paper). Better voltage and current waveforms are possible and the internal frequency range for high current (> 50 A) low voltage (< 3 V) supplies, less restricted.

The supply was developed as a compensation supply for a compensated Darlington pair for 2000A switching.

I.) INTRODUCTION

A feature of the standard base drive technology, is that the efficiency is very low [6, 7]. It was shown previously [4] that in applications such as low voltage high current switches it is much more efficient to make use of compensated Darlington switching than direct base drive or normal Darlington switches. Although it is possible to achieve a comparable efficiency to compensated Darlington pairs in transformer-coupled direct base drives in the base current range up to some 100A [6,7], turn-on and turn-off of the base current supply of say 400A (2000 A switching) at the switching frequency presents several problems. Since the compensation supply in a compensated Darlington- although being of the same current rating as the direct base drive supply (Fig 1) - is simply a continuous supply, it is an attractive alternative to investigate. For compensated Darlington pairs a low voltage high current supply is needed (output voltage 1.5V, 400A for a switching of 2000A). In a supply for this current range the internal frequency range is limited by the high current and low voltage on the secondary which will tolerate only a very small leakage inductance.

A method to overcome this is the use of matrix transformers [1]. Matrix transformers consist of more than one core to set up a matrix board of transformers. The idea is to replace the standard **multi primary turn transformer** with a **single primary turn multiple core transformer** where the secondaries are placed in parallel.

This then, enables spreading the given transformer core and winding bulk for a certain ratio, over a larger surface area in a flat, thin form rather than leading to a customary bulk standard transformer. Good coupling between secondary and primary is possible. Leakage inductance is reduced and commutation time between secondary diodes is greatly reduced.

As an example: for 400A current turned off in 0.1 μ s :

dI/dt is 4000 A/μ s, while if 20 transformers in a matrix rated at 20A each are used this can be reduced to $200\,A/\mu s$ for each transformer.

This is much lower and consequently much better current waveforms can be achieved. A better output voltage, short rise times and an efficiency of 60% can be expected. Typical applications for this type of power supply would be :

(i) a compensation supply for compensated Darlingtons. [4]

(ii) direct base drive for bipolar transistors. [6]

(iii) base drive for high current Darlingtons. [7]

II.) CONSIDERATIONS FOR LOW VOLTAGE HIGH CURRENT SUPPLIES.

A.) Compensated Darlington

In low voltage high current transistor applications it is suggested that a compensated Darlington pair is used as the main switching element [4]. Higher efficiencies of up to 50 % can be achieved in the combined base drive and compensation power supplies. This is particularly advantageous at low voltages (< 150 V) and high currents (500 - 2000 A).

To use the compensated Darlington topology in an application of 2000A 150V, with a current gain of 5, means a compensating voltage supply of 1V to 2V and 400A output.

The compensated Darlington overcomes the major disadvantages of a high on state voltage of a Darlington pair and thus the losses involved. The fast switching capabilities of a Darlington can be maintained by appropriate design and control [4].

The loss factor can be defined [4] as : $n = \dfrac{P_k}{V_{be}\, I_k}$.

P_k = Total input power of compensating supply

V_{be} = Saturated base emitter voltage

I_k = Base current supplied.

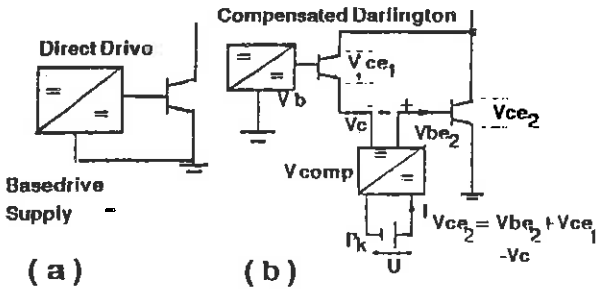

Fig.1 (a)Direct base drive (b)Compensated Darlington pair

For the supply a value of n from 1 to 3 would be a good working value for the compensating supply. A loss factor of 2 was chosen as design parameter.

Take V_{be} = 1.5V (Medl DT800-300)

I_k = 400 A

Calculating P_k as 800 W, it means that the compensating supply must have an efficiency in excess of 50 %.

B.) di/dt Limitations On Supply.

In low voltage supplies the rise and fall times of currents are often limited by the inductance in the circuit.

If the mosfets T1,T2 (see Fig 2) are turned on and off within 100 ns , at a frequency of 100 kHz,then it would be ideal to have the secondary rectifiyng diodes commutate within 100 ns.

The commutation time does not increase losses, but causes a certain output voltage drop, therefore reducing the average voltage. If leakage inductance L1 and L2 is assumed to be the same, and the supply of 400 A at 1 V is considered (at this voltage and current the load can be considered as an inductive load) it is seen that for the diodes to commutate within 500ns, a leakage inductance of 2.5 nH is required.

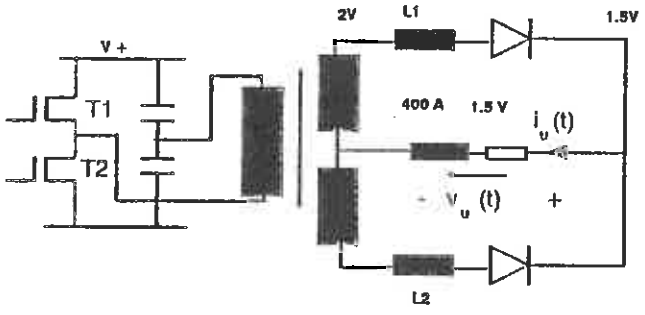

Fig.2 Schematic of compensating supply

It is not feasible to build a transformer of this current rating to have such a low leakage inductance and be practicable.

At a switching frequency of 100kHz the time for a half-period is 5 μs . Allowing a maximum of 500ns commutation time, 10 % commutation time means a 10 % loss on the average output voltage.

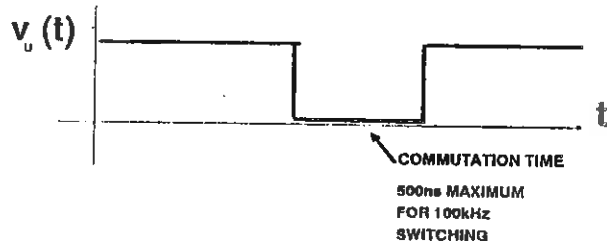

Fig.3 Output voltage during commutation time

C.). Reducing Commutation Time.

Leakage inductance and low voltages is the main element that increases commutation time in the rectifying diodes.

Using a standard transformer and say paralleling a couple of outputs to deliver a total current of 60A can also reduce the di/dt in each and make the supply more integrable with single turn output conductors [5]. In the 400A supply this would still be a problem. Choosing the units to be 20 A (allowable leakage inductance of approx 15 to 20 n H), it boils down to 20 outputs. It would be impractical to tap 20 outputs from a single transformer. It is clear that to obtain a good low voltage supply , an alternative approach will have to be used , leading to the concept of matrix transformers[1]. These were then considered further for the design.

III.) DESIGN OF A 400A 1.5V SUPPLY

The important points that are considered in the design are cost, availability of components, efficiency, size and volume, switching topology, layout and construction

A.) Cost And Selection Of Diodes

To limit the number of diodes, centre tapped rectification is used. Therefore each diode will only conduct during alternate half cycles . Under assumption of a square wave output and an ideal transformer the following applies.

$I_{eff} = 0.707 \times I_{max} = 282$ A , $I_{ave} = 200$ A

DIODES	V	I	V cond	$I \times V_{cond}$ Losses (W)	Total Needed	Total price perunit
12CTQ45	45	12	0.77	370	20	1.76
18CP	50	18	0.85	428	14	1.99
18TQ45	45	18	0.75	378	28	3.95
20CTQ45	45	20	0.76	364	12	1.59
30CP30	30	30	0.74	355	8	1.32
30CTQ40	40	30	0.82	355	8	1
40CPQ45	45	40	0.57	273	6	1.98
60HQ	100	60	1	400	4	1.32
19TQ45	15	19	0.3	120	40	4.49

TABLE 1. Diodes considered for output rectification.

The diodes are selected for the average current which is 200A . From table 1, the best results seem to be the two in one package at a current of approximately 20 A. In earlier discussions it was selected that 20A per transformer seemed to be reasonable for the best practical dI/dt, this correlates with the availability of the diodes. Although diodes with higher current ratings reduce the number of diodes to be used it would increase the dI/dt of each transformer .

B.) Selection Of Core

The choice would be a core that is easily integrable in a flat structure with the optimum combination of tight coupling and low leakage inductance. For swithing at high frequencies

(> 100kHz), the selection boiled down to either a tube core or a couple of flat integrable cores as shown in Fig. 4.

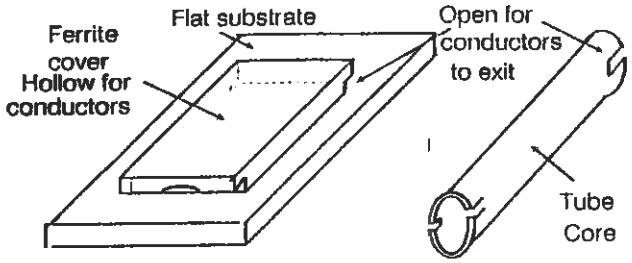

Fig. 4 Integrable core and tube core

1) Tube Cores: Tube with 3C6 material was selected for the first iteration. It is a soft ferrite material that could be cut to shape with available equipment. A working temperature of 100 ^{o}C, and a flux density of 100mT were chosen as design parameters. Switching at 100khz will require a core area of $A = 50mm^2$

With an outside diameter of 10 mm and a wall thickness of 2.75 mm, a minimum length of 18mm is required to give $A = 50mm^2$.

Although tube cores were selected, an integrable system requires a core that is flat and economical to mass produce, as chosen for the second iteration.

C.) Efficiency

Diodes with a voltage drop of 0.6V at 20 A (according to specifications) were used in the experimental design, giving a power loss of

$P_{loss} = 240W$ at $P_{out} = 600\,W$

The maximum efficiency that can be achieved is

$$\eta_{max} = \frac{P_{out}}{P_{out} + P_{loss}} = \approx 65\ \%$$

when neglecting switching and core losses. The experimental work reported later will show that other losses are small. Similarly with the use of ultra low voltage (0.3V @ 20A) Schottky diodes, an efficiency of approximately 80 % can be achieved.

D.) Size And Volume

It was decided to build the supply on an A4 size heat sink (8" * 11"). Construction and layout are shown in Figures 5 - 7. Two layers of cores were placed above each other. The rectifying diodes of layer 2 were each lifted by means of a small heatsink. The main heatsink itself was used as the positive terminal and a copper plate as common for the 400A output.

E.) Switching topology.

The selected topology is a half bridge as shown in Fig 2. The matrix transformer with 20 tube cores required 2 primary turns per cell instead of the 4 that would have been necessary in the case of a full bridge topology, thus simplifying the construction and reducing the leakage inductance which is proportional to the square of the number of turns.

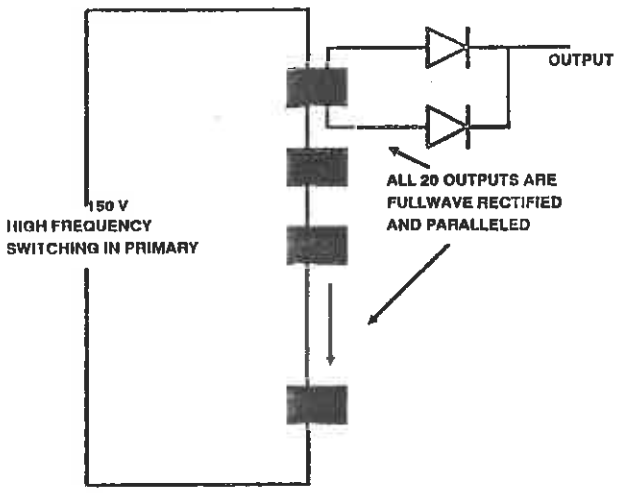

Fig.5 400A Matrix transformer

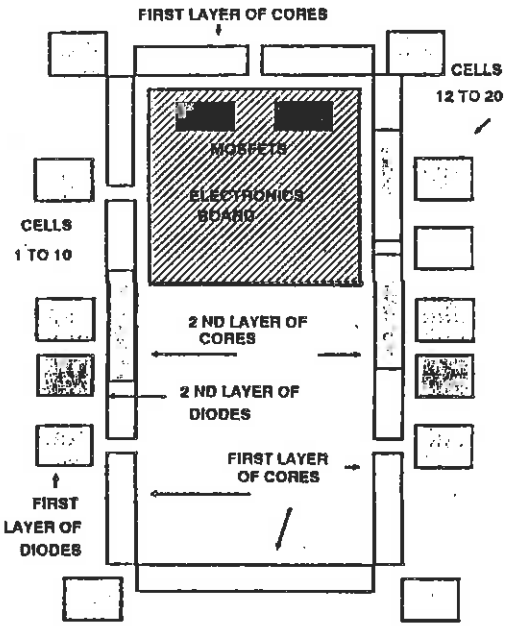

Fig.6 Matrix transformer layout

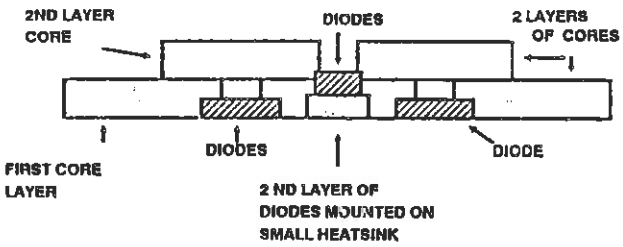

Fig.7 Diodes lifted by heatsinks

E.) Calculation Of Copper Area For Conductors

At high frequency switching it is often an advantage to use litz wire. In matrix tansformers this can be applied as well, but for reasons of heat dissipation and ease of construction, it was preferred to make use of single conductors, but to take precaution for penetration depth, a minimum diameter is required. Penetration depth at 100 kHz is

$$\delta = \frac{66.1}{\sqrt{f}} \quad = 0.21\ mm$$

This gives the diameter as

$$D = 2R \ = 2x\ R = \frac{1}{0.42} \times \left(\frac{A}{\pi} + 0.044\right)$$

The primary winding with an effective current of 10A and the secondary winding with effective currents of 15 A each, therefore required wires of 1.35 mm and 2.1 mm diameter respectively. This was a compromise between current density and available window area.

G.) Core Length And Magnetizing Current

The minimum core length that is allowable was calculated as 18 mm. To allow for the cutting of grooves for bringing wires out a minimum length of 30mm was selected, but an average of 40mm for construction. The wall thickness is 2.75 mm

$$A_{eff} = 20_{cores} \times 40 \times 2.75\ mm = 2200\ mm^2$$

Total magnetic path length

$$= 2\pi R \quad = 2\pi \frac{(10-4.5)}{2} \quad = 22.75 \text{mm}$$

at 100mT and 100 ^{o}C μ_a is2500 for 3C6 material. The magnetising inductance is then

$$L_M = \frac{\mu_o \mu_a n^2 A_e}{l_e} \quad = 1.22 \text{ mH}$$

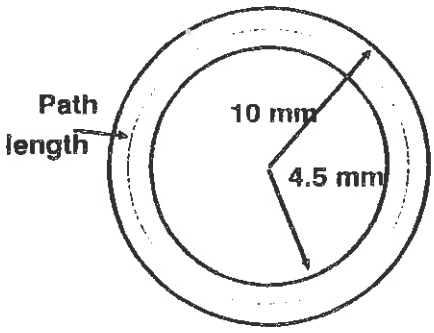

Fig. 8 Core size

The peak magnetising current is then

$$I_M = \frac{V_{in}}{4 \times L_M \times f_o} \quad = 154 \text{mA}$$

H.) Selection Of Switching Element

Switching at high frequencies leaves very few options but mosfets and therefore the mosfet IRF 640 with 200V blocking voltage and 18A continuous current with on resistance 0.18 ohm was selected. An input voltage of the order of 150 V was selected, since this will also be the supply voltage for which the entire switch is designed.

IV.) EXPERIMENTAL RESULTS

A.) Effects Of Mounting And Layout On The Results.

The voltage over all the output diodes was measured with different current loads , to determine the power distribution and calculate the leakage inductance [Fig 6]

At full load the maximum commutation time was found to be approximately 500ns. (This is the commutation effect on the load voltage side). If the whole supply is taken as a single supply that delivers 400 A at 1.5 V that gives an effective leakage inductance of 1.88nH. The leakage inductance was determined by measuring the commutation time over the rectifying diodes of each cell and also measuring the voltage. By knowing V, dI/dt, L_s can be calculated . (Both leakage inductance components of a cell was asumed to be the same).

It is clear that it would be practically impossible to build up a single supply that can deliver so much current at one volt with the same leakage inductance. The leakage inductance for each individual matrix transformer cell varies from 20 to 60 nH. The result is the same as a single leakage inductanc of 1.88nH.

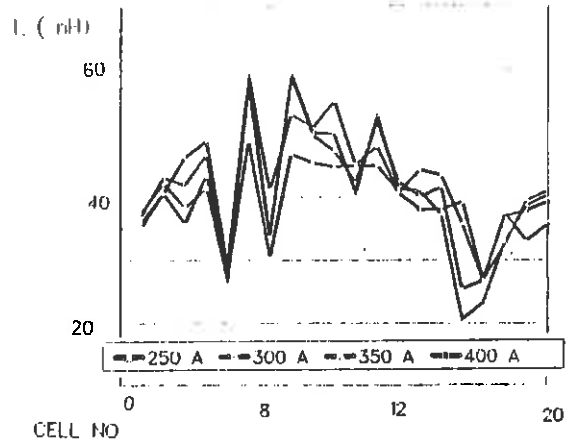

Fig 9 Leakage Inductance L_s

if the leakage inductance is referred to the primary, with a winding ratio a = 0.025, then $L_p = \frac{L_s}{a^2} \quad = 2.99\,\mu H$

Leakage inductance is defined as the uncoupled leakage flux giving for the coupling coefficient.

$$K = 1 - \frac{L_{leak}}{L_M} = 1 - \frac{L_p}{L_M}$$

The magnetising inductance was calculated as 1.22 mH with the referred leakage inductance of 2.99μH this gives K = 0.9975.

Referring to Fig 9 it can be seen that the leakage inductance of cells 12 to 20 seems to be less than for cells 1 to 12. By further investigation it was found that the ground plane formed by the copper plate was not completely centered, and is a little closer to cells 12 to 20 - therefore closing the secondary loop smaller and reducing leakage inductance.

B.) Power Balance

In a system that was built up with standard Schottky diodes, with a saturation voltage of 0.6 V @ 20 A, it was shown that a maximum efficiency of 65 % can be achieved, excluding con-

ducting , and switching losses. (Will be shown to be very small experimentally.)

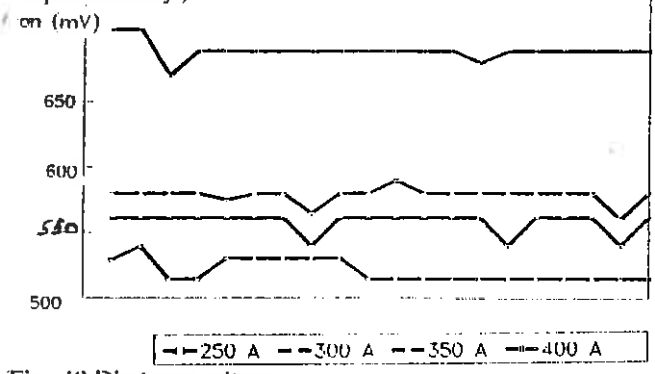

Fig . 10 Diode on voltage

The on voltage of the diodes was measured at different loads to determine the power dissipation and distribution in the supply. The on voltage of the diodes was found to be approximately the same, therefore it was accepted that the load current divided equally through all 20 cells. The losses in the diodes made up most of the losses followed by the copper and core losses and then the switching losses (Appendix A). Although the losses increased with load, the percentage ratio stayed constant. The measurment procedures are described in appendix B and the measured values are listed in appendix A.

C.) Efficiency

The efficiency was found to be between 55% and 60 % as shown in Fig. 11, with the copper and core losses plus primary and secondary switching losses never more than 10 %.

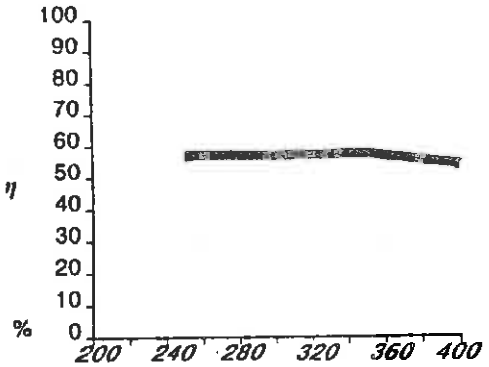

Fig. 11 Efficiency as function of output dc current I(u)

The larger part of the losses of approximate 35 % occurred in the rectifying diodes, bearing out the conclusion that lower diode drop can effect a substantial improvement.

D.) Current rise times

The supply was originally designed to be a compensating supply for a compensated Darlington pair. The supply must be able to supply current response as needed. The output load is 5 m ohm. It is difficult to make a full load test , because the output busbar and current shunt is an impedance by itself and by placing a current shunt in the line of the busbar the structural inductance is increased and plays a dominant role. Fig 12 shows current rise time . It was earlier shown that the leakage inductance in the supply itself is 1,88 nH. Thus the supply must have a good response, much better than the results show. Another current test was done to determine the structural inductance from the linear current rise and ouput voltage and was determined as: L = 210 n H

This corresponds to the linear physical dimensions of approximately 200mm for the load assembly. In the practical system the compensation supply has been mounted very close to the main transistor, in order to achieve minumum rise time for output current.

The physical measurements at full load were done using as a load a 1000A diode and heatsink-assembly, fed by a copper busbar from the output including the said current shunt. No output filtering is included.

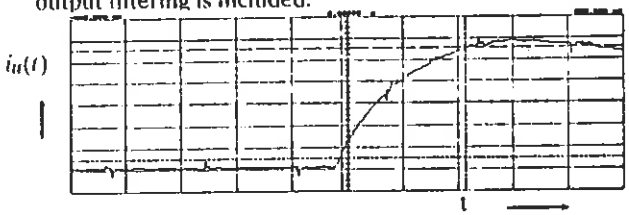

Time: 50 μs/div Current: 88.5 A/div

Fig . 12 Current rise time.

E.) Voltage And Current Waveforms

The output voltage and currents were determined at different loads as shown in figures 13-16 for 300A & 450A.

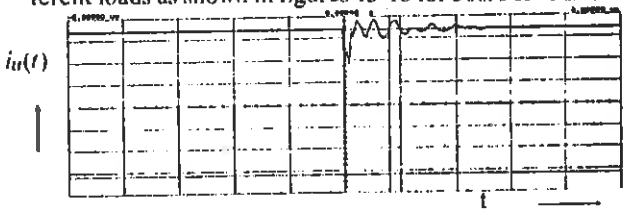

Time: 100 ns/div Current: 88.5 A/div

Fig . 13 Current 300 A

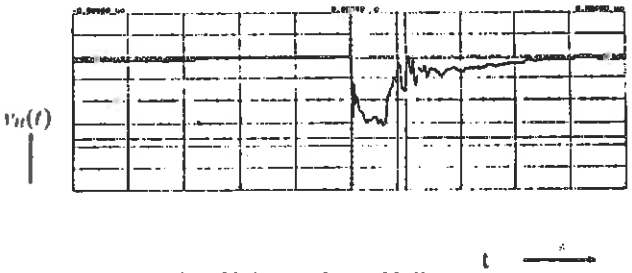

Time: 500ns/div Voltage: 300 mV/div

Fig . 14 Output voltage (load current = 300 A)

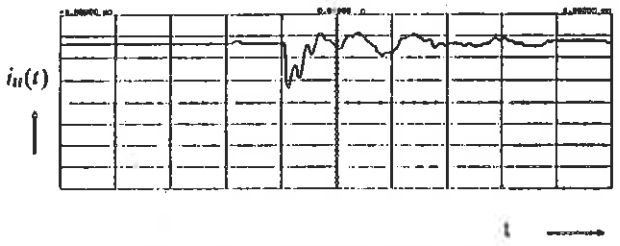

Time: 200 ns/div Current: 88.5 A/div

Fig . 15 Current 400A

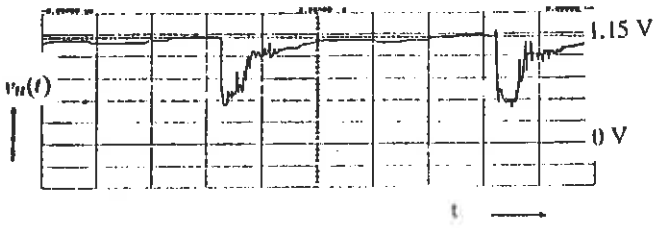

Time: 1 μs/div Voltage 300mV/div

Fig . 16 Voltage 400 A

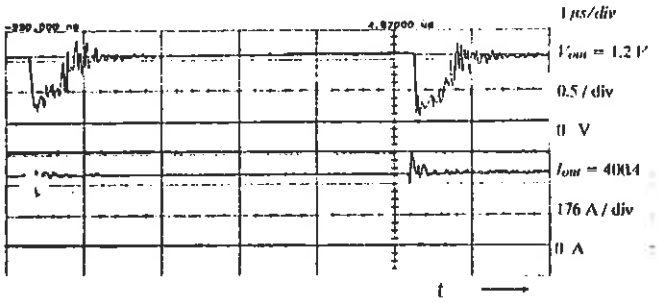

Time : 1 μ s/div Upper : Voltage 500 mv/div

Lower : Current 176 A/div

Fig . 17 400A Load current and voltage

V.) CONCLUSION

A 600W halfbridge push pull converter is presented, which provides a constant voltage of 1.5 V and current of 400A and operates at 100kHz with an efficiency of between 55 and 60 %. This is possible because of the application of the concept of matrix transformers and because of the operation at higher frequencies.

EMI is reduced because of the low parasitics of the transformer. The production of the transformer would be easier than a conventional one . Placing the transformer around the control electronics reduces space and enables optimum layout. Single turn primary increases integration capabilities

It has been proven that matrix transformers have major advantages in the area of integrability of high current low voltage supplies, with many advantages like distributed heat dissipation. (Reducing the chances of thermal runaway) . High frequency switching decreases electromagnetic component size and reduces weight and volume.

The major losses were in the rectifying diodes ,(as shown a maximum of only 65% could be achieved with the diodes used), but these diodes can easily be replaced with ultra low voltage Schottky diodes which have an on voltage of approx 0.3 V @ 20A, meaning an increase of efficiency to approx 80 %.

As Schottky diodes are easily available in the range of 20 A to 50A, the method of matrix transformers enables the use of these diodes in higher current supplies

VI.) REFERENCES

[1] E Herbert and K.K. Sum; " Design and application of matrix transformers and inductors ."; Seminar presented at the Fourth International High Frequency Power Conversion Conference, Naples, Florida, May 15 - 18 , 1989

[2] R.J. Smith " Circuits devices and systems. "; Wiley , Fourth edition 1983 p 606 - 608

[3] Philips ferroxcube databook ,C4 1988, Databook

[4] H.W van der Broek, J.D van Wyk, J.J. Schoeman " On the steady - state and dynamic characteristics of bipolar transistor power switches in low-loss technology, " IEE Proceedings., Vol 132 Pt.B No 5, September 1985

[5] H.W van der Broek, K Löhn, F Chevalier, H. Dethienne, W.Lemmens "A compact high performance 300W/5V switched mode power supply" Proceedings, Third European Conference on Power Electronics and Applications, (EPE 1989), October 1989, Aachen Germany pp 1455-1459

[6]P.H. Swanepoel, J.D. van Wyk , J.J. Schoeman ." Transformer coupled direct base drive technology for high power high voltage bipolar transistor pwm - convertors" IEEE Transactions on Industry Applications, Vol 25 (4) Nov-Dec 1989, pp1158-1166.1

[7] R.B. Prest , J.D. van Wyk " Base drive for high current low loss bipolar power transistor switches " ,IEEE Transactions on Power Electronics, Vol 3 (2) April 1989 pp137-146

VII.) APPENDIX A

Measured Results

LOAD (A)	250	300	338	384
Effeciency	56.9 %	56.8 %	56.8 %	54.2 %
Core, Switching losses (W)	39.7 9.6 %	36.9 7.35 %	38 6.5 %	35 5 %
Diode (W)	130 31.7%	167 33.3 %	200 34.5%	261 37%
FET (W)	7.3 1.8%	12.11 2.41%	14 2.4 %	28 3.91%
P(out) (W)	233	286	328	384
P(in) (W)	410	502	580	708
V(Fet) (V)	1.9	2.4	2.5	3.7
V(In) (V)	132.3	140	145	154
I(In) (A)	3.1	3.6	4	4.6
V (Out) (V)	0.935	0.95	0.97	1.00

VIII.) APPENDIX B

Loss Measuring Procedures.

The voltages and currents at different measuring points and loads were determined . The input voltage came from a DC variable supply and was measured with a 300 V voltmeter and the current with a 10 A ammeter. The input current was confirmed with a Hall effect current probe and the voltage with an oscilloscope measurement. The voltage over the primary transformer winding was measured with a 400MHz Oscilloscope and the current through the winding was measured with a Hall effect current probe to determine the conducting current in the mosfets. The on voltage of the mosfets was determined by a method of using a diode from a low voltage supply and measuring the drain source voltage drop during conduction. The output voltage was measured with a 400 MHz Oscilloscope, and the output current was measured by means of a 113μ ohm series current shunt . The voltage drop over every diode was measured with the oscilloscope and the average on voltage of the diodes was used to determine the losses in the rectifying diodes.

The input power, output power , diode losses (conducting) and mosfet losses (conducting) could be determined fairly accurately and the rest was accepted to make up the conducting , copper and switching losses.

A HYBRID PHASE ARM POWER MODULE WITH NON-LINEAR RESONANT TANK

J.A. FERREIRA, A. VAN ROSS, J.D. VAN WYK
Energy Laboratory, Rand Afrikaans University,
P.O. Box 524, Johannesburg 2000, South Africa

Abstract - A soft switching concept for a phase arm module, suitable for switching frequencies in the ultrasonic range, is introduced. Apart from series smoothing capacitors on the supply the only additional components to the switches and diodes of the phase arm is a parallel nonlinear resonant tank. A major feature is that the installed switching power of the semiconductors is close to 1 p.u. PWM is obtained through control of the saturation depth of the saturating inductor.

ULTRASONIC CONVERTER TECHNOLOGY AT LARGER POWERS

The recent past has seen important advances in converter technology for higher switching frequencies, especially by using resonant circuits [1]. These converters are extremely well suited to power conversion in the frequency range spanning the ultrasonic region to some mehahertz [2] in the lower power range. The use of conventional, linear resonant circuits unfortunately always is accompanied by the fundamental limitation of an increase in the installed switching power of the devices in the converter due to an increase in current or voltage associated with the resonant circuit, as well as the disadvantage of handling a multiple of the load power in the resonant part of the converter itself. The penalties in the power range above 1kW are such that a strong incentive exists for investigating other possibilities. A notable renewal in this approach has been the resonant link converter [3], in which the resonant tank does not pass the load power, but is determined by secondary considerations related to converter operation, control and switching devices. It has been convincingly demonstrated that this concept can be applied to higher power ratings, using a range of switching devices [4,5]. Although the resonant link converter in its original form also leads to an excessive installation of device switching power, changes in circuit topology and control [6] have convincingly demonstrated an extension of the technology that reduces the installed switching power to levels comparable to that of hard-switched converters. This unfortunately involves installing one or more additional active switches [7,8]. An alternative approach to the problem of both reducing switching losses and keeping excessive dissipation due to switching losses out of the switching component - in order to increase the converter switching frequency - has been the use of inductive and capacitive snubber circuits [9,10]. In this case, however removal of the stored energy in these elements in the ultrasonic range has been shown to require regenerative snubbers [11]. This complicates the power circuit and leads to so many disadvantages that it has not become an accepted technology for high power converters in the ultrasonic frequency range. Using non-linear, saturable capacitances to reduce turn-off dissipation and extend RCD snubber technology to the ultrasonic range is an elegant solution [12], but suffers at present from lack of a suitable component. The idea of using non-linear components in circuits for soft switching, in order to shape desired characteristics, remains attractive, however [13]. Using a non-linear inductor in a resonant circuit made to achieve soft switching in a converter was first introduced by the authors in a multikilowatt circuit previously [14]. Subsequently the topology of a non-linear resonant converter received attention [15]. The introduction of a new generic converter topology, extending the previous ideas - and especially that of the resonant pole [16] - followed [18], confirming the use of a non-linear resonant tank in an ultrasonic high power pulse width modulated converter. Although at lower power levels, other contributions have also confirmed the original proposal [14] of using a non-linear resonant tank in a selfoscillating converter [17].

The present paper now extends the work on the generic converter topology [18] to obtain a hybrid phase arm power module to achieve soft switching in converters. The control possibilities, optimal use of the characteristics of circuit components and the elimination of the modulated current source are investigated.

THE NONLINEAR RESONANT INVERTER PHASE ARM

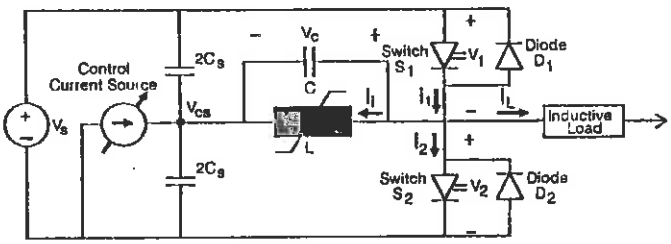

Fig 1. Diagram of the Nonlinear Resonant Phase Arm

The basic circuit of the nonlinear resonant phase arm as introduced in reference [18] is shown in Fig. 1. The output of the circuit is a PWM waveform with equal average voltage as V_{cs}. A major feature of this topology is that it achieves soft switching without having to overdimension the semiconductor component ratings, while at the same time it keeps the circuit complexity down and requires passive components with relatively small VA ratings. The inverter phase arm functions as an integral unit complete with an effective smoothing capacitor Cs across the supply. It has been designated a "Hybrid Phase Arm Power Module" since it can serve as a functional building block in more complex single and multi phase converter systems.A feature of this version of the circuit is the method of control, namely with an external control current source as indicated in the circuit diagram. If the average current through the nonlinear inductor L would not be equal to zero the rate of change of the voltage V_{cs} would be proportional to this average inductor current and stable operation would not be achieved. In the above circuit the average current level of the inductor is determined by an algorithm which ensures soft switching and minimal current stresses on the semiconductor switches and not enough levels of freedom in control exist to stabilize and modulate V_{cs}; hence the inclusion of a control current source.

In Fig. 2 simulated waveforms, which have also been experimentally verified in a previous paper [18], are shown. It is repeated as background to the basic principle of operation of the inverter phase arm which is to be developed further in this paper. The inductor is modelled as a two level inductance and the load as a constant current source. Typical waveforms of currents and voltages labelled in Fig. 1 are as shown in Fig. 2. The operation can be divided into different intervals of operation.

Interval 1: Switch 1 is on and the current flows through the switch. At the end of the interval the switch is turned off.

Interval 2: Charging of the capacitor causes soft turn-off of switch 1. At the end of interval the capacitor is fully charged and the free wheel diode parallel to switch 2 takes over the current.

Interval 3: Since the free wheel diode conducts, switch 2 can be turned on without losses. The diode current consists of the

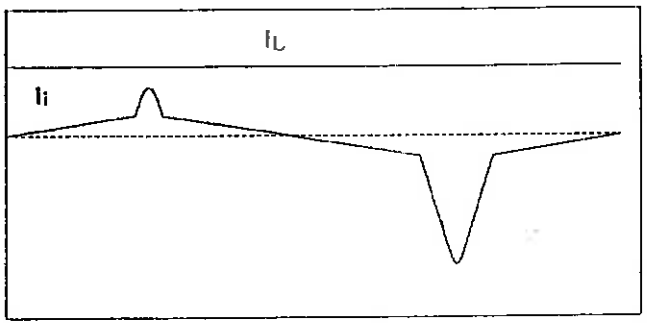

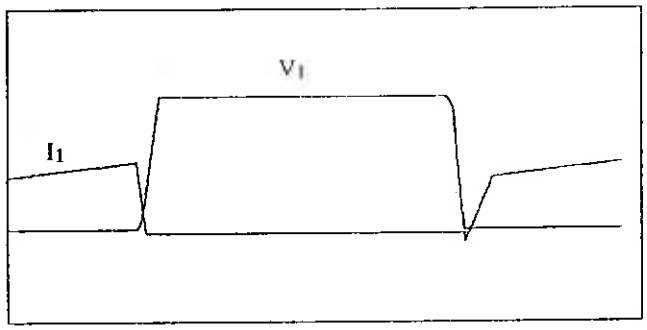

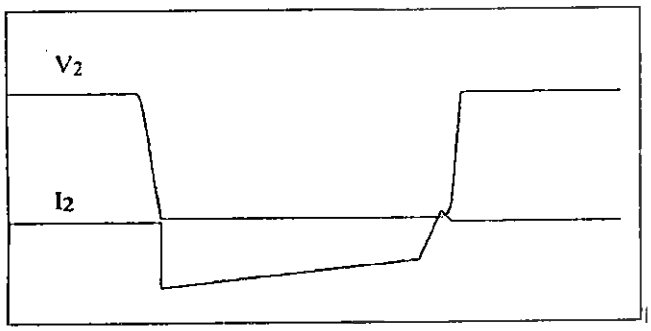

Fig. 2 Circuit waveforms

load current and inductor current and increases slightly due to the build up of inductor current during this interval.

Interval 4: At the beginning of this interval the inductor saturates. The inductor current amplitude increases rapidly, the combined current of the load and inductor changes sign, and consequently the switch 2 starts conducting. After the current has built up sufficiently, switch 2 is turned off. Note that the current in the switch is smaller than the current peak in L.

Interval 5: Charging of C causes soft turn-off of switch 2. At the end of the interval the capacitor is fully charged and the free wheel diode parallel to switch 1 takes over the current.

Interval 6: At the beginning of this interval, the Diode 1 conducts and Switch 1 can be turned on without stress. The inductor current decreases rapidly, unsaturates and Switch 1 conducts again.

OPTIMAL USE OF CHARACTERISTICS OF CIRCUIT COMPONENTS

A major objective of the phase arm module is to keep the ratings of the circuit components minimal for a given maximum output power, and to find a topology which makes optimal use of the components according to their inherent characteristics determined both by physics and state of the art. The converter circuit of Fig. 1 potentially satisfies many of these conditions.

Saturating Inductor (L)

A feature of this particular circuit which distinguishes it from most other power converters, and in particular for converters rated at 1kW and larger, is the inclusion of a saturating inductor. The following advantages are obtained by using a non-linear saturating inductor rather than a linear one:

- Less variation in switching frequency
- Smaller VA rating of inductor
- Smaller rms current in inductor
- Smaller current stresses in switches and diodes

Definitions

The inductor is modelled as a two level inductance with:

σ = per unit current level at which the inductor saturates,

K = the ratio of inductance before saturation and after saturation

α = per unit current when the inductor current adds to the load current through a switch-diode pair

β = per unit current when the inductor current opposes the load current through a switch-diode pair

Current peaks in inductor

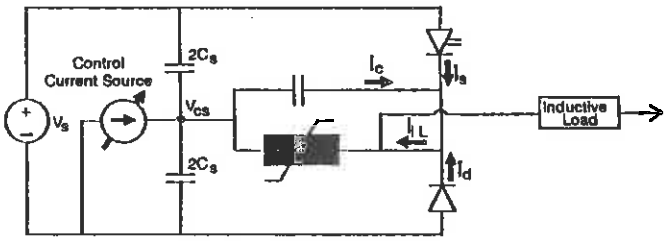

Fig. 3 Circuit diagram during switch over

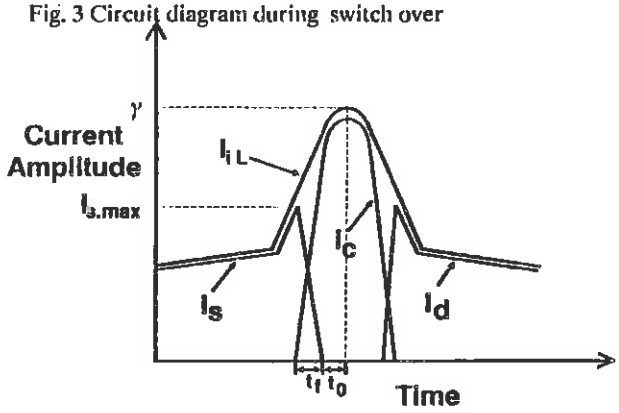

Fig. 4 Switch over transient

The current waveforms of I_1 (current through switch 1 and diode 1), I_2 (current through switch 2 and diode 2) and I_c (capacitor current) add together to give the combined load and inductor current, i_{iL} as shown in Figure 3. It should be noted that the peak value of γ is larger than the switch turn off current $I_{s,max}$ and is given by the following equation:

$$\gamma = \frac{V_c(tf)}{Z}\sin\omega t_0 + I_{iL}(tf)\cos\omega t_0 \qquad (1)$$

where $t_0 = \frac{1}{\omega}\tan^{-1}\left(\frac{V_c(tf)}{I_{iL}(tf)Z}\right)$ (2)

and $V_c(tf) = \left(V(d) + \frac{I_{s,max}}{tf\,\omega}\right)\cos\omega tf - \frac{I_{s,max}}{tf\,\omega}Z$ (3)

$$I_{iL}(tf) = \left(\frac{V(d)}{Z} + \frac{I_{s,max}}{tf\,\omega}\right)\sin\omega tf \qquad (4)$$

$$V(d) = dV_s \text{ or } (1-d)V_s \qquad (5)$$

depending on the switch.

$$Z = \sqrt{\frac{L}{C}} \qquad (6)$$

$$\omega = \frac{1}{\sqrt{LC}} \qquad (7)$$

with d ≡ duty cycle of PWM.

Switching frequency

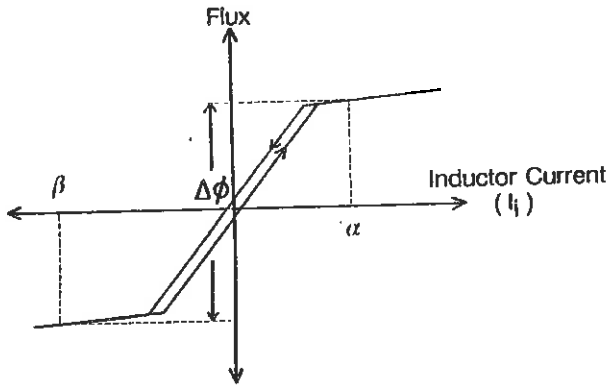

Fig. 5 Inductor current versus core flux

The nonlinear resonant inverter topology is essentially self oscillating since switch over is initiated when a certain value of I_1 or I_2 is detected. This reflects unto the inductor currents in that during steady state the peak inductor currents are fixed and will only change if the load current or PWM duty cycle is changed. One switching cycle is accompanied by a positive and negative excursion of flux as indicated in Fig. 5. During the interval when S_1 or D_1 is conducting the applied voltage across L is V_{cs} (= dV_s) so that for this interval:

$$t_1 = constant \times \frac{\Delta\Phi}{d} \qquad (8)$$

Similarly for the interval when S_2 or D_2 is conducting:

$$t_2 = constant \times \frac{\Delta\Phi}{(1-d)} \qquad (9)$$

The switching frequency f_s is therefore proportional to the following relationship:

$$f_s = constant \times \frac{d(1-d)}{\Delta\Phi} \qquad (10)$$

The switching frequency is dependent on the duty cycle which is a feature of this topology. It is however desirable to contain the frequency variation due to variation in $\Delta\Phi$, which occurs when α and β are modulated. In this respect the saturating characteristic of the inductor can be used to limit frequency variation by confining operation on the small slope after saturation in the first and third quadrant.

Snubber Capacitor (C)

The capacitor, C, serves as a turn-off snubber and is dimensioned to give low losses in the power semiconductor switches, thus permitting high frequency operation. Since turn-off is always conducted when the inductor has saturated, a steep current slope is present at turn-off which means that the standard snubber analysis is not applicable to this topology. The expression for turn-off losses in this case is as follows:

$$P = f_s I_{s,max}\left[V(d) + \frac{I_{s,max}}{tf\,\omega}Z\right)\left(\frac{tf}{2} + \frac{\cos\omega tf - 1}{tf\,\omega^2}\right] \qquad (11)$$

Semiconductors (S_1, S_2, D_1, D_2)

The stress conditions of the semiconductor elements in this topology are close to ideal. The maximum applied voltage to the switches (S_1 and S_2) is the supply voltage. The maximum current through the switches and diodes is determined by the control strategy and some freedom of design exists. If the frequency stability considerations described in par. 3.1.3 are applied the switch would be turned off at the onset of saturation at full load in which case the maximum current stress would be $(1 + \sigma)$ p.u.

Soft switching of all semiconductors permits operation at high frequencies and improves reliability. Lossless turn-on of the switches (or zero voltage switching) is achieved while a large turn-off snubber is applied for lowloss switching. Through saturation of the inductor soft reverse recovery of the diodes is achieved.

CONTROL OF CONVERTER WITH CONTROL CURRENT SOURCE

The version of this converter described in par. 2 of this paper and reference [18] is essentially self oscillating since the current in the switches are monitored and when it exceeds a certain preset value they are turned off. Under these conditions the voltage V_{cs} (see Fig. 1) is uncontrolled and it is necessary to control it with an additional source referred to as "control current source".

Approximations to simplify analysis

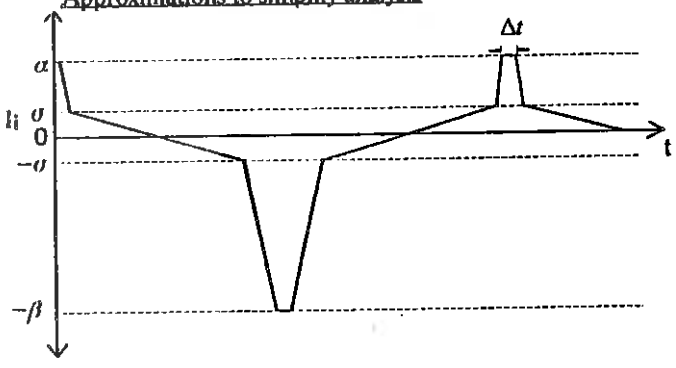

Fig. 6: Simplified inductor current waveforms.

The complete analysis of the converter is complicated and some approximations concerning its operation need to be introduced to simplify the analysis:

i) The circuit resistance is ignored

ii) All the slope transitions of the inductor current are abrupt

iii) The sinusoidal shape of the inductor waveform crests is approximated by a flat waveform crest, Δt, which is expressed as a percentage of the switching period (see Fig. 6).

iv) α and β are only dependent on the output current and independent of duty cycle. In practice the peak switch current (e. g. I_s in Fig. 5) is controlled in this manner. Since the difference between the peak current in a switch and the peak of the combined load and inductor current (γ - $I_{s,max}$ in Fig. 4) is dependent on the duty cycle α and β will also be dependent on the duty cycle. This dependency is generally not large and is ignored in this paper in order to enhance its clarity. The difference is defined as the following constant:

$$\varepsilon = \gamma - I_{s,max} = constant\ value \tag{12}$$

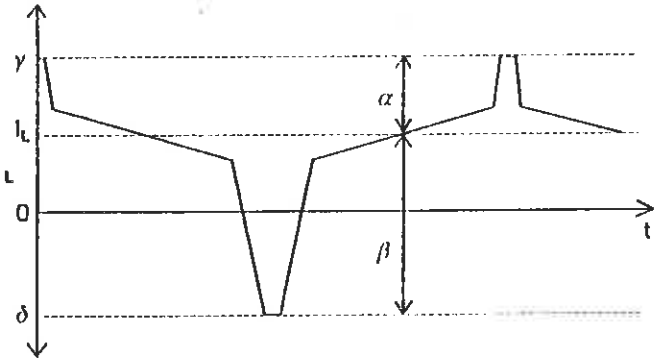

Fig. 7: Simplified combined inductor and load current waveforms.

The combined inductor and load current waveform is shown in Fig. 7. The current peaks γ and δ are important and are monitored by the control. δ has a certain minimum value δ_{min} which is required for zero voltage switching. As discussed under assumption (iv), the peak values of γ and δ need to be limited in order to contain the current stresses on the switches. The maximum values are designated by γ_{max} and δ_{max}. Applying the principle that turn off is always conducted when the inductor is saturated or at least at the onset of saturation, the maximum peak current I_{iL} becomes:

$$\Delta_{max} = \gamma_{max} = \delta_{max} = 1 + \sigma + \varepsilon \tag{13}$$

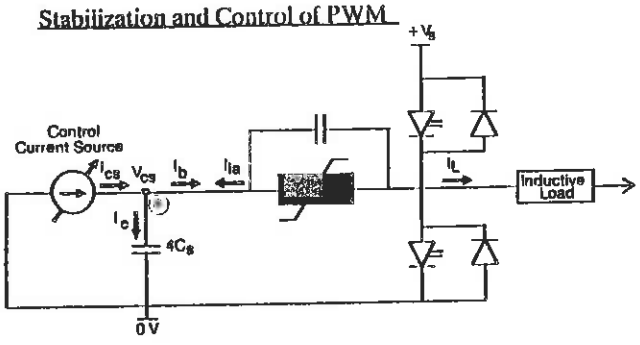

Fig. 8 Equivalent circuit for control analysis

The circuit of Fig. 1 can be simplified by parallelling the two capacitors of value $2C_s$ each into a single capacitor, $4C_s$, in order to analyze the ac behaviour of node a. As is shown in Fig. 8, the control current source supplies a current I_{cs} into node a, which controls the voltage V_{cs} of this node. I_{cs} branches into two components at node a, namely, I_c which flows into the capacitor $4C_s$ and I_b which flows into the resonant tank. The purpose of the bias current I_b is to counter the average current sourced by the non-linear resonant tank which is equal to I_{ia} and is given by the following expression:

$$I_{ia} = \frac{\alpha^2 - \beta^2 + \tau(\alpha - \beta)}{2[\alpha + \beta + \tau + 2\sigma(K-1)]} \tag{14}$$

$$\text{where } \tau = \frac{\Delta t}{1 - \Delta t}[\alpha + \beta + 2\sigma(K-1)] \tag{15}$$

The above expression assumes that switching only occurs when the inductor is saturated for reasons of limiting the frequency variation as outlined in par 1.1.3. If α and β are permitted to vary linearly with load current as follows;

$$\alpha = \alpha_0 - I_L \tag{16}$$

$$\beta = \beta_0 + I_L \tag{17}$$

where α_0 , β_0 ≡ Inductor peaks at zero load current,

then the average current can be expressed as follows :

$$I_{ia}(I_L) = \frac{[\alpha_0^2 - \beta_0^2 + \tau(\alpha_0 - \beta_0)] - 2I_L(\alpha_0 + \beta_0 + \tau)}{2[\alpha_0 + \beta_0 + 2\sigma(K-1)]} \tag{18}$$

Note that with this control scheme the switches are turned off at constant peak currents irrespective of the load. During the part of the cycle where the load current flows through the switch the peak current at turn off has been set equal to $(1+\sigma)$ which seems to be a good compromise between current stresses on the semiconductor switch devices and containing switching frequency variation. β can cover a range of values. The minimum value requirement that β must satisfy is that there should be enough inductive energy to ensure that the voltage polarity across C can be reversed to ensure zero voltage turn-on of the next half cycle.

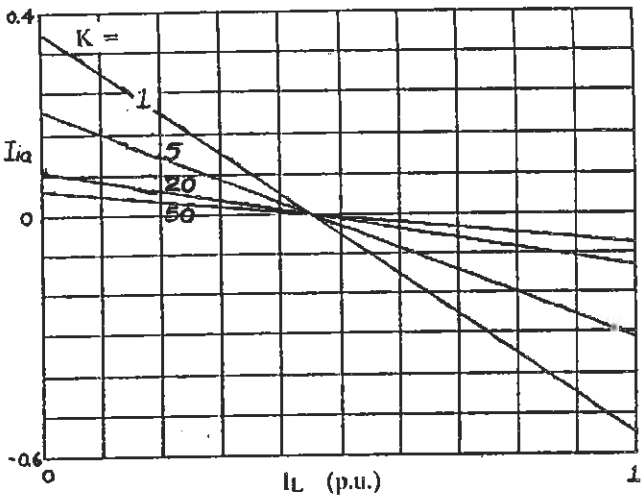

Fig. 9 Family of input-output current curves for different values of K ($\beta_0 = 0.4$, $\sigma = 0.2$, $\varepsilon = 0.3$)

It is desirable to keep the bias current as small as possible because it has direct bearing on the rating of the current source. The slope of the bias current is inversely dependent on a second

order polinomial of K which makes it desirable to have an inductor with a large K value, as can be appreciated from the graph of Fig 9. Vertical displacement of the input-output current curves can be obtained by keeping β constant while Iia is varied, as is shown in Figure 10.

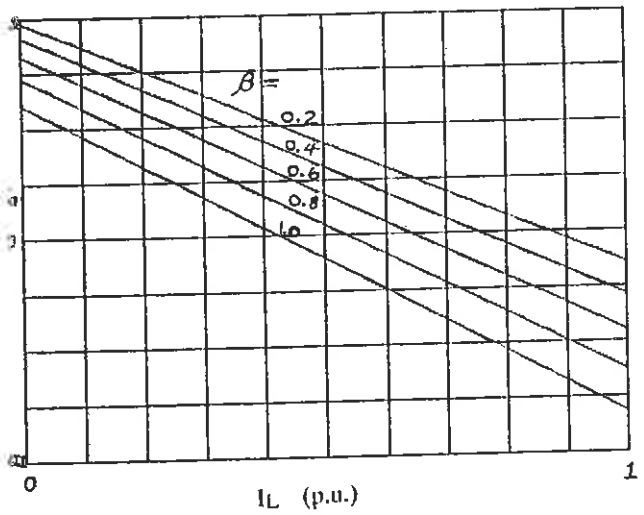

Fig. 10 Family of input-output current curves for different values of β_0 ($K = 20$, $\sigma = 0.2$, $\varepsilon = 0.3$)

ELIMINATION OF CONTROL CURRENT SOURCE

The basic nonlinear resonant inverter discussed functions essentially as a hybrid switchmode amplifier, since the output is a PWM waveform with the same average value as V_{cs}, the input stage consists of the control current source, and the gain is given by the family of curves shown in Fig. 9 and 10. Obvious questions are whether it is not possible to improve the gain by introducing feedback or feedforward and finally if it is not possible to completely discard the control current source.

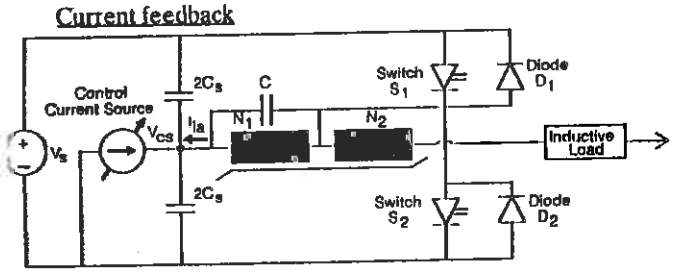

Fig. 11 Circuit with current feedback

A portion of the output current can be fed back to the resonant tank by adding a second winding to the saturating inductor as shown in Fig. 11. Depending on the polarity, the feedback current can either add or subtract from the average current, I_{ia}, flowing in the inductor, so that zero bias current is possible as has been experimentally illustrated (Fig. 12).

The feedback is a linear function of current, due to the characteristic of the current transformer, and by setting the feedback ratio;

$$\text{i)}\ f = \frac{\alpha_0 + \beta_0 + \tau}{[\alpha_0 + \beta_0 + 2\sigma(K-1)]} , \qquad (19)$$

$$\text{ii)}\ \alpha_0 = \beta_0 , \qquad (20)$$

the average inductor current can be completely cancelled with the feedback and no bias current is necessary.

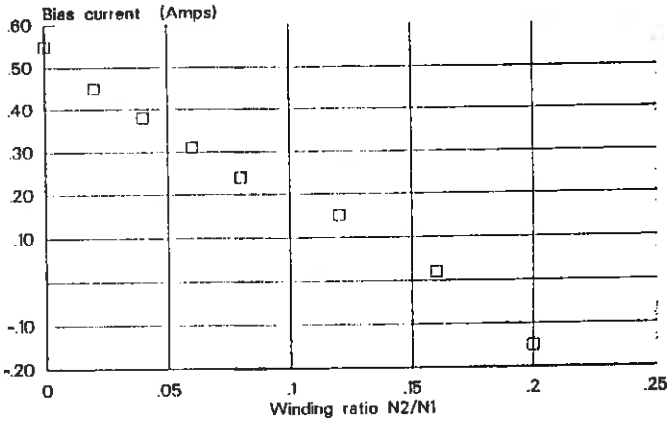

Fig. 12 Bias current from control current source required to sustain 65% duty cycle and 4A at output versus number of feedback turns on a small 50V experimental prototype

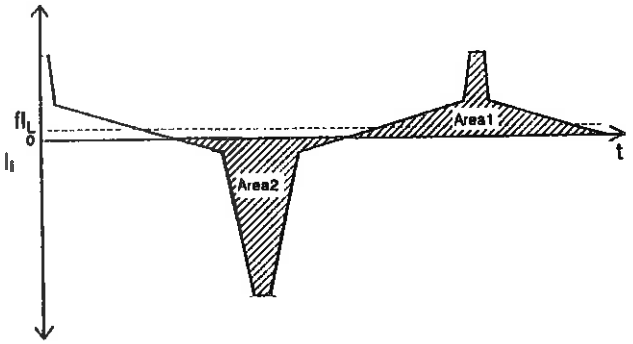

Fig. 13 The effect of feedback on the inductor current

The effect of the feedback is to adjust the current through winding N_1 (I_i) of the mutual inductor to give zero average value under all load conditions as indicated in Fig. 13.

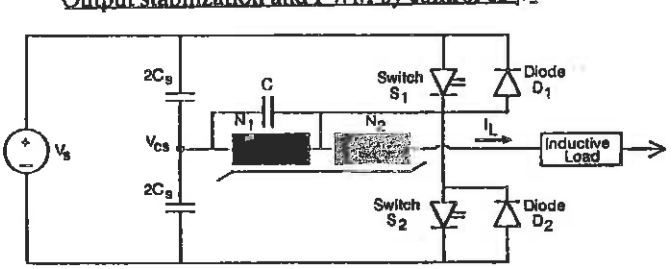

Fig. 14 Phase arm power module without modulating current source.

The control current source can be eliminated completely if, in addition to zero bias current, a way can be found to generate sufficient control current, I_c, to modulate V_{cs} and the PWM duty cycle. The only variables to achieve this control are modulation of α and β . α has the following dynamic range:

$$\sigma + \varepsilon < \alpha + I < \Delta_{max} \qquad (21)$$

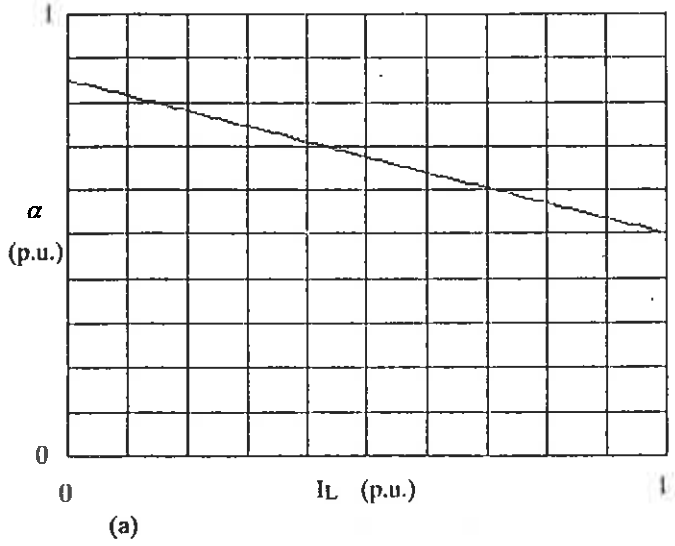

(a)

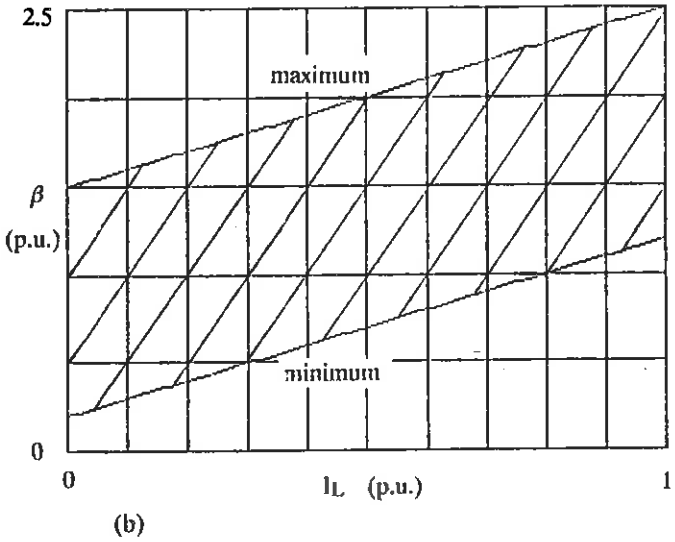

(b)

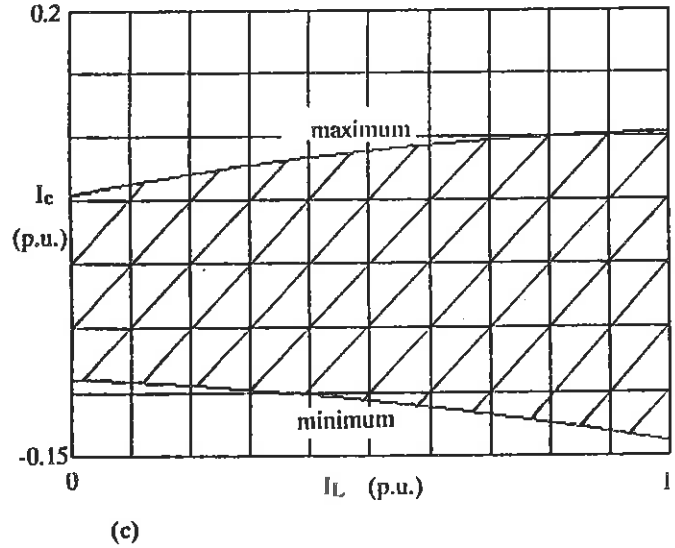

(c)

Fig.15 Graphic representation of (a) load dependency of α (b) value range of β and (c) value range of I_c for (K = 20, $\sigma = 0.2, \beta_0 = 0.2, \varepsilon = 0.3, \Delta t = 5\%$)

The following dependency of α on the load current needs to be introduced for maximum dynamic range of I_c:

$$\alpha = \frac{\Delta_{max} + \delta_{min}}{2} + I\left(\frac{\Delta_{max} - \delta_{min}}{2} - 1\right) \qquad (22)$$

β has the following optimum dynamic range:

$$\delta_{min} \le \beta - I \le \Delta_{max} \qquad (23)$$

Fig. 15(c) shows the range of control current as function of load current that can be achieved with controlling for certain circuit parameters. The slew rate for changing PWM is consequently determined by the ability to change the voltage across $4C_s$:

$$\frac{d(PWM)}{dt} = \frac{dV_c}{dt} = \frac{I_c}{4C_s} \qquad (24)$$

CONCLUSIONS

A hybrid phase arm power module has been desribed, which can be used in ultrasonic frequency inverters. Soft switching is achieved by using a single non-linear resonant tank per phase arm, and pulse width modulation is achieved by controlling the depth of saturation in the saturating inductor. A prominent feature of this topology is that the installed rating of the switches are close to 1 per unit which can be an important economic factor at larger powers.

7.0 REFERENCES

[1] R. Orugati, F.C. Lee, "Resonant power processors Parts I and II", IEEE Trans. Industry Applications, vol. IA-21, (No.6) Nov/Dec 1985, pp.1453-1471.

[2] W.A. Tabisz, P. Gradzki, F.C. Lee, "Zero-voltage switched quasi-resonant buck and fly-back, converters - experimental results at 10MHz", Conf. Record, IEEE PESC '87, (Blacksburg VA, June 1987), pp.404-413.

[3] D.M. Divan, "The resonant dc link converter - a new concept in static power conversion", IEEE Trans. Industry Applications, vol.25 (no.2) March/April 1989, pp.317-325.

[4] J.A. Deacon, J.D. van Wyk, J.J. Schoeman, "An evaluation of resonant snubbers applied to GTO-converters", IEEE Trans. Industry Applications, vol.25 (no.2) March/April 1989, pp.292-297.

[5] A. Mertens, D.M. Divan, "A high frequency resonant dc link inverter using IGBT'S", Proceedings, 2nd International Power Electronics Conference (IPEC) Tokyo, April 1990, pp.152-160.

[6] M. Kheraluwala, D.M. Divan, "Delta modulation strategies for resonant link inverters", Conf. Rec. IEEE PESC-87, Blacksburg, June 1987, pp.271-277.

[7] D.M. Divan, G. Skibinski, " Zero switching loss inverters for high power applications", IEEE Trans. Industry Applications, vol.25 (No.4) July 1989, pp. 634-636.

[8] J.S. Lai, B.K. Bose, "An induction motor drive using an improved high frequency resonant dc link inverter", Conf. Rec. IEEE PESC-90, San Antonio, June 1990, pp.792-799.

[9] W. McMurray, "Selection of snubbers and clamps to optimise the design of transistor switching converters", IEEE Trans Industry Applications, vol.IA-16 (no.4) July/Aug 1980, pp. 513-523.

[10] C.G. Steyn, "Analysis and optimization of regenerative linear snubbers", IEEE Trans. Power Electronics, vol.4 (no.3) July 1989, pp.362-376

A THYRISTOR DRIVEN PULSER FOR MULTI-KILOWATT LASERS

Piet H. Swart and Hubertus M. von Bergmann.

Rand Afrikaans University, Group for Pulse and Laser Technology, Laboratory for Systems, Johannesburg.

ABSTRACT

Excimer- and CO_2 TEA pulse lasers require excitation pulses with voltage rise times of 100 ns and peak voltage levels of more than 40 kV for efficient excitation. The corresponding electrical inputs extend to multikilowatt levels of average powers. To achieve these levels, primary switching must be carried out at tens of kA and multiple kV levels and at repetition rates of several kHz. These requirements place extreme demands on the active switching elements employed in the pulser for primary pulse conversion. Under these conditions, thyratron lifetimes are drastically limited and endeavours to overcome these limitations have led to the development of an all solid state driven pulser. The solid state driven pulser employs a modular, thyristor switched, pulse power supply unit for primary pulse conversion and a four stage series magnetic pulse compressor to transform the pulses into a domain compatible with excimer laser excitation.

1. OBJECTIVES

The main objective of the research is directed at the development of solid state switched industrial excimer laser systems with average optical output powers extending beyond 1 kW and multi kW CO_2 TEA lasers, in which solid state switching technology is employed exclusively in conjunction with electromagnetic series pulse compression. The emphasis is placed on the development of solid state switches as a result of the short life expectancy of conventional thyratrons and the consequent high replacement cost of these units in a conventional pulser employing thyratron switches for primary pulse conversion[4]. Electrical excitation pulses, with voltage rise times below 120 ns, energies of more than 20 J, and average electrical power levels above 40 kW, at a repetition rate of 2 kHz are required to achieve the objective.

2. PULSE COMPRESSION

Resonant Energy Transfer

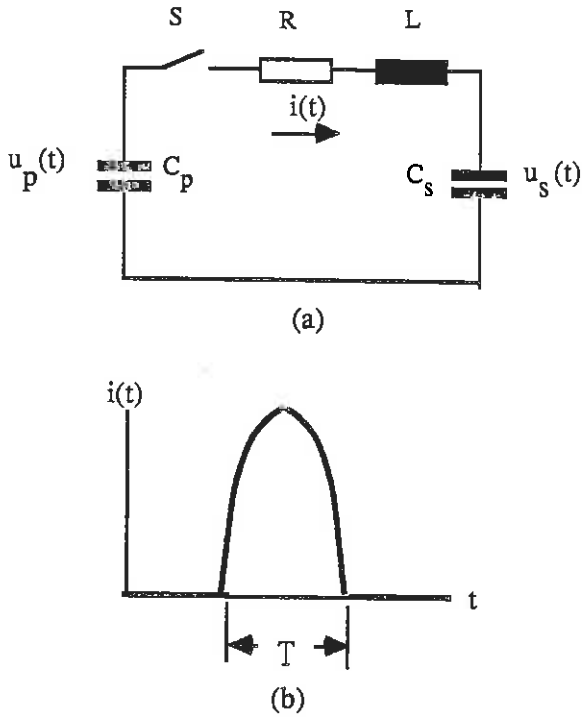

Figure 1 - Lossy resonant transfer.

It has been shown that the usual lossless treatments of resonant energy transfer, adopted in pulse compressor analysis, lead to inconsistencies with experimental observations and the authors have developed the "lossy analysis" for implementation in their modelling[2]. In accordance with this analysis, the half-sinusoidal loop current, shown in fig. 1(b), in the series resonant transfer loop of fig. 1(a) is given by:

$$i(t)=U_p\sqrt{\frac{C_T}{L_s}}\sin\omega t \quad \ldots\ldots (1)$$

with U_p the primary capacitor voltage at switch closure time, L_s the loop inductance, and ω the natural damped frequency of oscillation. C_T is the equivalent series loop capacitance.

The primary- and secondary capacitors respectively discharge and charge with co-sinusoidal voltage profiles of:

$$u_p(t)=U_p\left[1-\frac{1}{L_sC_1}\left(\frac{1}{\alpha^2+\omega^2}-\frac{1}{\omega\omega_0}e^{-\alpha t}\cos(\omega t+\phi)\right)\right] \quad \ldots\ldots (2)$$

and

$$u_s(t)=U_p\left[\frac{1}{L_sC_2}\left(\frac{1}{\alpha^2+\omega^2}\,\omega\;\omega_0 e^{-\alpha t}\cos(\omega t+\phi)\right)\right] \quad \ldots\ldots (3)$$

in which ϕ is the initial phase angle, α the damping coefficient, and ω_0 the undamped angular oscillation frequency of the loop. The pulse width, or pulse transfer time of the loop is the half-sinusoidal time of the current profile, coinciding also with the voltage transfer time.

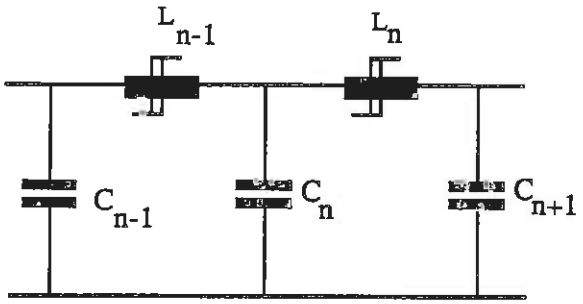

Figure 2 - Multistage series compression.

Pulse Compression

Placing several resonant transfer loops in tandem, makes the secondary capacitor of the previous loop the primary of the following as shown in the compressor in fig. 2. In this way, successive transfers can be accomplished from one loop to the next if isolation is provided in the adjacent loops whilst transfer is taking place.

This can be brought about by utilizing saturable inductors, designed to saturate when transfer into the primary capacitor of each loop is complete. In its unsaturated state, the inductor presents a large impedance and effectively blocks current flow. A small saturation current will, however, flow, and lead to saturation in accordance with:

$$\int_0^T u\,dt = NA_e\Delta B \quad \ldots\ldots (4)$$

in which T is the pulse width of the previous transfer loop, N is the number of turns on the inductor, A_e its effective magnetic cross-section and ΔB the available flux excursion that the inductor core material can undergo before saturating. Magnetic materials, with square BH-curves are preferred in pulse compression applications because of their sharp saturating characteristics. By grading down the saturated inductance in each loop by design, the pulse width of successive loops can be reduced, with commensurate increase in current levels.

By substituting for the final time in eq's (2) and (3), the final primary and secondary capacitor voltages after transfer are respectively obtained:

$$u_p(T)=U_p\left(1-\frac{1+e^{-\alpha T}}{1+k}\right) \quad \ldots\ldots (5)$$

$$u_s(T)=U_p\frac{k(1+e^{-\alpha T})}{1+k} \quad \ldots\ldots (6)$$

It has been shown that to achieve complete energy transfer in a lossy loop, the following relationship must hold[2]:

$$k=\frac{C_p}{C_s}=e^{-\alpha T} \quad \ldots\ldots (7)$$

Comprehensive spreadsheet modelling techniques have been developed for the modelling and design

of a pulser consisting of a Resonant Regulating Pulse Power Supply (R^2P^2) unit and a series magnetic pulse compressor (SMPC) in accordance with the above lossy theory. The R^2P^2 unit carries out primary pulse conversion at a level of 1 kV by means of thyristor switches and transforms these pulses to the 42 kV level required by the pulse compressor.

3. THE ALL SOLID STATE SWITCHED PULSER

Fig. 3 shows a simplified circuit diagram of the all solid state switched pulser, consisting of an R^2P^2 pulse power supply and a four stage series magnetic pulse compressor[5].

The four stage pulse compressor

A prototype four stage compressor has been constructed. The four modules, which are clearly shown in the photograph of fig. 5, are housed in a cylindrical alloy enclosure, also shown, through which mineral oil is circulated for insulation and cooling.

The saturable inductors utilize amorphous toroidal cores, separated by machined spacers. The inductor windings consist of specially constructed striplines to reduce conduction losses. The ceramic interstage capacitors are arranged in circular banks between conductive plates, connecting each capacitor bank to earth and to the two adjacent inductors, as shown in the diagram of fig. 6. Each stage of the compressor consists of an inductor and an interstage capacitor. The separate stages are modular, with each module connecting to the next through high current plug connectors for ease of assembly and maintenance.

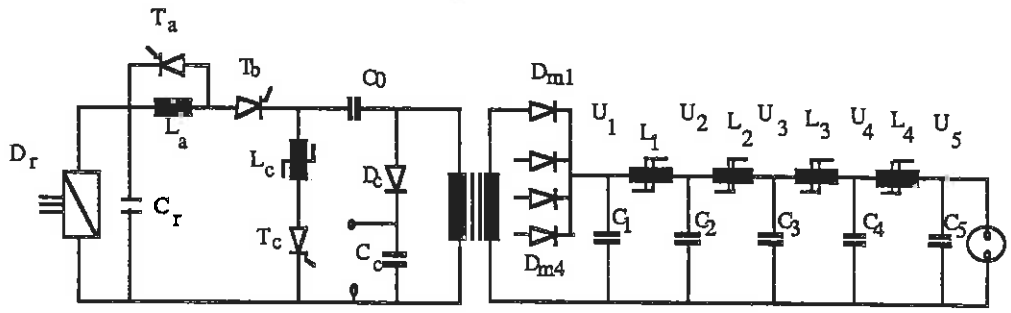

Figure 3. Simplified diagram of the all solid state switched pulser.

Operation of the series pulse compressor, as well as details of the design strategy used, has already been reported in the literature [2]. Table 1 reflects salient design parameters relating to the all solid state driven pulser. The data reflected in table 1, has been condensed from the appropriate spreadsheet model. The "loop numbers" in table 1 correspond to the four loops in the pulse compressor, with loop 1 formed by C_1, L_1 and C_2. Loop 4 is the final loop, delivering the charge finally to the peaking capacitor C_5. The columns "H.V. side" and "L.V. side" respectively refer to parameters in the secondary and in the primary of the pulse transformer in the R^2P^2 unit. The "charging" column reflect parameters relating to the charging circuit of the pulse power supply.

The pulse power supply unit

Only one R^2P^2 module is shown in the diagram in fig. 1, but the four diodes D_{m1} to D_{m4} permit four modules to be time multiplexed into the single pulse compressor. The modular approach is favoured for maintenance purposes. It also permits sharing of the total power required by the individual modules and makes it possible to use low power commercially available semiconductor devices for primary pulse conversion. In the present instance, the average input power required by the pulse compressor is in the order of 50 kW at a repetition rate of 2 kHz. Each of the 4 modules are only required to switch 12,7 kW, operating at a pulse repetition rate of 500 Hz.

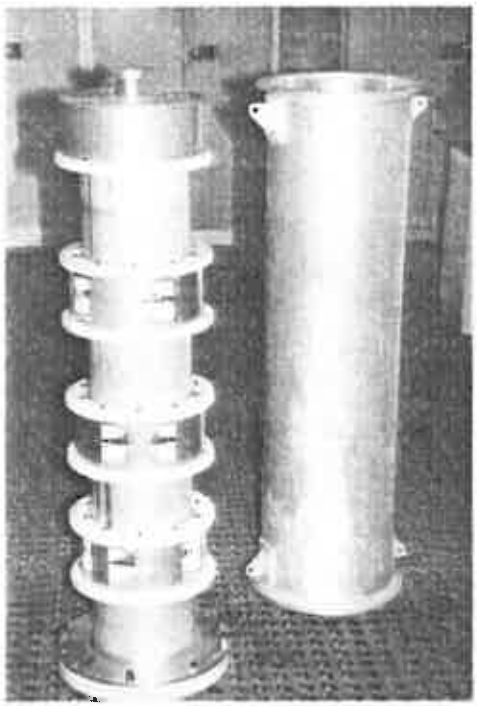

Figure 4. prototype four stage compressor

Operation of the R^2P^2 unit has been examined in the literature[1,5]. With reference to fig. 3, operation can be summarised as follows: Full-wave three phase rectifier D_r furnishes dc-voltage to the circuit of about 530 V, smoothed by reservoir capacitor C_r. The charging thyristor T_b resonantly charges primary capacitor C_0 through inductor L_a (with T_a off). Transfer of the charge in C_0 is also brought about resonantly to C_1 by triggering of the transfer thyristor T_c. The necessary inductance for LC-resonance is supplied in this transfer loop by the leakage inductance of the step-up pulse transformer.

Only one R^2P^2 module is shown in the diagram in fig. 1, but the four diodes D_{m1} to D_{m4} permit four modules to be time multiplexed into the single pulse compressor. The modular approach is favoured for maintenance purposes. It also permits sharing of the total power required by the individual modules and makes it possible to use low power commercially available semiconductor devices for primary pulse conversion. In the present instance, the average input power required by the pulse compressor is in the order of 50 kW at a repetition rate of 2 kHz. Each of the 4 modules are only required to deliver 12,7 kW, operating at a pulse repetition rate of 500 Hz.

Table 1 - Salient design parameters of the four stage compressor.

	Compressor loop number				Power supply		
Description	4	3	2	1	H.V. side	L.V. side	Charging
Pulse energy[J]	20	22.6	23.8	24.6	25.4	27.6	29.6
Pulse time	180ns	361ns	1.49µs	7.98µs	42.2µs	42.2µs	1.88ms
Pulse voltage [V]	39700	41600	42900	44000	44300	875	456
Peak current[A]	9977	4971	1201	224.8	42.54	2083	43.7
RMS current[A]	134	94.4	46.4	20.09	8.74	214	30.9
Average current[A]	2.28	2.28	2.28	2.28	2.28	27.9	27.9
Av. power [kW]	40	45.2	47.6	49.2	12.7	13.8	14.8

Pulse voltage regulation is furnished by the regulating (dequeing) thyristor T_a which, when triggered during the second half of the charging cycle, force commutates T_b and circulates the current through charging inductor L_a.

The R^2P^2 unit could be regarded as an extension to the pulse compressor rather than as a separate unit, as it also utilizes resonant energy transfer in its operation and has current and voltage

waveforms similar to that of the compressor.

Fig. 5 shows a photograpgh of the 2 kHz prototype R^2P^2 pulse power supply. Each of the two cabinets shown in fig. 5 is capable of delivering 25.4 kW of pulse power at 1 kHz and is self contained with its own Pulse Generation and Control (PGC) section, input power section, cooling oil circulation system, oil-to-water heat exchanger, and programmable logic controller (PLC). The PLC's and oil circulation systems, conveniently housed in the power supply cabinets, are being extended to also control the operation of the laser and to monitor gas flow, fan operation and other functions necessary to the operation of the laser.

5. EXPERIMENTAL RESULTS

Pulse Compressor

The composite oscillogram of fig. 6 combines two separate oscillograms with identical time bases. The waveforms are shown for the voltages v_1 to v_5. (Refer to fig.3.) of the 4 stage pulse compressor[4].

The voltage waveforms shown in fig. 6 correlate well with the designed values of peak voltage and pulse time. Losses in the different stages are of acceptable values and an overall efficiency of 77% has been measured, corresponding to and input pulse energy of 25,4 J with 20 J delivered to the laser.

Pulse power supply unit

Analysis carried out with the peak primary pulse voltage set at 1000 V, yielded a figure of 27,2 J input pulse energy to the pulse transformer, and an output pulse energy of 22,2 J delivered into the pulse compressor first stage. This is representative of an energy-efficiency of 85% for the transfer stage. Measurements carried out on input energy from the mains, relative to the initial energy stored in the primary capacitor before transfer, show an efficiency of 91%. From these figures, the total efficiency for the R^2P^2 unit is calculated to be 77%. When delivering 50 kW of output pulse power, the wallplug input is thus 65 kW, of which 15 kW must be removed by cooling.

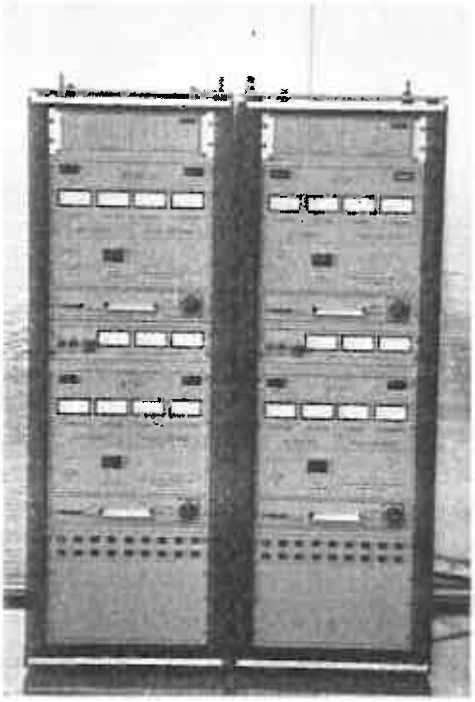

Figure 5. Prototype 2 kHz R^2P^2 Power supply

Pulse voltage variation on the input pulses to a multistage series compressor, leads to pulse time jitter on the output to the laser, as a result of a variation in the pulse propagation time through the compressor. This variation in propagation time is brought about by a variation in hold-off in the different stages. Pulse time jitter becomes problematical with large compression factors, such as is encountered in the multistage compressor discussed in this paper and may extend to several microseconds if the input pulse voltage is not accurately maintained at a given level.

Low pulse voltage variation, delivered to the pulse compressor is essential to the pulse time jitter-free operation of multistage pulse compressors. The low pulse voltage variation required, is achieved through active de-queing[1]. Low pulse voltage variation is one of the main features of the R^2P^2 power supply unit. Maximum pulse voltage variation of as low as 40 V in 40 kV (0,1%) was

measured under normal, full-power operating conditions on this unit and modifications are presently being undertaken to reduce this figure down to 4 V in 40 kV (0.01%).

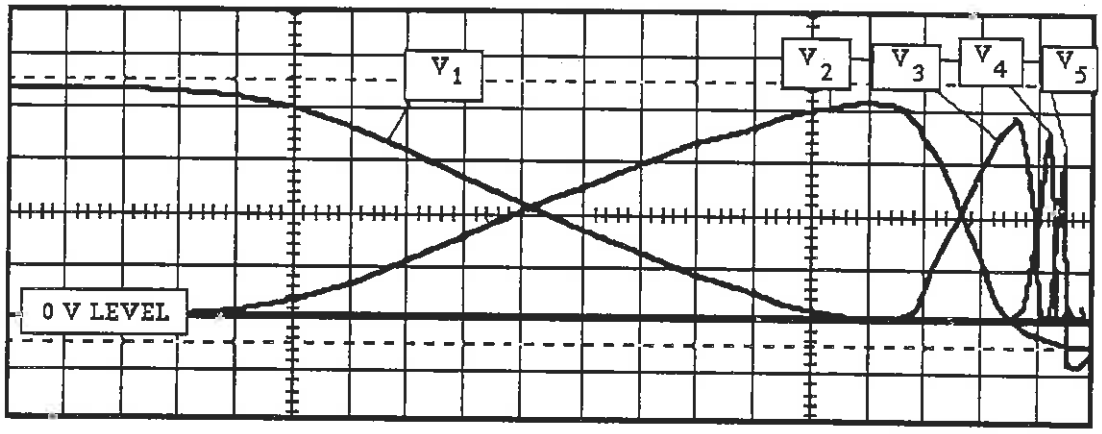

Figure 6. Composite oscillogram of voltage profiles on experimental compressor. Voltage scale: 5 kV/div. Time scale: 500 ns/div.

6. REFERENCES

1. Bredenkamp, G.L., Swart, P.H., von Bergmann, H.M., "A resonant Pulse Power Supply with Pulse-Energy Regulation", Proc. 6-th IEEE Pulsed Power Conference, pp. 723-726, 1987.
2. Swart, P.H., Bredenkamp, G.L., von Bergmann, H.M., "Spreadsheet design, numerical simulation and practical evaluation of a lossy series pulse compressor" Proc. 6th IEEE Pulsed Power Conference, pp. 680-683, IEEE,1987.
3. H.M. von Bergmann and P.H. Swart, "High Repetition Rate Excimer and CO_2 TEA lasers", SPIE, 1023, pp. 51-54, 1989.
4. Swart, P.H., von Bergmann, H.M., "Comparative evaluation of pulsing circuits for kHz excimer laser systems", Proc. 7th IEEE Pulsed Power Conference, pp. 293-296, IEEE, 1989.
5. H.M. von Bergmann and P.H. Swart, "Pulsing circuits for high power, high repetition rate lasers", Proc.4-th International Conference on 'Power Electronics and Variable Speed Drives', pp 472-477,IEE, 1990.
6. Henry T. Tromp, Piet H. Swart and Hubertus M. von Bergmann, "Bipolar pulsing circuits for high power, high repetition rate lasers", Proc. 19-th Power Modulator Symposium, San Deigo, CA, 26 - 28 June, 1990.

A TWO DAMPER EQUIVALENT FOR A MULTI DAMPER CIRCUIT CONFIGURATION

F.L.C. Badenhorst and F.S. van der Merwe

Abstract: When deducing operational equations for a machine with multiple damper bars starting from the constructional detail of the machine, one ends up with two equations for the stator, one for the field winding and one for each D-axis and Q-axis damper circuit. On the other hand standard textbook techniques to analyze the dynamic behaviour of an alternator use only five equations to describe the machine. The problem is to relate the impedance matrix allowing for multiple dampers to the impedance matrix allowing only for one D- and one Q-axis damper circuit. A reduction in the number of circuits in the model of the machine will affect the predicted dynamic response. The challenge is to do this without unduly changing the predicted performance. In this paper a mathematical procedure is described whereby this simplification can be done. As an example the reduction from five damper circuits to two damper circuits is studied. Simulated results using the original set of equations as well as the two damper circuits equivalent under dynamic conditions for different designs will be presented to demonstrate the accuracy of the proposed technique of circuit reduction.

LIST OF SYMBOLS

θ	Rotor position
ϕ	Position in airgap
L	Inductance
R	Resistance
V	Voltage or voltage matrix
I	Current or current matrix
Z	Impedance or impedance matrix
i	Instantaneous current
e	Instantaneous voltage
λ	Flux linkage
Φ	Flux
B	Flux density
P_e	Permeance per unit area
W	Magnetic energy
P	Power

1. INTRODUCTION

The standard textbook unified machine theory addresses a machine with five windings, namely the stator d- and q-axis windings, the field winding, and the d- and q-axis damper windings. Practical machines, however, have multiple damper bars requiring multiple damper circuits when modelling the machine. To relate these machines to the standard textbook theory, the damper windings must be reduced to only two. The actual number of damper windings must be replaced by two windings in such a way that the equivalent matrix still gives a good representation of the original machine under all conditions. In this article, a way will be shown to find a mathematical 2-damper winding equivalent of an original five damper winding machine. Simulated results of the equivalent machine compared with the simulated results of the original machine will be given.

2. POSITION OF DAMPER BARS

The machine discussed in this article has two d-axis and three q-axis damper windings on the rotor. The positions of the damper bars on the poles are shown in figure 1. Table 1 gives the angle covered by each damper winding according to the electrical angles shown in figure 1.

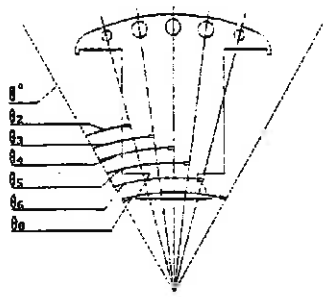

Figure 1: Sectional view of pole to show damper bar positions

Table 1: Position of damper bars on poles

Damper bars	Angle
D1	$\theta_3 \rightarrow \theta_5$
D2	$\theta_2 \rightarrow \theta_6$
Q1	$-\theta_2 \rightarrow \theta_2$
Q2	$-\theta_3 \rightarrow \theta_3$
Q3	$-\theta_4 \rightarrow \theta_4$

The reduction of the d-axis damper windings will be easier than the q-axis windings and it will be used to find a method to reduce the number of windings.

3. REDUCTION OF D-AXIS DAMPER WINDINGS

One needs to find a mathematical equivalent for the original windings that will give a good representation of the characteristics of the original circuits. This means that the energy stored and the power dissipated in the equivalent winding must be the same as in the original windings.

Consider the circuit shown in figure 2. This represents the two d-axis damper windings of the machine. Each circuit consists of an inductance and a resistance. The inductance consists of a leakage component and a mutual component. The resistance consists of a mutual component as well as a separate component which together forms the total resistance of the circuit. From figure 2 the following equations can be derived:

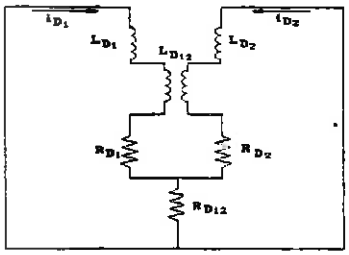

Figure 2: RL-circuit representation of d-axis damper circuit

$$R_{D_{11}} = R_{D_1} + R_{D_{12}} \qquad L_{D_{11}} = L_{D_1} + L_{D_{12}}$$

$$R_{D_{22}} = R_{D_2} + R_{D_{12}} \qquad L_{D_{22}} = L_{D_2} + L_{D_{12}}$$

From the relationships given above the equations for the induced voltages can be written as

$$e_{D_1} = L_{D_{11}}\frac{di_{D_1}}{dt} + L_{D_{12}}\frac{di_{D_2}}{dt}$$

$$e_{D_2} = L_{D_{21}}\frac{di_{D_1}}{dt} + L_{D_{22}}\frac{di_{D_2}}{dt} \qquad 3.1$$

In searching for a method to replace the 2 damper windings by 1 equivalent winding, it was found that a good estimation of dynamic response is obtained when it is

$$e_{D_1} = \left(K_{D_1} \int_{\Theta_3}^{\Theta_5} P_\phi(\phi)\, d\phi + K_{D_2} \int_{\Theta_1}^{\Theta_5} P_\phi(\phi)\, d\phi \right) \cdot \frac{di_{D_a}}{dt}$$

$$e_{D_2} = \left(K_{D_1} \int_{\Theta_3}^{\Theta_6} P_\phi(\phi)\, d\phi + K_{D_2} \int_{\Theta_2}^{\Theta_6} P_\phi(\phi)\, d\phi \right) \cdot \frac{di_{D_a}}{dt} \qquad 3.21$$

From these equations follows that the ratio of e_1 to e_2 is a constant

$$K_{VF} = \frac{e_{D_1}}{e_{D_2}} = \frac{\left(K_{D_1} \int_{\Theta_3}^{\Theta_5} P_\phi(\phi)\, d\phi + K_{D_2} \int_{\Theta_3}^{\Theta_5} P_\phi(\phi)\, d\phi \right)}{\left(K_{D_1} \int_{\Theta_3}^{\Theta_6} P_\phi(\phi)\, d\phi + K_{D_2} \int_{\Theta_2}^{\Theta_6} P_\phi(\phi)\, d\phi \right)} \qquad 3.22$$

This constant gives a relationship between the voltages induced in the two damper circuits. From this relationship and equation 3.1 follows that

$$K_{D_1} L_{D_{11}} \frac{di_{D_a}}{dt} + K_{D_2} L_{D_{12}} \frac{di_{D_a}}{dt} = K_{VF} \left(K_{D_1} L_{D_{12}} \frac{di_{D_a}}{dt} + K_{D_2} L_{D_{22}} \frac{di_{D_a}}{dt} \right)$$

or

$$K_{D_1} L_{D_{11}} + K_{D_2} L_{D_{12}} = K_{VF} * (K_{D_1} L_{D_{12}} + K_{D_2} L_{D_{22}}) \qquad 3.23$$

This equation together with equation 3.5 give two equations with two unknown quantities. The values of the two constants can hence be found.

4. Q-AXIS WINDINGS

The reduction will be done in the same way as with the D-axis, but the number of circuits are now three instead of only two. This makes the mathematics much more complicated.

As with the D-axis currents, the assumption is again made that the three currents have the same waveshape in time. The equivalent current is again taken as the sum of the three currents, thus

$$i_{Q_a} = i_{Q_1} + i_{Q_2} + i_{Q_3} \qquad 4.1$$

and must hence also have the same waveshape in time. This leads to:

$$i_{Q_1} = K_{Q_1} i_{Q_a} \qquad 4.2$$

$$i_{Q_2} = K_{Q_2} i_{Q_a} \qquad 4.3$$

$$i_{Q_3} = K_{Q_3} i_{Q_a} \qquad 4.4$$

From equations 4.1 - .4 follows that

$$K_{Q_1} + K_{Q_2} + K_{Q_3} = 1 \qquad 4.5$$

4.1 EQUIVALENT SELF INDUCTANCE

The same concept used with the d-axis will be used here. The energy stored in the equivalent impedance must be the same as the energy stored in the original impedances. The energy stored in the equivalent circuits can hence be written as

$$W_{Q_T} = \tfrac{1}{2} L_{Q_a} i_{Q_a}^2 \qquad 4.8$$

The energies stored in the separate windings are

$$W_{Q_1} = \tfrac{1}{2} [L_{Q_{11}} i_{Q_1}^2 + L_{Q_{12}} i_{Q_1} i_{Q_2} + L_{Q_{13}} i_{Q_1} i_{Q_3}]$$

$$W_{Q_2} = \tfrac{1}{2} [L_{Q_{22}} i_{Q_2} i_{Q_1} + L_{Q_{22}} i_{Q_2}^2 + L_{Q_{23}} i_{Q_2} i_{Q_3}]$$

$$W_{Q_3} = \tfrac{1}{2} [L_{Q_{13}} i_{Q_1} i_{Q_3} + L_{Q_{23}} i_{Q_2} i_{Q_3} + L_{Q_{33}} i_{Q_3}^2] \qquad 4.9$$

By substituting the currents with equations 4.2 - 4, one gets

$$W_{Q_1} = \tfrac{1}{2} [K_{Q_1}^2 L_{Q_{11}} + K_{Q_1} K_{Q_2} L_{Q_{12}} + K_{Q_1} K_{Q_3} L_{Q_{13}}] i_{Q_a}^2$$

$$W_{Q_2} = \tfrac{1}{2} [K_{Q_1} K_{Q_2} L_{Q_{21}} + K_{Q_2}^2 L_{Q_{22}} + K_{Q_2} K_{Q_3} L_{Q_{23}}] i_{Q_a}^2 \qquad 4.10$$

$$W_{Q_3} = \tfrac{1}{2} [K_{Q_1} K_{Q_3} L_{Q_{13}} + K_{Q_2} K_{Q_3} L_{Q_{23}} + K_{Q_3}^2 L_{Q_{33}}] i_{Q_a}^2$$

Substituting these equations into equation 4.8 leads to

$$\tfrac{1}{2} L_{Q_a} i_{Q_a}^2 = [\tfrac{1}{2} (K_{Q_1}^2 L_{Q_{11}} + K_{Q_2}^2 L_{Q_{22}} + K_{Q_3}^2 L_{Q_{33}}) + K_{Q_1} K_{Q_2} L_{Q_{12}} + K_{Q_1} K_{Q_3} L_{Q_{13}} + K_{Q_2} K_{Q_3} L_{Q_{23}}] i_{Q_a}^2 \qquad 4.11$$

from which the equivalent self inductance is found to be

$$L_{Q_a} = K_{Q_1}^2 L_{Q_{11}} + K_{Q_2}^2 L_{Q_{22}} + K_{Q_3}^2 L_{Q_{33}} + 2K_{Q_1} K_{Q_2} L_{Q_{12}} + 2K_{Q_1} K_{Q_3} L_{Q_{13}} + 2K_{Q_2} K_{Q_3} L_{Q_{23}} \qquad 4.12$$

4.2 EQUIVALENT MUTUAL INDUCTANCES

The q-axis damper windings have only mutual coupling with the q-axis stator winding. The voltage induced in the stator winding by currents in the damper windings is

$$e_{qQ} = M_{qQ_1} p i_{Q_1} + M_{qQ_2} p i_{Q_2} + M_{qQ_3} p i_{Q_3} \qquad 4.13$$

Substituting the currents with equations 4.2 - 4 gives

$$e_{qQ} = \left[M_{qQ_1} K_{Q_1} + M_{qQ_2} K_{Q_2} + M_{qQ_3} K_{Q_3} \right] p i_{Q_a} \qquad 4.14$$

The voltage induced in the stator due to the equivalent mutual inductance and current can be written as

$$e_{qQ_a} = M_{qQ_a} p i_{Q_a} \qquad 4.15$$

From this equation and equation 4.14 the equivalent mutual inductance is found to be

$$M_{qQ_a} = K_{Q_1} M_{qQ_1} + K_{Q_2} M_{qQ_2} + K_{Q_3} M_{qQ_3} \qquad 4.16$$

4.3 EQUIVALENT RESISTANCE

As before, the power dissipated in the equivalent resistance must be the same as the total power dissipated in the original resistances. Thus

$$P_{Q_a} = R_{Q_a} i_{Q_a}^2 = P_{Q_1} + P_{Q_2} + P_{Q_3} \qquad 4.17$$

The power dissipated in the three separate windings are

$$P_{Q_1} = i_{Q_1}^2 R_{Q_{11}} + i_{Q_1} i_{Q_2} R_{Q_{12}} + i_{Q_1} i_{Q_3} R_{Q_{13}}$$

$$P_{Q_2} = i_{Q_2} i_{Q_1} R_{Q_{21}} + i_{Q_2}^2 R_{Q_{22}} + i_{Q_2} i_{Q_3} R_{Q_{23}} \qquad 4.18$$

$$P_{Q_3} = i_{Q_3} i_{Q_1} R_{Q_{31}} + i_{Q_3} i_{Q_2} R_{Q_{32}} + i_{Q_3}^2 R_{Q_{33}}$$

By substituting the currents in these equations with equations 4.2 - 4, the power dissipated in the equivalent circuit can now be written as

$$P_{Q_T} = i_{Q_a}^2 R_{Q_a} = [K_{Q_1}^2 R_{Q_{11}} + K_{Q_2}^2 R_{Q_{22}} + K_{Q_3}^2 R_{Q_{33}} + 2(K_{Q_1} K_{Q_2} R_{Q_{12}} + K_{Q_1} K_{Q_3} R_{Q_{13}} + K_{Q_2} K_{Q_3} R_{Q_{23}})] i_{Q_a}^2 \qquad 4.19$$

A TWO DAMPER EQUIVALENT FOR A MULTI DAMPER CIRCUIT CONFIGURATION

F.L.C. Badenhorst and F.S. van der Merwe

Abstract: When deducing operational equations for a machine with multiple damper bars starting from the constructional detail of the machine, one ends up with two equations for the stator, one for the field winding and one for each D-axis and Q-axis damper circuit. On the other hand standard textbook techniques to analyze the dynamic behaviour of an alternator use only five equations to describe the machine. The problem is to relate the impedance matrix allowing for multiple dampers to the impedance matrix allowing only for one D- and one Q-axis damper circuit. A reduction in the number of circuits in the model of the machine will affect the predicted dynamic response. The challenge is to do this without unduly changing the predicted performance. In this paper a mathematical procedure is described whereby this simplification can be done. As an example the reduction from five damper circuits to two damper circuits is studied. Simulated results using the original set of equations as well as the two damper circuits equivalent under dynamic conditions for different designs will be presented to demonstrate the accuracy of the proposed technique of circuit reduction.

LIST OF SYMBOLS

ϑ	Rotor position
ϕ	Position in airgap
L	Inductance
R	Resistance
V	Voltage or voltage matrix
I	Current or current matrix
Z	Impedance or impedance matrix
i	Instantaneous current
e	Instantaneous voltage
λ	Flux linkage
Φ	Flux
B	Flux density
P_ϕ	Permeance per unit area
W	Magnetic energy
P	Power

1. INTRODUCTION

The standard textbook unified machine theory addresses a machine with five windings, namely the stator d- and q-axis windings, the field winding, and the d- and q-axis damper windings. Practical machines, however, have multiple damper bars requiring multiple damper circuits when modelling the machine. To relate these machines to the standard textbook theory, the damper windings must be reduced to only two. The actual number of damper windings must be replaced by two windings in such a way that the equivalent matrix still gives a good representation of the original machine under all conditions. In this article, a way will be shown to find a mathematical 2-damper winding equivalent of an original five damper winding machine. Simulated results of the equivalent machine compared with the simulated results of the original machine will be given.

2. POSITION OF DAMPER BARS

The machine discussed in this article has two d-axis and three q-axis damper windings on the rotor. The positions of the damper bars on the poles are shown in figure 1. Table 1 gives the angle covered by each damper winding according to the electrical angles shown in figure 1.

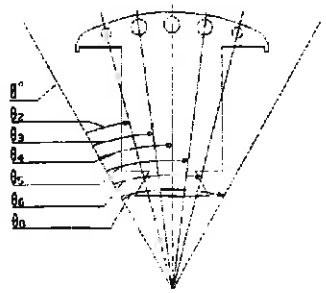

Figure 1: Sectional view of pole to show damper bar positions

Table 1: Position of damper bars on poles

Damper bars	Angle
D1	$\vartheta_1 \rightarrow \vartheta_2$
D2	$\vartheta_2 \rightarrow \vartheta_3$
Q1	$-\vartheta_2 \rightarrow \vartheta_2$
Q2	$-\vartheta_2 \rightarrow \vartheta_1$
Q3	$-\vartheta_4 \rightarrow \vartheta_4$

The reduction of the d-axis damper windings will be easier than the q-axis windings and it will be used to find a method to reduce the number of windings.

3. REDUCTION OF D-AXIS DAMPER WINDINGS

One needs to find a mathematical equivalent for the original windings that will give a good representation of the characteristics of the original circuits. This means that the energy stored and the power dissipated in the equivalent winding must be the same as in the original windings.

Consider the circuit shown in figure 2. This represents the two d-axis damper windings of the machine. Each circuit consists of an inductance and a resistance. The inductance consists of a leakage component and a mutual component. The resistance consists of a mutual component as well as a separate component which together forms the total resistance of the circuit. From figure 2 the following equations can be derived:

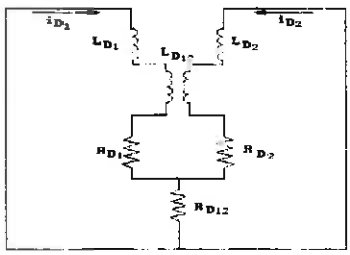

Figure 2: RL-circuit representation of d-axis damper circuit

$$R_{D_{11}} = R_{D_1} + R_{D_{12}} \qquad L_{D_{11}} = L_{D_1} + L_{D_{12}}$$

$$R_{D_{22}} = R_{D_2} + R_{D_{12}} \qquad L_{D_{22}} = L_{D_2} + L_{D_{12}}$$

From the relationships given above the equations for the induced voltages can be written as

$$e_{D_1} = L_{D_{11}}\frac{di_{D_1}}{dt} + L_{D_{12}}\frac{di_{D_2}}{dt}$$

$$e_{D_2} = L_{D_{21}}\frac{di_{D_1}}{dt} + L_{D_{22}}\frac{di_{D_2}}{dt} \qquad 3.1$$

In searching for a method to replace the 2 damper windings by 1 equivalent winding, it was found that a good estimation of dynamic response is obtained when it is

assumed that the two damper currents have as an approximation the same waveshapes in time. The equivalent current must therefore also have the same waveshape in time and is taken as the sum of the two separate currents, thus

$$i_{D_e} = i_{D_1} + i_{D_2} \qquad 3.2$$

Based on the above, the two damper currents can each be written as a constant factor times the equivalent current.

$$i_{D_1} = K_{D_1} i_{D_e} \qquad 3.3$$

$$i_{D_2} = K_{D_2} i_{D_e} \qquad 3.4$$

From the preceeding two equations follows that

$$\begin{aligned} K_{D_1} i_{D_e} + K_{D_2} i_{D_e} &= i_e \\ \therefore \quad K_{D_1} + K_{D_2} &= 1 \end{aligned} \qquad 3.5$$

3.1 EQUIVALENT SELF INDUCTANCE

The energy stored in the equivalent circuit must have the same value as the total energy stored in the original circuits. From this the energy stored in the equivalent circuit can be written as

$$W_{D_e} = \tfrac{1}{2} L_{D_e} i_{D_e}^2 \qquad 3.6$$

The energy stored in the original windings is

$$\begin{aligned} W_{D_1} &= \tfrac{1}{2} L_{D_{11}} i_{D_1}^2 + \tfrac{1}{2} L_{D_{12}} i_{D_1} i_{D_2} \\ W_{D_2} &= \tfrac{1}{2} L_{D_{21}} i_{D_1} i_{D_2} + \tfrac{1}{2} L_{D_{22}} i_{D_2}^2 \end{aligned} \qquad 3.7$$

By substituting equations 3.3 and 3.4 into this equation one gets

$$\begin{aligned} W_{D_1} &= \tfrac{1}{2} L_{D_{11}} K_{D_1}^2 i_{D_e}^2 + \tfrac{1}{2} L_{D_{12}} K_{D_1} K_{D_2} i_{D_e}^2 \\ W_{D_2} &= \tfrac{1}{2} L_{D_{21}} K_{D_2} K_{D_1} i_{D_e}^2 + \tfrac{1}{2} L_{D_{22}} K_{D_2}^2 i_{D_e}^2 \end{aligned} \qquad 3.8$$

This equation and equation 3.6 lead to

$$\tfrac{1}{2} L_{D_e} i_{D_e}^2 = \tfrac{1}{2} K_{D_1}^2 L_{D_{11}} i_{D_e}^2 + \tfrac{1}{2} K_{D_2}^2 L_{D_{22}} i_{D_e}^2 + K_{D_1} K_{D_2} L_{D_{12}} i_{D_e}^2 \qquad 3.9$$

from which the equivalent self inductance can be found as

$$L_{D_e} = K_{D_1}^2 L_{D_{11}} + K_{D_2}^2 L_{D_{22}} + 2 K_{D_1} K_{D_2} L_{D_{12}} \qquad 3.10$$

3.2 EQUIVALENT MUTUAL INDUCTANCES

The equivalent mutual inductances between the equivalent damper circuit and the stator or field, can be deduced from the voltages induced in the stator or field windings due to currents flowing in the damper circuits. The relevant equations are

$$\begin{aligned} e_{aD} &= M_{aD_1} p i_{D_1} + M_{aD_2} p i_{D_2} \\ e_{FD} &= M_{FD_1} p i_{D_1} + M_{FD_2} p i_{D_2} \end{aligned} \qquad 3.11$$

with p the derivative operator. Substituting the currents from equations 3.3 and .4 gives

$$\begin{aligned} e_{aD} &= M_{aD_1} K_{D_1} p i_{D_e} + M_{aD_2} K_{D_2} p i_{D_e} \\ e_{FD} &= M_{FD_1} K_{D_1} p i_{D_e} + M_{FD_2} K_{D_2} p i_{D_e} \end{aligned} \qquad 3.12$$

The voltages induced via the equivalent mutual inductance and current can be given as

$$\begin{aligned} e_{aD_e} &= M_{a_e} p i_{D_e} \\ e_{FD_e} &= M_{FD_e} p i_{D_e} \end{aligned} \qquad 3.13$$

From the previous four equations, the equivalent mutual inductances are found to be

3.3 EQUIVALENT RESISTANCE

$$\begin{aligned} M_{aD_e} &= K_{D_1} M_{aD_1} + K_{D_2} M_{aD_2} \\ M_{FD_e} &= K_{D_1} M_{FD_1} + K_{D_2} M_{FD_2} \end{aligned} \qquad 3.14$$

The power dissipated in the equivalent circuit must have the same magnitude as the power dissipated in the original circuits. Thus

$$\begin{aligned} P_{D_e} &= R_{D_e} i_{D_e}^2 \\ &= P_{D_1} + P_{D_2} \end{aligned} \qquad 3.15$$

The power dissipated in the separate windings are

$$\begin{aligned} P_{D_1} &= R_{D_{11}} i_{D_1}^2 + R_{D_{12}} i_{D_1} i_{D_2} \\ P_{D_2} &= R_{D_{12}} i_{D_1} i_{D_2} + R_{D_{22}} i_{D_2}^2 \end{aligned} \qquad 3.16$$

Substituting these two equations and equations 3.3 and 4 into equation 3.15 results in

$$\begin{aligned} R_{D_e} i_{D_e}^2 &= R_{D_{11}} i_{D_1}^2 + R_{D_{22}} i_{D_2}^2 + 2 R_{D_{12}} i_{D_1} i_{D_2} \\ &= K_{D_1}^2 R_{D_{11}} i_{D_e}^2 + K_{D_2}^2 R_{D_{22}} i_{D_e}^2 + 2 K_{D_1} K_{D_2} i_{D_e}^2 \end{aligned} \qquad 3.17$$

from which the equivalent resistance is found to be

$$R_{D_e} = K_{D_1}^2 R_{D_{11}} + K_{D_2}^2 R_{D_{22}} + 2 K_{D_1} K_{D_2} R_{D_{12}} \qquad 3.18$$

3.4 CALCULATING CURRENT CONSTANTS

It now remains to determine expressions for the constants K_{D1} and K_{D2}. To do this, consider the equations for the voltages induced in the damper windings (eq. 3.1), but now written in terms of the flux linkages of the coils.

$$\begin{aligned} e_{D_1} &= \frac{d\lambda_{D_1}}{dt} = \frac{d\lambda_{D_{11}}}{dt} + \frac{d\lambda_{D_{12}}}{dt} \\ e_{D_2} &= \frac{d\lambda_{D_2}}{dt} = \frac{d\lambda_{D_{21}}}{dt} + \frac{d\lambda_{D_{22}}}{dt} \end{aligned} \qquad 3.19$$

The flux linkage of a coil can be calculated by integrating the flux density over the area of the coil, which then gives the flux linkage of a single turn. Multiplying this with the number of turns gives the total amount of flux linked by the coil. The following set of equations gives a general method of calculating the flux linkage of a coil.

$$\begin{aligned} \lambda &= N \int_{\psi_1}^{\psi_2} B(\phi)\, r L_{axial} d\phi \\ &= N r L_{axial} \int_{\psi_1}^{\psi_2} F P_\phi(\phi)\, d\phi \\ &= N r L_{axial} \int_{\psi_1}^{\psi_2} N i P_\phi(\phi)\, d\phi \\ &= N^2 r L_{axial} \int_{\psi_1}^{\psi_2} P_\phi(\phi)\, d\phi \;.\; i \end{aligned} \qquad 3.20$$

where
- N = number of turns
- r = radius of armature
- L_{axial} = axial length of machine
- $B(\phi)$ = flux density distribution in airgap
- $P_\phi(\phi)$ = permeance per unit area
- ψ_1, ψ_2 = start and end points of angle covered by coil

For the damper windings the number of turns is one. The start and end points of the angle covered by the coil can be found from table 1. The induced voltages in the two circuits can hence be written as

from which the equivalent resistance is found to be

$$R_{Q_e} = K_{Q_1}^2 R_{Q_{11}} + K_{Q_2}^2 R_{Q_{12}} + K_{Q_3}^2 R_{Q_{13}} + 2K_{Q_1}K_{Q_2}R_{Q_{12}} + 2K_{Q_1}K_{Q_3}R_{Q_{13}} + 2K \quad 4.20$$

4.4 CALCULATING CURRENT CONSTANTS

To calculate the current constants, consider the following equations for the voltages induced in the stator q-axis by the Q-axis damper currents.

$$e_{Q_1} = \frac{d\lambda_{Q_1}}{dt} = \frac{d\lambda_{Q_{11}}}{dt} + \frac{d\lambda_{Q_{12}}}{dt} + \frac{d\lambda_{Q_{13}}}{dt}$$

$$e_{Q_2} = \frac{d\lambda_{Q_2}}{dt} = \frac{d\lambda_{Q_{21}}}{dt} + \frac{d\lambda_{Q_{22}}}{dt} + \frac{d\lambda_{Q_{23}}}{dt} \quad 4.21$$

$$e_{Q_3} = \frac{d\lambda_{Q_3}}{dt} = \frac{d\lambda_{Q_{31}}}{dt} + \frac{d\lambda_{Q_{32}}}{dt} + \frac{d\lambda_{Q_{33}}}{dt}$$

The flux linkages are calculated in the same way as described in paragraph 4.4 for the d-axis damper windings. Equation 4.21 then changes to

$$e_{Q_1} = 2\left(K_{Q_1}\int_{\theta_0}^{\theta_2} P_\phi d\phi + K_{Q_2}\int_{\theta_0}^{\theta_2} P_\phi d\phi + K_{Q_3}\int_{\theta_0}^{\theta_2} P_\phi d\phi\right)\frac{di_{Q_e}}{dt} \quad 4.22$$

$$e_{Q_2} = 2\left(K_{Q_1}\int_{\theta_0}^{\theta_2} P_\phi d\phi + K_{Q_2}\int_{\theta_0}^{\theta_2} P_\phi d\phi + K_{Q_3}\int_{\theta_0}^{\theta_2} P_\phi d\phi\right)\frac{di_{Q_e}}{dt} \quad 4.23$$

$$e_{Q_3} = 2\left(K_{Q_1}\int_{\theta_0}^{\theta_2} P_\phi d\phi + K_{Q_2}\int_{\theta_0}^{\theta_3} P_\phi d\phi + K_{Q_3}\int_{\theta_0}^{\theta_4} P_\phi d\phi\right)\frac{di_{Q_e}}{dt} \quad 4.24$$

The following substitutions are made to simplify the mathematics:

$$F_{Q_1} = \int_{\theta_0}^{\theta_2} P_\phi d\phi; \quad F_{Q_2} = \int_{\theta_0}^{\theta_3} P_\phi d\phi; \quad F_{Q_3} = \int_{\theta_0}^{\theta_4} P_\phi d\phi \quad 4.25$$

From these above equations then follows the following two equations giving the ratios between the induce voltages.

$$\frac{e_{Q_1}}{e_{Q_2}} = \frac{F_{Q_1}}{K_{Q_1}F_{Q_1} + K_{Q_2}F_{Q_2} + K_{Q_3}F_{Q_2}} = F_{Q_{12}} \quad 4.26$$

$$\frac{e_{Q_1}}{e_{Q_3}} = \frac{F_{Q_1}}{K_{Q_1}F_{Q_1} + K_{Q_2}F_{Q_2} + K_{Q_3}F_{Q_3}} = F_{Q_{13}} \quad 4.27$$

The equations for the voltages induced in the three circuits are

$$e_{Q_1} = L_{Q_{11}}\frac{di_{Q_1}}{dt} + L_{Q_{12}}\frac{di_{Q_2}}{dt} + L_{Q_{13}}\frac{di_{Q_3}}{dt}$$

$$e_{Q_2} = L_{Q_{21}}\frac{di_{Q_1}}{dt} + L_{Q_{22}}\frac{di_{Q_2}}{dt} + L_{Q_{23}}\frac{di_{Q_3}}{dt} \quad 4.28$$

$$e_{Q_3} = L_{Q_{31}}\frac{di_{Q_1}}{dt} + L_{Q_{32}}\frac{di_{Q_2}}{dt} + L_{Q_{33}}\frac{di_{Q_3}}{dt}$$

By substituting the currents from the relationships in equations 4.2 - 4, the equation now becomes

$$e_{Q_1} = K_{Q_1}L_{Q_{11}}\frac{di_{Q_e}}{dt} + K_{Q_2}L_{Q_{12}}\frac{di_{Q_e}}{dt} + K_{Q_3}L_{Q_{13}}\frac{di_{Q_e}}{dt}$$

$$e_{Q_2} = K_{Q_1}L_{Q_{21}}\frac{di_{Q_e}}{dt} + K_{Q_2}L_{Q_{22}}\frac{di_{Q_e}}{dt} + K_{Q_3}L_{Q_{23}}\frac{di_{Q_e}}{dt} \quad 4.29$$

$$e_{Q_3} = K_{Q_1}L_{Q_{31}}\frac{di_{Q_e}}{dt} + K_{Q_2}L_{Q_{32}}\frac{di_{Q_e}}{dt} + K_{Q_3}L_{Q_{33}}\frac{di_{Q_e}}{dt}$$

Relate the voltage equations in equation 4.28 to each other according to equations 4.26 and .27 to get the following two equations.

$$L_{Q_{11}}K_{Q_1} + L_{Q_{12}}K_{Q_2} + L_{Q_{13}}K_{Q_3} = F_{Q_{12}}*(L_{Q_{11}}K_{Q_1} + L_{Q_{12}}K_{Q_2} + L_{Q_{13}}K_{Q_1}) \quad 4.30$$

$$L_{Q_{11}}K_{Q_1} + L_{Q_{12}}K_{Q_2} + L_{Q_{13}}K_{Q_3} = F_{Q_{13}}*(L_{Q_{13}}K_{Q_1} + L_{Q_{23}}K_{Q_2} + L_{Q_{33}}K_{Q_1}) \quad 4.31$$

These two equations together with equation 4.5 give three equations with three unknown values. From this the values of the three constants can now be calculated.

5. PERFORMANCE PREDICTION WITH EQUIVALENT CIRCUITS

The response of the damper currents after a sudden short-circuit, are displayed in the graphs in figures 3 and 4. Figure 3 display the response of the d-axis damper circuit currents and figure 4 the response of the q-axis damper circuit currents. From the graphs can be seen that the currents do not have the same waveshapes as was assumed. The difference in shape is the most significant for the sub-transient part just after the short-circuit. After a while, the waveshapes are quite similar. This would hence mean that the response of the reduced matrix would differ in the sub-transient part, but should be fairly accurate for the transient part of the dynamic response of the machine.

The original damper circuits are replaced by the mathematical equivalent to form a five by five impedance matrix. To verify the accuracy of the method, the dynamic response of the machine is calculated with the same program as before, but with the reduced impedance matrix. The results are then compared with the results of the original machine. In the rest of the figures the results for two different machines are shown. The second machine is an experimental machine with a dynamic response that differs from the first machine. This gives more value to the verification process.

The waveforms calculated with the reduced matrix as well with the original matrix are displayed on the same graph. Figure 5 & 6 are for the standard generator and the next two for the second generator.

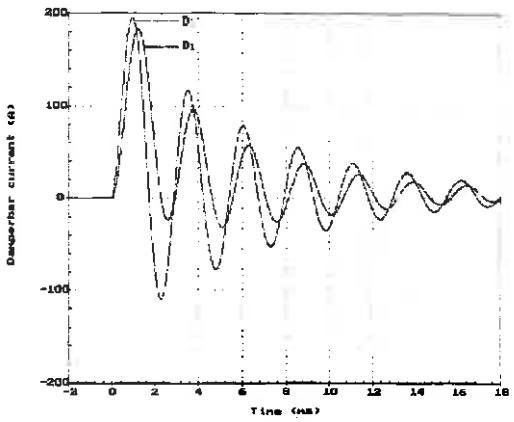

Figure 3: D-axis damper circuit currents after short-circuit

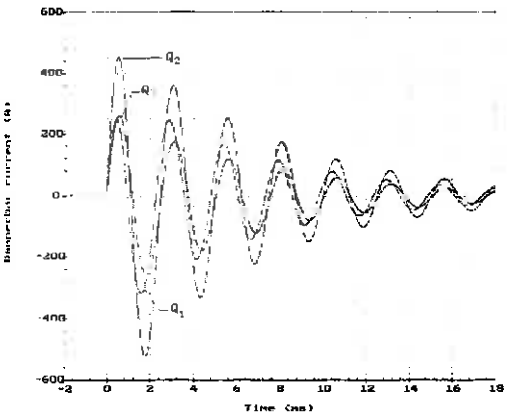

Figure 4: Q-axis damper circuit currents after short-circuit

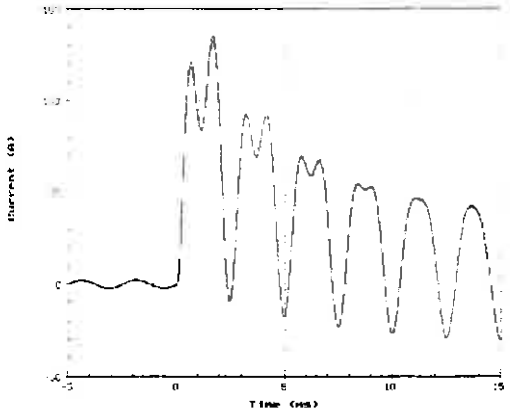

Figure 5: Armature currents of first generator after short-circuit

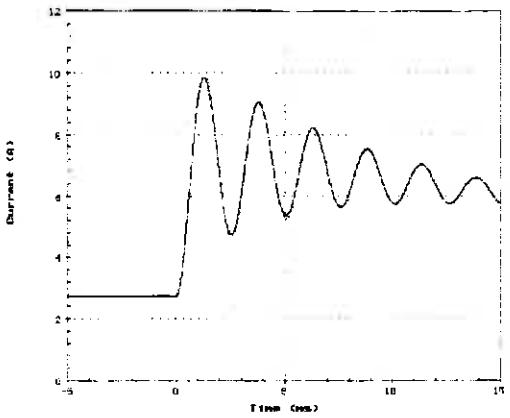

Figure 6: Field currents of first generator after short-circuit

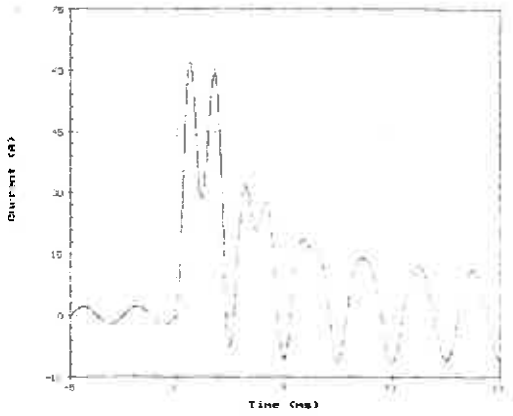

Figure 7: Armature currents of second generator after short-circuit

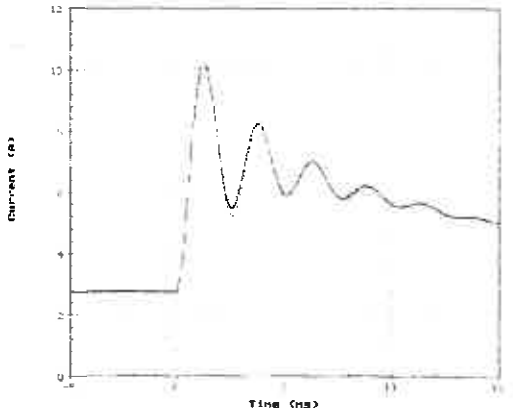

Figure 8: Field currents of second generator after short-circuit

6. CONCLUSIONS

As predicted, the sub-transient response of the reduced matrix differ slightly form the original response. For a terminal short-circuit, all the effective reactances are d-axis quantities. As described earlier, the d-axis damper bars force the stator flux into the airgap immediately after the fault. This creates the leakage reactance which determine the initial swing of the stator current. The difference between the actual waveshapes and the assumed waveshapes in this region is the reason for this difference in dynamic response of the currents. After the decay of the sub-transient component, the assumed waveshapes differ very little from the real waveshapes and the response of the reduced matrix is very accurate.

The error between the original and the reduced matrices is less than 5 % for both the armature and field currents. This method of reducing the matrix to an equivalent matrix thus gives a good representation of the response of the machine under the worst conditions. For conditions where the change in load is not so drastic, as in no-load to full-load, the effect of the sub-transient component does not play such a big role, and the response of the reduced matrix will be more accurate than with the short-circuit.

This is thus a good method of relating the original machine to an equivalent machine which is the same as the standard textbook unified machine theory.

DESIGN OF HIGH SPEED HOMOPOLAR SYNCHRONOUS MOTOR

M HIPPNER R G HARLEY G D JENNINGS

Department of Electrical Engineering, University of Natal, Durban

ABSTRACT

The paper deals with the design of a high speed homopolar synchronous machine with the help of a finite element method. Details of the finite element model are presented, and the results of finite element analysis are used for performance calculations. Examples of calculations are included.

1. INTRODUCTION

Drives utilising Field Oriented Control are finding increased use in high performance applications. The last part of such a drive is always an electrical machine. For this application permanent magnet synchronous motors as well as induction motors can be considered. The homopolar synchronous motor may be an interesting alternative.

The rotor of a homopolar motor is shown in Fig. 1 a. It can be manufactured as a solid one-piece iron forging or may be laminated. The stator of the machine houses a three phase winding similar to an induction motor stator. The iron core, however, is subdivided into two parts, as can be seen in Fig. 1 b. The field (excitation) winding has the form a solenoidal coil, located in between the two laminated stator cores.

The homopolar motor is a synchronous machine in which the saliency of the rotor causes changing flux linkages within the stator winding. Thus, the flux excited by the field coil is pulsating between a positive maximum and a positive minimum. A two dimensional projection of the three dimensional flux pattern is shown in Fig. 1 b. In order to generate the same flux changes in both stator sections, the rotor poles on the left half of the rotor are displaced by 180 electrical degrees in tangential direction with respect to the poles of the right half of the rotor. The induced voltages can thus be added.

The double pole pitch (one period) of a conventional synchronous machine corresponds to the azimuthal distance between two adjacent rotor teeth. The rotational speed is determined by the supply frequency and the total number of teeth on the rotor.

The advantage of the homopolar motor is its robust construction. The disadvantage is the moderate amplitude of the flux modulation in the air gap, resulting in a relatively low utilisation of the magnetic circuit.

2. DESIGN WITH THE HELP OF FINITE ELEMENT ANALYSIS

The performance of an electrical machine is critically dependent on its magnetic flux distribution. Furthermore, knowing the magnetic flux density distribution within machine the designer can use the magnetic materials in the more economic way. For these two reasons every effort should be made to calculate the magnetic flux distribution as accurately as possible.

Finite element model

A three dimensional analysis should be used for the homopolar machine because of the three dimensional distribution of magnetic field within machine. Unfortunately, a 3-D finite element (FE) package is expensive. Therefore, the 3-D FE model has been replaced by two 2-D FE models [4].

One FE model represents the cross section of the machine along its main axis. This model has been used for the excitation winding calculations, as well as for the final determination of the shaft and frame dimensions. The second FE model represents the machine's cross section perpendicular to the machine axis (axial cross section). The later will be described in detail, because it yields more useful information.

Fig. 2 shows the FE model's axial cross section. Because of symmetry the analysis of the half cross section is enough. The vector potentials on boundaries AB and CD are constant and equal to A_1 and A_2 respectively. The difference between A_1 and A_2 is proportional to the magnetic flux which enters the rotor tooth. On other boundaries the natural Neumann boundary conditions have been applied [2].

The nonlinear FE analysis has been performed for both no-load and load conditions. For load conditions the current distributions in the stator slots have been adjusted to give the required power angle.

The results of the above analysis are presented in Fig. 3 and Fig. 4. Fig. 3 a and b show the magnetic flux lines for no-load and load respectively. The magnetic flux distribution for no-load is symmetrical, whilst for load conditions the flux distortion due to the stator MMF is visible. The same effect can be seen in Fig 4 , where the distribution of the magnetic flux density along the air gap is presented. Furthermore the influence of stator slots is visible.

3. UTILISATION OF FE ANALYSIS FOR CALCULATION OF MACHINE PERFORMANCE

Voltage induced in stator winding

The phase induced voltage (EMF) is the time derivative of the stator flux linkages. The flux linkages for any stator coil can be found from the difference between the vector potentials of the two sides forming the coil [5, 6]. The vector potential for each coil side is the average of the vector potentials over the area of the coil side. The procedure for computation can be summarised as follows:

(a) calculate the instantaneous values of stator phase currents related to the present rotor position
(b) perform the FE analysis

(c) calculate the flux linkages for each coil belonging to the same phase
(d) calculate the flux linkage ψ_{ph} for the whole stator phase summing up coil flux linkages
(e) change the rotor position by the angle α
(f) repeat steps (a) to (e) until the rotor complete a turn of 2Π electrical degrees
(g) apply Fourier analysis [3] to the function $\psi_{ph}(\alpha)$
(h) calculate the voltages induced in the stator phase by each harmonic of the flux linkage
(i) calculate the RMS value of each harmonic of generated voltage
(j) calculate the RMS value of the phase EMF

The above method is very accurate because it accounts for the complicated geometry of the machine, for the nonlinearity of the magnetic materials as well as the change of the stator MMF wave with time.

Electromagnetic torque

The electromagnetic torque can be calculated using the method of virtual work [7] :

$$T = \partial W_c / \partial \alpha \qquad (1)$$

where W_c is the magnetic coenergy and α is the elementary rotational displacement of the rotor. The magnetic coenergy is usually calculated by the FE program. In practice the calculation is done as follows:

(a) perform FE analysis for two rotor positions different by the small angle α
(b) subtract the two coenergy values by the angle α
(c) multiply the result by the active stator length

Core loss

Since the FE program calculates the magnetic flux density for each finite element of the machine model, the overall core loss can be found easily as the sum of elementary core losses for each element within the core.

To calculate the elementary loss in an element one of the well known classical formulae can be used, for example [1] :

$$P_{Fe} = a\ f\ B^2 + b\ (g\ f\ B)^2 \qquad (2)$$

where P_{Fe} = core loss
f = frequency
B = peak value of flux density within element
g = lamination thickness
a, b = constants dependent on the properties of the material.

Pulsation losses on the rotor surface

These losses occur in the iron because of the fluctuation of the magnetic flux resulting from the presence of slots. At the rotor surface the flux density varies between a maximum B_{max} under the tooth and a minimum B_{min} under the slot opening (compare Fig. 4). the amplitude of this fluctuation is :

$$B_o = (B_{max} - B_{min}) / 2 \qquad (3)$$

and can be obtained directly from the flux density plot (Fig 4). For more accurate calculations Fourier analysis should be applied and each harmonic of B_o should be used for loss calculation.

Then according to [1] pulsation losses per square meter, P_s, can be calculated using expression:

$$P_s = k_s (Q_s n)^{1.5} (B_o \tau_s)^2 \qquad (4)$$

where Q_s = number of stator slots
n = rotor speed, rpm
τ_s = slot pitch
k_s = constant = 23.3 for steel forgings, and 2.5 for 0.5 mm laminations

4. CONCLUSIONS

The usefulness of a finite element method for design of high performance electrical machines has been shown.

Further studies are needed to improve the methods of performance calculations, especially to make them less time consuming.

The approach presented can be applied to other types of electrical machines.

REFERENCES

1. Levi E : Polyphase Motors - a direct approach to their design. John Wiley & Sons, 1984

2. Silvester P P, Ferrari R L : Finite Elements for Electrical Engineers. Cambridge University Press, 1983

3. Rice J R : Numerical Methods, Software, and Analysis: IMSL Reference Edition. McGraw-Hill, 1983

4. Frank U V, Fuchs E F : Design of a Homopolar Machine with Nearly Closed Stator Slots Using Numerical Field Analyses in Both Axial and Coaxial Cross-section. Conference proceedings.

5. Fouad F A, Nehl T W, Demerdash N A : Magnetic Field Modeling of Permanent Magnet Type Electronically Operated Synchronous Machines Using Finite Elements. IEEE PAS-100, no 9, September 1981, pp. 4125-35

6. Binns K J, Kurdali A : Permanent-magnet a.c. generators. Proc. IEE, vol. 126, No. 7, July 1979

7. Mizia J, Adamiak K, Estham A R, Dawson G E : Finite Element Force Calculation: comparison of methods for electrical machines. IEEE MAG-24, No 1, January 1988, pp. 447-450

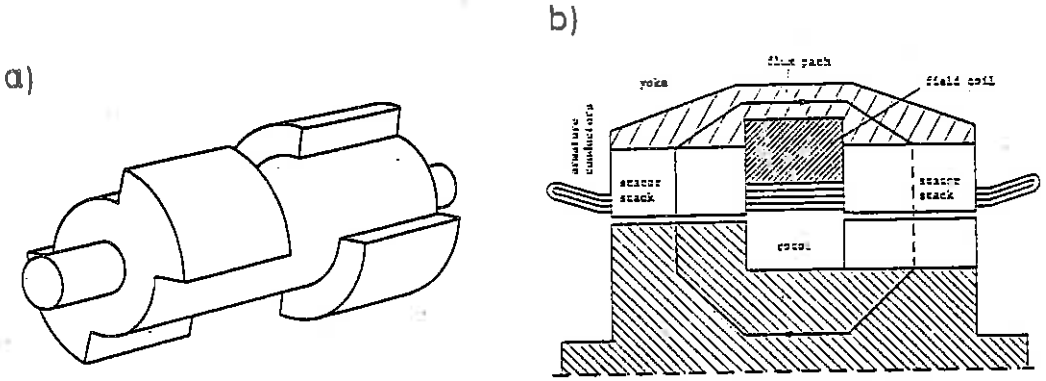

Fig. 1. Homopolar synchronous motor : a) rotor, b) coaxial cross section

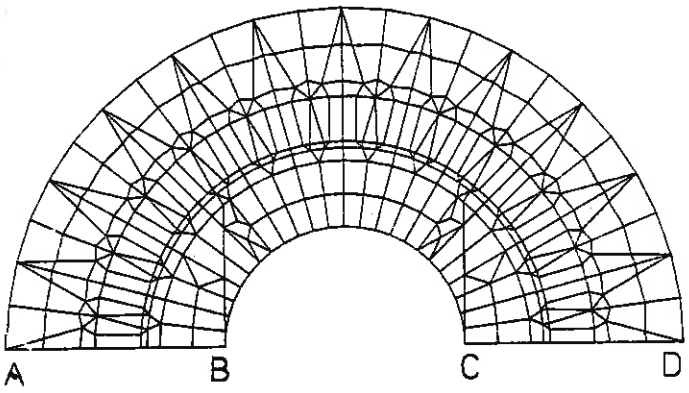

Fig. 2. Finite element model of a homopolar synchronous motor - coaxial cross section

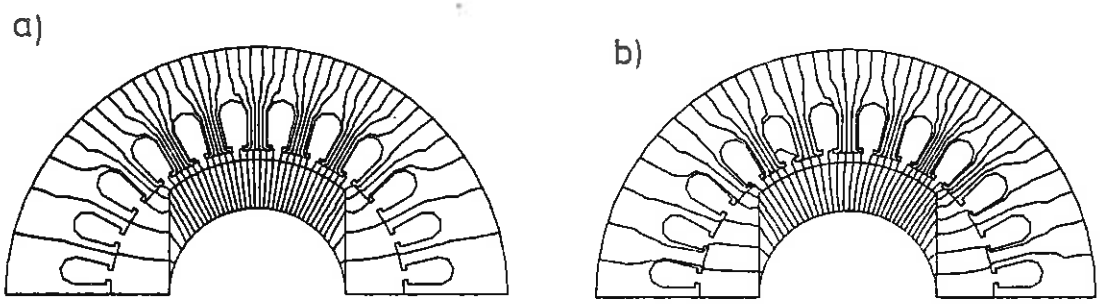

Fig. 3. Magnetic flux distribution within coaxial cross section : a) no-load, b) load

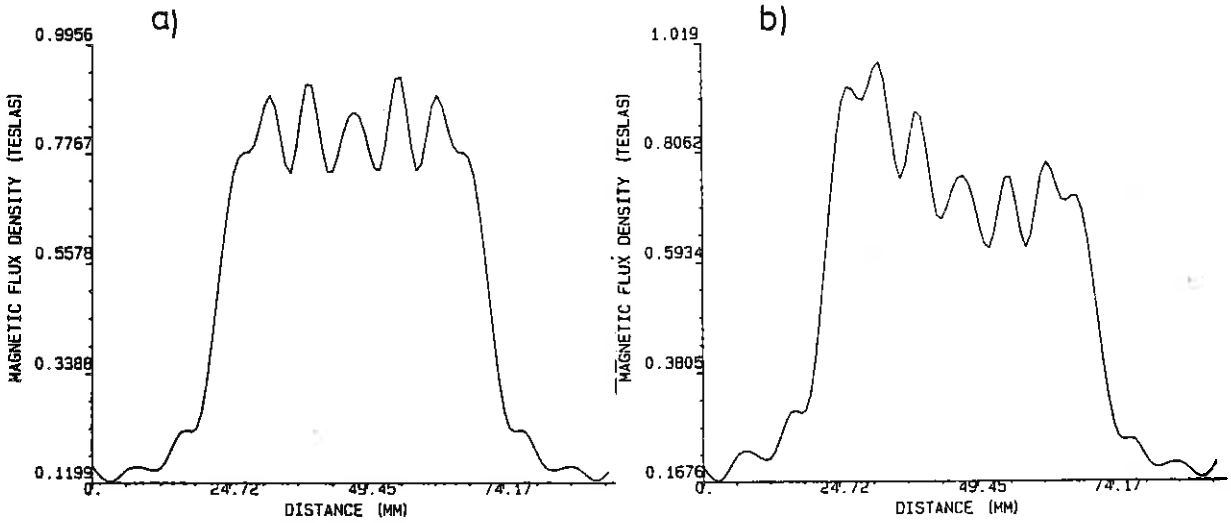

Fig 4. Magnetic flux density distribution along air gap : a) no-load, b) load

THE EFFECTS OF INDUCTION MOTOR AND RL LOADS ON THE DAMPING OF SSR TORSIONAL OSCILLATIONS

R.E.Fairbairn
University of Natal, King George V Ave., Durban 4001.

ABSTRACT This paper is an introductory study into the the effects that induction motor and RL loads have on the damping of SSR phenomena for a chosen power system network consisting of a turbo-alternator connected to an infinite busbar through a series compensated transmission line. A series of small signal test cases are examined in which the alternator's mechanical shaft is considered as lumped-inertial and as multi-inertial. The results show that for the considered system network the effects of an induction motor load are different from that of a simple RL load and that the assumption that the alternator's shaft is lumped inertial can lead to erroneous predictions.

INTRODUCTION

The economics of transmitting electrical power through an electrical power line is governed by numerous factors, and engineers faced with (possibly existing) long transmission lines often find that series compensation capacitors are a favorable option for improving the level of power transmission. Unfortunately, the insertion of series capacitance into a power line that contains resistive and inductive components results in a resonant circuit. Furthermore, any alternators connected to the line also contain resonant elements (in particular a turbo-alternators mechanical shaft) which will interact with the line's electrical resonant circuit. The interaction between a transmission line and the alternators connected to it can be broadly called Subsynchronous Resonance (SSR). The phenomena of SSR lead to two incidents of generator shaft failure in Nevada, USA, which has resulted in a great deal of research effort being put into SSR analysis.

The cost of providing SSR counter-measures is very high and Power Utilities have to make economic decisions that are based upon practical experience and/or computer studies. If, for example, it can be shown that induction motor's provide additional damping for SSR oscillations then an alternator that is connected to a load that consists largely of induction motors may be considered as less likely to experience SSR problems. Furthermore, should the need arise for a specific power network, it should be possible to predict the maximum level (critical compensation level, CCL) of capacitor compensation that can be (safely) connected to the network beyond which SSR phenomena will occur.

A Power Utility may have to use calculated guesswork in order to estimate what percentage of the load, supplied by a particular alternator/power-station, consists of rotating induction motors as apposed to RL loads. What may complicate matters further is that the percentage of induction motor load may vary periodically. This paper illustrates that induction motor loads as apposed to RL loads effect power system networks in a different manner, which means that for a particular load bus the induction motor and RL load contributions must be known in order to accurately predict the system performance.

The method chosen to study the small signal stability of each test case in this paper is that of eigenanalysis. References [1] and [2] report extensively on this method of analysis.

SYSTEM CONFIGURATION

Remote communities often have electrical power networks that are connected to a large power system grid via a long transmission line. Such communities will often have a local power station, which supplies power to the local load, while any power deficit/surplus in the local network flows through the transmission line. In order study such a system it seems pragmatic to consider the power station as a single alternator and the local load as a single RL load and/or a single induction motor. For this reason this paper consists of a study of the simple two machine system of Fig 1, which consists of a remote synchronous machine at node 4 connected through a long transmission line to an infinite busbar. The synchronous machine supplies power to a local load bus that is connected via a feeder to node 3. The local load bus is considered to consist of static RL load and/or dynamic induction motor load. The transmission line may or may not have series capacitor compensation. See the Appendix for the machine parameters and the line parameters (unless otherwise specified).

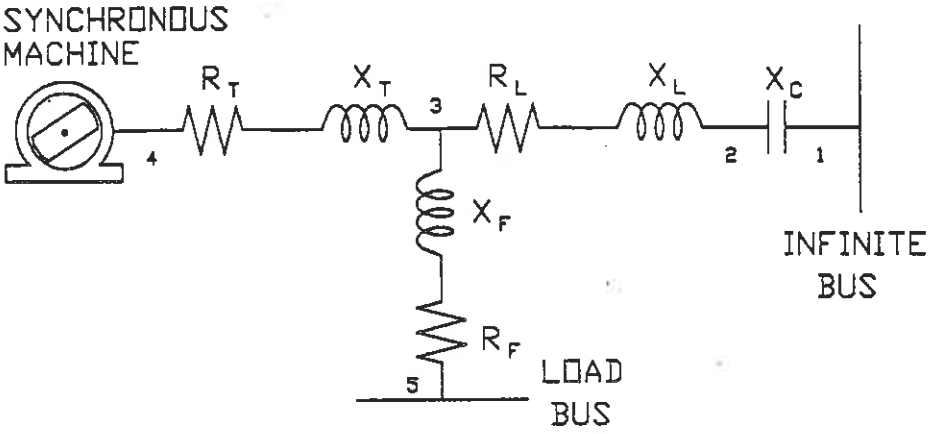

Fig 1 The power system network chosen to investigate the effects of dynamic induction motor loads and/or static RL loads.

RESULTS

The eigenanalysis results are presented in a set of five test cases that are structured in a sequential fashion and are presented in Table 1. Each of the five test cases are performed with the alternator having a lumped-inertial shaft and then with a multi-inertial shaft. Although for the results obtained individual eigenvalues cannot be related directly to particular parts of the system, according to reference [2] certain eigenvalues are influenced more by particular system parameters than others. Thus, for each case the eigenvalues illustrated in Table 1 may be classified into the following categories [1][2]

Group (a) *oscillatory modes close to the synchronous frequency.* These modes of oscillation are associated with the resistor-inductor elements of the network and the stator parameters of the alternator/induction motor.

Group (b) *frequency modes that are associated with the machine torsional system.* These modes define the alternator's/induction motor's rotor response to small disturbances.

Group (c) *real time-constants.* These modes are related to the rotor windings of the generator and induction motor.

For all the test cases analyzed the alternator generates a real power of 0.8 p.u. at a voltage of 1.0 p.u. into the system. Likewise the load bus draws (0.56+j0.30) p.u. power from the network whether the load is an RL load or an induction motor load.

TEST CASE A
No Load Bus and no Series Capacitors

This eigenanalysis is performed using the network of Fig 1, with no series capacitors in the transmission line and with the load bus disconnected from node 3. For, this test case since no capacitive reactance is included the transmission line reactance, X_L, is reduced to 0.5 p.u. (NB. when the capacitive reactance, X_C=–0.5, is included in later test cases X_L is increased to 1.0 p.u.).

The results of this test case clearly illustrate that the differences between the eigenvalues when the alternator's shaft is multi–inertial as apposed to lumped–inertial (for the chosen network) lie in group (b).

TEST CASE B
RL Load Bus and no Series Capacitors

This test case is performed using the same conditions as outlined in test case A, except with a RL load bus connected through a feeder to node 3. Comparison of the results obtained with those of test case A indicate an additional eigenvalue pair, EL, situated in group (a). This additional eigenvalue pair appears at the same position for both multi–inertial and lumped–inertial cases.

TEST CASE C
Induction Motor Load Bus and no Series Capacitors

This test case is performed using the same conditions as outlined in test case A, except with the an induction motor load connected through a feeder to node 3. The inclusion of the dynamic induction motor load yields three further eigenvalues, when compared with test case A. One of these additional eigenvalues, EI, lies in group (a), much the same as is observed with the inclusion of an RL load (ie.case B), but it lies in a different position. This means that the induction machine load has a different effect on the impedance of the network than does the RL load. The other two additional eigenvalues, MI and EI, lie in groups (b) and (c) respectively, and are associated with the responses of the induction machine's rotor inertia and rotor windings respectively [3].

Mode M0 is the hunting mode of the alternator. For both alternator shaft models this mode is more damped for the induction motor load (test case C) than for the RL load (test case B). However, examination of Table 1 shows that, for a multi–inertial shaft, modes M1, M2, M3 are less damped for RL load case than for an induction motor load case, while modes M4 and M5 are the same in both cases.

The magnetic stability mode, M, which becomes unstable if the alternator is operated at excessive values of leading reactive power, is less stable in the RL load case than the induction motor load case

TEST CASE D
RL Load Bus and Series Capacitors

This case is the same as that of test case B, except with the inclusion of series capacitors in the transmission line. The line parameters may be found in the Appendix. In comparison to test case B the inclusion of the series capacitors causes the synchronous flux eigenvalue pair E to 'split in two' to form the 'so called' supersynchronous flux and subsynchronous flux eigenvalue pairs (E1 and E2 respectively). Once again the examination of the relevant cases in Table 1 indicates that both multi-inertial and lumped-inertial cases are similar in groups (a) and (c), but that the modes of group (b) differ. SSR manifests itself in two forms, namely that of Torsional Interaction, TI, and Induction Generator Effect, IGE. TI involves the movement of the mechanical modes of the multi-inertial shaft, of group (b), into the right half plane, while IGE involves the movement into the right half plane of the subsynchronous mode, E2 [2]. From Table 1 it becomes clear that the lumped inertia model is only capable of predicting IGE. Also, since TI usually occurs at a much lower value of capacitor compensation level than IGE the lumped inertia model is not sufficient to predict the critical series capacitor compensation level, beyond which SSR will occur.

TEST CASE E
Induction Motor Load Bus and Series Capacitors

This test case was performed with the same conditions as that of D except with the RL load replaced with an induction motor load, which draws the same power from the network. Once again the inclusion of series capacitors has caused the synchronous mode, E, to be replaced by the supersynchronous and subsynchronous modes, E1 and E2 respectively. For both alternator shaft models the induction motor load yields lower damping values for E1 and E2 than does the RL load. This appears to indicate that as far as IGE is concerned the induction motor load is less stable than the equivalent RL load. On the other hand in order to analyze TI the modes of group (b) have to examined. Table 1 shows that mode M1 is more stable with the induction motor load case than with the RL load case, whereas the reverse is the case when considering modes M2 and M3. In order to make any far reaching conclusions about the instability of RL loads versus induction motor loads eigenvalue loci should be obtained for different values of capacitor compensation.

CONCLUSIONS

When analyzing SSR phenomena it is important to model alternator shaft's correctly. The assumption that an alternator's shaft is lumped inertial means that the SSR torsional interaction phenomena (TI) is neglected.

The eigenanalysis results of this study, up to date, do not demonstrate clearly enough the effects of induction motor loads versus RL loads, but they do imply that the induction motor load is less stable than the RL load. The results do demonstrate the need to model a load bus in the correct manner.

Further research will involve eigenvalue scans in order to determine the critical series capacitor compensation levels for each mode. As far as SSR is concerned this should give an indication as to the errors involved in representing a load bus as an RL load as apposed to as an induction motor load.

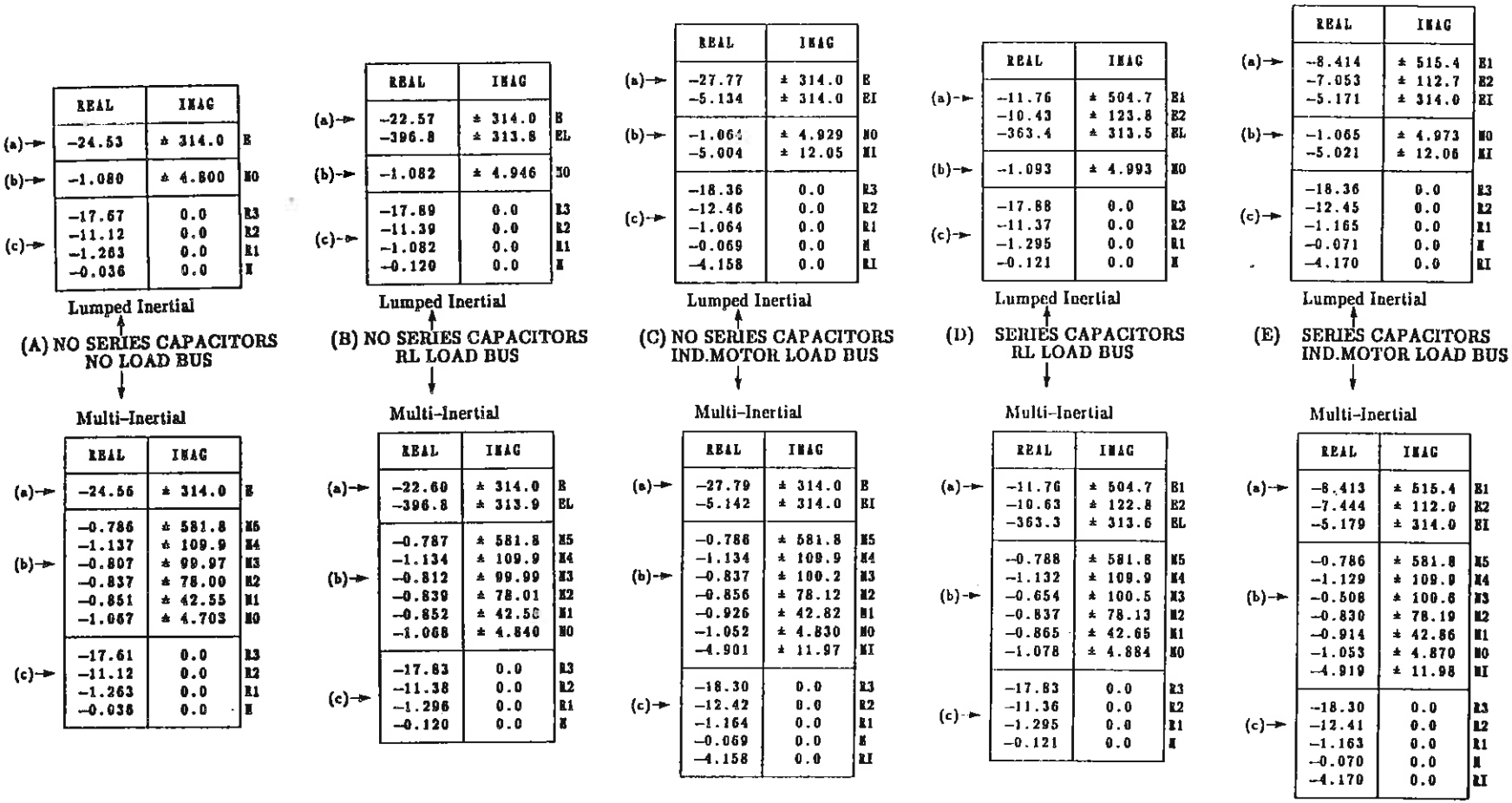

Table 1 Results of five test eigenanalysis test cases performed on the network of Fig 1

APPENDIX

SYNCHRONOUS MACHINE PARAMETERS

r_a	=0.003	p.u.
x_a	=0.22	p.u.
x_{md}	=2.226	p.u.
x_{mq}	=2.06	p.u.
x_f	=0.19	p.u.
r_f	=0.000984	p.u.
x_{kd}	=0.13	p.u.
r_{kd}	=0.015	p.u.
x_{kq1}	=0.59	p.u.
r_{kq1}	=0.00545	p.u.
x_{kq2}	=0.06	p.u.
r_{kq2}	=0.011	p.u.

INDUCTION MACHINE PARAMETERS

r_1	=0.0057	p.u.
x_1	=0.144	p.u.
x_{md}	=3.64	p.u.
r_2	=0.0088	p.u.
x_2	=0.097	p.u.
H	=2.0	secs.
D	=0.0	

Load Characteristic:-
$[0.05 + 0.9\omega^2]$ p.u.

SYNCHRONOUS MACHINE MECHANICAL DATA (modal form)

$\underline{D_m}$ = diag(.5681E–01 .2695E–01 .2006E–01 .1525E–01 .1949E–02 .3626E–03)
$\underline{f_m}$ = diag(.0000E+00 .6681E+01 .1237E+02 .1583E+02 .1749E+02 .9259E+02)
$\underline{J_m}$ = diag(.3616E–01 .1716E–01 .1277E–01 .9712E–02 .1240E–02 .2309E–03)

$$\underline{Q} = \begin{bmatrix} .10000E+01 & .10000E+01 & .10000E+01 & .10000E+01 & .10000E+01 & .10000E+01 \\ -.10000E+01 & -.83391E+00 & -.17435E+00 & .67230E+00 & .95355E+00, & .95881E+00 \\ .10000E+01 & .43028E+00 & -.85274E+00 & -.92504E-02 & .74578E+00 & .76006E+00 \\ -.52021E+00 & -.34693E-01 & .30688E+00 & -.63923E+00 & .96922E+00 & .10000E+01 \\ .10000E+01 & -.13872E+00 & .56328E-01 & -.27280E-01 & .26603E-01 & .27641E-01 \\ .62556E-07 & -.18426E-08 & .28293E-05 & -.40667E-03 & .52110E-01 & -.10000E+01 \end{bmatrix}$$

TRANSMISSION LINE PARAMETERS

$R_L + jX_L$ = (0.06+j1.0) p.u. , X_C = – 0.5 p.u.
$R_F + jX_F$ = (0.001+j0.1) p.u. , $R_T + jX_T$ = (0.001+j0.1) p.u.

REFERENCES

[1] M A Lahoud, 'The Analysis and Control of Synchronous and Asynchronous Machines in Power Systems', PhD thesis, University of Natal, Durban, 1982.

[2] G D Jennings, 'Modeling and Analysis of Turbogenerators in Single Machine and Multi-Machine Subsynchronous Resonance Studies', PhD thesis, University of Natal, Durban, 1987.

[3] G Gross, C F Imparato and P M Look, 'A tool for the Comprehensive Analysis of Power System Dynamic Stability', IEEE Transactions PAS-101, 1982, pp.226-234.

[4] M A Lahoud and R G Harley, 'Transmission Line Resonances as Influenced by Induction Motor Load Modeling in a Multigenerator-Multimotor Power System', Electrical Power Systems Research, July 1984.

EFFECT OF LOAD DIFFERENCES ON ROTOR OSCILLATIONS OF PARALLEL TURBOGENERATORS

G D JENNINGS R G HARLEY

Department of Electrical Engineering
University of Natal

1. ABSTRACT

The damping of torsional oscillations in two parallel generating units using a single common controlled shunt reactor is investigated. The shunt reactance is regulated using either a speed signal from one of the generating units or a combined speed signal from both units. The effect of load differences and torsional mode frequency differences between the units on the performance of a controller designed assuming truly identical units is investigated.

Results indicate that for the controller using only a single generator speed signal as input, it is better for the damping of a particular mode to take the input signal from the generator with the higher mode frequency for that mode. When the generator speed signals are combined to form the controller input, then mode frequency differences do not detract from the controller's performance but load differences do.

Keywords: SSR, Torsional Oscillations, Countermeasures

2. INTRODUCTION

Torsional oscillations in turbogenerators have been the subject of a great deal of research, particularly since the shaft failures at Mohave in the early seventies due to Subsynchronous Resonance (SSR). The potentially destructive nature of these oscillations has resulted in much attention being given to possible countermeasures [1]; the most promising one appears to be the use of a controlled shunt reactor [2-6]; either in the form of one shunt reactor per generator unit or one common reactor for several units.

The majority of studies dealing with torsional oscillations and SSR have dealt with single machine systems. In power stations where there have been two or more parallel identical turbogenerators simulations traditionally lump them into a single equivalent unit [7]. This is particularly true when designing countermeasures for multiple identical units where the computational effort in the design procedure is often drastically increased with additional model complexity [6]. However the equivalent turbogenerator model is a valid simplification only for truly identical units [7] but may be inaccurate even for small differences between the units [5,8,9]. In real systems there are always differences between turbogenerator parameters due to manufacturing tolerances, moreover under unequal loading conditions the damping of nominally identical units may be vastly different.

Differences between the parameters of turbogenerators and in their operating points introduces phase and amplitude variations in their speed signals [5,8,9]. Having each generator with its own shunt reactor and associated controller [6] results in phase and amplitude differences in the generator speed signals being inconsequential to the performance of the controllers, however the costs of such a scheme render it impractical. The alternative is a single shunt reactor serving several generators in parallel and which is controlled by a speed signal either from only one of the generators [5] (single speed controller) or a combination of speed signals from all the generators [6] (multi speed controller). Reference [5] showed that phase variations between generator speed signals caused by unequal loading could cause a shunt reactor with single speed controller to further excite torsional oscillations in one of the turbogenerators.

Reference [5] considered only load differences between two identical units which have a common shunt reactor with a single speed controller while Ref [6] considered a shunt reactor with multi speed controller but assumed only truly identical units. This paper extends the understanding in this area by considering the effects of differences in torsional mode frequency between parallel generators on the operation of a single speed controller as well as investigating the effect of load differences and frequency differences on a shunt reactor with multi speed controller.

This paper is not concerned with the design of controllers but uses a controller designed previously for truly identical units using optimal output feedback techniques [6] and considers its performance when the generators are not truly identical.

The analysis is performed using a multi-machine program that includes full d,q modelling of generators, modelling of network transients, shunt reactors and their associated controllers and a modal representation [10] of turbogenerator shaft dynamics. It is important to note that this modal representation is not the "single mode at a time" type of analysis described as the "modal method" in Ref [3] but is equivalent to the "all modes method" mentioned in Ref [3] and does consider the coupling between the different torsional modes.

The modal representation has a distinct advantage in this study over the conventional model of lumped inertias interconnected by flexible shafts since it is not possible with the conventional model to make independent changes in individual mode parameters; changing any parameter in the conventional model alters all the parameters of all the modes. Hence it is not possible with the conventional model to investigate small differences in mode frequency alone while all other shaft parameters stay the same. This limitation is overcome by the direct use of the modal representation in the multi-machine program.

Transient and eigenvalue calculations are performed to predict the performance of the two control strategies (single speed controller and multi speed controller) when the turbogenerators are not truly identical. Results show that if a shunt reactor with single speed controller is used and there is a difference in mode frequencies between the generators then it is preferable (for the stabilization of a particular mode) to take

the speed signal from the generator with the higher mode frequency. Furthermore, for a shunt reactor with multi speed controller, mode frequency differences do not have much affect on the operation of the controller but unequal loading (damping differences) may cause the anti-modes to become unstable.

3. THEORY

Figure 1 shows a schematic diagram of the system studied. It consists of two 1072 MVA turbogenerators connected through a single transmission line to an infinite busbar with a common shunt reactor at the terminals of the generators.

3.1 Generator Electrical Model

The method of analysis used in the multi-machine program is based on an earlier scheme [11] which allowed the systematic modelling of line transients and machine dynamics and was extended to investigate small-signal stability.

Each generator is represented by the well known [12] two-axis model with one d-axis and two q-axis damper circuits. However, in the two-generator system, the d-q axes of the individual generators rotate at different speeds so the stator variables of the generators are therefore transformed into a common synchronously rotating reference frame. Variables inside each generator are analyzed in the particular machine's own rotor reference frame.

In the common reference frame each generator is represented by the stator phase resistance in series with an equivalent inductance and an equivalent nonlinear voltage source which does not neglect stator transformer-voltage and speed-voltage terms. Readers are referred to Ref [13,14] for a detailed description of the generator modelling.

3.2 Shunt Reactor Controller

The modulated inductance L_s of a controlled shunt reactor can be written as [4]:

$$L_s = L_{sn}(1+u_s) \qquad u_s \geq -0.5 \tag{1}$$

where u_s is the output of the shunt reactor controller and L_{sn} is the nominal value of the shunt inductance. The method for determining the size of X_{sn} (or L_{sn}) is described in Refs [4,6,15] and in this case X_{sn} is calculated as 3.64 pu corresponding to a steady-state rating for the shunt reactor of 295 MVA and a peak rating of 590 MVA.

The controller is modelled in state space form as:

$$p\underline{z} = [A_c]\underline{z} + [B_c]\underline{u_c} \tag{2}$$

where $\underline{z}$ are the controller states and $\underline{u_c}$ is an input vector of generator speed deviations. The output of the controller is given by:

$$u_s = \underline{C_c}^t\underline{z} + \underline{D_c}^t\underline{u_c} \tag{3}$$

The controller is designed using optimal output feedback techniques assuming a single equivalent turbogenerator and is fully described in Refs [6,15]. The controller parameters obtained from the design are:

$$[A_c]=\begin{bmatrix}-52.5 & 0\\ -5760 & -600\end{bmatrix},\ [B_c]=\begin{bmatrix}0.5 & 0.5\\ 192 & 192\end{bmatrix},\ \underline{C_c}=\begin{bmatrix}9.6\\ 2\end{bmatrix},\ \underline{D_c}=\begin{bmatrix}-0.32\\ -0.32\end{bmatrix}$$

For only a single speed controller, $[B_c]$ becomes a vector and $\underline{D_c}$ a scalar such that:

$$\underline{B_c}=\begin{bmatrix}1\\ 384\end{bmatrix} \qquad D_c = -0.64$$

A detailed description of how the shunt reactor is included in the network state equations is given in Ref [13].

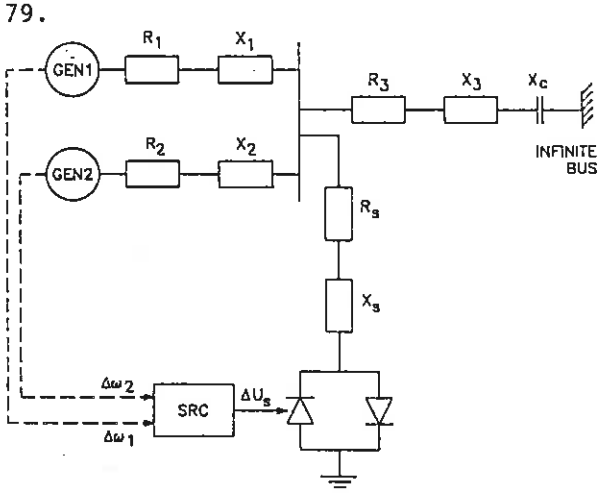

Fig 1 Two generator – one shunt reactor system.

3.3 Generator Mechanical Model

The mechanical system of each turbogenerator is described using a modal shaft representation; the derivation and description of which has been presented in Refs [10,13]. In the modal model, the shaft dynamic behavior is described by 'n' 2nd order differential equations where 'n' is the number of modes and each equation describes the dynamics of a particular mode.

It should be stressed that this modal representation is equivalent to the "all-modes method" mentioned in Ref [3] where instead of entering into the program shaft stiffnessess and inertias for an interconnected spring-mass model, the mechanical parameters are read in as frequency, damping, inertia and mode shape of each torsional mode. In this respect the torsional modes are decoupled when the machine is not synchronized but in the eigenvalue and transient studies when the turbogenerator is synchronized, all the modes are analyzed simultaneously and are coupled through the electrical network.

The dynamics of mode 'i' is described by [10]:

$$p^2q_i + 2\sigma_i pq_i + (2\pi f_i)^2 q_i + \underline{Q}_i^t\underline{T}/J_{mi} = 0 \tag{4}$$

where: q_i is the mode angle
f_i is the mode frequency
σ_i is the mode damping
J_{mi} is the mode inertia
$\underline{Q}_i$ is the mode shape vector

and $\underline{T}$ is a forcing torque vector comprising the mechanical torques from the turbine stages and the generator electrical torque. The physical shaft angular displacements (speeds) can be determined from a weighted combination of the mode angular displacements (speeds) with the weightings determined by the mode shape vectors.

3.4 Method of Analysis

The state equations of the generator electrical and mechanical systems are combined with the state equations of the network and shunt reactor controller to form the non-linear state-space formulation of the entire system [13]. These state-space equations are used to perform non-linear transient simulations.

For small-signal studies the state equations of the entire system are linearized about a steady-state operating point [13]. The linearized equations are used to calculate the eigenvalues

and eigenvectors of the system. From the eigenvectors the generators' mechanical mode shapes are extracted and these illustrate the difference in amplitude and phase between the generator rotor speed oscillations. These differences are presented as the phase deviation, θ, being the angle of gen–1 rotor speed oscillations w.r.t gen–2 rotor speed oscillations, and the amplitude ratio, Δ, defined as:

$$\Delta = 100(AMP1 - AMP2)/AMAX \quad \% \qquad (5)$$

where AMP1 = amplitude of gen–1 rotor speed oscillations
AMP2 = amplitude of gen–2 rotor speed oscillations
AMAX = maximum of AMP1 and AMP2

Δ therefore varies from +100% when gen–2 has zero amplitude of oscillation in the particular mode to –100% when gen–1 has zero amplitude of oscillation in that mode. A value of 0% indicates that the generators have equal involvement in the mode.

4. RESULTS

4.1 Identical Generators

As an initial study the two generators are considered to be both identical and at the same operating point with a terminal active power of 0.6 pu and a terminal voltage of 1.1 pu; for all calculations the infinite busbar voltage is 1.0 pu.

The system eigenvalues are calculated both with and without the controller in operation as the compensation level ($100.X_c/X_3$ % in Fig 1) is varied from 20% to 100% and a few of the relevant eigenvalue loci are shown in Fig 2. The loci calculated without the controller are labelled –C while those calculated with the controller are labelled +C. The anti–modes (labelled A) are the same, both with and without the controller and are unaffected by changes in the compensation level. This is expected since for identical machines at the same operating point the anti–mode oscillations are equal in magnitude and 180° out of phase. The controller is clearly effective in stabilizing the torsional modes, since for each of the three modes it moves the entire locus of eigenvalues completely into the left–half plane.

In order to verify the small–signal calculations, the transient response of the system was calculated with and without the controller for a temporary 10% drop in the infinite busbar voltage at a compensation level of 90% and the resulting rotor speed deviations are shown in Fig 3. At this compensation level the eigenvalues predict an unstable mode 1 without the controller (mode 1 eigenvalue = 1.69 + j42.4) and this is evident in the transient results in Fig 3.

The results in this section pertaining to the system with a controller were calculated with a single speed controller. However, they are identical to those that would be obtained with a multi speed controller since the generator rotor speed oscillations are identical and thus taking the sum of the two speeds is the same as taking twice one of their speeds.

4.2 Non–Identical Generators – Single Speed Controller

Difference in damping: As a first dissimilarity between the two generators in Fig 1 we consider a difference in their damping since this is the most obvious difference that occurs due to different degrees of loading. Generator 1 has just been synchronized (0.01 pu power) while generator 2 is operating at high load (0.9 pu power). The assumed mode dampings of gen–1 are all 0.0 s^{-1} while those of gen–2 are 0.4 s^{-1}.

Figure 4 shows the amplitude ratio and phase deviation of the common modes for the system without a controller as the compensation level is varied from 20% to 100%. Mode 2 is the most affected by the damping difference with up to 60° phase deviation between generator speed signals and 60% difference in their amplitudes.

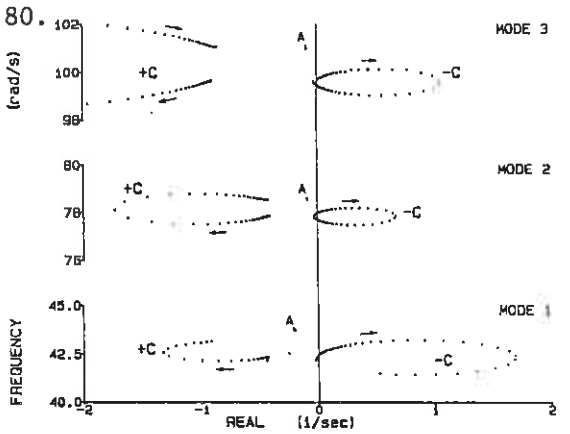

Fig 2 Eigenvalue loci as the compensation level ($100.X_c/X_3$ in Fig 1) is varied from 20% to 100%
A – Anti modes both with and without controller
+C – Common modes with controller in operation
–C – Common modes without controller in operation.

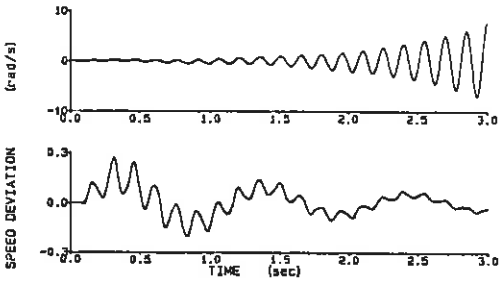

Fig 3 Generator rotor speed deviation of identical units at the same operating point subjected to a temporary 10% drop in the infinite bus voltage at a compensation level of 90%; top – no controller; bottom – with controller.

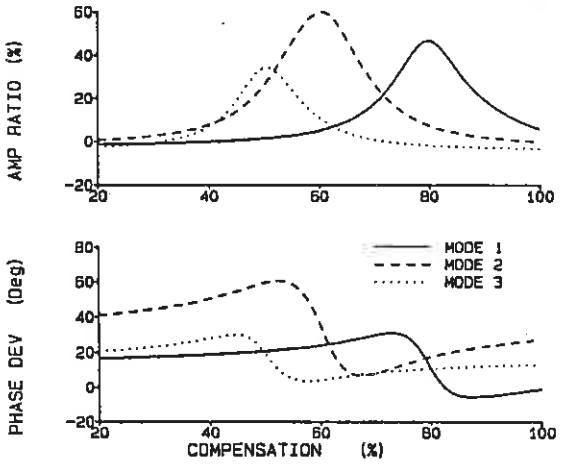

Fig 4 Amplitude ratio and phase deviation as a function of compensation level when gen–1 is supplying 0.01 pu real power (assumed mode dampings 0.0 s^{-1}) and gen–2 is supplying 0.9 pu real power (assumed mode dampings 0.4 s^{-1}).

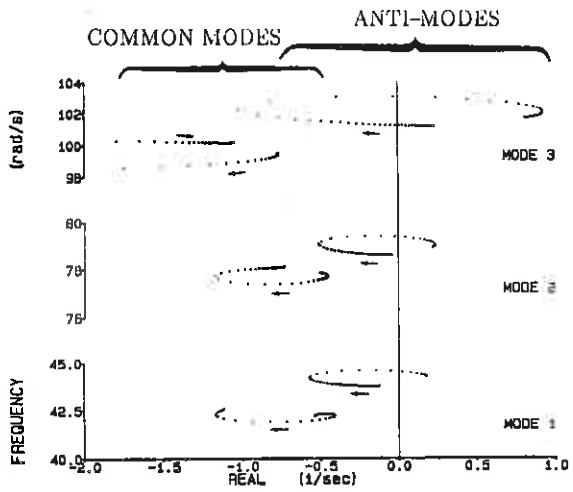

Fig 5 Eigenvalue loci calculated with a single speed controller using gen-1's rotor speed as input when the generators are at unequal loads as in Fig 4.

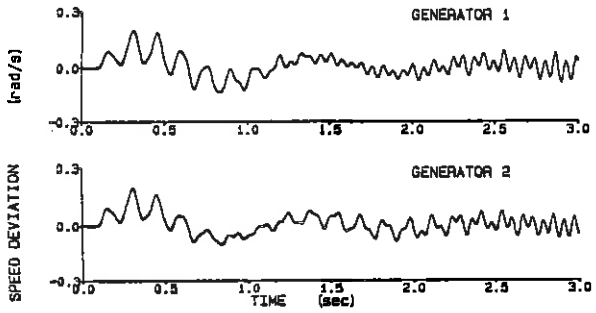

Fig 6 Generator rotor speed deviations for a temporary 10% drop in the infinite bus voltage at a compensation level of 90% when there is a single speed controller using gen-1's rotor speed in service and the generators are at unequal loads as in Fig4.

The eigenvalue loci calculated for the same compensation level variation when the single speed controller is in operation using the gen-1 rotor speed deviation signal as input are shown in Fig 5. The phase and amplitude difference in the speed signals has clearly detracted from the operation of the controller and it now has a destabilizing effect on the anti-modes indicated by their movement towards and into the right-half plane. Mode 3 is now unstable at both low and high compensation levels (since it starts and ends in the right-half plane).

The eigenvalue calculations are again verified by calculating the transient response of the system for a temporary 10% drop in the infinite busbar voltage at a compensation level of 90%. The eigenvalues predict mode 2 and mode 3 unstable (0.24+j78.9 and 0.86+j101.7 respectively) and this is confirmed in the generator rotor speed deviation signals shown in Fig 6.

Using generator-2's speed deviation (rather than that of generator-1) as the input signal to the controller also results in all three modes being destabilized. The results in this section have illustrated the severe adverse affect which differences in damping can have on the operation of a shunt reactor with single speed controller being used to damp oscillations in multiple units; they agree with those reported in Ref [5].

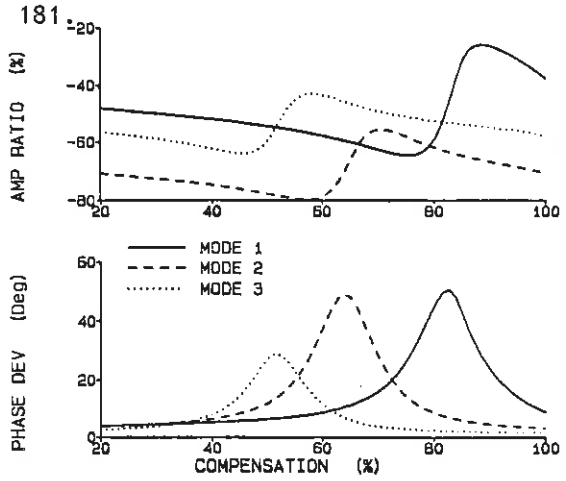

Fig 7 Amplitude ratio and phase deviation as a function of compensation level when the generators are at the same operating point but gen-2's mode frequencies are 0.2 Hz lower that those of gen-1.

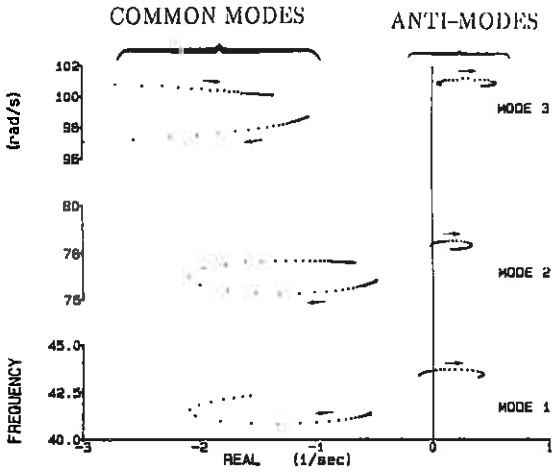

Fig 8 Eigenvalue loci calculated for a single speed controller using gen-2's rotor speed as input when the generators are at the same operating point but gen-2's mode frequencies are 0.2 Hz lower than those of gen-1.

Difference in frequency: Differences in mode frequency between nominally identical units occur due to manufacturing tolerances and values up to 0.2 Hz are not uncommon. These differences appear small and it is tempting to consider them insignificant, especially against the large damping differences that occur.

To investigate the effects of frequency difference, gen-2's mode frequencies are all reduced by 0.2 Hz from their values quoted in the Appendix. The amplitude ratio and phase deviation of the common modes are shown in Fig 7 as the compensation is varied from 20% to 100%. As in the case of damping differences we see large variations between the amplitude and phase of the rotor speed signals with mode 2 showing up to 80% difference in amplitudes and mode 1 up to 50° phase deviation.

Figure 8 shows the eigenvalue loci, calculated for the same compensation level variation, when the single speed controller using the gen-2 speed deviation signal as input is in operation.

As in the case with damping differences, the controller causes destabilization of the anti-modes but the system stability is even worse in this case with mode 3 being unstable over the entire compensation range.

The eigenvalue calculations are again verified by calculating the transient response of the system for a temporary 10% drop in the infinite busbar voltage at a compensation level of 90%. The eigenvalues predict all 3 modes unstable (0.37+j43.7, 0.23+j78.2 and 0.48+j100.66) and this is confirmed in the generator rotor speed deviation signals shown in Fig 9.

In the case of damping differences the results were not significantly affected by which generator speed deviation signal is used as an input to the controller; this is not the case for frequency differences. Fig 10 compares the real part of the anti-modes (most undamped modes) when gen-1's speed is used as the control input (top) with the case when the control input is taken from gen-2 instead (bottom). Clearly using the higher frequency generator speed signal yields a more stable system with only mode 1 going unstable over a small compensation range. Thus if it is wished to implement a system with a common controller that uses only a single generator speed signal to damp oscillations in multiple units, then these results indicate that for the stabilization of a particular mode it is beneficial to take the control signal from the generator with the highest mode frequency. In a real system it is likely that one generator will have some mode frequencies higher and others lower in which case it would probably be best to take the control signal from the generator with the highest mode frequency for the most troublesome mode. Further studies are needed though to determine whether this result holds in general or whether it is peculiar to this particular controller and system.

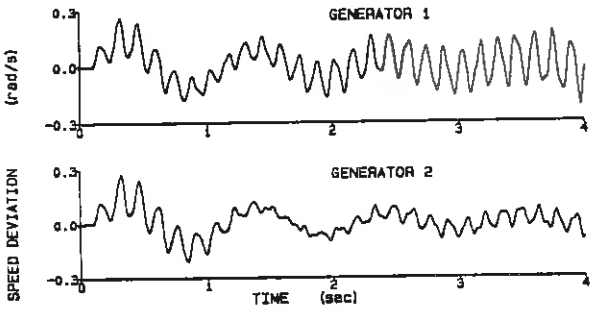

Fig 9 Generator rotor speed deviations for a temporary 10% drop in the infinite bus voltage at a compensation level of 90% when there is a single speed controller using gen-2's rotor speed in service and the gen-2's mode frequencies are 0.2 Hz lower than those of gen-1.

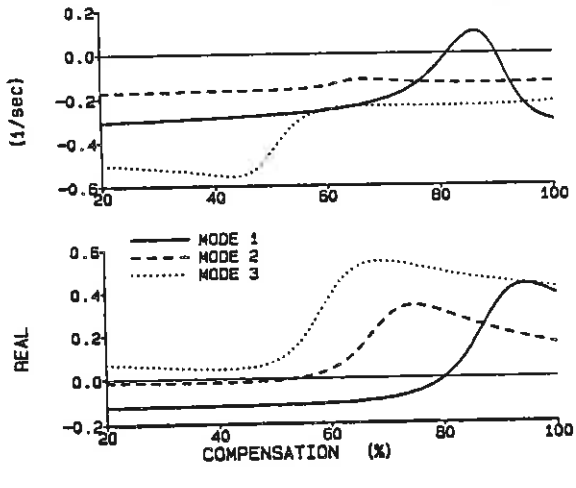

Fig 10 Real parts of anti-modes calculated for a single speed controller using gen-1's rotor speed as input (top) and gen-2's rotor speed as input (bottom), when gen-2's mode frequencies are 0.2 Hz lower than those of gen-1.

4.3 Non-Identical Generators – Multi Speed Controller

Consider now the case where both generator speeds are used to form the input to the common controller. Such a controller was designed in Ref [6] assuming identical units but was not tested for the case of dissimilarities between the generators. The previous section has shown that differences between the generators causes a phase shift and amplitude difference in their speeds. It may be argued that the phase deviation between the speed signals will cause a certain amount of cancellation in the summation of these signals to form the input to the controller and will therefore detract from the effectiveness of the controller.

Another line of thought is that any cancellation which occurs when the generator speed signals are summed will be matched by a corresponding cancellation when the generator armature currents sum together at the common high voltage busbar. Thus the input signal to the controller will always be representative of the current flowing into the network from the power station and it is that current which interacts with the transmission line resonances. This theory suggests that phase and amplitude differences between the speed signals should not effect the operation of the controller.

Difference in damping: Figure 11 shows the eigenvalue loci calculated for the same damping difference and compensation variation as in the previous section but with the multi speed controller. The common mode damping is practically identical to that obtained with identical generators (see Fig 2) thus supporting the notion that the summation of the generator speed signals corresponds to the summation of the armature currents resulting in the input signal to the controller being proportional to the current flowing in the transmission line.

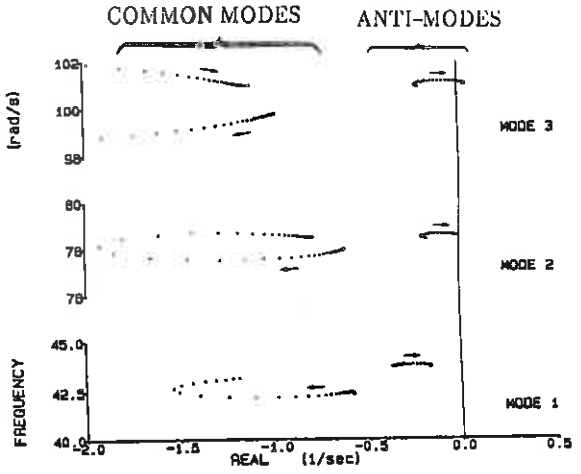

Fig 11 Eigenvalue loci calculated for a multi speed controller when generator-1 is supplying 0.01 pu real power (assumed mode dampings 0.0 s^{-1}) and generator-2 is supplying 0.9 pu real power (assumed mode dampings 0.4 s^{-1}).

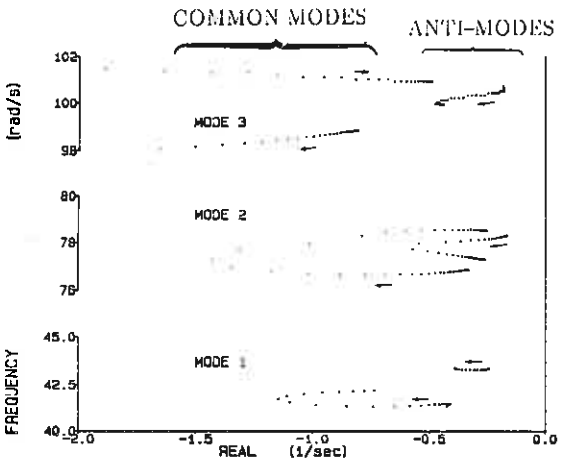

Fig 12 Eigenvalue loci calculated for a multi speed controller when gen-2's mode frequencies are 0.2 Hz less than those of gen-1.

There is however a marked reduction in damping of the anti-modes (seen by the movement of the anti-modes towards the right-half plane) and mode 3 does in fact go unstable at a very high compensation level, however it is a marked improvement on the single speed controller result in Fig 5.

Difference in frequency: A different situation exists when there is a mode frequency difference between units as seen in Fig 12. In this case the system is stable over the whole compensation range.

Results in this section have shown that even if the generator speed signals are summed to form the controller input, phase and amplitude variations between the generator speed signals may cause the anti-modes to go unstable.

5. CONCLUSIONS

This paper has investigated the damping of SSR oscillations in a power station with two generating units using a single common controlled shunt reactor at the high voltage bus when there are dissimilarities between the generating units. The dissimilarities include differences in damping that may occur due to unequal loading and differences in torsional mode frequency due to manufacturing tolerances.

The controller used in this paper was designed assuming identical generators and using optimal output feedback techniques. The input to the controller was considered to be either a single speed deviation signal from one of the generators or a combination of the two generator speed deviation signals. Eigenvalue and transient results show that for this system and controller designs :

(a) The controller with only a single speed signal from one of the two generator rotors as input is effective when the machines are identical but may be ineffective when there are differences between the generators which cause phase and amplitude variations in their speeds.

(b) If a single generator speed signal is used as input to the controller and there is a difference between the generator's mode frequencies, then a mode is more effectively damped if the speed signal is taken from the generator with the higher mode frequency.

(c) Using an input signal to the controller comprising the sum of the two generator speed signals enables the controller to be effective even with phase and amplitude differences between the generator speed signals caused by mode frequency differences. However in the case of damping differences, the controller causes a reduction in the damping of the anti-modes and may result in them becoming unstable.

Further studies are needed to determine the extent to which these results are peculiar to the particular system and controller. It is clear though that assuming identical units in the design of the controller leads to unacceptable errors. The control problem of non-identical units can be overcome by a single shunt reactor and controller for each unit [6]. An alternative is to use a design procedure which takes into account uncertainties in system parameters. Such a procedure using Quantitative Feedback Theory techniques is described in Ref [16].

6. REFERENCES

[1] IEEE Subsynchronous Resonance Working Group, "Countermeasures to Subsynchronous Resonance Problems", IEEE Trans, Vol PAS-99, pp 1810-1818, 1980.

[2] O Wasynczuk, "Damping Subsynchronous Resonance using Reactive Power Control", IEEE Trans, Vol PAS-100, pp 1096-1104, 1981.

[3] A E Hammad and M El-Sadek, "Application of a Thyristor Controlled Var Compensator for Damping Subsynchronous Oscillations in Power Systems", IEEE Trans, Vol PAS-103, pp 198-212, 1984.

[4] T H Putman and D G Ramey, "Theory of the Modulated Reactance Solution for Subsynchronous Resonance", IEEE Trans, Vol PAS-101, pp 1527-1535, 1982.

[5] M R Iravani, "Torsional Oscillations of Unequally-Loaded Parallel Identical Turbine-Generators", IEEE Trans, Vol PS-4, No 4, 1989.

[6] J C Balda, R G Harley, E Eitelberg, "Damping Torsional Oscillations in Two Interacting Neighbouring Turbogenerators", IEEE Trans, Vol EC-2, No 1, pp 108-115, 1987.

[7] G D Jennings, R G Harley, D C Levy, "Subsynchronous Resonance of a Power Station With Two Identical Generating Units", IEE Proc, Vol 133, Pt.C, No 1, pp 33-43, 1986.

[8] D N Walker, C E J Bowler, D H Baker, "Torsional Dynamics of Closely Coupled Turbine-Generators", IEEE Trans, Vol PAS-97, pp 1458-1466, 1978.

[9] G D Jennings and R G Harley, "Torsional Interaction Between Non-Identical Turbine Generators", IEEE Transactions on Power Systems, Vol 5, No 1, pp 133-139, Feb 1990.

[10] G D Jennings, R G Harley, D C Levy, "Sensitivity of Subsynchronous Resonance Predictions to Turbo-Generator Modal Parameter Values and to Omitting Certain Active Subsynchronous Modes", IEEE Trans, Vol EC-2, No 3, pp 470-479, 1987.

[11] N Jaleeli-Parshci, E Vaahedi and D C Mac-Donald, "Multi Machine System Transient Behaviour" IEEE 1977 PICA Conference, Toronto, Canada, pp 51-58.

[12] B Adkins, R G Harley, "The General Theory of Alternating Current Machines: Application to Practical Problems", Chapman and Hall, London, ISBN 0-412-15560-5, 1975.

[13] G D Jennings, "Modelling and Analysis of Turbogenerators in Single Machine and Multi-Machine Subsynchronous Resonance Studies", PhD Thesis, University of Natal, Durban, South Africa, 1987.

[14] M A Lahoud and R G Harley, "Analysis Techniques for the Dynamic Behaviour of a Mulitgenerator System", Transactions SAIEE (South Africa), Vol 74, Part4, pp 83-87 ,1983.

[15] J C Balda, "Subsynchronous Resonance of Turbogenerators with Particular Reference to a few Selected Countermeasures", PhD Thesis, University of Natal, Durban, South Africa, 1985.

[16] E Eitelberg, J C Balda, E S Boje and R G Harley, "Stabilizing SSR Oscillations with a Shunt Reactor Controller for Uncertain Levels of Series Compensation", IEEE Transactions on Power Systems, Vol 3, No 3, pp 936-943, Aug 1988.

7. APPENDIX

Generator electrical parameters (base MVA = 1072):

X_d	=2.466 pu	X_{kd}	=0.13 pu	X_{kq1}	=0.59 pu
X_q	=2.28 pu	R_{kd}	=0.015 pu	R_{kq1}	=0.00545 pu
X_a	=0.22 pu	X_{fd}	=0.19 pu	X_{kq2}	=0.06 pu
R_a	=0.003 pu	R_{fd}	=9.84E-4 pu	R_{kq2}	=0.011 pu

Mechanical parameters (base MVA = 1072):

Mode	Frequency (Hz)	Inertia (pu)
0	0.0	0.036
1	6.68	0.017
2	12.37	0.012
3	15.84	0.0097

Mode shapes:

Mode	HP	LP1	LP2	LP3	GEN	EXC
0	1.00	1.00	1.00	1.00	1.00	1.00
1	-1.00	-0.83	-0.17	0.67	0.95	0.96
2	1.00	0.43	-0.85	-0.01	0.75	0.76
3	0.52	0.03	-0.31	0.64	-0.97	-1.00

Torque:

dist(%)	33.7	21.6	18.8	25.9	0.0	0.0

Transmission system parameters (base MVA = 1072):

R_1	$=R_2$ =0.001 pu	X_1	$=X_2$ =0.13 pu
R_3	=0.092 pu	X_3	=1.003 pu
R_s	=0.0052 pu	X_s	=3.64 pu

THE ON SITE LEAKAGE CURRENT PERFORMANCE OF INSULATORS OF VARIOUS DESIGNS AND MATERIALS AS A FUNCTION OF WEATHER DATA

J.P. Holtzhausen, O.C.T. Potgieter & J.M. Smith

University of Stellenbosch, South Africa.

In order to evaluate the effect of coastal pollution on power line insulators an insulator test station was established on the west coast of South Africa about 250 km from Cape Town. The station is in a winter rainfall area with build-up of pollution during the dry summer months.

The 30 minute highest leakage currents are stored on a continuous basis together with weather data using a dedicated microprocessor based data logger. Insulators of different designs, materials and specific creepage lengths (including synthetic composite insulators), are used as test samples.

Results of a period longer than a year are presented and interpreted together with the relevant weather data. The effects of humidity and natural rain washing are confirmed. The ageing of materials is also analysed.

INTRODUCTION:

This paper reports on the continued operation of the pollution leakage current monitoring station at Elandsbaai. As was earlier reported [1], this station is at a site where severe saline coastal pollution is prevalent. The highest leakage current pulse occuring on each insulator during each 30 minute interval is stored in RAM until downloaded to a portable computer at three weekly intervals.

The main objective of this project is to collect data on leakage current activity. The performance of different types of insulators and different materials will thus be compared in a harsh environment. The results will be analysed in terms of the performance and ageing of the different insulators.

PROGRESS:

Fairly successful operation of the station was achieved during the past year. The site was visited seven times between December 1989 and June 1990. The weather data obtained from the weather station

was unreliable but data was fortunately available from an agricultural weather station 10 km away.

Details of the test insulators and their performance since commissioning of the station in May 1989 is given in Table 1.

TABLE 1: PERFORMANCE OF INSULATORS AT ELANDSBAAI:

POSITN.	INSULATOR NAME	NO OF SHEDS	CREEPAGE LENGTH	mm/KV	DATE OF SUSP.	DATE OF F/O	I-MAX [A]	I-H [A]	TIME TO F/O (mnths)
1	PORC LONGROD(160/60)	17/22	1748	25.69	19/05/89	09/11/89	2.8	F/O	5.7
		22/22	2880	33.26	09/11/89(a)		4.7	1	
2	PORC LONGROD(160/60)	13/22	1701	19.65	19/05/89	15/08/89	1.6	F/O	3
		13/22	1701	19.65	21/09/89(e)	26/10/89	1.6	F/O	1
		22/22	2880	33.26	09/11/89(a)		4.7	1.1	
3	CYCLO-ALIPHATIC	FULL	2290	26.44	19/05/89	01/12/89	3.0	F/O	6.3
			2290	26.44	03/01/90(b)	15/05/90(d)	3.0	F/O	4.5
4	SILICON RUBBER	17/17	2700	25.24	19/05/89		2.7	0.1	
5	PORC TRACTION LR	2x12	2060	23.78	19/05/89	09/11/89	2.4	F/O	5.7
		2x12+6	2575	25.75	09/11/89(a)		2.8	0.85	
6	PORC TRACTION LR	1x12+8	1717	19.82	19/05/89	26/10/89	1.7	F/O	5.7
		3x12	3090	35.68	09/11/89(a)		5.4	0.5	
7	EPR ?	FULL	2225	25.99	19/05/89	19/01/90(d)	2.9	F/O	5.2
8	EPR ?	FULL	1960	22.63	19/05/89	22/06/89(d)	2.2	F/O	1
9	STD GLASS C & P	7	7x280	22.63	24/05/89	09/11/89	2.2	F/O	5.5
		9	9x280	29.1	09/11/89(a)	03/01/90	3.6	F/O	1.8
		9	9x280	29.1	03/01/90		3.6	0.5	
10	STD GLASS C & P	6	6x280	19.4	24/05/89	09/11/89	1.6	F/O	5.5
		8	8x280	25.86	09/11/89(a)	01/12/89	2.8	F/O	<1.0
		8	8x280	25.86	03/01/90(c)	09/02/90(d)	2.8	F/O	2
11	STD GLASS C & P (GREASED)	7	7x280	22.63	24/05/89		2.2	0.1	
12	STD GLASS C & P (GREASED)	6	6x280	19.4	24/05/89		1.6	0.1	

(a): CREEPAGE LENGTH INCREASED & CLEANED
(b): CLEANED & RE-ENERGISED AFTER F/O
(c): ONE DISK REPLACED
(d): DISCONNECTED AFTER F/O
(e): NEW INSULATOR FITTED AFTER F/O

Insulators 7 and 8 are composite synthetic insulators of unknown origin. Initially, frequent flashovers occurred and it was soon necessary to increase the creepage length of most of the insulators. The insulators are protected by series explosive fuses that disconnect an insulator from the supply when the current exceeds a value of the order of 1 ampere. The leakage current activity versus time for various insulators are given together with the weather data in figures 1 and 2.

A major maintenance operation of the station was undertaken during September 1990 and at the same time new insulators were suspended. At the time the surface of the insulators were inspected.

DISCUSSION OF RESULTS:

With reference to Table 1, it is generally accepted that flashover is inevitable if the leakage current exceeds I-max, given by

$$I\text{-max} = ((mm/kV)/15,32)^2.$$

In this equation "mm/kV" refers to the specific creepage length measured along the surface of the insulator and the highest line to line voltage of the three phase system on which the insulators are used. As has been mentioned, it was necessary to increase the specific creepage length on some insulators.

It will be noted that the best performance is given by the silicon grease coated glass cap and pin insulators and the silicon rubber insulators. This can be ascribed to the water repellency of the silicon rubber and grease. During inspection the silicon rubber insulators appeared to be water repellent despite a visibly polluted and weathered appearance. This has also been reported by Kindersberger [2], who also claims that silicon rubber regains its hydrophobicity after a resting period.

The surface of the cyclo-aliphatic insulators became rough during weathering and therefore easily wettable. As the full length of the cyclo-aliphatic insulator was used it was unfortunately not possible to increase its specific creepage length.

It should be noted that insulator no. 3 (cyclo-aliphatic) was only re-energised a month after the start of the cycle represented in figure 1 (d). As the cyclo-aliphatic insulator failed on day 77 of the second time period, a spike was apparently produced which was also registered by the other channels. Another explanation is that a severe pollution event occurred that affected all insulators.

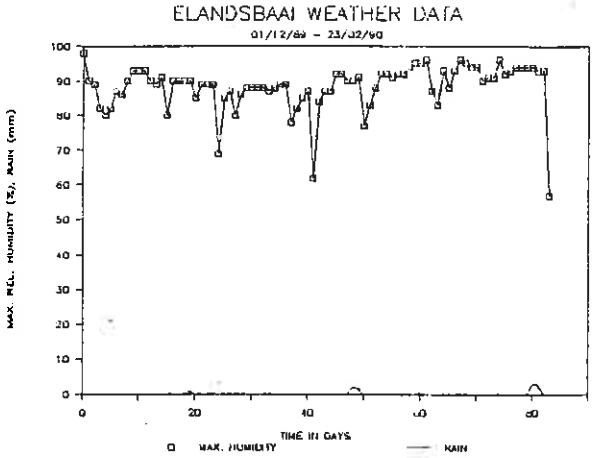

a) Weather data

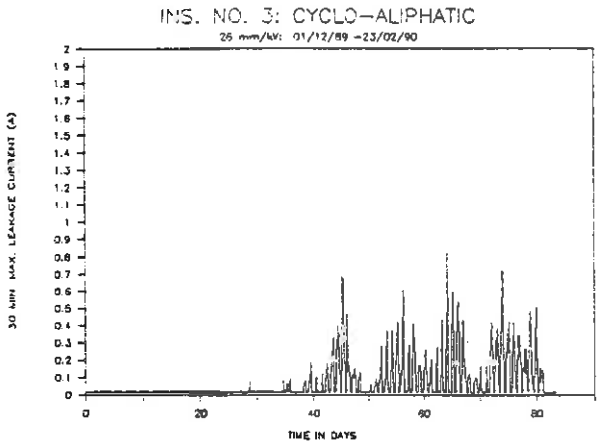

d) Cyclo-aliphatic insulator

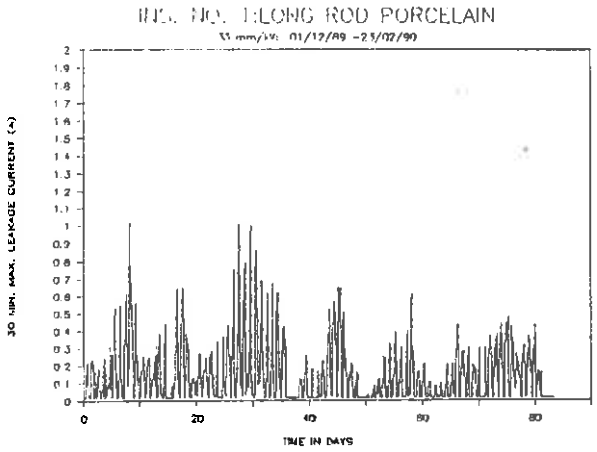

b) Porcelain long rod insulator

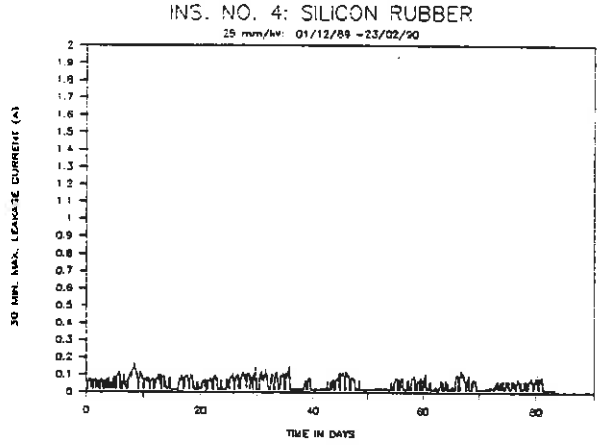

e) Silicon rubber insulator

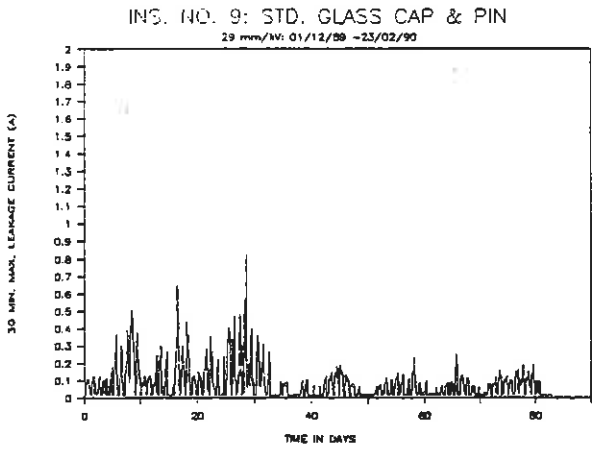

c) Cap and pin insulator

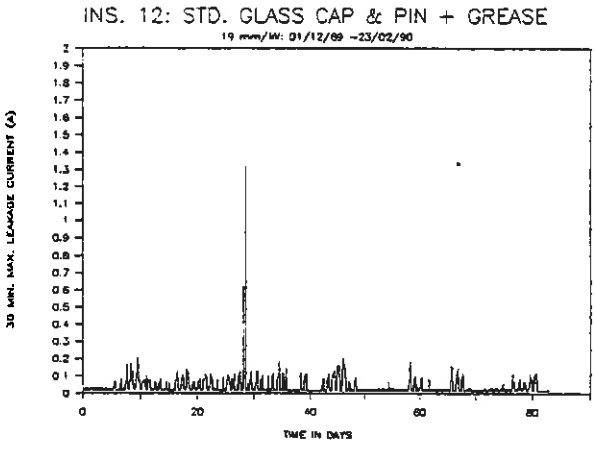

e) Cap and pin ins. (greased)

Fig. 1: Weather data and leakage currents for period 01/12/89 - 23/ 02/ 90.

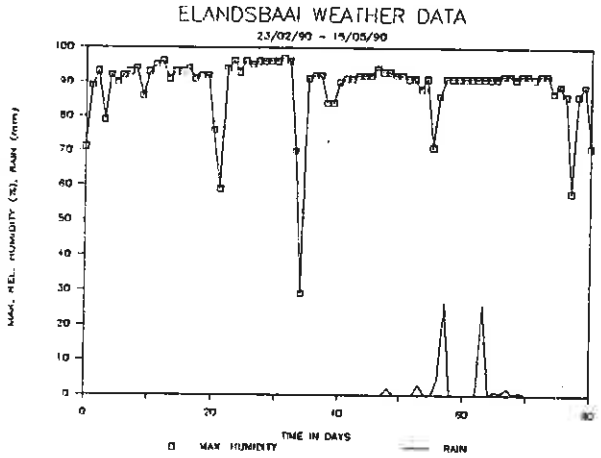

a) Weather data

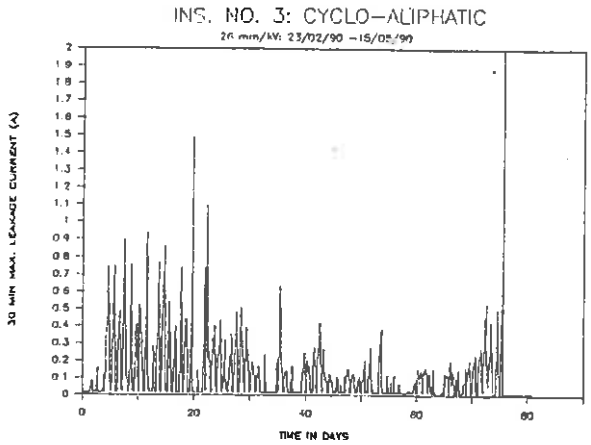

d) Cyclo-aliphatic insulator

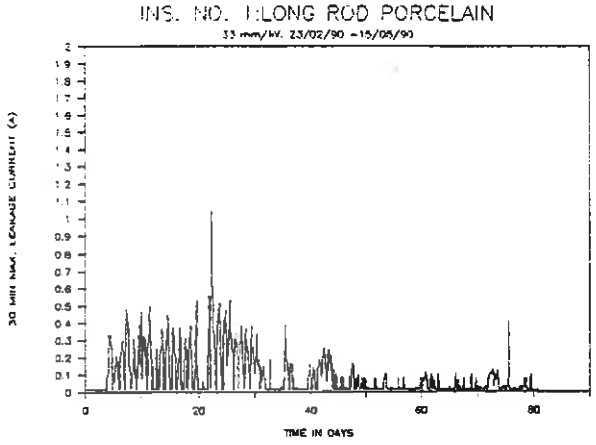

b) Porcelain long rod insulator

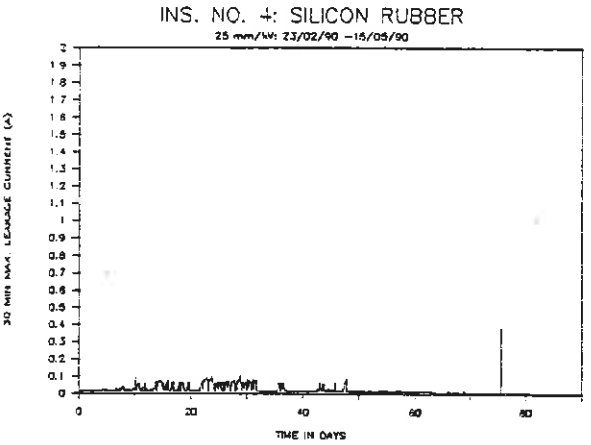

e) Silicon rubber insulator

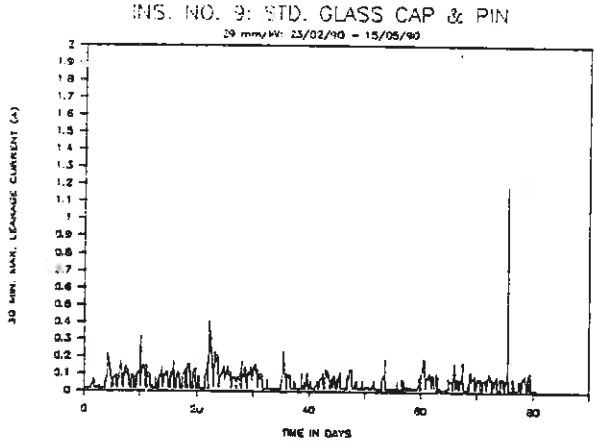

c) Cap and pin insulator

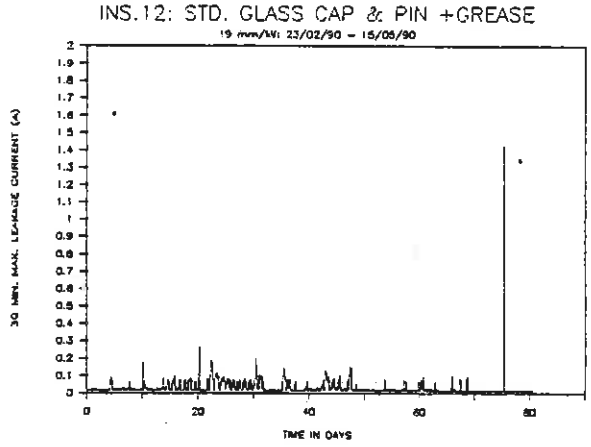

e) Cap and pin ins. (greased)

Fig. 2: Weather data and leakage currents for period: 23/02/90 - 15/05/90

Unfortunately, the weather station at Elandsbaai has not been operating satisfactorily. Weather data is however available from a weather station at an agricultural farm in the 10 km from the station.

With reference to figures 1 and 2, the correlation among the leakage current activity of the various insulators is striking. The highest leakage currents coincide with times of high humidity while leakage currents are lower after rain. As can be seen, the relative humidity is very high, often above 90 %. The humidity at Elandsbaai is possibly even higher than that measured at the experimental farm.

Data from the directional dust deposit gauge was collected during every site visit. The average pollution from the various wind directions were in the following ratios:

N = 40 %, E = 15 %, S = 26 % and W = 19 %

These readings also confirmed that the pollution index decreased with increase in rainfall.

CONCLUSION:

It is clear that for most types of insulators a specific creepage length in excess of 30 kV/mm must be used at a site such as this one. Silicon rubber insulators with a specific creepage of 25 mm/kV give a good performance. The silicon grease coated glass cap and pin insulators with a 19,4 mm/ kV creepage length perform surprisingly well.

REFERENCES:

1. Holtzhausen, J. P., et al, "Insulator Pollution: Monitoring of Leakage Currents during artificial and site test Conditions", SAUPEC 90, paper 3.4, January 1990, University of STELLENBOSCH /

2. Kindersberger, J., et al, "Effect of hydrophobicity on Insulator performance", Sixth International Symposium on High Voltage Engineering", paper 12.01.

ACKNOWLEDGEMENT:

This research is being done with the support of the National Energy Council of the R.S.A.

CONTINUOUS ON SITE MONITORING OF INSULATOR SURFACE CONDUCTANCE AND LEAKAGE CURRENTS.

J.P. Holtznausen and D.C.T. Potgieter

University of Stellenbosch, South Africa.

ABSTRACT:

An insulator pollution monitoring apparatus was designed and built to measure the surface conductance of test insulators while producing artificial wetting of the insulators. The apparatus can be used to facilitate site severity measurement and can be used as a pollution warning device.

The insulators are only energised for a few cycles only to prevent the formation of dry bands. The control of the measurement cycle and data logging is effected by a dedicated microprocessor.

The apparatus will be used at a site where the 30 minute highest leakage currents of a different set of insulators are also continuously monitored. The surface conductance measurements will be compared with the leakage currents.

INTRODUCTION:

The presence of conducting layers on the surface of insulators leads to the deterioration of the quality of power line insulation [1]. This layer could be due to a moist wind-driven salt spray at the coast. It is however more often in the form of a dry layer which is at first deposited and subsequently becomes conducting during humid and foggy conditions. Dry deposition of pollution is typical for industrial, desert and also for most coastal localities.

In some areas problems are being experienced with the rapid build-up of dry pollution on the insulators. During subsequent damp periods excessive leakage currents flow which can eventually lead to flashover. Insulator monitoring systems, based on the measurement of leakage currents [2] or surface conductance [3] are ineffective in these cases as no leakage currents flow during dry periods while in damp periods flashover can develop without sufficient warning.

It is therefore necessary to incorporate an artificial wetting feature into an insulator monitoring scheme. Artificial wetting of insulators while in service in order to measure leakage currents is not advisable as this may trigger unnecessary flashovers. A separate apparatus with its own step up transformer

is therefore required. Similar equipment was developed in Italy [4].

It is not considered practical to leave insulator energised during wetting in order to measure leakage current as any current or flashover may develop. It was therefore decided to use the method of surface conductance measurement, developed in Italy [4], whereby the transformer is only energised for a few cycles during conductance measurement.

The use of this apparatus at the same site together with a continuously energised leakage current measuring device will also provide useful information on the relationship between surface conductance and leakage current.

DESCRIPTION OF INSULATOR POLLUTION MONITORING APPARATUS (IPMA):

The heart of the apparatus is a 220 / 11000 V , 5 KVA step- up single phase distribution transformer, which is housed in a sheet metal rectangular box. The high voltage output of the transformer is taken through the top of the box via bushings. Two

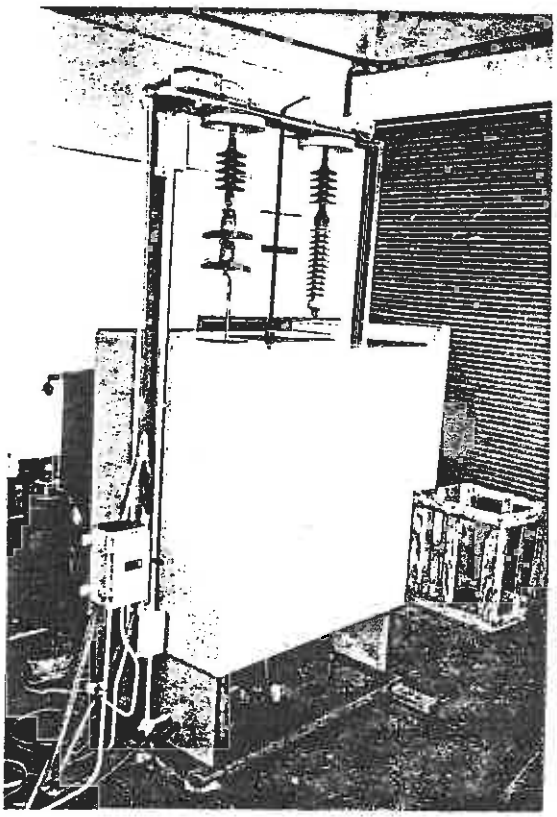

Figure 1: Photograph of IPMA with fog chamber in lowered position.

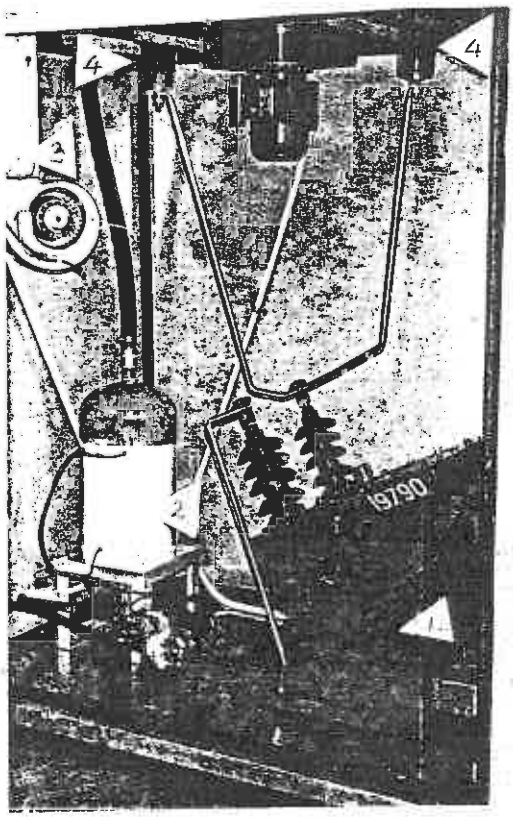

Figure 2: Equipment enclosure with side panel removed, showing arrangement of various items: 1: transformer, 2: steam generator, 3: fan / heater, 4: bushings.

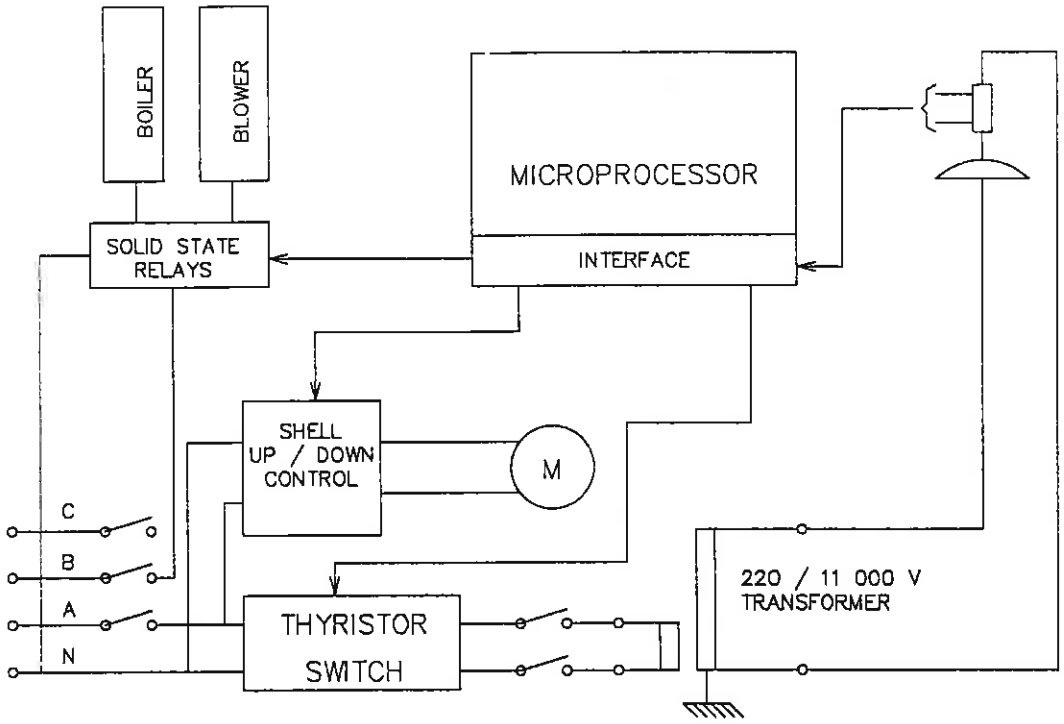

Fig 3: Schematic diagram of supply and control circuits for IPMA.

test insulators of different shape, two glass cap and pin discs and a porcelain long rod insulator are suspended above the box as can be seen in Fig. 1.

The leakage currents flow to ground via 4,7 ohm resistors. The voltages across these resistors are fed to the data logging equipment.

A rectangular moving fog chamber of slightly larger dimensions than the equipment housing described above encases the housing when in the normal lowered position.

During a measuring cycle when steam fog is generated, the fog chamber is raised to completely cover the test insulators. The fog chamber is manufactured from polystyrene sheets , laminated with glass fibre reinforced epoxy resin.

The chamber is raised by means of a motor driven helical screw. A

feature of the design is that the lifting gear of the fog chamber takes up a minimum of space in the equipment housing.

The fog generator is an electrode type heater, using fresh water for each test cycle to avoid the formation of sediments in the boiler.

The arrangement of the equipment in the housing can be seen in figure 2.

The electronics and instrumentation is housed in a separate weatherproof glass fibre kiosk.

CONTROL AND OPERATION OF IPMA:

A schematic diagram of the control circuits is given in figure 3.

The operation and data logging is controlled by a dedicated microprocessor. Communication with the microprocessor during initialising and data downloading is by means of a portable personal computer. During initialising various options, e.g. the time between measurement cycles are available. Normally one test cycle will be done every day.

The sequence of automatic steps during a typical test cycle is as follows:

a) Refill water boiler up to upper electrode.

b) Switch on water boiler.

c) Raise fog chamber.

d) The thyristor switch, energising the transformer is switched on for three 50 Hz cycles and the maximum leakage current is recorded during the second cycle.

e) Step d) is repeated at intervals specified during initialization (typically every 30 seconds), until the difference between consecutive readings is less than a specified percentage.

f) The last value is stored together with the relevant voltage.

g) The fan and heater is started to dry the insulators.

h) The salt fog chamber is lowered.

The recorded current and voltage values are stored in RAM until

downloaded to a portable personal computer.

Operational checks and preliminary commissioning tests in the workshop has been completed.

FIELD INSTALLATION OF IPMA:

The apparatus will be installed on the west coast at a site next to Koeberg Power Station at the same site where ESKOM and the University of Stellenbosch operated an insulator test station for a number of years. A power supply will be obtained from the Regional Services Council 11 kV line and ESKOM will assist in re-establishing the site.

A mobile leakage current monitoring station has been in operation in Kuils River for more than a year [9]. As it has now been established that a very low level of pollution prevails at that site, plans are in hand to move that facility also to the Koeberg test site. This will present an excellent opportunity to compare leakage current results with the surface conductivity measurements. Weather data will also be available from the nearby Koeberg Power Station weather station.

Commissioning of the Koeberg facility is scheduled for the first week of January 1991.

CONCLUSION:

A useful facility has been developed that should generate useful research results, that will, when interpreted together with leakage current data, lead to better understanding of insulator behaviour.

REFERENCES:

1. Holtzhausen J. P. et al, "Insulator Pollution: Monitoring of leakage currents during artificial and site test conditions", SAUPEC90 , paper 3.4.

2. Verma, P., "Highest leakage current impulse as criterion for the insulation performance of polluted insulators", CIGRE 33-73 (WG 04) (6) IWD.

3. Sforzini M. et al, " A statistical approach for insulator design in polluted areas", IEEE Trans. on Power Apparatus and Systems", Vol. PAS-102, No. 9, September 1983, pp 3157 - 3166.

4. Bertazzi et al, " A device for the automatic measurement of

Surface conductivity of insulators", Sixth International Symposium on High Voltage Engineering, New Orleans, September 1989, paper 47.39.

ACKNOWLEDGEMENTS:

This research is being done with the support of the National Energy Council of the R.S.A.

CORRELATION BETWEEN PARTIAL DISCHARGES AND RADIO-INTERFERENCE VOLTAGES FOR OVERHEAD LINE INSULATORS

JC VAN ALPHEN JT RAUBENHEIMER * F KNOETZE *

DEPARTMENT OF ELECTRICAL ENGINEERING, UNIVERSITY OF PRETORIA
PRETORIA, REPUBLIC OF SOUTH AFRICA

INTRODUCTION

Overhead lines have often been a source of nuisance in interfering with radio and TV reception, which particularly affects the public living or working in the immediate vicinity of power lines. Normal practice is to survey the line by visual inspection for obvious failures such as broken strands or dislodged components, and to carry out field strength measurements.

Where persistent complaints point to a particular type of insulator failure, this would normally either be referred to the manufacturer or an investigation is launched with regard to the possible cause for radio interference. The trouble might for instance be the result of bad workmanship in fastening the conductor to the head of the insulator, or an ill-fitting pin in a pin insulator resulting in a gap outside design limits in the dielectric path.

Manufacturers have overcome some of these problems by designing preformed wire fittings which make the connection of conductor to insulator less dependent on workmanship, or fitting the hole in the pin insulator with a metal thimble into which is screwed the lead-headed pin.

THE CYCLO-ALIPHATIC INSULATOR

With the advent of cyclo-aliphatic insulators, another problem has made its appearance. These insulators might contain voids, or display an erosion phenomenon caused by leakage current or corona discharges, a phenomenon which has been relatively unknown when employing the well-known classical materials such as porcelain and glass.

The students set out to investigate the hypothesis whether a correlation exists between radio-interference voltage (RIV) and partial discharge (PD) for each type of insulator. Should there be a persistent pattern of complaints from these newer type of insulators of composite materials due to either radio-interference or insulation failure, it would be advantageous to be able to pinpoint measured RIV to a possible cause, which may for these insulators partial discharge.

THE WOOD POLE LINE

Cyclo-aliphatic line insulators have found wide acceptance in certain electricity supply undertakings because of their advantage in being light, robust and easy to handle. These insulators have, when used as an insulator with earthed pin, a reduced insulation level. Their main application is, however, in wood pole line constructions in which wood provides an additional path of insulation.

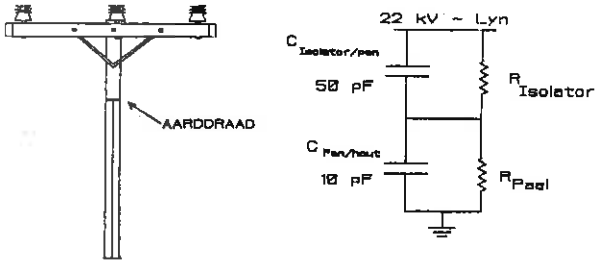

FIG 1 - 22 kV WOOD POLE STRUCTURE USING TWO WOOD POLE SECTIONS AS ADDITIONAL INSULATION IN SERIES WITH INSULATOR

Fig 1 shows a typical construction in which an insulating path is provided by a section of wood pole between phases and between phase and ground.

It was therefore considered that the investigation should first elucidate whether this combination of insulator and wood pole section has any significant effect on the possible generation of radio-interference.

Fig 1 shows the representative circuit for this combination. If it were to be assumed that the leakage resistances across the insulator and wood pole section are infinite, the voltage impressed upon the pin due to capacitive voltage distribution would be considerable, of the order of $^{4}/_{5}$th of line voltage, and the voltage across the insulator only about $^{1}/_{5}$th.

---

*) Co-authors Raubenheimer and Knoetze are final-year students of the Department Electrical Engineering of the University of Pretoria. As a project in fulfilment of the requirements of their B Eng degree, they spent considerable time and effort in conducting their investigations at NETFA (the National Electrical Test Facility: Apollo), a facility of the SABS near Olifantsfontein. The results of their investigation are to be attributed to the guidance and whole-hearted support received from AC Britten PrEng, Chief Consultant, Engineering Investigations of ESKOM who arranged for the supply of a wood pole structure and hardware, and to P du Preez MSc, Head of High Voltage Technology of NETFA, who made part of the High Voltage laboratory and measuring equipment available for this project.

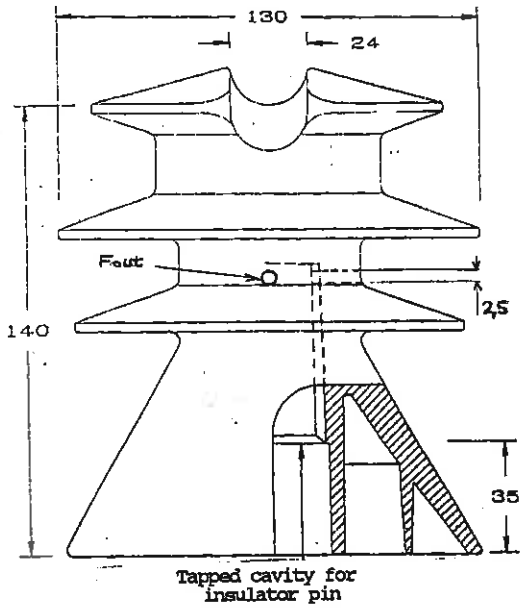

FIG 2 - CYCLO-ALIPHATIC PIN TYPE INSULATOR (artificial fault created by drilling a 2,5 mm hole in insulator body)

The pin, which has not been designed in terms of RIV performance should it be live, might make a considerable contribution to the RIV level of the combination. Against this, the reduced voltage across the insulator would reduce its contribution to RIV.

THE RIV MEASURING CIRCUIT

A 22 kV wood pole structure with cyclo-aliphatic line insulators as in Fig 2 and earth strap as in Fig 1 was set up in the laboratory. Each insulator was fitted with a length of stranded conductor, clamped to the insulator by a preformed wire wrap. The ends of the conductor, each about 2 m long, were terminated in an RIV-free electrode.

The circuit used for the RIV measurements is given in Fig 3. A pi-filter was used to ensure that measurements are not influenced by mains born interference signals. The 0,813 nF capacitance is provided by the bushing of the test transformer and the 1 nF capacitor is the measuring capacitor for voltage measurements.

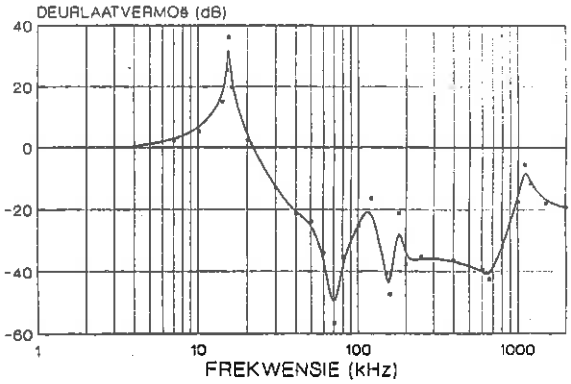

FIG 4 - AMPLIFICATION CHARACTERISTIC OF FILTER IN HIGH VOLTAGE TEST CIRCUIT (Reverse of Attenuation characteristic)

Fig 4 shows the amplification of the filter, which is -38 dB at 500 kHz.

RIV measurements were carried out in conformance with IEC 437 and the relevant CISPR standards. The instrument used was a Schwarzbeck FSME 1515 narrow band receiver with a bandwidth of 9 kHz.

The RIV method uses a quasi-peak voltmeter operating at a fixed frequency, usually 1 MHz or 0,5 MHz. The quasi-peak feature permits the evaluation of peak values of random pulses, in which the peak value is weighted by the relative frequency of occurrence.

Fig 5 shows the elements of the quasi peak filter, in which the time constants RC and R_1C are 1 ms and 160 ms respectively in accordance with CISPR 1.

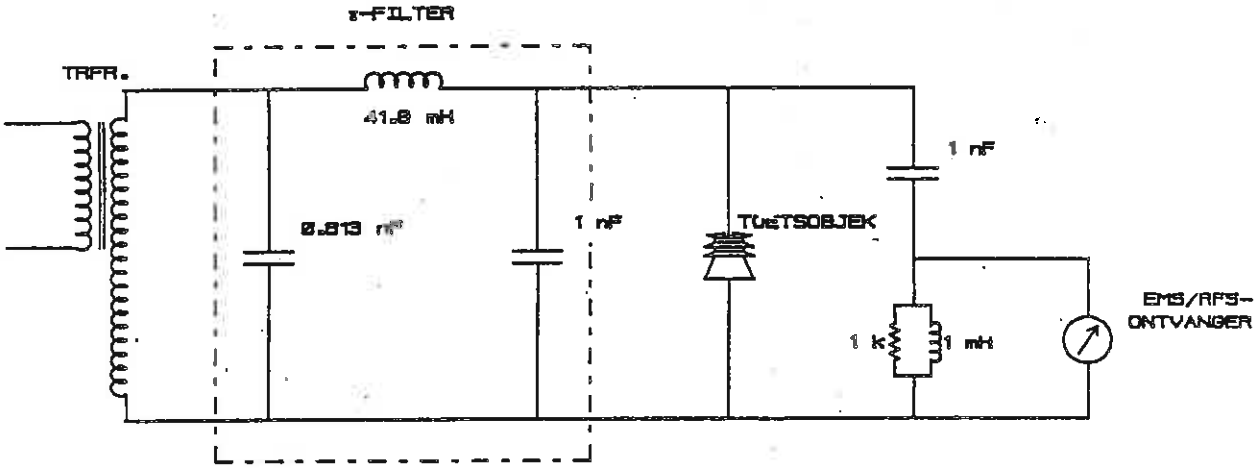

FIG 3 - RADIO INTERFERENCE MEASURING CIRCUIT (650 kV transformer on the left and 100 pF high voltage capacitors for voltage measurement and as blocking capacitor)

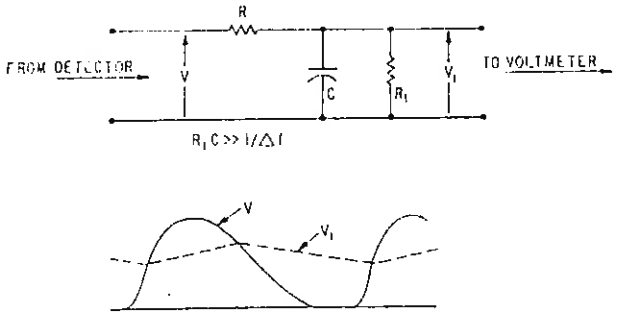

FIG 5 - QUASI-PEAK FILTER ELEMENTS FOR RIV MEASURING CIRCUIT (CISPR 1)

Before commencing the experiment, a signal generator was inserted in the place of the insulator and a calibration carried out. The following table gives the results.

FREKWENSIE MHz	BEREKEND dB/µV	GEMEET dB/µV
0.97	78.5	78
0.97	82,5	82
0.97	91.6	92

RIV PERFORMANCE OF WOOD POLE LINE

It was first determined at which frequency the experiment should be carried out. Graph 1 shows that the noise produced by the line lies mainly in the 0,5-1,0 MHz band. This confirms IEC's preference for RIV measurements to be carried out at 0,5 MHz.

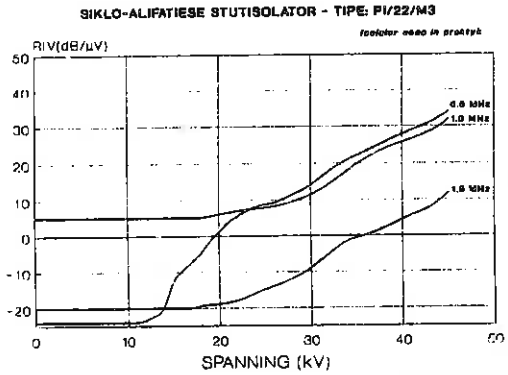

GRAPH 1 RIV MEASURED AT VARIOUS FREQUENCIES vs APPLIED VOLTAGE TO INSULATOR CONDUCTOR

The wood pole structure, in which the insulator is in series with the insulation of a section of wood pole, may give rise to three conditions in service which were simulated as follows (see Graph 2):

(1) as in practice with dry and clean insulator and wood (see curve denoted "praktyk");

(2) the insulator being conducting (e.g. due to moisture condensation or pollution) whilst the insulation resistance of the wood is high, this condition being simulated by the shorting out of the insulator, i.e. the pin is at full line potential (see curve denoted "kortgesluit");

(3) the reverse of (2), i.e. the wood pole path being shorted out, i.e. the pin is earthed (see curve denoted "ge-aard")

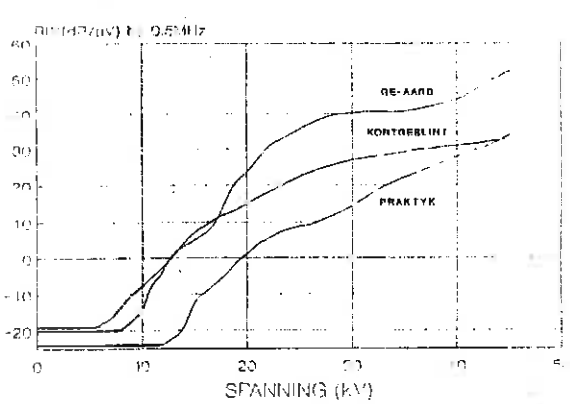

GRAPH 2 RIV MEASURED AT 0,5 MHz UNDER VARIOUS CONDITIONS OF INSULATOR AND WOOD PATH (Pin earthed, insulator shorted out and installed as in practice)

The curves give a clear picture of an acceptable RIV performance of this 22 kV line with typical cyclo-aliphatic pin insulators as shown in Fig 2.

In this study, RIV which may be generated by extraneous sources such as irregular surface pollution, dry bands or droplets, is ignored.

The RIV generated at normal 22 kV service voltage, which is equivalent to 14 kV to earth, under the extreme conditions "ge-aard" and "kortgesluit" is about 5 dB. The recommended RIV limit for medium voltage lines is 30 dB, which indicates that the RIV performance of this line is well within limits.

THE PD MEASURING CIRCUIT

PD measurements were carried out on insulators, which were again mounted in situ as for the RIV measurements, i.e. with conductor fitted as in service, except that in this case the pin was earthed throughout.

The measuring circuit is given in Fig 6, using a TETTEX 9120 partial discharge bridge system in order to suppress to greater or lesser degree extraneous signals. Measurements were conducted in conformance to IEC 270. Because the capacitance of the insulator is extremely small, in order to match the coupling capacitor of 100 pF with the arm containing the insulator, a capacitor of 100 pF was connected in parallel to the insulator. In this manner the two arms of the bridge were reasonably balanced, which enhances the rejection of extraneous signals.

In contrast with the RIV method, the instrument used for measurement of partial discharges has a wide band detector with a relatively flat response in the frequency range from 70 to 300 kHz.

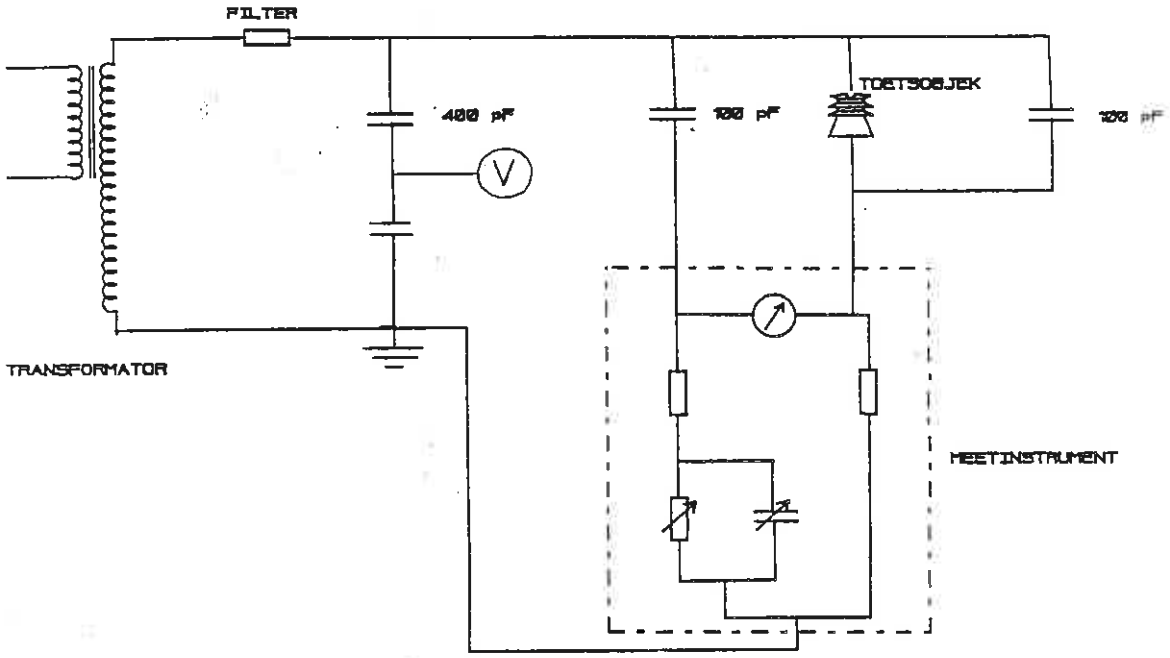

FIG 6 - PARTIAL DISCHARGE MEASURING CIRCUIT (BALANCED BRIDGE METHOD)

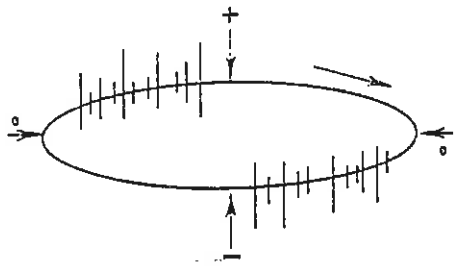

FIG 7 - TYPICAL ELLIPSE DISPLAY OF PD ON LEADING SLOPE OF 50 Hz SINE WAVE

The position of partial discharge superimposed on the power frequency sine wave may enable the operator to determine whether the signals emanate from corona (usually on the crest of the sine wave) or as a result of discharges in voids in the insulation (usually on the slope of the sine wave, see Fig 7).

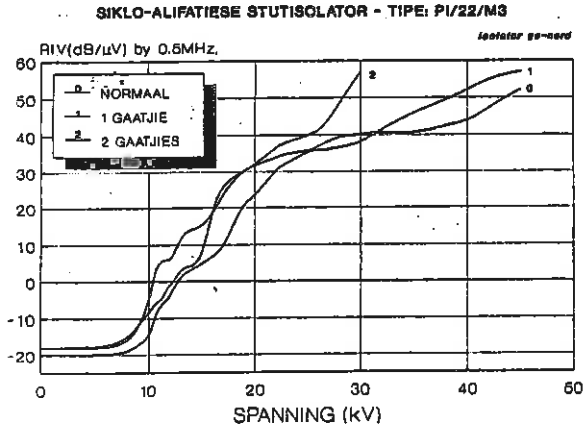

GRAPH 3 RIV MEASURED AS A FUNCTION OF APPLIED VOLTAGE WITH SOUND AND "FAULTY" INSULATOR (curves 2 and 3 with holes)

PD vs RIV FOR CYCLO-ALIPHATIC INSULATOR

The next exercise was to determine whether a correlation could be established between PD and RIV for the cyclo-aliphatic insulator as shown in Fig 2. Measurements were conducted on the insulators in situ on the wood pole structure with the line conductor fitted and the pin earthed, see Graph 2 "ge-aard".

Graphs 3 and 4 show the relationship of RIV and PD vs applied voltage respectively. The measurements were first made on the sound insulator. Thereafter, a fault in the insulator was simulated by drilling a hole by means of a tungsten tipped drill in the position indicated in Fig 2 as "fout", and the measurements repeated.

The experiment was repeated by adding a second hole in a higher position. The experiment with two holes had to be terminated at 30 kV due to imminent flashover of the insulator.

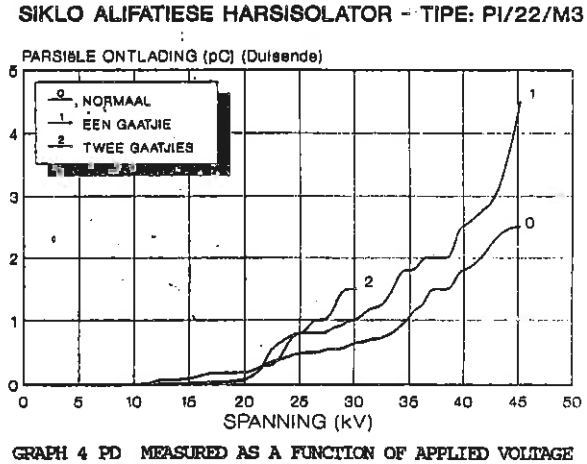

GRAPH 4 PD MEASURED AS A FUNCTION OF APPLIED VOLTAGE WITH SOUND AND "FAULTY" INSULATOR (curves 2 and 3 with holes)

As far as RIV is concerned, the onset voltage of RIV with the faulty insulator is about 2 kV lower, but there is no significant change in the shape of the curve of measured RIV vs applied voltage.

There appears to be no significant difference in onset voltage in the measured PD, being about 23 kV. Considering the low levels of PD, the change between sound and faulty insulator is barely significant.

Studying the pattern of PD on the sine wave, it was significant that the pattern of discharges was not materially different between the sound insulator and the "faulty" insulator.

INSULATOR SIGNATURES

The object of the exercise is to establish whether for each type of insulator, and for each typical fault which may occur in the insulator, a signature relationship between PD and RIV could be established.

Because transmission line nuisance is commonly related to RIV, a laboratory in which the RIV of an insulator can be measured is usually more readily available to the maintenance engineer than when measuring of PD is required.

With the increasing use of composite insulators, such as made of cyclo-aliphatic resins, it may be possible to establish a signature register which would enable the engineer, judging by the shape of RIV as a function of applied voltage, to make an assessment of whether or not there is a significant PD contribution to RIV, and possibly what type of fault might be the cause of this.

Cyclo-aliphatic and other types of composite insulators have not yet been long enough in service to establish a pattern of insulation failure. Literature research gave little evidence that much work has been done in establishing a correlation between RIV and PD.

The need for a signature register may therefore have to be reassessed after further work has been done.

CONCLUSION

Within the time available for this project and within the constraints of being remote from NETFA, the following conclusions may be drawn:

(a) The experiment was initially aimed at simulating service conditions. In order to be able to separate RIV and PD generated by the insulator from extraneous noise such as emanating from the conductor and the manner in which the conductor is fitted to the insulator, it will be necessary to continue the experiments, using a discharge free connection to the live end of the insulator.

In this way, a noticeable difference might be observed in correlation, when testing a sound and a faulty insulator.

(b) Once an acceptable criterion for distinguishing between sound and faulty conditions has been established, insulators rejected in the field should then be examined in order to determine whether a "signature" of correlation between PD and RIV can be established for each type of failure.

At the time of the project, no such rejects were available.

(c) An attempt was made to plot PD against RIV for a cyclo-aliphatic insulator and an equivalent glas disc insulator, see Graphs 5 and 6. Whilst there is a definite difference in pattern, Graph 5 fails in indicating a significant change in pattern between a sound an a "faulty" insulator. This might, of course, be the result of the unwanted contribution made by the conductor, as discussed in (a) above.

(d) Since there is barely any reference in the literature to the methods proposed in the project, at this stage it remains to be seen whether the method can ever be employed with success. Even if this is not the case, the results have, it is hoped, contributed to the knowledge base with regard to RIV and PD behaviour of insulators used in typical wood pole structures.

SIKLO-ALIFATIESE STUTISOLATOR - TIPE: PI/22/M3

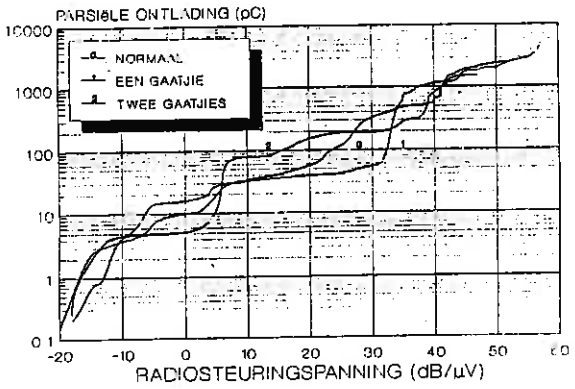

GRAPH 5 CYCLO-ALIPHATIC INSULATOR SIGNATURE IN TERMS OF PD vs RIV FOR THE THREE INSULATOR CONDITIONS AS IN GRAPH 3

GLASTREKISOLATOR - TIPE: BS-2510

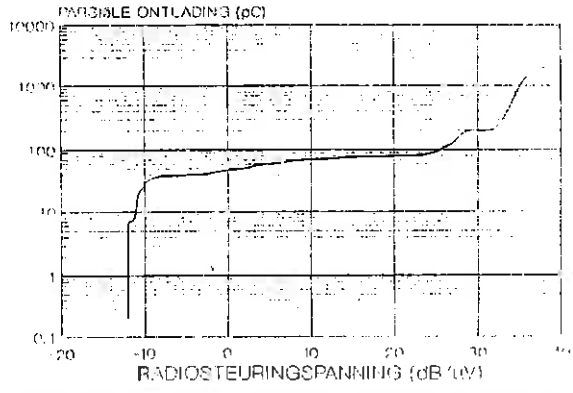

GRAPH 6 GLASS DISC INSULATOR SIGNATURE IN TERMS OF PD vs RIV (no fault introduced in insulator

BIBLIOGRAFIE

1. D.A. Nattrass, "Partial Discharge Measurement and Interpretation.", IEEE Electrical Insulating Magazine, vol.4, no.3, p10-23, 1988.

2. L.D. Bobrovskaya, N.S. Larionova, "Influence of Partial Discharges on ageing of Epoxy Insulation at High Frequencies.", Soviet Electrical Engineering, vol.57, no.9, p113-117, 1986.

3. T. Tanaka, "Internal Partial Discharge and Material Degradation.", IEEE Transactions on Electrical Insulation, vol.EI-21, no.6, p899-905, December 1986.

4. T. Tanaka, T. Okamoto, "Novel Partial Discharge Measurement Computor-aided Measurement Systems.", IEEE Transactions on Electrical Insulation, vol.EI-21, no.6, p1015-1019, December 1986.

5. G.H. Vaillancourt, A. Dechamplain, R.A. Malewski, "Simultaneous Measurement of Partial Discharge and Radio-Interference Voltage.", IEEE Transanctions on Instrumentation and Measurement, vol.IM-31, no.1, p49-52, March 1982.

6. R.J. Van Brunt, S.V. Kulkarni, "Method for Measuring the Stochastic Properties of Corona and Partial Discharge Pulses.", Rev. Sci. Instrum., vol60, no.9, p3012-3023, September 1989.

7. E. Kuffel, W.S. Zaengl, "High Voltage Engineering Fundamentals.", First edition, p422-462, 1988.

8. R. Malewski, G.H. Vaillancourt, D. Train, "Comparison of Three Techniques of Partial Discharge Measurements in Power Transformers.", IEEE Transactions on Power Apparatus and Systems, vol. Pas-104, no.4, p900-909, April 1985.

9. R.Bartnikas, "Detection of Partial Discharges (Corona) in Electrical Apparatus.", IEEE Transactions on Electrical Insulation, vol. 25, no.1, p111-124, Febr. 1990.

10. U. Bannet, M. Beyer, "Partial Discharges measured with an Automated Measuring System in Epoxy Resin and Polyethylene.", IEEE Transactions on Electrical Insulation, vol.23, no.2, p215-225, April 1988.

11. D. König, I. Quint, P. Rösch, B. Bayer, "Surface Discharges on Contaminated Epoxy Insulators.", IEEE Transactions on Electrical Insulation, vol.24, no.2, p229-237, April 1989.

12. M.G. Comber, R.J. Nigher, "Radio Noise", Transmission Line Reference Book, Chapter 5, Second Edition.

13. J.S.T.Looms, Insulators for High Voltages, 1988.

14. Publication 437, "Radio interference test on high voltage insulators.", International Electrotechnical Commission, First Edition, 1973.

15. SABS 177, "Isolators vir bogrondse lyne met 'n nominale spanning van meer as 1000 V.", Deel 3, 1990.

16. IEC Standard, "Partial discharge measurement", Publication 270, p1-56, 2de uitgawe, 1981.

17. J.H. Mason, "Discharge Detection and Measurement.", Electrical Review, p802-806, 31 Mei 1968.

18. R.T. Harrold, T.W. Dakin, "The relationship between the picocoulomb and microvolt for corona measurements on HV transformers and other apparatus.", p187-198.

19. E.M. Dembinski, J.L. Douglas, "Calibration and comparison of partial discharge and radio - interference measuring circuits.", Proc. IEEE, vol.115, no.9, p1332-1340, 9 September 1968.

20. Engineering Investigations, "Radio interference from polluted insulators.", E.I. Enertek, vol.1, no.3, November 1989.

21. J. Golinski, R. Malewski, D. Train, "Measurements of RIV on large EHV apparatus in high voltage laboratory.", IEEE Transactions on Power Apparatus and Systems, vol.Pas-98, no.3, p817-822, Mei/Junie 1979.

IMPULSE FLASHOVER OF POLLUTED INSULATION

D.A. Hoch
University of the Witwatersrand

D.A. Swift
University of Natal

ABSTRACT

Information extracted from published research has been combined with new results obtained from a simple experiment to arrive at an approximate expression for the lightning wave pollution flashover voltage of a short string of porcelain disc insulators. This voltage, expressed relative to the dry flashover value, is given as a function of both the pollution severity and the height above sea level. Some comparative data are provided for the switching surge case.

These findings have been used to assess the likelihood of faults occurring on power systems due to these short-duration overvoltages.

Features of the flashover process have been briefly discussed. from which some aspects in need of further investigation have been identified.

1. INTRODUCTION

Although it is known that wet pollution appreciably reduces the flashover performance of practical insulators, the cause has not been identified when the energization is either the lightning wave or the switching surge; the explanation generally accepted for the much studied pollution flashover under normal service stressing is not valid because of the time factor.

Further, for all types of waveform there is a dearth of information concerning the influence of altitude on the value of the flashover voltage.

Both of these aspects are currently under investigation by CIGRE Working Group 33-07.

The impulse flashover of a polluted service insulator probably comprises : (a) the sparkover of dry bands, which may have been previously established on the surface by the normal service stressing (b) the extension of the discharge across the wetted part of the surface (c) the breakdown of the air-gaps between both the sheds and the ribs of a shed.

To determine the relative importance of the various parameters of this complex process, the paper reviews the relevant data for insulators and air-gaps and provides new results obtained for the flashover across a representative surface of electrolyte. The mechanism of flashover across the electrolyte and the relevance of this information to power system faults are briefly discussed.

2. INSULATOR DATA

The effect of short duration overvoltages on a polluted insulator can be best assessed by comparing the magnitude of that voltage (peak value of waveform, at 50% probability of flashover) required to produce flashover with the corresponding value for the insulator when clean.

Examples, based on data provided in reference [1], of such comparisons for positive polarity impulses applied to a 9 unit string of disc insulators (alternatively called cap and pin insulators) are shown in Figure 1 as a function of pollution severity, expressed in the various scales used by CIGRE Working Group 33-04 [2].

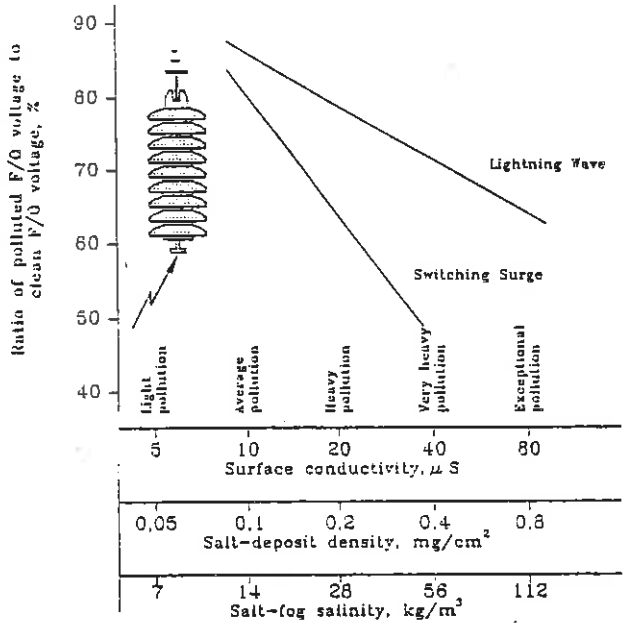

Figure 1 : Reduction in the positive polarity impulse strength due to pollution, for a 9 unit string of standard 10" x 5.75" disc insulators without pre-established dry bands; note, clean F/O voltage = 850 kV for the impulse wave and = 500 kV for the switching surge.

The general findings from investigations made at low altitude on various string-lengths of disc insulators are :

* Both the lightning wave and the switching surge flashover values decrease with the increase in pollution severity. For very heavy pollution and no dry bands, the reduction from the clean flashover value is about 30% for the lightning wave [1] and about 50% for the switching surge [1], [3], [4], [5]

* Prior established dry bands cause a further lowering of the flashover strength; for very heavy pollution, this additional reduction is about 10% for the lightning wave [1] and about 15% for the switching surge [1], [3], [4].

Another useful comparison is the ratio of the impulse flashover voltage to the corresponding normal stressing value. Such information for the ac reference case is illustrated in Figure 2, as a function of the duration of the impulse waveform (stated as the time for which the voltage is greater than 50% of the peak value); again these data are for disc insulators, no dry bands and low-altitude air conditions. Also included on this diagram, are a few results

[6] that apply to the corresponding temporary AC overvoltage condition (in this case the duration is the time for which the 50 Hz voltage is applied before flashover occurs).

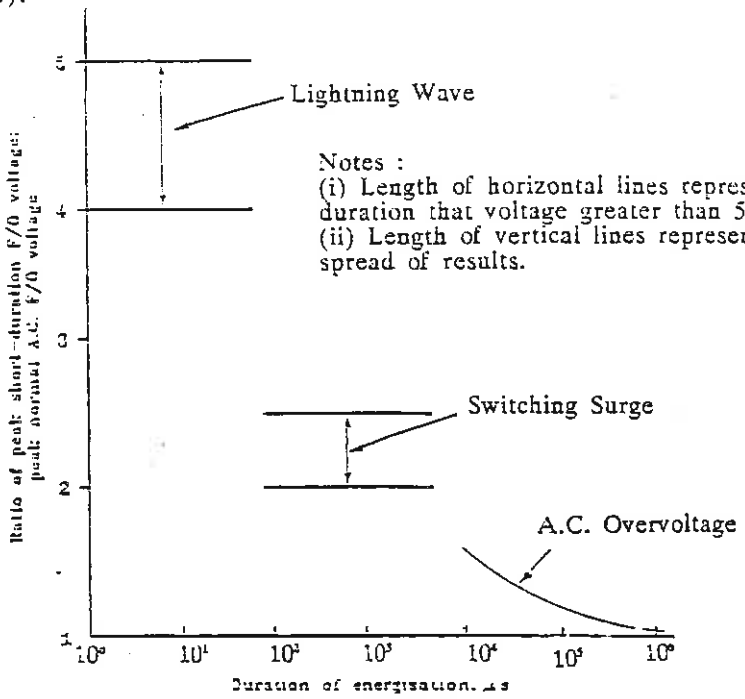

Figure 2 : Comparison of the short duration stressing strength for positive polarity impulses with the normal AC stressing strength, for a 9-unit string of disc insulators without pre-established dry bands on a very heavily polluted surface; note, peak normal AC F/O voltage = 100 kV.

This figure shows that for very heavy pollution :

* The peak impulse voltage/peak AC voltage ratio is 4 to 5 for the lightning wave but only 2 to 2.5 for the switching surge.

* The impulse voltage data are consistent with those for AC overvoltage stressing.

Further, a summary of related data is :

* Negative polarity flashover voltages are typically 10 to 20% greater than positive polarity values, for both the lightning wave and the switching surge.

* For a variety of insulator types, the order of merit is the same for lightning wave, switching surge and normal AC voltage.

* Linearity of flashover voltage with string length up to 25 disc insulators is not usually preserved for switching surges.

* The flashover strength with switching surges decreases a little (10%) as the time to peak increases by an order of magnitude and time to half wave by a factor of 3.

* Flashover occurs on the tail of the waveform. For example, for a string of 9 standard disc insulators, the time lag at the 50% flashover level is typically 20 μs for the 1/50 μs lightning wave and about 1000 μs for the 350/3500 μs switching surge.

By using the mathematical model of surface-water evaporation proposed by Texier and Kouadri [7], it is reasoned that altitude has no appreciable effect on the formation of these important dry bands for the relevant range of conditions.

3. GAP DISCHARGES

Under certain types of weather (e.g. mist, rain), the electrodes of an air-gap discharge on a polluted insulator are likely to be water droplets, and their shape determines the stress enhancement in the air. Such droplets can become highly distorted by the pre-applied AC field [8], thereby appreciably lowering - possibly by a factor of 4 - the impulse breakdown strength of these numerous small gaps.

Although the conductivity of the water is unlikely to have much effect on the shape and size of the water drops, it does effect the conductance of these electrodes and so an increase in pollution severity causes a corresponding increase in voltage across the other part of the circuit, thereby enhancing the likelihood of the flashover.

As the basic electric strength of the air is a function of its density, the further reduction of this portion of the impulse flashover voltage can be represented by a factor F given, for conditions relevant to South Africa, as :

$$F \sim 1 - 10^{-4} H \quad \text{.....(1)}$$

where H is the height above sea level in meters.

4. FLASHOVER ACROSS AN ELECTROLYTE

In a representative experimental arrangement , the electrical discharge across a brine surface occurred from an energized point electrode - which was mounted just above the electrolyte, thereby simulating initiation at a dry band - to an earthed bar electrode, which was immersed within the electrolyte and shaped to achieve a near-uniform field at its boundary with the water. The electrolyte was sufficiently deep in the rectangular trough to avoid complications due to an increase in its temperature.

The relationship of lightning wave flashover voltage to water conductivity essentially comprises three distinct parts. Firstly, there is a more than 50% decrease from the dry flashover value of the surface even though the water is only weakly conducting. This is followed by a more gradual decrease in flashover strength as the water becomes more conducting. Finally there is an increase in flashover voltage when the water becomes very conducting; i.e. there is the impression of the start of a U-curve.

The detailed quantification of this dramatic decrease in the flashover voltage due to simply wetting the surface has not yet been investigated. Although the trough was filled with de-ionised water, the conductivity increased very substantially during the multiple-shot testing procedure used to determine the flashover voltage; that is, the products of the discharge (probably oxides of nitrogen) were polluting the water. A more sophisticated arrangement is needed to obviate this problem.

The middle part of the characteristic has been investigated in some detail. The 50 % probability value of the flashover voltage for a 1/50 μs impulse wave has been determined as a function of surface conductivity by using the standard up-and-down method for a 50 shot procedure. Identical experiments have been performed at essentially sea level and at an altitude of 1700 m; i.e. 17% reduction in air density. Figure 3 shows the results, expressed as a percentage of the flashover voltage, at sea level, of the dry surface of the trough.

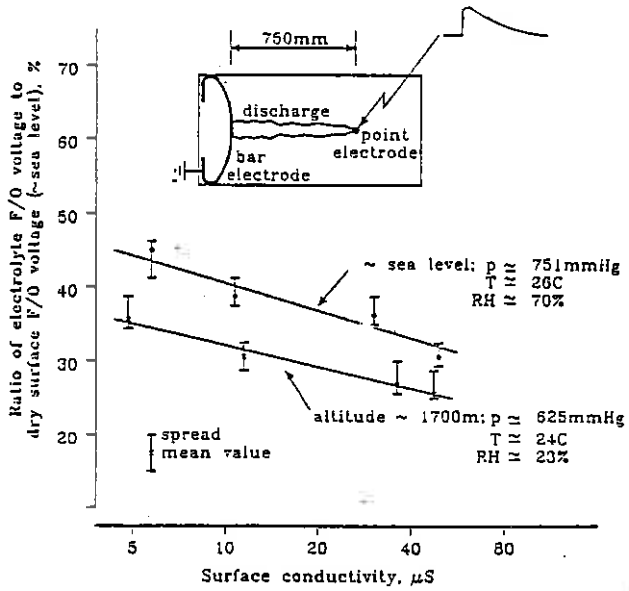

Figure 3 : Flashover performance of an air/water interface for positive polarity lightning wave impulses; note, dry flashover voltage of insulator surface = 454 kV for sea level condition.

These results show that the flashover voltage at the higher altitude is between 15 and 20 % lower than the corresponding sea-level value. Also, some additional results indicate that negative polarity impulse voltages are substantially higher than the positive polarity ones. Further, the time taken to complete the flashover (as indicated by the collapse of the voltage waveform) increased as the water conductivity increased; e.g. this time was ~ 50 μs at a surface conductivity of 30 μS. On the basis of an average stress (i.e. voltage divided by flashover path length), these results (750 mm path length) for the sea level case are about 10 % lower than corresponding data reported for a 100 mm path length [9].

The third stage of the characteristic has not yet been adequately investigated, but the turning point in the curve seems to occur at 50 to 100 μS. Also there is some evidence to suggest that for some voltage withstand cases the discharge tip becomes arrested during its propagation across the surface; of note, a similar situation has been observed on practical insulators - and in some cases the flashover path was completed by the AC energization [1].

5. DISCUSSION

For a practical insulator with no pre-established dry bands, the current information indicates that the flashover voltage, V(F/O), under impulse energization can be expressed as :

$$V(F/O) = V(D/B) + V(ES) + V(AG) \quad .....(2)$$

where V(DB), V(ES) and V(AG) are the components due to the dry bands, the electrolyte surface and the air gaps respectively.

From the information reviewed in section 2:

$$V(DB) = 0.1 \text{ to } 0.15 \times V(F/O) \quad .....(3)$$

Inspection of the data presented in Figure 3 shows that, for the lightning wave, the flashover voltage across the electrolyte, V(ES), and the pollution severity, S, are related as :

$$V(ES) \propto S^{-p} \quad .....(4)$$

where p is a constant.

Further, the data contained in Figure 1 indicate that the switching surge case can be similarly represented. That is, the relationship for both the lightning waveform (LW) and the switching surge (SS) is the same as that for AC or DC stressing [10]. The value of p for the relevant situations is given in Table 1.

Table 1 : Value of constant p in equation 4 for various cases

Arrangement	Insulator			Electrolyte	
Energization	LW	SS	AC	LW	DC
p	0.14	0.4	0.33	0.15	0.34
Reference	[1]	[1]	[1]	*	[11]

* - current paper, Fig 3. average value of sea-level and high altitude data.

Therefore, although the lightning wave flashover performance of insulators clearly deteriorates as the pollution severity increases, the change is nothing like as great as that for the AC and DC cases. In contrast, the decrease in the switching surge strength as the surface becomes more polluted is even greater than that for normal service stressing.

Denoting the dry/clean flashover voltage as V(D) and assuming that both the flashover voltage for porcelain is approximately equal to that of tufnol and the arrangements can be equated, then the ratios of V(ES) + V(AG): V(D) for the lightning wave case are obtained from Figure 1 - by subtracting V(DB), equ. 3 - and Fig. 3 respectively. Using this approach :

$$V(AG) \sim V(ES) \quad ..... (5)$$

The data of figure 3 also show that the lightning wave flashover voltage across the electrolyte reduces with air density in approximately the same proportion as that of a normal air gap; i.e. that factor F given in equ. 1 also applies to the wetted surface of an insulator.

For the electrically weakest case of pre-established dry bands (EDB), the generalized equation for the lightning-wave flashover voltage, V(F/O,EDB,H), of a service insulator - situated at any practical altitude - can be obtained by combining equations 1 through 5 and again using the data of Figure 3. Expressed relative to its dry flashover voltage at sea-level, V(D), this expression is :

$$V(F/O,EDB,H):V(D) \sim 0.8 \times (S/10)^{-0.15} \times (1 - 10^{-4} H) \quad ...(6)$$

where S is in microsiemens and H is in metres above sea level.

The mechanism of pollution flashover under normal stressing is essentially that of a circuit instability leading to the propagation of an arc root over the surface of an electrolyte. The instability arises because the electric field of an arc decreases as its current magnitude increases. Arc root propagation is a relatively slow process such that the flashover time for AC and DC voltages is usually more than 10 ms. for practical insulators (Fig 2; AC overvoltage curve). Clearly, this is much too slow a process for the lightning wave case. Although the tip of the impulse discharge is not in direct contact with the electrolyte , it is, nonetheless, capacitively coupled to it by image charges. Further, the electric field of the spark decreases as its transport current increases. Therefore, these factors may explain the role of the series conductance provided by the electrolyte.

Dry bands on the surface of the insulator are caused by Joule heating due to the leakage current; they form at the places of maximum power density and/or minimum water coverage. When the insulator is suddenly energized, the time delay before they form is part of the total time taken to complete the flashover process. Therefore, the shorter the pulse duration, the greater the overvoltage has to be to provide the necessary energy of evaporation. Alternatively, if these dry bands have been pre-established by other means - on service insulators, usually by the normal service stressing - then less overvoltage is needed to complete the flashover process. Although this reasoning qualitatively explains the observations, supporting quantitative analysis remains to be done.

The consensus of opinion of the researchers in this field is that most of the pollution flashover faults of power systems are caused by the normal service stressing. The argument is partly statistical, in that high pollution severity and impulse energization do not often occur simultaneously. The other factor concerns the ratio of the magnitude of the impulse voltage to that of normal service voltage. The data presented in Fig. 2 show that this ratio must be greater than four for the lightning wave and two for the switching surge, for an impulse flashover to be at all likely. IEC specification 71 (1972) - of note, it relates to low-altitude conditions, shows that the basic insulation level ratio for system voltages of 145 kV, 420 kV and 765 kV is 6.4, 4.3 and 3.4 respectively for the lightning wave; the corresponding ratio is 3.1 at 420 kV and 2.3 at 765 kV for the switching surge. Therefore there is a distinct probability that severely polluted insulation does flashover under voltage impulses, especially for the lower voltage systems.

The influence of altitude can be assessed by noting (equ 6) that the impulse strength is likely to decrease linearly with height above sea-level. Therefore if the insulation were to be designed solely on AC considerations - for which air density may not be so important - then there would be an enhanced likelihood of impulse flashover.

The current results obtained for the electrolyte show close similarities to those obtained for the lightning wave flashover performance of wood poles. In particular, wetting lowers the impulse strength of the wood by up to 60% [12] -cf. 55% for tufnol, Fig 3 - and an increase in altitude from sea level to 1700 m lowers the strength of the pole by 18% [13] - cf. 15 to 20% for the water surface, Fig 3.

6. CONCLUSIONS

Based on the limited amount of information available for analysis, the magnitude of the impulse voltage required to flash over a polluted and wet insulator can be considered as comprising three components. Ten to fifteen percent of this voltage is associated with the formation of dry bands on the insulator; the remainder, is reasoned to be divided approximately equally between the breakdown of the various air gaps and the extension of the discharge across the wetted surface.

The impulse strength decreases with increasing pollution severity, in a form appreciable to that of normal service stressing. For a nine-unit string of porcelain disc insulators, this variation for lightning wave energization is a little greater than that of the AC case. However, the switching surge process needs to be examined further, especially as some features seem to be complex (eg. non-linearity of voltage with string length).

The lightning wave flashover voltage of an electrolyte surface - used here to provide a simple model of the well wetted part of the insulator - was found to vary with air density by an extent very similar to that of a normal air-gap. Consequently, it is argued that the impulse flashover of a practical insulator can be likewise regarded, thereby enabling the effect of altitude to be calculated.

The possibility of pollution flashover faults occurring on power networks due to lightning wave and switching surge events seems possible for the lower system voltages.

The experiments into the impulse strength of an air/water interface have identified aspects at the low and the high conductance values of the electrolyte that warrant further investigation in the quest to determine the flashover mechanism, both for polluted insulators and wetted wood poles.

REFERENCES

[1] Lushnicoff, N.L. and Parnell, T.M. - IEEE Vol PAS-90, No 4, pp 1619 -1627, 1971.
[2] CIGRE Working Group 33-04, Electra No 64, p132, 1979.
[3] Okado, T. and Koga, S. - IEEE Trans VOL. PAS-89, No.3, pp 437-441, 1970.
[4] Ely, C.H.A. and Roberts, W.J., Proc. IEE, Vol 115, No 11, pp 1667 -1671, 1968.
[5] Macchiararoli, B. and Turner, F.J., IEEE Trans Paper 71, TP 141-PWR, 1971
[6] CERL data, private communication
[7] Texier, C. and Kouadri, B. - IEE PROC Vol 133 Pt A, No. 5, pp 285-290, 1986
[8] Swift, D.A., Fourth Int. Sym. on High Voltage Engineering, Paper 44-07, 1983.
[9] Guan, Z., Warren, L., Bagdahdi, A.A.J. and Gouldsbra, D.R., Sixth Int Sym on High Voltage Engineering, Paper 33-03, 1989.
[10] Lambeth, P.J., Proc IEE Vol 188, No 94, pp 1115, 1971.
[11] CERL data, private communication
[12] AIEE Committee report, IEEE Trans PAS-75 Pt III, pp 16-21, 1956.
[13] Holtzhausen, J.P. and Englebrecht, C.S., Sixth Int Sym on High Voltage Engineering, Paper 12-06, 1989.

Ionic Current-induced punctures in toughened glass insulators

J.P. Reynders

1 Introduction

High voltage direct current (HVDC) transmission lines have become significant features in many large electric power systems. There are today fourteen major long-distance HVDC schemes in operation around the world. Service voltages range from 200kV to 600kV and the insulation is either glass or porcelain cap-and-pin strings. A small number of long rod composite insulators are also used. Toughened glass cap-and-pin insulators dominate, comprising roughly two-thirds of the total number installed. Service experience has shown that the spontaneous failure rate of these insulators on HVDC schemes is 10 to 40 times greater than that experienced with similar insulators used in HVAC networks.

2 Service Statistics

A comprehensive survey of the performance of HVDC insulators has been undertaken by Cigré Working Group 33-04 (1). An examination of these statistics shows:

i In areas where the pollution may be regarded as light, there is an indication that the failure rate decreases with time. Typical initial failure rates range between 0,10% and 0,15% p.a. and these declined to between 0,01% and 0,04% p.a. after periods of 10 or more years in service. This is a clear indication that the insulators contained a latent defect which was responsible for the failures. With the passage of time the insulators containing these defects fail and are replaced with sound insulators. A failure rate of 0,02insulators on HVAC lines.

ii In areas where the pollution is heavy, extremely high failure rates persist, even after periods of 10 or more years in service. These failure rates can be as high as 0,8% p.a. This implies that there is a factor associated with the operation of the line which causes the insulators to fail.

3 Failure Analysis

Two comprehensive studies (2)(3) have been undertaken to investigate failure modes. It has been found that the failures invariably propagate from a small inhomogeneity or inclusion which is trapped in the glass. Under clean or very lightly polluted conditions, the failures all emanate from the head of the insulator (Zone 1, Figure 1) (2) while with polluted insulators the majority of failures emanate from the portion of the insulator adjacent to the cap-and-pin but not in the head (Zone 2, Figure 1) (3).

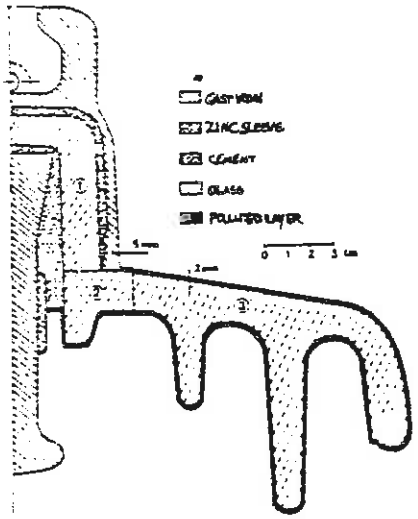

Figure 1 : Insulator Crossaction
Zone 1 : Contained between the cap and the pin.
Zone 2 : Portion of the external disk closest to the metal parts.
Zone 3 : Remaining part of the disk.

Under clean or lightly polluted conditions, the area of highest electrical stress in the glass is in Zone 1 whereas under polluted conditions, Zone 2 experiences an extremely severe stress because the surface of the glass nearest to the cap-and-pin becomes heavily eroded as a result of dry-band arcing and the pollutant adheres to these roughened surfaces and is not removed by natural washing. (4) These erosion channels act as extensions of the cap or pin and high electric stress and high current densities exist at their extremities. Any inhomogeneities or inclusions in Zone 2 are therefore potential sites for failure initiation.

A further point to be borne in mind with HVDC insulators is that the voltage distribution along the length of the string can be grossly non-uniform. The leakage current through the body of the insulators is extremely small and the distribution is determined largely by the surface leakage current. This in turn is influenced by the degree of pollution and its moisture content on each disk. The deposition of pollution and the absorption of moisture is never uniform and it has been found that flashover can occur across a single disk in a string. (5) 6).

In summary, it has been found that the failures are associated with:

- the presence of high local electric stress
- the presence of an inhomogeneity or inclusion in the area of high electric stress.

4 Failure Mechanism

A toughened glass insulator is formed by super cooling the molten glass in a mould. As a result of this rapid cooling, the surface layers of glass contract much more rapidly than the inner layers of glass. The finished insulator consists, therefore, of an outer skin a few millimetres thick, which is in mechanical tension and the inner portion of insulator, which is in compression. It is this stress distribution which gives the mechanical strength and toughness to the insulator. However, any mechanism which causes a redistribution of the internal mechanical stress within the insulator, can lead to a spontaneous shattering of the glass.

A mechanism of failure in terms of ion accumulation and depletion has been proposed. (7) An inclusion or inhomogeneity is most likely have a resistivity which is less than that of the glass body. This means that there will be an increased current density at the site of the inhomogeneity. The current carriers in the glass are sodium or potassium ions and under DC stress, these will accumulate on one side of the inhomogeneity and be depleted from the other side. Since these ions are significantly larger in size than the silicone atoms which make up the bulk of the glass, their accumulation will cause an increased compressive stress, while their depletion will cause an increased tensile stress. Over a period of time, there will be a redistribution of mechanical stress at the inhomogeneity site. This will change the normal stress pattern caused when the glass was super cooled during the forming of the insulator and will lead to shattering. In the case of pollution related erosion channels on the surface of the insulator, high leakage currents will exist at the extremities of these erosion channels. Accumulation and depletion of ions will therefore be present at these positions and also lead to shattering of the insulator.

A simple experiment (7) was conducted to demonstrate this mechanism. Flat glass samples 4,0mm thick and 200mm square were used in the arrangement shown in Figure 2. The holes into which the brass point electrode was fitted were made using a high speed diamond drill, or a brass bit and grinding paste. Samples were hardened by thermal shock after the drilling of the hole. Before the samples were used, a standard period of at least four weeks was allowed to preclude failures as a result of residual mechanical stress. None failed in this way. However, some did fail shortly after being placed in the test rig as a result of the slight mechanical pressure exerted by the point electrode and these were excluded from the experiment. The glass used is the same as that used for AC cap-and-pin insulators and its composition includes the following:

SiO_2	approximately	70%
Na_2O	approximately	14%
CaO	approximately	7%
K_2O	approximately	1%

A voltage of 30kV was maintained between the point and the plane with the point negative. The experiments were done in an air-conditioned laboratory with a temperature maintained in a range 20-22°C and the relative humidity at approximately 15%.

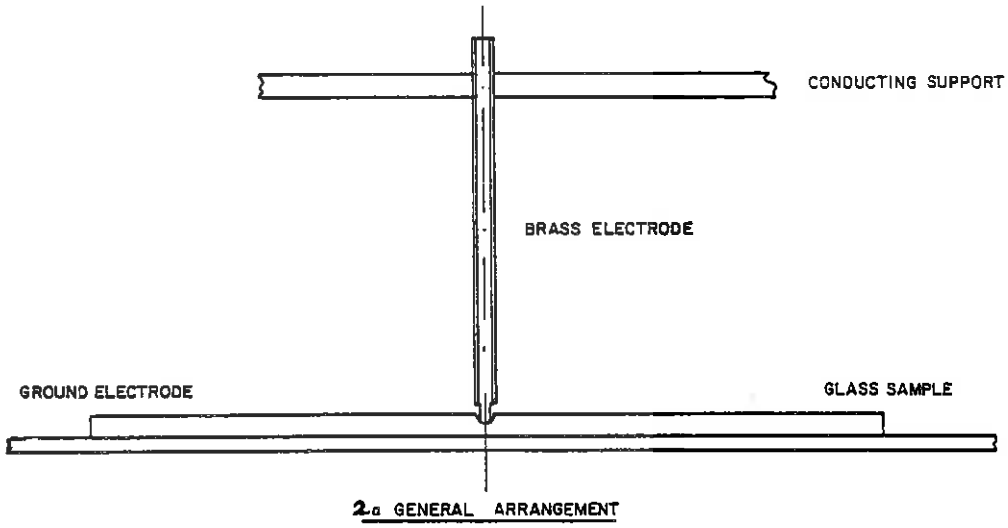

2a GENERAL ARRANGEMENT

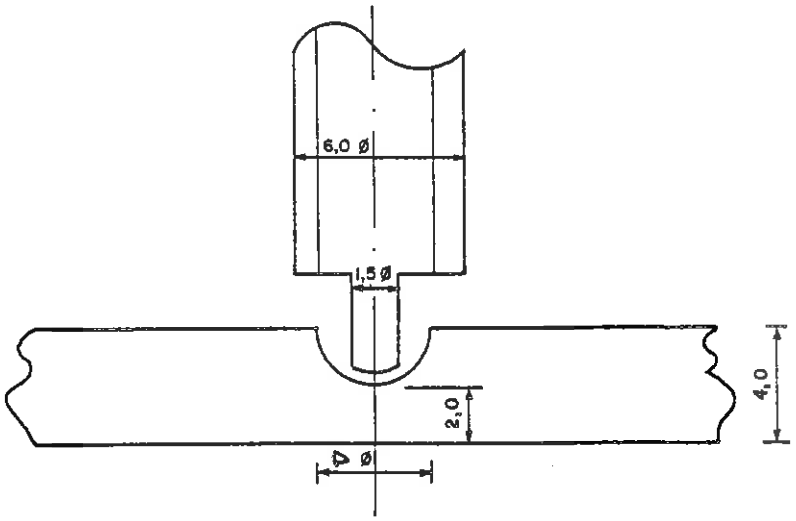

2b DETAILS OF HOLE AND ELECTRODE

FIGURE 2 EXPERIMENTAL SET-UP

Excluding the samples which failed immediately after being placed in the test rig, 13 were tested of which 11 failed. The failure statistics are shown in Table 1.

Sample No.	Dimensions Dmm (As in Fig.1.)	Days to Failure
1	1,8	5
2	1,8	8
3	1,8	8
4	1,8	10
5	1,8	22
6	1,8	20
7	1,8	35
8	1,8	8
9	1,8	14
10	3,0	16
11	4,5	27
12	3,0	>93
13	3,0	>93

Table 1 : Time to Failure of Samples

Photograph 1 shows the fracture in a typical sample. Complete shattering of the glass sheet occurred. The example in the photograph was reassembled after the shattering.

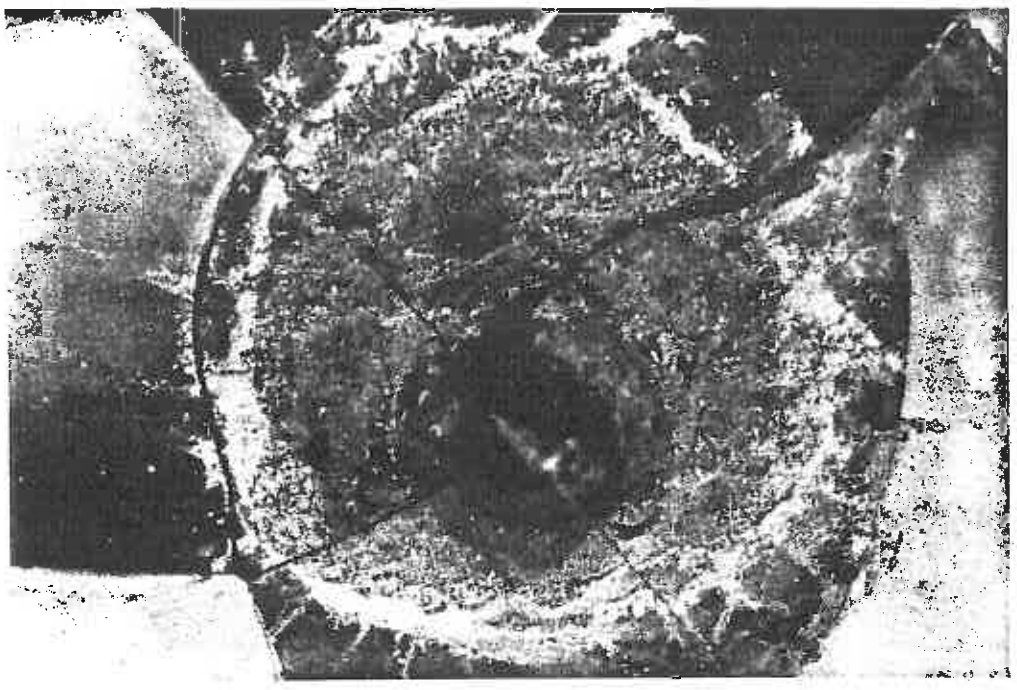

Photograph 1 : Failure site in sample. Mag 50X

Some samples were removed for surface chemical analysis prior to failure. Figure 3

shows the points on the surface of the sheet and the hole where analysis was performed. As expected, positions marked 1 showed a composition which represented the bulk composition of the glass. Position 3 at the bottom of the hole showed an enormous increase in sodium and potassium ions. (7)

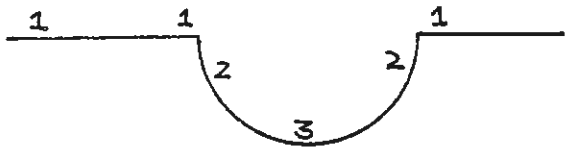

Figure 3 : Locations for Chemical Analysis

5 Remedial Measures

Clearly the purity of the glass is an important factor. In addition to the quality of the raw materials used in the formation of the glass, the quality of the refractory material in the furnace must be such that decomposition does not take place and contaminate the melt.

A further important measure is to reduce the ionic current in the glass. This can be done by reducing the concentration of sodium and potassium (these are the major ionic components). In addition since potassium ions are larger than sodium ions, the mobility in the glass body is much less than that of sodium ions. The replacement of sodium ions with potassium ions therefore, also reduces the ionic current. These measures have led to the production of high resistivity toughened glass insulators and although service experience is still fairly limited, indications are that their performance is vastly superior to that of the conventional HVDC toughened glass insulator. For example, on the Skaggerak line the failure rate of conventional HVDC glass insulators averaged at 0,41% p.a. (1) These insulators were replaced with high resistivity glass insulators in 1988 and todate none of the high resistivity insulators have failed.

6 Conclusion

1. Ion accumulation and depletion causes shattering of HVDC toughened glass insulators.

2. This shattering can be reduced by minimising the defects in the glass body and by the use of high resistivity glass compositions.

7 References

1. Reynders, J.P., Peixoto, C.A.O., De Decker, D., Marrone, G. "Failure of cap-and-pin insulators subjected to HVDC" to be published in Elektra in 1991.

2. Mailfert, R., Pargamin, L., Riviere, D. "Electrical reliability of DC line insulators", IEEE Trans on Electrical Insulation, V EI-16, No. 3, June 1981, pp. 267-276.

3. Peixoto, C.A.O., Pargamin, L., Marrone, G., Carrara, G. "Failure of transmission line cap-and-pin insulators under DC stresses", IEEE T and D Conference 1986, Paper 512-8.

4. Knudsen, M., Lundquist, J., Sherif, E. "Environmental effects of HVDC overhead lines", Report 36-02 Cigré Session 1980.

5. Fukushma, M., Sunaga, Y., Sasano, T., Sawada, Y. "AN, RI and TVI from a single unit flashover HVDC suspension insulation strings", IEEE Trans on Power Apparatus and Systems, V PAS 96, No. 4, July/August 1977, pp. 1233-1241.

6. Reynders, J.P., Meal, D.V. "Anomolous failure of toughened glass HVDC insulators", Fifth International Symposium on High Voltage Engineering, Braunschweig, August 1987, paper 5201.

J.P. Reynders
January 1991
ionic.tex

Investigations Towards a Better understanding of Very Fast Transient Breakdown in SF_6

G.L van der Zel & J.P Reynders
Department of Electrical Engineering
University of the Witwatersrand
January 1991

Abstract

Recent results examining the reduction in breakdown under VFTs (Very Fast Transients) to below that of LIs (Lightning Impulses) are presented. The results represent the initial stage of a systematic study of the three distinguishing features of VFTs, ie. the rapid rise, oscillating tail and weak damping. The paper focuses on results that isolate the effect of the rapid rise by excluding the influence of the oscillating tail and weak damping. The conclusions lead the way towards future tests on the latter features. The goal is to apply these results to GIS (Gas Insulated Substations) design, practices and diagnosis.

1 Introduction

This paper presents the recent experimental results examining the difference in breakdown under VFTs and LIs. The goals are firstly to determine the conditions under which VFTs are more critical than LIs and secondly to understand the mechanisms behind this breakdown. This information will be applied to aid GIS design, operating practices and diagnosis.

Experiments performed by various research bodies (including our laboratory) [1,2,3,4] have shown that under non-uniform field conditions VFTs can be more severe that LIs. Since LIs play a major role in GIS insulation co-ordination, the possibility of a more severe overvoltage must be investigated thoroughly. There is, at present, no consensus on this matter [2,5,6,7,8]. This is due to two major factors: Firstly, the scarcity of experimental data in SF_6 under VFTs; secondly, the lack of a standard VFT test waveform. Parameters such as rise-time, tail oscillations and damping vary with GIS geometry and hence vary from test to test. Since the roles of these parameters on breakdown are not known, comparisons of results are difficult.

A systematic study has thus been initiated where each of these aspect of VFTs is isolated and examined. This will highlight the aspects dominant in lowering the breakdown voltage of VFTs to below that of LIs.

VFTs differ from LIs in three major ways:

- VFTs have a very rapid rise time compared to LIs (10s of ns compared to approximately a microsecond)

- VFTs have a high frequency oscillating tail with a frequency dependant on station geometry (6MHz dominant frequency for our configuration)

- VFTs have a long decay time (ms), dependant on connected equipment.

It is important to know which of these three aspects plays the dominant role in lowering the breakdown voltage under VFTs. Once that is known, the mechanisms behind the breakdown can be investigated. This information will be vital in the following areas:

- Predicting potentially dangerous station layouts, (layout dictates the frequency of the tail)

- Adapting particular switching sequences to reduce the stress on the station (since VFTs are generated by disconnector switching operations).

- Developing commissioning tests for GIS that provide a higher sensitivity to problem sites.

This paper initiates this study by examining the effect of the rapid rise of the VFT in a non-uniform field. Breakdown under a LI is compared to that of a rapidly rising pulse with the same decay time (50 μs). The effects of tail oscillations and low damping are thus excluded.

To confirm that VFTs are more severe that LIs only in non-uniform fields, an experiment in a quasi-uniform field is also presented.

2 Experimental Set-up

All tests were performed in industrial grade 275kV GIS fitted with an SF_6 insulated bushing (Details in [9]). Only the more critical case of positive polarity on the more highly stressed electrode is considered. A 9 Stage Marx Impulse Generator was connected to the bushing. The final section of duct was fitted with a coaxial sleeve, forming the coaxial test gap (180/110mm). Industrial-grade SF_6 was used in the test-gap.

A radiation source of 100mCi Cs 137 was directed at the test-gap to provide additional initiatory electrons for specific tests. A disconnector switch was positioned between the bushing and the test gap. When the disconnector was closed, the Impulse Generator connected directly to the test gap, generating a lightning impulse (1.2/50 μs) in the test gap. By opening and adjusting the disconnector switch gap, breakdown across the switch could be achieved close to the peak of the LI. The rapid voltage collapse across the switch resulted in a waveform with a very rapid rise (80 ns) but identical decay (50 μs) in the test gap. An example of both the LI and the rapid rising pulse is shown in Figure 1.

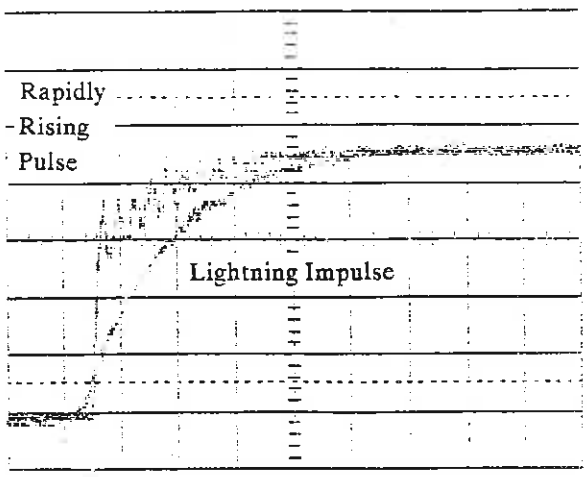

Figure 1 Sample Lightning Impulse and Rapidly Rising Pulse (0.2 μ s/div, 50kV/div)

Voltage was measured by means of a capacitive divider (500MHz Bandwidth) and a Digital Oscilloscope (1GS/s, 50kB memory). For the quasi-uniform field tests, a bus-bar of industrial-grade surface roughness was used in the coaxial sleeve. For the non-uniform field tests, a 2mm long 1mm diameter tungsten rod was mounted on the centre bus- bar in the coaxial sleeve.

3 Results

3.1 Quasi-Uniform Field Conditions

Performance of SF_6 in a coaxial geometry (ie a quasi-uniform field) is important for the design of GIS. LIs are most commonly used as the dimensioning overvoltage and hence it is important to confirm that VFTs don't have a lower breakdown voltage than LIs under these conditions.

Since the largest difference in breakdown voltage between LIs and VFTs has been found for pressures less than 3 bar [1], a pressure of 1 bar was maintained in the coaxial test-gap. Due to the large critical volume in this geometry (along the entire length of bus-bar), supplementary initial electrons from the radiation source were not required.

The volt-time curve for LIs was obtained and compared to the volt-time curve previously obtained under VFTs [10]. 6 minutes were left between each voltage application to allow the ions to reach their equilibrium densities [11]. The two curves are shown in Figure 2. The hatched area contains the breakdown points under VFTs. Two important results can be drawn. Firstly confirmation that, under quasi-uniform fields, VFTs and LIs have similar breakdown voltages. Secondly, evidence of a far greater scatter in breakdown voltages for VFTs than for LIs. This latter observation is currently under investigation.

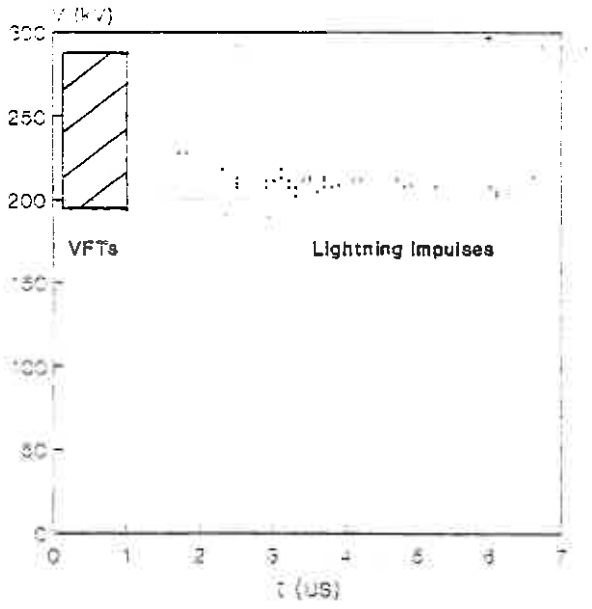

Figure 2 Volt-time curves for Lightning Impulses and VFTs under quasi-uniform fields

3.2 Non-Uniform Fields

Previous research on the difference in breakdown between LIs and VFTs was performed using a point-plane geometry [4]. Extrapolation of these results to the typical in-service fault condition of a field enhancement in a coaxial geometry (Free Conducting Particles) is difficult. To overcome this problem, a geometry as close to this in-service condition was adopted in the laboratory. This consisted of a small tungsten tip mounted onto the centre bus-bar of the quasi-uniform test arrangement (as described in Section 2).

In non-uniform field conditions VFTs have been shown to be more critical than LIs [1,2,4]. The purpose of the present investigations is to identify the dominant aspect (and later, hence the dominant mechanism) of VFTs that causes this lowering of the breakdown voltage.

The rapid rise is the aspect examined in this paper and is achieved by comparing the breakdown level of a rapidly rising pulse (0.08/50 µs) with that of a LI (1.2/50 µs). The two waveforms are shown in Figure 1. The generation of both is describe in Section 2. This comparison enables us to exclude the effects of the VFTs oscillating tail and weak damping and to isolate the effect of the rapid rise-time.

It has been shown [12] that for impulse breakdown comparisons, U_{50} values can be misleading and should be supplemented by comparisons of lower probability breakdown values. It was further shown that because of the small critical volume about the point, reliable low probability results can only be obtained if the gap is strongly irradiated.

Taking note of these findings, a 100mCi Cs 137 radiation source was placed facing the tungsten rod, outside the GIS enclosure. The radiation level in the test-gap was concluded to be strong enough firstly by comparisons with other laboratories' radiation intensities [12] and secondly by observing a dramatic reduction in the statistical time lag of the

gap when radiated (all breakdowns occurred on the waveform fronts. Without radiation, breakdown times had a wide spread and times of up to 12 μs were recorded.) U_{50}, U_{20} and U_{min} (the lowest breakdown voltage recorded in a test) were obtained for both waveshapes at pressures of 1.5bar and 2.5bar.

Comparisons of the breakdown probability values (U_{50}, U_{20} and U_{min}) of the LI with that of the 0.08/50 μs pulse showed that there was no measurable difference in the dielectric strength of SF_6 between the two waveforms.

This result indicates that the rapid rise-time of the VFT cannot, on its own, explain the reduction in breakdown to below that of LIs. The oscillating tail and weak damping are thus vital and must be further investigated.

4 Conclusion

Progress has been made in understanding both the impact and the reasons for the impact of VFTs or GIS. In particular,

- VFTs have been confirmed as being no more severe than LIs under quasi-uniform fields (ie in a clean GIS).

- Under non-uniform fields, the role of the rise-time of the VFT has been examined and has been shown to play, on its own, a minor role in lowering the breakdown voltage to below that of LIs.

Tests are under-way to examine the roles of the oscillating tail and the weakly damped tail. The findings will guide the investigations into the dominant mechanisms involved in the breakdown under VFTs. The goal is the application of these results to improve GIS design, practices and diagnostics.

5 References

1. H.Hiesinger. "Statistical time-lag in case of very fast transient breakdown", Sixth International Symposium on High Voltage Engineering, August 1989, Paper 32.23.

2. H.Hiesinger, R.Witzmann. "Very fast transient breakdown at a needle shaped protrusion", Conference on gas discharges and their applications, Venice, 1988, p323-326.

3. G.Luxa et Al. "Recent research activity on the dielectric performance of SF_6 with special reference to Very Fast Transients", 1988 Cigre Session, Paper 15-06.

4. G.L.van der Zel, J.P.Reynders. "The effect of surface imperfections on the breakdown strength of SF_6 under very fast transients", Sixth International Symposium on High Voltage Engineering, August 1989, Paper 22.24.

5. J.Nelson, B.Railing, J.Sollia Demacedo. "Divergent field behaviour of SF_6 subjected to steep fronted surges", Conference record of 1986 IEEE International Symposium on Electrical Insulation, Washington DC, June 9-11, 1986.

6. W.Pfeiffer, V.Zimmer, P.Zipfl. "Insulating characteristics of SF_6 and SF_6/N_2 mixtures for very fast transient voltages (VFTs)", Sixth International Symposium on High Voltage Engineering, August 1989, Paper 49.06.

7. A.Gibert, J.Dupuy, G.Riquel. "Dielectric Behaviour of SF_6 Point-Plane Gap Subjected to Fast Rising Impulse Voltage", Sixth International Symposium on High Voltage Engineering, August 1989. Paper 25.04.

8. G.Riquel, Z.Ren, L.Lefrancois. "Comparison between VFT and Lightning impulse breakdown voltages for GIS insulation in the presence of defects on live conductors", Sixth International Symposium on High Voltage Engineering, August 1989, Paper 23.09.

9. J.P.Reynders, J.Mepplink. "Characteristics of disconnect switch transients and control of the consequent electromagnetic interference" Open conference on EHV transmission systems, Paper No. 6, 1987.

10. S.D.Nielson, H.Wardley. "Breakdowns in a coaxial gap due to disconnector transients and simulation of VFTs using ATP", Department of Electrical Engineering, University of the Witwatersrand, 4th year report No. 50P/90, 1990.

11. J.Kindersberger, W.Taschner. "Impulse voltage breakdown in SF_6 with AC and DC bias voltages", Symposium on GIS Technology and Practice, Toronto, 1985.

12. I.Chalmers, O.Farish, S.MacGregor. "The effect of impulse waveshape on point-plane breakdown in SF_6", Gaseous Dielectrics IV, Pergamon Press, 1984.

Acknowledgements

The authors would like to thank ESKOM (EI) for the funding of portions of this work.

ELECTRICAL BREAKDOWN DATA FOR A NOVEL INSULATING FLUID

D.A. Hoch J.P. Reynders

University of the Witwatersrand

ABSTRACT

This paper reports on the results of an experimental investigation into the dielectric properties of mineral oil/perchlorethylene mixtures. The primary aim of this work is to identify that mixture which displays the highest dielectric breakdown stress under both uniform field and divergent field electrode geometries. The mixture of 35% perchlorethylene to 65% mineral oil is found to be the strongest dielectric under both geometries. The variation in dielectric breakdown stress with temperature has been ascertained to ensure that the observed improvements are retained at high temperatures. Thermal properties of the novel mixture have been briefly investigated and preliminary results are presented.

1. INTRODUCTION

The need for a non-flammable, low-toxicity liquid dielectric has long been identified and has been the subject of on-going research by the authors for several years. This initial research investigated a novel dielectric fluid comprising a 1:1 mixture by volume (v/v) of pentaerythritol ester and perchlorethylene. This work demonstrated that the mixture had a higher dielectric strength under most conditions than a typical mineral oil [1]. Further, this mixture was less sensitive to typical contamination (moisture, increased acidity and particles) than mineral oil. The combination of this low-flammable fluid with the totally non-flammable perchlorethylene resulted in a fluid that, according to classical definitions [2], may be classed as non-flammable. Unfortunately, the ester carried a significantly higher cost than mineral oil. In order to find a more economically viable non-flammable replacement for mineral oils, a potential mixture of mineral oil with perchlorethylene is currently being investigated. Further, important data on the breakdown behaviour of other low-flammable liquids (paraffinic hydrocarbons and silicones) is being collected.

Mixtures of perchlorethylene with mineral oil have already been investigated by EPRI [3] but the mixture developed in this work carried a very high loading of perchlorethylene (75% by volume). Two commercially available liquids based on perchlorethylene have been developed overseas, one being primarily highly purified perchlorethylene with proprietary stabilisers added, the other being a mixture of perchlorethylene with various chlorofluorocarbons [3]. Recent cutbacks and the expected ultimate ban on the use of CFC's by all industries make the second mixture unsuitable for use in transformers and both fluids suffer from cost disadvantages.

In spite of the developmental work performed on these liquids, not much experimental work has been performed or published on the electrical breakdown strength of these liquids under conditions likely to be encountered in a practical transformer. The only data readily available is that data relating to standard specifications for transformer dielectrics i.e. sphere to sphere breakdown voltages, tan delta, volume resistivity and permittivity. No published data has been located concerning behaviour in highly divergent fields.

The purpose of this work is to present much needed data on this particular subject while examining whether the quantity of perchlorethylene added to mineral oil may be reduced significantly while still retaining an acceptable degree of fire retardance. This paper does not address the fire retardance issue but does examine electrically optimum perchlorethylene/mineral oil mixtures.

2. EXPERIMENTAL PROCEDURES FOR DIELECTRIC STRENGTH DETERMINATION

It is generally accepted that the dielectric strength of a mineral oil under highly purified conditions is not retained with time as the oil absorbs gases and moisture from the surrounding atmosphere. In a fully sealed unit the problems of moisture absorption are mainly solved but the header gas used to fill the space above the oil (typically dry nitrogen) will be absorbed into the oil thereby decreasing the breakdown strength considerably. The question is therefore under what conditions should a mineral oil be tested i.e. highly purified or with dissolved gases present. It would appear that the liquid containing dissolved gases is more representative of the condition of the oil to be found in a transformer. This work has investigated both conditions in order to provide comparative for the breakdown strengths between a highly purified mineral oil and the fluid in the as delivered condition when mixed with industrial grade perchlorethylene.

The purification procedure followed was not as rigourous as used by many researchers but nevertheless good correlation between our data and data published elsewhere for highly purified liquids has been achieved. The purification procedure essentially comprised a heating stage of 80°C for one hour, the liquid then being allowed to cool under a vacuum of less than 1 millibar for two hours. After removal from the vacuum chamber, the liquid is immediately introduced into the test cell. Ten minutes settling time is allowed before the first voltage application. By following this procedure, a high degree of repeatability was achieved (mean breakdown strengths within 4% between separate samples). Mineral oil, the ester and the paraffinic oil were the only liquids treated this way, the volatility of perchlorethylene making it unsuitable for high vacuum treatment.

The silicone oil tested (DC 200/100) was purified by heating the liquid to 100°C for two hours and then cooling under partial vacuum (0.7 bar) back to room temperature. Again good repeatability was achieved in terms of the mean breakdown voltages for each sample of the fluid treated in this way.

Two electrode geometries were utilised for the determination of dielectric strength : one, a quasi-uniform field geometry comprising two 12.5 mm spheres with a gap length of 2.5 mm; the second, a divergent field geometry comprising a point-sphere electrode (20 mm diameter sphere) with a gap length of 25mm.

The reported breakdown voltages were determined by the application of a ramped a.c. voltage to the test geometry (rate of rise of voltage being 2.5 kV/sec) until breakdown occurred. Between six and ten such applications were performed on one cell filling, the reported breakdown voltage being the arithmetic mean of the achieved breakdown voltages. After each breakdown, the liquid in the cell was stirred to remove the breakdown debris from the electrode gap. Only one minute was allowed between voltage applications for the liquid to settle.

3. EXPERIMENTAL RESULTS

The results for the highly purified liquids and uniform field geometries are shown in Table 1. The acceptance values of breakdown strength for each fluid are also given and are obviously typical for each liquid when tested in the as supplied condition.

TABLE 1 : BREAKDOWN DATA FOR PURIFIED LIQUID DIELECTRICS : UNIFORM FIELD

LIQUID	CLASSIFICATION	BREAKDOWN STRENGTH (kV rms)	TYPICAL VALUE (kV rms)
Mineral oil	Flammable	76	30
Paraffinic oil	Low-flammable	47	45
Ester	Low-flammable	54	45
Silicone	Low-flammable	64	40
Formel(™)	Non-flammable	-	50

The typical values reported in the above table are the minimum acceptance values for each liquid, these values being obtained either from the appropriate standards (e.g. BS148 or [4]) or from [3].

As may be seen, breakdown voltages far in excess of the acceptance value for the liquids in the as supplied condition are achieved after extra purification. The breakdown measurements recorded for both the silicone liquid and the mineral oil correspond very well with results obtained by other researchers using highly purified liquids [4]. Further tests performed on each liquid in the as delivered condition (the only processing being a filtration stage through an 8 micron sintered borosilicate glass filter enabling high efficiency filtration at high temperatures) produced the results given in Table 2.

TABLE 2 : BREAKDOWN DATA FOR LIQUIDS AS SUPPLIED : UNIFORM FIELD

LIQUID	BREAKDOWN STRENGTH (kV rms)
Mineral oil	54
Parafinnic oil	36
Ester	45
Silicone	45

The low breakdown voltage measured for the paraffinic hydrocarbon is undoubtedly due to the exposure of the liquid to contamination (probably moisture). The result for mineral oil could also be obtained by exposing a sample of the highly purified oil with the breakdown voltage given in Table 1 (76 kV) to the atmosphere (T = 24°C, RH = 35%) for 24 hours. This indicates clearly the fact that a highly purified oil is not typical of what we expect in a transformer.

The repeatability achieved in the breakdown tests enabled us to do comparative tests of mineral oil/perchlorethylene mixtures with a high degree of confidence. For these tests, the liquids were tested in the as delivered condition - only filtration down to 8 microns was performed. The concentration of perchlorethylene was increased from 20 % to 50 % and the change in breakdown voltage noted.

4. DISCUSSION

The results for the uniform field tests are shown in Figure 1 while those for the divergent field tests are shown in Figure 2. The variation in breakdown strength with temperature for the optimum mixture (35% perchlorethylene / 65% mineral oil) for both geometries is shown in Figures 3 and 4.

It is quite clear from Figures 1 and 2 that, of the mixtures investigated, the mixture comprising 65% mineral oil:35% perchlorethylene v/v (i.e. 1,85:1 v/v) displayed a significantly higher mean breakdown strength under both geometries. A concentration of 40% perchlorethylene to 60% mineral oil also displayed very high breakdown voltages. Figures 3 and 4 clearly indicate that the optimum mixture of 1,85:1 retains its superior dielectric strength between 20°C and 80°C. Of particular interest is the breakdown strength at 60°C since at this temperature the breakdown strength of the mineral oil approaches that strength reported in Table 1 for the highly purified case. At 20°C the optimum mixture is 18% stronger than pure mineral oil, while at 60°C it is still 10% stronger. It is also important to note that the mixture essentially displays a very similar breakdown strength versus temperature characteristic as the mineral oil. This dependence of mineral oil breakdown stress is well documented [5]. The ability of mixtures of perchlorethylene with other liquids to significantly improve the breakdown behaviour while retaining the same general breakdown characteristics in terms of sensitivity to temperature changes has previously been noted by the authors [1].

The significant increase in breakdown strength for the optimum mixture is more pronounced under the divergent field geometry where an increase of 33% over the pure mineral oil is noted at 20°C and an increase of 26% at 60°C.

with other liquids to significantly improve the breakdown behaviour while retaining the same general breakdown characteristics in terms of sensitivity to temperature changes has previously been noted by the authors [1].

The significant increase in breakdown strength for the optimum mixture is more pronounced under the divergent field geometry where an increase of 33% over the pure mineral oil is noted at 20°C and an increase of 26% at 60°C.

An important point to note from the results presented here is that the results obtained purely from the quasi-uniform electrode geometries may be misleading in terms of the performance of the liquid under larger gap distances and more divergent fields. As an example, the introduction of 20% v/v of perchlorethylene to mineral oil leads to a lowering of the breakdown strength under the quasi-uniform field (by 9% at 20°C), while under the divergent geometry an increase of 9% is realised.

This data implies that clearances may be reduced considerably while still maintaining dielectric integrity. Before such size reduction is performed in the design of a transformer, it is essential to determine the thermal characteristics of the fluid.

5. THERMAL PERFORMANCE OF THE OPTIMUM MIXTURE

The thermal performance of the 1.85:1 mixture has been investigated in the first instance via the retrofitting of a small 6.6 kV, 15 kVA transformer. Two such transformers were made available for the tests. The transformers were loaded by running them back to back i.e. supplying the low voltage side of the first transformer and loading on the low-voltage side of the second transformer. Hence the first transformer (the one containing the perchlorethylene/oil mixture) supplies both the load current as well as the losses of both transformers. The new fluid should therefore be subjected to slightly higher thermal stresses than the mineral oil. Initial indications are that under full load conditions the thermal performance of the two liquids is very similar in these particular transformers with the perchlorethylene/oil mixture displaying a slightly faster rise in top oil temperature than the oil filled unit. Both top oil and winding temperature rises were very similar for both transformers. The faster thermal time constant of the perchlorethylene/oil mixture should result in lower mean winding temperatures under temporary overload conditions. Under a heavy overload (50% for two hours starting from room temperature) the perchlorethylene/oil mixture displayed a mean winding temperature rise 3°C lower than the mineral oil filled unit.

We clearly need to measure the losses in each transformer before we can reach too many conclusions about the thermal performance of the new mixture. However, it is quite clear from the initial tests performed that the thermal performance will not be significantly worse than mineral oil if it is indeed not better. It would appear, therefore, that the new mixture may be suitable for retrofitting existing transformers and introducing the liquid into existing designs without major modifications.

6. REQUIRED FURTHER WORK ON THE NEW FLUID

The introduction of significant quantities of perchlorethylene into a low-flammable liquid (an ester) introduces a very high degree of fire retardance (this has been observed in previous experimental work performed on the 1:1 mixture of perchlorethylene and pentaerythritol ester utilising the British Naval Engineering Specification NES 713 to investigate flammability and toxicity) and we would also expect it to increase the fire retardance of mixtures of mineral oil and perchlorethylene. This increase in fire retardance needs to be investigated, again with regard to optimizing the performance as a function of perchlorethylene concentration. Further, issues relating to the toxicity of the mixture need to be addressed especially where the mixture is exposed to a fire causing decomposition of the perchlorethylene. Gases generated under heavy arcing also need to be determined.

In previous work by the authors on perchlorethylene, the ability of perchlorethylene to extinguish partial discharges impinging on the liquid in an air-filled cavity was noted [7]. The performance of oil/perchlorethylene mixtures also needs to be addressed in terms of this extinction mechanism to ascertain how effective this mechanism will be compared to the pure perchlorethylene investigated previously as well as the performance in a practical situation.

7. CONCLUSIONS

The following conclusions may be drawn from the experimental results presented here :

- A mixture comprising 35% perchlorethylene to 65% mineral oil v/v results in significantly increased mean breakdown voltages under uniform and divergent field conditions.

- This increased strength is retained with temperature up to 80°C.

- Indications are that the thermal properties of the optimum mixture will make it a suitable fluid for retrofit operations.

8. ACKNOWLEDGEMENTS

The authors would like to acknowledge the work performed by Messers Northrop and Paravano, who obtained certain of the data presented here as part of their fourth year thesis work. We would also like to express our appreciation to ESKOM for the two transformers used in the heat run tests.

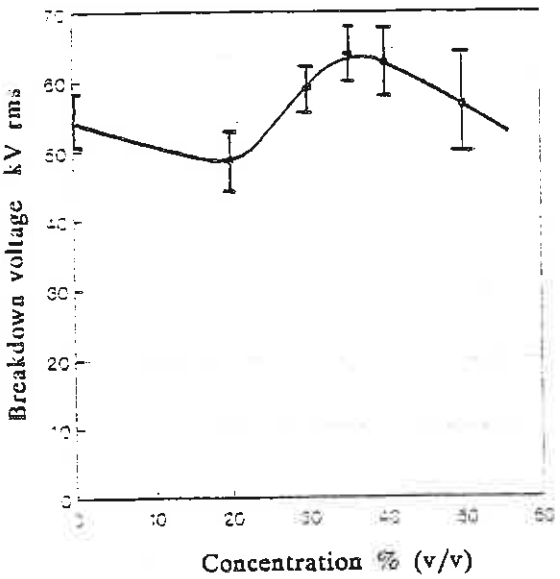

FIGURE 1 : Variation in mean breakdown voltage with increasing perchlorethylene concentration : Sphere-sphere electrodes : 2.5 mm gap : 20°C

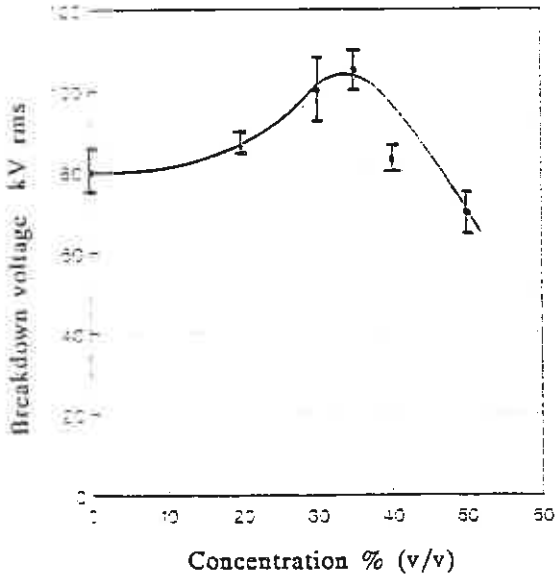

FIGURE 2 : Variation in mean breakdown voltage with increasing perchlorethylene concentration : Point-sphere electrodes : 25 mm gap : 20°C

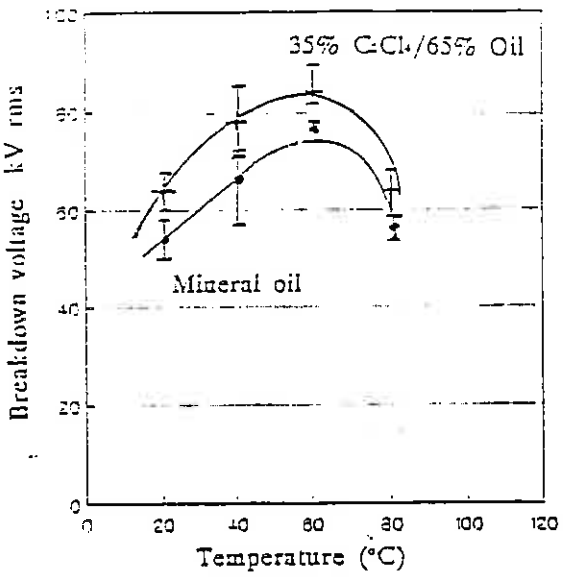

FIGURE 3 : Variation in mean breakdown strength versus temperature for the 35% perchlorethylene : 65% mineral oil mixture : Sphere-sphere electrodes : 2.5 mm gap

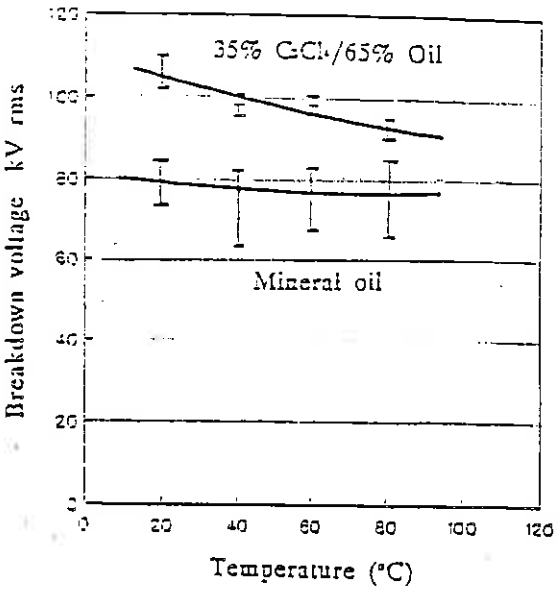

FIGURE 4 : Variation in mean breakdown strength versus temperature for the 35% perchlorethylene : 65% mineral oil mixture : Point-sphere electrodes : 25 mm gap

9. REFERENCES

[1] Hoch, D.A. and Reynders, J.P., Breakdown behaviour of a non-flammable synthetic liquid under conditions of particle and moisture contamination, Paper 13-07, Proceedings of Sixth International Symposium on High Voltage Engineering, New Orleans, USA, 1989.

[2] British Standard 2000 Part 34, 1986.

[3] The low-flammabilty transformer, ERA Report 87-0021, 1987.

[4] Draft ESI Standard 35-00, Standard for Formel NF Filled Transformers, May 1984.

[5] Binns, D.F., A review of recent research into the electrical properties of synthetic ester fluids, Paper 3, One day international seminar on Dielectric Fluids for Transformers, London, 2nd June, 1983

[6] Clarke, F.M., Insulating Materials for Design and Engineering Practice, John Wiley and Sons, 1962.

[7] Ruffini, A., Hoch, D.A., Reynders, J.P., Partial discharge behaviour of halogenated liquids, Paper 13.14, Proceedings of Sixth International Symposium on High Voltage Engineering, New Orleans, USA, 1989.

Consideration of the Transient Skin Effect in Co-axial SF_6 Insulated Systems, and an Analysis of this Effect in Various Types of Conductor

JP Reynders and IR Jandrell
University of the Witwatersrand, Johannesburg

Abstract

While the normal skin effect results in the so-called AC resistance of a conductor (R_{AC}), the transient skin effect results in the transient resistance of the conductor (R_{TR}). It is shown that, in the determination of R_{TR}, a very important parameter is the time that it takes the fields to penetrate the conductors. In particular, it is shown that the steady state condition is reached in vastly differing times for different conductor materials. For aluminium, copper, mild steel and 3CR12, the coefficient of velocity of current penetration, h, the velocity of penetration, v_p, and the transient skin depth, δ', are quantified. These parameters are of concern when modelling transients with very fast rise times. Particular consideration is given to conductors incorporating ferromagnetic materials, as the transient skin effect is shown to be particularly marked in this case. The effect of relative permeability is noted.

Keywords

SF_6, skin effect, transient, very fast transients, ferromagnetics coatings, permeability

1 Introduction

Both the time and frequency domain have been shown to offer accurate techniques of simulating the transient performance of gas insulated systems /1/. In particular, it has become possible to model very fast transients (VFTs) very accurately. However, while much emphasis has been on the transmission and reflection of transient phenomena along the conductors in a system, little emphasis has been on the time-dependent current penetration into the conductors themselves. Recent work on the measurement of VFTs in SF_6 insulated systems has shown that disparate results may be obtained if the time taken for the establishment of the magnetic fields within the conductors is ignored /2/. A model for the transient skin effect is discussed in terms of its accuracy and relevance to this type of transient event. Furthermore, the effectiveness of the transient resistance as an attenuating influence is discussed for various types of system.

In order to experimentally examine the effects of a ferromagnetic coating upon the attenuating characteristic of a section of duct, tests were conducted in two similar systems. In one, the busbars were fabricated from aluminium, and in the other from mild steel. The tests were conducted at voltages which ensured that the peak magnitude reached by the transients was in excess of 200 kV. This ensures an initial step voltage of magnitude similar to that used in previous predictions /3/.

The fact that a significant difference was detected between the measured and the predicted results, particularly in the mild steel system, made it clear that the diffusion of the electric current into the busbars had to be accounted for.

2 An Overview of the Skin Effect in Co-axial Conductors

Of particular concern to anyone interested in modelling the skin effect in conductors is the detail that is desired for the particular application. For example, it is important to distinguish between the so-called AC resistance (R_{AC}) and the transient resistance (R_{TR}) of the conductors. Both have been the subject of numerous investigations /4//5//6//7/, and are defined in terms of the field penetration into the conductors. Importantly, determination of R_{AC} implies a steady state phenomena - frequency dependent, but not time dependent. R_{TR} is associated with a time dependent effect that would ultimately result in $R_{TR}=R_{AC}$ if the stimulation were to continue for sufficiently long. In the choice of the most suitable model to use for a particular application, care must be taken to assess the relevance of the model against the accuracy that can be expected.

In the determination of R_{TR}, a very important parameter is the time that it takes the fields to penetrate the conductor, as the value of R_{TR} represents the resistance seen by the current caused to flow in the conductor by the diffusion of the flux into them. This implies the association of a time constant with the development of the fields within the conductors. A simple model clearly showing this effect has been proposed by Yen, Fazarinc and Wheeler /7/. For a continuous length of co-axial line where the inner and outer conductors are fabricated from the same homogeneous material, the line is divided into N sections. Each of the N sections consists of M partial resistors and M-1 partial inductors derived directly from the skin effect differential equations. This concentric ring definition of a co-axial line, as well as the skin effect equivalent circuit, is shown in *figure 1*.

A number of important observations pertaining to this model can be made:

- The effective resistance of the line is a function of time, where the partial resistances and partial inductances dictate the time constants associated with the transient current distribution within the conductor.

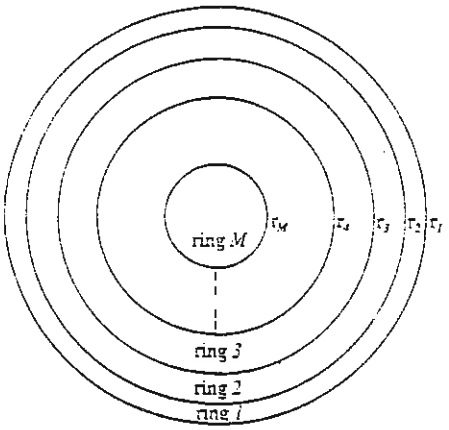

(a)

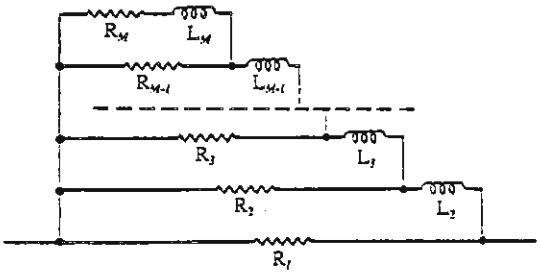

(b)

Figure 1 : (a) Concentric ring definition of the centre conductor of a coaxial system, and (b) the skin effect equivalent circuit /7/.

- The current distribution at DC is uniform, as expected, and the DC resistance, R_o, is given by the parallel combination of the partial resistors.
- The high frequency resistance is limited to the resistance of the outermost ring.
- Under transient conditions, the current distribution is valid for an instant in time, and the series resistance, R_{TR}, is thus also valid only for that instant.
- The partial resistances and inductances must be related to constant physical parameters of the material - the conductivity (σ) and permeability (μ) respectively.

For the systems of interest, it is important to quantify the time taken for establishment of the steady state condition under stimulation by a step wave with a very fast risetime. In this consideration, the steady state skin depth, δ, is an important parameter as it dictates the thickness of the layers required in order to usefully model the transient component of the skin effect. Clearly, if δ were 10μm, then each layer in the model should be thinner than this in order to introduce the time dependent effect. The velocity at which the current penetrates the conductors is thus important.

3 A Consideration of the Coefficient of Velocity of Current Penetration, *h*

Miller has shown from the skin effect differential equations for a cylindrical conductor, that for any (conductive) material a coefficient of current penetration (or diffusion), h, may be determined /4/. Thus the velocity of current penetration, v_D, may be defined:

$$v_D = \frac{h}{\sqrt{t}}$$

where: v_D = current penetration velocity [m/s]. (Recall that the current propagates along the conductor in the direction of current flow. v_D defines the velocity of current penetration (diffusion) from the conductor surface into the conductor in a direction normal to the axial direction of current flow.)

h = coefficient of current penetration [m/$\sqrt{s}$].

t = time [s].

Two important observations may be made:

- v_D is not a constant, but decreases with time inversely as the square root of time.
- At any time the approximate depth to which current has penetrated (diffused), δ', may be defined as:

$$\text{ie} \qquad \delta' = 2h\sqrt{t}$$

Thus, in order to be able to predict the transient skin depth, δ', and the velocity of penetration, v_D, it is necessary to determine the coefficient of velocity of current penetration, h, for the materials of interest. Values of h may be determined from the following relationship:

$$h = \frac{1}{\sqrt{\mu_o \mu_R \sigma}}$$

It should be noted from the above relationship that the relative permeability, μ_R, is an important parameter in the equation. The implications of this are that, in predicting values of h, a value of μ_R must be chosen. Actual skin effect modelling of current carrying ferromagnetics under transient conditions has not been achieved, and experimental results are limited to the lower frequency ranges /6/. Values of h for various materials are shown in *Table 1*. It can be clearly seen that a variation in permeability of 1000 can alter the value of h by a factor of $\sqrt{1000}$.

Table 1 : Coefficient of velocity of current penetration for four materials. In the case of ferromagnetics, values of μ_R used in the evaluation are noted.

Material	Conductivity [S/m]	μ_R	h [m/√s]
Aluminium	$3,5 \times 10^7$	1	0,150
Copper	$5,8 \times 10^7$	1	0,117
Mild Steel	$1,0 \times 10^7$	1	0,282
		10	0,089
		100	0,028
		1000	0,009
		2000	0,006
3CR12	$1,8 \times 10^6$	1	0,665
		10	0,210
		100	0,066
		1000	0,021

4 Current Penetration Velocity (v_D) and Transient Skin Depth (δ')

Using values of h determined above, v_D is shown in *figure 2* as a function of time for three materials - copper, aluminium and mild steel. In the case of the mild steel, the relative permeability has been assumed to be a constant of 1000.

The velocity of penetration is significantly more rapid in the copper and aluminium than in the steel. Furthermore, v_D is approximately 1,25 times more rapid in aluminium than in copper. Based on this information, it is important to quantify the time taken to reach the steady state skin depth in the materials. Due to the nature of the formation of a VFT, it is not the oscillation frequency that is of concern - rather it is the range of frequencies associated with the risetime of the initial step.

It is furthermore important to consider the effect of permeability on the velocity of penetration. It should be stressed that while the surface "layer" of a ferromagnetic material may have saturated, the deeper regions of the material, being unaware of the penetrating flux, present an unsaturated value of permeability to the flux. The effect of permeability on the v_D is shown for mild steel and 3CR12 in *figures 3* and *4* respectively.

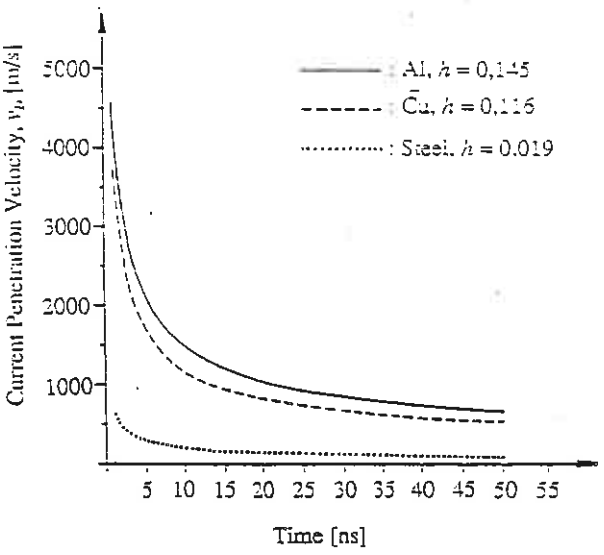

Figure 2 : Velocity of current penetration into a conductive material as a function of time, shown for three materials.

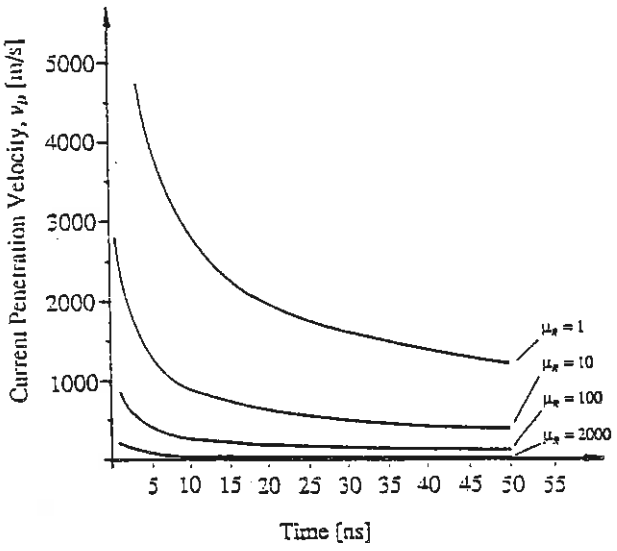

Figure 3 : Velocity of current penetration into mild steel shown as a function of time for different values of μ_R.

The Fourier spectrum of a typical VFT is shown in *figure 5*. The highest frequency components are associated with the very fast rising edge of the transient. The component at 15MHz is associated with the oscillation frequency of the system in which the VFT was recorded. The value of the steady state skin depth, δ, is thus dictated by frequencies of 25MHz and greater (based on the accepted range of initial risetimes for VFTs). Consequently, concern must be with the time taken for the current to diffuse to a depth of $\leq 17\mu m$. Thus, any time domain model must accurately account for the current penetration

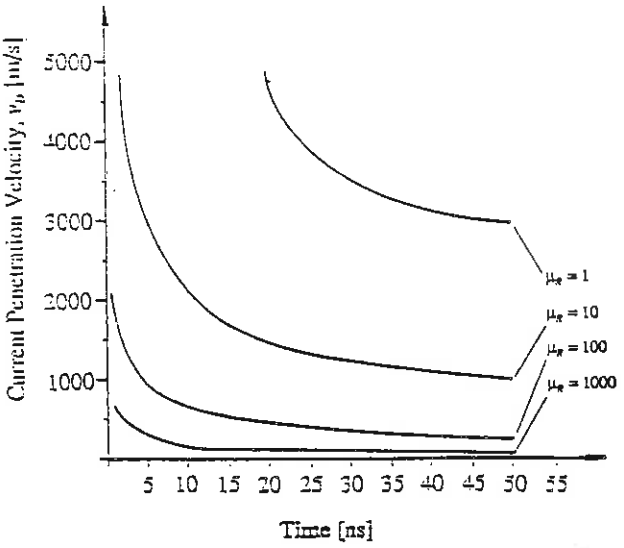

Figure 4 : Velocity of current penetration into 3CR12 shown as a function of time for different values of μ_R.

to this depth. In particular, the frequencies associated with the very fast rising edge must be accounted for. For the system used in this investigation, the risetime of the initial step was in the order of 5ns, implying that δ be set by frequencies of $\geq$100MHz. Under these conditions, δ is $\leq$8,5µm. Clearly shown in *figure 6* is the very rapid current penetration into an aluminium system. The steady state skin depth is reached in a short time. While the penetration into the steel is slow, the steady state skin depth is also small. The depth to which the current has penetrated is shown as a function of time in *figure 6*.

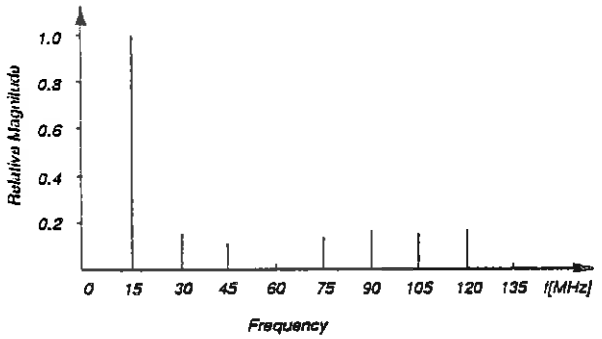

Figure 5 : The Fourier spectrum of a typical VFT /8/.

The transient skin depth is shown for mild steel and 3CR12 in *figures 7* and *8*. Once again, emphasis is placed on the effect of μ_R.

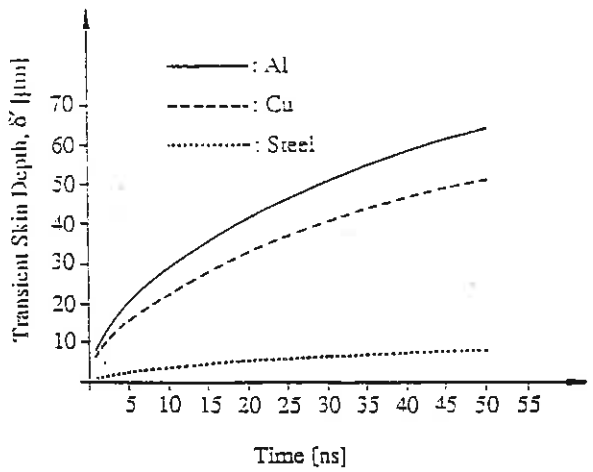

Figure 6 : Depth to which current has diffused into a conductive material, shown as a function of time for three materials.

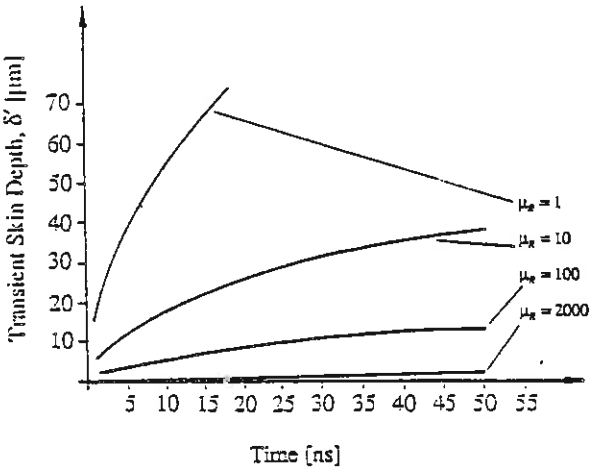

Figure 7 : Depth to which current has diffused into mild steel, shown as a function of time for differing values of μ_R.

5 Discussion

Previous work /3/ has shown the importance of the factor $\mu_R\sigma$. Particular emphasis was placed on the increase in the risetime and the decrease in the peak magnitude of surge and pulse waveforms as they were transmitted along a single continuous section of busduct. It is apparent from the above analysis that in the case of the transient skin effect, the relative permeability of the material plays a particularly important role.

While it was previously noted that saturation effects within the ferromagnetics would adversely affect the attenuating properties of the coating /9/, it must be appreciated that the transient component of the skin effect will enhance the attenuation. This is because the attenuation is governed by the actual depth of penetration into the

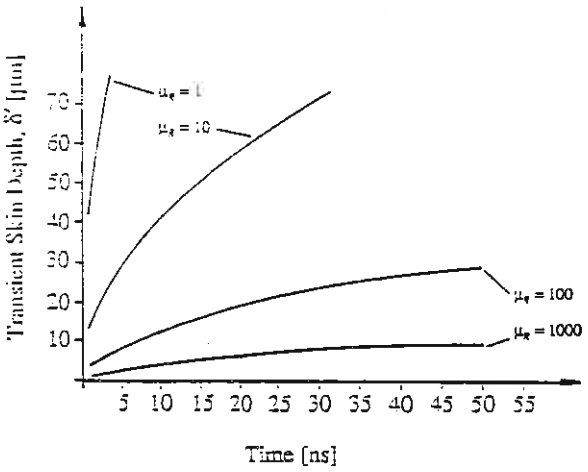

Figure 8 : Depth to which current has diffused into 3CR12, shown as a function of time for differing values of μ_R.

coating material at any instant in time. Consequently, while the outer layer (for example a fraction of a micrometer of the coating) may indeed be saturated, the deeper layers will be presenting unsaturated values of relative permeability to the penetrating flux, effectively slowing down the current penetration. This naturally results in a high series resistance for a long period of time.

While the technique illustrated in *figure 1* does present a viable approach to modelling the transient skin effect, it can be seen in the light of the above discussion that, in order to ensure accurate modelling of VFTs with risetimes in the 5-20ns range and having durations of some microseconds, the time constants associated with the skin effect model (and hence the time step Δt) would need to be very short indeed. It has also been shown that the steady state skin depth for an aluminium system is reached during a time span equivalent to the risetime of the initial step. Furthermore, inclusion into the model of the effects of coatings is not trivial. All these limit the usefulness of this technique applied to GIS busducts. It nevertheless ensures an appreciation of both the physical processes involved and the limitations of frequency domain modelling of transient events.

In the case of ferromagnetics it is particularly difficult to model the transient event. While the steady state skin depth can be accurately determined with a knowledge of the flux density under the anticipated conditions, it should be noted that the permeability changes markedly under the influence of the penetrating flux. The increased attenuation recorded in the laboratory is ascribed to the influence of the unsaturated deeper layers of the ferromagnetic coating.

It is thus concluded that, in order to accurately model the transient skin effect in current carrying ferromagnetics, it is necessary to allow differing values of relative permeability to be used in each layer of the model. Furthermore, it is necessary to allow those values to be adjusted in time as the simulation progresses. It is also clear that any model used in the simulation of VFTs must be carefully utilised if ferromagnetics are present. In particular, care must be taken in selecting a suitable value of relative permeability. It appears that, due to the nature of the VFT, accurate results are to be expected using existing modelling techniques in cases where the steady state skin depth is reached rapidly. Where the time taken to reach this steady state value is long (with respect to the initial rise time), the time dependent penetration of the flux must be accounted for. However, the increased time for penetration may make it possible to utilise a time step in accordance with the frequency range associated with the VFTs. Where rapid penetration to steady state value occurs, the time step must be selected in order that the initial risetime is made up of a multiple of this step. It is not feasible to realise such a simulation technique.

Conclusion

Laboratory test results using ferromagnetic busbars have shown an increased attenuation over predictions. The enhanced attenuation may only be justifiably accounted for by using a higher value of μ_R in the simulation. This has the effect of constricting the transient to an even thinner layer near the surface of the conductor. This is precisely the nature of R_{TR}. The coefficient of velocity of current penetration has been quantified for a number of materials. Using this coefficient, the transient skin depth and the velocity of current penetration for copper, aluminium, mild steel and 3CR12 have been determined. The marked influence of relative permeability is noted. While the assumption that the flux is instantaneously established within the busbars has been found to correlate well with observations made in an aluminium system, in the ferromagnetic case the transient skin effect is strong. This is characteristic of unsaturated ferromagnetics. During the transient event, the deeper layers of the conductors have not yet saturated, and hence present a high permeability to the flux as it penetrates and ultimately saturates them. This effect is an advantage in this application. It is concluded that in the case of ferromagnetics, the enhanced attenuating characteristics can be attributed to the transient skin effect described in this paper.

References

/1/ Jandrell IR, Reynders JP. "Travelling wave model for very fast transient overvoltages in co-axial busducts." Paper 25.07, sixth ISH, New Orleans, August/September 1989.

/2/ Jandrell IR, Reynders JP. "Consideration of the skin effect in high voltage coaxial systems under transient and steady state conditions and its impact on steep travelling waves." Paper submitted to the London Institution of Electrical Engineers (IEE).

/3/ Reynders JP, Jandrell IR. "The degradation of undesirable features of disconnect transients by means of a ferromagnetic skin." SAIEE Trans Vol 79, no 1, July 1988.

/4/ Miller KW. "Diffusion of electric current into rods, tubes, and flat surfaces." AIEE Transactions, Vol 66, 1947.

/5/ Nahman NS. "A discussion on the transient analysis of coaxial cables considering high-frequency losses." IRE Trans, Vol CT-9, June 1962.

/6/ Malewski R. "Measurements of transient skin effect within nonlinear conductors." Paper T72 128-2, IEEE winter meeting, New York, January/February 1972.

/7/ Yen C-S, Fazarinc Z, Wheeler RL. "Time-domain skin-effect model for transient analysis of lossy transmission lines." IEEE Proc Vol 70, no 7, July 1982.

/8/ Reynders JP, Meppelink J. "Characteristics of disconnect switch transients and control of the subsequent electromagnetic interference." Paper 6, CIGRÉ Open Conference on EHV Transmission Systems, Johannesburg, October 1987.

/9/ Jandrell IR, Reynders JP. "The attenuation of high frequency transient voltages in co-axial SF_6 insulated systems." Paper 12.05, fifth ISH, Braunschweig, August 1987.

Acknowledgements

The authors would like to thank ESKOM for financial support. They would also like to thank BBT for the supply of the SF_6 insulated high voltage test system in which the results discussed here were recorded.

ON-LINE HYDROGEN GAS-IN-OIL MONITOR

M. J. Van de Venter J. P. Reynders

University of the Witwatersrand

ABSTRACT

This paper describes available techniques for on-line monitoring of current transformers. Dissolved gas-in-oil analysis has been determined as a viable monitoring technique. In particular a monitor has been developed specifically to measure hydrogen concentration dissolved in the oil. Design and operation of the monitor is described.

INTRODUCTION

Due to the amount of failures of current transformers in the last few years, a research project was initiated to investigate the design and implementation of a cheap on-line monitor for current transformers. The only commercial unit available is the Hydran hydrogen on-line monitor at a approximate cost of R40 000. Since the smaller current transformers cost in the same region, the cost of the Hydran cannot be justified. Therefore the cost of the unit is of prime importance.
A summary of the survey for different techniques that can be used to monitor transformers is given with the conclusions thereof.
This is followed by the specific aims of the MSc(ENG). A description of the final design and experimental apparatus is given.
The results of the experiments done so far and initial conclusions are finally presented.

1 Condition monitoring of transformers

Four techniques are generally used to assess the condition of transformers : Gas-in-oil (GIO) analysis, High Performance Liquid Chromatography (HPLC) analysis, Partial Discharge and Power Factor measurements.

1.1 Gas-in-oil analysis

Soon after transformers were introduced, they were immersed in oil to cool them and improve dielectric strength. The oil is an integral part of the insulation. Faults in the transformer - partial discharge, heating etc results in the breakdown of the oil into various hydrocarbons. Gas-in-oil analysis is used to test for the concentration of various key hydrocarbon gases. There are various methods for intrepreting the results of the GIO analysis. These include :

- Setting allowable limits for amount and rate of

production of various hydrocarbon gases.
- Setting a limit for amount and rate of production of Total Combustible Gases (TCG).
- Checking for key hydrocarbon gases.
- Ratio tests of various hydrocarbon gases.
- Gas patterns of concentration plotted against particular gas.

1.2 HPLC Analysis

A short coming of GIO analysis is that the ratio of the various gases produced will indicate the type of fault, but not what type of materials are involved. Also GIO analysis cannot differentiate between low temperature thermal decomposition of insulation and long-term oxidation of oil.
HPLC allows heavier hydrocarbons to be separated and identified which are specific products of overheating in insulation. The most common stable hydrocarbon as a result of cellulose degradation is Fururaldehyde. The relation between Furfuraldehyde and its relation to acidity, degree of polymerisation and thermal ageing has been established.

1.3 Partial Discharge Measurements

Generally partial discharge measurements are taken by a Radio Influence Voltage (RIV) meter.
Precise comparison of results on different transformers cannot be compared because the results is a function of the transformer rating and design parameters. A reliable method has been developed to measure partial discharges in current transformers on a common bus.

1.4 Power Factor Measurements

The power factor of electrical insulation has been recognized as a good indicator of its serviveablility. Any degradation will increase its power factor. Power factor measurement at line voltages has not been used extensively because of the difficulty of obtaining a suitable reference for each measurement. A computer based on-line power factor monitor has been designed by Tennessee Valley Authority that avoids the difficultes of former measuring equipment.

1.5 Acoustical Emission Analysis

The ageing of electrical insulation materials is connected with structural degradation and molecular changes. This results in quantum and phonon emission. A sound detection is possible useing complex sensitive sensors.

2 CONCLUSIONS ON MONITORING TECHNIQUES

High Performance Liquid Chromatography promises to be useful in the future, but lacks the development of Gas Chromatography. Also a on-line monitor built on HPLC principles will be bulky and expensive due lack of off the shelf parts.

Partial discharge measurements are not reliable because even though a higher partial discharge measurement will indicate a higher probability of a fault, there is no definite correlation. Also background noise is very high in the field and can easily swamp out the actual measurement. An exception to this is a technique developed for current transformers connected to a common bus that allows the common noise to be filtered out. This only useful for transformers close together on a common bus and again there is the problem of wether the measurements are a reliable indication of a fault.

Power factor measurement promises to be a useful tool but still requires further testing. Also the present implementations are expensive.

Aoustical Emission Analysis is still in it's infancy and only a single fault can be distinquished in transformers. Further investigations have to be carried out in order to find solutions for analysing superpositions of two or more sources with different intensities. The hardware required for on-line monitor is also relatively expensive.

The over whelming evidence indicates that gas-in-oil analysis is the most reliable indication of most faults in oil filled transformers.

3 SPECIFIC AIMS

The design approach to on-line monitor will be based on the following considerations :

- Because of the number of transformers in the field, the cost of the on-line monitor is very important, especially with respect to the cost of the transformer.
- The design should be reliable and based on sound theoritical and practical considerations.

Because of the cost of large transmission and generation transformers, the cost of a complete on-line monitor using a ratio test is not a problem, but for a CT this will be prohibitively expensive. Designing and building a such a monitor will be duplicating commercially available designs and there is also the problem of a limited University budget.
On the other hand designing and building a on-line monitor for current transformers has the following advantages :

- There is a very definite need for current transformer on-line monitor due to amount of recent failures.
- Current transformers are cheap and therefore require a very cheap on-line monitor design.
- Even though there are comercially available designs, they are very expensive. (greater than R30 000)
- There is a total lack of information on gas limits, ratio limits for current transformers. The information provided in the previous chapters are almost exclusively for high voltage transformers.

- Also there is very little information on where the oil should taken from. (even for high voltage transformers)

In conclusion the design of a on-line monitor will be for a low cost gas-in-oil monitor for current transformers. Because of the cost considerations, only one gas will be monitored. The overwhelming evidence points to hydrogen as being the most suitable gas for detection.
The experiments that are to be performed are used to determine the following :

- most suitable position for the monitor.
- most suitable membrane for the monitor.
- does the position of the partial discharge affect the amount of hydrogen produced.
- approximate relationship between the amount of hydrogen produced and the level of partial discharge.
- time response for the sensing of the hydrogen.

4 TEST FACILITIES

A short description of the apparatus used is given in the following two sections.
First a short description of the hydrogen sensing apparatus is given. Finally the experimental CT setup is described.

4.1 Sensor Apparatus

There are two versions of the sensor apparatus, one with a permeable membrane (Figure 4.1.1) and one without. (Figure 4.1.2)

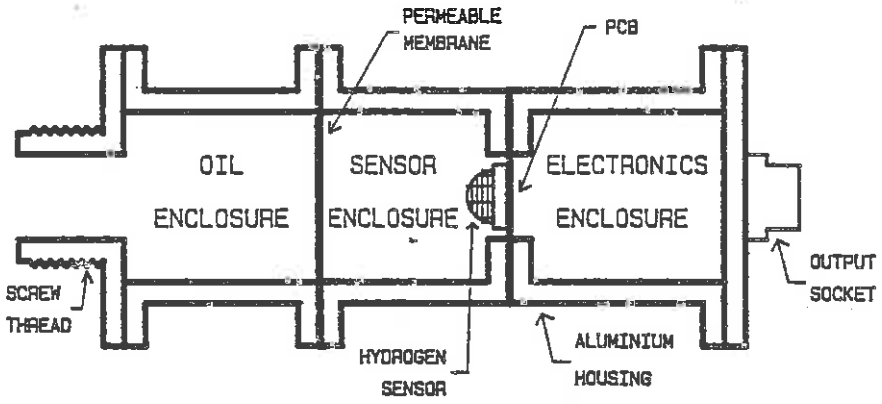

Figure 4.1.1 Sensor apparatus with membrane

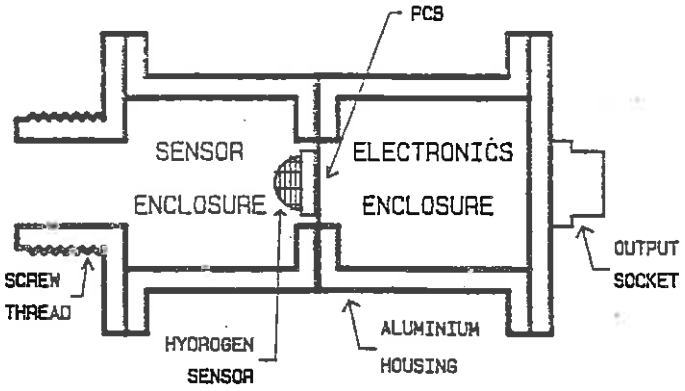

Figure 4.1.2 Sensor apparatus without membrane

The sensor apparatus with the membrane is used to test for the hydrogen concentration at the various ports on the experimental apparatus. The sensor apparatus without the membrane is used to test the hydrogen concentration in the air space above the oil in the experimental apparatus.

The hydrogen sensor consists of a heated semiconductor tube. The heater is supplied by a switch-mode power supply. A linear power supply dissaipates too much heat in the confined area.
The semiconductor tube changes resistance according to the amount of hydrogen detected. The output is buffered before being converted into a 4 - 20 mA loop. The temperature sensor output is converted into a separate 4 - 20 mA loop. All supply and output wires have overvoltage and noise protection.

4.2 EXPERIMENTAL CURRENT TRANSFORMER

A experimental current transformer apparatus is used to simulate fault conditions for the hydrogen experiments. This consists of a tube 1.5 m high, 0.3 m in diameter with four ports. (Figure 4.2.1) The hydrogen sensor is bolted to the one of the four ports. A discharge is created in the oil to simulate a fault. The height of this can be adjusted and is connected to a partial discharge measuring instrument.

5 INITIAL RESULTS

Suitable hydrogen sensors have been located and calibrated.
Various permeable membranes have been tested. Eventually a special membrane was manufactured at E.I. that has an excellant rate of diffusion with high mechanical strength.
At the moment experiments are been conducted to determine the following :

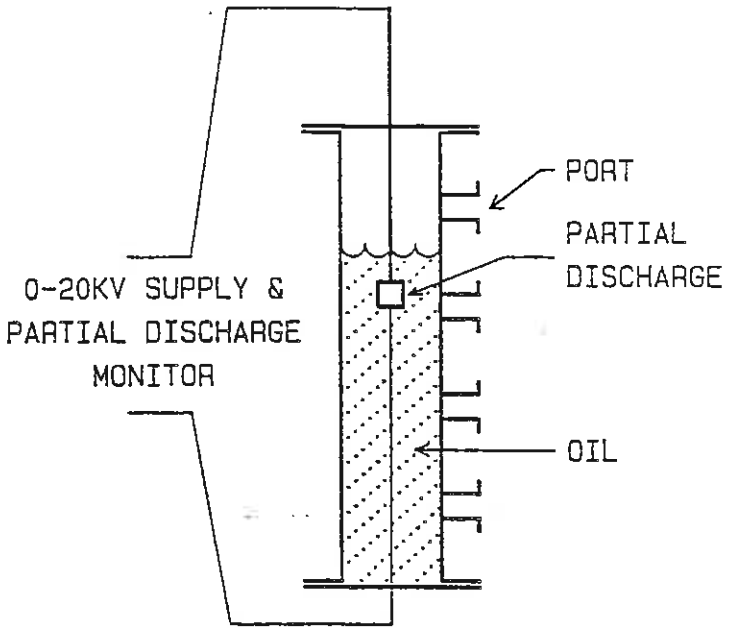

Figure 4.2.1 Experimental Apparatus

- Relationship between the hydrogen concentration in the oil and the hydrogen concentration measured.
- Does the position of the sensor affect the readings.
- Does the position of the partial discharge affect the readings.
- Time response to measure the hydrogen concentration.

6 INITIAL RESULTS

Suitable hydrogen sensors have been located and calibrated. Various permeable membranes have been tested. Eventually a special membrane was manufactured at E.I. that has an excellant rate of diffusion with high mechanical strength.
At the moment experiments are been conducted to determine the following :

- Relationship between the hydrogen concentration in the oil and the hydrogen concentration measured.
- Does the position of the sensor affect the readings.
- Does the position of the partial discharge affect the readings.
- Time response to measure the hydrogen concentration.

7 CONCLUSION

The final estimated cost of the unit will be approximatly R4000 for analog processing and R6000 - R7000 with a digital datalogger. This is well below the cost of other commercial devices. The hydogen on-line monitor promises to play an important role in preventing expensive damage of equipment or loss of lives in the future.

THE USE OF SPREAD SHEET PROGRAMMES IN ELECTRICAL ENGINEERING EDUCATION

M J Case and R Herman

INTRODUCTION

Projects or tasks are a valuable method of introducing electrical engineering principles and techniques. These projects are often associated with the use of the computer. A problem that often arises is that much time is spent in coding software to input information and to extract the results. The actual engineering, mathematical or statistical issues occupy a significantly small part of the programme.

Some general purpose and inexpensive spread sheet programmes are now available for personal computers which can be applied to a wide variety of electrical engineering problems. Once mastered, the input and output facilities are easy to use. Certain characteristics of the spread sheet concept make it particularly suitable for the solution of some typical electrical engineering problems. The way in which these problems are solved also enables the student or engineer to observe the process in a step-by-step fashion and develop a better understanding of the concepts.

SPREAD SHEET FEATURES

The basic premise for the use of spread sheet programmes is that any problem that can be resolved into an equation or set of equations can be solved on a spread sheet package. Characteristics which make the packages specifically useful are the following:-

- **Input/output facilities.** Irrespective of the format of the problem on hand, the cellular approach ensures ease of inputting data and extracting results. This is often a time consuming activity in writing dedicated programmes.

- **Mathematical and statistical functions.** A large variety of functions are available to perform most of the required mathematical operations.

- **Graphic facilities.** These packages have excellent graphic facilities. These include simple X-Y graphs (up to 6 variables on the same graph), pie graphs, histograms, polar diagrams, log-lin and log-log graphs. The plotting of these graphs can be done on even modest printers. These facilities make the presentation of results more lucid to both the student and the teacher.

- **Tabular structure.** The tabular structure of the spread sheet provides a convenient way to apply the "what-if" approach. This can make a valuable contribution to the learning process.

- **Macros.** These are used to programme the procedures of a particular spread sheet. Once a specific spread sheet has been tried and tested, it can be automated with the use of macros and can become a useful dedicated programme.

These principles have been applied and found to be useful in a several courses. A number of diverse applications are described in the paper. These include the solution of state variable equations in circuits, fault calculations in power systems and protection co-ordination calculations in power systems.

CASE STUDY 1 - CIRCUIT ANALYSIS

The circuit shown in Fig. 1 is taken from a standard textbook (1). Three state variables are present. The zero-state responses may be found by Euler's method.

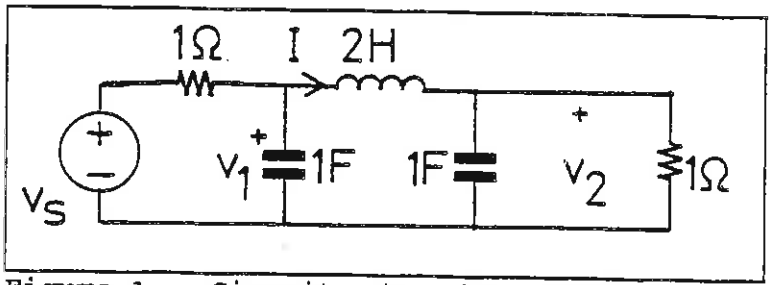

Figure 1: Circuit to be analyzed by spreadsheet

The following state equations can easily be found:

$$\frac{di(t)}{dt}=\frac{1}{2}(v_1-v_2);\ \frac{dv_1(t)}{dt}=-i-v_1+v_s;\ \frac{dv_2(t)}{dt}=i-v_2$$

Euler's method requires initial conditions which are entered as I1(0) etc in the spreadsheet. The time increment is del T. The formulae are entered and copied to the end of the spreadsheet; results are given in table 1 while table 2 shows some of the formulae.

Figure 2 shows the response to a 1 volt step input; this may altered by altering the number in cell E3.

TABLE 1

Printout of the first few rows of the state-variable solution to a simple network problem; the rows are 1,2 etc starting at the top; columns are A,B etc from left to right

Bobrow P.333 Example 7.10				
I1(0)	V1(0)	V2(0)	Del T	Vs
0.000	0.000	0.000	0.5	1.00
T	I	V1	V2	
0.000	0.000	0.000	0.000	
0.500	0.000	0.500	0.000	
1.000	0.125	0.750	0.000	
1.500	0.313	0.813	0.063	

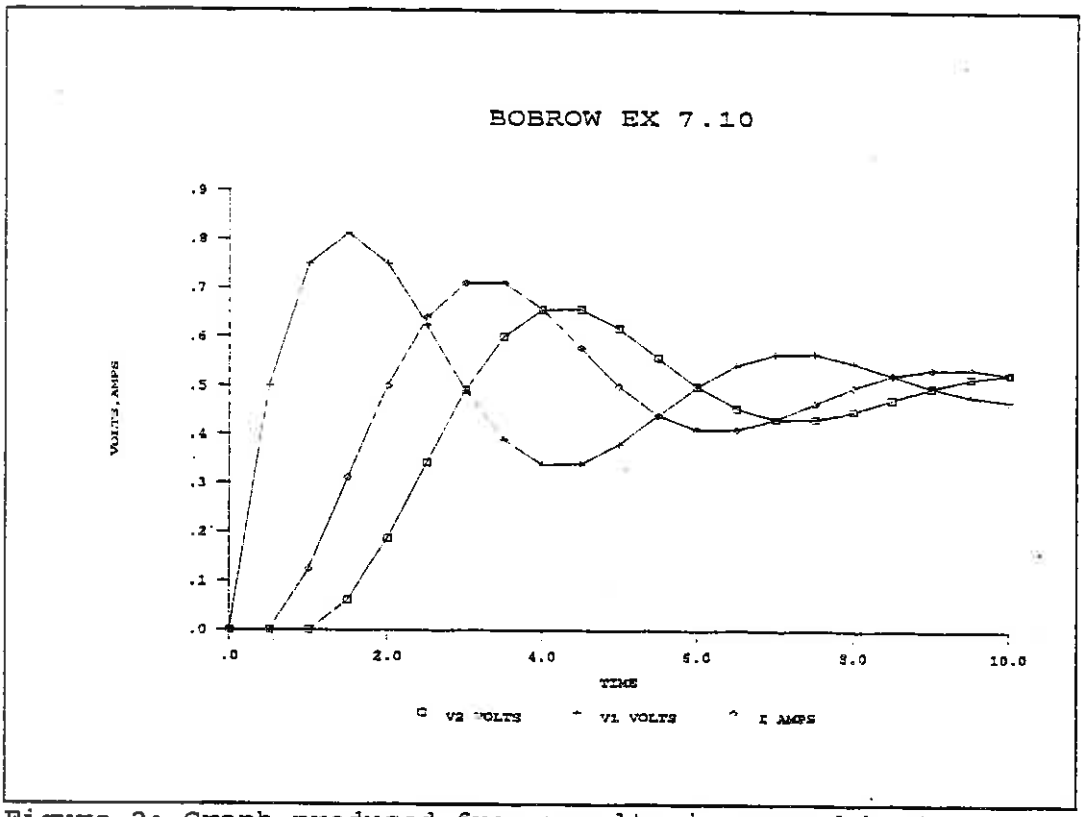

Figure 2: Graph produced from results in spreadsheet.

The advantage of the spreadsheet is shown by the output waveforms in fig.1. The ease wherewith these graphs are created is a great improvement on the problems involved in writing your own software.

The student merely selects a few operations from the menus and examines the results. If not as hoped for, it is a simple matter to carry out any wanted alteration. The "view" or "look" command displays the results on the screen and is often all that is needed. The effects of any alteration to the circuit parameters can easily be viewed.

TABLE 2: THE FORMULAE IN THE SPREADSHEET

	A	B	C	D	E
1					
2	I1(0)	V1(0)	V2(0)	DEL T	Vs
3	0	0	0	0.5	1
4	T	I	V1	V2	
5	0	+A3	+B3	+C3	
6	+A5+$D$3	+B5+0.5*(C5-D5)*$D$3	+C5+($E$3-B5-C5)*$D$3	+D5+(B5-D5)*$D$3	
7	+A6+$D$3	+B6+0.5*(C6-D6)*$D$3	+C6+($E$3-B6-C6)*$D$3	+D6+(B6-D6)*$D$3	
8	+A7+$D$3	+B7+0.5*(C7-D7)*$D$3	+C7+($E$3-B7-C7)*$D$3	+D7+(B7-D7)*$D$3	
9	+A8+$D$3	+B8+0.5*(C8-D8)*$D$3	+C8+($E$3-B8-C8)*$D$3	+D8+(B8-D8)*$D$3	

CASE STUDY 2 - FAULT CALCULATIONS

For this example a network from a classical text is used [3]. According to common practice only reactances are considered.

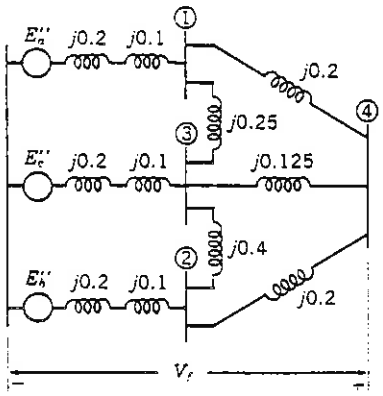

Figure: 3 Power system reactance diagram

The admittance matrix, Y_{BUS}, is constructed in the usual way and entered into the work sheet in rows and columns. The matrix manipulation facility in the spread sheet programme allows for the inversion of matrices up to 90 x 90 elements. Y_{BUS} is now inverted into a selected range giving Z_{BUS}. Generally the prefault voltages are taken to be $1\angle 0^{o}$ p.u. The three-phase symmetrical fault currents at any node, i, is then simply given by

$$If = 1/z_{ii} \text{ p.u.}$$

The voltage at any node j as a result of a fault at node i is given by

$$V_j = 1 - z_{ji}/z_{ii}$$

where z refers to the element in Z_{BUS}. The procedure can be extended to cover asymmetrical faults as well.

Results obtained in this way may be used in further studies such as protection relay co-ordination.

CASE STUDY 3 - PROTECTION CO-ORDINATION

In time-graded overcurrent protection schemes two relay constants, or settings have to be specified - the current setting and the time multiplier. The correct computation of these settings ensures that the inverse time relays will be co-ordinated with one another.

A practical method of doing this is to set out the calculations in tabular form. This suggests the suitability of the spread sheet format. The additional graphics features enables the resultant time-current curves to be displayed on log-log graphs. A radial distribution system depicted in figure 4 is used as an example. The procedure followed for the determination of the settings can be found in standard texts on the subject [4].

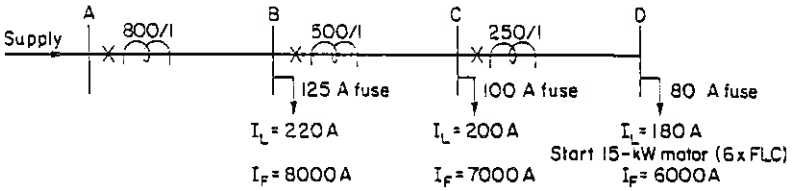

Figure: 4 Radial distribution system

The current setting is chosen from a consideration of the long term overload current and the CT ratio. From the standard inverse characteristics of the overcurrent relays the time multiplier is ascertained. A portion of the work sheet used for this exercise is shown in figure 5. The resultant time-current graph is shown in figure 6.

```
      IDMT PROTECTION CO-ORDINATION SPREAD SHEET
Fill in the details at the arrows (<--) and press F9
Press F10 to view the graph of time vs current

SUPPLY   [A]      [B]      [C]      [D]
---------¦w-------¦w-------¦w-------¦-->
         800/1    500/1    250/1

      ** SUMMARY OF SETTING  **
PLUG SET   100.00   100.00   125.00
TIME X       0.35     0.26     0.13

CURRENTS:  A        B        C        D
Iload              220.00   200.00   180.00 <--
I O/L              220.00   200.00   320.00 <--
Ifault    8000.00  7000.00  6000.00          <--

CT'S           800      500      250          <--

CURRENT SETTINGS - % :
Nominal         83       84       80
O/Load          84       95      116
Discrim t      0.4      0.4      0.4      0.3 <--
CHOSEN %       100      100      125          <-- **
PSM             10       14     19.2
PSM - f         10       16     22.4
TMS           0.35     0.26     0.13
TRIP TIME     1.05     0.65     0.29               **
```

Figure: 5 Work sheet for case study 3

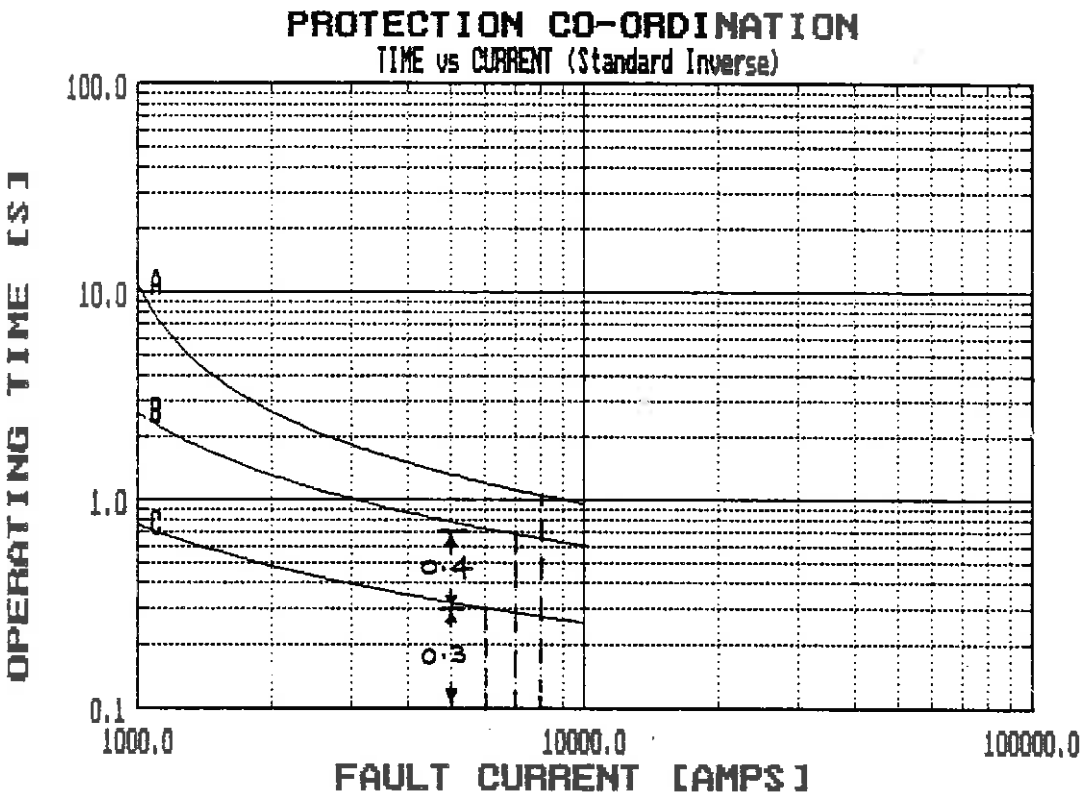

Figure: 6 Time - current curve of relays

CONCLUSION

In this brief survey some of the features of spread sheet software have been discussed. This method of setting out and solving electrical engineering problems has been found to be most instructive. It teaches the student to approach the calculations in a logical and systematic way. It also assists in observing the effects of parameter changes within the solution procedure.

REFERENCES

1 Bobrow, L.S.: "Elementary linear circuit analysis", Holt,Rinehart, Winston, New York.

2 Orvis, W.J: "1-2-3 for scientists and engineers", Sybex, Alameda CA, 1987.

3 Stevenson, W.D.: "Elements of power system analysis", 4th ed, McGraw-Hill, 1982.

4 Davis, T.: "Protection of industrial power systems", Pergamon Press, 1984.

MODELLING, NON-LINEAR SIMULATION AND DYNAMIC PERFORMANCE OF A CURRENT CONTROLLED PERMANENT-MAGNET SYNCHRONOUS MOTOR DRIVE

M.J. Kamper and F.S. van der Merwe
(University of Stellenbosch)

Abstract - The dynamic performance of a commercial permanent magnet synchronous motor (PMSM) drive is presented. The measured speed and phase current responses of the PMSM are given. The results show that the phase currents build up within 1 ms to their maximum values after a step input speed command. Transfer function models of the PMSM and speed controller of the drive system have been obtained. Computer simulations of the response of the drive system are presented, with due allowance for all important non-linearities, amongst others, the saturation of the motor phase currents due to the maximum capability of the inverter. The non-linear simulation results of the entire current controlled drive system show extremely good similarity with measured results.

1. Introduction

With the introduction of the Neodymium-Iron-Boron (NdFeB) based permanent magnets in 1983, renewed attention has been given to the use of permanent magnets in electrical machines. The coercivity (900 kA/m), remanence (1,2 Tesla) and energy product (300 kJ/m³) of NdFeB magnets are significant improvements. These improvements permit reductions in motor frame size for the same output power. A major advantage is the reduction in magnet thickness, which is less than 10 mm for producing air-gap flux densities between 0,8-1,0 T [1]. Another major advantage of the NdFeB magnets is that these magnets, unlike the SmCo magnets, contain no strategic minerals and thus should cost less. According to Mhango [2] NdFeB costs about ten times more than Ferrite and 3½ times less than SmCo.

Current research indicates that when high energy NdFeB or SmCo magnets are used in electrical machines, these machines exhibit attractive torque-to-inertia ratio, power density and efficiency characteristics compared to induction machines and wound rotor synchronous machines. An important aspect concerning servo applications is the peak to rated torque ratio of the electrical machine. The experimental results of Sebastian and Slemon [1] show for a 5 hp NdFeB PMSM that a linear relationship exists between torque and current, up to eight times rated torque, where the stator current is 6 per unit. Such impressive torque characteristic makes these machines very suitable for high performance servo applications. This peak to rated torque ratio is more than twice that obtained for an equivalent induction machine with the same per unit stator current.

It is the aim of this paper to bring about the dynamic performance of a commercially available 2 kW PMSM drive. The PMSM drive is a closed-loop speed control system. Secondly, the transfer function models for the entire PMSM drive system have been obtained. For the model of the PMSM the well-established d-q model for wound rotor synchronous machines without damper windings is adapted. Further, the drive system is simulated taking into account the non-linearities like, amongst others, the non-linear d-q equations and the finite current delivering capability of the inverter. The simulated speed and current responses of the drive for step input speed commands are presented.

2. Description of the PMSM Drive

The PMSM drive is a voltage-fed, current controlled system. The drive basically consists of a 3-phase inverter with control circuits, and a 12 pole, 2 kW, 30 Nm peak permanent magnet machine with position resolver (see fig. 1). The rotor contains high energy SmCo magnets.

With the rated torque equal to 10 Nm, the peak to rated torque ratio of the PMSM is equal to 3. Within the torque range up to 30 Nm, a linear relationship between torque and current is found for the machine. The maximum output current of the inverter is 32 A rms. The PWM current controller closes a current loop around three phases of the stator windings to output a balanced 3-phase sinusoidal stator current. The switching frequency of the power transistors is 5 kHz.

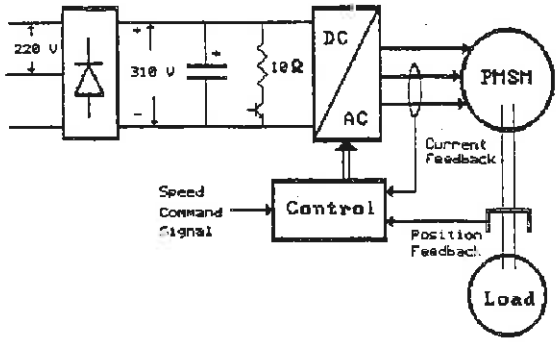

Figure 1: The PMSM Drive System

The speed controller compares desired speed with actual speed of the motor and gives accurate speed tracking over

a wide bandwidth. The parameters of the cascade PI-compensator of the speed-controller are adjustable by potentiometers for optimum motor response. An inertia through gearbox load is connected to the machine, also to evaluate the PMSM drive in a closed-loop position control system. This aspect is not covered in the paper.

3. Mathematical Model for the PMSM

The PMSM considered here is a SM without field and damper windings on the rotor and with a sinusoidal back EMF produced by the permanent magnets on the rotor. Hence, the mathematical model of the PMSM is similar but more simple than that of the wound rotor SM. By adopting Park's transformation, all stator variables (voltages, currents, and flux linkages) can be transformed, or referred, to a frame of reference fixed in the rotor. The time-varying inductances of a synchronous machine can only be eliminated if the reference frame is fixed in the rotor. By this transformation the 3-phase stator windings are replaced by fictitious 2-phase (d-q) windings rotating with the rotor. The d-q variables can be obtained from the a-b-c variables, and vice versa, through the Park and inverse Park transform defined below:

$$\begin{bmatrix} f_q \\ f_d \\ f_o \end{bmatrix} = 2/3 \begin{bmatrix} \cos(\alpha) & \cos(\alpha - 2\pi/3) & \cos(\alpha + 2\pi/3) \\ \sin(\alpha) & \sin(\alpha - 2\pi/3) & \sin(\alpha + 2\pi/3) \\ 1/2 & 1/2 & 1/2 \end{bmatrix} \begin{bmatrix} f_a \\ f_b \\ f_c \end{bmatrix} \tag{1}$$

$$\begin{bmatrix} f_a \\ f_b \\ f_c \end{bmatrix} = \begin{bmatrix} \cos(\alpha) & \sin(\alpha) & 1 \\ \cos(\alpha - 2\pi/3) & \sin(\alpha - 2\pi/3) & 1 \\ \cos(\alpha + 2\pi/3) & \sin(\alpha + 2\pi/3) & 1 \end{bmatrix} \begin{bmatrix} f_q \\ f_d \\ f_o \end{bmatrix} \tag{2}$$

The angle α in equations (1) and (2) is the electrical angle in radians between the rotating q-axis and the fixed phase a-axis. By using the transform equations (1) and (2), the following d-q equations are obtained for the PMSM with the direction of positive stator currents taken into the machine [3, 4] (Note that for a balanced 3-phase wye-connected winding the zero component voltages and currents do not exist):

$$v_q = r_s i_q + L_q \, d/dt(i_q) + (L_d i_d + \lambda_m)\omega_s \tag{3}$$

$$v_d = r_s i_d + L_d \, d/dt(i_d) - L_q i_q \omega_s \tag{4}$$

In these equations the d-q parameters v, i and L refer respectively to voltages, currents and inductances. The d-q inductances depend on the rotor configuration [5]. With the permanent magnets mounted on the surface of a round rotor, which is the case of the PMSM under consideration, the d-q inductances are the same and is given by:

$$L_d = L_q = L_{s\ell} + L_m \tag{5}$$

where $L_{s\ell}$ = phase leakage inductance of stator
and L_m = phase magnetizing inductance of stator

Note that due to the large air-gap of the PMSM, the magnetizing inductance is small (of the same order as the leakage inductance) and can be taken as a constant under steady-state and transient conditions, as is the case with the leakage inductance.

Further, r_s is the stator phase resitance, λ_m is the peak value of the flux linkage established by the permanent magnets as viewed from the stator phase windings and ω_s is the electrical synchronous speed in rad/s. The relationship between ω_s and the rotor speed ω_r is

$$\omega_s = p\omega_r \tag{6}$$

with p = number of pole pairs

The electromagnetic torque of the PMSM is given by:

$$T_e = (3/2)p\left[\lambda_m i_q + (L_d - L_q) i_d i_q\right] \tag{7}$$

The term $(L_d - L_q) i_d i_q$ refers to the reluctance torque component of the electromagnetic torque. This torque component becomes zero if either i_d is forced to zero, which is normally the case, or if $L_d = L_q$. In such cases equation (7) reduces to:

$$\begin{aligned} T_e &= (3/2)p\lambda_m i_q \\ &= K_t i_q \end{aligned} \tag{8}$$

Note that λ_m can be taken as a constant due to the large effective airgap which makes the armature reaction effect negligible. λ_m is given by

$$\lambda_m = L_m i_m \tag{9}$$

where i_m = equivalent current source for the magnet.

Equation (8) is similar to the torque equation of a separately excited dc machine. Finally, the equation for the machine dynamics is given by

$$J\, d/dt\,(\omega_r) = T_e - T_L \qquad (10)$$

where T_L is the load torque and J is the moment of inertia.

In fig. 2 the equivalent d-q circuits for the PMSM are shown. Normally i_d is forced to zero by a negative v_d voltage. A negative i_d current will weaken the airgap flux and will lower the speed voltage of the circuit of fig. 2a.

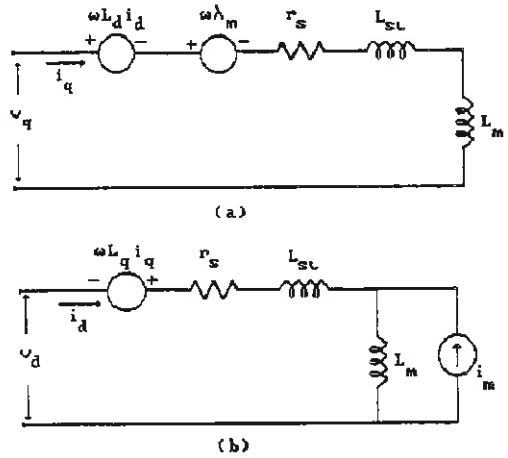

Figure 2: Equivalent d-q circuits for the PMSM.

In fig. 3 the complete d-q block diagram of the PMSM is shown. Hence, it is clear that the machine model is non-linear as it contains product terms such as speed with i_d and i_q.

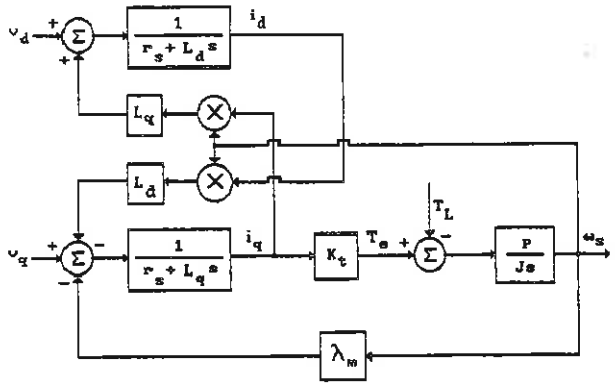

Figure 3: Complete d-q block diagram of the PMSM in terms of transfer functions ($L_d = L_q$).

4.0 Approximate Model for Speed Control Drive

For the PMSM drive system described in par. 2 a few approximations can be made to simplify the model for the complete speed control drive. Firstly, the mechanical time constant of the particular load connected to the machine is about 30 times longer than the electrical time constant of the stator winding. The electrical time constant thus can be ignored. Together with this a good approximation is to assume that the current controller will force the actual phase currents equal to the desired (command) phase currents, or in other words to assume that $i_q = i_q^*$ and $i_d = i_d^* = 0$, where '*' denotes command. This assumption will only be valid when the speed of the machine is well below base speed, where the counter EMF is low.

There is, however, an important aspect which can not be ignored namely the finite current capability of the inverter. This non-linearity or saturation in the current capacity of the inverter must be considered in the simulation of the speed control drive.

With all the assumptions above the model of the complete speed control drive simplifies to that shown in fig. 4. The actual rotor speed is fed back and compared with the command speed. In cascade with the speed error a lag compensator is used in the system, which directly controls the q-axis current command. The non-linearity in the current command, however, ensures that the command never exceeds the maximum current capability of the inverter. It was found for the system that the saturation current level is different under motoring mode (45 A) and dynamic braking mode (28 A).

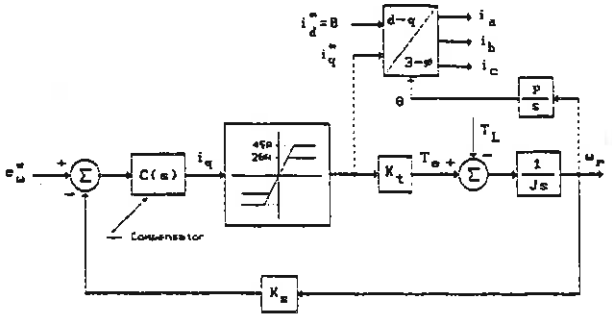

Figure 4: Block diagram of the simplified speed control model.

5. Dynamic Performance of the PMSM Drive

The dynamic response of the PMSM drive system of par. 2 is evaluated by giving step input speed commands to the system and recording the speed and phase current responses. The measured results are shown in figures 5 to 7. The non-linearities in the actual speed curves are clearly visible

and are due to torque disturbances caused by the non-linearities in the mechanical system. From fig. 5 a slight overshoot in the actual speed curve is observed, caused by the lag compensator of fig. 4 which gives second-order characteristic responses to the system.

It is seen from fig. 6 that during dynamic braking the amplitude of the phase currents is limited to 28 A, i.e. the dynamic braking torque of the drive is lower than the motoring torque. The dynamic braking resistor of fig. 1 therefore can only absorb a limited amount of braking power. In motoring mode, the current saturation level is increased to 45 A, which results in maximum motor torque. Further in fig. 6 the reversal of the phase sequence of the inverter can be seen from the current curve when the direction of machine rotation is reversed.

From figures 5 and 6 it is found that the deceleration of the system is higher than the acceleration, despite the fact that the electric braking torque is lower than the motoring torque. This discrepancy can be explained by the difference in the coulomb friction torque of the gearbox under acceleration and deceleration conditions, i.e the gearbox has the characteristics of a worm gearbox (also known as a diode gearbox). During deceleration the relative high coulomb friction torque of the gearbox adds to the negative electric braking torque of the machine (see fig. 4), consequently with a high deceleration.

In fig. 7 it is observed that the phase currents build up within 1 ms to their maximum values just after the step input speed command. The response of the PMSM drive on command is thus very rapid. Note that the frequency of the phase current of fig. 7 corresponds with the speed of the 12-pole machine.

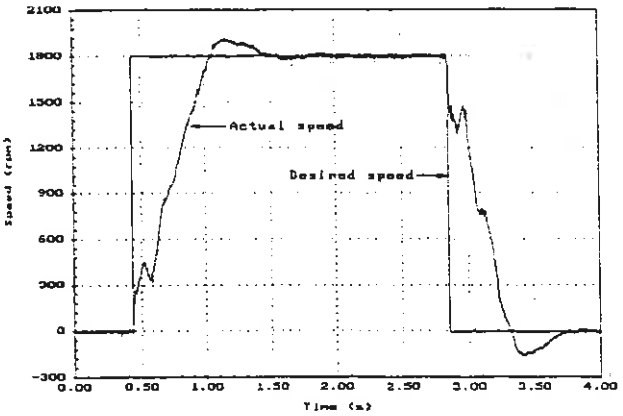

Figure 5: Measured speed response of the PMSM

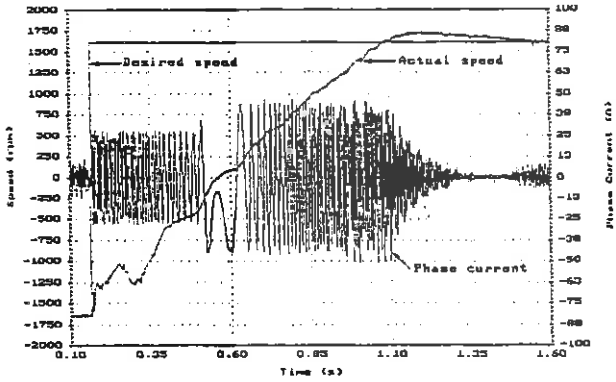

Figure 6: Measured speed and current response of the PMSM under dynamic braking and motoring.

6. Simulation Results

For the simulation of the system the simplified model of fig. 4 is used, taking into account the non-linear current command. The part of the model of fig. 4 connected in dotted lines is used to obtain the a-b-c current variables. The load torque is taken as a conditional coulomb friction torque, depending on if the system is accelarating or decelarating. The only unknowns of fig. 4 are the parameters of the lag compensator. These parameters were approximately identified from the second-order overshoot response of fig. 5, together with some further adjustments, with the following result:

$$C(s) = \frac{100\,(s+5)}{(s+3{,}5)} \qquad (11)$$

In figures 5 and 6 the speed of the machine is kept below 1800 rpm, which is well below the base speed of 3000 rpm. The assumption in fig. 4, therefore, that the actual

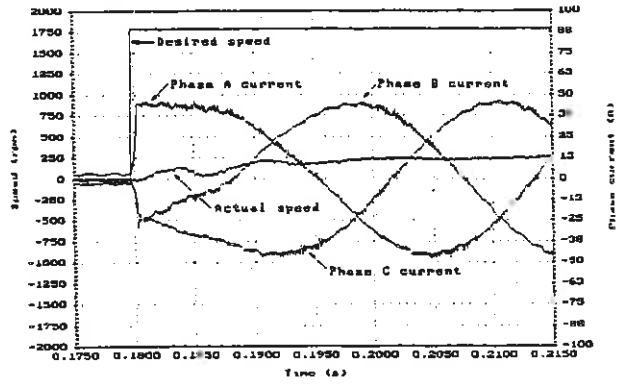

Figure 7: Measured speed and current response of the PMSM at time of the step input speed command.

current is equal to the desired current due to the relatively low counter EMF at low speeds, is acceptable.

For the simulation a "Non-linear Identification Through Simulation" (NISIM) [6] computer package is used, using only the simulation part of this package. The non-linear feedback control model (like fig. 4) is entered in block diagram form with the help of a graphic editor, from where the simulation is done using numerical methods. Almost any kind of non-linearity can be chosen from the menu and used in the block diagram.

In figures 8 and 9 the simulated results are shown for comparision with the measured results of figures 5 and 6. Clearly, the simulated results show good correlation with the measured results.

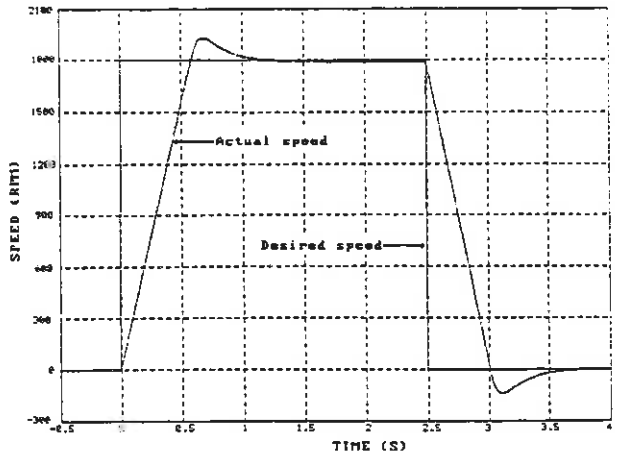

Figure 8: Simulated speed response of the PMSM drive.

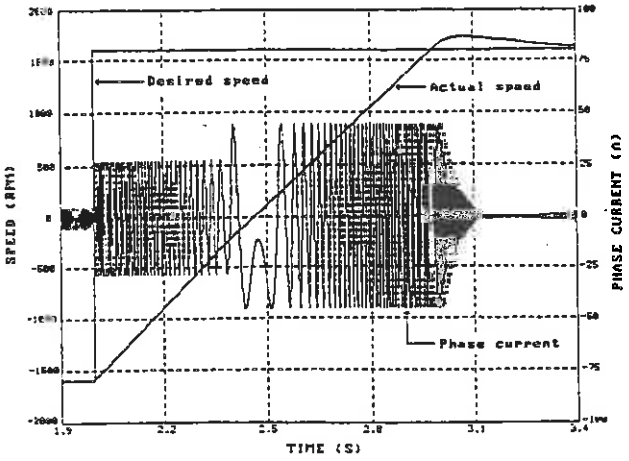

Figure 9: Simulated speed and current response of the PMSM drive under dynamic braking and motoring.

7. Complete Current Control Simulation

It must be clear, however, that under certain conditions the assumptions made in par. 4 will be invalid. For example, when the mechanical time constant becomes short, the effect of the stator winding time constant becomes more important. Also, at high speeds, where the counter EMF is high, the current controller will tend to saturate in part of the cycle due to the finite voltage capability of the inverter. These effects have to be considered in the simulation.

With due allowance for the stator winding time constant, the complete block diagram of fig. 3 must be used. However, with the use of this block diagram the instantaneous d-q voltages must be known. The d-q voltages are directly determined by the current controller of the system. The current controller and thus every instant of a power switch opening or closing must be simulated to predict accurately the changes in the d-q voltages and currents. In order to obtain this the entire non-linear drive system is simulated by using the block diagram of fig. 10.

In fig. 10 the desired d-q currents, which are determined by the speed controller, are transformed to a-b-c currents using equation (2) ($\theta = \alpha$). These desired currents are compared with the actual a-b-c currents, and the current errors are then used by the current controllers to directly determine the V_{ao}, V_{bo} and V_{co} terminal voltages with respect to the dc bus midpoint. These voltages are used to obtain the instantaneous line-to-neutral phase voltages (neutral disconnected) by means of the following well-known equations:

$$\begin{aligned} V_{an} &= 1/3(2V_{ao} - V_{bo} - V_{co}) \\ V_{bn} &= 1/3(2V_{bo} - V_{co} - V_{ao}) \\ V_{cn} &= 1/3(2V_{co} - V_{ao} - V_{bo}) \end{aligned} \qquad (12)$$

By using equation (1) the a-b-c phase voltages of equation (12) are transformed to the actual d-q voltages. From here the real d-q currents and speed response of the system can be predicted, using the complete d-q circuit of fig. 3. Finally the d-q currents are transformed backwards to obtain the real a-b-c currents.

For the current controllers the hysteresis or PWM type of current controllers can be used in the simulation. In fig. 11 the simulated phase current responses to a step input speed command are shown. Hysteresis current controllers are used with the hysteresis band set at 1,5 A. The effect of the stator winding time constant is clearly seen in the building up of the phase currents within 1 ms. This corresponds very well with the measured 1 ms response of fig. 7. The hysteresis current controllers, however, give rise to large ripples in the current waveforms shown in fig. 11. A maximum line current error of 3 A is observed,

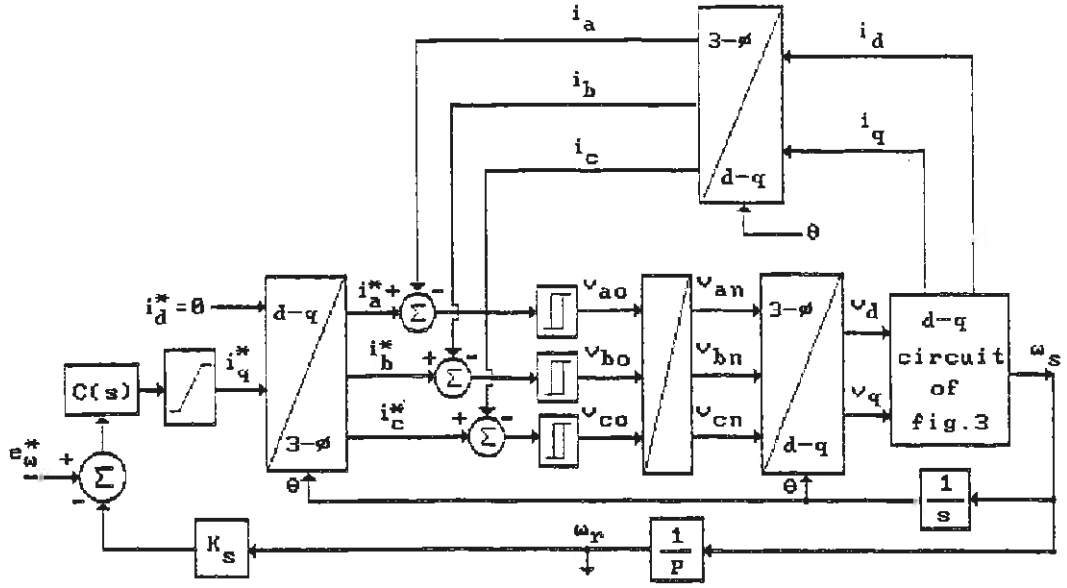

Figure 10: Block diagram for the simulation of the entire drive system.

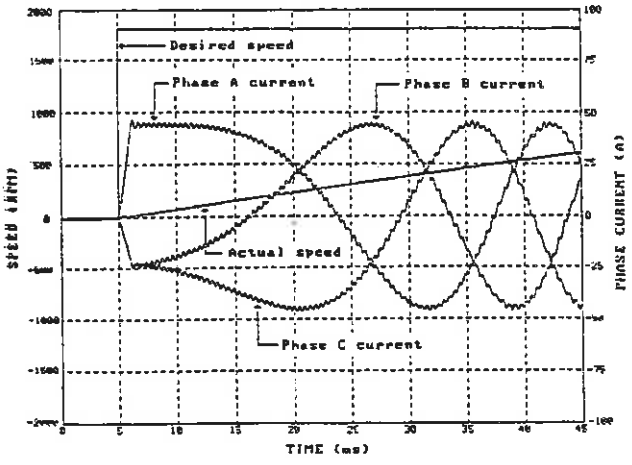

Figure 11: Simulated speed and current responses of the PMSM drive using three independent hysteresis controllers (band = 1,5 A).

which is double the hysteresis band. This behaviour, however, is typical of what happens for a system without a neutral connection using three independent hysteresis controllers [7].

8. Conclusions

The first conclusion drawn from the simulated results is that the mathematical d-q model of the PMSM, given by fig. 3, is an accurate model which can be used under steady-state and transient conditions. An important aspect, which becomes evident from the measured and simulated results, is the linear relationship between torque and current (K_t is constant), up to 3 times rated torque for the machine under consideration. This is due to the large airgap of the PMSM which makes the armature reaction effect negligible even at high values of stator current. The rotor field flux, therefore, can be considered as constant. In coherence with this the d-q inductances can be taken as constants in the model under transient conditions, due to the large airgap and relatively large slot openings.

The second conclusion reached, is the importance of the due allowance for the non-linearities of the entire drive system. The non-linearities in, for example, the current and voltage capability of the inverter becomes dominant under transient conditions and can not be ignored in the simulation of the dynamic performance of the drive. Also the non-linearities in the current controllers and thus the switching of the terminal voltages must be considered.

Thirdly, from the measured results, the PMSM shows excellent dynamic performance. The response of the PMSM on command (reaction time of 1 ms) is very rapid, which is the result of a constant field and low d-q inductance values. The PMSM drive system therefore is extremely suitable for the use in high-performance servo applications.

NOMENCLATURE

i_d, i_q	direct- and quadrature-axis stator currents (A)
v_d, v_q	direct- and quadrature-axis stator voltages (V)
L_d, L_q	direct- and quadrature-axis stator inductances (H)
L_m	phase magnetizing inductance of stator (H)
$L_{s\ell}$	phase leakage inductance of stator (H)
r_s	stator resistance (Ω)
T_e	electromagnetic torque (Nm)
T_L	load torque (Nm)
J	moment of inertia ($Kg.m^2$)
p	number of pole-pairs
ω_s	synchronous speed (rad/s)
ω_r	rotor speed (rad/s)
λ_m	maximum flux linkage established by the permanent magnet as viewed from the stator phase windings (Wb.turn)
K_t	torque/current constant (Nm/A)
K_s	voltage/speed constant (V/rad/s)
α, θ	electrical angle between rotating q-axis and fixed phase a-axis (rad)

APPENDIX: System Parameters

Rated motor torque = 10 Nm
Rated motor power (at 3000 rpm) = 2 kW
Maximum motor speed (no-load) = 3500 rpm
Rotor inertia = 8,4 $kg.cm^2$
Load inertia = 878 $kg.cm^2$
$L_d = L_q$ = 4,47 mH
r_s = 0,71 Ω
p = 6 pole-pairs
K_t = 0,73 Nm/A
K_s = 0,0238 V/rad/s
λ_m = 0,0811 V/rad/s

ACKNOWLEDGMENT

The authors acknowledge the following persons for their contribution to the paper: Mr. A.F. Kotze, mr. O.M. Strydom, who developed the simulation program, and prof. J.J. du Plessis (all from the University of Stellenbosch).

REFERENCES

[1] Sebastian, T. and Slemon, G.R.: "Transient Modeling and Performance of Variable-Speed Permanent-Magnet Motors", IEEE Trans. Ind. Appl., Jan/Feb 1989, vol. 25, no. 1, pp. 101-106

[2] Mhango, L.M.C.: "Performance and Recent Advances of a Class of Brushless DC Motor with NdFeB Magnets", ICEM Pisa, Sept. 1988, vol. 3, pp. 105-110

[3] Krause, P.C.: "Analysis of Electric Machinery", McGraw-Hill, 1986

[4] Pillay, P. and Krishnan, R.: "Modeling, Simulation, and Analysis of Permanent-Magnet Motor Drives, Part I: The Permanent-Magnet Synchronous Motor Drive", IEEE Trans. Ind. Appl., March/April 1989, vol. 25, no.2, pp. 265-273

[5] Takeda, Y., Morimoto, S., Hirasa, T. and Puchi, K.: "Most Suitable Control Method for Permanent Magnet Synchronous Motors", ICEM Pisa (Italy), Sept. 1988, vol. 3, pp. 53-58

[6] Strydom, O.M.: "A document that describes the program used for evaluation of Nonlinear Identification through Simulation (NISIM)", Internal document, Dept. of Electronic Eng. Univ. of Stellenbosch, May 1990

[7] Brod, M.B. and Novotny, D.W.: "Current Control of VSI-PWM Inverters", IEEE Trans. Ind. Appl., May/June 1985, vol. IA-21, no. 4, pp. 562-570

DIGITALE BEHEER VAN 'N 3-FASE DINAMIESE DRYWINGSFILTER ONDER TOESTANDE VAN ONSIMMETRIESE, NIE-SINUSVORMIGE LASSTROME

JG ROOS GL VAN HARMELEN JHR ENSLIN

DEPARTEMENT VAN ELEKTRIESE INGENIEURSWESE
UNIVERSITEIT VAN PRETORIA
PRETORIA, REPUBLIEK VAN SUID AFRIKA

UITTREKSEL

Digitale PWM stroomvoorspellingsbeheer van 'n dinamiese drywingsfilter in 'n hibriede kompensator-installasie word ondersoek. Die vermoë van die aktiewe drywingsfilter, wat gebaseer word op 'n 3-fasige spanningsgevoerde PWM-wisselrigter, is ± 40 kVA. Hierdie drywingsfilter word aangewend in 'n hibriede-kompensator-installasie wat bestaan uit 'n 3-fasige tiristor-beheerde-reaktiewe-bron met 'n vermoë van ongeveer 60 kVA_r gekombineer met die 40 kVA dinamiese drywingsfilter (DDF). Hierdie hibriede-kompensator-installasie word aangewend om te kompenseer vir onsimmetriese, nie-sinusvormige lasstrome sodat 3-fasige, simmetriese, sinusvormige strome met eenheidsarbeidsfaktor vanaf die toevoer getrek word. Die vermoë van die demonstrasielas is ongeveer 100 kVA. Die funksionering en verwagte vertoningskarakteristieke van die DDF word in hierdie skrywe aangespreek.

INLEIDING

Die kompensasie van fiktiewe drywing by hoër-drywing nie-lineêre laste (F > 100 kVA) onder dinamiese toestande lewer nog steeds probleme op [2,3,4,5]. Die dinamiese responsie van die kompensatorstelsels is omgekeerd eweredig aan die drywingsvermoë van die omsetters. Dit is om hierdie rede dat aandag geskenk word [2,3] aan die ontwikkeling van koste-effektiewe hibriede-kompensators gebaseer op die parallelwerking van tiristor-beheerde-reaktiewe-bronne (TBR) en dinamiese drywingsfilters (DDF) [2,6]. Die TBR word gebruik om te kompenseer vir reaktiewe drywing by hoër drywingsvlakke, terwyl die DDF aangewend word om te kompenseer vir hoër-orde harmonieke (> 5°) onder dinamiese toestande teen laer drywingsvlakke.

Die werking en verwagte vertoningskarakteristieke van 'n totaal digitaal beheerde, spanningsgevoerde PWM-wisselrigter wat geïmplementeer word in die beheerlus van 'n dinamiese drywingsfilter, word in hierdie skrywe aangespreek. Hierdie DDF besit ook die vermoë om stelsels met nie-sinusvormige spannings te kompenseer.

In vorige werk is aangetoon [3] dat die bepaling van netwerkparameters, nl. die konduktansie G en susseptansie B, binne 312 μs afgelei kan word met behulp van toegewyde syferseinverwerkers (TMS320C25), en dit kan gebruik word om dinamiese drywingsfilters intyds te beheer onder dinamiese lastoestande. Die werk wat in hierdie skrywe aangespreek word, handel oor die implementering van digitale PWM-stroom-aanpasbeheer van 'n 3-fasige DDF onder onsimmetriese dinamiese lastoestande.

HIBRIEDE-KOMPENSATOR

'n Blokdiagrammatiese voorstelling van die hibriede-kompensator word in figuur 1 getoon. Die kompensator bestaan basies uit 3 boublokke, nl. die tiristor-beheerde-reaktiewe-bron, die dinamiese drywingsfilter en die hibriede-kompensator-beheerder. Die DDF word saamgestel uit 'n standaard industriële-tipe 6-skakelaar spanningsgevoerde wisselrigterbrug met 'n vermoë van 40 kVA. Vir doeleindes van hierdie projek is die wisselrigter opgegradeer om aan die vereistes van 'n hoër skakelfrekwensie (10 kHz) te voldoen.

Die totale beheerder bestaan uit drie afsonderlike beheerders in twee hierargiese vlakke. Die eerste is die bepaling van die ekwivalente netwerkparameters en dus die berekening van die verwysingseine aan die DDF en die TBR omsetters. Die tweede vlak bestaan uit twee onafhanklike beheerders, waar die eerste die vuurhoek α vir

die tiristore in die 3-fasige TBR bereken . Die TBR word gebruik om te kompenseer vir reaktiewe drywing. Die tweede beheerder bereken die PWM basisstuurseine vir die 3-fasige DDF wisselrigter-skakelaars.

Die prakties-geïmplementeerde DDF funksioneer eintlik as 'n stroombron wat 3-fasige onsimmetriese strome aan die netwerk lewer, of daaruit absorbeer, om te verseker dat sinusvormige strome vanaf die toevoer getrek word. Harmonieke tot so hoog as die 20°-orde (1 kHz) sal uitgefilter word. Daarvoor is 'n PWM-skakelfrekwensie van ten minste 10 kHz nodig om goeie dinamiese gedrag te verseker. Die GS-spanning oor die stam-kapasitor C_f in die wisselrigter word intyds gemonitor en op 'n vasgestelde spanningsvlak beheer d.m.v. 'n energie-uitruilingsproses tussen die kapasitor en die 3-fase netwerk.

Die PWM-wisselrigter word in die stroom-modus beheer, omdat 3-fase stroomverwysingseine vanaf die oorhoofse beheerder ontvang word. In plaas van die analoog-gebaseerde stroom-histerese PWM-beheerder [8], word van 'n digitale PWM-stroomvoorspellingsbeheertegniek [1] gebruik gemaak wat op 'n TMS320E15 toegewyde syferseinverwerker geïmplementeer word.

DIGITALE BEHEERSTRATEGIE VIR DIE DINAMIESE DRYWINGSFILTER

Omdat die oorhoofse beheerder op 'n TMS320C25 toegewyde syferseinverwerker geïmplementeer word, sou dit sinvol wees om die beheer van die dinamiese drywingsfilter ook te baseer op 'n soortgelyke mikroverwerker. Daar is baie voordele met só 'n digitale PWM-beheeralgoritme, soos aanpasbaarheid tussen die PWM-beheerder en die hoofbeheerder, netwerkparameterafskatting, buigbaarheid in die sin dat programmatuur maklik verander kan word en eliminering van dryf- en EMI probleme wat gewoonlik met analoogbeheerders ondervind word. Die analoog-intervlak tussen die oorhoofse beheerder en die analoog-gebaseerde histerese beheerder word dus uitgeskakel, sodat die ses drywingstransistors in die wisselrigter nou direk vanaf 'n mikroverwerker gestuur word.

'n Stroomvoorspellingsbeheertegniek wat gebaseer is op die sogenaamde ruimte-vektor-modulasie ("Space vector modulation") [1,7,9] word ondersoek om die digitale beheer van die PWM-wisselrigter uit te voer. In beginsel kan 'n stel van 3-fasige golfvorms voorgestel word as 'n enkele roterende vektor in die komplekse vlak. As hierdie beginsel toegepas word op 'n 6-skakelaarwisselrigter soos getoon is in figuur 1, kan gesien word dat daar 8 moontlike diskrete uitsetspanningstoestande kan onstaan, wat ooreen kom met die agt moontlike kombinasies wat daar bestaan tussen die 6 skakelaars. Twee van hierdie toestande is nul spanningsvektore ($\overline{V}_0$,$\overline{V}_7$) waar al drie boonste skakelaars of al drie onderste skakelaars gelyk aan is, terwyl die orige ses spanningsvektore 60° uitmekaar versprei is in die komplekse vlak, soos getoon is in figuur 2.

Enige spanningsvektor binne hierdie heksagon kan verkry word deur die volt-sekonde integraal van die vier spanningsvektore aangrensend aan daardie verlangde spanningsvektor in die spesifieke sektor, vektories te bereken. So byvoorbeeld kan die spanningsvektor $\overline{V}$ in figuur 2 verkry word uit die volgende uitdrukking

$$\overline{V}\cdot T = \overline{V}_0\cdot t_0 + \overline{V}_x\cdot t_x + \overline{V}_y\cdot t_y + \overline{V}_7\cdot t_7 \qquad (1)$$

waar T die skakelperiode van die wisselrigter is en $T = t_0 + t_x + t_y + t_7$. Omdat t_0 en t_7 ooreenkom met nul-vektore, kan hulle gelyk aanmekaar gestel word sodat $t_0 = t_7 = \frac{1}{2}\cdot t_z$.

Die heksagon word in ses sektore onderverdeel waar elke sektor begrens word deur die twee vektore $\overline{V}_x$ en $\overline{V}_y$ soos getoon is vir sektor 1 in figuur 2. Die hoek α word telkens gemeet vanaf die vektor $\overline{V}_x$ tot by die verlangde spanningsvektor $\overline{V}$ in die sektor. Die onderskeie tye wat vektore $\overline{V}_x$, $\overline{V}_y$, $\overline{V}_0$ en $\overline{V}_7$ moet bestaan, word as volg bereken [9]

$$t_x = k\cdot\sin(\alpha + 120^\circ) \qquad (2)$$

$$t_y = k\cdot\sin(\alpha) \qquad (3)$$

$$t_z = T - t_x - t_y \qquad (4)$$

$$k = \frac{\sqrt{3}\cdot T\cdot|\overline{V}|}{V_{GS}} \qquad (5)$$

waar V_{GS} die GS-stamspanning van die wisselrigter is. Om dus die bogenoemde tye te kan bereken, moet die grootte $|\overline{V}|$ en die fasehoek van die verlangde roterende spanningsvektor $\overline{V}$ bekend wees. Dit word verkry uit

$$|\overline{V}| = \sqrt{(ReV^2 + ImV^2)} \qquad (6)$$

$$\arg(\overline{V}) = \text{bgtan}\left[\frac{ImV}{ReV}\right] \qquad (7)$$

waar ReV en ImV onderskeidelik die reële en imaginêre gedeeltes van die spanningsvektor $\overline{V}$ in die komplekse vlak is. Die hoek α word telkens bereken uit $\arg(\overline{V})$ sodat $0^\circ \leq \alpha \leq 60^\circ$ in elke sektor, omdat $0^\circ \leq \arg(\overline{V}) \leq 360^\circ$.

Die stroomvoorspellings-beheertegniek kom daarop neer dat die verskil tussen roterende verwysingstroomvektor en die werklike stroomvektor bereken word, waaruit die verlangde spanningsvektor bereken word om daardie foutstroomvektor na nul te reduseer. Hierdie berekenings is gebaseer op die eenvoudige stroombaan van 'n elektiese netwerk. Die verlangde spanningsvektor, $\overline{V}_k$, word bereken uit

$$\overline{V}_k = \overline{e}_k + [L/T]\cdot[\overline{i}^*_{k+1} - \overline{i}_k] + R\cdot\overline{i}_k \qquad (8)$$

waar $\overline{e}_k$ die ruimtevektor van die 3-fase netwerk is gedurende die k^{de} monsterperiode, $\overline{i}^*_{k+1}$ is die verwysingstroomvektor gedurende die $(k+1)^{ste}$ monsterperiode en $\overline{i}_k$ is die werklike stroomvektor gedurende die k^{de} monsterperiode. L is die totale induktansie en R die totale weerstand van die uitsetfilter, opstap-transformator en netwerk. T is die monsterperiode, wat 100 μs is in hierdie geval.

Die netwerkparameters L en R moet binne 'n redelike akkuraatheid bekend wees. Met die beskikbare syferseinverwerker kan hierdie parameters gereeld geïdentifiseer word m.b.v. 'n parameter-identifikasieroetine.

Om vergelykings 2-8 te kan oplos, moet die waardes van die lynspannings, die werklike uitsetstrome van die DDF, die verwysingstrome vir die DDF en die GS-stamspanning van die wisselrigter bekend wees. Vir doeleindes van hierdie projek word V_{ab}, i_{ad}, i_{bd} en V_{as} (sien figuur 1) d.m.v. 12-bis A/D omsetters elke 100μs gemonster, versyfer en in die TMS320E15 geheue gestoor vir verdere verwerking. Die stroomverwysingseine word d.m.v. 'n digitale stam direk vanaf die oorhoofse TMS320C25 hibriede-kompensatorbeheerder verkry.

Die digitale PWM-beheerder bereken dus die waardes van t_x, t_y en t_z wat bepaal hoe lank die onderskeie transistors in die wisselrigter moet aan/af wees. Die keuse van transistors wat geskakel moet word, berus op die posisie van die verlangde spanningsvektor in die komplekse vlak, m.a.w. inligting i.v.m. die sektor moet ook bekend wees. Dit word maklik verkry uit die fasehoek van die spanningsvektor. Die waardes van die drie berekende tye word m.b.v. drie 8-bis tellers afgetel. Die uitsette van die drie tellers asook die sektorinligting adresseer geheueposisies in 'n EPROM waarvan die uitset die ses transistors direk stuur. Figuur 3 toon die apparatuur vir hierdie mikroverwerker-transistorintervlak.

SIMULASIE VAN DINAMIESE DRYWINGSFILTER

Die voorgestelde stroomvoorspellingsbeheer-algoritme is m.b.v. die syferrekenaar-simulasiepakket ACSL gesimuleer. 'n Blokvormige, onsimmetriese 3-fase las met 'n vermoë van ongeveer 50 kVA, 'n GS-stamspanning van 600 V, 'n 1:2 opstaptransformator, 'n skakelfrekwensie van 10 kHz en minimum filtering van die werklike DDF strome is gesimuleer.

Figuur 4 toon die nie-sinusvormige, onsimmetriese lasstrome van fases A en B (66 A/div). Die lasstroom van fase C is die negatiewe som van hierdie twee. Die 3-fase stroomverwysingseine en die werklike DDF strome vir die DDF word in figuur 5 getoon (55 A/div). Die gekompenseerde sinusvormige, simmetriese toevoerstrome vir fases A en B word in figuur 6 getoon (60 A/div). Met beter filtering sal die 10 kHz rippel op die toevoerstrome ge-elimineer kan word.

Dit is duidelik uit die gesimuleerde resultate van die verwysing- en uitsetstrome van die DDF in figuur 5 dat die aangevraagde strome baie akkuraat gevolg word met 'n baie klein fasevertraging. Hierdie vertraging is een monsterperiode (100 μs) lank omdat die mikroverwerker op huidige waardes van die veranderlikes werk en dan eers in die volgende periode beheer daarop uitoefen.

Op hierdie stadium is praktiese resultate nog nie beskikbaar nie.

OPSOMMING

Dinamiese drywingsfilters word in hibriede-kompensators aangewend om onder dinamiese toestande te kompenseer vir hoër-orde harmonieke wat ontstaan a.g.v. nie-lineêre, nie-sinusvormige lasstrome. Die funksionering en verwagte vertoningskarakteristieke van 'n totaal-digitaal-beheerde dinamiese drywingsfilter gebaseer op 'n standaard 6-skakelaar spanningsgevoerde PWM-wisselrigterbrug word in hierdie skrywe aangespreek. 'n Digitale strcomvoorspellings-beheeralgoritme gebaseer op die ruimtevektor-modulasietegniek word m.b.v. 'n toegewyde TMS320E15 syferseinverwerker geïmplementeer. Simulasieresultate van die digitaal-beheerde dinamiese drywingsfilter word getoon.

Die digitale PWM-stroomvoorspellingsbeheertegniek blyk uit die simulasieresultate heeltemal suksesvol te wees. Deur hierdie digitale beheertegniek te implementeer kan 'n baie elegante totaal digitaal beheerde hibriede-kompensator verkry word met baie voordele bo analoogbeheerders.

VERWYSINGS

[1] H Le-Huy, LA Dessaint: "An adaptive current control scheme for PWM synchronous motor drives: Analysis and simulation", IEEE Trans. on Power Electronics, vol. 4, no. 4, pp 486-495, Oct. 1989.

[2] JHR Enslin, JD van Wyk: A new control philosophy for power electronic converters as fictitious power compensators", IEEE Trans. on Power Electronics, vol. 5, no. 1, pp 88-97, Jan. 1990.

[3] JHR Enslin, GL van Harmelen: "Real-time, dynamic control of dynamic power filters in supplies with high contamination", Proc. of 21st IEEE Annual Power Electronics Specialists Conference (PESC-90), San Antonio, Texas, USA, pp 887-894, 10-14 June 1990.

[4] G Dinkel, R Gretch: "Kompensator für Oberschwingungen und Blindleistung", ETZ Archiv, vol. 9, no. 1, pp 9-14, 1987.

[5] M Depenbrock: "Kompensation schnell veränderlicher Blindströme", ETZ-A, vol. 98, no. 6, pp 418-421, 1977.

[6] DA Marshall, JD van Wyk, D Vermooten, FP Venter: An experimental study of a hybrid Power compensator", Proc. of ICHPS IV, Budapest, Hungary, 4-6 October 1990, pp 134-140.

[7] H van der Broeck, H.Ch Skudelny, GV Stanke: "Analysis and realization of a pulsewidth modulator based on voltage space vectors", IEEE Trans. on Industry Applications, vol. IA-24, no. 1, pp 142-150, Jan./Feb. 1988.

[8] DM Brod, DW Novotny: "Current control of VSI-PWM inverters", IEEE Trans. on Industry Applications, vol. IA-21, no. 4, pp 562-570, May/June 1985.

[9] PG Handley, JT Boys: "Space vector modulation : An engineering review", IEE Fourth International Conference on Power Electronics and Variable Speed Drives, no. 324, pp 87-91, 17-19 July 1990.

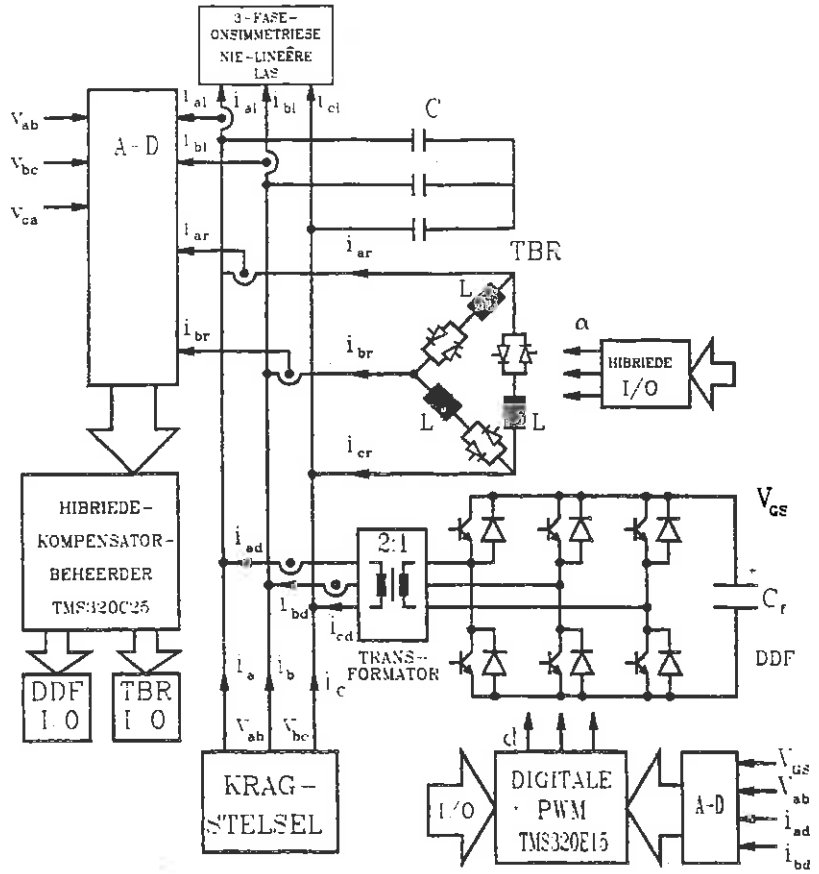

Fig. 1. Blokdiagram : Hibriede-kompensator.

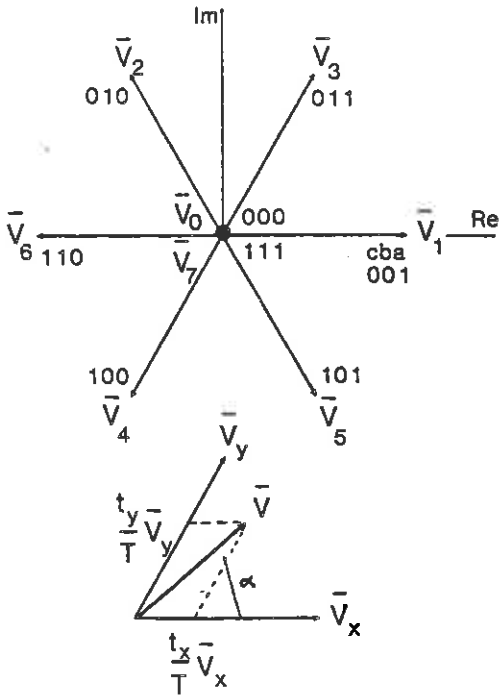

Fig. 2. Spannings-ruimte-vektore in die komplekse vlak.

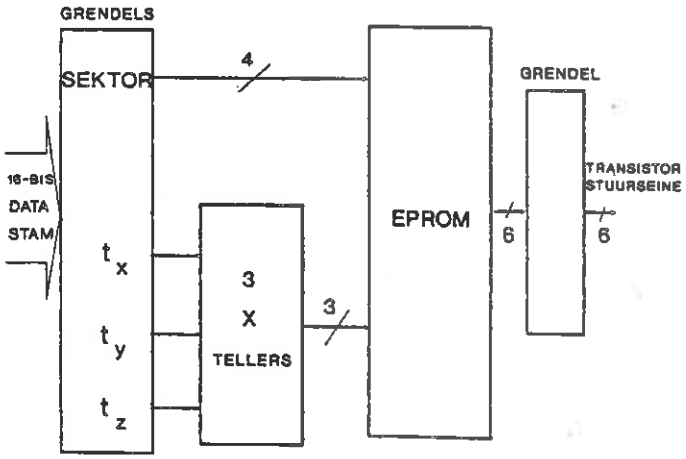

Fig. 3. Apparatuur vir mikroverwerker-transistorintervlak.

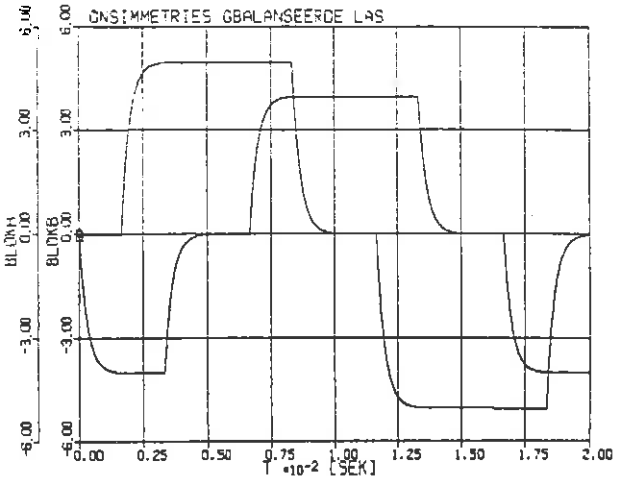

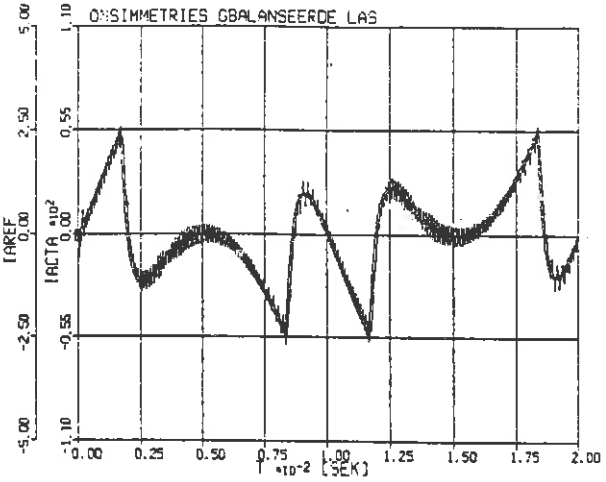

Fig. 4. Gesimuleerde nie-sinusvormige, onsimmetriese 3-fase lasstrome (66 A/div).

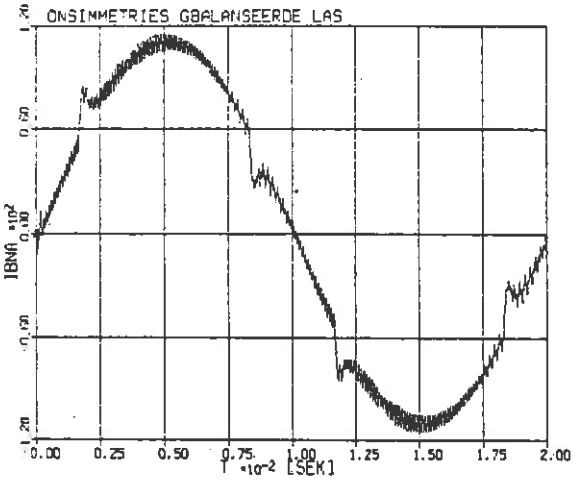

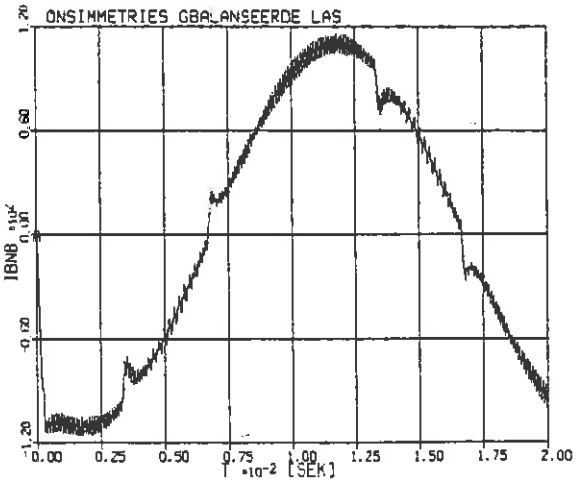

Fig. 6. Gesimuleerde gekompenseerde toevoerstrome vir fase A en B (60 A/div).

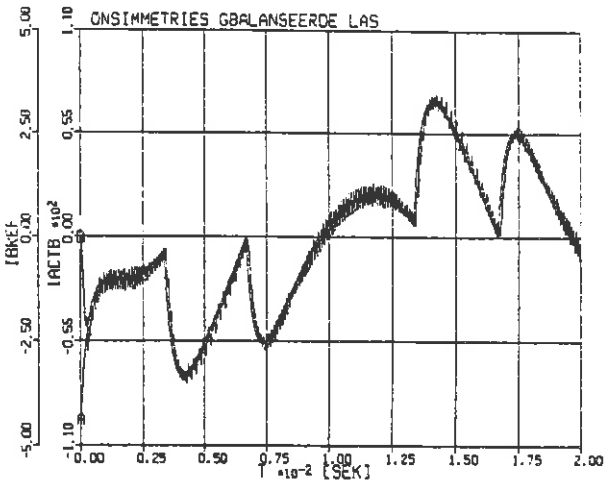

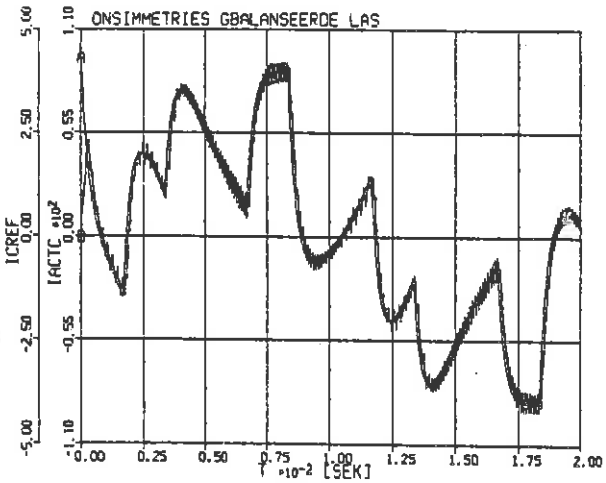

Fig. 5. Gesimuleerde aangevraagde- en werklike DDP uitsetstrome vir fases A, B en C (55 A/div).

HARDWARE DEVELOPMENT FOR INVESTIGATION OF CONTROL ALGORITHMS FOR AC MACHINES.

D.C. Pentz J.G. Roos

DEPARTMENT OF ELECTRICAL ENGINEERING
UNIVERSITY OF PRETORIA
SOUTH AFRICA

ABSTRACT

Hardware development for digital implementation of a current adaptive control scheme is done for a permanent magnet synchronous machine (PMSM). A three phase voltage source inverter receives the digital control signals directly from the fully digitalized controller without the use of analogue interfaces. Hardware requirements for implementation of the current adaptive control scheme are discussed.

INTRODUCTION

The need for highly responsive machine drives in the medium to high power range (above 20kW) have become very important in recent years due to the development of high power highly responsive servo systems. DC machines are generally used in highly responsive machine applications because of the relative simplicity of control schemes for DC machines.

However the need to investigate alternative methods of AC machine control have become very important due to several advantages of the AC machine compared to the DC machine. The potential of the AC machine to show better dynamic responses than DC motors can be subscribed to the fact that the machine inertia is much less than that of a DC machine with comparable size.

Furthermore AC machines are more generally used in the industry because of lower maintenance and initial cost compared to that of DC machines. Torque vector control strategies have been implemented with great success in the past [2] and the possibility to fully digitalize the obtained controller is investigated.

The advantage of the control scheme is that problems usually experienced with analogue controllers of this kind can be eliminated. Furthermore the current ripple caused by the current adaptive control scheme under static conditions is much less than that of a hysteresis controller.
This provides a much smoother torque characteristic during static operating conditions. [1]

More advantages and disadvantages of a digital controller are discussed later in this paper. A micro computer based controller is proposed for implementation of the control algorithms.

PMSM CONTROL SYSTEM

Refer to figure 1 for a block diagram of the current system.
A 12kW peak PMSM is fed from a suitable industrial type voltage fed inverter. A high resolution position sensor is fitted to the rotor of the machine.

CONTROL STRATEGY

The position of the rotor is fed back to the micro computer and the speed is derived through normal differentiation. A digitally implemented PI controller is used to close the speed loop and to determine the torque request (T_{ref}) from the difference in the actual and the wanted rotor speed. (See figures 1 and 2)

The torque vector control strategy is proposed in the literature and the basic equations for the PMSM used are shown in [2]. This control algorithm was directly implemented to provide two of the three phase current request signals (ia_{ref} and ib_{ref}) from the torque request.

CURRENT ADAPTIVE CONTROL

These reference current signals were previously sent to a current hysteresis controller where the current loop was closed and the PWM control signals generated for control of the inverter. The main objective of the controller built was to close the current loop inside the micro computer based digital controller. The PWM control signals are then generated by the computer and sent directly to the inverter in a digital form.

The current adaptive control scheme is proposed by Hoang Le-Huy [1] and is based on a space vector modulation technique [3 and 4]. Figure 3 shows the machine and inverter model. The magnitude and angle of a space vector $\underline{V}$ is calculated mainly from the difference between the reference and the actual phase current in the machine. (See figure 4) The equation is also shown in figure 4.

The switching intervals for the inverter switches are then calculated from the components of this space vector and are used to provide the inverter with 10kHz PWM control signals which will ensure a minimization of the current error as quick as possible.

SIMULATIONS

Simulations performed on this algorithm can be seen in papers produced by Le-Huy [1]. The author have also simulated the control scheme and a result of both static and dynamic characteristics is shown in figure 6. The effect of current ripple have not been simulated and can thus not be seen. A block diagram of the simulation is shown in figure 5.

HARDWARE IMPLEMENTATION OF THE ALGORITHM

A TMS320E15 micro computer based controller is proposed by the author for investigation of PWM control algorithms in general. Figure 7 shows a block diagram of the whole controller. The controller was divided into several control modules.

The micro computer is used to do the numbercrunching as well as the control of data on the central data bus. The resolver to digital converter provides a high resolution digital value of the actual rotor position. Three analogue to digital converters are used to read in the different values shown in figure 7. The three digital to analogue converters are mainly used in the development stage of the software to read out different parameters for visual display. A central high frequency switch mode power supply distributes power to the different modules.

DIGITAL PWM INTERFACE

A block diagram of this interface is shown in figure 8. The calculated switching intervals together with the sector position of the rotating voltage vector $\underline{V}$ are sent to the address lines of an EPROM which is programmed with all the different switching configurations of the inverter switches. The outputs of the EPROM are directly latched and serve as PWM control signals for the inverter.

DISADVANTAGES

Mainly two disadvantages are connected to the digital implementation of the current adaptive control strategy as proposed in [1]. Firstly it is expected that the dynamic responses of the machine drive would not be the same as for hysteresis control.

Furthermore the parameters of the machine have to be known to a great degree of accuracy and the algorithm in itself is not sensitive the changes in machine parameters due to temperature changes.

ADVANTAGES

Both the mentioned disadvantages can be overcome by the following solutions. The steady state current ripple of the adaptive current control scheme is not as high as for hysteresis control. The two different controllers can be kept on standby and activated by the micro computer under the different conditions.

The effect of changing parameters can be compensated for by using parameter estimation techniques.
The parameters of the machine can thus be determined quite often during operation and made available for the control algorithm. The above solutions cannot be implemented in analogue controllers because of the complexity of such circuits. The controller can also be used in various PWM inverter applications and can be adapted easily for any required need.

CONCLUSION

The object of this project was to build a digital controller for investigation of digital control algorithms. Such a control scheme was discussed, simulated and the hardware have been built for implementation of the control scheme. Disadvantages and advantages of the controller and current control scheme have been discussed.

REFERENCES

[1] Hoang Le-Huy and L.A.Dessaint, "An adaptive current control scheme for PWM synchronous motor drives: Analysis and simulation," IEEE Trans. Power Electron. Vol.4, No.4, October 1989.

[2] J.G.Roos and J.H.R.Enslin, "Analysis, simulation and practical evaluation of torque vector control strategies for medium power, highly responsive PMSM drives."

[3] H.W.v.d.Broeck, Hans-Christoph Skudelny, G.V.Stanke, Analysis and realization of pulse width modulator based on voltage space vectors," IEEE Trans.Ind.appl. Vol.24, No.1, January/February 1988.

[4] J.Grando, R.G.Harley, G.Diana, "Understanding and designing an space vector pulse width modulator to control a three phase inverter," Department of Electrical Engineering, University of Natal.

FIGURES

FIGURE 1 PMSM CONTROL SYSTEM

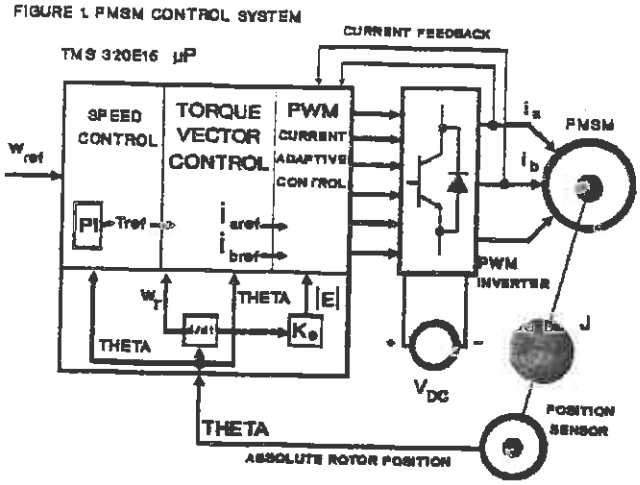

FIGURE 2 PROGRAM STRUCTURE

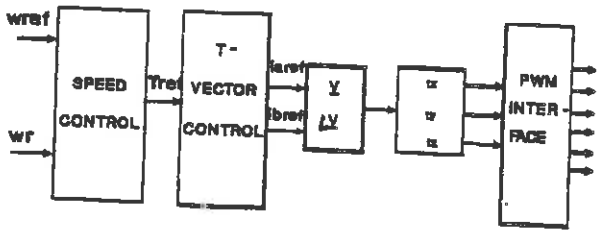

FIGURE 3. MACHINE AND INVERTER MODEL

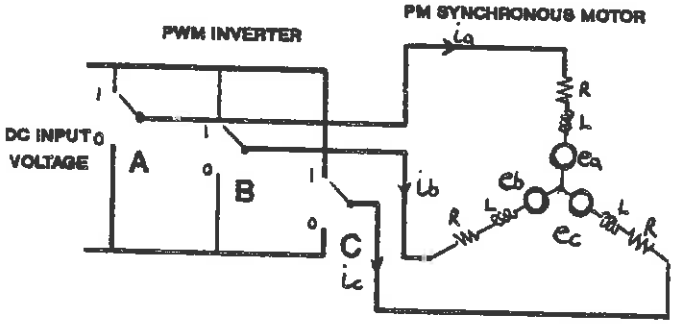

FIGURE 4. ADAPTIVE CURRENT CONTROL SCHEME

$$\underline{V} = \underline{e} + (L/T) * (\underline{i}_{ref} - \underline{i}) + (R * \underline{i})$$

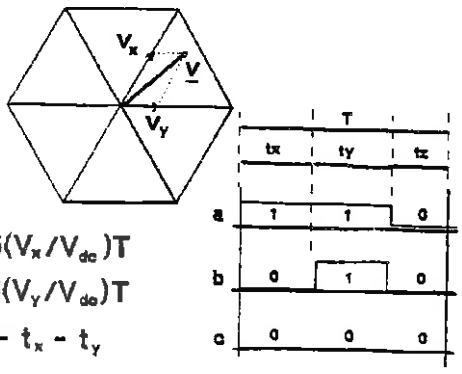

$$t_x = 1.5(V_x/V_{dc})T$$

$$t_y = 1.5(V_y/V_{dc})T$$

$$t_z = T - t_x - t_y$$

FIGURE 5. SIMULATION BLOCK DIAGRAM

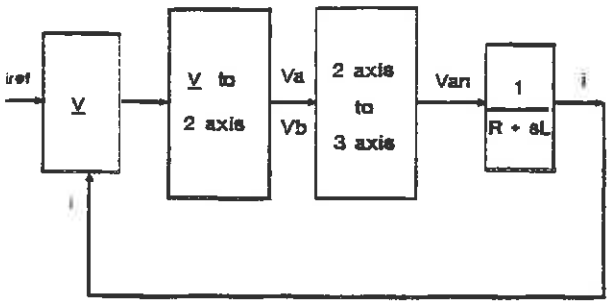

FIGURE 6. SIMULATION RESULTS

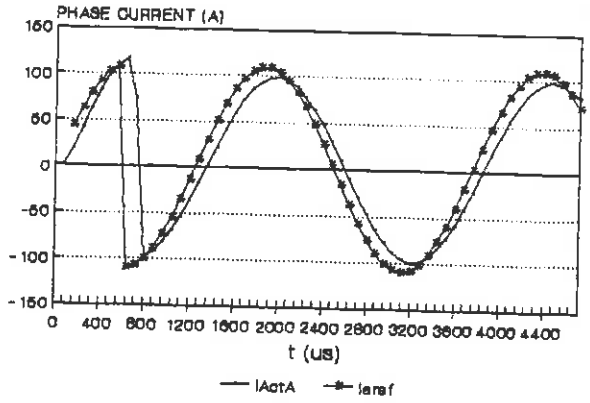

DYNAMIC AND STATIC CHARACTERISTICS

FIGURE 7. HARDWARE REQUIREMENTS

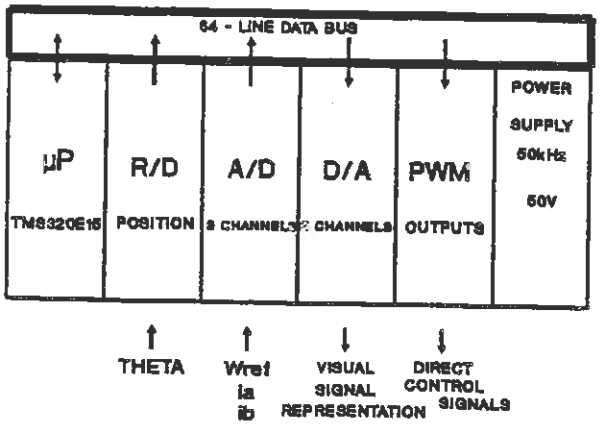

FIGURE 8. PWM - INTERFACE

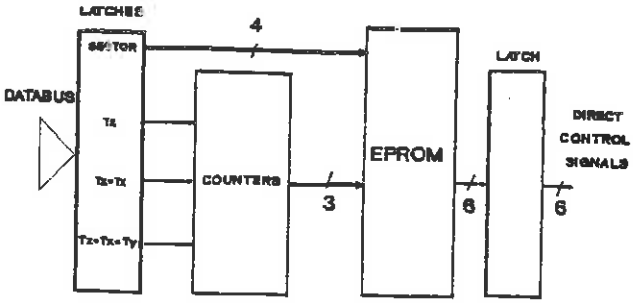

PERFORMANCE OF A PWM INVERTER CONTROL ASIC.

D R Woodward, R G Harley, D C Levy, G Diana

Electrical Engineering Department
University of Natal
Durban 4001

1. INTRODUCTION.

The current trend towards microprocessor based digital control of inverters [1,2] for AC drive applications, has led to a demand for devices to relieve the microprocessor of the work load of generating the control signals for the inverter. The purpose of such a device would be to allow the current loops of the controller to be changed from a software to a hardware based implementation. Control signal operations such as pulse width modulation (PWM) pattern generation, dead time compensation, switching device minimum-on-time monitoring and turn-off-delay compensation would be removed to hardware. The parameters of these control signals would still however be under the complete control of software. The microprocessor could then be fully dedicated to implementing the control strategy of the AC drive, and the more exotic features such as self commissioning, online calibration and tuning, and self diagnostics required by the modern AC drive market.

A device to generate the control signals for an inverter is currently available and is produced by Hanning Elektro Works. This paper describes this device, as well as the interface requirements of this device to the Analogue In Loop (AIL) Interface system [3]. The AIL Interface system is a locally available general purpose, digital controller, and was used as a convenient test bed for the Hanning device. A basic outline of this system will also be given. The paper concludes by discussing the performance of the Hanning device.

2. HANNING 3 PHASE PULSE WIDTH MODULATOR ASIC.

2.1 GENERAL DESCRIPTION.

The Hanning PWM application specific integrated circuit (ASIC) is a gate array containing approximately 8000 active gates, manufactured in 2um CMOS technology. The entire ASIC is contained in a 40 pin DIL package and it has the following specifications :

a) Generates 3 phase PWM control signals for an inverter, using Space Vector Modulation.

b) The inverter output voltage, frequency and phase angle are completely controllable, and may be described in cartesian or polar form.

c) Inverter switching frequency is variable up to a maximum of 18 kHz.

d) Dead band compensation and minimum on time monitoring.

e) Turn off delay compensation.

f) 8 or 16 bit microprocessor interface.

2.2 FUNCTIONAL DESCRIPTION OF THE PWM ASIC.

The functional block diagram of the PWM ASIC [4] is shown in FIG. 1. The input quantities include; the inverter output voltage (described in cartesian form by U1 and U2), the inverter output frequency F, and a desired phase angle offset phio. The output signals to the inverter accomodate both the upper (u1, u2, u3) and lower (l1, l2, l3) devices in each leg of the inverter.

Initially various status words defining the parameters of minimum-on-time, turn-off-time, dead-band-time and switching frequency are loaded into the ASIC from a microprocessor, (an interface is provided to allow the ASIC to be connected to a support microprocessor). Once pulse generation is enabled by sending a control word from the microprocessor to the ASIC, these predefined parameters along with the input quantites of U1, U2, F and phio are used to generate the necessary switching waveforms for the inverter. The input quantities to the ASIC are updated every cycle of the control algorithm executing on the microprocessor. During the switching pulse calculation phase, the cartesian voltage vector described by U1 and U2 is transformed into polar coordinates. The polar angle of the voltage vector is added to the output of an integrator which calculates a phase angle from the required output frequency F. This integrator can be preset by the value of phio from the microprocessor. The sum of the two angles is transformed by a set of nonlinear functions representing the phase potentials at maximum modulation. The resulting potentials are then multiplied by the amplitude of the voltage vector Uo. The resulting signals are then passed to the pulse generation block, which produces the control signals for the inverter. Minimum-on-time monitoring, dead-band and turn-off-delay compensation [5] are administered within this final block.

3. THE ANALOGUE IN LOOP INTERFACE SYSTEM.

3.1 SYSTEM CONCEPT.

The Analogue In Loop Interface (AIL) system [3,6] is a controller suitable for general control applications. The system consists of a number of processing elements along with I/O interfaces. The processing elements are transputers, a microprocessor with an instruction throughput of 10 MIPS / 1.5 MFLOPS [7]. These transputers can be connected together to form parallel processing networks. Due to the general applicability of the AIL system, a number of interfaces are provided. These include analogue-to-digital (AD), digital-to-analogue (DA) and digital-to-digital (DD) interfaces. The various interfaces are connected to the transputers via Inmos communication links [7]. The digital nature of the AIL control system requires that there be a common timebase available to all the system components. The AIL system has a number of ways of ensuring synchronism betwwen its various components. These include a common 5 Mhz clock for all the transputers, an "AIL clock" generated from the common 5 Mhz clock and distributed to all the AIL interfaces, and a broadcast channel (physically an Inmos communications link [7]), connected to all the system components allows synchronised starting and stopping of the system.

The time step of the control algorithm (implemented on the system), is derived from the AIL clock and is software programmable in steps of 125uS. Hence the AIL clock essentially governs the sampling rate of the system. An important point to

note, is that due to timing overheads generated in firmware within the system, the AIL clock frequency is limited to 8 kHz.

4. THE AIL / HANNING PWM ASIC INTERFACE.

4.1 HARDWARE INTERFACE OVERVIEW.

Each of the AIL interface cards consist of the same basic "AILCELL" to which is added the specific components required to convert it into an AD, DA or DD interface. The AILCELL is based on an 8031 microcontroller with support peripherals to allow it to communicate with the transputer via communication links. The particular function (AD, DA or DD) is interfaced directly to the 8031 microcontroller bus structure. To interface the Hanning PWM ASIC to the system, the ASIC is connected to the microcontroller bus in place of a currently supported function. This matter is simplified by the fact that the ASIC has a built-in 8 bit microprocessor interface. The precise details are trivial, however for the microcontroller to communicate with the PWM ASIC correctly it must do so at precise times within the PWM ASIC's timing cycle. Thus the PWM ASIC provides a synchronising signal to the microcontroller to enable correct data transfer between the two devices. The PWM ASIC generates this signal at twice the frequency of the switching signals for the inverter, since it requires data twice during a single PWM cycle. This limits the maximum inverter switching frequency to approximately 4 kHz, since the software executing on the microcontroller has to cycle at 8 kHz to transfer the required data. This cycle time is barely achievable with the 8031 microcontroller which has a basic instruction cycle time of 1uS. It is interesting to note that to achieve the maximum switching frequency of the PWM ASIC (18 kHz), the data transfer rate would have to be 36 kHz and at each transfer instance approximately 10 uS would be available to transfer six 16 bit data words, (the remaining cycle time is used internally by the PWM ASIC). Thus for high performance systems requiring switching frequencies of this order, the microprocessor supporting the PWM ASIC will have to have a very small instruction cycle time and be able to support high bandwidth I/O.

4.2 SOFTWARE INTERFACE OVERVIEW.

The software interface allows the user to change the parameters of the inverter output (voltage magnitude, phase angle and frequency) online. Software running on the PC based transputer host card allows parameters to be passed to the 8031 microcontroller on the AIL interface card containing the PWM ASIC, via the transputer communications link. The microcontroller executes firmware from a support eprom in the AILCELL. The parameters are then passed to the PWM ASIC. A block diagram of the entire system from the user interface to the inverter load is shown in FIG. 2.

5. RESULTS.

The control signals from the PWM ASIC were connected to a 3 phase insulated gate bipolar transistor (IGBT) inverter, with a DC link voltage of 140 volts. The three phase star connected inverter load consisted of an R - L series combination for each phase with R = 25 ohms and L = 62 mH. The results of the phase current measurements for various output frequencies are shown in FIG. 3 and FIG. 4. The results shown in FIG. 3 are for an inverter switching frequency of 4 kHz, whilst those shown in FIG. 4 are for an inverter switching frequency of 1 kHz.

6. DISCUSSION.

The waveforms of FIG. 3 show that for common inverter output frequencies (up 100Hz), the phase current waveforms are essentially free from switching noise. However at higher frequencies (1 kHz), switching noise becomes more apparent but does not totally distort the waveform. This could be improved by increasing the inverter switching frequency, but this is not possible due to the limitations mentioned in SECTION 4.1. Decreasing the switching frequency to 1 kHz causes the switching noise on the waveforms to increase as shown in FIG. 4; this would limit the maximum inverter output frequency, in this case to about 250 Hz.

7. CONCLUSIONS.

The Hanning PWM ASIC provides a means of moving the current control loops from a software to a hardware implementation, whilst still maintaining complete control of the various parameters. The results show that acceptable phase current waveforms can be produced by the ASIC, thus allowing the microcontroller to handle other tasks, provided that it can transfer data to the ASIC fast enough.

8. REFERENCES.

[1] Stefanovic V R, "Industrial AC Drives - Status of Technology", Proceedings of the 6th Conference on Power Electronics and Motion Control (PEMC'90), Budapest, Hungary, Oct 1990, vol3, pp 653 - 664.

[2] Leonhard W, "High Performance Digital Motion Control with Electrical Servo Drives", Proceedings of the 6th Conference on Power Electronics and Motion Control (PEMC'90), Budapest, Hungary, Oct 1990, vol1, pp 1 - 12.

[3] Mostert S, "The Analogue In Loop Interface System Manual", Revision 3.0, Stellenbosch University 1990.

[4] Kiel E, Schumacher W, Gabriel R, "PWM Gate Array for AC Drives", Proceedings EPE 1987.

[5] Dodson R C, Evans P D, Tabatabaei Yazdi H, Harley S C, "Compensating for Dead Time Degradation of PWM Inverter Waveforms", IEE Proceedings, March 1990, vol137, pp 73 - 81.

[6] Woodward D R, "Development of a Transputer based Controller for AC Drives", Proceedings of the South African Universities Power Engineering Conference (SAUPEC'90), January 1990, Stellenbosch, South Africa.

[7] Inmos, "Transputer Reference Manual", Inmos 1989.

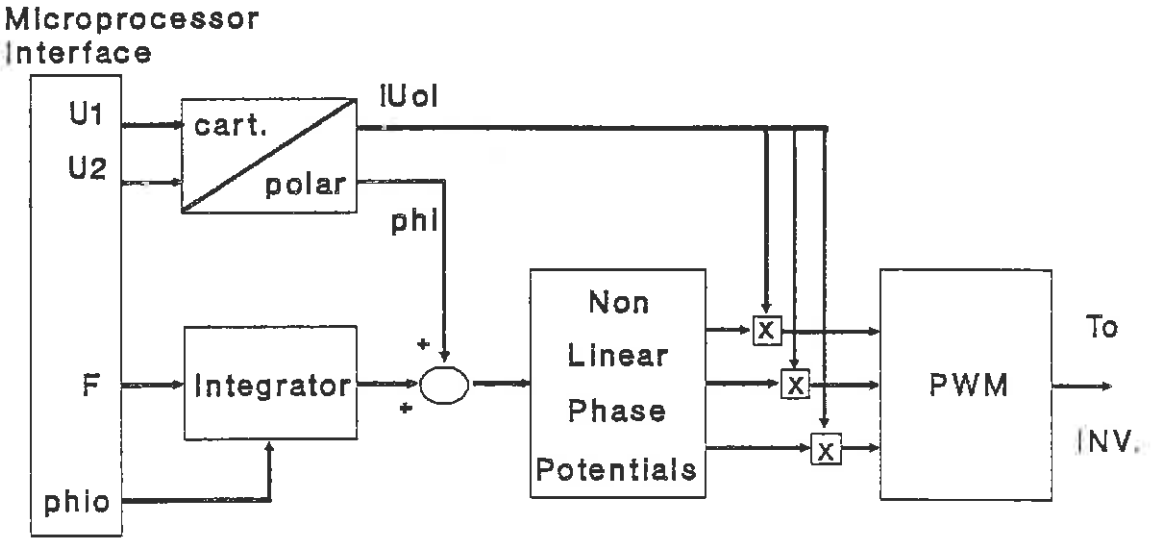

FIGURE 1. Functional Block Diagram of the PWM ASIC.

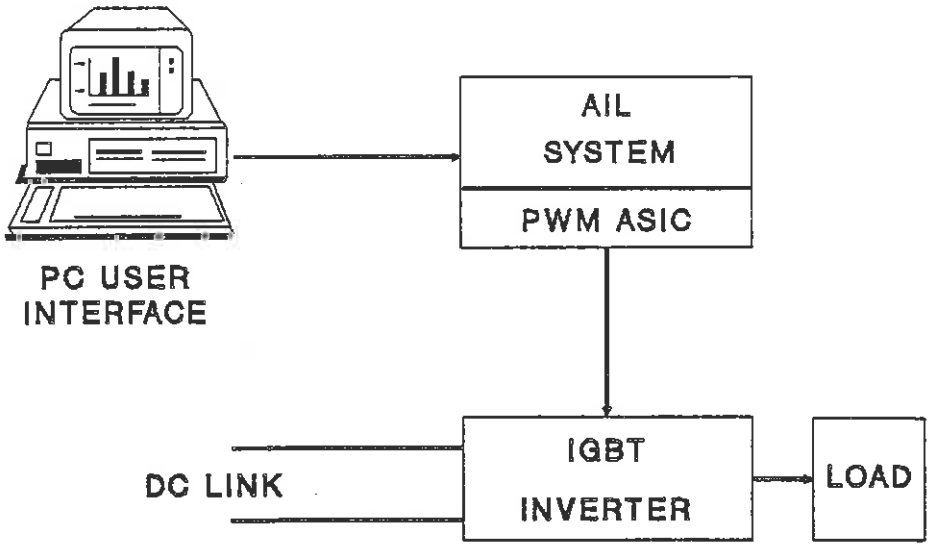

FIGURE 2. Block Diagram of the Complete System.

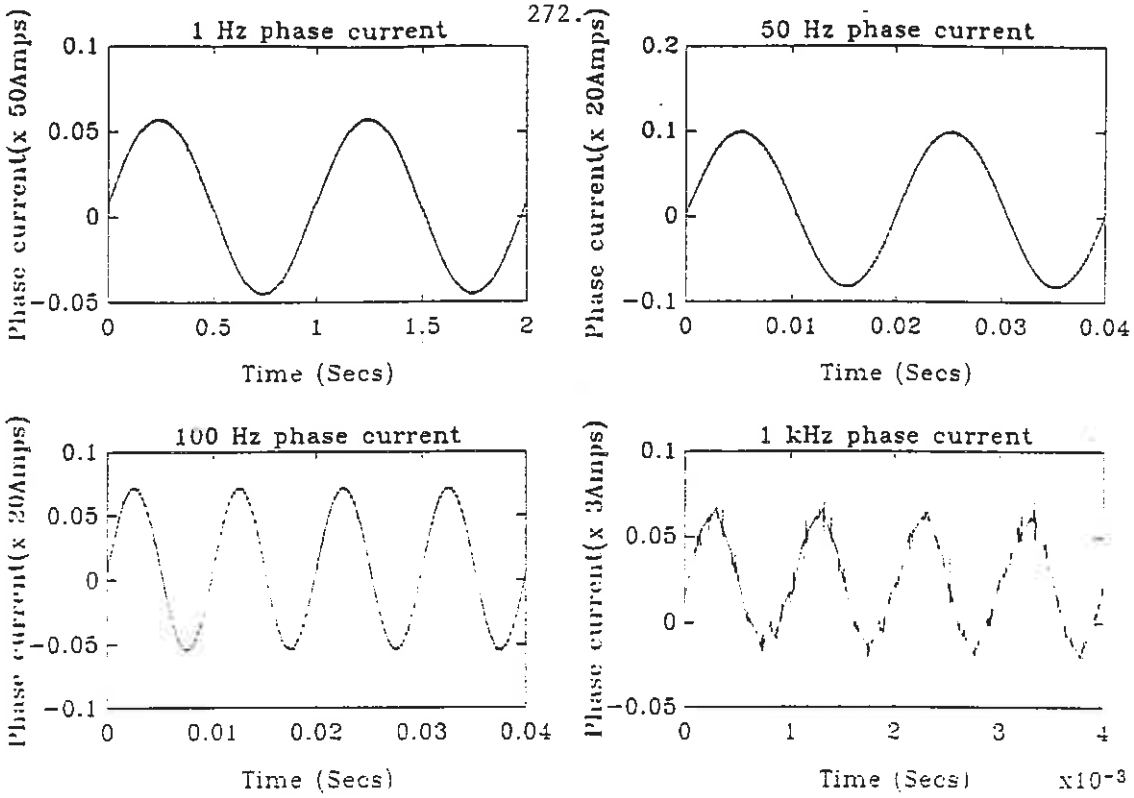

FIGURE 3. Inverter Phase Currents for various output frequencies and an inverter switching frequency of 4 kHz.

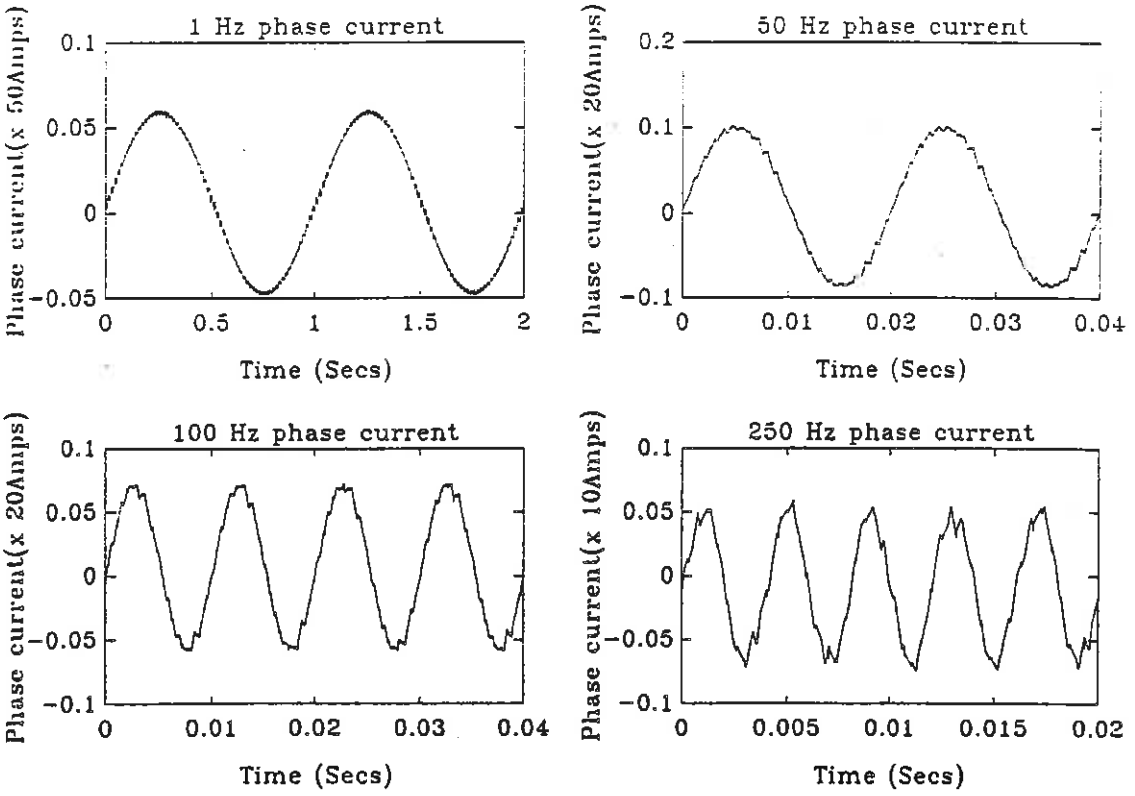

FIGURE 4. Inverter Phase Currents for various output frequencies and an inverter switching frequency of 1 kHz.

CALCULATIONS OF CROSS MMF OF ARMATURE WINDING FOR PERMANENT MAGNET DC MOTORS

J.F. GIERAS, E.E. MOOS, and M. WING

Department of Electrical and Electronic Engineering
University of Cape Town
Rondebosch 7700

ABSTRACT

Calculations of the cross (quadrature) MMF of the armature of a DC commutator permanent magnet (PM) machine have been discussed. Three different approaches have been considered. The first analytical approach approximates the airgap magnetic flux density - MMF curve using two linear segments. The second one utilizes Froelich's equation. The third approach uses a numerical analysis.

A PC based computer program for the performance calculation for PM DC motors has been worked out. Three approaches have been used to take into account the cross armature reaction. Calculations have been made for a small DC motor with segmental permanent magnets. The numerical and based on Froelich's equation approach show close correlation.

1 EFFECT OF ARMATURE REACTION ON OPERATING POINT

The progress in hard magnetic materials technology opens a wide field of application of permanent magnet (PM) DC machines. The trend is strong because of the inherent simplicity of the construction, higher efficiency, and smaller size compared with wound-field machines.

The operating point for a PM with coordinates (B_u, $-H_m$) can be located using the demagnetization curve (second quadrant of the B-H loop), permeance lines and recoil line. Fig.1 shows how to find the operating point for a PM magnetized inside a DC motor. The following symbols have been used: B_r = residual magnetic flux density, B_m = magnetic flux density of the PM assumed to be uniform through its volume, B_u = useful magnetic flux density, H_c = coercive force, H_a = magnetic field intensity corresponding to MMF of armature H_m = equivalent magnetic field intensity corresponding to the MMF of PM, H_{amax} = equivalent magnetic field intensity corresponding to maximum MMF of armature, σ_l = leakage factor [1,2], λ_t = permeance for total magnetic flux (useful + leakage) λ_g = permeance of the airgap for useful flux.

The MMF of armature

$$F_a = H_a h_m = F_{aq} \pm F_{ad} \pm F_{aK} \quad (1)$$

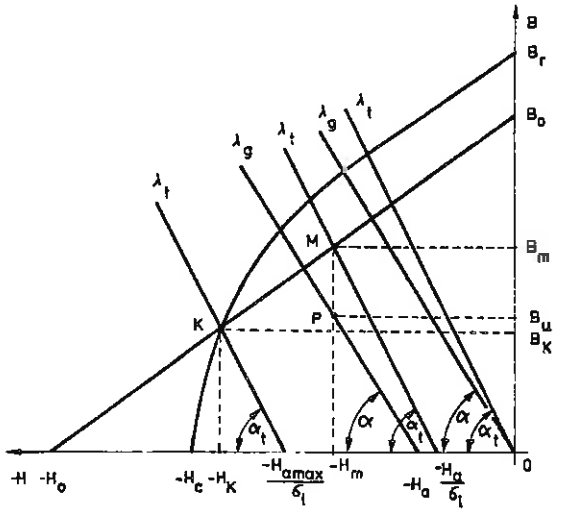

Fig. 1. Demagnetization curve, permeance lines and recoil line. Permanent magnet is magnetized inside a DC motor

holds three components: F_{aq} = cross (quadrature) MMF, F_{ad} = direct-axis MMF, and F_{aK} = direct axis MMF of the coils sections being commutated. The sign "+" is for a generator, the sign "-" is for a motor, and h_m is the height of PM (two poles).

The MMF of PM

$$F_m = H_m h_m \qquad (2)$$

must counterbalance the magnetic voltage drop per pole pair

$$F_p = \Phi_g / \lambda_g \qquad (3)$$

where Φ_g = airgap magnetic flux per pole, λ_g = permeance of the airgap with saturation of magnetic circuit being included, and the MMF of armature, i.e.

$$F_m = F_p + F_a \qquad (4)$$

The point K (Fig. 1) which is given by the intersection of the demagnetization curve and the total permeance line is usually determined for plugging, when

$$F_{amax} = H_{amax} h_m = F_{aq}(I_{amax}) + F_{ad}(I_{amax}) + F_{aK}(I_{amax}) \qquad (5)$$

The armature current for plugging can reach the following value [3]

$$I_{amax} = (0.6 \ldots 0.9)(V_T + E_g)/\Sigma R_a \qquad (6)$$

where V_T = terminal voltage, E_g = generated EMF, ΣR_a = resistance of armature circuit.

2 CROSS MMF OF ARMATURE WINDING

If the brushes are set along the geometrical neutral axis and the magnetic circuit is non-saturated, the cross MMF of the armature winding per pole pair is

$$F_{aq} = A\tau \qquad (7)$$

where $A = f(I_a)$ is the armature electric loading [1-5], I_a is the armature current and τ is the pole pitch.

The armature cross MMF in motors distorts the main field, weakening it under the trailing edge. If the magnetic

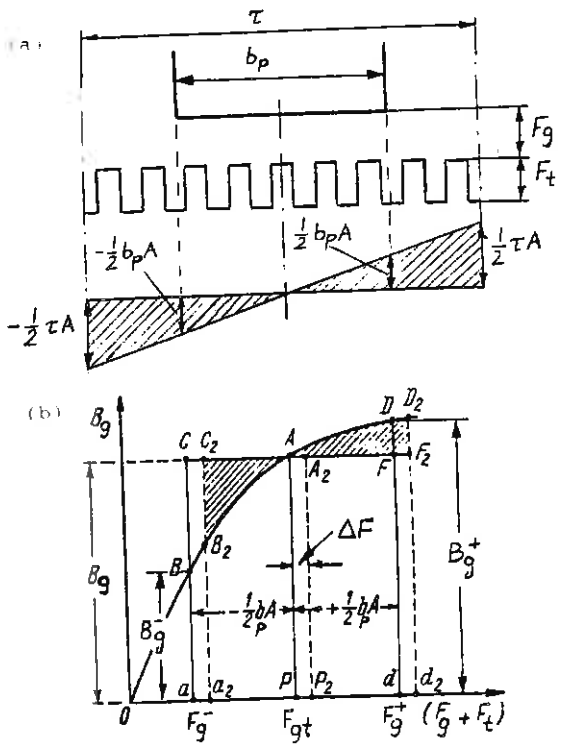

Fig. 2. Determination of demagnetizing effect of cross armature reaqction

circuit is saturated the reluctance of the leading edges of the poles grows quicker than it reduces under the trailing edges.

The curve B_g plotted against $(F_g + F_t)$ (Fig. 2b), where B_g = airgap magnetic flux density, F_g = magnetic voltage drop across the airgap, F_t = magnetic voltage drop along the armature tooth, is used for evaluation of the demagnetizing effect of cross armature reaction. Since rectangle aCFd has a base proportional to pole arc b_p, and a height equal to B_g, its area can serve as a measure of the flux at no-load. In the same manner the area of the curvilinear tetragon aBDd serves as a measure of the flux under load. If the machine is saturated, then the triangles ACB > AFD. To obtain the same magnetic flux and EMF E_g under load as with

no-load, the MMF of the excitation system must be somewhat higher, say, by ΔF, i.e. the MMF of PM of a loaded machine must be

$$F_m = F_{mo} + \Delta F \qquad (8)$$

where F_{mo} is the MMF of PM for no-load. To determine this increase it is sufficient to move rectangle aCFd to the right so that area $AC_2B_2 = AF_2D_2$. The areas of rectangles $aCFd$ and $a_2C_2F_2d_2$ and of the curvilinear tetragon $a_2B_2D_2d_2$ are equal and hence the airgap flux and also the EMF E recover their initial values owing to the increase ΔF in the MMF of PM. The increase ΔF compensates the effect of cross armature reaction

$$\Delta F = 0.5\, F_{aq} \qquad (9)$$

since F_g and F_t are for a single airgap and a single tooth respectively.

The results of evaluating the F_{aq} published so far, e.g. [4]

$$F_{aq} \sim b_p A/b_g \qquad (10)$$

or [5]

$$F_{aq} \sim b_p A/(3\, b_g) \qquad (11)$$

where

$$b_g = (B_g^+ - B_g^-)/(2B_g^+ - B_g^- - B_g^-) \qquad (12)$$

are rather rough and not convergent one with the other. In the next Sections the authors present more accurate approaches to this problem.

3 METHOD OF LINEAR LINE-SEGMENTS OF CALCULATING THE CROSS MMF

The portions AB and AD_2 of the characteristic $B_g = f(F_g + F_t)$ shown in Fig. 2 are approximated by line segments, as in Fig. 3. Since

$$(0.5b_p A - \Delta F)b_l = (0.5b_p A + \Delta F)b_r \qquad (13)$$

and

$$\tan\delta_l = \frac{b_l}{(0.5b_p A - \Delta F)} = \frac{B_g^+ - B_g^-}{0.5b_p A} \qquad (14)$$

$$\tan\delta_r = \frac{b_r}{(0.5b_p A + \Delta F)} = \frac{B_g^+ - B_g^-}{0.5b_p A} \qquad (15)$$

the MMF of cross armature reaction is expressed by the following equation

$$F_{aq} = b_p A(b_g - \sqrt{b_g^2 - b_g}) \qquad (16)$$

where b_g is according to eqn. (12).

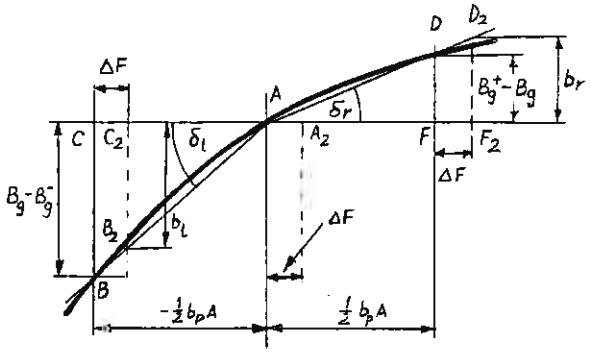

Fig. 3. Approximation of the $B_g = f(F_g + F_t)$ curve by two line-segments

4 CALCULATION OF CROSS MMF USING FROELICH'S EQUATION

For the Froelich's equation of the form

$$B(F) = \frac{a\,F}{1 + b\,F} \qquad (17)$$

where $n = i, i+1, \ldots, j-1, j, \ldots, k-1, k$, the known data points (F_n, B_n) are taken from the $B_g = F(F_g + F_t)$ curve. A least squares fit is performed on these selected points to determine the unknown coefficients a and b in eqn. (17), i.e.:

$$a = \frac{\sum_{n=i}^{k} B_n F_n \sum_{n=i}^{k} B_n F_n - \sum_{n=i}^{k} B_n \sum_{n=i}^{k} B_n F_n}{\sum_{n=i}^{k} F_n \sum_{n=i}^{k} B_n F_n - \sum_{n=i}^{k} F_n \sum_{n=i}^{k} B_n^2} \qquad (18)$$

$$b = \frac{\sum_{n=i}^{k} B_n F_n \sum_{n=i}^{k} F_n - \sum_{n=i}^{k} F_n \sum_{n=i}^{k} B_n}{\sum_{n=i}^{k} F_n \sum_{n=i}^{k} B_n F_n - \sum_{n=i}^{k} F_n \sum_{n=i}^{k} B_n^2} \qquad (19)$$

The areas AB C and AD F in Fig. 2 should be equal. By writing equations for the two areas, evaluation of them and setting the two equal, one can obtain the following equation for the cross armature reaction

$$F_{aq} = \frac{1}{2} b_p A \left[\frac{1 + \exp(-\alpha)}{1 - \exp(-\alpha)}\right] - F_{gt} - \frac{1}{b} \quad (20)$$

where

$$\alpha = b_p b_a A \left(1 - \frac{b}{a}\right) \quad (21)$$

and F_{gt} is according to Fig. 2.

5 NUMERICAL APPROACH OF CALCULATING THE CROSS ARMATURE REACTION

Straight lines between successive points are used to approximate the characteristic $B = f(F_g + F_t)$. Denoting in Fig. 2 the area ABC by S_l, the area ADF by S_r, the area APaB by A_l, the area ADdP by A_r, and using trapezoidal rule, the the following equations can be written

$$S_l = B_g (F_{gt} - \bar{F}_g) - A_l \quad (22)$$

and

$$S_r = A_r - B_g (F_{gt} - \bar{F}_g) \quad (23)$$

where

$$A_l = \frac{1}{2}(F_i - \bar{F}_g)(B_i + \bar{B}_g) + \sum_{n=i}^{j-1}(F_{n+1} - F_n)(B_{n+1} + B_n) + \frac{1}{2}(F_{gt} - F_j)(B_j + B_g) \quad (24)$$

$$A_r = \frac{1}{2}(F_{gt} - F_{j+1})(B_{j+1} + B_g) + \sum_{n=j+1}^{k-1}(F_{n+1} - F_n) \times (B_{n+1} + B_n) + \frac{1}{2}(\bar{F}_g - F_k)(\bar{B}_g - B_k) \quad (35)$$

Depending on the areas $\bar{S}_l$ and $\bar{S}_r$, the MMFs $\bar{F}_g$ and $\bar{F}_g$ will be shifted to the left or right by an amount. This amount and the direction of the shift will be determined by the bisection method. This method (an iteration process) calculates the areas S_l and S_r until the difference between them is negligible.

For the motor operating in the saturation region, the iteration process is as follows:

A. Initialise $\bar{F}_l$ as $\bar{F}_g$, F_r as F_{gt} and F_{mid} as $0.5(F_l + F_r)$;

B. Compare the areas S_l and S_r and then redefine

$\bar{F}_g$ as F_{mid}

$\bar{F}_g$ as $(F_g + F_{mid} - \bar{F}_g)$

F_l as F_{mid} if $S_l > S_r$ or F_r as F_{mid} if $S_l < S_r$

F_{mid} as $0.5(F_l + F_r)$

C. Calculate areas S_l and S_r

The procedure from step B onwards is then repeated. The iteration process is terminated upon, e.g.

$$|S_l - S_r| < 10^{-5}$$

The MMF of cross armature reaction is

$$F_{aq} = F_{mid} - \bar{F}_g \quad (36)$$

where $\bar{F}_g$ is the initial value of $\bar{F}_g$.

6 COMPUTATIONS

The PC based program (Fig. 4) starts by prompting the user to enter the shape of the PMs. The user is then asked to enter the name of the file containing specific data on the dimensions of the rotor, stator and PMs, as well as the dimensions

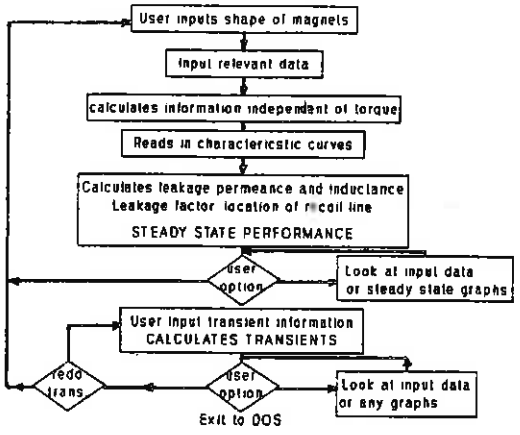

Fig. 4. Flow chart for computer program

of the armature slots and armature winding parameters. The demagnetization curve of the PM, the magnetization curve and the specific losses curve vs the magnetic flux density of the rotor laminations are inputs to the program from data files containing points of the specific curves. The steady state performance is then calculated for a range of torque values from close to zero up to a chosen value usually greater than the rated torque value. The user is also asked to select the method by which the cross armature reaction is to be calculated. The output data of the steady state simulation, such as input power, output power, efficiency, armature current and rotor speed all against output shaft torque can then be observed in graphical form. The transient simulation is done for a specified time interval with a specified load torque and load moment of inertia. The output data of the transient simulation as e.g. speed or armature current vs time can now be displayed in graphical form.

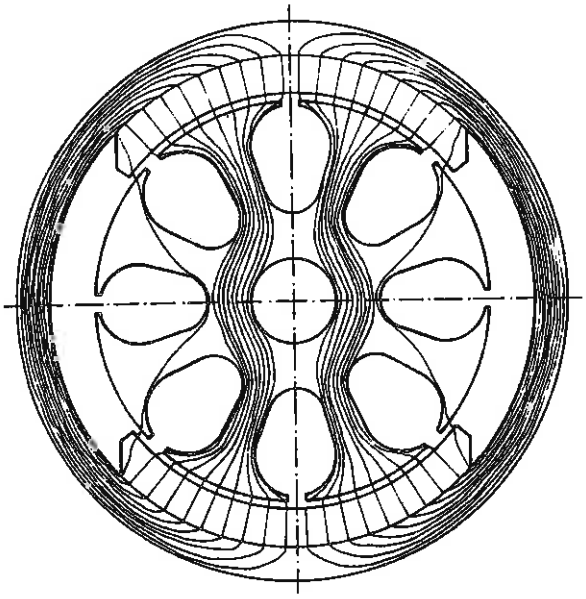

Fig. 5. Magnetic circuit of a 8-W two-pole DC motor with segmental permanent magnets

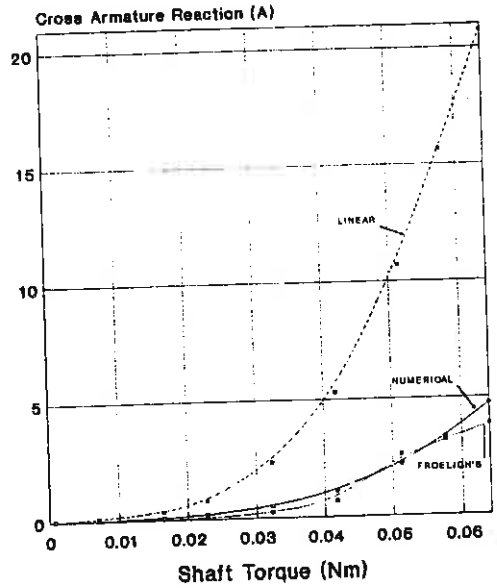

Fig. 6. Cross MMF of armature winding as a function of shaft torque

The calculations have been done for 8-W PM DC motor for automobile blower [2] the magnetic circuit of which is shown in Fig. 5. A comparison (Fig. 6) has been made between the calculated values for cross armature reaction using linear, Froelich's and numerical methods. The steady state (Fig.7) and transient (Fig. 8) simulation results have been compared for the three methods of calculating the cross armature reaction. Comparison of steady state performance obtained from experimental results is shown in Fig. 9. It does not make any practical difference which method of including of the cross armature reaction has been used. In Fig. 9 this has been calculated using line segment approximation according to eqn. (16).

7 CONCLUSIONS

All the methods described in Sections 3,4, and 5 give similar results. The Froelich's approximation and the numerical

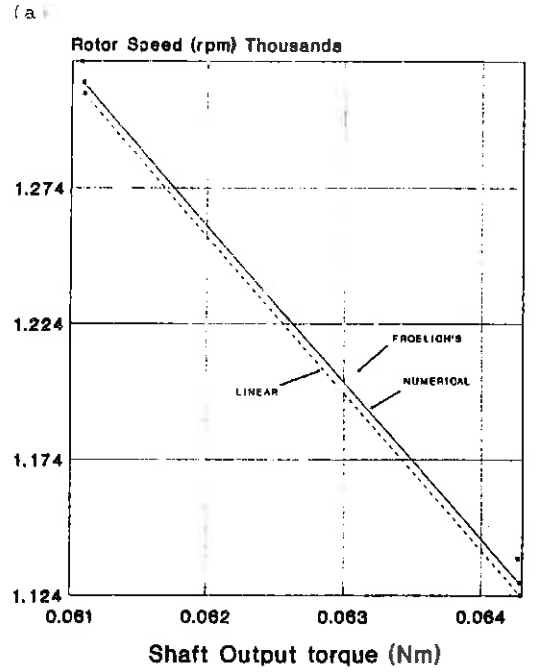

Fig. 7. Calculated steady-state performance: (a) speed vs shaft torque; (b) armature current vs shaft torque

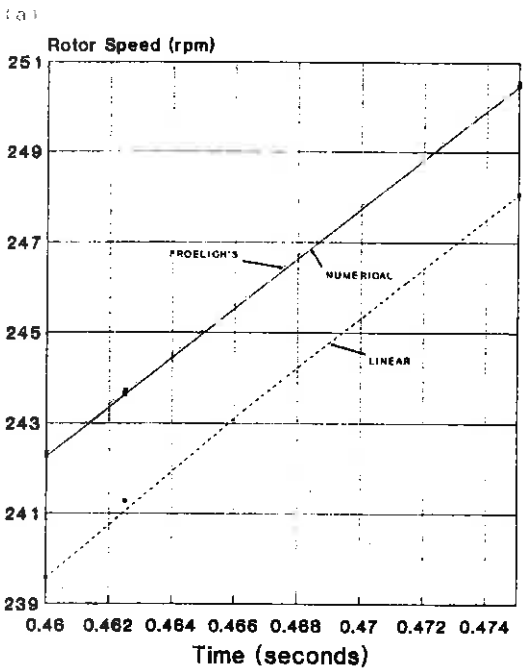

Fig. 8. Calculated transient performance for moment of inertia 0.001 kgm²: (a) speed vs time; (b) armature current vs time

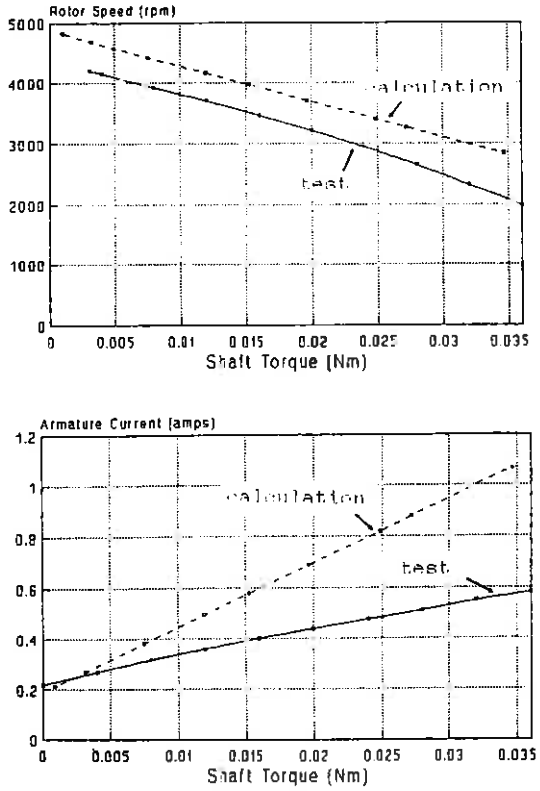

Fig. 9. Steady state performance obtained from calculations and measurements

method show a good correlation over the whole range of torque values. The linear method on the other hand deviates to an extend from the values obtained using the numerical and Froelich's methods. It can thus be recommended to use numerical method or method based on Froelich's equation rather than that utilizing linear approximation. However, all three methods in practice give very close results in calculating the steady state performance. This is due to the fact that the MMF of armature winding does not affect the airgap useful magnetic flux density in any significant way in this PM DC motor . Note that the y axis in Figs. 7 and 8 has been extended (compare Fig. 9).

REFERENCES

1 Kostenko M., and Piotrovsky L.: "Electrical machines", vol 1, Mir Publishers, Moscow, 1974

2 Gieras J.F.:"Performance calculation for small dc motors with segmental permanent magnets", SAIEE Transactions, submitted for publication

3 Balagurov V.A., Galteyev F.F., and Larinov A.N.: "Permanent magnet electrical machines" (in Russian), Energia, Moscow, 1964

4 Gogolewski Z., and Gabryś W.: "DC machines" (in Polish), PWT, Warsaw, 1960

5 Voldek A.I.: "Electrical machines" (in Russian), Energia, Leningrad, 1974

AN INVESTIGATION INTO IMPROVING THE COMMUTATION OF A D.C. MACHINE

G.M.J.Parsley C.F.Landy

INTRODUCTION

The most effective way of ascertaining the efficacy of the commutation of a D.C. machine is to suject it to the so called "black band" test. This test involves sujecting the machine to various loads in the range of roughly 0.2 pu to 2 pu. At each particular load the interpole windings are seperately excited and a range of of interpole winding currents are determined that result in little or no commutator sparking. This is the so called black commutation region and, plotting these regions over the entire load range will produce the black band.

It is the shape of this black band and which portion of the machines' load current line falls within it that gives a good indication of how the machine is commutating. Over- or under-commutation is easily discernable as well as interpole magnetic saturation.

It is ironic that the black band test provides a very clear picture of commutation ills but offers no indication of the cause or remedy of these ills. It is therefore the purpose of this research to identify those factors that influence the black band test.

THEORY

According to Jones [1] [2], the magnetic effects of the particular coil undergoing commutation in the armature of a DC Machine is in space quadrature with the magnetic effects of armature reaction. Jones further proposes that, during a particular commutation period, the DC Machine may be regarded as a primative slip ring machine functioning about the neutral axis and puts forward the schematic of the machine as shown in Fig 1

Referring to fig 1, coil 1 is the main field winding, coil 2 is the interpole winding, coil 3 represents the armature windings, and coil 4 represents the particular armature winding undergoing commutation and short circuited by the brushes as indicated. The most general form of the equations describing this machine are:

$$\begin{matrix} V_1 \\ V_2 \\ V_3 \\ V_4 \end{matrix} = \begin{matrix} R_1 + pL_1 & pM_{12} & pM_{13} & pM_{14} \\ pM_{21} & P_2 + pL_2 & pM_{23} & pM_{23} \\ pM_{31} & pM_{32} & R_3 + pL_3 & pM_{34} \\ pM_{41} & pM_{42} & pM_{43} & R_4 + pL_4 \end{matrix} \begin{matrix} I_1 \\ I_2 \\ I_3 \\ I_4 \end{matrix}$$

where the mutual inductances between coils are indicated by M and inductances by L. The time derivative $\frac{d}{dt}$ is indicated by p in the usual way.

During a commutation period the angle θ can be regarded as small and deviating slightly as a fraction of arc occupied by one commutator segment in the neutral axis of the machine. This slight deviation, coupled with the assumption that the pole shoes of the main poles and the interpoles differ in geometry, will cause changes in the mutual inductances of the machine experiencing such a changing magnetic environment due to a slight change in θ. The exception in this regard is the mutual inductance between the main field and interpol field, M_{12}. These coils are in space quadrature and their magnetic environments are not functions of the armature angle θ, making pM_{12} and pM_{21} equal to zero.

Considering the conditions pertinent to the execution of a "black band" test we have:

The main field current I_1, the interpole current I_2, and the armature current I_3 are all constant, ie time invariant.

The current I_4 in the coil undergoing commutation is varying with time and should ideally change from $-I_3$ to $+I_3$ within the commutation period T_c.

With these constraints and considering each mutual inductance in the following manner,

$$pM = \frac{dM}{dt} = \frac{dM}{d\theta}\,\frac{d\theta}{dt} = \omega M'$$

$$where\ \omega = \frac{d\theta}{dt}\ and\ M' = \frac{dM}{d\theta}$$

The describing equations can be stated as:

Field Volts	$V_1 = R_1I_1 + \omega M'_{13}I_3 + M_{14}pI_4$	1
Interpole Volts	$V_2 = R_2I_2 + \omega M'_{24}I_4$	2
Armature Volts	$V_3 = \omega M'_{13}I_1 + R_3I_3 + \omega M'_{34}I_4$	3
Com Coil Volts	$V_4 = \omega M'_{24}I_2 + \omega M'_{34}I_3 + (R_4 + L_4p)\ I_4$ . . .	4

Referring to eqn 3, $\omega M'_{13}I_1$ is the internally generated voltage.

R_3I_3 is the normal voltage drop across the internal impendence of the armature.

The term $\omega M'_{34}I_4$ is the significant voltage of the black band phenomenon. At the end of the commutation period T_c, if I_4, the current in the coil undergoing commutation, is equal to the armature current I_3, no voltage difference will exist between the brush and commutator segment just leaving the brush. This would be perfect commutation.

If $I_4 \neq I_3$, a voltage of $\omega M'_{34}\ (I_4 - I_3)$ will arise and, if it is sufficiently large, a spark will occur.

In order to determine wheather sparking will occur it is necessary to compare the magnitudes of I_4 and I_3 at the end of the commutation period T_c. This means considering eqn 4.

V_4 is an external voltage applied to the coil undergoing commutation. Since no such voltage is being applied, indeed, the coil is short circuited by the brushes, this voltage is zero.

Rewriting eqn 4 with the interpole current I_2 in the opposite

direction to the armature current I_3, (ie bucking), we get

$$\frac{dI_4}{dt} + \frac{R_4}{L_4} I_4 = \frac{\omega}{L_4} (M'_{24} I_2 - M'_{34} I_3)$$

The solution to this differential equation is

$$I_4 = \frac{\omega}{R_4} (M'_{24} I_2 - M'_{34} I_3) + Ae^{-\frac{R_4}{L_4} t}$$

In order to resolve the constant A, consider the following

At the start of commutation, ie at t = 0, $I_4 = -I_3$
so that

$$I_4 = \frac{\omega}{R_4} (I_2 M'_{24} - I_3 M'_{34}) - [I_3 + \frac{\omega}{R_4} (I_2 M'_{24} - I_3 M'_{34})] e^{-\frac{R_4}{L_4} t}$$

and the final value of current in the coil undergoing commutation occurs at $t = T_c$, the total commutation time.

Therefore the voltage of commutation is,

$$V_c = \omega M'_{34} (I_4 - I_3)$$

$$= \omega M'_{34} [\frac{\omega}{R_4} (I_2 M'_{24} - I_3 M'_{34}) - [I_3 + \frac{\omega}{R_4} (I_2 M'_{24} - I_3 M'_{34})] e^{-\frac{R_4}{L_4} T_c} - I_3] \quad ..5$$

Note that this voltage, as expected, depends on I_2 and I_3, the interpole and armature currents respectively. Other factors are the speed ω, the brush resistance R_4, M'_{24} and M'_{34}. These last two factors represent the following rotational inductances, about the neutral axis.

$$M'_{24} = \frac{dM_{24}}{d\theta}\Big|_{\theta=0} \qquad M'_{34} = \frac{dM_{34}}{d\theta}\Big|_{\theta=0}$$

Apart from the windings that exist on the armature and

interpoles, M_{24} and M_{34} are greatly influenced by the physical geometry of the machine. These mutual inductances and their variation about the neutral axis are incredibly difficult to determine on an actual machine,and,having determined them,one is still at a loss as to how to adjust them to obtain better commutation. It is thus necessary to consider a finite element analysis model of the machine. Using this model it should be possible not only to determine M_{24} and M_{34} and their variations about the neutral axis but also determine what factors of machine geometry can be rearranged to adjust these values for better commutation.

The effectivety of these rearrangments will have to be tested in each case by deciding on a voltage of commutation,V_c,(usually about 20 volts) and solving eqn 5 for various values of I_2 and I_3 to obtain this. In other words,simulating and plotting the black band. The final test would be to construct a machine according to the geometry determined by finite element analysis and compare the actual black band with the simulated one.

References:

1. C V Jones: "Analysis of Commutation for the Unified Machine Theory", Proc IEE 108c; 1(1958).

2. C V Jones: "The Unified Theory of Electrical Machines", Butterworths 1967.

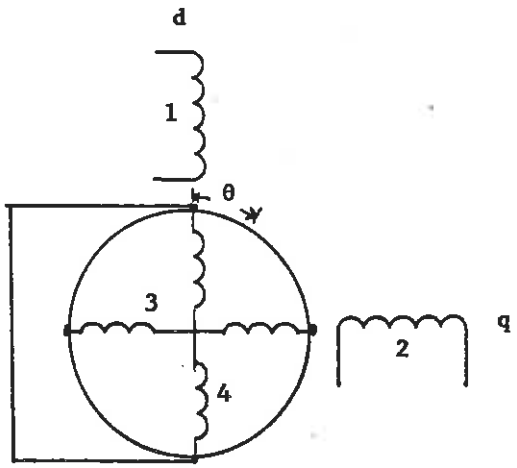

FIG 1: EQUIVALENT PRIMATIVE MACHINE SCHEMATIC

BIPOLAR PULSING CIRCUITS FOR HIGH POWER HIGH REP RATE LASERS

H.T.W. Tromp, P.H. Swart and H.M. von Bergmann
Systems Laboratory, Rand Afrikaans University, P.O. Box 524
Johannesburg, 2000, Republic of South Africa

Abstract

Series pulse compression is ideally suited for transforming the switching requirements of multi-kilohertz and multi-kilowatt excimer and CO_2 TEA lasers into regimes where commercial thyristors can be utilized economically for primary pulse conversion.

A major drawback of series Melville compressors which are conventionally employed are core losses, especially in the final stages, bottlenecking the average power throughput capability. In order to achieve optimal hold-off, the saturable inductor cores have to be reset between successive pulses, requiring two full flux excursions per pulse. A simple modification, introducing pulses with alternative polarity, accomplishes intrinsic resetting, and in addition leads to the requirement of only a single flux excursion per pulse. As magnetic core losses are directly related to the cyclic magnetization frequency, core losses are effectively halved by utilizing bipolar operation. Alternatively viewed, a pulser operating in the bipolar mode will yield the same level of average power with half the core losses, compared to the unipolar case.

The introduction of non-linear interstage capacitors into a Melville line will lead to a reduction in hold-off requirement in successive stages, because of the resulting non co-sinusoidal charging voltage profiles, with their lower $\int v dt$ requirement. A major difficulty associated with the use of non-linear capacitors in this application though, is the requirement of dielectric resetting. Again bipolar operation (intrinsically) solves this problem and enables the utilization of non-linear capacitors, that would otherwise be problematic. By means of bipolar opperation thus, two major important objectives are collectively achieved, namely increased efficiency and a reduction in inductor core volume.

This paper presents analytical and experimental work, carried out in the above regard.

Introduction

Series pulse compression, utilizing saturable amorphous magnetic cores and linear interstage capacitors, is ideally suited for transforming the switching requirements of multi-kilohertz and multi-kilowatt excimer and CO_2 TEA lasers, into regimes where commercial thyristors can be utilized economically for primary pulse conversion. The series, or Melville line [1] configuration, has been adopted on account of its relative simplicity, to develop thyristor driven excimer and CO_2 TEA laser pulsers capable of delivering average powers in excess of 40 kW at pulse energies extending beyond 20 J. Recent successes in overcoming difficulties in gas flow dynamics have indicated that pulse repetition rates above 2 kHz are feasible for excimer and CO_2 TEA lasers [2]. Peak attainable repetition rates and average power levels are presently restricted by heat losses in the inductor cores, especially in the final stages of multistage compressors.

In conventional unipolar multistage series pulse compressors, additional core resetting is usually necessary to achieve full hold-off capability of the saturable inductors. Because of the resetting requirements in unipolar pulsing, two full flux excursion, with their associated eddy-current and hysteresis losses, are necessary for each pulse. By alternating the polarity of the pulses, however, intrinsic resetting is achieved, as each pulse resets the cores for the next. Using this scheme, pulse repetition rates can be doubled without increasing magnetic and dielectric losses. By utilizing bipolar pulsing output power levels can be raised drastically. In the laser, uv-preionization and electrode structures can be designed to accommodate bipolar excitation, without adversely affecting the modal and directional stability of the laser beam.

Aside from the major asset of increased power capability, furnished by the bipolar compressor, it also exhibits other valuable features. The most important is that of intrinsic core resetting, obviating the necessity of additional reset windings and power supplies, yet furnishing peak flux excursion and thereby assuring optimum core volume utilization. It also opens the venue for employing non-linear capacitors through which higher compression factors can be achieved with the same core volume. As non-linear capacitors also exhibit hysteresis however, resetting of their dielectrics will be necessary for optimum compression. This resetting is intrinsically achieved by bipolar pulsing.

A scaled-down bipolar multistage compressor, utilizing linear as well as non-linear interstage capacitors, has been experimentally evaluated. Analytical and experimental results are presented.

Theoretical Considerations

Bipolar Series Pulse Compression

In order to obtain maximum compression per unit core volume in the series pulse compressor, it is essential to

maximize the flux excursion. In Z-type core materials, with high remanence ratio (B_r/B_s), this requirement can usually be realized effectively with static or dynamic resetting [1], carried out extrinsically, or intrinsically in the case of unipolar operation. In this case, hold-off in the inductor is furnished by the flux swing from $-B_r$ to B_s as shown in the magnetization curve in fig.1. With magnetic materials in which the remanence ratio is lower, such as in ferrites, the available flux excursion is reduced, with a consequent reduction in hold-off. If each successive pulse, however, is of opposite polarity, magnetization will alternate in polarity and will in effect furnish resetting for successive pulses. If pulses follow rapidley enough in time, flux excursions beyond the B_r - B_s range for the magnetic materiaal in question, can be achieved.

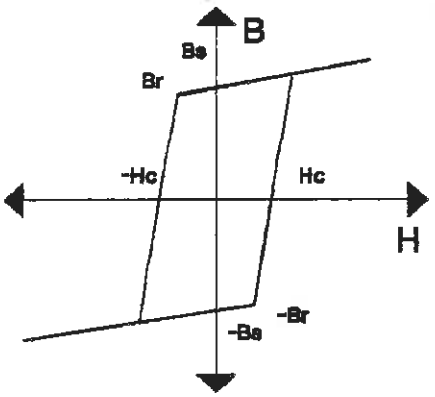

Figure 1. Typical Z type magnitization.

In unipolar operation, the excursion from $-B_r$ to B_s is utilized in the inductor, to furnish the necessary synchronizing hold-off. Unfortunately, each flux excursion, be it that required for hold-off, or that due to resetting, forms part of the magnetization cycle and assists in enclosing the magnetization loop. In the case of bipolar operation, each successive pulse will force magnetization in the opposite direction. Where pulses required two excursions and one full cycle of magnetization with unipolar operation, bipolar operation will require only one full flux excursion per pulse and only one cycle of magnetization will result for each two successive pulses handled by the inductor.

When operated at pulse widths below 150ns, as in the case of final stage inductors of pulse compressors driving laser circuits at high repetition rates, excessive core losses report as the result of the high frequency content in the inductor. The average power capability of compressors is usually limited by the rate at which the heat generated by the magnetization losses can be removed. The higher conduction losses in the windings at higher repetition rates, usually present less of a problem and can more easily be accomodated.

A bipolar pulser configuration

Fig. 2 shows, in simplified diagrammatic form, the bipolar pulser configuration that has been used. This configuration [3] is a modification on the unipolar pulser previously designed by the PULSTEK[2] group. The four stage compressor is of conventional design. The Resonant, Regulating Pulse Power (R^2P^2) supply unit still operates in accordance with initial design, but in the case of the bipolar configuration shown, it utilizes a centre tapped transformer and an additional pair of transfer- and charging thyristors, T_{b2} and T_{c2} respectively, to generate the negative pulses. The de-queing thyristor T_a serves the unit for both polarities.

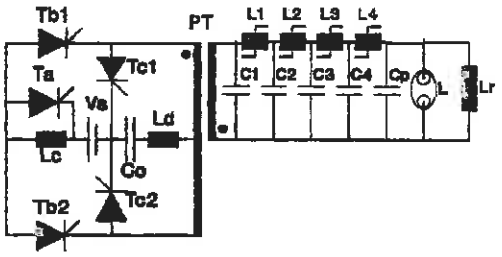

Figure 2. Bipolar power supply and pulse compressor (Only T_{b2} and T_{c2} was added and the transformer was furnished with a centre-tap to enable bipolar operation).

Charge transfer from the primary capacitor C_0 to high voltage capacitor C_1 takes place resonantly. The polarity of the charge transferred to C_1 will be opposite, depending on whether T_{c1} or T_{c2} is triggered. With the dot orientation shown, C_1 will be charged positively (top plate positivaly charged)during the cycle when T_{c1} is triggered. Propagation of this charge takes place through the compressor in the conventional way, resulting in C_1 being discharged and the inductors all retained at positive remanence. Thyristor T_{b2} is triggered next, recharging C_0 resonantly through inductor L_c from the source V_s. The charging current now flows in the same direction as the previous pulse current and, as a result of the relatively large charging pulse width, serves to push the four saturable inductors L_1 to L_4 (seen to be in series) past remanence, into

1 Static resetting implies constant magnetization of the core in the opposite direction to that brought about by the pulse, by means of a d.c. current in the main winding, or through a secondary winding. Dynamic resetting is carried out by pulsing the core in the opposite direction through external means or intrinsically by the normal operation of the circuit.

2 Group for Pulse and Laser Technology of the Rand Afrikaans University, Johannesburg, South Africa.

positive saturation. Inductor L_r serves to provide a conducting path for the relatively long charging (resetting) pulse. As in the case of the unipolar configuration, the de-queing thyristor T_a is triggered to terminate the charging cycle when capacitor C_0 has reached a predetermined voltage.

When transfer thyristor T_{c2} is triggered, charge is again transferred to C_1, but this time with negative polarity. This negative pulse again propagates through the compressor in the normal way. Hold-off is maximized in each inductor, as each successive pulse is of opposite polarity and each pulse finds the inductors in their maximum reset condition.

Aside from the advantages mentioned above, bipolar compression, utilized by means of the configuration shown in fig. 2, offers another valuable feature. Two transfer thyristors now switch the power previously handled by a single one. With peak repetitive current capability of thyristors being one of the major constrains in the design of low- initial pulse width, high power thyristor pulsers, this feature lifts the average power ceiling attainable in their designs.

Non-linear interstage capacitors

The voltage charging profiles of recipient capacitors in series resonant loops, employing non-linear capacitors (in which capacitance reduces with increasing voltage) require lower hold-off of the inductors in successive loops than in the case of linear capacitors. Fig. 3 compares two voltage charging profiles. V_{cl} represents the co-sinusoidal secondary capacitor charging voltage curve in a series resonant loop with linear capacitors [4]. The curve V_{cnl} depicts the charging voltage waveform in the same loop, but with capacitors in which the capacitance decreases by 80% when fully charged. The waveform is no longer co-sinusoidal and it is evident that the hold-off $\int v dt$, represented by the area under the curve, is reduced in comparison.

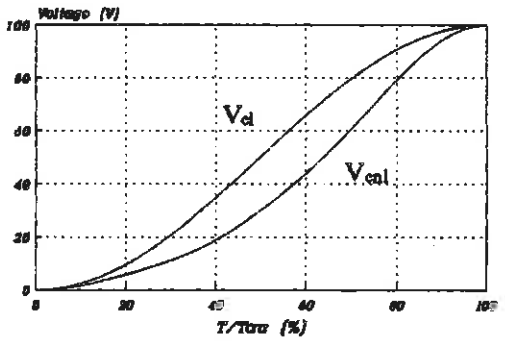

Figure 3. Comparison between the voltage charging profiles for linear (V_{cl}) and non-linear (V_{cnl}) capacitors

The main advantage offered by non-linear interstage capacitors in a series compressor configuration, is a reduction in required magnetic core volume, by virtue of a reduction in the hold-off requirement of the inductors. As the cost of magnetics feature high in economic compressor design, any saving in this respect is well worth considering. When used in the final stage of a series compressor, non-linear peaking capacitors offer faster equivalent voltage risetimes, further reducing the required overall compression factor.

Presently the dielectric with the highest degree of non-linearity, used in our research has been that clasified as a Z5W type 2 by the EIA. The non-linear dependency of capacitance on voltage, for this type of capacitor, as determined in the laboratory, is shown in fig.4.

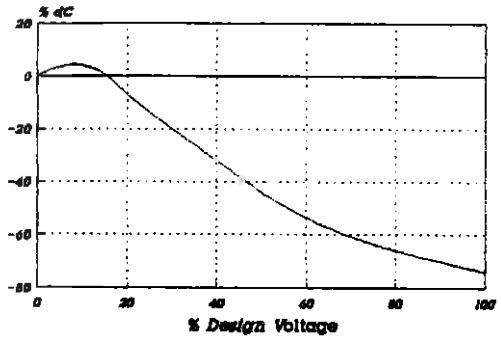

Figure 4. Change in capacitance vs DV voltage of a non-linear capacitor.

Conventional high voltage ceramic capacitors, when used in the non-linear regimes are expected to have a dramatically reduced life expectancy, since in order to achieve sufficient non-linearity with barium titanate ceramics, dielectric stresses well beyond those presently employed, will have to be accomodated. Life expectancy under these conditions can only be guessed at at this stage. As there are presently no commercial high voltage non-linear capacitors available, additional research and development is indicated in this field, before configurations employing non-linear capacitors, such as those envisaged here, can be constructed.

Additional problems, associated with non-linear capacitors when used in the present context, among others, are their high degree of temperature dependency. Typical variations in capacitance of as high as 1.16% per degree C is shown to occur in the above mentioned dielectric [5]. Such variation can have unpredictable consequences in compressor operation, and correct matching of interstage capacitors under varying operating conditions, will be difficult to achieve. Correct matching, however, is essential for complete energy transfer between stages in multistage compressors and failure in achieving it, results in unacceptable pulse jitter.

As the operation of non-linear capacitors does not lend itself to analytical analysis, the bulk of investigation,

testing and design of compressor configurations, is dependent on numerical integration. Suitable analytical techniques are still presently being sought to assist in this work. New designs and investigations are presently carried out by means of an iterative numerical integration method, in which configurations are simulated in terms of one, or more variables, to furnish behavioral data which are matched against the other required parameters of the system.

In order to compare the saving in magnetic volume, brought about by employing non-linear capacitors, non-linear simulation of a single pulse compression loop was carried out in accordance with previously developed methods [6]. Capacitance to voltage dependence was furnished to the program in look-up tables. Data were derived from suppliers, as well as from experimental verification in the laboratory. The parameters of one such simulation is compared in table 1 with the analytical parameters of an equivalent system using only linear capacitors. In this excercise, the basis of comparison is the required volume of magnetic core material, to achieve identical compression with other identical parameters, such as pulse time, pulse voltage and pulse energy.

As shown in table 1, the saving in core volume from 8.76 cm^3 in the case of the 'linear' compressor to 7.88 cm^3 in the case of the 'non-linear' compressor, represents a magnetic saving of 10%. The simulation was carried out with non-linear capacitors which had a reduction in capacitance at full voltage of only 70%. As much as 90% of capacitance change has been measured experimentally. This indicates that even greater potential savings should be possible

Table 1

Comparison of magnetic material requirements when employing linear and non-linear capacitors. Components adjusted for identical Pulse Energy, Pulse Voltage and Pulse Time.

	Non-Linear	Linear	Units
Pulse Time	1.85	1.85	μs
Pulse Energy	0.94	0.94	J
Compression Ratio	2	2	
Voltage	2000	2000	V
Initial Capacitance	1.0	.047	μF
Saturated Inductance	1.0	1.47	μH
Hold-off loop n+1	1.46	1.85	mV.s
Hold-off loop n	2.91	3.70	mV.s
Flux Excursion	2	2	T
Number of turns	21	24	
Internal Diameter	2.3	2.3	cm
External Diameter	4.3	4.3	cm
Effective Length	1.02	1.02	cm
Toroid Height	1.90	2.11	cm
Effective Area	6.93	7.71	cm^2
Effective Volume	7.88	8.76	cm^3

Experimental Results

A scaled down experimental compressor, utilizing the configuration of fig. 2, was used to test the theoretical assertions made above. The same inductors were used throughout, but comparative tests were carried out by operating the compressor in unipolar as well as in bipolar mode, with linear, as well as with non-linear capacitors.

Temperature tests confirmed that the amount of heat generated in operating the system at double the repetition rate during bipolar operation, was commensurate with that generated at half the repetition rate during unipolar operation. The anticipated increased hold-off, however, was not realized, possibly because of discontinuity in exitation of the cores. As previously stated, it was anticipated that by holding an inductor core in negative saturation, a greater flux excursion (and hold-off) could be achieved, than by merely holding it at negative remanence. Continuity in exicatation could only be achieved by increasing the fequency, or by extending the pulse width.

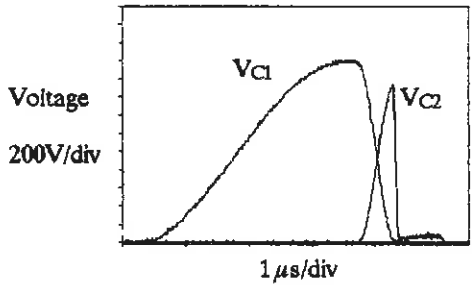

Figure 5. Positive pulse during bipolar operation with linear capacitors.

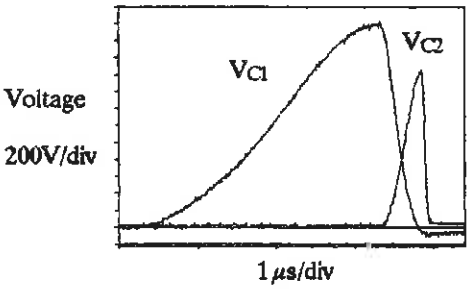

Figure 6. Positive pulse during bipolar operation with non-linear capacitors.

The oscillogram of fig's. 5 and 6 respectively show voltage waveforms across capacitors C_1 and C_2 (refer fig. 2), for the linear and non-linear configurations. Scrutiny of the waveforms indicates an increase in the peak pulse voltage, especially that of C_1. This higher pulse voltage was achieved with identical synchronization to that of the linear case. Calculations, however, indicate an increase in the pulse energy. Calculations, based on these

waveforms, indicate a potentional saving of 5% in magnetic volume. This potentional saving has, however, not been verified experimentally yet, as it involves a complete and accurate redesign of the whole compressor.

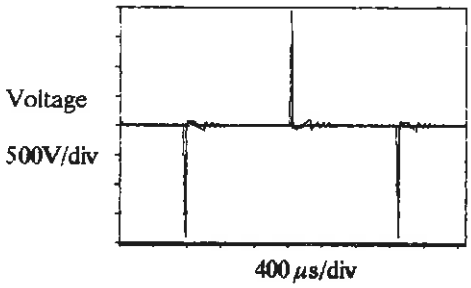

Figure 7. Voltage across capacitor C_1 (Fig. 2) during bipolar operation.

Fig. 7 presents an oscillogram of the C_1 voltage (refer fig. 2) which shows that, in spite of oscillations due to incorrect capacitor matching, the peak attainable hold-off has not deteriorated. This seems to indicate that the inevitable incorrect capacitor matching of temperature dependant non-linear capacitors can be effectively overcome.

Future Developments

The following developments are presently being considered :

(1) Development of analytical methods, by means of which non-linear capacitor operation can be investigated in pulse compression.

(2) Development and testing of high voltage non-linear capacitors that will furnish extended life expectancy in pulse compressor operation.

(3) Implementation of bipolar compression in the full scale pulsers presently operated by PULSTEK.

References

[1] W. S. Melville, The use of saturable reactors as Discharge Devices for Pulse Generators, Proc. Institute for Electrical Engineers (IEE London), 1951 Vol. 98, pt.3.

[2] H. M. von Bergmann, P. H. Swart, High repetition rate excimer and CO_2 TEA lasers, Proc. of the International Conference on Lasers '89, New Orleans, Dec. 3-8 1989.

[3] G. L. Bredenkamp, P. H. Swart, H. M. von Bergmann, A Resonant Power Supply with Pulse-Energy Regulation, Proceedings of the 6-th IEEE Pulse Power Conference, Arlington, Virginia, June 29 - July 1, 1987.

[4] P. H. Swart, G. L. Bredenkamp, H. M. von Bergmann, Computer Spreadsheet Design, Numerical Simulation and Practical Evaluation of a Lossy Series Pulse Compressor, Proceedings of the 6-th IEEE Pulse Power Conference, Arlington, Virginia, June 29 - July 1, 1987.

[5] Beck Electronics Ltd., Single Layer Ceramic Capacitors and assemblies, Brochure, August 1986.

[6] P. H. Swart, G. L. Bredenkamp, M. A. Oberholzer, Digital Simulation of General Non-linear Systems, Proceedings of the 12-th South African Symposium on Numerical Mathematics, Umhlanga Rocks, South Africa.

'N GESTANDAARDISEERDE HEKSTUURBAAN VIR DIE BIPOLÊRE ISOLEER-HEKTRANSISTOR (BIHT)

E.P. Wilke, P.C. Theron, J.D. van Wyk, J.A. Ferreira, J.J. Schoeman
Laboratorium vir Energie, Fakulteit Ingenieurswese, Randse Afrikaanse Universiteit, Johannesburg

1 INLEIDING

Onlangs is 'n nuwe skakelelement ontwikkel met die doel om die komplementerende eienskappe van die bipolêre transistor en die MOHVET ("MOSFET") te kombineer. Hierdie komponent is ontwerp om die hoë aan-toestand verliese van die MOHVET te oorkom terwyl die hekstuurbaan so eenvoudig as moontlik gehou word. Die komponent se inset is spanningsbeheerd, soos 'n MOHVET, terwyl die uitsetstroom se eienskappe dieselfde is as vir 'n bipolêre transistor. Hieruit spruit die naam bipolêre isoleerhektransistor of BIHT ("IGBT" in Engels). Die komponent staan ook bekend as 'n IGT, MOSIGT, COMFET (conductivity modulated FET), GEMFET (gain modulated FET) en IGR (insulated gate rectifier).

Die *i-v* karakteristieke van 'n BIHT in die voorwaartse rigting vertoon kwantitatief soortgelyk aan die van 'n bipolêre transistor behalwe vir die feit dat die beherende parameter 'n inset spanning nl. hek-bron spanning is in plaas van 'n inset stroom. Die i_d- v_{GS} kurwe van 'n BIHT is identies aan die van 'n drywings MOHVET. Die kurwe is redelik lineêr oor die grootste gebied van die kollektorstroom. Die kurwe word nie-lineêr slegs by lae kollektorstrome waar die hek-emitter spanning die drempelspanning bereik. As die hekspanning minder as die drempelspanning is, is die BIHT in die af-toestand. Die maksimum hekspanning wat aangelê mag word, word gewoonlik beperk deur die maksimum kollektorstroom wat toegelaat mag word in die BIHT.

Die BIHT bied heelwat voordele bo 'n bipolêre transistor en 'n MOHVET in medium drywing (10-100kW) en medium frekwensie (tot 50 kHz) drywingsomsetters. Om hierdie skakelaars te bedryf moet daar dus gelet word op die werking en skakeleienskappe, onder normale en kortsluittoestande, van hierdie element.

2 SKAKELKARAKTERISTIEKE

Die spanning en stroom golfvorms tydens aanskakeling van die BIHT stem baie ooreen met dié van 'n MOHVET. Hierdie gedrag is verwag aangesien die BIHT hoofsaaklik soos 'n MOHVET optree oor die grootste deel van die aanskakel interval.

Die spanning- en stroomgolfvorms tydens die afskakeling van die BIHT word getoon in fig.1. Die aangeduide volgorde van eers 'n styging in die kollektor-emitterspanning

na sy blokkeer toestandswaarde voor enige vermindering in die kollektorstroom is identies met wat gebeur met alle skakelelemente wat in verlagingsmutators gebruik word. Die aanvangstydintervalle, $t_{d(af)}$ en t_{rv} word gereël deur die MOHVET gedeelte van die BIHT.

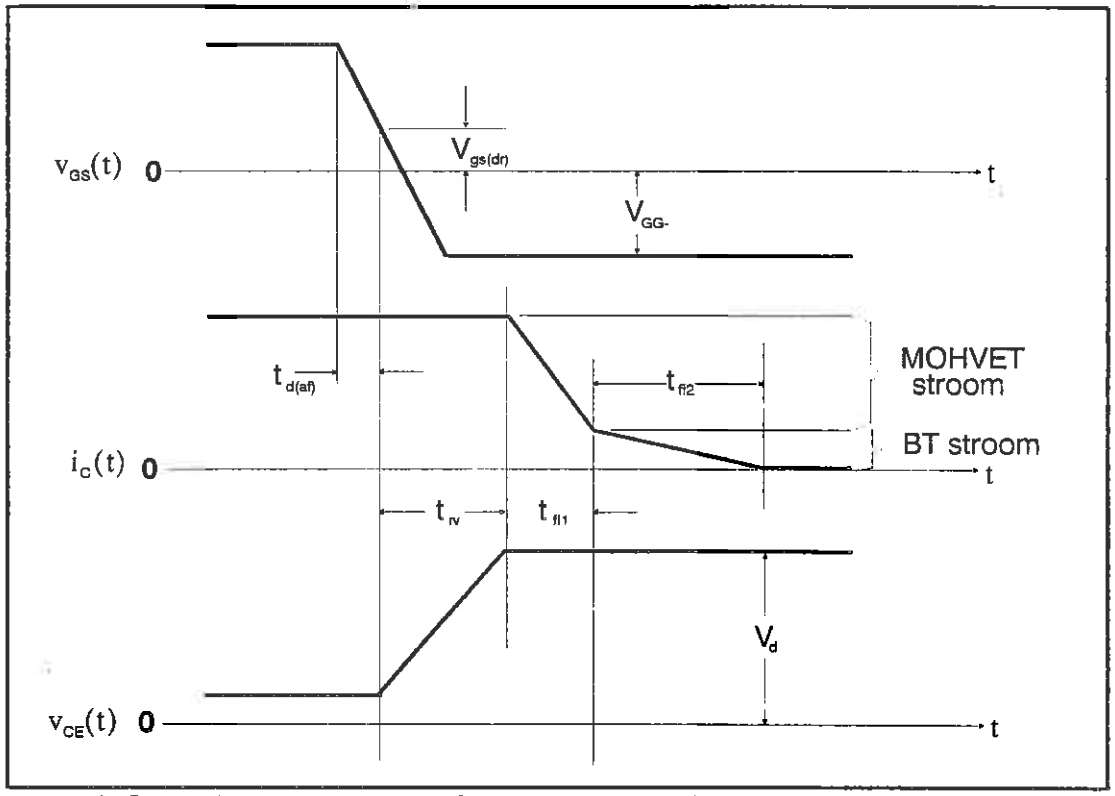

figuur 1 Spanning- en stroomgolfvorms van 'n BIHT tydens afskakeling

Die grootste verskil tussen die afskakeling van die BIHT en die van die drywings-MOHVET kan waargeneem word in die putstroom golfvorm waar daar tussen twee duidelike tydintervalle onderskei kan word. Die vinnige val wat plaasvind gedurende die t_{fi1} interval korrespondeer met die afskakeling van die MOHVET gedeelte van die BIHT. Die stroomstert wat waargeneem kan word tydens die t_{fi2} interval is as gevolg van die gestoorde lading in die n^- epitaksiale gebied. Aangesien die MOHVET gedeelte afgeskakel is en daar geen truspanning oor die BIHT aangelê word wat 'n negatiewe putstroom kan genereer nie, is dit nie moontlik om die gestoorde lading te verwyder deur middel van draer verplasing nie.

3. VOORSTELLE VIR HEKSTUURBANE

In hoë drywingstoepassings word die skakelelemente of aktiewe komponente ideaal slegs as skakelaars gebruik. Dus word bedryf van die skakelelemente in die lineêre gebied vermy deurdat dit slegs hoër verliese veroorsaak. Die primêre funksie van die hekstuurbaan is dus om die BIHT aan of af te skakel en in die verlangde toestand te hou.

Om die invloed van die millerkapasitansie te onderdruk is dit nodig om die hek van die BIHT negatief te trek tydens die afgeskakelde toestand. Daarom is 'n hekstuurbaan nodig wat , na gelang van die insetsein, die hek van die BIHT oplaai na +15V tydens die aantoestand, en ontlaai na -15V tydens die aftoestand. Hierdie hekspanning is t.o.v. die emitter van die BIHT. Om die skakelverliese te minimiseer is dit verder nodig dat elke aan- of afskakeling baie vinnig geskied. Daarom moet die uitsetimpedansie van die stuurbaan so laag as moontlik wees [4].

'n Verdere noodsaaklikheid van 'n hoëdrywing BIHT fase-arm is die galvaniese isolasie van die hekstuurbaan. Vir die spanningsvoeding word dus 'n swewende spanningsbron met ingeboude elektrostatiese skerm aangewend. Alhoewel veseloptiesekabel heelwat duurder is as beide 'n pulstransformator en 'n opto-isolator, word dit wel aangewend vir die volgende redes:
1. Die parasitiese kapasitansie tussen die sender en ontvanger word ten volle geëlimineer.
2. Deurbraakspanning is 'n funksie van die lengte van die kabel.
Hieruit volg dus dat dv/dt asook deurbraakspanning oorwegings uitgesluit word [4]. Verder is die gestuurde seine immuun teen elektromagnetiese steurings deurdat slegs die polarisasie van die ligsein beïnvloed kan word [1].

Verskeie topologieë is moontlik om die verlangde skakeling te bewerkstellig [4,p39], [2], [3], maar omdat die hekstuurbaan toepassing sal vind in die hoë drywingsgebied, is dit nodig om die mees stabiele en betroubare topologie uit te sonder.

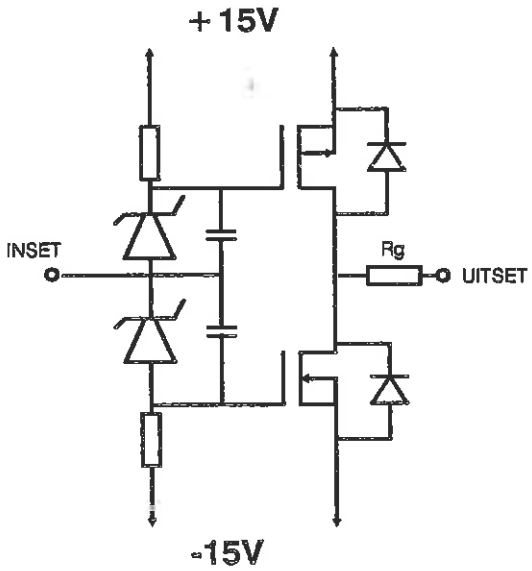

figuur 2 Hekstuurbaan

Figuur 2 toon die uitsetstadium van die hekstuurbaan . MOHVET M1 en M2 word om die beurt geskakel, na gelang van die inset wat of +15V of -15V is, en dus funksioneer die uitsetstadium as 'n omkeerder met 'n spanningswins van een. Indien albei MOHVET'e gelyktydig aanskakel sal deurgeleiding plaasvind wat die bron kortsluit. Om deurgeleiding te voorkom moet genoegsame dooietyd ingebou word. Dit is waar albei

MOHVET'e gelyktydig afgeskakel is. Hierdie eienskap word bewerkstellig deur die gebruikmaking van die twee zenerdiodes. Tydens skakeling van die inset sal albei MOHVET'e ten volle afgeskakel wees terwyl die inset tussen -4V en +4V is. Hierdie "dooietydgebied" van 8V, asook die feit dat albei MOHVET'e nie gelyktydig aangeskakel kan wees nie, word dus verkry.

Albei die kapasitore word aangewend om die skakeling vinniger te laat geskied. Die weerstande is nodig om die zenerdiodes in die aktiewe gebied te hou en om albei MOHVET'e afgeskakel te hou tydens die geval waar 'n inset totaal afwesig is.

Hierdie uitsetstadium verskaf die verlangde skakeltye wat, indien nodig, aangepas kan word deur die verandering van Rg waar 'n ander dv/dt verlang word. Omdat die aanweerstand van die MOHVET'e laag is, word die verlangde lae uitsetimpedansie verkry. Die maksimum skakelfrekwensie wat bereik kan word is >1 MHz, en daar is geen beperking op die minimum skakelfrekwensie nie.

4. KORTSLUITGEDRAG

Die gedrag van die BIHT tydens kortsluiting is met behulp van twee verskillende metodes ondersoek. Die doel van hierdie toetse is om te bepaal watter tipe beskerming in die hekstuurbaan ingebou moet word indien die BIHT aan 'n kortsluiting onderwerp sou word. Eerstens word 'n spanning oor die kollektor-emitter van die BIHT aangelê sonder 'n las. 'n Vinnige vryloopdiode word ook oor die BIHT geplaas. Die BIHT word gestuur deur 'n vinnige hekpuls wat die BIHT vir ongeveer 5us aangeskakel hou met 'n herhalingsfrekwensie van 2 kHz.

Die maksimum stroompiek wat verkry is vir 'n 30A/600V BIHT was om en by 45A met 'n bronspanning van 220V. Dit het egter na vore gekom dat die spanningsval oor die BIHT baie min verander tydens skakeling. Die BIHT het dus na regte oombliklike drywingsverliese van ongeveer 5kW vir 5us gehad. Indien die BIHT vir 'n lang tydperk aan hierdie toets onderwerp was, het die BIHT uitgebrand as gevolg van te hoë bedryfstemperature.

Die tweede toetsmetode maak gebruik van 'n oorstroombeskermingsbaan (m.b.v. 'n tiristor). Tydens hierdie metode word die BIHT by die hek aangeskakel en styg die stroom deur die BIHT totdat die tiristor wat in parallel met die BIHT geplaas is aanskakel en die kortsluitstroom deur die BIHT verwyder en in hierdie toestand bly totdat 'n sekering smelt.

Die resultate van hierdie toets word voorgestel in fig.3. Die kollektorstroom styg tot 100A binne 2us. Hierna skakel die tiristor aan en neem I_C af. Piekstrome van meer as 120A is met behulp van hierdie toets verkry vir dieselfde BIHT wat in die eerste toets gebruik is. Dit is dus duidelik dat BIHT'e redelik bestand is teen hoë kortsluitstrome vir kort tydperke. Kortsluitbeveiliging is egter in die stuurbaan ingebou wat die BIHT binne 5us kan afskakel indien 'n fouttoestand sou voorkom. In die volgende paragraaf word die beveiliging wat toegepas is meer volledig bespreek.

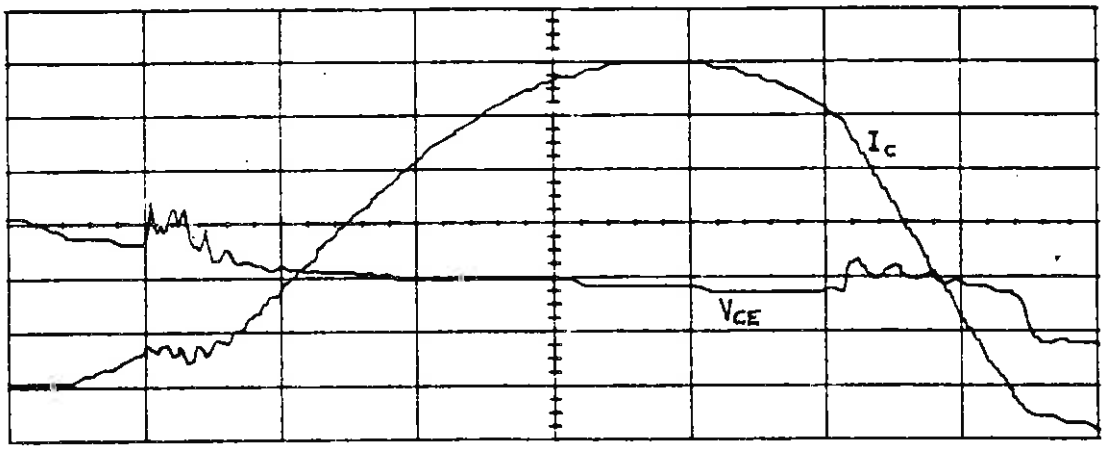

figuur 3 I_C en V_{CE} tydens kortsluiting
Tydskaal : 500 ns/div
Stroomskaal (I_C) :17 A/div
Spanningskaal (V_{CE}) : 50 V/div

5. BEVEILIGINGSBANE.

Die beveiligingsbane het ten doel om die BIHT'te te beskerm teen vernietiging sodra 'n fouttoestand voorkom.

Omdat 'n beveiligingsbaan of beskermingsnetwerk 'n onvermydelike komponent van enige hekstuurbaan in hoë drywingstoepassings is, was daar gepoog om dit te integreer in die stuurbaan om sodoende die minimum aantal komponente te verkry asook om die effektiwiteit van die beskerming optimaal te verhoog.

Terwyl die BIHT aangeskakel is, monitor die beveiligingsbaan die aanspanning. Sodra die aanspanning van die BIHT dan hoër as 'n sekere voorafbepaalde waarde is, word die toestand van die wipbaan verander wat die BIHT onmiddelik afskakel en afgeskakel hou, ongeag die inset na die stuurbaan.

Omdat 'n sekere tydsduur verloop vandat die fouttoestand waargeneem word totdat die BIHT afgeskakel word, is dit nodig om die di/dt te beperk. Dus is dit nodig dat 'n sekere minimum verspreide induktansie tussen die afvlakkapasitore en die skakelelemente teenwoordig is.

Vervolgens word die volledige hekstuurbaan met geïntegreerde beveiligingsbaan getoon in figuur 4.

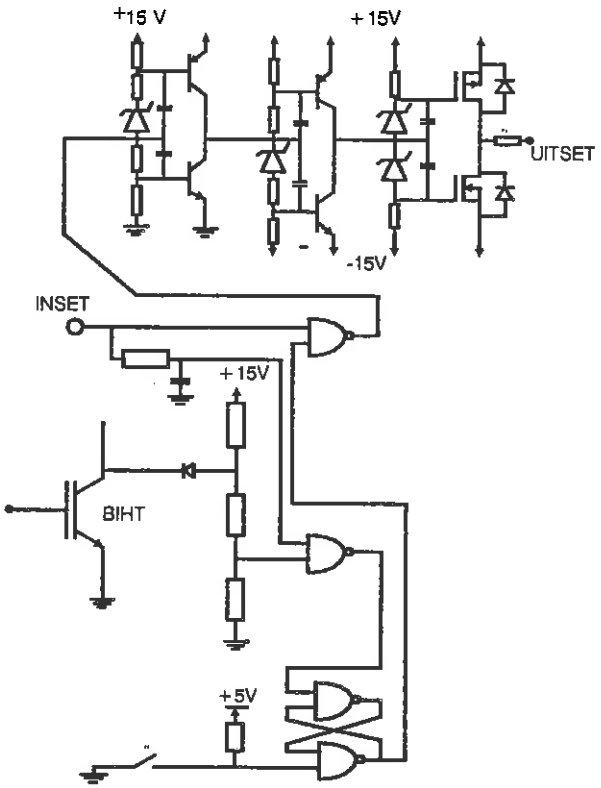

Figuur 4 Hekstuurbaan met geïntegreerde beveiligingsnetwerk.

6 AFSKERMING EN ISOLASIE

As gevolg van die vinnige skakeltye en hoë frekwensies wat voorkom tydens die beheer van die BIHT is dit noodsaaklik dat alle aardlusse so kort as moontlik gehou word. Sodoende sal steurseine tot 'n minimum beperk word. 'n Beter metode om hierdie probleem op te los is om die verskillende kragbronne te isoleer van mekaar. Onderlinge aardlusse sal dus op hierdie manier uitgeskakel word. Albei stuurbane per fase-arm sal dus geïsoleerd van mekaar wees. 'n Voorstelling van 'n enkele geïsoleerde kragbron kom voor in fig.5.

'n Gewone blokgolfgenerator (4047) word gebruik om die 200 kHz sein te genereer wat MOHVET'e T1 en T2 om die beurt skakel. As gevolg van die hoë skakelfrekwensie word slegs 'n klein hoë frekwensie transformatorkern benodig. Die voordeel van hierdie topologie is dat slegs een kragbron gebruik word om twee kragbronne (+15 en -15V) te genereer. D1 tot D4 is hoë spoed MUR1100 diodes. Daar moet wel groot aandag geskenk word aan die afskerming van die transformator aangesien die spannings by hoë waardes kan sweef wat kan veroorsaak dat daar spanningsdeurbraak in die transformator kan plaasvind. Die uitset van die gelykrigterbrug word na 7815 en 7915 spanningsreguleerders gestuur en met die kapasitore afgevlak.

'n Groot probleem is ondervind met afskerming. As gevolg van die hoë skakelfrekwensie van bostaande stroombaan kan ruis maklik deur onafgeskermde verbindings opgetel word. Hierdie probleem kan veral voorkom by baie vinnige vergelykers vir

gebruik in veseloptika. Hierdie probleem is opgelos deur al die verbindingsdrade in die stelsel af te skerm en deur afvlakkapasitore direk op die bronne van die beheer- en stuurbane te plaas. Daar moet egter daarop gelet word dat 'n sekere stelsel wel goed afgeskerm kan word om steurseine te beperk maar daar moet in gedagte gehou word dat so 'n stelsel moonlik naby 'n ander stelsel gebruik moet word wat nie teen hierdie tipe steurings beskerm is nie en moet daar moontlik na 'n ander alternatief gekyk word vir die isolering van die kragbronne. 'n Voorstel is die gebruik van gewone 220V/50Hz afgeskermde transformators.

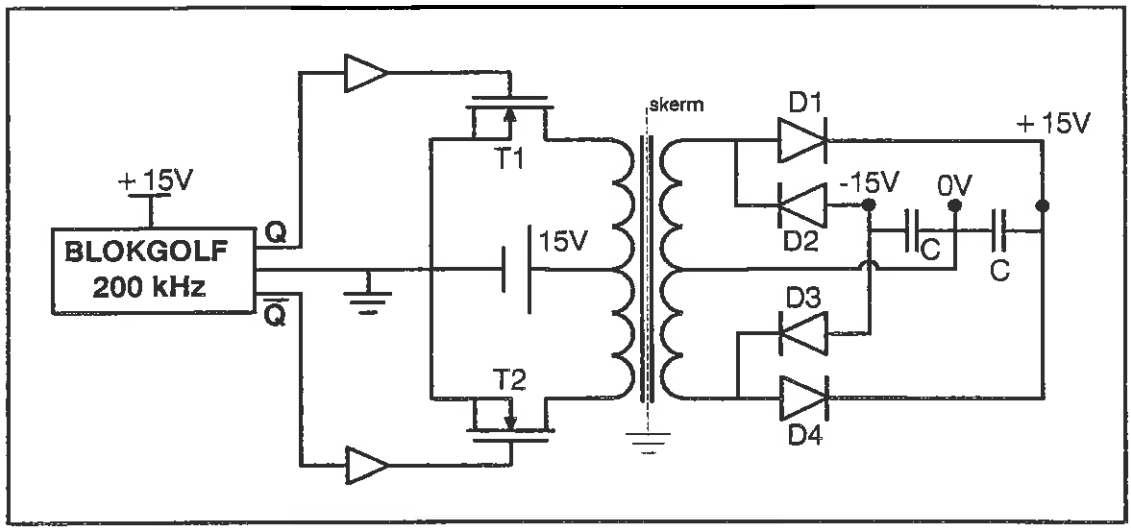

figuur. 5 Geïsoleerde kragbron

VERWYSINGS

1. DAWSON F P.
IPEC-90 Protection of High Power IGBT and Mosfet gate drivers against line disturbances.
pp775-782.

2 International Rectifier.
High Voltage MOS Gate driver.
Data sheet No. PD-6.011B.

3. MOHAN N, UNDELAND T M, ROBBINS W P.
POWER ELECTRONICS: Converters, Applications and Design.
Hfst. 21 en 24.

4. PEMC'90
IGBT-Modules in Inverters: Concepts, Gate drive, Fault protection. pp35-41

5 HEFNER, A R; BLACKBURN,D L.
An analytical model for the steady-state and transient characteristics of the power insulated-gate bipolar transistor.
SOLID-STATE ELECTRONICS, Vol.31 No.10 01/10/1988 p.1513-1532.

Reluktansiemeter om Touspannings te Bepaal.

C.H. van As

OPSOMMING

´n Elektroniese instrumentasie stelstel bestaan uit ´n aantal komponente wat gesamentlik gebruik word om ´n meting te doen. Die instrumentasie stelsel bestaan uit basies drie hoof elemente: die insettoestel, prosesseringsgedeelte en dan die uitsettoestel. Tydens ´n meting lewer die insettoestel ´n elektriese sein wat proporsioneel is aan die meganiese verandering waaraan dit onderhewig was aan die prosesseringsgedeelte. Hier word die sein verwerk tot ´n meer aanvaarbare formaat vir die uitset.
Die insette vir meeste instrumentasie stelsels is gewoontlik nie elektries van aard. Om elektriese metodes en tegnieke vir metings te bebruik moet die nie-elektriese grootheid omgesit word in ´n elektriese sein deur ´n toestel wat ´n omsetter genoem word. Per definisie kan ´n omsetter voorgestel word as ´n toestel wat wanneer dit geaktiveer word deur energie in ´n stelsel dit energie in dieselfde of ´n ander vorm oordra tot ´n tweede stelsel. Die energieoordrag kan elektries, meganies, chemies, opties of termies van aard wees.

Om die regte omsetter te kies is die belangrikste stap wat geneem moet word om akkurate resultate te verkry.Die keuse van omsetter hang af van:

a) Wat is die fisiese grootheid wat gemeet moet word?
b) Watter omsetter tegniek kan die beste gebruik word om hierdie grootte te meet?
c) Watter akkuraatheid word benodig vir die meting?

Wanneer ´n mens te doen kry met ´n probleem waar trekkragte in ´n staalkabel gemeet moet word wat reeds onder spanning verkeer kan dit heelwat probleme veroorsaak. Die meeste meetinstrumente is van so aard dat die kabel gesny moet word om hulle te installeer. ´n Tipiese voorbeeld hiervan is weegbrûe. Voorbeelde van toepassingsmoontlikhede is:

a) Trekkragte in ankerkabels van bruê, torings ens.

b) Nie vernietiggende toetse.
c) Hystoestelle en nog vele meer.

"ABSTRACT"

Wanneer die trekkragte in ´n staalkabel bepaal moet word, moet daar in die meeste gevalle vernietigende toets gedoen word. Om dit te probeer verhoed is ons besig om ´n draagbare meetinstrument te ontwikkel wat die voordele sal hê dat;

1) Die meetinstrument opgestel en ´n meting gedoen kan word terwyl die kabel onder spanning verkeer.
2) Spanningsmetings kan gedoen word in verskillende soorte buigbare toue.

TEORETIESE BESKRYWING

Voorgestelde oplossing

Indien dit moontlik is om twee steunpunte onder die kabel te plaas terwyl daar ´n drukkrag tussen die punte uitgeoefen word waarvan die grootte bekend is, is dit moontlik om die trekkrag in die kabel te bepaal. Die drukkrag/trekkrag tussen die steunpunte kan op verkeie maniere verkry word hetsy meganies of elektries, maar dit moet op so ´n wyse gedoen word dat dit meetbaar is.

Indien die kabel tussen drie steunpunte vervorm word kan die trekkrag in die kabel gemeet word, indien die vervormingskrag aan ons bekend is.

Wiskundige model

Fig. 1 Skematiese voorstelling.

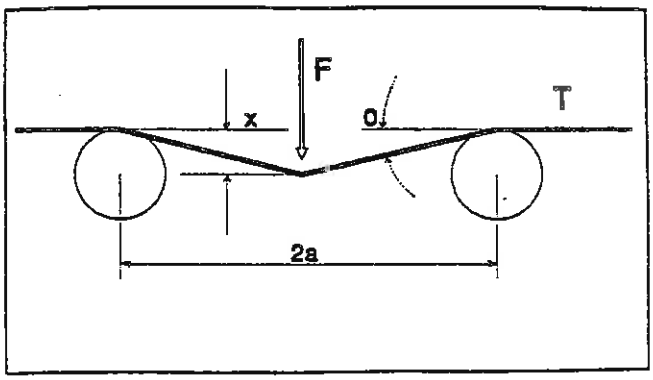

Die gevraagde parameter is T wat die trekkrag in die trou voorstel.
Om T te bereken uit die veranderlikes F en x kan die vlg benaderings gevolg word.

Tan θ = x/a
Maar indien θ klein is kan ons sê dat
$\theta \approx x/a$

Verontagsaam die wrywing oor die steunpunte, dus kan ons die verwantskap tussen F en T as volg benader.

Sin θ = F/T

Dus omdat θ klein is volg dat:

$\theta \approx x/a \approx F/T$

Hieruit kan gesien word dat x en F bepaal moet word om T te bereken.
Om die drukkrag tussen die steunpunte te verkry is 'n aktuator gebruik. Dit is dus moontlik om F te bereken. Beskou die onderstaande skets ter verduideliking van die afleidings.

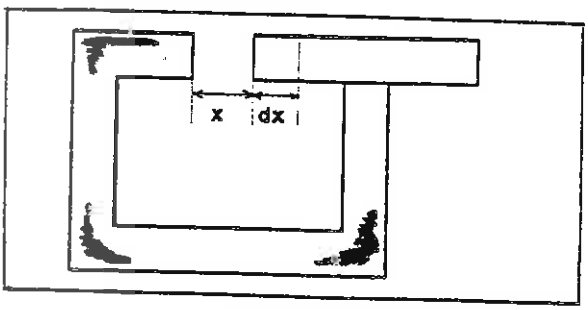

Werk gedoen = $F\delta x$
Die energie teenwoordig $\frac{1}{2}\Phi I = \frac{1}{2}LI^2$
As x vergroot met dx sal L verklein met 'n waarde dL (Induktansie is omgekeerd eweredig aan x)
Die energie $\delta WP_r = \frac{1}{2} I^2 dL$
Sodra x vergroot met 'n konstante NI sal die vloed (Φ) dus verlaag met $d\Phi$. Die vloedkoppelings sal dus verander. Die

verandering in spanning is so dat dit 'n stroomvloei sal veroorsaak wat dan die verandering in vloed sal teëwerk. Die magnetiese baan poog om energie terug te plaas in die bron.

$VIdt = I\,dL/dt = I^2dL$
I^2dL in die toevoerstelsel en
$\frac{1}{2}IdL/2$ is wat gelewer word.
Dus $Fdx = \frac{1}{2}I^2dL$
en $\lim F = \lim \frac{1}{2}I^2\,dL/dx$
$F = \frac{1}{2}I^2dLdx$
$= dW_F/dx$
$dW = \frac{1}{2}\,BHAdx$
$Fdx = \frac{1}{2}BHAdx$
$F = \frac{1}{2}BHA$
$= B^2A/2\mu_o$
In die eksperimentele opstelling is 'n E kern as aktuator gebruik.

Ontwerpsberekeninge

Fig. 2 Magnetieseringskurwe

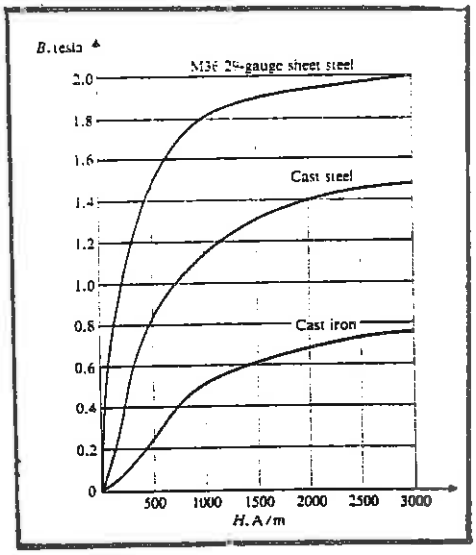

Fig. 3 Afmetings van E kern.

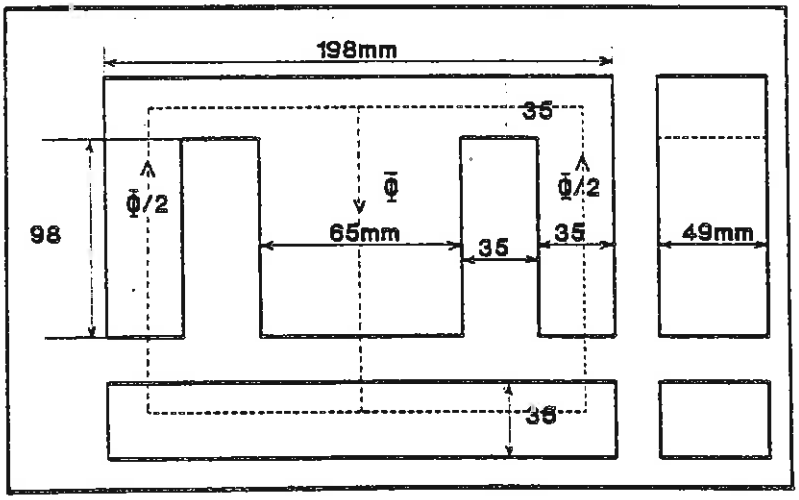

Beskou die aktuator in fig 3

Beide van die kern en sluitstuk is van M -36/M-19 transformator plaat gemaak.
Lekvloed en vervorming kan geignoreer word in die luggapings.
Die sluitstuk moet so bevestig word dat die lengte van die luggaping ´n maksimum grootte van 5 mm sal bereik.
´n Gelykstroom word deur die spoel gestuur sodat ´n vloeddigtheid van 1,2 T in die luggaping opgewek word.

Vloeddigtheid in die staal is
B_s = T/pakkingsfaktor
Lengte van die vloed pad is = l_s
Die MMK nodig in die staal is:
f = Hl
Die totale vloed in die magnetiese stelsel is:
Φ_T = BA
Die reluktansie van die luggapings in die magnetiese pad is:

$$R_g = \frac{l_g}{\mu_o A_g}$$

Die MMK nodig in die luggapings is

$$f_g = \Phi R_g$$

Die Totale MMK is
$f_T = f_s + f_g$
Deur die stroom (I) te kies is die aantal windings N:
f_T = NI
Dus kan F bereken word as al die gegewens bekend is
$F = B^2/2\mu_o$ N/m²
Die totale deursnee area van die luggapings is 2A
Met die sluitstuk in die posisie soos getoon is
die totale krag:
$F = 2AF_n$
Vir die opstelling soos getoon in fig .3 kan daar m.b.v. die bostaande afleidings die drukkrag F tussen die steunpunte bepaal word.

Fig 4 Omsetter.

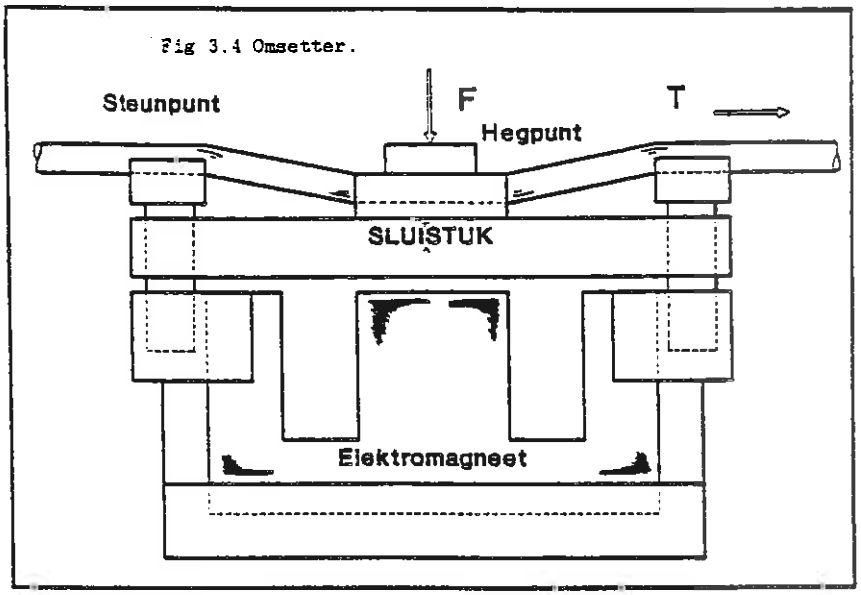

Om die trekkrag te bepaal het ons F en x nodig soos reeds al verduidelik is. Uit die wiskundige model het ons reeds gesien wat die verwantskap tussen F en x is. Indien x vergroot vir 'n gegewe T neem die hoek θ toe en dus moet F vergroot dit is dus nodig om x konstant te hou wat gedoen kan word deur die sluitstuk te beheer. Indien die luggaping tydens 'n toets gesluit word, is dit egter nie moontlik om m.b.v. die stroom in die spoel die krag (F) te bepaal nie. Om die sluitstuk te beheer is dit nodig om die posisie daarvan te bepaal. Dit kan gedoen word d.m.v. 'n lineêre verplasingsomsetter of om die reluktansie eienskappe van die magnetiesebaan te gebruik.

Fig.5 Blokdiagram van stelsel.

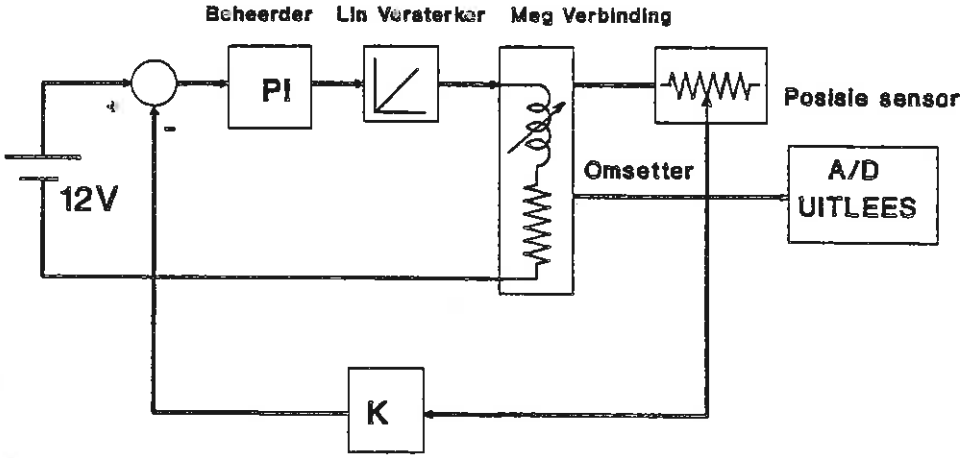

Fig.6 Stroombaan.

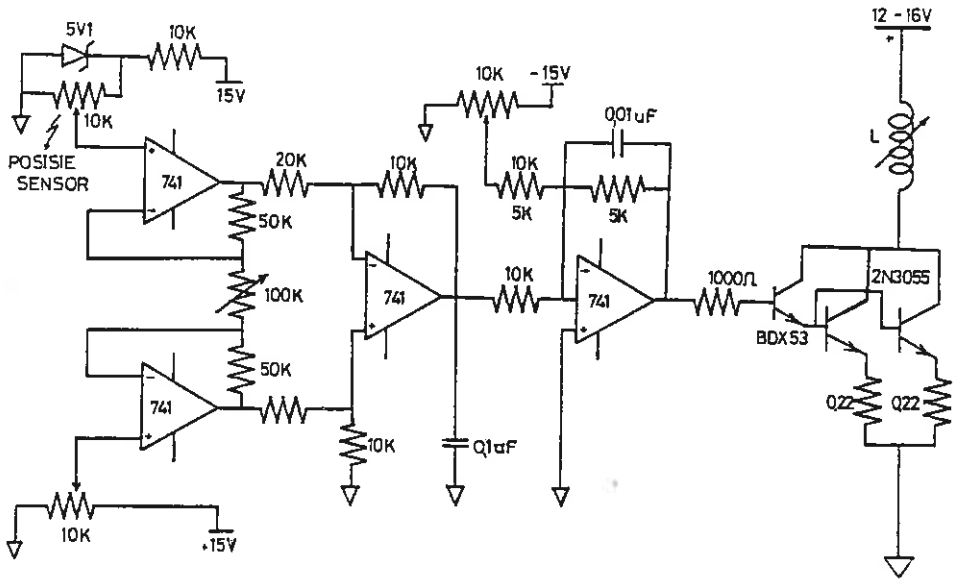

Indien die verlangde posisie met 'n spanning vergelyk word kan die sluitstuk beheer word deur hierdie spanning en die terugvoer spanning vanaf die posisie sensor met mekaar te vergelyk. Deur die twee spannings te sommeer kan die verskil wat as foutsein dien dan gebruik word om die versterker te stuur.

PRAKTIESE RESULTATE

Die verwantskap tussen F en I is nie lineêr. M.b.v. die terugvoerbaan word daar gepoog om die stelsel te lineêriseer.

EKSPERIMENTELE RESULTATE

Massa (kg)	Stroom (A)	Stroom (A)	Stroom (A)	Stroom (A)
200	2.6	2.32	2.51	2.48
301	2.81	2.83	2.8	2.77
400	3.42	3.4	3.34	3.31
500.6	3.61	3.64	3.67	3.6
600.1	3.9	3.86	3.95	3.91
700.7	4.19	4.15	4.2	4.1
836	4.44	4.45	4.4	4.38
946	4.81	4.78	4.65	4.73

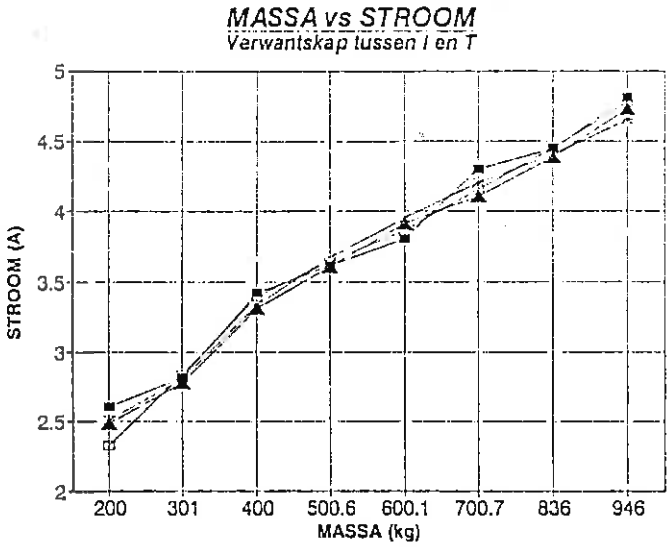

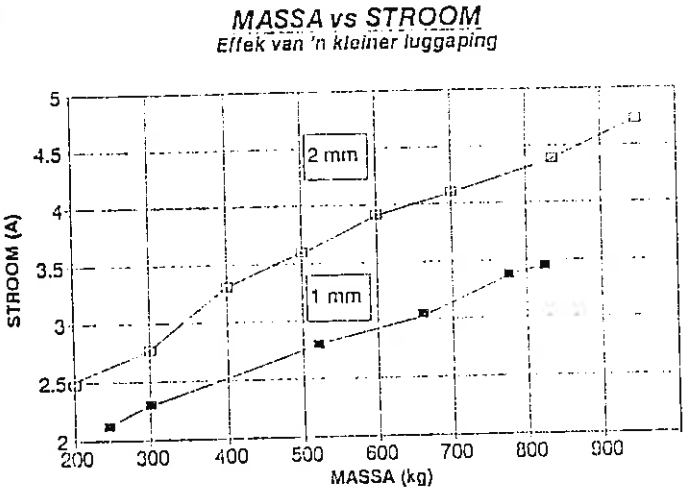

RESULTATE (I vs M met 1 en 2 mm luggapings)

Massa (kg)	Stroom (A) 1mm	Stroom (A) 2mm
200		2.48
245	2.12	
300	2.3	2.77
400		3.31
500.6		3.6
520	2.8	
600.1		3.91
660	3.05	
700.7		4.1
775	3.38	
824	3.45	
836		4.38
946		4.73

OPSOMMING

Die voordeel van 'n terugvoerstelsel is dat dit nie lineêre stelsels lineêriseer.

LITERATUURVERWYSINGS

Slemon G.R.en Straughen A. "Electric Machines" Addison-Wesley, 1982.

Cooper W.D, Helfrick A.D. "Electronic intrumentation and measurement techniques" Prentice-Hall 1985.

Bentley J.P. "Principles of measurement systems" New York 1989.

HAGGIE RAND "KABELS"

"Introduction to Transducers for Instrumentation" Statham Instruments, Inc., Los Angeles.